Introduction to Powder Storage and Flow

Carl Wassgren, Ph.D.

School of Mechanical Engineering

585 Purdue Mall

Purdue University

West Lafayette, IN 47907-2088

U.S.A.

wassgren@purdue.edu

For Alex and Ben

Contents

CHAPTER 1

Introduction

Welcome to this introduction to powder storage and flow! These notes are meant to introduce someone with little exposure to particulate systems to the main issues involved in powder storage and flow. These notes should be accessible to students with a junior-level university engineering background or above. Most chapters involve some content from calculus, ordinary differential equations, and mechanics of materials. However, these notes are not meant to be an advanced or comprehensive text on powder storage and flow. It's simply meant to be an introduction to help the next generation of engineers and scientists learn the basics. I encourage the reader to make use of the many references throughout the notes, especially the books by Nedderman [1] and Schulze [2], which I've used extensively to improve my own understanding of the topic. Lastly, these notes are a work-in-progress. I've provided them online as a freely-available PDF file and plan to update them frequently with corrections and additions. I'm open to constructive comments. If you wish to show your appreciation for these notes, then I encourage you to help the next generation by donating your time or money to your favorite educational institution.

This first chapter is focused on motivation for the topic. Most people have had little exposure to the study of particulate materials and I've found it helpful to compile statistics and background on the topic. The technical content of the notes starts in Chapter 2.

Two additional notes before getting started: (1) I've included hypertext links within these notes to reference web sites and videos. These links were active when the notes were prepared, but with the internet being ephemeral, unfortunately some of these links may not work for you. (2) In case you have an interest, I also have notes available for thermodynamics, fluid mechanics, and gas dynamics, entitled appropriately as Notes on Thermodynamics, Fluid Mechanics, and Gas Dynamics. I have supporting course-related web sites (Thermodynamics I and Introductory Fluid Mechanics) with lecture and example videos. Enjoy!

1.1. Why do we care about Particle Science, Engineering, and Technology (PSET)?

Particle Science, Engineering, and Technology is defined by the Particle Technology Forum as "...that branch of science and engineering dealing with the production, handling, modification, and use of a wide variety of particulate materials, both wet or dry, in sizes ranging from nanometers to centimeters. Its scope spans a range of industries to include chemical, petrochemical, agricultural, food, pharmaceuticals, mineral processing, advanced materials, energy, and the environment." Without a strong PSET background, the design and manufacture of many materials and products would not be economically viable or even possible (Figure 1.1).

To illustrate the importance of PSET, the following collection of miscellaneous statistics has been compiled:

- "Some 75% of chemical manufacturing processes involve small solid particles (fine particles) at some point." [3].
- Approximately one-half of the products and at least three-quarters of the raw materials in the chemical industry are in granular form [1].
- In 1992, DuPont found that 62% of its 3,000 products involved particulate materials [4].
- A minimum of 40% or $61B of the value added by the chemical industry is linked to particle technology (*Chemical Economics Handbook*, cited in [4]).
- Figure 1.2 plots the average start-up time of facilities processing fluids, i.e., gases and liquids, which was approximately five times shorter than the average start up time for facilities handling particulate

FIGURE 1.1. Photographs of various particle-based materials and products.
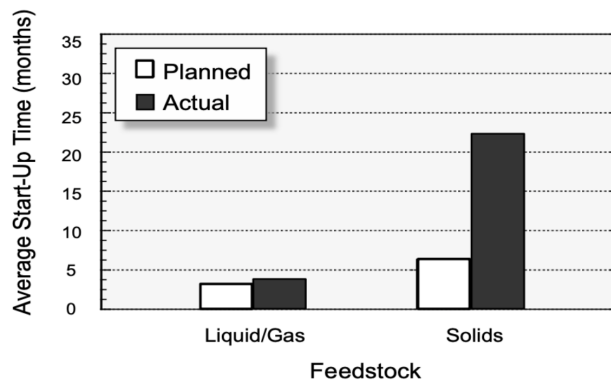
FIGURE 1.2. The planned and actual start-up times for facilities processing fluids and those processing particulate materials. Figure from [5].

materials, i.e., solids. Furthermore, the planned and actual start-up time for fluids facilities was nearly the same while the planned start-up time for particulate material processing facilities was much shorter than the actual start-up time. The large difference between planned and actual start-up times reflects the challenges in designing and operating particulate material unit operations.

- Figure 1.3 plots the year-end design performance of facilities handling fluids, refined solid feed material, i.e., particulate material that has been pre-processed, and raw solid feed material. Facilities handling fluids operated between 60% and 110% of their design rate, with 90% at the median performance level. In contrast, facilities processing refined solid materials ranged between 0% and
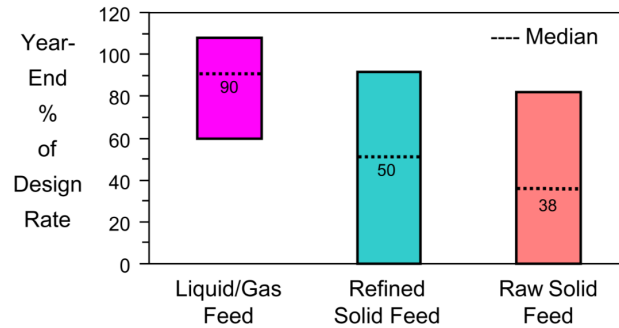
Figure 1.3. Influence of feed material on the performance of new facilities. Figure from [6].

90% of the design rate with a median performance of 50%. Facilities handling raw solid feeds performed even worse, with a range between 0% and 80% with a median of 38%.

- Grinding of particles consumes 1.3% of U.S. electrical power production, with more than 50% devoted to minerals (*National Materials Advisory Board Report*, cited in [4]).
- Approximately 50% of the world's energy resources come from granular materials, such as soils and rocks. [7].
- Sand and gravel account for 68% to 85% of all materials mined from the earth [8].
- Each year over 1,000 silos, bins, and hoppers fail in North America [9].
- In 2020, the world produced nearly 181 million metric tons of urea in particulate form, which is widely used in agricultural fertilizers [10].
- In North America and the Oceania region, approximately 500 million metric tons of cereal grains, which are in granular form, are lost during distribution, processing, and other stages of handling [11].
- In 2017, 1134 million tonnes of corn was produced globally. According to the U.S. Corn Harvest Quality Report, 8.8% of the corn kernels were chipped or had cracks, decreasing the useful grain yield. This damage was due in part to mechanical loads occurring during grain harvesting and handling [12].
- Approximately 50% of the world's energy resources are derived from granular systems such as soils, grains, and biomass [7].
- The pharmaceutical industry relies extensively on particulate materials, with approximately 90% of drug products consisting of solid dosage forms [13], meaning that they are produced from particulate materials.
- From a study of the pharmaceutical industry, "...two [economic] models effectively bound the range of potential future benefits from greater manufacturing efficiency and estimate that, for example, a 30% reduction in manufacturing costs will generate between $1.0 and $12.3 trillion in social value to the United States." [14].
- Approximately 30% of pharmaceutical materials are lost due to powder segregation, which is the unintentional de-mixing of powder components [15].

Clearly, there is incentive from a range of industries to improve our knowledge for how to design products and processes involving particulate materials.

1.2. Why do we need academic programs focused on PSET?

Most engineers and scientists have experience with fluids and solids, but not particulate materials. The lack of proper training can result in products and operations designed using improper assumptions for material behavior. As a result, significant trial and error and scale-up testing are required.

FIGURE 1.4. The IFPRI-compiled list of training topics, in order of decreasing priority. Powder flow is considered to be the most important topic across all audiences.

Unfortunately, few U.S. undergraduate academic programs focus on PSET topics. Other countries, such as Germany, England, Australia, and Japan, include aspects of PSET in their undergraduate engineering curricula. Although some U.S. universities now have graduate research programs in PSET, they are not widespread and courses supporting the fundamentals of PSET are still uncommon. Presumably, with improved PSET education, we can expect more effective and novel particle-based products and manufacturing methods.

1.3. What PSET topics are of most interest?

The International Fine Particle Research Institute (IFPRI), a consortium consisting of dozens of companies that process particulate materials, surveyed their members and found that powder flow is the most relevant PSET topic across all audiences (Figure 1.4). Hence, the focus of the remainder of these notes is on *powder storage and flow.*

1.4. What methods are used to predict powder flow behavior?

The most common method for predicting powder flow is to perform empirical testing. This approach generally involves performing a design of experiments study and fitting the resulting data. The results from these types of studies are usually not generalizable, i.e., they can only be used for the tested material in the tested system. However, if those conditions are satisfied, then the resulting empirical fits can provide rapid, accurate predictions as long as extrapolation is not required.

Analytical models demonstrate good understanding of the system physics and explicitly show how various parameters are related. In addition, calculations using analytical models are often quick to perform. However, usually analytical modeling requires significant simplifying assumptions regarding material behavior and operating conditions which can reduce the model's accuracy and generalizability.
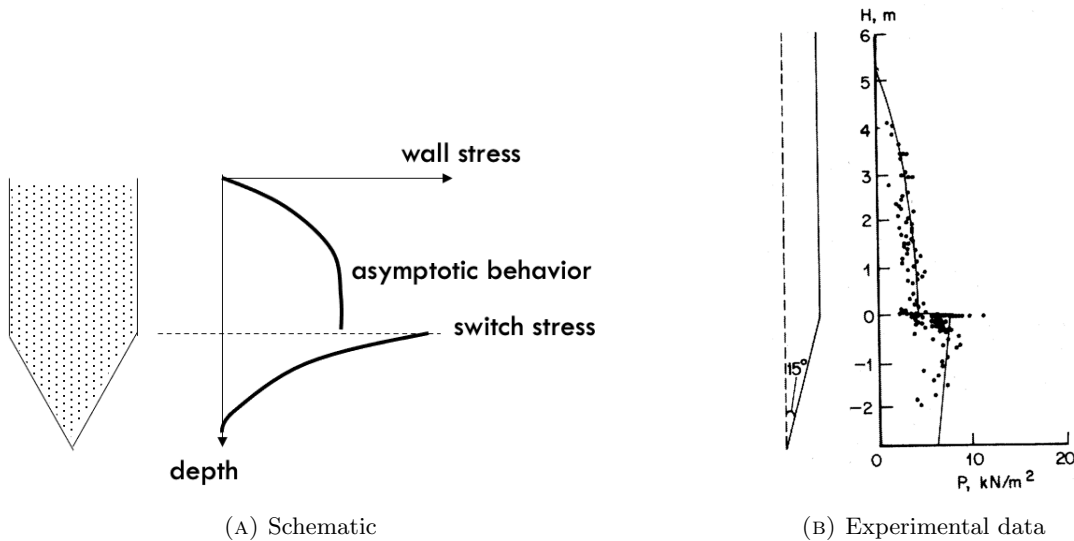
(A) Schematic

(B) Experimental data

Figure 1.5. Typical wall normal stress distributions in a hopper.

Computational modeling also demonstrates a good understanding of the system physics, but the relationship between parameters may not be as clear as in analytical models. Computational models also require simplifying material and system assumptions, but these assumptions are usually less restrictive than the ones required for analytical models. The downsides of computational models are that they can be time-consuming to perform and usually require some familiarity with numerical methods. The remainder of these notes focus on analytical models for powder storage and flow with some supporting empirical correlations.

1.5. Examples of Unusual Powder Behavior

Before presenting powder storage and flow models, it is helpful to introduce some of the unusual characteristics found with particulate materials. Several of these unusual behaviors are presented in this section.

When a particulate material discharges from a hopper (a device for temporarily storing particulate material, typically consisting of a converging section located below a vertical section; Figure 1.5), the normal stresses at the wall increase with depth in the vertical section, but approach an asymptotic value for a sufficiently deep bed of material. This behavior is quite different than what would occur for an incompressible liquid such as water where the stresses increase linearly with depth. At the transition between the vertical and converging sections, the wall stress increases abruptly, a phenomenon known as a *switch stress*. Again, this behavior is significantly different than what occurs for a liquid. Approaching the converging section apex, the wall stress decreases to zero.

Depending on the material and system characteristics, particulate materials discharging from a hopper can display several flow patterns. Two of these patterns are shown in Figure 1.6. If the walls are sufficiently steep, then mass flow occurs. In mass flow, all of the material is in motion, although the velocity profile is not necessarily uniform across a lateral section. In contrast, in funnel flow (aka core flow) stagnant regions of material exist adjacent to the wall and flow only occurs in an inner core region. Funnel flows occur when the hopper walls are too shallow. A nice video showing the two different flow patterns is available at https://youtu.be/qneDHMWeZ70. Mass flow is usually preferable to funnel flow since it offers many advantages, which is discussed further in Chapter 7.

Designing hoppers to produce mass flow is not as trivial as it may seem. L. ter Borg [16] performed a series of hopper discharge tests on 500 different particulate materials and tabulated the percentage of hoppers that produced mass flow for different hopper wall half angles (measured from the vertical; Figure 1.7). He found that a 45° angle hopper, a typical angle many people would guess for a reasonable design, had zero mass

(A) Mass flow.

(B) Funnel (aka core) flow.
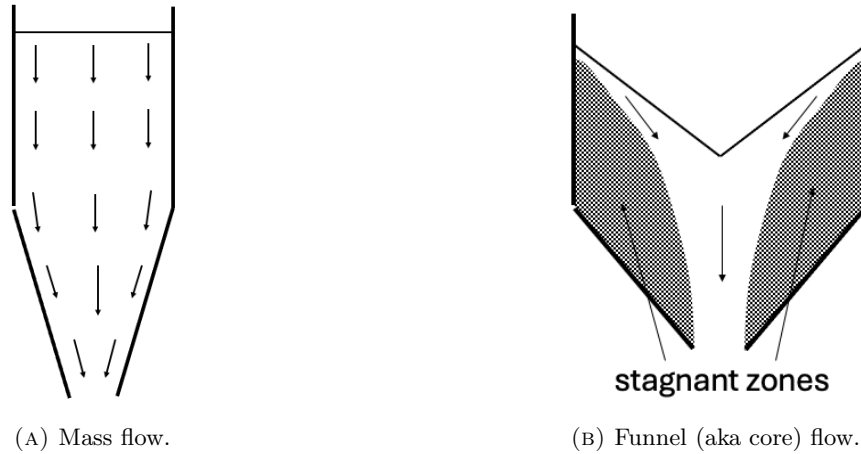
FIGURE 1.6. Two common flow patterns in a hopper.
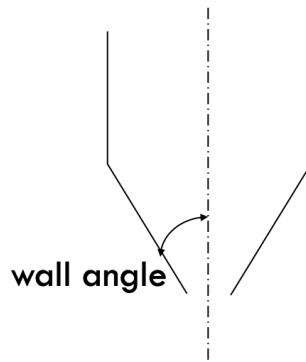
FIGURE 1.7. Illustration showing the hopper wall half angle measured from the vertical.

Angle from the vertical (°)	% of hoppers in mass flow
45	0
30	25
20	50
15	70

TABLE 1.1. The percentage of materials that resulted in mass flow for different hopper wall half angles from the vertical (Figure 1.7). The data was collected by L. ter Borg and presented in the lecture notes by Jacob [16].

flow cases (Table 1.1). Even a hopper wall angle of 15° from the vertical resulted in only 70% of the hoppers producing mass flow. Designing for mass flow is discussed in Chapter 9.

An extreme case of funnel flow, known as a rathole (aka a pipe), is shown in Figure 1.8. When a rathole occurs, the material only flows through a narrow flow channel while most of the material remains stagnant. Ratholes are particularly problematic since a collapsing rathole can cause structural damage to the hopper. Furthermore, the falling material may become fluidized by entraining air between the particles and flow uncontrollably from the exit (known as flooding).

(A) Schematic.

(B) Photograph from above.

FIGURE 1.8. Examples of ratholes. Both images are courtesy of B. Hancock.

FIGURE 1.9. A photograph showing a cohesive bridge in a hopper.

If the hopper outlet size is too narrow, then a cohesive bridge may form (Figure 1.9) which prevents the material above the bridge from discharging. A design method for avoiding cohesive bridging is presented in Chapter 9.

Vibration is often used to induce flow in hoppers. The vibration can be applied by attaching an unbalanced motor or other device to the hopper wall or, more inelegantly, by pounding on the walls with a sledgehammer (Figure 1.10). The hammer marks on hopper walls are called hopper rash.

The following videos show how various particulate-based products are manufactured. Note that these links may become inactive over time.

- Detergents: https://www.youtube.com/watch?v=EPNpgTmjA2I
- "Pills": https://www.youtube.com/watch?v=XMkYEFwadG0
- Flour: https://www.youtube.com/watch?v=kFP-KBPwn3E
- Gypsum board: https://www.youtube.com/watch?v=46OwU7zGMlw
- Grain harvesting: https://www.youtube.com/watch?v=RMU0goBWRjY
- Chocolate: https://www.youtube.com/watch?v=ZtMfiWDQHT8
- 3D metal printing: https://www.youtube.com/watch?v=aSjjrEni_sY
- Batteries: https://www.youtube.com/watch?v=q8laRePW618

The examples given in this section demonstrate that particulate materials are not only common, but behave significantly differently than fluids.
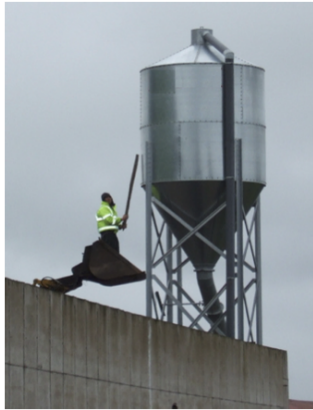
(A) Source: [17]   (B) Source: [18]   (C) Source: [19]

(D) Source: [19]   (E) Source: [20]

Figure 1.10. Various photos showing people pounding on hopper walls in an attempt to promote promote flow.

1.5.1. Summary

Summarizing the main points from this chapter:

- Particle science, engineering, and technology (PSET) is a broad topic found in many industries.
- Most engineers, particularly in the U.S., have little background on how to design for particulate systems.
- Powder flow is a particularly important topic in PSET.
- Particulate system behavior can be significantly different from fluid system behavior.

Bibliography

[1] R. Nedderman, <u>Statics and Kinematics of Granular Materials</u>. Cambridge University Press, 1992. DOI: [10.1017/CBO9780511600043](10.1017/CBO9780511600043).

[2] D. Schulze, <u>Powers and Bulk Solids: Behavior, Characterization, Storage and Flow</u>, 2nd. Springer, 2021. DOI: [10.1007/978-3-030-76720-4](10.1007/978-3-030-76720-4).

[3] R. Nelson, "Why study particle science?," 1999. [Online]. Available: http://web.archive.org/web/20110814145406/http://www.erpt.org/misc/whystudy.htm.

[4] B. Ennis, J. Green, and R. Davies, "The legacy of neglect in the U.S.," <u>Chemical Engineering Progress</u>, pp. 32–43, Apr. 1994.

[5] E. Merrow, "Linking R&D; to problems experienced in solids processing," <u>Chemical Engineering Progress</u>, vol. 81, pp. 14–22, 1985.

[6] T. Bell, "Challenges in the scale-up of particulate processes – an industrial perspective," <u>Powder Technology</u>, vol. 150, pp. 60–71, 2005.

[7] R. Blumenfeld, S. Edwards, and S. Walley, "The Oxford handbook of soft condensed matter," E. Terentjev and D. WeitZ, Eds., pp. 167–231, 2015. [Online]. Available: https://doi.org/10.1093/oxfordhb/9780199667925.013.5.

[8] F. Krausmann, S. Gingrich, N. Eisenmenger, K. Erb, H. Haberl, and M. Fischer-Kowalski, "Growth in global materials use, gdp and population during the 20th century," <u>Ecological Economics</u>, vol. 68, no. 10, pp. 2696–2705, 2009. DOI: 10.1016/j.ecolecon.2009.05.007.

[9] T. Knowlton, J. Carson, G. Klinzing, and W.-C. Wang, "The importance of storage, transfer, and collection," <u>Chemical Engineering Progress</u>, vol. 90, no. 4, pp. 44–54, 1994.

[10] Statistica. "Production of urea worldwide from 2009 to 2020." (2023), [Online]. Available: https://www.statista.com/statistics/1287028/global-urea-production/ (visited on 03/15/2023).

[11] J. Gustavsson, C. Cederberg, U. Sonesson, R. van Otterdijk, and A. Meybeck. "Global food losses and food waste." (2011), [Online]. Available: http://www.fao.org/docrep/014/mb060e/mb060e00.pdf (visited on 04/26/2023).

[12] Z. Chen, C. Wassgren, and R. Ambrose, "A review of grain kernel damage: Mechanisms, modeling, and testing procedures," <u>Transactions of the ASABE</u>, vol. 63, no. 2, pp. 455–475, 2020.

[13] Pharmapproach. "Understanding pharmaceutical dosage forms." (2021), [Online]. Available: https://www.pharmapproach.com/understanding-pharmaceutical-dosage-forms (visited on 04/26/2023).

[14] J. Vernon, W. Hughen, and A. Trujillo, "Pharmaceutical manufacturing efficiency, drug prices, and public health: Examining the causal links," <u>Drug Information Journal</u>, vol. 41, pp. 229–239, 2007.

[15] M. I. Corporation. "Understanding and solving segregation effects in pharmaceutical solid-dosage form operations." (2018), [Online]. Available: https://www.pharmaceuticalonline.com/doc/understanding-and-solving-segregation-effects-%20in-pharmaceutical-solid-dosage-form-operations-0001 (visited on 04/26/2023).

[16] K. Jacob, <u>Bin and hopper design</u>, Lecture Notes, Mar. 2000.

[17] E. McGee, "The benefits of powder characterization," <u>SHAPA Technical Bulletin Number 14</u>, 2009. [Online]. Available: https://www.shapa.co.uk/technical-downloads/Updated%5C%20Papers%5C%20May%5C%202015/powder_characterisation.pdf.

[18] B. H. R. W. Arnott. "Ask an engineer: How do i protect my storage silo and feed hopper from baked in design flaws?" (2019), [Online]. Available: https://www.bulkhandlingreview.com.au/ask-an-

engineer-how-do-i-protect-my-storage-silo-and-feed-hopper-from-baked-in-design-flaws/ (visited on 04/26/2023).

[19]   Jenike and Johanson. "What is poor flow?" (2023), [Online]. Available: https://jenike.com/solutions/solve-or-prevent-poor-flow/ (visited on 04/26/2023).

[20]   Bulk Solids Flow (link no longer active). (2013), [Online]. Available: http://www.bulksolidsflow.com/index.php?option=com_content&view=article&id=5&Itemid=3 (visited on 09/02/2013).

CHAPTER 2

Powder Flow Indices

2.1. What is powder "flowability"?

Flowability is a term used to describe how well a powder flows. One hears the term in the context of hopper flow, die filling, screw feeding, and other powder handling behavior. There is no single standard for measuring a powder's flowability and many methods are qualitative or comparative, as shown in Figure 2.1. Indeed, how well a powder flows depends on the powder's properties and the local stress conditions. Thus, we can't say how well a powder will flow without considering both material properties and system conditions.

The following sections review common methods that have been proposed for quantifying a powder's flowability. One important method, shear cell testing, is not described in this chapter and instead an entire chapter (Chapter 8) is devoted to the topic.

2.2. Indices vs. Properties

Before discussing methods for evaluating flowability, it is important to first clarify the difference between indices and properties. Let's say you're unfamiliar with fluid mechanics and need to determine how a fluid will flow in a variety of situations. One approach would be to develop a series of physical "simulations" to assess fluid flow behavior in commonly encountered systems. For example, Figure 2.2 shows three flow systems: liquid discharging from a vessel, liquid flowing through a pipe, and an impeller stirring a liquid in a container. These tests provide quantitative information, e.g., the time required to discharge the vessel, the flow rate through the pipe, and the torque required to rotate the impeller, and can be used to compare

FIGURE 2.1. The traditional assessment of powder flowability consists of an experienced worker tumbling a jar of powder and, based on that person's experience, assessing the powder's "flowability". This photograph is courtesy of B. Hancock.
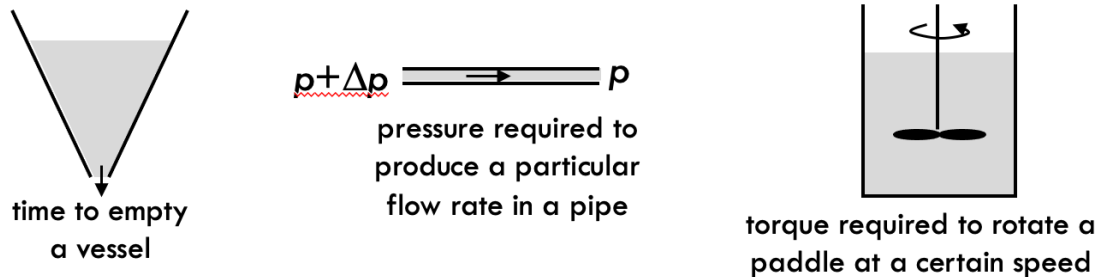
FIGURE 2.2. Examples of common systems that might be used to create liquid flow indices.

the "flowability" of different liquids, but they don't provide fundamental properties and can't be used to quantitatively design new systems. Such non-fundamental measurements are often termed "indices", e.g., the Vessel Discharge Index, the Pipe Flow Index, and the Stirring Index.

To know what quantities are fundamental to a material and how to devise methods for measuring these quantities, we must first have a modeling framework. For an incompressible, Newtonian fluid, that framework is the Navier-Stokes equations,

$$\rho \left[\frac{\partial \mathbf{u}}{\partial t} + (\mathbf{u} \cdot \nabla) \, \mathbf{u} \right] = -\nabla p + \mu \nabla^2 \mathbf{u} + \rho \mathbf{g}, \tag{2.1}$$

where $\mathbf{u}$ is the fluid velocity, t is time, p is the fluid pressure, and $\mathbf{g}$ is the gravitational acceleration. Here we see there are two fundamental material-related quantities in the model: density (ρ) and dynamic viscosity (μ). These fundamental material parameters in the model are called "properties". Using the model, we can devise simple experiments that an be used to measure each of the properties, e.g., using a hydrometer to obtain the density or a viscometer to obtain the viscosity. With the fundamental properties and the model, we can, in principle, predict flow behavior in any system.

Unfortunately, the modeling framework for particulate materials isn't as developed as it is for fluid mechanics. We do have soil mechanics models available for quasi-static particulate material systems at high pressures, but the models are often simplified, difficult to implement, or require many, sometimes difficult-to-measure properties. Powder flow indices tend to be defined for systems at low pressures, consistent with powders flowing at free surfaces. There are also kinetic theory models for dilute, energetic flows, but again, these are often highly simplified and require particle-level properties, which can be difficult to obtain. Thus, we must frequently rely on index-style measurements and then either use them in a comparative manner, e.g., Powder A has an index value less than Powder B's value, or experimentally correlate the indices to processes of interest, e.g., performance in manufacturing pharmaceutical tablets. This chapter describes some of the index-style properties that have been proposed. Subsequent chapters focus more on fundamentals.

2.2.1. A Side-note on Property Values

Although these notes do not focus on characterization measurements, two measurement-related items are worth noting:

(1) Proper material sampling is essential for obtaining reliable characterization measurements. The Golden Rules of Sampling [1] should always be followed.
(2) Be wary of using published property data for particulate materials. The properties of particulate materials depend not only on chemical composition, but also on the surrounding environmental conditions, e.g., temperature and humidity, and the loading history of the material, e.g., how it was produced, whether or not it has been subject to attrition or previous compression, etc. It is a best practice to measure the properties of the material you're handling under the conditions the material will be subject to, e.g., temperature, humidity, and storage time. Values reported in the
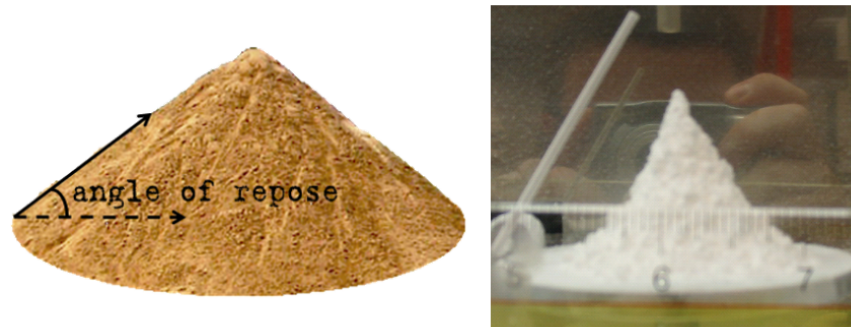
Figure 2.3. (left) A well-defined angle of repose for a cohesionless material. (right) A cohesive powder's angle of repose is not well defined. For this powder, the angle of repose is larger near the peak and smaller near the base.

literature can be useful for first-cut design estimates, but detailed design should use measurements on the actual material.

2.3. Angles of Repose

An angle of repose is the largest, stable angle of a powder's free surface with respect to the horizontal. A smaller angle of repose generally implies better flow characteristics. Free flowing materials generally have a well-defined angle of repose; however, cohesive powders do not, which makes the angle of repose value questionable (Figure 2.3).

Although angles of repose are often reported, their use for assessing flowability is questionable. Hiestand [2] states that "for pharmaceutical materials the angle of repose [as a flowability measure] is satisfactory only with powders whose flow characteristics are so good that one seldom needs the measurement." Similarly, Jenike [3] states, "... In fact, it [the angle of repose] is only useful in the determination of the contour of a pile, and its popularity among engineers and investigators is due not to its usefulness but to the ease with which it is measured." Despite the criticisms, since it has been used by some to assess flowability, the following list is provided to describe a few of the many different methods used for measuring the angle of repose:

- **Poured Angle of Repose**: The poured angle of repose is found by pouring a powder from some elevation onto a flat plate and measuring the angle that the powder's slope makes with respect to the horizontal (Figure 2.4a).
- **Angle of Fall**: The angle of fall is the angle of repose for a powder mound that has been poured onto a surface and then impacted (Figure 2.4b). The powder will slump somewhat in response to the impact.
- **Angle of Spatula**: The angle of spatula is the angle of repose for a powder that has been formed by slowly lifting a spatula out of a powder bed (Figure 2.4c).
- **Drained Angle of Repose**: The drained angle of repose is the angle of repose formed by the powder retained in a flat-bottomed bin after discharge (Figure 2.4d).
- **Dynamic Angle of Repose**: The dynamic angle of repose is the angle of repose for a continuously avalanching powder, such as what one might find in a rotating drum (Figure 2.4e).

Note that the schematics in Figure 2.4 are idealizations. As stated previously, cohesive powders do not generally have a well defined angle of repose. Furthermore, in a dynamic angle of repose experiment, a cohesive powder will not avalanche continuously and instead will build-up to a large angle then collapse in a large avalanche event, then repeat the cycle, often in an erratic manner. These avalanche events are used in another flowability index and are discussed further in Section 2.6.
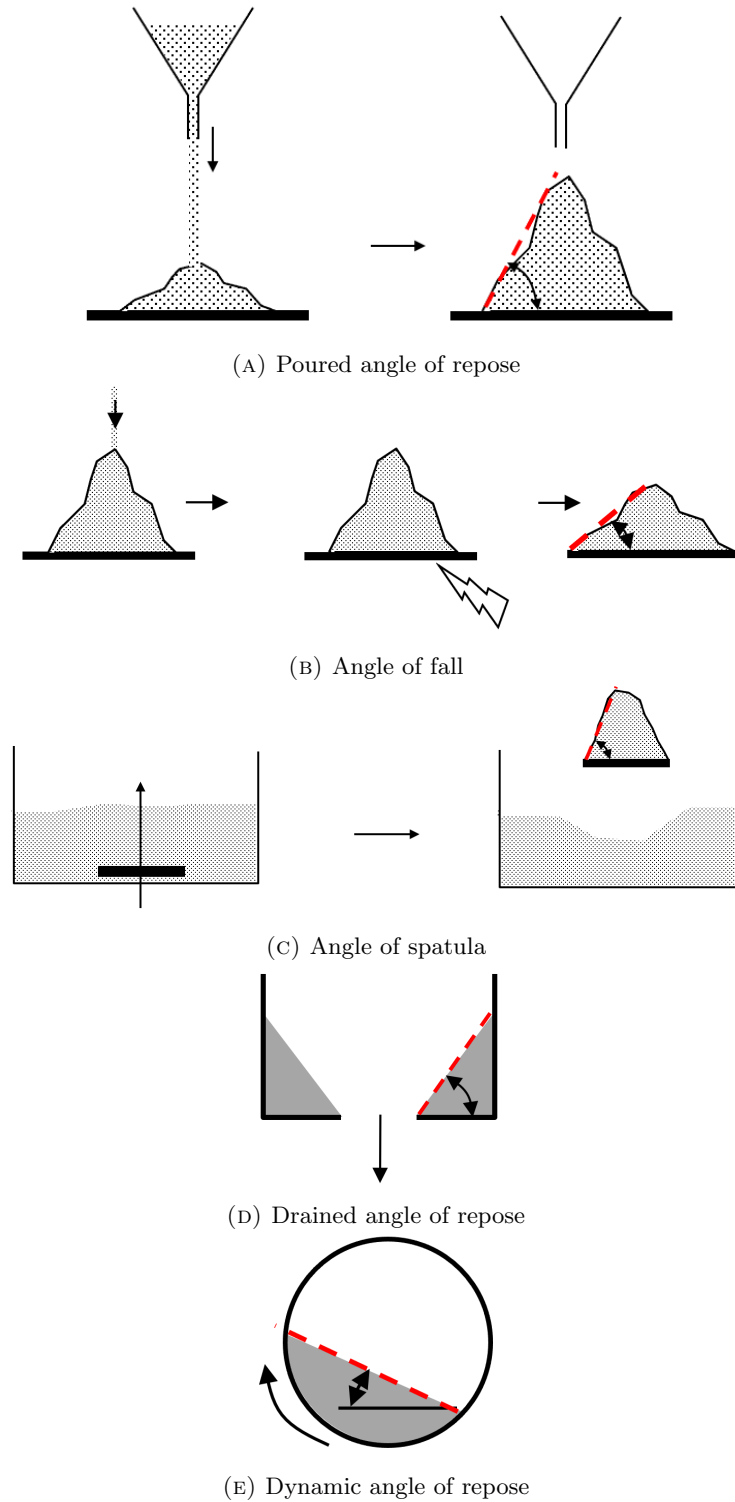
(A) Poured angle of repose

(B) Angle of fall

(C) Angle of spatula

(D) Drained angle of repose

(E) Dynamic angle of repose

FIGURE 2.4. Schematics for various methods for measuring angles of repose.

Material	Angle of Repose (deg)
sodium chloride	34 ± 1
sucrose	35 ± 1
lactose 100	38 ± 2
lactose 325	41 ± 1

TABLE 2.1. Typical values for the poured angle of repose [4].

Notes:

(1) Commercial testers are available for measuring angles of repose such as the Micron Powder Characteristics Tester PT-X, the GranuHeap, the GranuDrum, and the PowderPro A1. Note that these notes are not endorsing any particular device nor claim to list all possible commercial devices, but only mention a few here so the reader can conveniently examine what these commercial devices look like and how they operate.

(2) Crude estimates of the angle of repose can be made using a protractor or calculated from the measured locations of the powder heap peak and base. More precise measurements can be made from processing a digital image of a powder heap. Digital processing has the added advantage of being able to examine the local slope fluctuations in addition to the average slope.

(3) For a cohesionless material, the angle of repose is equal to the material's angle of internal friction, a topic discussed in Chapter 4.

(4) Example values for the poured angle of repose are given in Table 2.1.

2.4. Carr's Flowability and Floodability Indices

Carr indices are empirical formulas proposed by Carr [5] for describing a powder's flowability and floodability. A powder's <u>floodability</u> is the powder's tendency to fluidize in air and produce liquid-like flow. Carr based his formulas on the behavior of more than 2800 dry materials. The full Carr index analysis approach is rarely used nowadays, although the Carr compressibility is still used frequently. Despite not being widely used, a description of the methods for determining the flowability and floodability indices is presented in this section for completeness.

2.4.1. Carr's Flowability Index

Carr's flowability index is an empirically-derived score between 0 and 100, with 100 indicating excellent flow qualities, that combines measurements of a powder's:

- poured angle of repose,
- angle of spatula,
- compressibility, and
- either cohesion or coefficient of uniformity.

The poured angle of repose and angle of spatula are presented in the previous section and, thus, won't be discussed here. Instead, the powder's compressibility, cohesion (as defined by Carr), and coefficient of uniformity are described.

<u>Compressibility</u> is the change in a powder's bulk density between tapped and aerated states relative to the powder's tapped bulk density,

$$\text{compressibility} = \frac{\rho_{b,T} - \rho_{b,A}}{\rho_{b,T}} \approx \frac{\rho_{b,T} - \rho_{b,P}}{\rho_{b,T}} \tag{2.2}$$

where $\rho_{b,T}$ and $\rho_{b,A}$ are the tapped and aerated bulk densities, respectively. Note that the compressibility is often reported as a percentage. The aerated bulk density is the bulk density of the powder at incipient fluidization while the tapped bulk density is the powder's bulk density after being subject to a large number

FIGURE 2.5. (left) Powders gently poured into a container can support large void spaces if the particles are frictional or cohesive, resulting in a small bulk density. (right) After tapping, these voids collapse and the bulk density increases.

Flowability	compressibility (%)	Hausner ratio
excellent	5 - 10	1.05 - 1.11
good	11 - 15	1.12 - 1.18
fair	16 - 20	1.19 - 1.25
passable	21 - 25	1.27 - 1.33
poor	26 - 31	1.35 - 1.45
very poor	32 - 37	1.47 - 1.59
exceedingly poor	38 - 45	1.61 - 1.82

TABLE 2.2. Qualitative flow descriptions for different ranges of compressibility and Hausner ratio. The Hausner ratio is described in Section 2.5. This table is adapted from [2].

of small taps in a containing vessel. Because measuring a powder's aerated bulk density is not simple, the loosely packed poured bulk density, $\rho_{b,P}$, is often used instead. The loosely poured bulk density corresponds to the bulk density just after gently pouring the powder into a containing vessel. It's the initial powder bulk density at the start of the tapping sequence used to find the tapped bulk density.

Powders with significant frictional and cohesive interactions, which tend to decrease flowability, have a larger difference in their tapped and poured bulk densities. When the powder is gently poured into a vessel, the packing configuration can contain large pores if the particles are frictional or cohesive, resulting in a smaller bulk density (Figure 2.5). When tapped, these large pores collapse and increase the bulk density. Thus, a large compressibility implies poor flow behavior. Qualitative flow descriptions for different ranges of compressibility values are presented in Table 2.2. Compressibility values for various materials are presented in Table 2.3.

Carr quantified a powder's cohesion using the powder masses retained on three vibrating, stacked sieves subject to vibration,

$$\text{cohesion} := 5 \cdot (\text{mass on top sieve})(0.1 \text{ g}) + 3 \cdot (\text{mass on middle sieve})/(0.1 \text{ g})$$
$$+ (\text{mass on bottom sieve})/(0.1 \text{ g}). \tag{2.3}$$

The choice of sieve sizes depends on the powder's tapped and aerated bulk densities and powder compressibility (Table 2.4). A more cohesive material, which would result in worse flowability, will have more material retained on the upper and middle sieves and, thus, result in a larger value for cohesion.

For larger sized (aka coarse) particles, a uniformity coefficient is used in place of cohesion in Carr's algorithm. Uniformity is defined as the ratio of the width of sieve opening that passes 60% of the material (by mass) to the width of sieve opening that passes 10% of the material. Increasing uniformity results in increasing flowability.

To calculate the Carr Flowability Index, one sums the appropriate scores in Table 2.5. For example, if experiments gave the values in Table 2.6, then the Carr Flowability Index is 96, indicating excellent flowability: aid will not be needed for the material to flow, and the material is not expected to arch.

Material	Ref.	Comp. (%)	HR	Flow behavior
glass beads	[4]	4	1.04	excellent
sucrose	[4]	10	1.11	excellent
povidone	[6]	12	1.13	good
sodium chloride	[4]	15	1.18	good
microcrystalline cellulose (Avicel PH103)	[4]	19	1.23	fair
lactose (Pharmatose 100M)	[4]	20	1.25	fair
microcrystalline cellulose (Avicel PH102)	[7]	21	1.26	passable
microcrystalline cellulose (Avicel PH105)	[4]	22	1.28	passable
lactose (Pharmatose 325M)	[4]	23	1.30	passable
starch 1500	[7]	23	1.29	passable
maltodextrin (Maltrin M150)	[4]	24	1.32	passable
paracetamol	[6]	28	1.39	poor
microcrystalline cellulose (Avicel PH102)	[8]	29	1.41	poor
microcrystalline cellulose (Avicel PH101)	[8]	28-29	1.39-1.41	poor
lactose (Pharmatose 200M)	[4]	41	1.69	exceedingly poor

TABLE 2.3. Example compressibility (Comp.) and Hausner ratio (HR) values for various materials, including flow descriptions. The Hausner ratio is described in Section 2.5. References for the data are given in the second column.

Working bulk density (kg/m^3)	Sieve sizes (mesh)
160 - 400	40, 60 ,100
400 - 960	60, 100, 200
960 - 1440	100, 200, 325

TABLE 2.4. Sieve sizes used to determine the Carr cohesion value. The working bulk density is $\rho_{b,W} = \rho_{b,A} + (\rho_{b,T} - \rho_{b,A}) * (\text{compressibility})$. The mesh size is the number of openings per linear inch for the sieve. For example, a 200 mesh indicates 200 openings per linear inch. Accounting for the sieve wire diameter, 200 mesh corresponds to a $74\,\mu\text{m}$ opening in the US standard. It's a measure of particle size. To perform the test, one places 2 g of -200 mesh material (i.e., $< 74\,\mu\text{m}$ particle size) on the top-most sieve then vibrates the powder for a period of time.

2.4.2. Carr's Floodability Index

The Carr Floodability Index rates a powder's tendency to fluidize in air and flow like a liquid. Powders that are prone to flooding can be difficult to control since the flow behavior can rapidly transition from solid-like to liquid-like if air gets entrained into the powder. Like the Flowability Index, the Floodability Index ranges from 0 to 100. A score of 100 indicates the powder is very floodable.

The Floodability Index is based on the following measurements:

- Flowability Index,
- angle of fall,
- angle of difference, and
- dispersibility.

The angle of fall and Flowability Index have been previously discussed. The angle of difference is the difference between the poured angle of repose and the angle of fall, i.e.,

$$(\text{angle of difference}) = (\text{angle of repose}) - (\text{angle of fall}). \tag{2.4}$$

Flowability and Performance	Angle of Repose		Compressibility		Angle of Spatula		Uniformity Coeff.*		Cohesion**	
	Deg.	Points	%	Points	Deg.	Points	Units	Points	%	Points
Excellent, 90 - 100 pts	25	25	5	25	25	25	1	25		
Aid not needed	26 - 29	24	6 - 9	23	26 - 30	24	2 - 4	23		
Will not arch	30	22.5	10	22.5	31	22.5	5	22.5		
Good, 80 - 89 pts.	31	22	11	22	32	22	6	22		
Aid not needed	32 - 34	21	12 - 14	21	33 - 37	21	7	21		
Will not arch	35	20	15	20	38	20	8	20		
Fair, 70 - 79 pts	36	19.5	16	19.5	39	19.5	9	19		
Aid not needed (but vibrate if necessary)	37 - 39	18	17 - 19	18	40 - 44	18	10 - 11	18		
	40	17.5	20	17.5	45	17.5	12	17.5		
Passable, 60 - 69 pts	41	17	21	17	46	17	13	17		
Borderline. Material may hang up	42 - 44	16	22 - 24	16	47 - 59	16	15 - 16	16		
	45	15	25	15	60	15	17	15	< 6	15
Poor, 40 - 59 pts	46	14.5	26	14.5	61	14.5	18	14.5	6 - 9	14.5
Must agitate, Vibrate	47 - 54	12	27 - 30	12	62 - 74	12	19 - 21	12	10 - 29	12
	55	10	31	10	75	10	22	10	30	10
Very poor, 20 - 39 pts	56	9.5	32	9.5	76	9.5	23	9.5	31	9.5
Agitate more positively	57 - 64	7	33 - 36	7	77 - 89	7	24 - 26	7	32 - 54	7
	65	5	37	5	90	5	27	5	55	5
Very, very poor, 0 - 19 pts	66	4.5	38	4.5	91	4.5	28	4.5	56	4.5
Special agit., hopper or eng'g	67 - 89	2	39 - 45	2	92 - 99	2	29 - 35	2	51 - 79	2
	90	0	> 45	0	> 99	0	> 36	0	> 79	0

* Used with granular and powdered granular materials.
** Used with powders or where an effective cohesion can be measured.

TABLE 2.5. The Carr Flowability Index score table [5].

Measurement	Value	Score from Table 2.5
angle of repose	25°	25
compressibility	8%	23
angle of spatula	25°	25
uniformity coefficient	2	23
	Sum	**96**

TABLE 2.6. Measurement values for sand used in the example for calculating the Carr Flowability Index [5].

A floodable material typically has a small angle of fall since air trapped within the heap of powder causes the material to fluidize when the base is impacted. The larger the angle of difference, the more likely the material will be floodable.

The dispersibility is a measure of the scattering and dusting characteristics of a powder. The more dispersible a material is, the more floodable it is. Dispersibility is measured by dropping a 10 g sample of material en masse through a 4 in. diameter, 13 in. long cylinder from a height of 24 in. above a watch glass, which in turn is located 4 in. from the bottom of the cylinder (Figure 2.6). The material remaining on the watch glass is weighed and the dispersibility is found using,

$$(\text{dispersibility}) = 10 * [10 - (\text{mass remaining, in grams})]. \tag{2.5}$$

The algorithm for calculating the Floodability Index is similar to the one used to find the Flowability. The table for determining the scores and evaluating the floodability is given in Table 2.7.
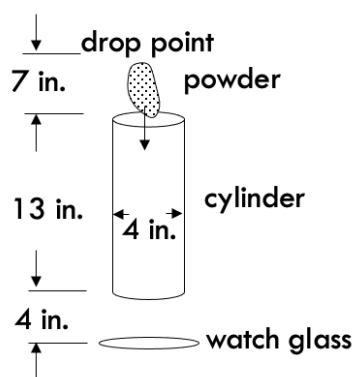
Notes:

FIGURE 2.6. A schematic illustrating the test used to evaluate a powder's dispersibility in the Carr Floodability Index.

Floodability and Performance	Flowability		Angle of Fall		Angle of Difference		Dispersibility	
	Units	Points	Deg.	Points	Deg.	Points	%	Points
Very floodable, 80 - 100 pts	60+	25	10	25	30+	25	50+	25
Positive rotary seal	59 - 56	24	11 - 19	24	29 - 28	24	49 - 44	24
will be necessary	55	22.5	20	22.5	27	22.5	43	22.5
	54	22	21	22	26	22	42	22
	53 - 50	21	22 - 24	21	25	21	41 - 36	21
	49	20	25	20	24	20	35	20
Floodable, 60 - 79 pts.	48	19.5	26	19.5	23	19.5	34	19.5
Rotary seal will	47 - 45	18	27 - 29	18	22 - 20	18	33 - 29	18
be necessary	44	17.5	30	17.5	19	17.5	28	17.5
	43	17	31	17	18	17	27	17
	42 - 40	16	32 - 39	16	17 - 16	16	26 - 21	16
	39	15	40	15	15	15	20	15
Inclined to flood, 40 - 59 pts	38	14.5	41	14.5	14	14.5	19	14.5
Rotary seal is desirable	37 - 34	12	42 - 49	12	13 - 11	12	18 - 11	12
	33	10	50	10	10	10	10	10
Could flood, 25 - 39 pts	32	9.5	51	9.5	9	9.5	9	9.5
Rotary seal probably needed	31 - 29	8	52 - 56	8	8	8	8	8
depending on drop, velocity	28	6.25	57	6.25	7	6.25	7	6.25
Won't flood, 0 - 24 pts	27	6	58	6	6	6	6	6
Rotary seal will	26 - 23	3	59 - 64	3	5 - 1	3	5 - 1	3
not be needed	< 23	0	> 64	0	0	0	0	0

TABLE 2.7. The Carr Floodability Index score table [5].

(1) A device that can measure all of the parameters required for evaluating the Carr Flowability and Floodability Indices is the Hosokawa Micron Powder Characteristics Tester.
(2) As stated previously, the full Carr Indices are not frequently used; however, the compressibility is a commonly reported quantity when evaluating powder flow behavior.

2.5. The Hausner Ratio

Perhaps the most commonly-used, easy-to-measure quantity used to evaluate flowability, at least in the pharmaceutical industry, is the Hausner ratio [9]. The Hausner ratio is defined as the ratio of the powder's

tapped bulk density ($\rho_{b,T}$) to the powder's aerated bulk density ($\rho_{b,A}$),

$$\text{(Hausner ratio)} := \frac{\rho_{b,T}}{\rho_{b,A}} \approx \frac{\rho_{b,T}}{\rho_{b,P}}. \tag{2.6}$$

As with the compressibility, it's much easier to measure the loosely poured bulk density and use that value in place of the aerated bulk density. The Hausner ratio is directly rated to the compressibility (Eq. (2.2)),

$$\text{(Hausner ratio)} = \frac{\rho_{b,T}}{\rho_{b,A}} = \frac{1}{1 - \frac{\rho_{b,T} - \rho_{b,A}}{\rho_{b,T}}} = \frac{1}{1 - \text{(compressibility)}}. \tag{2.7}$$

Notes:

(1) Table 2.2 lists qualitative flow behavior descriptions for various ranges of the Hausner ratio.
(2) Hausner ratio values for various materials are listed in Table 2.3.
(3) A variety of testers are available for measuring a powder's loosely poured and tapped bulk densities, e.g., Agilent 350 Tapped Density Tester, Autotap, SOTAX, and the GranuPack.
(4) The Hausner ratio can also be used to distinguish between Geldart Group A (aeratable, easy-to-fluidize, Hausner ratio < 1.25) and Group C (cohesive, difficult-to-fluidize, Hausner ratio > 1.4) powders. Powders with $1.25 <$ Hausner ratio < 1.4 are Group AC (transitional) powders [10].
(5) The Hausner ratio (and the compressibility) has been known to sometimes give erroneous flowability results.
  (a) If the cohesion strength between particles is greater than the separation forces generated by tapping, then the initial packing arrangement may not change leading to a small Hausner ratio and a prediction of good flowability when in fact the flowability is poor [4], [6]. An example material displaying this behavior is microcrystalline cellulose (Avicel PH103) [4].
  (b) If the cohesion between particles is significant, then the initial packing may already have a large initial bulk density so tapping won't decrease it significantly. The resulting small Hausner ratio is misleading since the flowability would be poor due to the large cohesion [6].
  (c) Non-cohesive, angular particles may pack loosely initially, but small perturbations could result in significant re-packing leading to a large Hausner ratio, indicating poor flowability. The flowability may still be good however [6]. An example of this type of material is pre-gelatinized starch [6].

The bulk density of a powder increases with the number of taps. In addition to the loosely poured and asymptotic tapped densities, it has been proposed that the rate at which densification occurs can provide additional information on flow behavior. Consider Figure 2.7 in which two compaction curves are shown. Both start and end at the same packing fractions, but the red curve approaches the asymptotic value faster than the green curve, presumably because the cohesion and frictional properties of the red curve material are less significant. Thus, the red curve material will likely have better flow behavior even though both materials have the same Hausner ratio. The authors [11] of this figure suggest that the function,

$$\eta_n = \eta_\infty - \frac{\eta_\infty - \eta_0}{1 + \ln\left(1 + \frac{n}{\tau}\right)}, \tag{2.8}$$

fits experimental data well while also having a physical underpinning [12], with η being the material's packing fraction (aka solid fraction, relative density), and n the number of taps. The relation has three fitting parameters: η_0, η_∞, and τ. The number of taps required to reach the average packing fraction may be found from Eq. (2.8),

$$\frac{1}{2}\left(\eta_0 + \eta_\infty\right) = \eta_\infty - \frac{\eta_\infty - \eta_0}{1 + \ln\left(1 + \frac{n_{1/2}}{\tau}\right)}, \tag{2.9}$$

$$\frac{1}{2}\left(\eta_0 - \eta_\infty\right) = \frac{\eta_0 - \eta_\infty}{1 + \ln\left(1 + \frac{n_{1/2}}{\tau}\right)}, \tag{2.10}$$

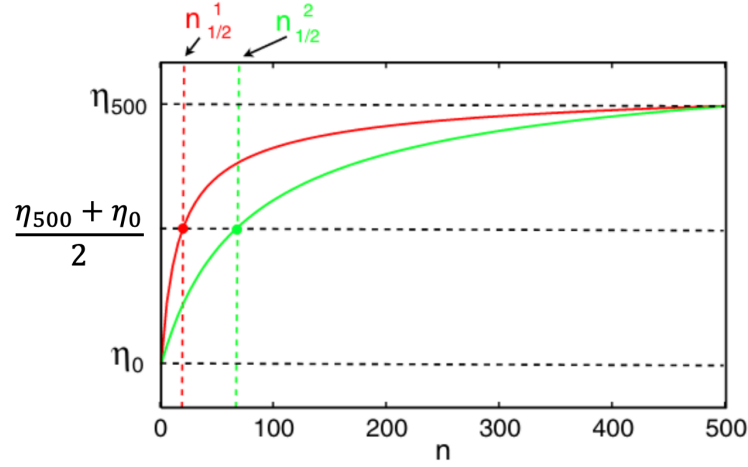$$\frac{1}{2}\left[1 + \ln\left(1 + \frac{n_{1/2}}{\tau}\right)\right] = 1, \tag{2.11}$$

FIGURE 2.7. Example plots of a powder's packing fraction as a function of the number of taps. Both powders start and end at the same packing fraction and, thus, have the same Hausner ratio. The rate at which the asymptotic packing fraction is reached is different, however. This figure is from [11], but with the average packing fraction expression on the vertical axis modified.

$$\ln\left(1 + \frac{n_{1/2}}{\tau}\right) = 1, \tag{2.12}$$

$$1 + \frac{n_{1/2}}{\tau} = e, \tag{2.13}$$

$$n_{1/2} = (e - 1)\tau. \tag{2.14}$$

Thus, smaller values for τ imply improved flow behavior for the same Hausner ratio since smaller values of τ result in a faster approach to the asymptotic value.

A different fit to the compaction curve is based on the work of Kawakita and Lüdde [13] who originally developed their relation for the uniaxial compaction of powders. This fit expresses the instantaneous compressibility of a powder,

$$C_n = \frac{\eta_n - \eta_0}{\eta_n}, \tag{2.15}$$

where η_n is the packing fraction of the powder after n taps, in the following form,

$$\frac{n}{C_n} = \frac{n}{a} + \frac{1}{ab}. \tag{2.16}$$

The parameter $a = C_\infty$ is the Carr compressibility (Eq. (2.2)), which is the compressibility after a large number of taps. This relation, like the previous one, has three fitting parameters: η_0, a, and b. Smaller values of a (compressibility) and $1/b$ imply better flowability. Note that when plotted in the form of Eq. (2.16), the slope of the data is equal to $1/a$ and the intercept on the vertical axis is $1/(ab)$ (Figure 2.8). Typical values for a and $1/b$ are listed in Table 2.8. Equation (2.16) may be re-arranged to evaluate the packing fraction explicitly,

$$\frac{n}{\frac{\eta_n - \eta_0}{\eta_n}} = \frac{n}{\frac{\eta_\infty - \eta_0}{\eta_\infty}} + \frac{1}{\left(\frac{\eta_\infty - \eta_0}{\eta_\infty}\right)b}, \tag{2.17}$$

$$\frac{1}{1 - \frac{\eta_0}{\eta_n}} = \frac{1}{1 - \frac{\eta_0}{\eta_\infty}} + \frac{1}{nb\left(1 - \frac{\eta_0}{\eta_\infty}\right)}, \tag{2.18}$$

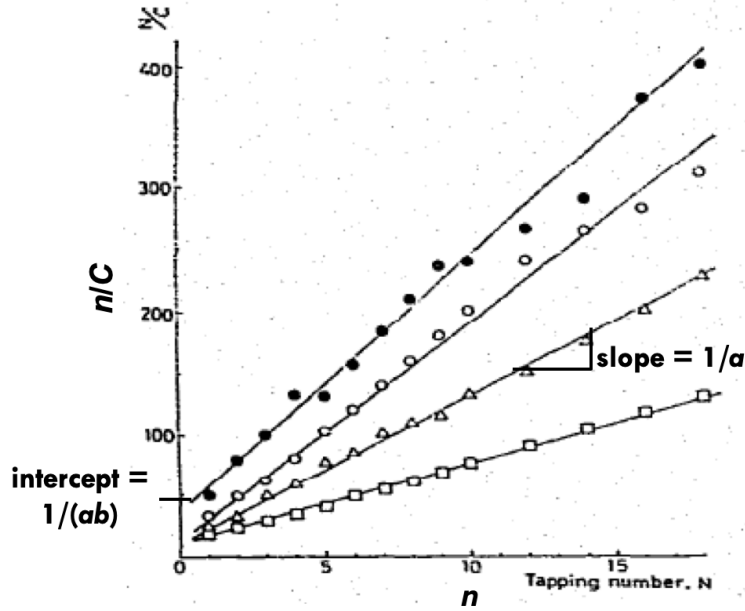$$1 - \frac{\eta_0}{\eta_n} = \frac{nb\left(1 - \frac{\eta_0}{\eta_\infty}\right)}{nb + 1}, \tag{2.19}$$

FIGURE 2.8. Plots of the instantaneous compressibility C_n (C in the figure), in the form of Eq. (2.16), as a function of the number of taps n for different materials. This plot is from [14].

	Substance	Particle diameter (mm)	Amount of additive or mixing ratio	$\dfrac{1}{ab}$	$\dfrac{1}{a}$	a	$\dfrac{1}{b}$
Single powder	Toporex	0.180		30	18.00	0.056	1.68
		0.254		50	19.20	0.052	2.60
	Skimmed milk	0.359		15	6.16	0.162	2.43
	Carborundum	0.127		18	7.81	0.128	2.30
	Sugar (sanontō)	0.191		7	2.50	0.400	2.80
	Granulated sugar (for coffee)	0.505		62	17.52	0.057	3.53
	Starch	0.074		19	2.98	0.336	6.38
	Magnesium stearate	0.003		27	4.10	0.244	6.59
	Calcium stearate	0.003		17	2.70	0.370	6.29
	Aluminum stearate	0.003		20	2.9	0.345	6.90
	Talc	0.003		15.5	2.55	0.392	6.08

TABLE 2.8. Values of the Kawakita constants for different materials [14].

$$\eta_n = \eta_0 \left[1 - \frac{nb\left(1 - \frac{\eta_0}{\eta_\infty}\right)}{nb+1} \right]^{-1}. \tag{2.20}$$

Yet a third proposed fit for tapped density comes from Philippe and Bideau [15]. They suggest the use of a stretched exponential function often used to study the relaxation of glasses,

$$\eta_n = \eta_\infty - (\eta_\infty - \eta_0) \exp\left[-\left(\frac{n}{n^*}\right)^m \right], \tag{2.21}$$

which has four fitting parameters: η_0, η_∞, n^*, and m. Having four fitting parameters can improve the fit accuracy compared to the previously discussed fits, which have three parameters each, but at the expense of having an additional parameter to consider.

Notes:

(1) To obtain a more accurate fit to tapped density data, more data should be included at the initial stages of tapping since that is when the bulk density changes most rapidly.

(2) The asymptotic packing fraction in the previously presented curve fits is never reached since an infinite number of taps would be required. However, we can calculate the number of taps required to reach 99% of the asymptotic packing fraction. For example, for Eq. (2.8),

$$0.99\eta_\infty = \eta_\infty - \frac{\eta_\infty - \eta_0}{1 + \ln\left(1 + \frac{n_{0.99}}{\tau}\right)}, \tag{2.22}$$

$$0.01\eta_\infty = \frac{\eta_\infty - \eta_0}{1 + \ln\left(1 + \frac{n_{0.99}}{\tau}\right)}, \tag{2.23}$$

$$1 + \ln\left(1 + \frac{n_{0.99}}{\tau}\right) = \frac{\eta_\infty - \eta_0}{0.01\eta_\infty} = 100\left(1 - \frac{\eta_0}{\eta_\infty}\right), \tag{2.24}$$

$$\left(1 + \frac{n_{0.99}}{\tau}\right) = \exp\left[100\left(1 - \frac{\eta_0}{\eta_\infty}\right) - 1\right] = \exp\left(99 - 100\frac{\eta_0}{\eta_\infty}\right), \tag{2.25}$$

$$n_{0.99} = \tau\left[\exp\left(99 - 100\frac{\eta_0}{\eta_\infty}\right) - 1\right]. \tag{2.26}$$

For Eq. (2.16), the number of taps required to reach $0.99\eta_\infty$ is,

$$\frac{n_{0.99}}{C_{0.99}} = \frac{n_{0.99}}{a} + \frac{1}{ab}, \tag{2.27}$$

$$n_{0.99}\left(\frac{1}{C_{0.99}} - \frac{1}{a}\right) = \frac{1}{ab}, \tag{2.28}$$

$$n_{0.99} = \frac{1}{ab}\left(\frac{aC_{0.99}}{a - C_{0.99}}\right) = \frac{1}{b}\left(\frac{C_{0.99}}{C_\infty - C_{0.99}}\right), \tag{2.29}$$

$$n_{0.99} = \frac{1}{b}\left(\frac{\frac{0.99\eta_\infty - \eta_0}{0.99\eta_\infty}}{\frac{\eta_\infty - \eta_0}{\eta_\infty} - \frac{0.99\eta_\infty - \eta_0}{0.99\eta_\infty}}\right), \tag{2.30}$$

$$n_{0.99} = \frac{1}{b}\left(\frac{\eta_\infty - \frac{\eta_0}{0.99}}{\eta_\infty - \eta_0 - \eta_\infty + \frac{\eta_0}{0.99}}\right), \tag{2.31}$$

$$n_{0.99} = \frac{1}{b}\left(\frac{\eta_\infty - \frac{\eta_0}{0.99}}{\frac{0.01}{0.99}\eta_0}\right), \tag{2.32}$$

$$n_{0.99} = \frac{1}{b}\left(\frac{0.99\frac{\eta_\infty}{\eta_0} - 1}{0.01}\right), \tag{2.33}$$

$$n_{0.99} = \frac{100}{b}\left(0.99\frac{\eta_\infty}{\eta_0} - 1\right). \tag{2.34}$$

Finally, for Eq. (2.21),

$$0.99\eta_\infty = \eta_\infty - (\eta_\infty - \eta_0)\exp\left[-\left(\frac{n_{0.99}}{n^*}\right)^m\right], \tag{2.35}$$

$$0.01\eta_\infty = (\eta_\infty - \eta_0)\exp\left[-\left(\frac{n_{0.99}}{n^*}\right)^m\right], \tag{2.36}$$

$$\frac{0.01\eta_\infty}{\eta_\infty - \eta_0} = \exp\left[-\left(\frac{n_{0.99}}{n^*}\right)^m\right], \tag{2.37}$$

$$\ln\left(\frac{0.01\eta_\infty}{\eta_\infty - \eta_0}\right) = -\left(\frac{n_{0.99}}{n^*}\right)^m, \tag{2.38}$$

$$\left[\ln\left(\frac{\eta_\infty - \eta_0}{0.01\eta_\infty}\right)\right]^{1/m} = \frac{n_{0.99}}{n^*}, \tag{2.39}$$

$$n_{0.99} = n^*\left\{\ln\left[100\left(1 - \frac{\eta_0}{\eta_\infty}\right)\right]\right\}^{1/m}. \tag{2.40}$$

The number of taps required to reach $0.99\eta_\infty$ may vary significantly depending on the choice of curve fit. Note that the n_{99} values can be used to compare approach rates to the asymptotic value, at least when the same fitting expression is used.

(3) When determining the fitting parameters numerically, initial estimates of the parameter values may be needed for convergence of the fitting algorithm, especially for more complex functions with multiple parameters. The initial estimate for η_0 can simply be the poured packing fraction, i.e., the first data point in the measurements. The fit for η_∞ can be approximated by assuming a Hausner ratio of 1.3, corresponding to passible flow behavior, which gives $\eta_\infty = 1.3\eta_0$. Estimates for other fitting parameters depend on the choice of fitting expression. An estimate for τ in Eq. (2.8) can be found by noting that,

$$\frac{d\eta_n}{dn} = \frac{\eta_\infty - \eta_0}{\left[1 + \ln\left(1 + \frac{n}{\tau}\right)\right]^2}\left(\frac{1}{1 + \frac{n}{\tau}}\right)\left(\frac{1}{\tau}\right) = \frac{\eta_\infty - \eta_0}{\left[1 + \ln\left(1 + \frac{n}{\tau}\right)\right]^2}\left(\frac{1}{\tau + n}\right), \tag{2.41}$$

so that at $n = 0$,

$$\left.\frac{d\eta_n}{dn}\right|_{n=0} = \frac{\eta_\infty - \eta_0}{\tau}, \tag{2.42}$$

$$\tau = \frac{\eta_\infty - \eta_0}{d\eta_n/dn|_{n=0}}. \tag{2.43}$$

Thus, calculating the initial slope from the measurement data along with the previously discussed approximations for η_0 and η_∞ provides a method for estimating τ.

For Eq. (2.16), initial estimates may be determined by first plotting the data using Eq. (2.16) as shown in Figure 2.8. A simple line fit can be used to estimate a and b. The parameter a is the inverse slope of the fitting line ($a = 1/(\text{slope})$) and b is related to the intercept, $1/(ab) = (\text{intercept})$. These values along with the previously discussed η_0 estimate can be used as the seed for a fitting algorithm.

Equation (2.21) can also be re-arranged to produce a linear fit for estimation purposes,

$$\frac{\eta_n - \eta_\infty}{\eta_\infty - \eta_0} = -\exp\left[-\left(\frac{n}{n^*}\right)^m\right], \tag{2.44}$$

$$\ln\left(\frac{\eta_\infty - \eta_n}{\eta_\infty - \eta_0}\right) = -\left(\frac{n}{n^*}\right)^m, \tag{2.45}$$

$$\ln\left(\frac{\eta_\infty - \eta_0}{\eta_\infty - \eta_n}\right) = \left(\frac{n}{n^*}\right)^m, \tag{2.46}$$

$$\ln\left[\ln\left(\frac{\eta_\infty - \eta_0}{\eta_\infty - \eta_n}\right)\right] = m\ln\left(\frac{n}{n^*}\right), \tag{2.47}$$

$$\ln\left[\ln\left(\frac{\eta_\infty - \eta_0}{\eta_\infty - \eta_n}\right)\right] = m\ln n - m\ln n^*. \tag{2.48}$$

Thus, when plotting the packing fraction in the form of the previous equation along with the estimates for η_0 and η_∞, the data should fall on a line with a slope of m and an intercept on the vertical axis of $-m\ln n^*$. These values can then be used as an initial guess for a fitting algorithm.

(4) In general, the stretched exponential function of Philippe and Bideau (Eq. (2.21)) works well at fitting tapped bulk density data and is the fit recommended by this author.
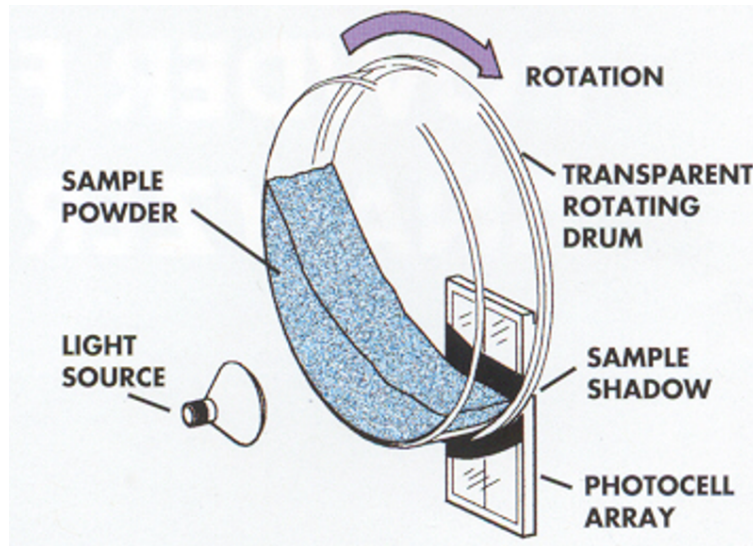
FIGURE 2.9. A schematic of a typical avalanche tester geometry [16]. Powder is contained within a rotating drum. In this particular device, the free surface of the powder is found from its shadow projected onto an imaging sensor.

2.6. Avalanche Testing

The previous methods of evaluating powder flow mostly use static or nearly static conditions. Avalanche testing has the powder in a flowing state when measurements are made. The test reproduces common handling conditions such as blending or granulating in a rotating drum and flow down a free surface.

A typical avalanche tester geometry is shown in Figure 2.9. Powder is contained within a drum that rotates at a prescribed speed such that powder circulates within the drum. The drum front and back walls are usually transparent so the powder movement can be monitored visually. In this particular device, a light on one side of the drum produces a shadow of the powder free surface on an imaging sensor. By monitoring the light intensity on the sensor, one can infer the dynamics of the free surface. A sudden change in the light intensity implies that an avalanche has occurred (Figure 2.10). An example of the light detector output as a function of time is shown in Figure 2.11a. A histogram of the time between avalanches in a 15 minute time period is shown for a particular powder in Figure 2.11b. The smaller the time between avalanches and the narrower the distribution of avalanche times (i.e., the smaller the standard deviation of avalanche times), the better the flowability. Figure 2.12 shows the mean and standard deviation of avalanche times for various materials.

Notes:

(1) Figure 2.13 provides an example for how avalanche time correlates with tablet weight variability in a pharmaceutical tableting operation. The larger the mean avalanche time, the greater the tablet weight variability, which is undesirable.
(2) Lavoie et al. [4] proposed testing at multiple drum speeds and define the following indices:

$$\text{Flowability Index} := \frac{1}{n} \sum_{i=1}^{n} \sigma_i, \tag{2.49}$$

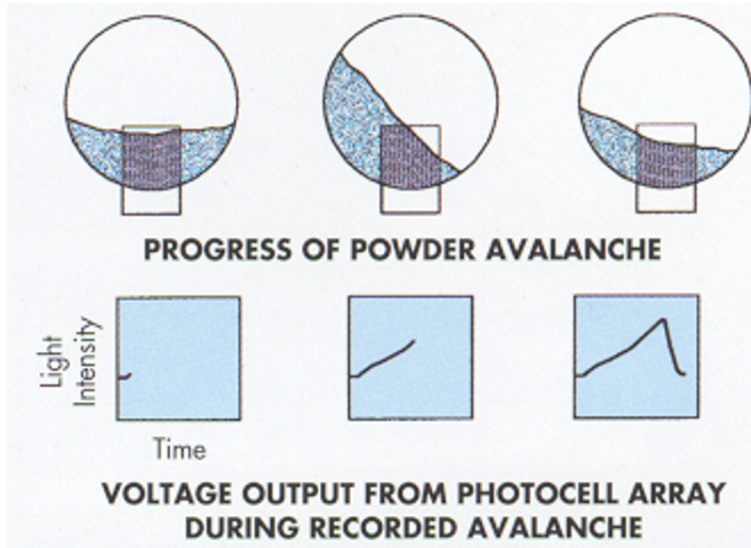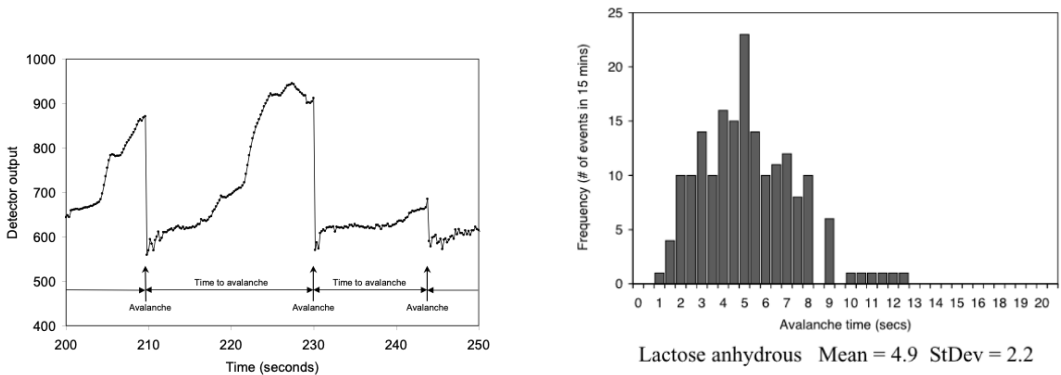$$\text{Cohesion Index} := \frac{1}{n} \sum_{i=1}^{n} m_i. \tag{2.50}$$

FIGURE 2.10. An illustration of how a powder avalanche is detected. This figure is taken from [16].

(A) An example of the light detector output as a function of time. Avalanche events are noted on the figure. This figure is from [16].

(B) A histogram for the avalanche time of lactose anhydrous over a 15 minute period. The smaller the mean avalanche time and the narrower the distribution, the better the flowability. This figure is from [16].

FIGURE 2.11. Typical avalanche time data [16].

where n is the number of different speeds tested, σ_i is the standard deviation of the time between avalanches at speed test i, and m_i is the mean time between avalanches at speed test i. Note that the time between avalanches is proportional to the drum speed [4] so the proposed indices are artificially weighted toward the slower speed values. The indices would be more useful if the time between avalanches is normalized by the drum rotation period before calculating standard deviations and means.

(3) Fill level can also make a difference in the avalanche times.

(4) The loading conditions on the powder are not well controlled. For example, the stress acting on any given region near the free surface, especially for cohesive powders, may vary in time as material collapses on top of it.
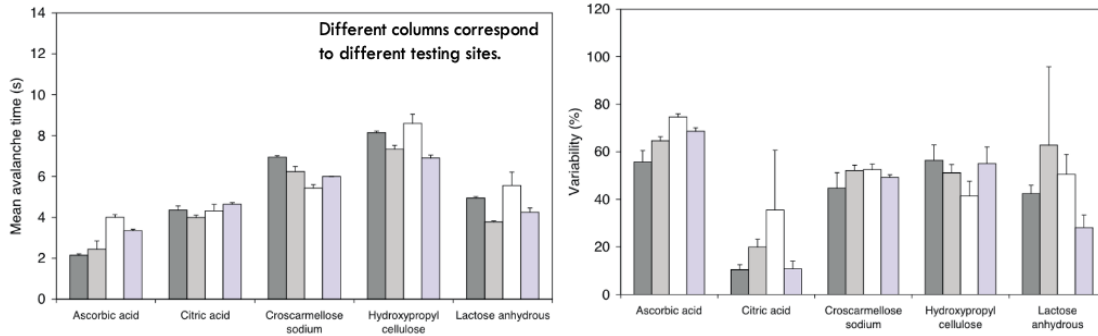
Figure 2.12. (left) The mean avalanche times for various pharmaceutical materials. The different bars correspond to measurements at different testing sites. (right) The corresponding standard deviations of the avalanche times. These figures are taken from [16].
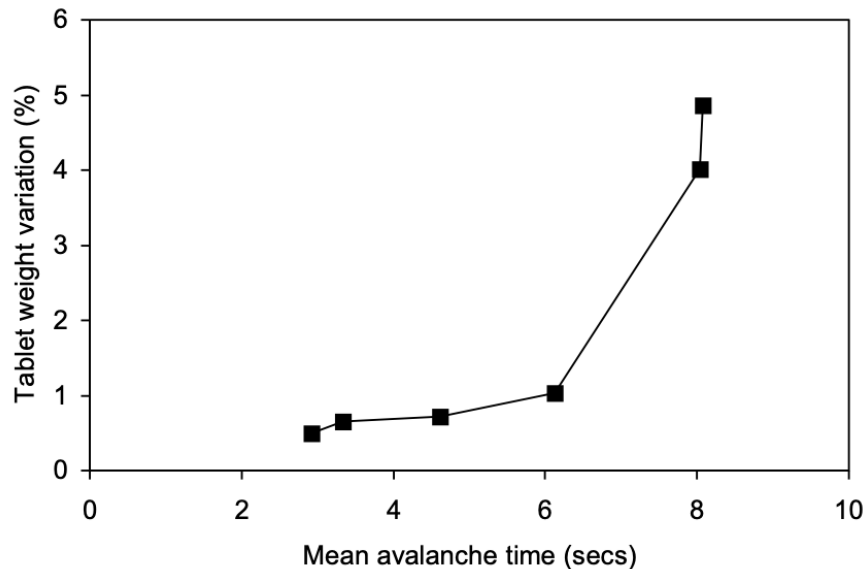

Figure 2.13. Tablet weight variation in a pharmaceutical tableting operation as a function of the material's mean avalanche time. This figure is taken from [17].

(5) Wall interactions can play a role in the avalanche behavior. For example, if the drum was frictionless, then the material in the drum wouldn't avalanche. A roughened boundary surface, e.g., using sandpaper or a mesh, is recommended to prevent slipping at the drum walls [18].

(6) If using a light-based avalanche detection method, the drum walls should remain free from sticking particles. Wiping the front and rear drum walls with an anti-static cloth can help reduce sticking due to electrostatic forces [18].

(7) Examples of avalanche testers include the TSI Aero-Flow (discontinued), Mercury Revolution, and the GranuDrum. There is also an avalanche tester that uses a load cell to detect avalanches rather than using an optical method.

Another approach to analyzing rotating drum avalanche data is to monitor the dynamic angle of repose and the variations in this angle. For example, when using the GranuDrum device, the free surface profile is analyzed in the following manner [19]:
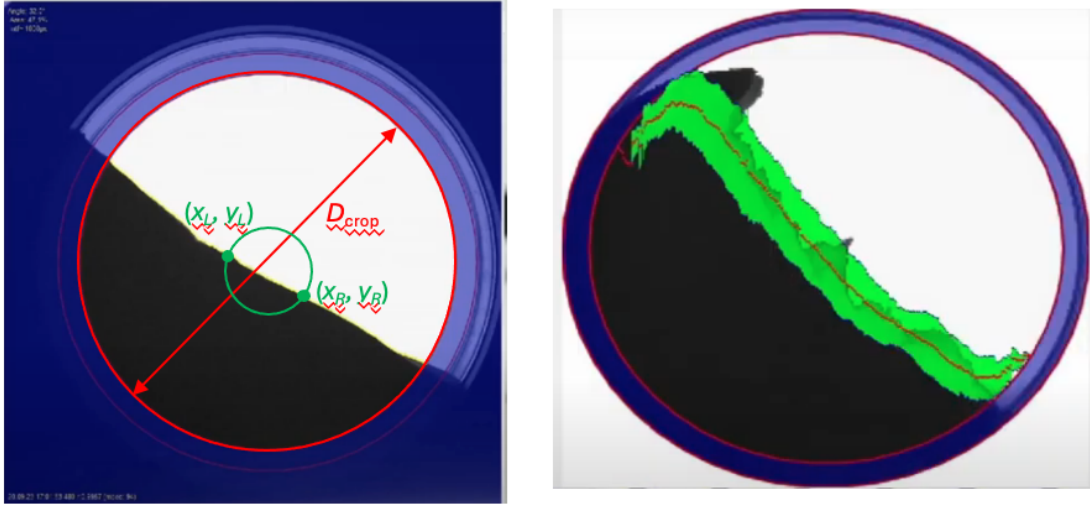
FIGURE 2.14. (left) A photograph from the GranuDrum device showing the crop diameter (red) and the diameter used to determine the average slope (green). (right) The green region is the range of all y locations of the free surface at each x location over many different images. The solid line in the figure is the mean of the y positions at the x locations. Images from [20].

(1) The region of the powder's free surface to be analyzed is identified using a "crop" diameter, D_{crop} (shown in red in Figure 2.14), in order to reduce boundary effects.

(2) The average surface slope, m_i, for image i is based on the positions of the left-most and right-most points intersecting a small circle near the middle of the drum (shown in green in Figure 2.14). Using a (forward difference) vector to connect two neighboring surface points, $\mathbf{v}_n = (x_{n+1} - x_n)\hat{\boldsymbol{i}} + (y_{n+1} - y_n)\hat{\boldsymbol{j}}$, the average vector for all of the surface points in image i is,

$$\overline{\mathbf{v}}_i = \frac{1}{N-1} \sum_{n=1}^{N-1} \mathbf{v}_n = \frac{1}{N-1} \sum_{n=1}^{N-1} [(x_{n+1} - x_n)\hat{\boldsymbol{i}} + (y_{n+1} - y_n)\hat{\boldsymbol{j}}], \qquad (2.51)$$

where N is the total number of surface points. Expanding the summation, one will find that all of the terms will cancel except for the end points, i.e., $(x, y)_N$ and $(x, y)_1$. Thus,

$$\overline{\mathbf{v}}_i = \frac{1}{N-1} [(x_N - x_1)\hat{\boldsymbol{i}} + (y_N - y_1)\hat{\boldsymbol{j}}]. \qquad (2.52)$$

The slope of this average surface vector is,

$$m_i = \frac{y_N - y_1}{x_N - x_1} = \frac{y_R - y_L}{x_R - x_L}. \qquad (2.53)$$

(3) Once many surface images have been collected, the mean and standard deviation of free surface y positions at each x location can be determined (Figure 2.14). The mean y position and standard deviation of the free surface at a particular x location are, respectively,

$$\overline{y}(x) = \frac{1}{I} \sum_{i=0}^{I} y_i(x), \qquad (2.54)$$

$$\sigma(x) = \sqrt{\frac{1}{I} \sum_{i=0}^{I} [y_i(x) - \overline{y}(x)]^2}, \qquad (2.55)$$

where I is the total number of images.
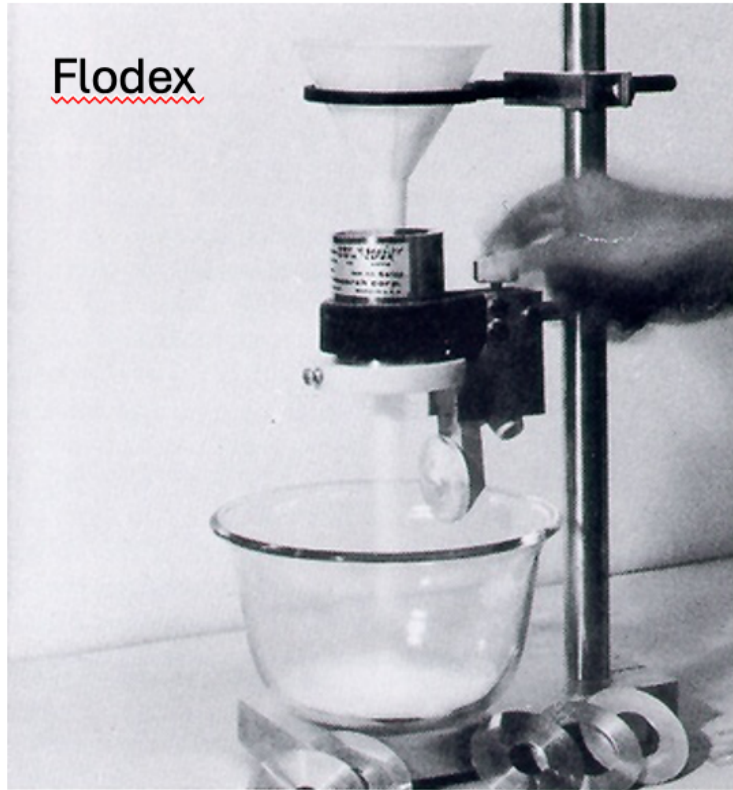
FIGURE 2.15. A photograph of a Flodex flow through an orifice device [21].

(4) The GranuDrum cohesion index (CI) is defined as,

$$CI := \frac{1}{D_{\text{crop}}} \sum_{\forall x} \sigma(x). \tag{2.56}$$

As the cohesion index decreases, the powder free surface is more consistent. Smaller average angles of repose and smaller cohesion index values correspond to better flow behavior.

2.7. Flow Through an Orifice

A flow through an orifice testing device consists of a small, flat-bottom cylindrical bin with a circular hole in the base (Figure 2.15). Flowability is quantified by the smallest diameter hole through which powder falls freely. Smaller diameters indicate better flow behavior.

Notes:

(1) In the traditional flow through orifice testing methodology, the critical hole diameter corresponds to when the material first flows through the hole in three consecutive tests. An alternate approach is to test the material multiple times and then plot the fraction of times that flow occurs, as shown in Figure 2.16. The index can be reported as the aperture opening corresponding to a particular fraction, e.g., 0.5 or 1.
(2) The device does not represent powder behavior under dynamic conditions [4].
(3) A flowing powder could become non-flowing when forced through small openings [4].
(4) Examples of commercial testers include the Flodex, Sotax, Gardco BEP2, and Hall flow meter.
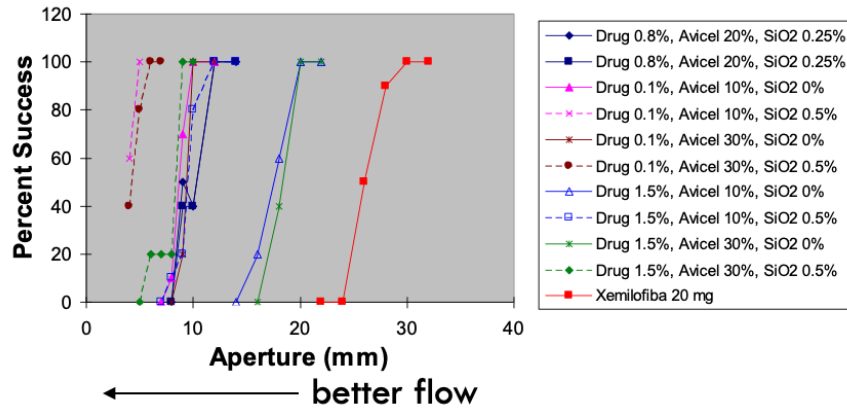(5) Example values from Flodex measurements are given in Table 2.9.

FIGURE 2.16. Flow through an orifice data for various pharmaceutical materials. The horizontal axis is the aperture diameter and the vertical axis is the percentage of times there was flow through the orifice. This plot is from [22].

Material	Min diameter for flow (mm)	Ref.
sucrose	< 4	[4]
commercial granulated sugar	4	[22]
sodium chloride	5	[4]
granulated active pharma blends	14-18	[22]
lactose (Pharmatose 100)	17	[4]
lactose (Pharmatose 325)	19	[4]
un-granulated active pharma blends	28-30	[22]
lactose (Pharmatose 200)	29	[4]
microcrystalline cellulose (Avicel PH105)	> 34	[4]

TABLE 2.9. The minimum orifice diameters to produce flow three consecutive times in a Flodex device. The last column lists the reference for the data.

2.8. Powder Rheometers

A powder rheometer is a device that measures powder flow behavior, often in a dynamic state. These devices are typically automated, which decreases the likelihood of operator bias. In addition, many commercial rheometers have the ability to test the powder in consolidated (i.e., densified) or aerated states as well as at various shear strain rates.

A typical powder rheometer device is shown in Figure 2.17. Here the powder is contained in a cylindrical vessel while a rotating blade is moved down and up through the bed. The force and torque required to move the blade through the bed and the blade displacement are monitored. These quantities are used to obtain the energy required to move the blade through the powder bed. The energy required to move the blade downward through the bed, which is in a confined state due to the presence of the container bottom and the blade pushing the powder downward, is called the "Basic Flowability Energy (BFE)". In general, powders with better flow behavior have a smaller BFE. Unfortunately, the BFE is not a fundamental property of the powder, but it can still be used as a comparative measure as well as in empirical correlations.

Notes:

(1) Examples of powder rheometers include the Freeman FT4 powder rheometer, the Anton Paar Rheometer with a powder cell, and the Stable Microsystems Powder Flow Analyser. These devices
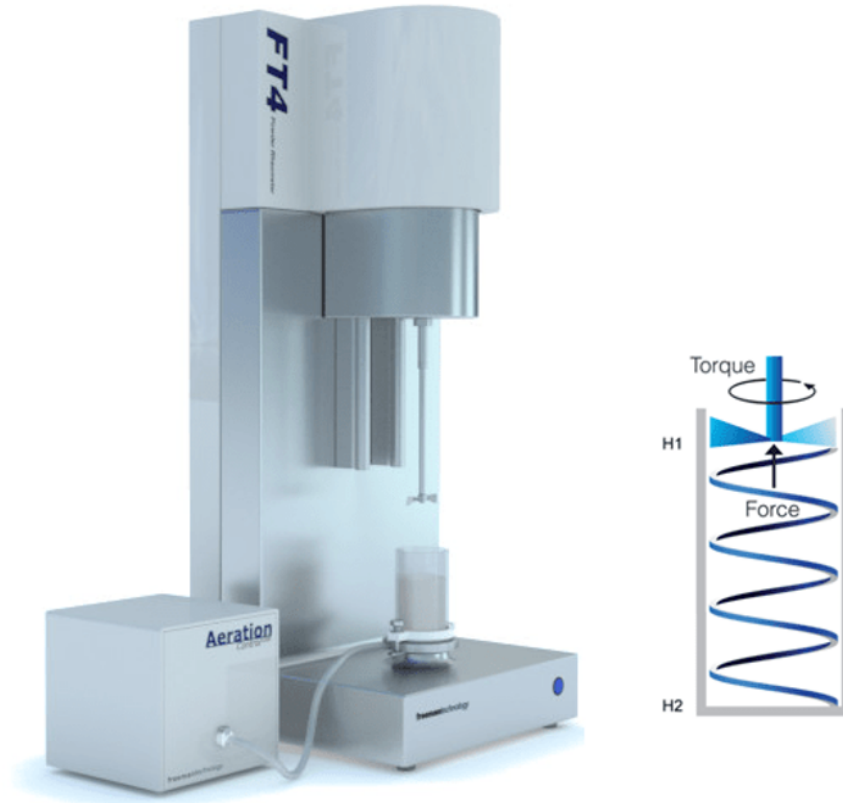
FIGURE 2.17. An example of a powder rheometer. This particular device is a Freeman FT4 powder rheometer [23].

also have the capability to perform shear cell testing (discussed in Chapter 8) as well as making compressibility and permeability measurements.

(2) Often the rotating blade is passed through the bed a couple of times to condition the bed prior to making energy measurements. This feature puts the powder in a more consistent state prior to making measurements, which is important for obtaining repeatable results. Other flowability measurement methods, such as the loosely poured bulk density or flow through an orifice, do not start with the powder in a well controlled, repeatable state.

(3) Powder rheometers can measure the powder behavior under various conditions. For example, the following indices have been proposed for testing the powder in various states of packing and at various speeds:

(a) Compaction Index (CI) := (the BFE for a consolidated sample)/BFE. The CI can range from nearly 1 to > 40, but $2 < CI < 6$ is more typical.

(b) Aeration Ratio (AR) := BFE/(the BFE for an aerated sample). The Aeration Ratio can vary widely, with values in the range $1.5 < AR < 1000$. An example of the BFE for various states of aeration and consolidation are shown in Figure 2.18.

(c) Specific Energy (SE) := the BFE per unit mass, but for the blade moving upward through the bed rather than downward. When moving upward through the bed, the powder is in an unconfined state since the blade acts to lift the powder and the free surface is unconfined.

(d) Flow Rate Index (FRI) := (the BFE at a blade speed 10 times smaller than the typical BFE test / the BFE at the normal blade speed. For an ideal powder: FRI = 1, indicating insensitivity to the strain rate induced by the blade. Some free flowing, coarse particles have FRI < 1. Most powders, and all cohesive powders, have FRI > 1 with typical values of $3 < FRI < 4$. At
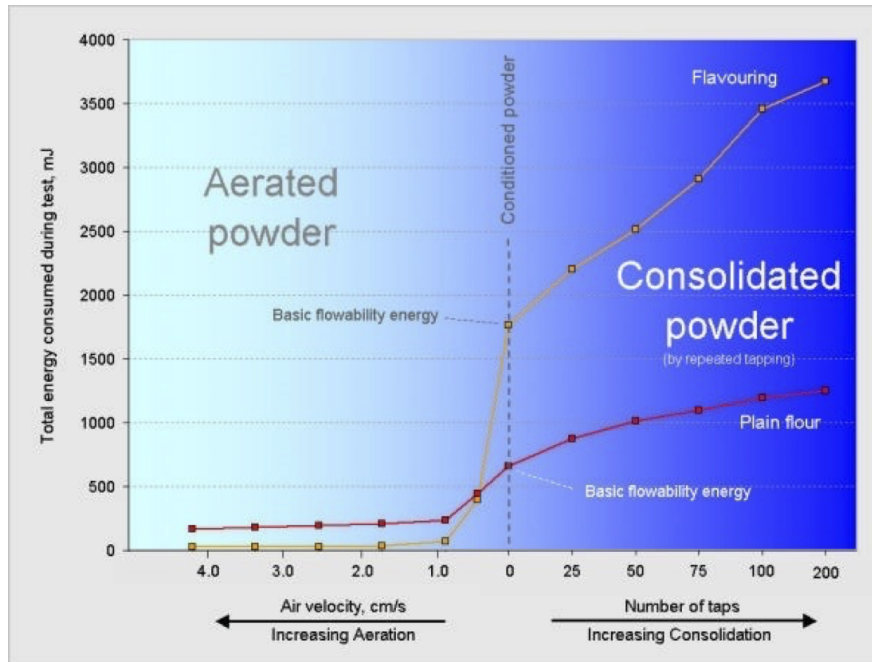
.

FIGURE 2.18. Measurements of the Basic Flowability Energy of flour and a flavoring powder in various states of aeration and consolidation [24]

slower speeds, the powder bed tends to be more consolidated and, thus, the resistance to the blade is greater. Figure 2.19 shows the strain rate sensitivity of glass beads of different size classes.

(e) Stability Index (SI) := the BFE after multiple transits through the bed / the BFE for the first transit. The stability index can examine if the powder properties change when being worked by the blade.

Note that other types of indices have also been proposed.

2.9. Summary

The following bullet points summarize the main points from this chapter.

- Powder flow indices are not fundamental properties of a powder. They don't fit into a modeling framework, but they are still useful in practice for ranking of flow behavior of materials and in empirical correlations. It is important to use/define an index with flow conditions similar to what occurs in practice.
- Common systems used in defining and measuring indices are typically defined at low pressures, consistent with free surface flow. Examples include:
  - various angles of repose,
  - the bulk density of poured and tapped powders,
  - the avalanching behavior in rotating drums,
  - flow through orifices, and
  - the energy required to rotate and move a stirring blade through the poweder.
- Another common system for quantifying powder flow behavior, the shear cell, is described in Chapter 8. Shear cells can measure properties that fit within a modeling framework, but the properties tend to be at pressures larger than those at a free surface.
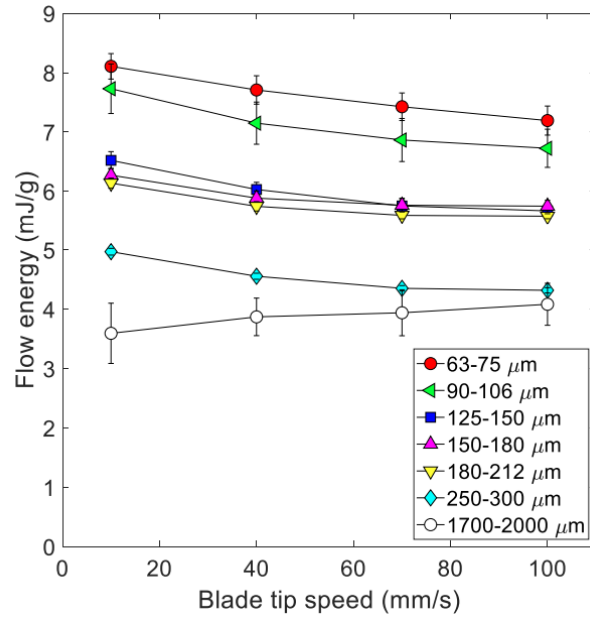
Figure 2.19. Measurements of the Basic Flowability Energy (downward blade movement) of glass beads of different size ranges [25].

2.10. Relevant Standards

- ASAE D274.1: Flow of Grain and Seeds Through Orifices
- ASTM D6393-14: Standard Test Method for Bulk Solids Characterization by Carr Indices
- ASTM D7481-18: Standard test methods for determining loose and tapped bulk densities of powders using a graduated cylinder.
- ASTM B0213-20: Standard test methods for flow rate of metal powders using the Hall flowmeter funnel
- USP 24 / NF 19: <616>Bulk and Tapped Density
- USP <1174>Powder flow.

Given the following experimental tapped bulk density data for Ti64 Grade 23 particles:

a. Fit the data using a curve of the form (Lumay et al., 2012),

$$\rho_{b,n} = \rho_{b,\infty} - \frac{\rho_{b,\infty} - \rho_{b,0}}{1 + \ln(1 + n/\tau)}$$

Report the values for $\rho_{b,0}$, $\rho_{b,\infty}$, and τ.

b. Fit the data using a curve of the form (Kawakita and Lüdde, 1971, re-arranged expression),

$$\rho_{b,n} = \rho_{b,0}\left[1 - \frac{nb\left(1 - \rho_{b,0}/\rho_{b,\infty}\right)}{nb + 1}\right]^{-1}$$

Report the values for $\rho_{b,0}$, $\rho_{b,\infty}$, and b.

c. Fit the data using a curve of the form (Philippe and Bideau, 2002),

$$\rho_{b,n} = \rho_{b,\infty} - \left(\rho_{b,\infty} - \rho_{b,0}\right)\exp\left[-\left(\frac{n}{n^*}\right)^m\right]$$

Report the values for $\rho_{b,0}$, $\rho_{b,\infty}$, n^*, and m.

d. On the same figure, plot the experimental data, each of the curve fits, and their asymptotic values.
e. Calculate the number of taps required to reach 99% of the asymptotic bulk density value.
f. Calculate the Hausner ratio and compressibility using each fit and provide a qualitative description of the expected flow behavior.

Note that it may help your fitting algorithm converge if estimates of the parameter values are provided as a starting point.

number of taps, n [-]	bulk density, ρ_b [g/cm³]
0	2.4038
5	2.4988
10	2.5259
15	2.5423
20	2.5530
25	2.5625
50	2.5915
100	2.6275
150	2.6499
200	2.6683
250	2.6827
300	2.6959
350	2.7056
400	2.7149
450	2.7215
500	2.7296

SOLUTION:
Using the Python code provided at the end of this solution, for the Lumay et al. (2012) fit,

$$\left(\rho_{b,0}, \rho_{b,\infty}, \tau\right) = \left(2.427\,\frac{g}{cm^3},\ 2.810\,\frac{g}{cm^3},\ 32.627\right).$$ (1)

$$n_{99} = 10099491.$$ (2)

Using these data, the Hausner ratio and compressibility values are,

$$HR = \frac{\rho_{b,\infty}}{\rho_{b,0}} \ => \ \boxed{HR = 1.16},$$ (3)

$$comp = 100\% * \left(\frac{\rho_{b,\infty}-\rho_{b,0}}{\rho_{b,\infty}}\right) \ => \ \boxed{comp = 13.6\%}.$$ (4)

For these Hausner ratio and compressibility values, the qualitative flow behavior is expected to be <u>good</u>.

For the Kawakita and Lüdde (1971) fit,

$$\left(\rho_{b,0}, \rho_{b,\infty}, b\right) = \left(2.439\,\frac{g}{cm^3},\ 2.725\,\frac{g}{cm^3},\ 0.033\right).$$ (1)

$$n_{99} = 317.$$ (2)

Using these data, the Hausner ratio and compressibility values are,

$$HR = \frac{\rho_{b,\infty}}{\rho_{b,0}} \ => \ \boxed{HR = 1.12},$$ (3)

$$comp = 100\% * \left(\frac{\rho_{b,\infty}-\rho_{b,0}}{\rho_{b,\infty}}\right) \ => \ \boxed{comp = 10.5\%}.$$ (4)

For these Hausner ratio and compressibility values, the qualitative flow behavior is expected to be <u>good</u>.

For the Philippe and Bideau (2002) fit,

$$\left(\rho_{b,0}, \rho_{b,\infty}, n^*, m\right) = \left(2.403\,\frac{g}{cm^3},\ 3.014\,\frac{g}{cm^3},\ 1179.2, 0.315\right).$$ (1)

$$n_{99} = 38973.$$ (2)

Using these data, the Hausner ratio and compressibility values are,

$$HR = \frac{\rho_{b,\infty}}{\rho_{b,0}} \ => \ \boxed{HR = 1.25},$$ (3)

$$comp = 100\% * \left(\frac{\rho_{b,\infty}-\rho_{b,0}}{\rho_{b,\infty}}\right) \ => \ \boxed{comp = 20.2\%}.$$ (4)

For these Hausner ratio and compressibility values, the qualitative flow behavior is expected to be <u>passible</u>.
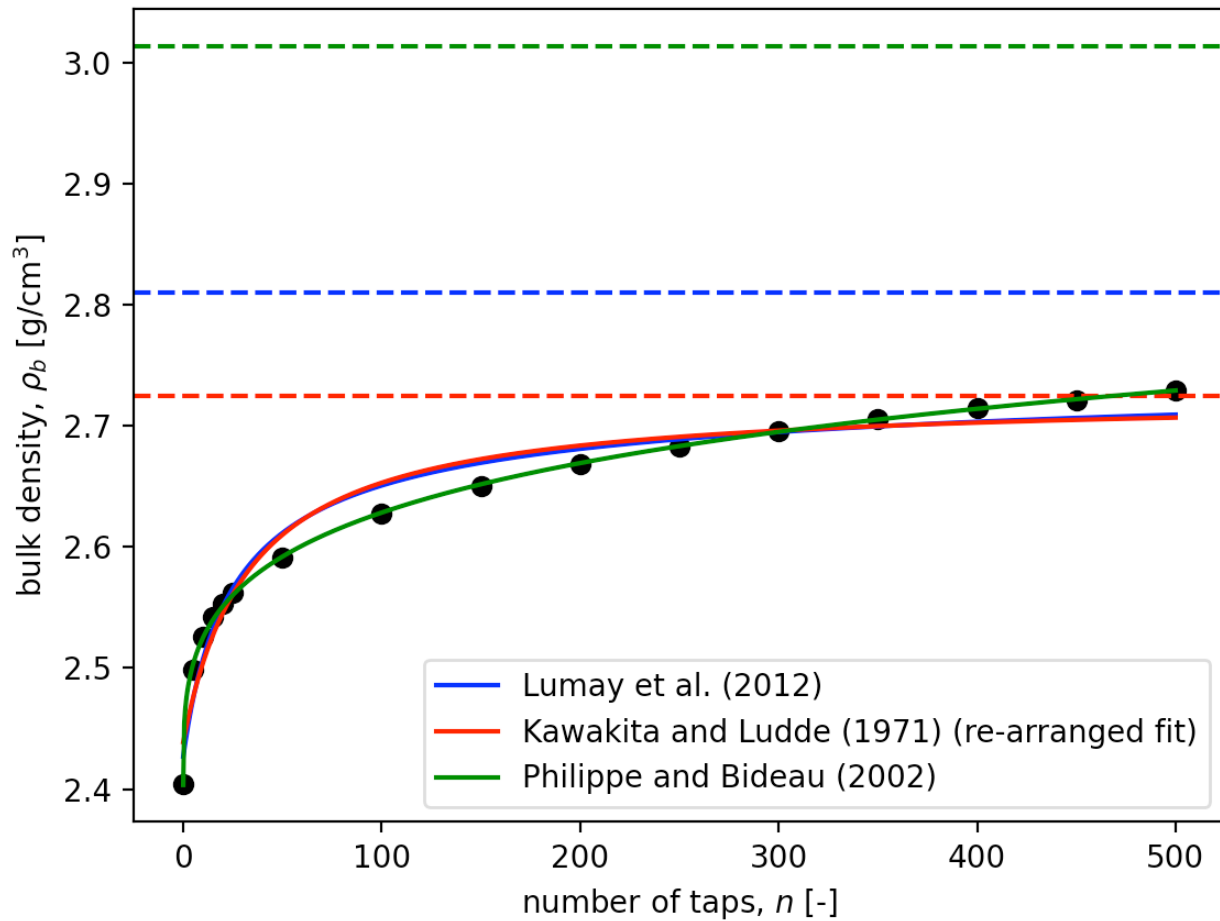
The Lumay (2012) and Kawakita and Lüdde (1971) fits give similar predictions over the data range, but don't fit the data very well. The Lumay asymptotic value is approximately 3% larger than the Kawakita and Lüdde value and, thus, the Hausner ratio and compressibility values are similar (both predict good flow behavior). The number of taps required to reach 99% of the asymptotic bulk density is vastly different, however. The Lumay fit requires over 10 million taps to reach this value while the Kawakita and Lüdde fit requires less than 400 taps.

The Philippe and Bideau (2002) fit is much better than the other two fits. The asymptotic bulk density is the largest of the three values and predicts passible flow behavior (consistent with the larger change in bulk density). The number of taps required to reach 99% of the asymptotic bulk density is approximately 39000.

The following plot is used to estimate the parameters for the Kawakita and Lüdde curve fit. When the data are plotted in the following form,

$$\frac{n}{C_n} = \frac{n}{a} + \frac{1}{ab}$$

where,

$$C_n = \frac{\rho_{b,n} - \rho_{b,0}}{\rho_{b,n}} \quad \text{and} \quad a = \frac{\rho_{b,\infty} - \rho_{b,0}}{\rho_{b,\infty}}$$

a straight line is expected with a slope of $1/a$ and intercept of $1/(ab)$. These values are used in the initial estimates in the fitting algorithm.
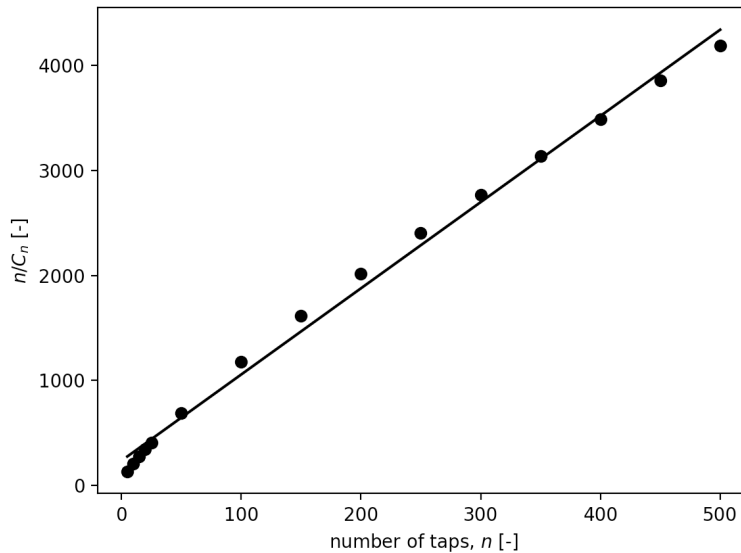
The following plot is used to estimate the parameters for the Philippe and Bideau curve fit. When the Philippe and Bideau fit is re-arranged in the following form

$$\ln \left[\ln \left(\frac{\rho_{b,\infty} - \rho_{b,0}}{\rho_{b,\infty} - \rho_{b,n}} \right) \right] = m \ln n - m \ln n^*$$

the data are expected to fall on a straight line with a slope of m and an intercept of $-m \ln n^*$. These values are used as initial estimates in the fitting algorithm.
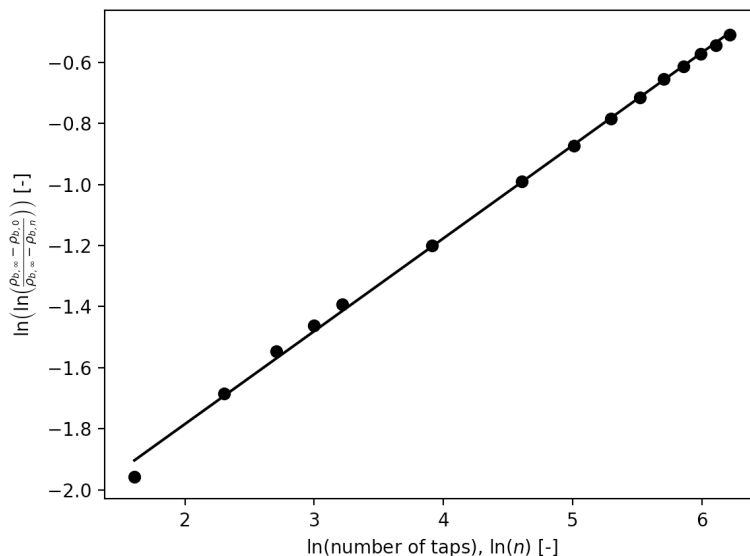
The following Python code was used to perform the fitting, calculations, and making the plots.

```
# PowderFlowIndices_01.py

import matplotlib.pyplot as plt
import numpy as np
from scipy.optimize import curve_fit

def LineFit(n, m, b):
    # A fit to a line with slope m and intercept b.
    return(m*n + b)

def Lumay_etal(n, rhob_0, rhob_inf, tau):
    # Curve fit of Lumay et al. (2012).
    # Returns rhob_n.
    return(rhob_inf - (rhob_inf - rhob_0)/(1 + np.log(1 + n/tau)))

def Kawakita_and_Ludde(n, rhob_0, rhob_inf, b):
    # Curve fit of Kawakita and Ludde (1971), re-arranged form.
    # Returns rhob_n.
    return(rhob_0/(1-(n*b*(1-rhob_0/rhob_inf))/(n*b+1)))

def Philippe_and_Bideau(n, rhob_0, rhob_inf, nstar, m):
    # Curve fit of Philippe and Bideau (2002).
    # Returns rhob_n.
    return(rhob_inf - (rhob_inf - rhob_0)*np.exp(-(n/nstar)**m))

def HR_FlowBehavior(HR):
    # A function to determine the qualitative flow behavior from the
    # Hausner ratio.
    if (HR <= 1.11):
        return('excellent')
    elif (HR <= 1.18):
        return('good')
    elif (HR <= 1.25):
        return('fair')
    elif (HR <= 1.33):
        return('passable')
    elif (HR <= 1.45):
        return('poor')
    elif (HR <= 1.59):
        return('very poor')
    else:
        return('exceedingly poor')

# The bulk density vs. number of taps data: [tap number, bulk
# density]. Units of bulk density are g/cm^3.
data = np.array([[0, 2.4038],
                 [5, 2.4988],
                 [10, 2.5259],
                 [15, 2.5423],
                 [20, 2.5530],
                 [25, 2.5625],
                 [50, 2.5915],
                 [100, 2.6275],
                 [150, 2.6499],
                 [200, 2.6683],
                 [250, 2.6827],
                 [300, 2.6959],
                 [350, 2.7056],
                 [400, 2.7149],
                 [450, 2.7215],
```

```
                        [500, 2.7296]])
n = data[:,0]  # number of taps
rhob = data[:,1]  # bulk density [kg/m^3]
n_fit = np.linspace(0, max(n), 1000) # used for the fits

# Plot the data.
plt.figure(1)
plt.plot(n, rhob, 'ko')  # plot the provided data.

# Fit the data using the Lumay et al. (2012) curve fit.  Provide
# initial estimates of the parameters to the fitting algorithm.
rhob_0_est = rhob[0]  # Using the first data point.
rhob_inf_est = 1.3*rhob[0]  # Assuming HR = 1.3.
tau_est = (rhob_inf_est - rhob_0_est)/((rhob[1]-rhob[0])/(n[1]-n[0]))
popt, pcov = curve_fit(Lumay_etal, n, rhob, p0=(rhob_0_est, rhob_inf_est, tau_est))
rhob_0, rhob_inf, tau = popt  # actual fitting parameters

print('Lumay et al. (2012):')
print('Estimated:  (rhob_0, rhob_inf, tau) = (%.3f g/cm^3, %.3f g/cm^3, %.3f)' %
(rhob_0_est, rhob_inf_est, tau_est))
print('Actual:  (rhob_0, rhob_inf, tau) = (%.3f g/cm^3, %.3f g/cm^3, %.3f)' % (rhob_0,
rhob_inf, tau))

# Calculate the number of taps required to reach 0.99 of the asymptotic value.
n_99 = tau*(np.exp(99-100*rhob_0/rhob_inf)-1)
print('n_0.99 = %d' % n_99)

# Print the Hausner ratio and compressibility.
HR = rhob_inf/rhob_0
comp = 100*((rhob_inf - rhob_0)/rhob_inf)
print('(HR, comp) = (%.3f, %.3f perc)' % (HR, comp))
print('Flow behavior is %s.' % HR_FlowBehavior(HR))
print('\n')

# Plot the fit.
plt.figure(1)
plt.plot(n_fit, Lumay_etal(n_fit, rhob_0, rhob_inf, tau), 'b-', label='Lumay et al.
(2012)')
plt.axhline(y=rhob_inf, color='blue', linestyle='--')  # asymptotic value

#####

# Fit the data using the re-arranged Kawakita and Ludde (1971) curve
# fit.  First, determine estimates for the parameters using the
# original form of the Kawakita and Ludde fit.
rhob_0_est = rhob[0]  # estimated initial bulk density
#  Calculate C_n. Note that the first data point is removed to avoid a NAN value.
C_n = np.divide((rhob[1:] - rhob_0_est), rhob[1:])
LHS = np.divide(n[1:], C_n)  # evaluate n/C_n
popt, pcov = curve_fit(LineFit, n[1:], LHS)  # fit the data
slope, intercept = popt
a = 1/slope
b_est = 1/(a*intercept)
rhob_inf_est = rhob_0_est/(1-a)

# Plot the intermediate figure used in estimating the parameters.
plt.figure(2)
plt.plot(n[1:], LHS, 'ko')
plt.plot(n[1:], LineFit(n[1:], slope, intercept), 'k-')
plt.xlabel('number of taps, $n$ [-]')
plt.ylabel('$n/C_n$ [-]')
```

```
# Now fit the data using the re-arranged Kawakita fit.
popt, pcov = curve_fit(Kawakita_and_Ludde, n, rhob, p0=(rhob_0_est, rhob_inf_est, b_est))
rhob_0, rhob_inf, b = popt  # actual fitting parameters
print('Kawakita and Ludde (1971) [re-arranged fit]:')
print('Estimated:  (rhob_0, rhob_inf, b) = (%.3f g/cm^3, %.3f g/cm^3, %.3f)' %
(rhob_0_est, rhob_inf_est, b_est))
print('Actual:  (rhob_0, rhob_inf, b) = (%.3f g/cm^3, %.3f g/cm^3, %.3f)' % (rhob_0,
rhob_inf, b))

# Calculate the number of taps required to reach 0.99 of the asymptotic value.
n_99 = 100/b*(0.99*rhob_inf/rhob_0-1)
print('n_0.99 = %d' % n_99)

# Print the Hausner ratio and compressibility.
HR = rhob_inf/rhob_0
comp = 100*((rhob_inf - rhob_0)/rhob_inf)
print('(HR, comp) = (%.3f, %.3f perc)' % (HR, comp))
print('Flow behavior is %s.' % HR_FlowBehavior(HR))
print('\n')

# Plot the fit.
plt.figure(1)
plt.plot(n_fit, Kawakita_and_Ludde(n_fit, rhob_0, rhob_inf, b), 'r-', label='Kawakita and
Ludde (1971) (re-arranged fit)')
plt.axhline(y=rhob_inf, color='red', linestyle='--')  # asymptotic value

#####

# Fit the data using the Philippe and Bideau (2002) curve fit.
# First find estimates for the fit parameters.
rhob_0_est = rhob[0]
rhob_inf_est = 1.3*rhob_0_est
LHS = np.log(np.log((rhob_inf_est - rhob_0_est)/(rhob_inf_est-rhob[1:])))  # avoid the
first point to avoid a NAN value
popt, pcov = curve_fit(LineFit, np.log(n[1:]), LHS)  # avoid the first point for n to
avoid a NAN value
slope, intercept = popt
m_est = slope
nstar_est = np.exp(-intercept/m_est)
# Plot the intermediate figure used in estimating the parameters.
plt.figure(3)
plt.plot(np.log(n[1:]), LHS, 'ko')
plt.plot(np.log(n[1:]), LineFit(np.log(n[1:]), slope, intercept), 'k-')
plt.xlabel(r'ln(number of taps), $\ln(n)$ [-]')
plt.ylabel(r'$\ln\left(\ln\left(\frac{\rho_{b,\infty}-\rho_{b,0}}{\rho_{b,\infty}-
\rho_{b,n}}\right)\right)$ [-]')

# Now fit the actual curve.
popt, pcov = curve_fit(Philippe_and_Bideau, n, rhob, p0=(rhob_0_est, rhob_inf_est,
nstar_est, m_est))
rhob_0, rhob_inf, nstar, m = popt  # actual fitting parameters

print('Philippe and Bideau (2002):')
print('Estimated:  (rhob_0, rhob_inf, nstar, m) = (%.3f g/cm^3, %.3f g/cm^3, %.3f, %.3f)'
% (rhob_0_est, rhob_inf_est, nstar_est, m_est))
print('Actual:  (rhob_0, rhob_inf, nstar, m) = (%.3f g/cm^3, %.3f g/cm^3, %.3f, %.3f)' %
(rhob_0, rhob_inf, nstar, m))

n_99 = nstar*(np.log(100*(1-rhob_0/rhob_inf)))**(1/m)
print('n_0.99 = %d' % n_99)
```

```
    # Print the Hausner ratio and compressibility.
    HR = rhob_inf/rhob_0
    comp = 100*((rhob_inf - rhob_0)/rhob_inf)
    print('(HR, comp) = (%.3f, %.3f perc)' % (HR, comp))
    print('Flow behavior is %s.' % HR_FlowBehavior(HR))
    print('\n')

    # Plot the fit.
    plt.figure(1)
    plt.plot(n_fit, Philippe_and_Bideau(n_fit, rhob_0, rhob_inf, nstar, m), 'g-',
    label='Philippe and Bideau (2002)')
    plt.axhline(y=rhob_inf, color='g', linestyle='--')  # asymptotic value

    # Add features to the plot.
    plt.figure(1)
    plt.xlabel(r'number of taps, $n$ [-]')
    plt.ylabel(r'bulk density, $\rho_b$ [g/cm$^3$]')
    plt.legend()  # show a legend

    plt.show()  # show the plots
```

Running the code gives the following output:
```
    >> python3 ./PowderFlowIndices_01.py
    Lumay et al. (2012):
    Estimated:  (rhob_0, rhob_inf, tau) = (2.404 g/cm^3, 3.125 g/cm^3, 37.955)
    Actual:  (rhob_0, rhob_inf, tau) = (2.427 g/cm^3, 2.810 g/cm^3, 32.627)
    n_0.99 = 10099491
    (HR, comp) = (1.158, 13.643 perc)
    Flow behavior is good.


    Kawakita and Ludde (1971) [re-arranged fit]:
    Estimated:  (rhob_0, rhob_inf, b) = (2.404 g/cm^3, 2.737 g/cm^3, 0.035)
    Actual:  (rhob_0, rhob_inf, b) = (2.439 g/cm^3, 2.725 g/cm^3, 0.033)
    n_0.99 = 317
    (HR, comp) = (1.117, 10.494 perc)
    Flow behavior is good.


    Philippe and Bideau (2002):
    Estimated:  (rhob_0, rhob_inf, nstar, m) = (2.404 g/cm^3, 3.125 g/cm^3, 2604.848, 0.304)
    Actual:  (rhob_0, rhob_inf, nstar, m) = (2.403 g/cm^3, 3.014 g/cm^3, 1179.250, 0.315)
    n_0.99 = 38974
    (HR, comp) = (1.254, 20.246 perc)
    Flow behavior is passable.
```

Bibliography

[1] T. Allen, Particle Size Measurement, 5th. London: Chapman & Hall, 1997, ISBN: 9780412729508.

[2] E. Heistand, Mechanics and Physical Principles for Powders and Compacts, 2nd. SSCI, West Lafayette, IN, 1991, ISBN: 9780967067124.

[3] A. Jenike, "Storage and flow of solids (Bulletin (123)," Bulletin of the University of Utah, vol. 53, no. 26, Nov. 1964.

[4] F. Lavoie, L. Cartilier, and R. Thibert, "New methods characterizing avalanche behavior to determine powder flow," Pharmaceutical Research, vol. 19, no. 6, pp. 887–893, 2002.

[5] R. Carr, "Evaluating flow properties of solids," Chemical Engineering Journal, vol. 72, pp. 163–168, 1965.

[6] Q. Li, V. Rudolph, B. Weigl, and A. Earl, "Interparticle van der waals force in powder flowability and compactibility," International Journal of Pharmaceutics, vol. 280, pp. 77–93, 2004.

[7] A. Schüussele and A. Bauer-Brandl, "Note on the measurement of flowability according to the european pharmacopoeia," International Journal of Pharmaceutics, vol. 257, pp. 301–304, 2003.

[8] I. Sinka, L. Schneider, and A. Cocks, "Measurement of the flow properties of powders with special reference to die fill," International Journal of Pharmaceutics, vol. 280, pp. 27–38, 2004.

[9] H. Hausner, "Friction conditions in a mass of metal powder," International Journal of Powder Metallurgy, vol. 3, pp. 7–13, 1967.

[10] D. Geldart, N. Harnby, and A. Wong, "Fluidization of cohesive powders," Powder Technology, vol. 37, no. 1, pp. 25–37, 1984.

[11] G. Lumay, F. Boshchini, K. Traina, et al., "Measuring the flowing properties of powders and grains," Powder Technology, vol. 224, pp. 19–27, 2012.

[12] J. Knight, C. Fandrich, C. Lau, H. Jaeger, and S. Nagel, "Density relaxation in a vibrated granular material," Physical Review E, vol. 51, no. 5, pp. 3957–3963, 1995.

[13] K. Kawakita and K. Lüdde, "Some considerations on powder compression equations," Powder Technology, vol. 4, no. 2, pp. 61–68, 1971.

[14] M. Yamashiro, Y. Yuasa, and K. Kawakita, "An experimental study on the relationships between compressibility, fluidity and cohesion of powder solids at small tapping numbers," Powder Technology, vol. 34, no. 2, pp. 225–231, 1983.

[15] P. Philippe and D. Bideau, "Compaction dynamics of a granular medium under vertical tapping," Europhysics Letters, vol. 60, no. 5, pp. 677–683, 2002.

[16] B. Hancock, K. Vukovinsky, B. Brolley, et al., "Development of a robust procedure for assessing powder flow using a commercial avalanche testing instrument," Journal of Pharmaceutical and Biomedical Analysis, vol. 35, pp. 979–990, 2004.

[17] E. Boothroyd, R. Doherty, R. Poynter, and M. Ticehurst, "Comparison of blend flow measured on the aeroflow with tablet weight uniformity," Journal of Pharmacy and Pharmacology, vol. 52S, no. 9, p. 174, 2000.

[18] K. Thalberg, D. Lindholm, and A. Axelsson, "Comparison of different flowability tests for powders for inhalation," Powder Technology, vol. 146, no. 3, pp. 206–213, 2004.

[19] A. Neveu, F. Francqui, and G. Lumay, "Measuring powder flow properties in a rotating drum," Measurement, vol. 200, no. 111548, 2022.

[20] The new rheometer for powder - GranuDrum, https://youtu.be/dn8jutBYdYI, Accessed: 2024-02-22.

[21]   http://203.147.186.54/html/Hanson/flodex_report.htm, Accessed: 2005-06-17.
[22]   A. Hlinak, Unit operations for dosage form manufacturing, Course notes for Purdue CHE 597P, 2005.
[23]   The impact of high-shear blenders on powder mixtures, https://www.azom.com/article.aspx?ArticleID=18738, 2019.
[24]   http://www.esum.com.cn/updata/Flowability.pdf.
[25]   M. Khala, "Characterising powder flow in dynamic processes," Ph.D. dissertation, University of Surrey, 2020.

CHAPTER 3

A Review of Stress and Mohr's Circles

The analysis of powder storage and flow involves the calculation of stresses, typically in two dimensional (planar and axi-symmetric) geometries. In preparation for these analyses, we'll review the following topics in this chapter:

- review of stress basics,
- two-dimensional Mohr's circles,
- principal stresses and principal planes, and
- plane stress and plane strain.

3.1. Review of Stress Basics

The reader is assumed to already have had some exposure to the concept of stress so only a brief review of some basic items is presented here. Any introductory text on strength of materials or solid mechanics will have further information on stresses, strains, and Mohr's circle analysis.

(1) A stress is a force magnitude per unit area and, thus, has example units of Pa, psi, psf, or bar.
(2) Stresses act on a surface and can be categorized as being either a normal stress or a tangential (aka shear) stress. Stresses are often written using the Greek symbol σ, although shear stresses are frequently written using a τ.
(3) The value of a stress at a point depends on the orientation of the (infinitesimally small) surface on which it acts. The directions are specified using the three ortho-normal components of the coordinate system, e.g., (x, y, z), (r, θ, z), or, more generally, $(1, 2, 3)$. The sign convention for stresses consists of two subscripts, e.g., σ_{ij}. The first subscript (i) identifies the direction of the unit normal for the surface on which the stress acts while the second subscript (j) identifies the direction of the stress acting on the surface. For example, the stress σ_{yz} is a stress acting on a surface with a normal vector pointing in the y direction with the stress pointing in the z direction. Normal stresses have repeated subscripts, e.g., σ_{zz} acts on a surface with a z unit normal with the stress pointing in the z direction, while shear stresses have different indices, e.g., τ_{23} acts on a surface with a normal in the 2 direction and points in the 3 direction. Examples of normal and shear stresses on a small cube of material are shown in Figure 3.1.
(4) In these notes, the sign convention for the stresses is as follows: (1) Positive normal stresses cause compression of the material element, i.e., act inward on the material element. (2) Positive shear stresses on a plane cause counter-clockwise rotation of the element about the plane's normal vector, e.g., positive shear stresses in the 1-2 plane cause counter-clockwise rotation about the 3 coordinate direction. Positive stresses on "positive" and "negative" cube faces are shown in Figure 3.1. This sign convention is often used in the soil mechanics literature.
(5) It can be shown from rotational equilibrium that the shear stresses using the sign convention stated in the previous note are anti-symmetric, i.e., $\tau_{ij} = -\tau_{ij}$ $(i \neq j)$.
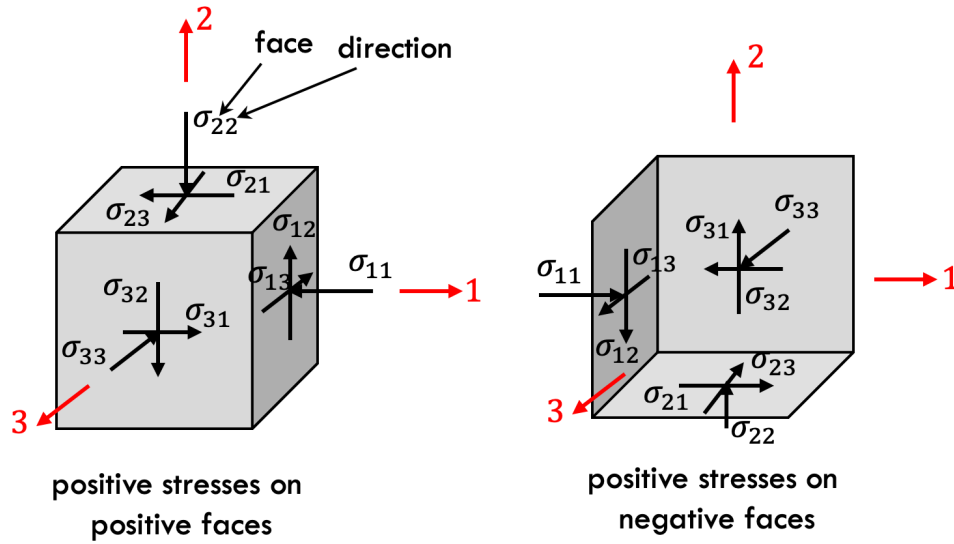
Figure 3.1. Left: Positively-oriented normal and shear stresses on cube faces with positively-oriented unit normals. Right: Positively-oriented normal and shear stresses on cube faces with negatively-oriented unit normals. The red arrows are the coordinate directions.
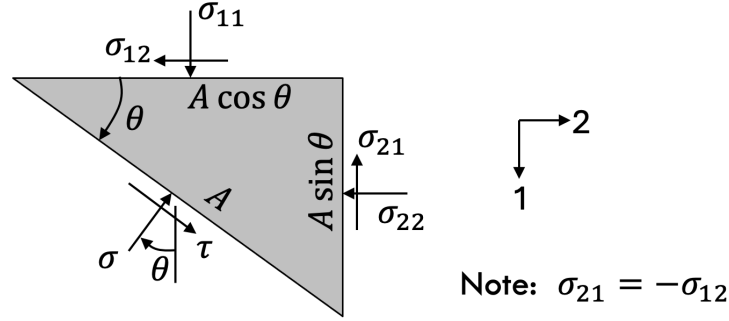
FIGURE 3.2. The wedge element used in the derivation of the two-dimensional Mohr's circle. A positive normal (σ) and shear (τ) stress are shown on the inclined surface.

3.2. The Mohr's Circle for a Two-dimensional Stress State

A Mohr's Circle is a graphical method for showing all of the normal and shear stress combinations at a point, depending on the orientation of the surface on which the stresses act. Although Mohr's circles can be generated for three-dimensional stress states, in these notes we'll only consider Mohr's circles for two-dimensional stress states.

Consider a force balance on the small wedge of material as shown in Figure 3.2. We wish to determine the normal and tangential stresses, σ and τ, acting on the surface area, A, which is inclined from the horizontal by an angle θ. Balancing forces on the element in the 1 and 2 directions, respectively,

$$\sum F_1 = 0 = (\sigma_{11})(A\cos\theta) - (\sigma_{21})(A\sin\theta) - (\sigma\cos\theta)(A) + (\tau\sin\theta)(A), \tag{3.1}$$

$$\sum F_2 = 0 = -(\sigma_{22})(A\sin\theta) - (\sigma_{12})(A\cos\theta) + (\sigma\sin\theta)(A) + (\tau\cos\theta)(A). \tag{3.2}$$

Now solve for σ and τ. First, multiply the first equation by $-\cos\theta$ and add it to the second equation multiplied by $\sin\theta$. Also divide through by the area A and note that $\sigma_{21} = -\sigma_{12}$,

$$\begin{aligned}0 = -\sigma_{11}\cos^2\theta &-\sigma_{22}\sin^2\theta - \sigma_{12}\sin\theta\cos\theta - \sigma_{12}\cos\theta\sin\theta \\ &+ \sigma\cos^2\theta + \sigma\sin^2\theta - \tau\sin\theta\cos\theta + \tau\cos\theta\sin\theta.\end{aligned} \tag{3.3}$$

Now make use of trigonometric identities and simplify,

$$\sigma = \sigma_{11}\cos^2\theta + \sigma_{22}\sin^2\theta + \sigma_{12}(2\sin\theta\cos\theta), \tag{3.4}$$

$$= \sigma_{11}\left[\frac{1}{2}(1+\cos(2\theta))\right] + \sigma_{22}\left[\frac{1}{2}(1-\cos(2\theta)\right] + \sigma_{12}\sin(2\theta), \tag{3.5}$$

$$\sigma = \left(\frac{\sigma_{11}+\sigma_{22}}{2}\right) + \left(\frac{\sigma_{11}-\sigma_{22}}{2}\right)\cos(2\theta)) + \sigma_{12}\sin(2\theta). \tag{3.6}$$

Similarly, multiply the first equation by $\sin\theta$ and add it to the second equation multiplied by $\cos\theta$. Also divide through by the area A, use $\sigma_{21} = -\sigma_{12}$, and make use of trigonometric identities,

$$\tau = -\sigma_{11}\cos\theta\sin\theta + \sigma_{22}\sin\theta\cos\theta + \sigma_{12}(\cos^2\theta - \sin^2\theta), \tag{3.7}$$

$$\tau = -\left(\frac{\sigma_{11}-\sigma_{22}}{2}\right)\sin(2\theta) + \sigma_{12}\cos(2\theta). \tag{3.8}$$

Combine the expressions for the normal and tangential stresses in the following manner,

$$\begin{aligned}\left[\sigma - \frac{1}{2}(\sigma_{11}+\sigma_{22})\right]^2 + \tau^2 =&\frac{1}{4}(\sigma_{11}-\sigma_{22})^2\cos^2(2\theta) + \sigma_{12}(\sigma_{11}-\sigma_{22})\sin(2\theta)\cos(2\theta) + \sigma_{12}^2\sin^2(2\theta) \\ &+ \frac{1}{4}(\sigma_{11}-\sigma_{22})^2\sin^2(2\theta) - \sigma_{12}(\sigma_{11}-\sigma_{22})\sin(2\theta)\cos(2\theta) + \sigma_{12}^2\cos^2(2\theta).\end{aligned} \tag{3.9}$$
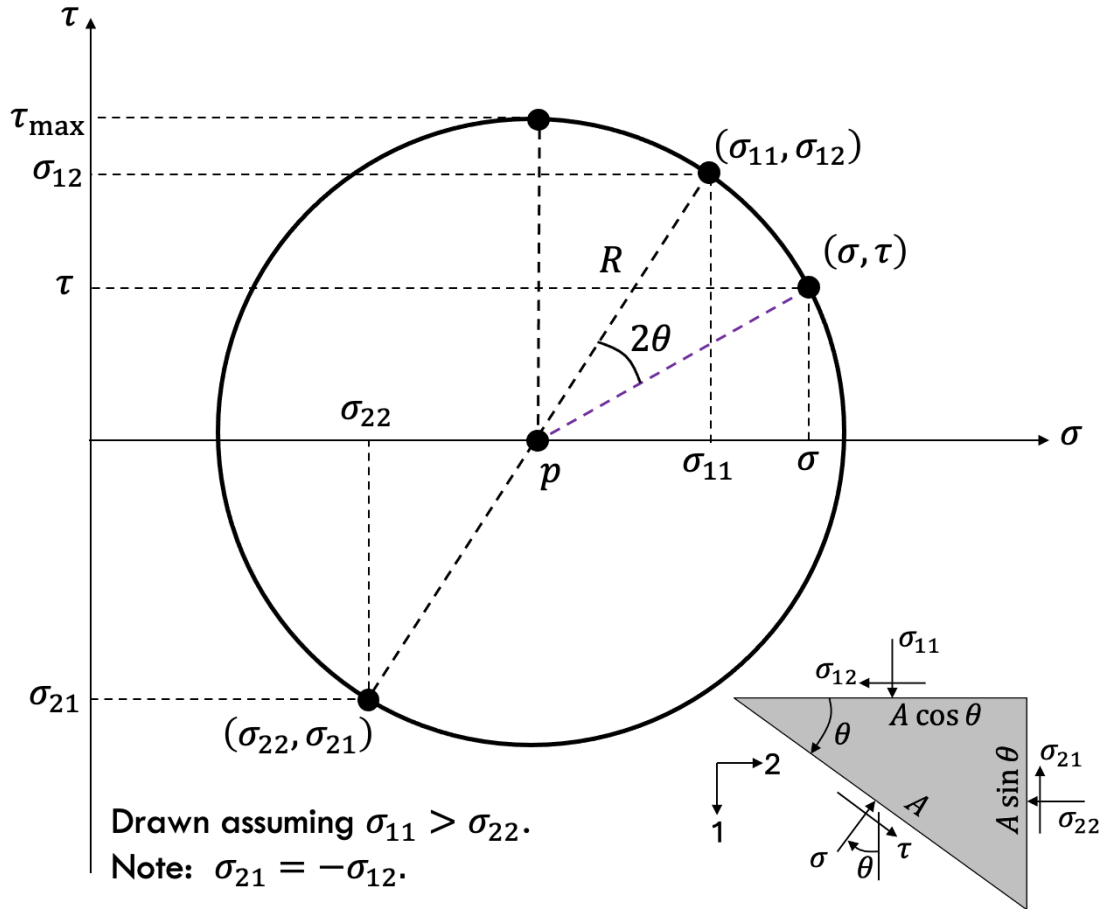
FIGURE 3.3. The Mohr's circle (left) for the two-dimensional stress state shown at the bottom right.

Simplifying gives,

$$\left[\sigma - \left(\frac{\sigma_{11} + \sigma_{22}}{2}\right)\right]^2 + \tau^2 = \left(\frac{\sigma_{11} - \sigma_{22}}{2}\right)^2 + \sigma_{12}^2. \tag{3.10}$$

This relation is the equation of a circle and is referred to as a Mohr's circle (Figure 3.3). The center and radius of the circle on a (σ, τ) plot are,

$$\text{center} = (p, 0) = \left(\frac{\sigma_{11} + \sigma_{22}}{2}, 0\right), \tag{3.11}$$

$$\text{radius} = R = \sqrt{\left(\frac{\sigma_{11} - \sigma_{22}}{2}\right)^2 + \sigma_{12}^2}. \tag{3.12}$$

It's important to recognize that the Mohr's circle shows all of the normal and shear stress combinations corresponding to different angles θ on the material element.

Notes:

(1) Mohr's circles are used extensively in the analysis of two-dimensional stress states. It's important for you to understand how to determine normal and shear stresses and relative orientations from a Mohr's circle.
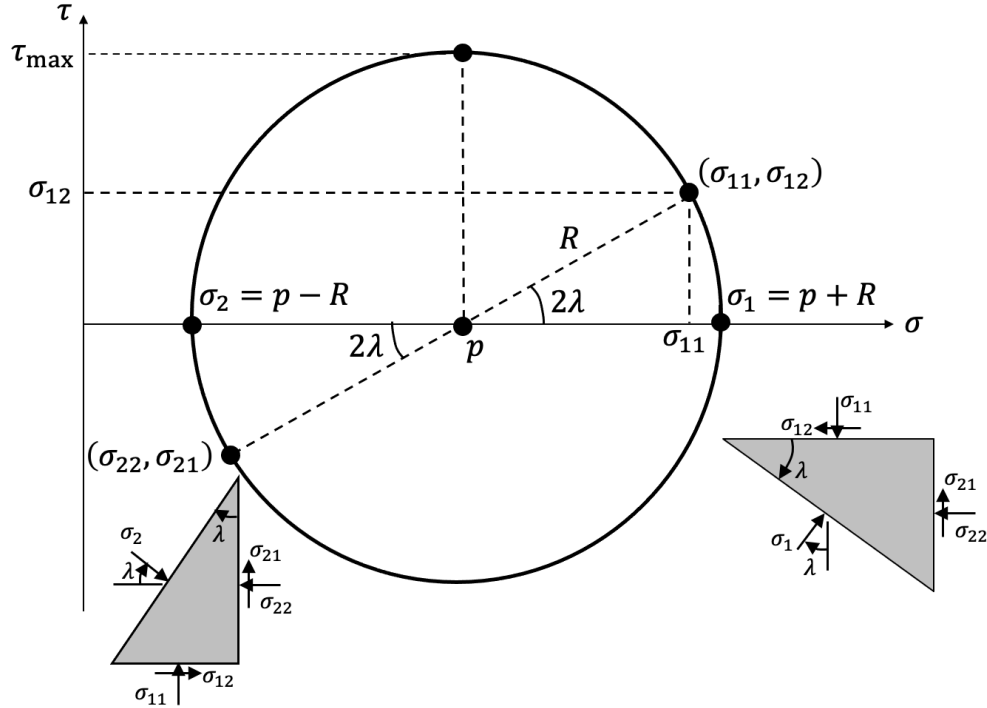
FIGURE 3.4. A Mohr's circle showing the location of the major and minor principal stresses.

(2) Angles in the Mohr's circle are oriented in the same relative direction as angles in the "real world", but are twice the magnitude. For example, in Figure 3.3 (bottom right) the plane on which (σ, τ) acts is rotated an angle θ (in the "real world") in the clockwise direction from the plane on which $(\sigma_{11}, \sigma_{12})$ acts. Thus, in the Mohr's circle, the stress state (σ, τ) is rotated an angle 2θ in the clockwise direction from the stress state $(\sigma_{11}, \sigma_{12})$. Note that since the stress states $(\sigma_{11}, \sigma_{12})$ and $(\sigma_{22}, \sigma_{21})$ are at right angles in the real world, they are located 180° apart in the Mohr's circle (and $\sigma_{21} = -\sigma_{12}$).

(3) The hydrostatic pressure, p, is defined as the average of the normal stresses,

$$p := \frac{\sigma_{11} + \sigma_{22}}{2}, \tag{3.13}$$

and $(p, 0)$ is the center of the Mohr's circle.

(4) Using the Mohr's circle, the magnitude of the maximum shear stress, $\tau_{\max}$, is equal to the Mohr's circle radius,

$$|\tau_{\max}| = R, \tag{3.14}$$

where R is given in Eq. (3.12).

It can be much easier to evaluate stresses and surface orientations using the geometry of a Mohr's circle rather than manipulating Eqs. (3.6) and (3.8).

3.3. Principal Stresses and Principal Planes

A principal plane is a plane on which there is only a normal stress, i.e., the tangential stress is zero on a principal plane. The normal stress on a principal plane is called a principal stress.

Notes:

(1) From the Mohr's circle (Figure 3.4) we observe that the maximum and minimum normal stresses are principal stresses. The values of the two principal stresses are,

$$\sigma_1 = p + R, \tag{3.15}$$

$$\sigma_2 = p - R, \tag{3.16}$$

where σ_1 is the larger of the two values, known as the <u>major principal stress</u>, and σ_2 is the smaller and is known as the <u>minor principal stress</u>.

(2) To find the orientation of the plane on which σ_1 acts relative to the plane on which $(\sigma_{11}, \sigma_{12})$ acts, we can use the Mohr's circle (Figure 3.4) to get the angle,

$$\tan(2\lambda) = \frac{\sigma_{12}}{\sigma_{11} - p}. \tag{3.17}$$

Thus, in the real world the major principal stress acts on a plane rotated an angle λ in the clockwise direction from the plane on which $(\sigma_{11}, \sigma_{12})$ acts. Similarly, the plane on which the minor principal stress acts is also at an angle λ (real world; 2λ on the Mohr's circle) in the clockwise direction from the plane on which the stress state $(\sigma_{22}, \sigma_{21})$ acts.

(3) The major and minor principal stresses are located $180°$ apart in the Mohr's circle and, thus, are $90°$ apart in the real world.

(4) Since the angle between the maximum shear stress and a principal stress is $90°$ in the Mohr's circle, it means that the maximum shear stress occurs on a plane that's oriented $45°$ from a principal plane in the real world.

A material element adjacent to a wall, inclined at an angle of $\alpha = 30°$ with respect to the vertical, is subject to the 2D stress state $(\sigma_{11}, \sigma_{22}, \sigma_{12}) = (10, 6, -1)$ kPa.

a.   Draw the 2D Mohr's circle corresponding to this stress state and identify the hydrostatic pressure and the stress states $(\sigma_{11}, \sigma_{12})$ and $(\sigma_{22}, \sigma_{21})$.

b.   Determine the normal and shear stresses (σ, τ) the wall exerts on the element using the Mohr's circle.

c.   Determine the major and minor principal stresses.
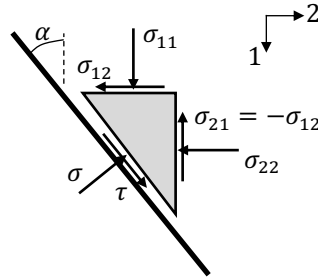
SOLUTION:

The hydrostatic pressure acting on the element (and the center of the Mohr's circle) is,

$$p = \tfrac{1}{2}(\sigma_{11} + \sigma_{22}) \implies p = 8 \text{ kPa}, \tag{1}$$

where $\sigma_{11} = 10$ kPa and $\sigma_{22} = 6$ kPa.

The radius of the Mohr's circle is,

$$R = \sqrt{\tfrac{1}{4}(\sigma_{11} - \sigma_{22})^2 + \sigma_{12}^2} \implies R = 2.24 \text{ kPa}, \tag{2}$$

where $\sigma_{12} = -1$ kPa.

The acute angle between the stress state $(\sigma_{22}, \sigma_{21})$ and the horizontal axis is (refer to the Mohr's circle),

$$\tan(2\lambda) = \frac{\sigma_{21}}{p - \sigma_{22}} \implies 2\lambda = 26.6°. \tag{3}$$

The angle between stress state $(\sigma_{22}, \sigma_{21})$ and stress state (σ, τ) is,

$$2\alpha = 60° \text{ (in the clockwise direction).} \tag{4}$$

From the Mohr's circle geometry,

$$\sigma = p - R\cos(2\lambda - 2\alpha) \implies \boxed{\sigma = 6.13 \text{ kPa}}, \tag{3}$$
$$\tau = R\sin(2\lambda - 2\alpha) \implies \boxed{\tau = -1.23 \text{ kPa}}. \tag{4}$$

The major and minor principal stresses are,

$$\sigma_1 = p + R \implies \boxed{\sigma_1 = 10.2 \text{ kPa}}, \tag{5}$$
$$\sigma_2 = p - R \implies \boxed{\sigma_2 = 5.76 \text{ kPa}}. \tag{6}$$

Note that the angle from the plane on which $(\sigma_{11}, \sigma_{12})$ acts and the major principal stress plane is,

$$2\lambda = 26.6°. \tag{7}$$

A plot of the Mohr's circle follows.
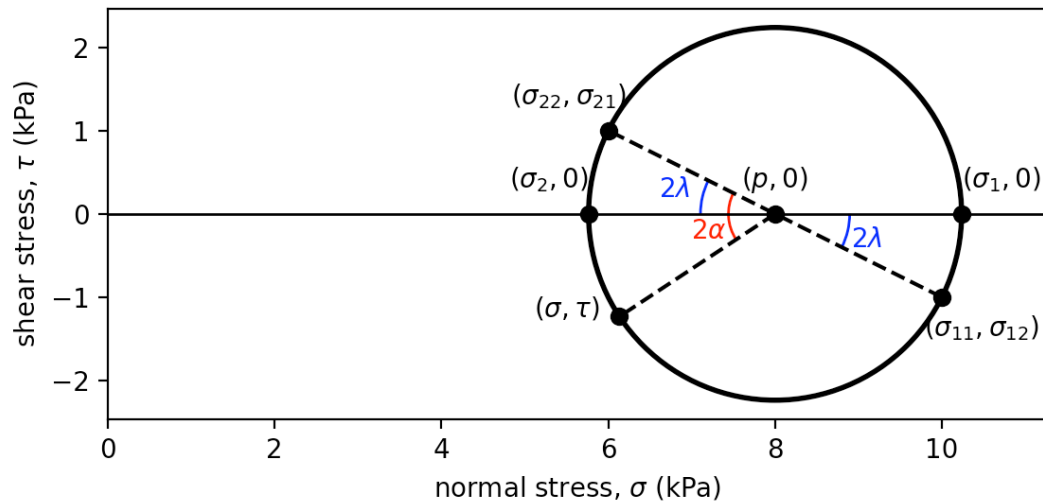
The following Python code was used to generate the Mohr's circle and perform the calculations.

```
# stress_03.py

import matplotlib.pyplot as plt
import matplotlib.patches as patches
import numpy as np

# The given stress state.
sigma_11 = 10  # kPa
sigma_22 = 6  # kPa
sigma_12 = -1  # kPa
alpha_deg = 30  # deg, real world wall angle from the vertical
sigma_21 = -sigma_12  # the other shear stress
alpha_rad = np.radians(alpha_deg)  # convert to radians

# Set up the plot.
figure, axes = plt.subplots()

# Determine the hydrostatic pressure and Mohr's circle radius.
p = 0.5*(sigma_11 + sigma_22)
R = np.sqrt(0.25*(sigma_11 - sigma_22)**2 + sigma_12**2)
print('p = %.3f kPa' % p)
print('R = %.3f kPa' % R)

# Find the real-world angle lambda between (sigma_22, sigma_21) and the horizontal axis.
lambda_rad = 0.5*np.arctan(sigma_21/(p - sigma_22))
lambda_deg = np.degrees(lambda_rad)
print('2*lambda = %.3f deg' % (2*lambda_deg))

# Determine the normal and shear stresses exerted by the wall.
sigma = p - R*np.cos(2*lambda_rad - 2*alpha_rad)
tau = R*np.sin(2*lambda_rad - 2*alpha_rad)
print('(sigma, tau) = (%.3f, %.3f) kPa' % (sigma, tau))

# Determine the major and minor principal stresses.
sigma_1 = p + R
sigma_2 = p - R
print('(sigma_1, sigma_2) = (%.3f, %.3f) kPa' % (sigma_1, sigma_2))

# Draw the Mohr's circle centered at (p, 0) with radius R.
MohrsCircle = patches.Circle((p, 0), R, fill=False, linewidth=2)
axes.set_aspect(1)  # Set the aspect ratio to one.
axes.add_patch(MohrsCircle)  # Add the Mohr's circle to the plot.

# Plot the location of the hydrostatic pressure.
```

```
    plt.plot(p, 0, color='k', marker='o')
    plt.annotate(r'$(p, 0)$', (p, 0), textcoords='offset points', xytext=(0,10), ha='center')  # Label the
    location.

    # Plot the location of (sigma_11, sigma_12).
    plt.plot(sigma_11, sigma_12, color='k', marker='o')
    plt.annotate(r'$(\sigma_{11}, \sigma_{12})$', (sigma_11, sigma_12), textcoords='offset points',
    xytext=(15,-15), ha='center')  # Label the location.

    # Plot the location of (sigma_22, sigma_21).
    plt.plot(sigma_22, sigma_21, color='k', marker='o')
    plt.annotate(r'$(\sigma_{22}, \sigma_{21})$', (sigma_22, sigma_21), textcoords='offset points',
    xytext=(-15,10), ha='center')  # Label the location.

    # Plot the locations of sigma_1 and sigma_2.
    plt.plot(sigma_1, 0, color='k', marker='o')
    plt.plot(sigma_2, 0, color='k', marker='o')
    plt.annotate(r'$(\sigma_1, 0)$', (sigma_1, 0), textcoords='offset points', xytext=(15,10),
    ha='center')  # Label the location.
    plt.annotate(r'$(\sigma_2, 0)$', (sigma_2, 0), textcoords='offset points', xytext=(-15,10),
    ha='center')  # Label the location.

    # Draw a line between the two given stress states.
    plt.plot([sigma_11, sigma_22], [sigma_12, sigma_21], color='k', linestyle='--')

    # Draw the angle 2*lambda from (sigma_22, sigma_21) and the minor principal stress.
    two_lambda_arc = patches.Arc([p, 0], 0.8*R, 0.8*R, angle=180-2*lambda_deg, theta1=0,
    theta2=2*lambda_deg, color='b', linestyle='-')
    axes.add_patch(two_lambda_arc)
    plt.annotate(r'$2\lambda$', (6.8, 0.2), textcoords='offset points', xytext=(0,0), ha='center',
    color='b')

    # Draw the angle 2*lambda from (sigma_11, sigma_12) and the major principal stres.
    two_lambda_arc = patches.Arc([p, 0], 0.8*R, 0.8*R, angle=-2*lambda_deg, theta1=0, theta2=2*lambda_deg,
    color='b', linestyle='-')
    axes.add_patch(two_lambda_arc)
    plt.annotate(r'$2\lambda$', (9.1, -0.4), textcoords='offset points', xytext=(0,0), ha='center',
    color='b')

    # Plot the location of (sigma, tau)
    plt.plot(sigma, tau, color='k', marker='o')
    plt.annotate(r'$(\sigma, \tau)$', (sigma, tau), textcoords='offset points', xytext=(-20,0),
    ha='center')  # Label the location.

    # Draw a radius from the Mohr's circle origin to (sigma, tau).
    plt.plot([p, sigma], [0, tau], color='k', linestyle='--')

    # Draw the angle from (sigma_22, sigma_21) to (sigma, tau).
    two_alpha_arc = patches.Arc([p, 0], 0.5*R, 0.5*R, angle=180-2*lambda_deg, theta1=0,
    theta2=2*alpha_deg, color='r', linestyle='-')
    axes.add_patch(two_alpha_arc)
    plt.annotate(r'$2\alpha$', (7.2, -0.3), textcoords='offset points', xytext=(0,0), ha='center',
    color='r')

    # Miscellaneous plot items.
    plt.xlabel('normal stress, $\\sigma$ (kPa)')  # Add the x-axis title.
    plt.ylabel('shear stress, $\\tau$ (kPa)')  # Add the y-axis title.
    plt.axhline(y=0, color='k', linewidth=1)  # Draw a horz line at y=0.
    plt.xlim([0, 1.1*(p+R)])  # Set the plot y-range.
    plt.show()  # Show the plot.
```

The output from the Python code is as follows:

```
>> python3 ./stress_03.py
p = 8.000 kPa
R = 2.236 kPa
2*lambda = 26.565 deg
(sigma, tau) = (6.134, -1.232) kPa
(sigma_1, sigma_2) = (10.236, 5.764) kPa
```

Sketch the Mohr's circle for the stress state in a material that is compressed by frictionless platens applying a normal stress σ. The sides of the material are unconfined. Identify the principal stresses and planes.
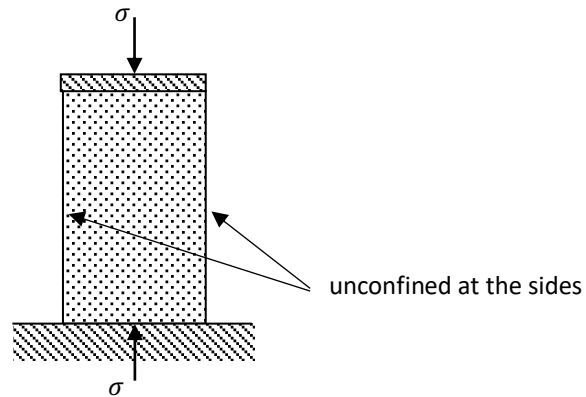
SOLUTION:
The Mohr's circle passes through the origin since no stresses are applied on the unconfined sides. The top/bottom and side surfaces are principal planes since no shear stresses are applied there.
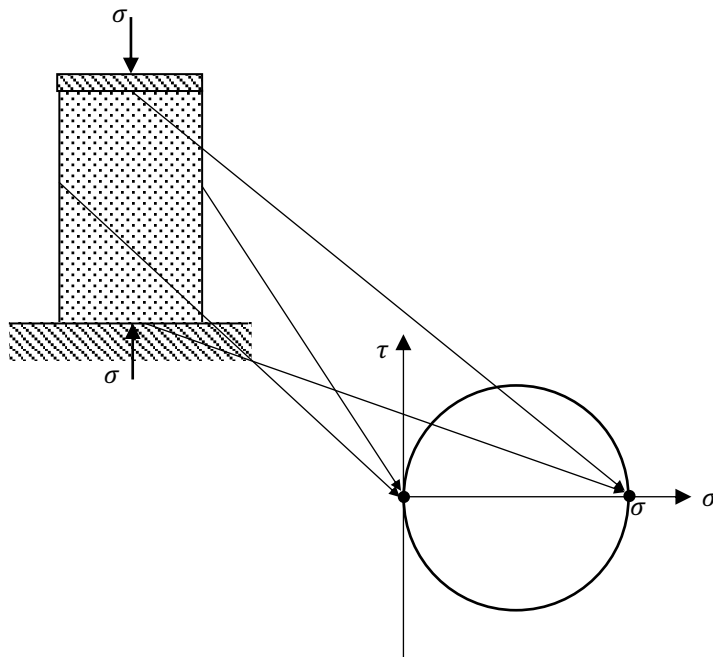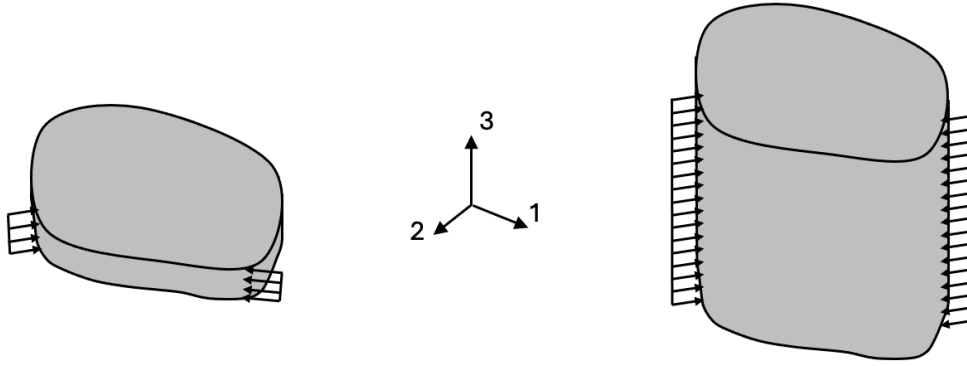
FIGURE 3.5. Sketches showing examples of plane stress (left) and plane strain (right).

3.4. Plane Stress and Plane Strain

Arbitrary stress states can be three-dimensional; however, there are two common geometries that result in two-dimensional stress states for which two-dimensional Mohr's circles can be used. When one dimension of an object is much thinner than the other two and the loading is uniform and in the plane of the object (Figure 3.5, left), then the object's stress state is two-dimensional since $\sigma_{33} = \sigma_{31} = \sigma_{32} = 0$. This two-dimensional stress state is called a <u>plane stress</u> state. The other common two-dimensional stress state occurs when the strain (i.e., relative deformation) in one direction of an object is constant (it could be zero) and loading is along the other two dimensions and uniform in the constant strain dimension (Figure 3.5, right). For this case, the normal stress in the constant strain dimension can be shown to be a function of the other two normal stresses, i.e., $\sigma_{33} = f(\sigma_{11}, \sigma_{22})$. In addition, $\sigma_{31} = \sigma_{32} = 0$. Thus, this state is also two-dimensional and is called a <u>plane strain</u> stress state. Many geometries of interest in powder handling can be approximated as being in plane strain and, thus, two-dimensional Mohr's circle can be be used in their analysis.

A wedge-shaped hopper and cylindrical bin are filled with material as shown in the following figures. Is the material in these geometries in a plane stress state, plane strain state, or neither?
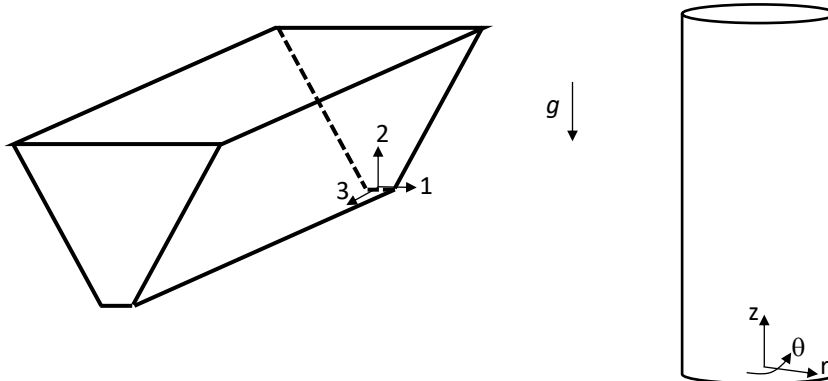
SOLUTION:
Wedge-shaped hopper: Because the geometry is <u>planar</u>, the material in the hopper is in a 2D <u>plane strain</u> condition. The following strain and stresses can be reasonably assumed: $\epsilon_{33} = 0$, $\sigma_{31} = \sigma_{32} = 0$.

Cylindrical bin: Because the geometry is <u>axi-symmetric</u>, the material in the hopper is in a 2D <u>plane strain</u> condition. The following strain and stresses can be reasonably assumed: $\epsilon_{\theta\theta} = 0$, $\sigma_{\theta z} = \sigma_{\theta r} = 0$.

3.5. Summary

The main points from this chapter are as follows:

(1) A stress is a force magnitude per unit area. On a given surface, normal and tangential stresses can be specified.

(2) The conventions used for stresses in these notes are:

    (a) The first subscript on the stress is the plane on which the stress acts and the second subscript is the orientation of the stress vector.

    (b) Positive normal stresses cause compression of the material element.

    (c) Positive shear stresses in a plane cause counter-clockwise rotation of the material element about the plane's normal vector, e.g., positive shear stresses acting in the 1-2 plane cause counter-clockwise rotation about the 3 coordinate direction.

(3) A Mohr's circle is a graphical representation of all of the normal and shear stress combinations on planes with different orientations. We'll only consider two-dimensional Mohr's circles in these notes since the geometries we'll consider can be modeled as two-dimensional. Angles in a Mohr's circle are twice their value in the real world but are in the same relative orientation. The advantage of using a Mohr's circle is that the Mohr's circle geometry and trigonometry can be easily used to find stresses and relative orientations rather than memorizing and manipulating more formulas.

(4) The tangential stress on a principal plane is zero. The corresponding normal stress is known as a principal stress. For a two-dimensional stress state, the larger of the two principal stresses is the major principal stress (σ_1) and the smaller is the minor principal stress (σ_2).

(5) Two frequently-assumed two-dimensional stress states are plane stress and plane strain. Plane stress typically occurs for thin objects with loading occurring in the plane. Plane strain occurs when one dimension of the object is much larger than the other two and loading occurs along the object's sides and is uniform in the long dimension.

CHAPTER 4

The Ideal Coulomb Material Model

The ideal Coulomb material model is a simple model for describing the yielding behavior of granular materials. Although it doesn't capture all of the complexities of real materials, it is still a good enough approximation to give useful predictions.

4.1. Features of the Ideal Coulomb Material Model

In an ideal Coulomb material, prior to yielding the material deforms elastically, for example, as a linearly elastic, isotropic solid. When the stress state acting on a material element (σ, τ) reaches a critical value, the material yields (aka fails or flows) plastically. For an ideal Coulomb material in two dimensions, yielding occurs when,

$$|\tau| = |\mu\sigma + c|, \tag{4.1}$$

where μ is the <u>internal friction coefficient</u> and c is the <u>(bulk) cohesion</u> of the material. An example of this yield locus in the $\sigma - \tau$ plane is shown in Figure 4.1.

Notes:

(1) The name "Mohr-Coulomb" model is often used interchangeably with the "ideal Coulomb" model.
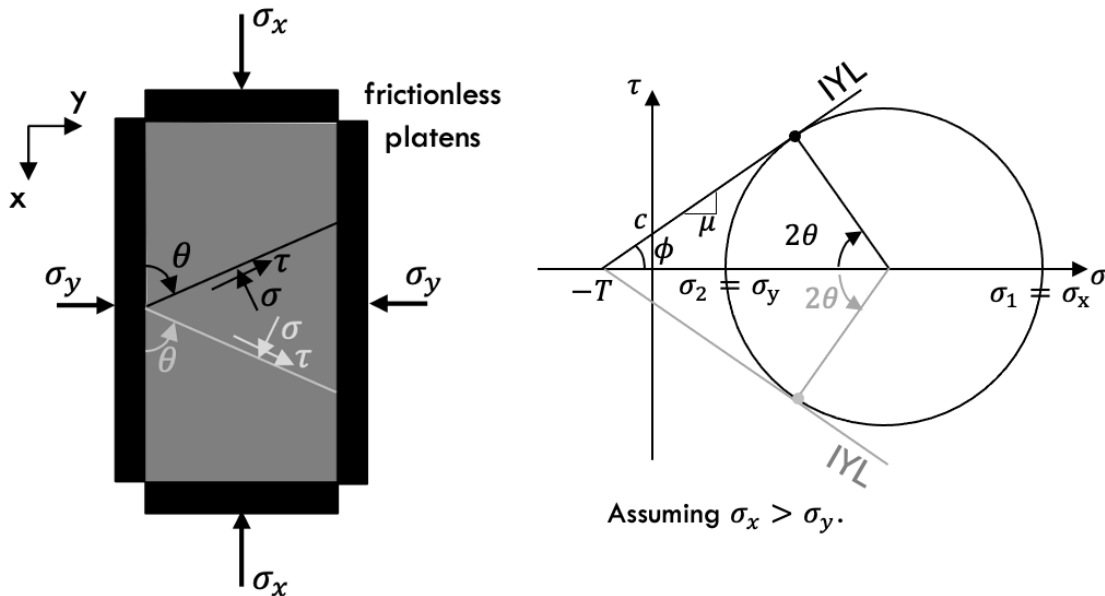
FIGURE 4.1. (left) A schematic showing a material subject to a two-dimensional, uniform stress state and the surfaces on which yielding occurs. (right) The corresponding Mohr's circle with the internal yield locus (IYL), internal friction coefficient (μ), cohesion (c), internal friction angle (ϕ), and tensile strength (T).

(2) Yielding in a real material typically occurs within a <u>shear band</u>, which is approximately 10 particle diameters thick. We model this shear band as being infinitesimally thin.

(3) In the ideal Coulomb material model, the shear stress is independent of the strain rate (speed) and shear strain (displacement) when yielding.

(4) Yielding occurs on two planes within the material; however, the extent of yielding need not be the same on both.

(5) The Mohr's circle for the material's stress state can only exist within the yield lines (no yielding, elastic deformation) or can be tangent to the yield lines (yielding at the intersection point). The Mohr's circle cannot go beyond the yield lines.

(6) A <u>cohesionless material</u> is one for which $c = 0$.

(7) The <u>internal friction angle ϕ</u> is related to the internal friction coefficient via,

$$\mu = \tan\phi. \tag{4.2}$$

(8) The <u>tensile strength</u> of the material, T (refer to Figure 4.1) is the maximum normal stress in tension that the material can withstand before yielding. Note that,

$$T = \frac{c}{\tan\phi}. \tag{4.3}$$

.

(9) In real materials, the internal yield locus is seldom a straight line and can show significant curvature as $\sigma \to 0$. Many IYL data are fit well using the <u>Warren-Spring Equation</u> (Figure 4.2),

$$\left(\frac{\tau}{c}\right)^n = \left(\frac{\sigma}{T}\right) + 1, \tag{4.4}$$

where c is the cohesion, T is the tensile strength, and $n \geq 1$ is a fitting parameter for the yield locus curvature. This expression simplifies to the ideal Coulomb material yield locus when $n = 1$. Note that the slope at $\tau = 0$ is infinite when $n > 1$ as shown by differentiating the previous equation,

$$\frac{n\tau^{n-1}d\tau}{c^n} = \frac{d\sigma}{T}, \tag{4.5}$$

$$\frac{d\tau}{d\sigma} = \left(\frac{c^n}{nT}\right)\frac{1}{\tau^{n-1}}, \tag{4.6}$$

$$\lim_{\tau \to 0, n > 1}\left(\frac{d\tau}{d\sigma}\right) \to \infty. \tag{4.7}$$

A linear yield locus is still frequently used in analytical work because of its simplicity and because many problems of interest, such as the stresses in large bins, are at normal stresses much greater than zero where the IYL curvature is negligible. However, if one is modeling free surface flows which have small normal stresses, then one should be mindful of the IYL curvature.

(10) Define the <u>effective angle of internal friction, δ</u>, as the angle of the Mohr's circle tangent line passing through the origin (Figure 4.3). This line is called the <u>Effective Yield Locus (EYL)</u>. The effective angle of internal friction can be related to the major and minor principal stresses,

$$p = \frac{1}{2}\left(\sigma_1 + \sigma_2\right), \tag{4.8}$$

$$R = \frac{1}{2}\left(\sigma_1 - \sigma_2\right), \tag{4.9}$$

$$\sin\delta = \frac{R}{p}, \tag{4.10}$$

$$\sin\delta = \frac{\sigma_1 - \sigma_2}{\sigma_1 + \sigma_2}. \tag{4.11}$$

Alternately, the previous equation may be re-arranged to give,

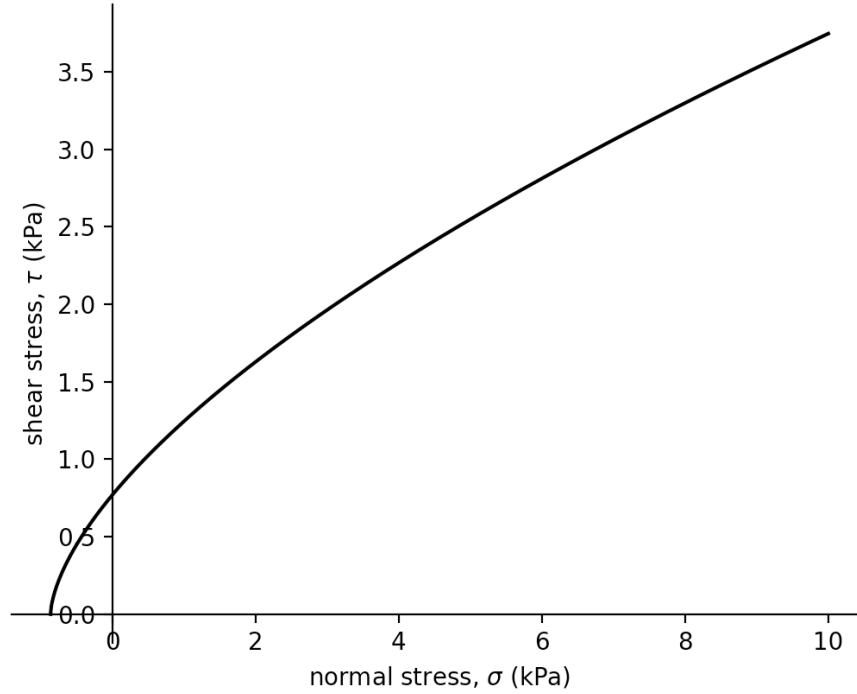$$\frac{\sigma_1}{\sigma_2} = \frac{1 + \sin\delta}{1 - \sin\delta}. \tag{4.12}$$

FIGURE 4.2. Internal yield loci following the Warren-Spring Equation (Eq. (4.4)). For this plot, $n = 1.6$, $c = 0.768$ kPa, and $T = 0.860$ kPa.
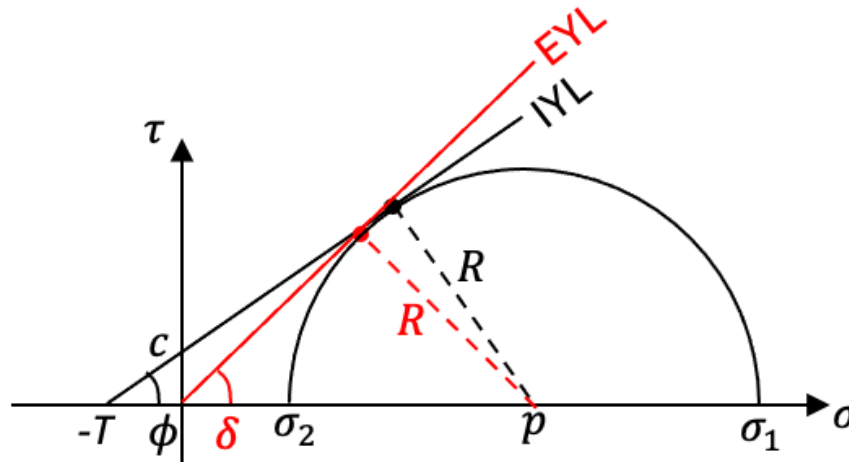

FIGURE 4.3. A Mohr's circle showing the effective yield locus (EYL) compared to the internal yield locus (IYL).

(a) For a cohesionless material, the internal friction angle and effective angle of internal friction are identical, i.e., $\phi = \delta$. For cohesive materials, $\delta > \phi$ since, from the geometry shown in Figure 4.3,

$$\sin \phi = \frac{R}{p + T} \qquad \text{and} \qquad \sin \delta = \frac{R}{p}, \tag{4.13}$$

Material	ϕ (deg)
wheat	15 - 30
wheat flour	28 - 42
granulated sugar	30 - 40
quartz sand	33 - 40
alumina	27 - 44
fly ash	25 - 35

TABLE 4.1. Typical values for the internal friction angle (ϕ). Data from McGlinchey [1].

Metal Powders	δ (°)	σ_{sd} (°)	δ_{min} (°)	δ_{max} (°)	ϕ (°)	σ_{sd} (°)	ϕ_{min} (°)	ϕ_{max} (°)
Stainless Steel 316L	28.6	0.5	28.0	39.7	28.5	0.4	27.8	29.3
Zinc powder	29.9	0.3	29.3	30.7	29.6	0.5	28.8	30.7
Aluminum powder	32.9	1.2	31.4	35.2	32.9	1.2	31.4	35.2
Tin powder	37.8	2.8	33.8	42.2	36.1	1.8	33.3	38.8
Copper powder	39.1	0.7	38.2	40.6	38.1	0.5	37.4	39.1
Manganese powder	39.4	0.4	38.9	40.6	38.6	0.6	37.9	40.4
Bronze powder	39.9	0.5	39.0	40.7	38.7	0.7	37.6	40.1
Iron powder	40.0	0.7	39.0	41.6	39.4	0.5	38.7	40.7
Titanium powder	42.9	0.9	41.4	45.1	41.9	0.7	40.6	43.7
Ferrite powder	48.1	1.6	45.8	51.1	39.1	0.6	37.6	40.0

TABLE 4.2. Typical values for the effective angle of internal friction (δ), standard deviation of δ measurements (σ_{sd}), minimum value of δ (δ_{min}), maximum value of δ (δ_{max}), internal friction angle (ϕ), standard deviation of ϕ measurements (σ_{sd}), minimum value of ϕ (ϕ_{min}), and maximum value of ϕ (ϕ_{max}). Data are for a variety of metal powders. Table from Zegzulka et al. [2].

Material Type	Number of Samples (N)	10th	50th	90th	Minimum	Maximum	Mean
All materials	123	40.0	46.0	59.6	35.0	74.0	47.8
Active blends	25	40.0	46.0	61.2	38.0	70.0	48.7
Active granulations	40	40.0	47.0	52.0	39.0	55.0	46.8
Active pharmaceutical ingredients	10	45.8	52.0	65.9	35.0	74.0	54.6

10th, 50th, and 90th are percentiles of the population.

TABLE 4.3. Typical values for the effective angle of internal friction (δ) for different types of pharmaceutical material. Table from Hancock [3].

$$\sin \delta = \left(1 + \frac{T}{p}\right) \sin \phi. \tag{4.14}$$

Note that for a cohesive material, δ has a large value when the hydrostatic pressure is small, but asymptotes to the internal friction angle for large pressures.

(11) Typical values for the internal friction angle (ϕ) and effective angle of internal friction (δ) are shown in Tables 4.1 – 4.3. McGlinchey [1] states, "Angles of internal friction typically range from about 20° for rounded objects to about 50° for angular products...and cohesion varies between extremely small values for coarse granular products to values of about 50 kPa for a stiff clay."

4.2. The Wall Yield Locus

In addition to yielding internally, a particulate material may also yield against a wall. For an ideal Coulomb material, the wall yield locus (WYL) can be written as,

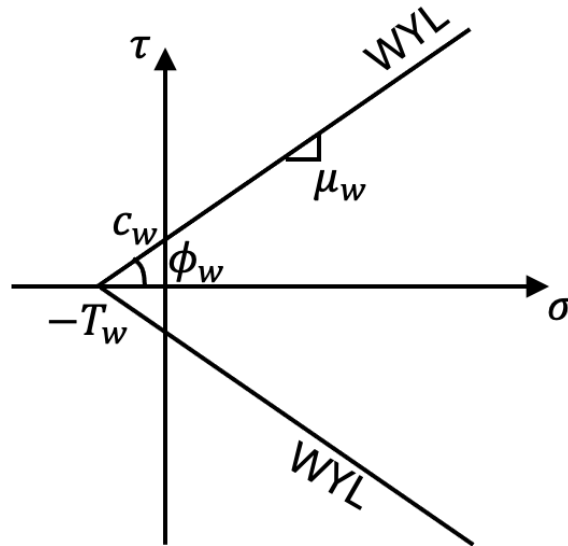$$|\tau| = |\mu_w \sigma + c_w|, \tag{4.15}$$

FIGURE 4.4. An example wall yield locus (WYL). The quantity μ_w is the wall friction coefficient, ϕ_w is the wall friction angle, c_w is the wall adhesion, and T_w is the wall tensile strength.

where μ_w is the material-wall friction coefficient and c_w is the adhesion between the material and wall. Figure 4.4 shows an example wall yield locus.

Notes:

(1) The wall friction coefficient is related to the <u>wall friction angle, ϕ_w</u>, via,

$$\mu_w = \tan \phi_w \tag{4.16}$$

(2) A common, alternate approach to quantifying the wall yield locus is to measure the wall friction angle, ϕ_w, from the origin of the $\sigma - \tau$ plot (Figure 4.5), similar to how the effective angle of internal friction is defined. Using this approach, the wall friction angle decreases as the normal stress increases, as shown in Figure 4.6.

(3) The internal yield locus (IYL) and wall yield locus (WYL) are not the same. The IYL sets the yield limit on any plane within the material, i.e., the Mohr's circle for any material element cannot extend beyond the IYL. The WYL sets the yield limit only on the wall plane for a material element adjacent to the wall. The Mohr's circle can extend beyond the WYL for planes not aligned with the wall.

(4) For a material element next to a wall (Figure 4.7), if the wall plane is aligned with points A, A', B, or B', then yield will occur at the wall. Wall planes oriented between AA' and BB' won't yield since they lie within the WYL (green arcs in the figure). It's not possible for the wall plane to have an orientation between AB or A'B' (red arcs) for a material element in static equilibrium.

(5) Since the Mohr's circle cannot extend beyond the IYL, a WYL outside of the IYL envelope can be interpreted as yielding in the material against a very thin layer of material stuck to the wall (Figure 4.8). Thus, effectively the WYL cannot extend beyond the IYL. We call a wall for which the WYL and IYL are the same a <u>fully rough wall</u> and $\phi_w = \phi$ and $c_w = c$.
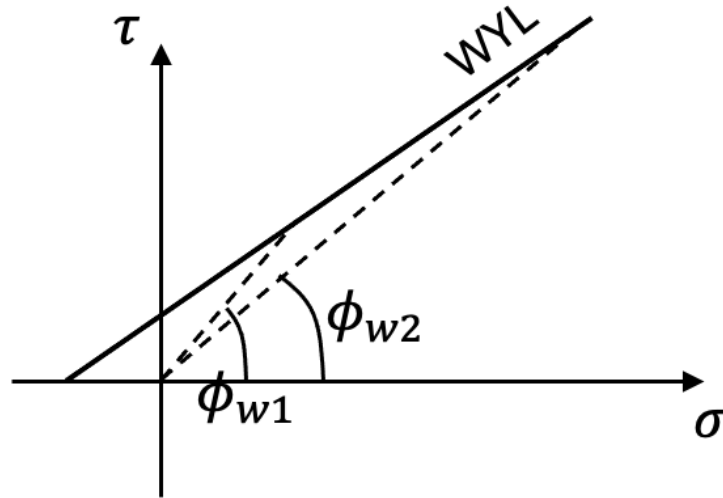
FIGURE 4.5. A common, alternate approach to presenting the wall yield locus is to measure the wall friction angle from the origin.
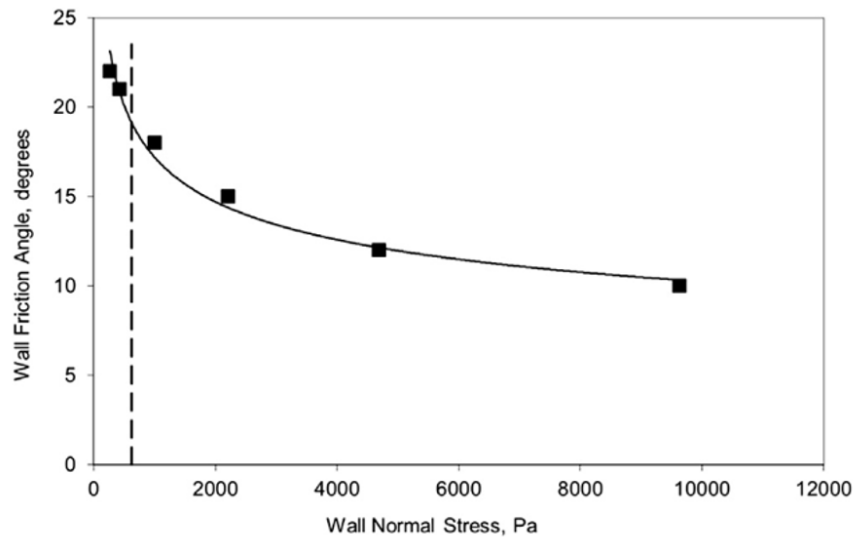
FIGURE 4.6. Measured wall friction angles (ϕ_w) as a function of wall normal stress (σ) for a typical active pharmaceutical powder blend. The vertical dashed line is a normal stress of 622 Pa, for which the wall friction angle is 19.1°. Wall friction angles for pharmaceutical powders against stainless steel 2B surfaces at 622 Pa are typically in the range $10° < \phi_w < 30°$ [3].

4.3. Active and Passive Stress States

Consider a block on a frictional inclined plane as shown in Figure 4.9. A force P is applied to the block and acts in the uphill direction. The block will remain static as long as,

$$\sum F_{\text{on plane}} = 0 = P - mg\sin\theta - \mu(mg\cos\theta) \qquad \text{(block about to slip uphill)}, \qquad (4.17)$$

$$\sum F_{\text{on plane}} = 0 = P - mg\sin\theta + \mu(mg\cos\theta) \qquad \text{(block about to slip downhill)}, \qquad (4.18)$$
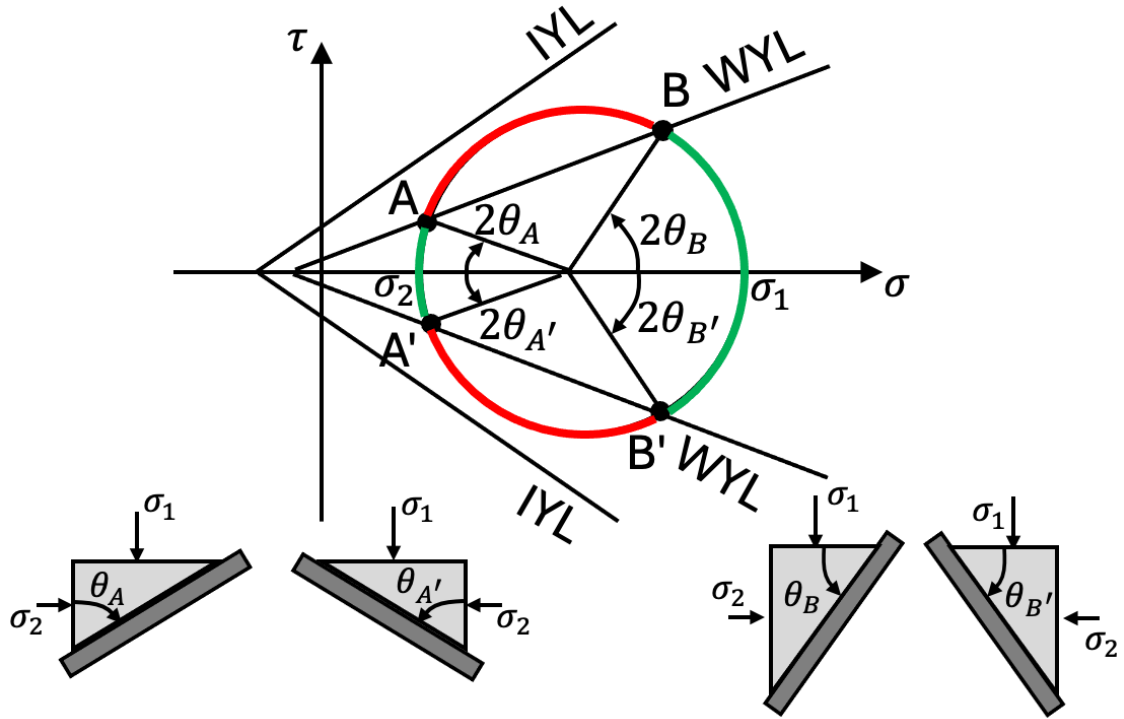
FIGURE 4.7. A Mohr's circle for a material element adjacent to the wall. For this element, the material does not yield internally since the Mohr's circle doesn't touch the IYL. If the wall plane has an angle coinciding with points A, B, A', or B', then the element will yield against the wall. If the wall plane has an angle between AA' or BB' (green arcs), then the element will not yield against the wall. Wall angles in the range AB or A'B' (red arcs) are not possible.
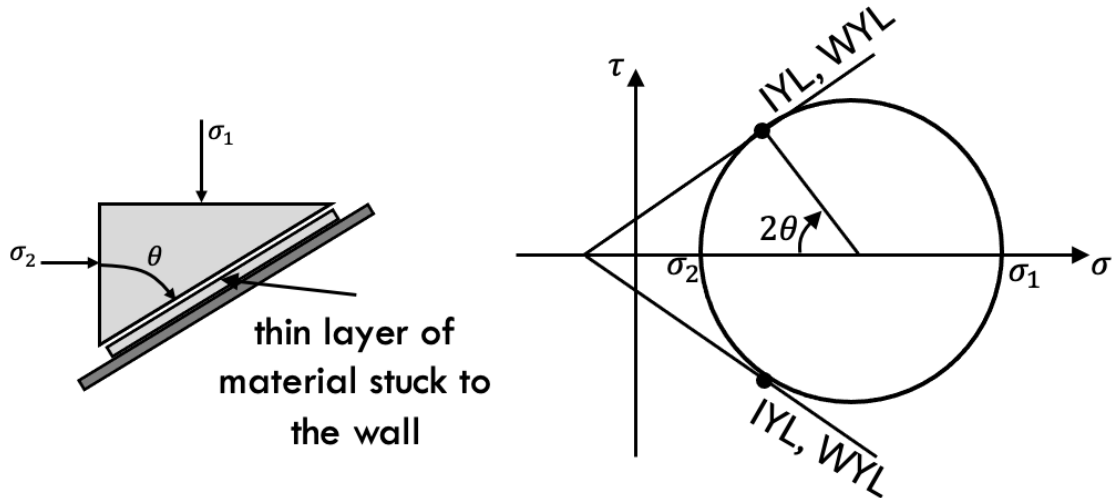
FIGURE 4.8. (left) An illustration of a fully rough wall where a thin layer of material is stuck to the wall and the material fails internally adjacent to the wall. (right) A Mohr's circle for a fully rough wall.
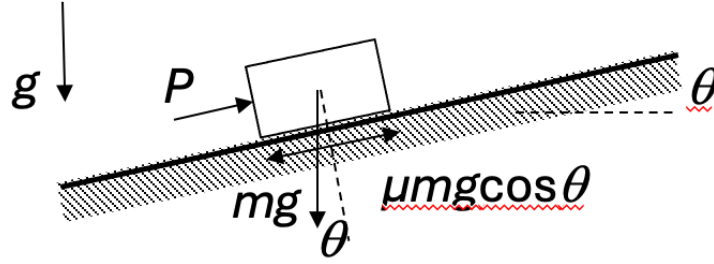
FIGURE 4.9. A static block on a frictional inclined plane.
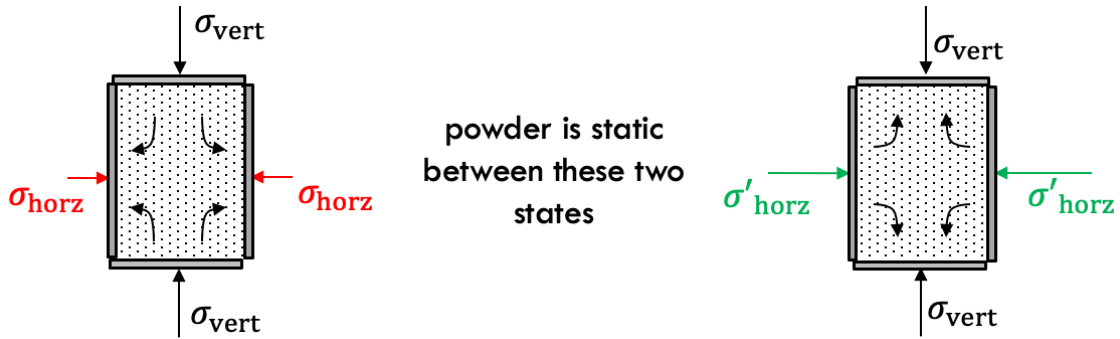
FIGURE 4.10. Powder contained between two frictionless containing walls. In the left system the powder is in active case since the powder is about to move in the opposite direction to the lateral force. The right system is in a passive state since the powder is about to move in the same direction as the applied force.

$$\therefore mg(\sin\theta - \mu\cos\theta) \leq P \leq mg(\sin\theta + \mu\cos\theta). \tag{4.19}$$

The lower limit corresponds to when the block is just about to slide downward on the incline. This case is called the active state since the block is moving in the direction opposite to the applied force. The upper limit corresponds to when the block is just about to move upward on the incline. This case is called the passive state since the block is moving in the same direction as the applied force. Without knowing the mechanical behavior of the block and surface, we can only determine the force P for these limiting cases.

Similar to the block, powder can also be static over a range between active and passive states. Consider a two-dimensional system with powder contained between two frictionless confining walls as shown in Figure 4.10. Since the walls are frictionless, the applied normal stresses are principal stresses. For this example, let σ_{vert}, which applies the driving force, remain constant, similar to how the block's weight in the previous example remains constant. In the case shown on the left-hand side of Figure 4.10, the powder is in an active state since the force required to hold the powder static is applied in the direction opposite to the powder's incipient movement. For this case, $\sigma_{\text{horz}} < \sigma_{\text{vert}}$. Now consider the right-hand system. For this case the powder is in a passive state since the lateral force acts in the same direction as the powder just prior to yielding. For this case, $\sigma_{\text{horz}} > \sigma_{\text{vert}}$. Between these two values for σ_{horz} the powder remains static. The Mohr's circles corresponding to the active and passive states are shown in Figure 4.11. For the given σ_{vert}, the powder is static for horizontal stresses between σ_{horz} and σ'_{horz}. It's also not possible to have horizontal stresses smaller than σ_{horz} or larger than σ'_{horz} for the given σ_{vert} since those would create Mohr's circles that extend beyond the internal yield locus.
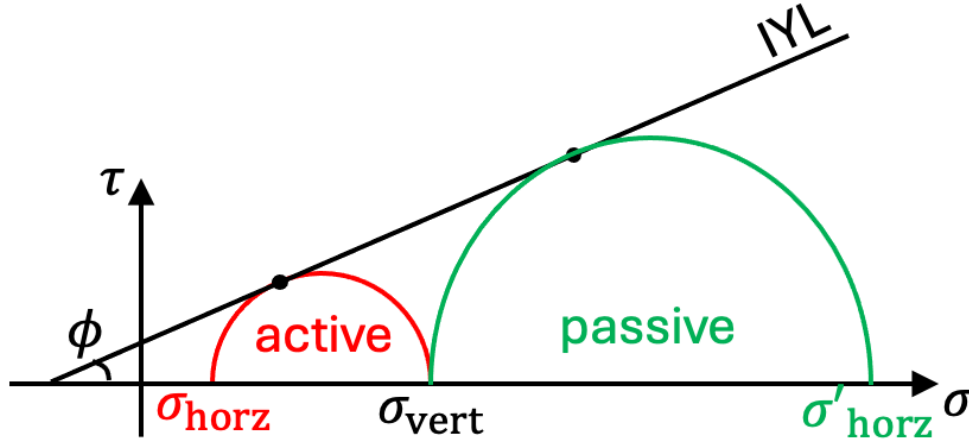
FIGURE 4.11. The Mohr's circles corresponding to the active and passive states shown in Figure 4.10.

4.4. Janssen's Constant

Now let's define a quantity known as Janssen's Constant, K, (named after H. Janssen [4], who investigated powder stresses in bins), which is the ratio of the lateral to vertical stress,

$$K := \frac{\sigma_{\text{lat}}}{\sigma_{\text{vert}}}. \tag{4.20}$$

In a particulate material, vertical stresses can be converted into lateral stresses via particle-particle contacts. For example, Figure 4.12 shows a photograph of photo-elastic disks compressed vertically. The polarization of light passing through a photo-elastic disk changes in response to stresses applied to the disk. In this image, disks are brighter when the internal stresses are larger and, thus, force chains, i.e., the paths along which forces are transmitted, can be observed. The image shows that some of the vertically applied force gets converted into a lateral force. The sketch in the figure illustrates how a vertical force on a particle can eventually become a lateral stress on a boundary due to the geometry of the contacts.

Notes:

(1) When the lateral and vertical stresses are principal stresses as in the previous section's example,

$$K_A = \frac{\sigma_{\text{horz}}}{\sigma_{\text{vert}}} = \frac{\sigma_2}{\sigma_1} < 1, \tag{4.21}$$

$$K_P = \frac{\sigma'_{\text{horz}}}{\sigma_{\text{vert}}} = \frac{\sigma_1}{\sigma_2} > 1, \tag{4.22}$$

where σ_1 and σ_2 are, respectively, the major and minor principal stresses. Making use of Eq. (4.12),

$$K_A = \frac{1 - \sin \delta_A}{1 + \sin \delta_A} < 1, \tag{4.23}$$

$$K_P = \frac{1 + \sin \delta_P}{1 - \sin \delta_P} > 1, \tag{4.24}$$

where δ_A and δ_P are the effective angles of internal friction for the active and passive cases. It's important to note that these expressions are specifically for the case when the vertical and lateral stresses are principal stresses. In general, that will not be the case, as is discussed in a following note.

(2) Active values for Janssen's constant are typically between 0.4 and 0.6. If no other information is given, it's reasonable to assume a value of $K_A = 0.4$ as a rough estimate.
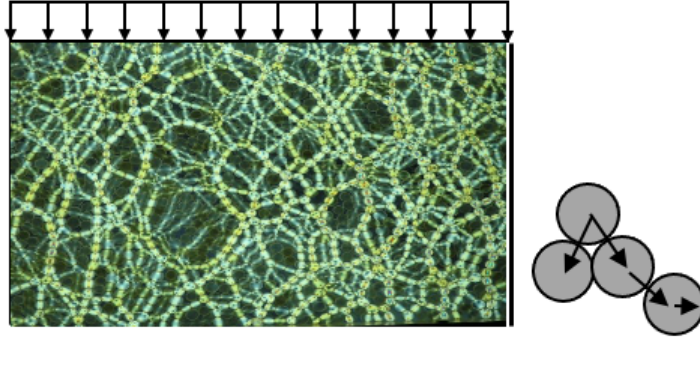
FIGURE 4.12. An image showing the internal stresses within photo-elastic disks as they are compressed. The larger the internal stress, the brighter the disk. The photo shows the force paths in the bulk material and demonstrates how loads applied in the vertical direction can result in loads in the lateral direction. The illustration at the bottom right also demonstrates how a vertical force on a particle can result in a lateral force against a vertical wall.
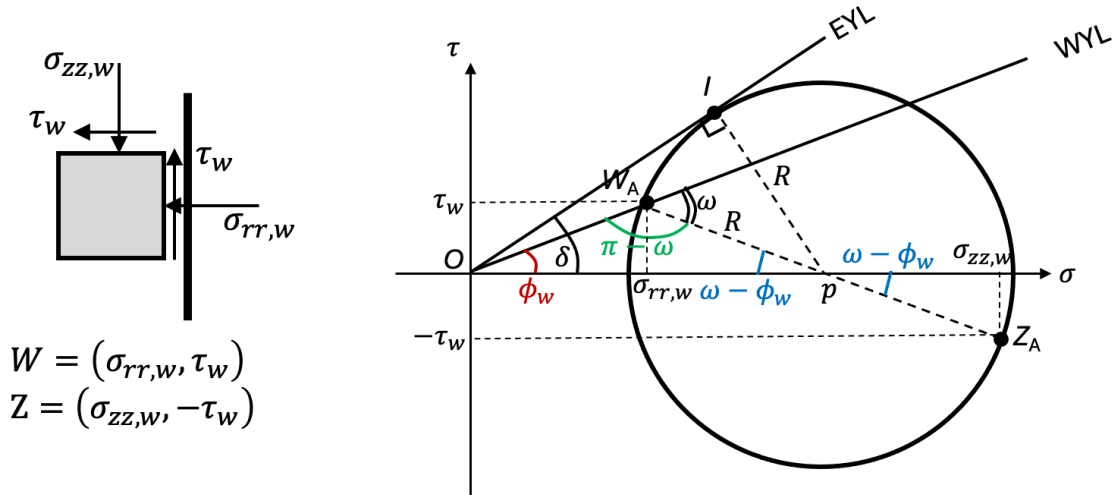

$$W = (\sigma_{rr,w}, \tau_w)$$
$$Z = (\sigma_{zz,w}, -\tau_w)$$

FIGURE 4.13. A Mohr's circle for a material element in the active state adjacent to a frictional, vertical wall. Recall that for the active state, $\sigma_{zz,w} > \sigma_{rr,w}$. The element is assumed to be yielding internally and at the wall.

(3) The recommendation by Eurocode 1 [5] for estimating the active Janssen's constant is to use the empirical relation,

$$K_A = 1.1(1 - \sin \phi), \tag{4.25}$$

where ϕ is the internal friction angle. The recommendation by the German Institute for Standardization [6], also based on empirical data is,

$$K_A = 1.2(1 - \sin \phi). \tag{4.26}$$

(4) Janssen's constant adjacent to a frictional wall (the radial and vertical normal stresses are not principal stresses) can be estimated using a Mohr's circle. For example, consider the Mohr's circle for a material element in the active state against the frictional, vertical wall ($\sigma_{zz,w} > \sigma_{rr,w}$) shown in Figure 4.13. The angle ω in the Mohr's circle can be found by applying the Law of Sines to the

triangle $\Delta OW_A p$,

$$\frac{\sin\phi_w}{R} = \frac{\sin(\pi - \omega)}{p} = \frac{\sin\omega}{p}, \tag{4.27}$$

$$\sin\omega = \frac{p}{R}\sin\phi_w. \tag{4.28}$$

From right triangle ΔOIp,

$$\sin\delta = \frac{R}{p}. \tag{4.29}$$

Substituting Eq. (4.29) into Eq. (4.28),

$$\sin\omega = \frac{\sin\phi_w}{\sin\delta}. \tag{4.30}$$

The angle between line segments $\overline{pW_A}$ and $\overline{pO}$ is found by noting that the sum of the interior angles of a triangle is π radians,

$$\angle W_A pO = \pi - \phi_w - (\pi - \omega) = \omega - \phi_w. \tag{4.31}$$

Now find the lateral normal stress at the wall ($\sigma_{rr,w}$) using the Mohr's circle geometry,

$$\sigma_{rr,w} = p - R\cos(\omega - \phi_w), \tag{4.32}$$

$$= p - p\sin\delta\cos(\omega - \phi_w) \qquad \text{(using Eq. (4.29))}, \tag{4.33}$$

$$\sigma_{rr,w} = p\left[1 - \sin\delta\cos(\omega - \phi_w)\right]. \tag{4.34}$$

Similarly, the vertical normal stress at the wall ($\sigma_{zz,w}$) is,

$$\sigma_{zz,w} = p + R\cos(\omega - \phi_w), \tag{4.35}$$

$$= p + p\sin\delta\cos(\omega - \phi_w) \qquad \text{(using Eq. (4.29))}, \tag{4.36}$$

$$\sigma_{zz,w} = p\left[1 + \sin\delta\cos(\omega - \phi_w)\right]. \tag{4.37}$$

Taking the ratio of Eq. (4.34) to Eq. (4.37) to form Janssen's constant at the wall,

$$K_{A,w} = \frac{\sigma_{rr,w}}{\sigma_{zz,w}} = \frac{p\left[1 - \sin\delta\cos(\omega - \phi_w)\right]}{p\left[1 + \sin\delta\cos(\omega - \phi_w)\right]}, \tag{4.38}$$

$$K_{A,w} = \frac{1 - \sin\delta\cos(\omega - \phi_w)}{1 + \sin\delta\cos(\omega - \phi_w)}. \tag{4.39}$$

A similar approach can be used to determine the Janssen constant for the passive case at the wall ($\sigma_{rr,w} > \sigma_{zz,w}$). The corresponding Mohr's circle is shown in Figure 4.14. For this case, the angle $\angle OW_P p$ is ω since triangle $\Delta W_P pW_A$ is isosceles. Furthermore, since the interior angles of the triangle add to π radians,

$$\angle W_P pW_A = \pi - 2\omega. \tag{4.40}$$

Since the angle along a line is also π radians, the angle from $W_p p\sigma_{rr,w}$ is,

$$\angle W_p p\sigma_{rr,w} = \pi - (\omega - \phi_w) - (\pi - 2\omega) = \omega + \phi_w. \tag{4.41}$$

Applying the Law of Sines to triangle $\Delta OW_p p$,

$$\frac{\sin\phi_w}{R} = \frac{\sin\omega}{p} \implies \sin\omega = \frac{p}{R}\sin\phi_w, \tag{4.42}$$

which is the same as Eq. (4.28). Equations (4.29) and (4.30) are also true for the passive case. The lateral normal stress at the wall using the Mohr's circle geometry,

$$\sigma_{rr,w} = p + R\cos(\omega + \phi_w), \tag{4.43}$$

$$= p + p\sin\delta\cos(\omega + \phi_w) \qquad \text{(using Eq. (4.29))}, \tag{4.44}$$

$$\sigma_{rr,w} = p\left[1 + \sin\delta\cos(\omega + \phi_w)\right]. \tag{4.45}$$

FIGURE 4.14. A Mohr's circle for a material element in the passive state adjacent to a frictional, vertical wall. Recall that for the passive state, $\sigma_{rr,w} > \sigma_{zz,w}$. The element is assumed to be yielding internally and at the wall.

The vertical normal stress at the wall is,

$$\sigma_{zz,w} = p - R\cos(\omega + \phi_w), \tag{4.46}$$

$$= p - p\sin\delta\cos(\omega + \phi_w) \qquad \text{(using Eq. (4.29))}, \tag{4.47}$$

$$\sigma_{zz,w} = p\left[1 - \sin\delta\cos(\omega + \phi_w)\right]. \tag{4.48}$$

Taking the ratio of Eq. (4.45) to Eq. (4.48) to form Janssen's constant at the wall,

$$K_{P,w} = \frac{\sigma_{rr,w}}{\sigma_{zz,w}} = \frac{p\left[1 + \sin\delta\cos(\omega + \phi_w)\right]}{p\left[1 - \sin\delta\cos(\omega + \phi_w)\right]}, \tag{4.49}$$

$$K_{P,w} = \frac{1 + \sin\delta\cos(\omega + \phi_w)}{1 - \sin\delta\cos(\omega + \phi_w)}. \tag{4.50}$$

Equations (4.39) and (4.50) may be combined to give a single expression for Janssen's constant adjacent to a vertical wall,

$$K_w = \frac{1 - \kappa\sin\delta\cos(\omega - \kappa\phi_w)}{1 + \kappa\sin\delta\cos(\omega - \kappa\phi_w)}, \tag{4.51}$$

where $\kappa = +1$ for the active state and $\kappa = -1$ for the passive state. A plot of Eq. (4.51) is shown in Figure 4.15 for various values of the effective angle of internal friction and the wall friction angle. Note that for the passive case when the wall friction angle is sufficiently large, i.e., when,

$$\tan\phi_w > \frac{R}{p} = \sin\delta, \tag{4.52}$$

which puts the point W_P to the left of the hydrostatic pressure p (Figure 4.14), then $K_{w,P} < 1$. The value of $K_{w,P}$ is still larger than $K_{w,A}$, however. Note that Eq. (4.51) reduces to Eqs. (4.23) and (4.24) when $\phi_w = 0$, i.e., when the walls are frictionless and the vertical and radial stresses at the wall are principal stresses. For a fully rough wall where $\phi_w = \delta$, Eq. (4.51) becomes,

$$K_{w,\text{fully rough}} = \frac{1 - \kappa\sin^2\delta}{1 + \kappa\sin^2\delta}. \tag{4.53}$$

Figure 4.15. Janssen's constant at the wall using Eq. (4.51) plotted as a function of the effective angle of internal friction for different wall friction angles. Active and passive cases are shown.

(5) Experimental values for the active Janssen's constant along with internal friction angles are given in Table 4.4 for various agricultural grains. The experimental values range between approximately 0.3 and 0.5. Also included in the table are estimates using the Eurocode recommendation (Eq. (4.25)), which tends to over-predict the experimental values. The experimental values for Janssen's constant are plotted in Figure 4.16 as a function of the internal friction angle along with various predictions for K_A, assuming the grain materials are cohesionless. The wall friction angle was not specified in the work so different values are assumed. The predictions from Eq. (4.51) provide good estimates for the experimental values and are more accurate than the predictions from the Eurocode (Eq. (4.25)) and German code (Eq. (4.26)) recommendations.

Table 4.5 presents active Janssen's constant values for various materials using different methods for filling the testing apparatus. The authors [8] observed that Janssen's constant decreases as the vertical stress approaches zero and asymptotes for large values of the vertical stress. The reported Janssen's constants in the table are measured at a vertical normal stress of 35 kPa. Note that the measured Janssen's constants range between approximately 0.3 and 0.6. The experiments showed that the filling method affects the measured Janssen's constant, which they attribute to the presence of shear planes in the sample when filling.

Table 4.6 provides additional active Janssen constant measurements for a wide variety of materials, specifically at a vertical normal stress of 35 kPa. The reported values of K_A are generally between $0.4 - 0.6$. Figure 4.17 plots the measured Janssen's constants as a function of the material's effective angle of internal friction (δ, or ϕ_e in the authors' work). The plot also includes various methods for estimating Janssen's constant, which are based on the effective angle of internal friction as opposed to the internal friction angle. Equation (4.26) does the best job of predicting the measurements, although the predictions tend to underestimate the experimental values. Figure 4.18 plots the predicted values against the measured values using the Mohr's circle analysis (Eq. (4.51)), the Eurocode recommendation (Eq. (4.25)), and the German DIN recommendation (Eq. (4.26)). The

Grain	Moisture content (w.b.) (%)	k_s	k_φ	φ (deg)
Barley	10	0.45 ± 0.02	0.59 ± 0.01	27.8 ± 0.4
	12.5	0.47 ± 0.03	0.57 ± 0.01	28.5 ± 0.5
	15	0.43 ± 0.02	0.53 ± 0.01	31.2 ± 0.3
	17.5	0.45 ± 0.03	0.54 ± 0.02	30.6 ± 1.0
	20	0.39 ± 0.03	0.51 ± 0.01	33.2 ± 0.5
Corn	10	0.48 ± 0.04	0.60 ± 0.01	26.7 ± 0.6
	12.5	0.40 ± 0.03	0.52 ± 0.01	31.7 ± 0.5
	15	0.36 ± 0.05	0.51 ± 0.02	32.0 ± 1.4
	17.5	0.34 ± 0.03	0.50 ± 0.02	33.4 ± 0.8
	20	0.30 ± 0.05	0.49 ± 0.03	33.6 ± 1.5
Oat	10	0.49 ± 0.03	0.68 ± 0.02	22.1 ± 1.1
	12.5	0.44 ± 0.04	0.68 ± 0.02	22.4 ± 0.9
	15	0.45 ± 0.03	0.65 ± 0.01	24.0 ± 0.5
	17.5	0.40 ± 0.03	0.65 ± 0.02	23.9 ± 1.0
	20	0.41 ± 0.06	0.61 ± 0.03	26.4 ± 1.7
Wheat	10	0.44 ± 0.02	0.62 ± 0.01	25.7 ± 0.3
	12.5	0.38 ± 0.01	0.61 ± 0.01	26.2 ± 0.4
	15	0.34 ± 0.02	0.60 ± 0.01	27.0 ± 0.5
	17.5	0.31 ± 0.02	0.50 ± 0.02	33.0 ± 1.0
	20	0.35 ± 0.01	0.46 ± 0.01	35.5 ± 0.5
Rape seeds	6	0.46 ± 0.02	0.64 ± 0.02	24.7 ± 0.5
	9	0.28 ± 0.04	0.54 ± 0.01	30.6 ± 0.4
	12	0.27 ± 0.02	0.52 ± 0.01	31.7 ± 0.7
	15	0.24 ± 0.02	0.47 ± 0.01	34.8 ± 0.7

TABLE 4.4. Experimental values (mean $\pm$ standard deviation) for Janssen's constant (k_s) and internal friction angle (ϕ) for various agricultural grains. Calculated values for Janssen's constant (k_ϕ) using the Eurocode expression (Eq. (4.25)) are also included. This table is from Horabik and Rusinek[7].

Filling procedure	bulk solid			
	glass beads	limestone powder	coarse limestone	plastic pellets
sieving	0.460	0.470	0.301	0.513
funnel, central	0.555	0.457	0.379	0.516
filling by portions	0.573	0.477	0.345	0.543
funnel, concentric	0.590	0.486	0.407	0.558

TABLE 4.5. Janssen constants for various materials using different experimental apparatus filling methods. The measurements are made at a vertical normal stress of 35 kPa. This table is from Kwade et al. [8].

models generally under-predict the measurements with the Mohr's circle analysis giving the worst predictions. The authors state that the model assumption that the material is yielding internally is a likely reason for the deviation.

Bulk Solid	Density of Bulk Solid at 35 kPa ρ_b [kg/m³]	Effective Angle of Internal Friction φ_e [°]	Wall Friction Angle (aluminium) φ_x [°]	Stress Ratio			Compression Angle φ_c [°]	Ratio of Principal Stresses λ_0
				λ_{35}	λ_{corr}	$(\lambda_{corr} - \lambda_{35})/\lambda_{35}$ [%]		
Active Coal	687	38	22	0.40	0.46	15.4	27	0.38
Adipic Acid	790	35	16	0.46	0.50	10.2	22	0.45
Aluminium Oxide (x < 0.06 mm)	1960	34	28	0.50	0.62	25.1	28	0.36
Aluminium Powder (< 0.06 mm)	1128	38	21	0.43	0.48	12.0	26	0.40
Aluminium Powder (0.1 - 2 mm)	1018	39	13	0.36	0.38	6.9	28	0.37
Basalt (1 - 3 mm)	1449	41	27	0.35	0.41	17.6	31	0.32
Brown Coal Dust	550	38	30	0.40	0.47	18.2	31	0.32
Broken Sand	1433	43	24	0.48	0.58	21.6	25	0.40
Burnt Clay Granulates, dry	429	43	26	0.32	0.36	13.4	32	0.30
Burnt Clay Granulates, moist	705	46	31	0.29	0.34	13.9	35	0.27
Cement PZ 35 F	1541	39	28	0.40	0.46	15.8	30	0.33
Cement Clinker	1751	40	22	0.46	0.53	17.1	25	0.41
Chalk Powder	1131	42	29	0.45	0.53	18.3	30	0.34
Dug Sand (0 - 2 mm), washed	1619	39	23	0.46	0.56	20.2	25	0.41
FGD - Gypsum	866	40	29	0.42	0.49	16.7	30	0.34
Fine Sand (0 - 1 mm)	1522	34	22	0.44	0.52	18.2	25	0.41
Glass Beads (x ≈ 1 mm)	1726	27	17	0.56	0.65	16.8	19	0.52
Hard Coal	847	42	20	0.36	0.39	9.0	29	0.35
Hard Coal (8% H_2O)	978	52	16	0.42	0.45	7.8	25	0.41
Hard Coal Flue Ash	1261	40	21	0.48	0.54	12.9	23	0.43
Limestone Powder	1386	40	26	0.46	0.52	13.2	28	0.37
Limestone (0.1 - 0.5 mm)	1391	33	20	0.38	0.43	13	27	0.37
Limestone (0.8 - 3.2 mm)	1376	40	16	0.37	0.40	9.6	27	0.37
Maize	748	34	15	0.48	0.53	10.8	21	0.47
Open-Hearth Coke	477	40	15	0.43	0.47	10.3	23	0.43
Plastic Granules, broken	535	42	15	0.34	0.36	7.4	29	0.34
Plastic Pellets (PP + PE)	511	20	8	0.52	0.55	6.3	18	0.53
Plastic Powder (PE, < 0.2 mm)	477	37	17	0.57	0.63	9.8	19	0.51
Plastic Pellets (PE)	568	36	8	0.49	0.52	5.7	19	0.50
Quartzite (0 - 3 mm)	1667	46	28	0.43	0.52	20.0	29	0.35
Rhine Sand (0 - 5 mm)	1677	39	23	0.45	0.54	18.5	25	0.41
Sawdust, fine	294	48	17	0.37	0.39	5.4	28	0.36
Sawdust, coarse	222	40	15	0.39	0.41	4.2	27	0.38
Silicon Carbide (x < 0.065 mm)	1406	36	29	0.48	0.61	26.9	29	0.34
Slag Granulates (2 - 4 mm)	1329	41	27	0.47	0.60	26.6	28	0.37
Sugar	860	39	24	0.44	0.53	20.3	26	0.39
Wheat Flour	778	37	13	0.36	0.38	4.9	28	0.36
Wheat	824	30	11	0.47	0.51	7.4	21	0.48
Zeolite 1	705	57	28	0.50	0.57	14.4	28	0.36
Zeolite 2	650	45	26	0.50	0.57	14.5	27	0.38
Zinc Oxide	845	46	35	0.37	0.41	11.5	36	0.26

TABLE 4.6. Measurements for different bulk solids of the bulk density (ρ_b), effective angle of internal friction (ϕ_e), wall friction angle against aluminum (ϕ_x), and three measures of Janssen's constant (λ_{35}, λ_{corr}, and λ_0). All values are measured at an applied vertical normal stress of 35 kPa. In the table λ_{35} is Janssen's constant based on the applied vertical normal stress of 35 kPa, λ_{corr} is Janssen's constant where the vertical stress is estimated at the location of the horizontal stress measurement, and λ_0 is Janssen's constant for uniaxial compaction that doesn't involve yielding. The compression angle ϕ_c is the angle through the origin tangent to the non-yielding Mohr's circles. This table is from Kwade et al. [9].
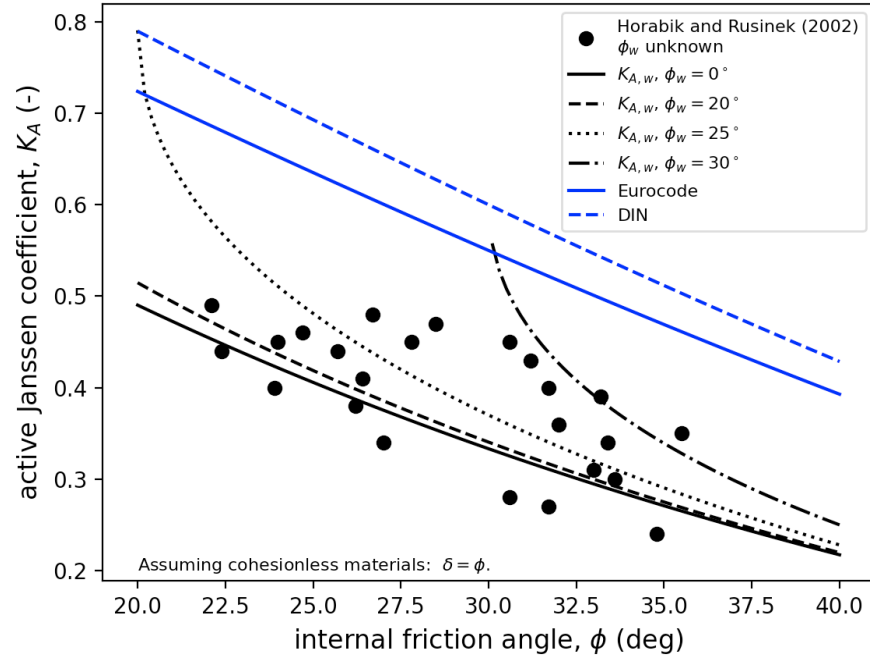
FIGURE 4.16. Measured Janssen's constants plotted as a function of the internal friction angle for various agricultural grain materials. These data are from Table 4.4. The curve fits are from Eqs. (4.51) (assuming cohesionless materials), (4.25), and (4.26).

4.5. Summary

Following is a summary of the significant points in this chapter:

(1) The Ideal Coulomb Material Model is often used in analyses for powder storage and flow.
(2) In the Ideal Coulomb model, yielding occurs within the material when $|\tau| = |\sigma \tan \phi + c|$ and at a wall when $|\tau| = |\sigma \tan \phi_w + c_w|$.
(3) The effective angle of internal friction δ is related to the ratio of the principal stresses when the material yields internally.
(4) Janssen's constant is the ratio of the lateral to vertical stresses. The active Janssen's constant typically has a value between $0.4 - 0.6$. There are various methods for estimating Janssen's constant. The effect of wall friction should be considered for improved prediction accuracy.
(5) A static powder stress state is bounded by active and passive stress states.
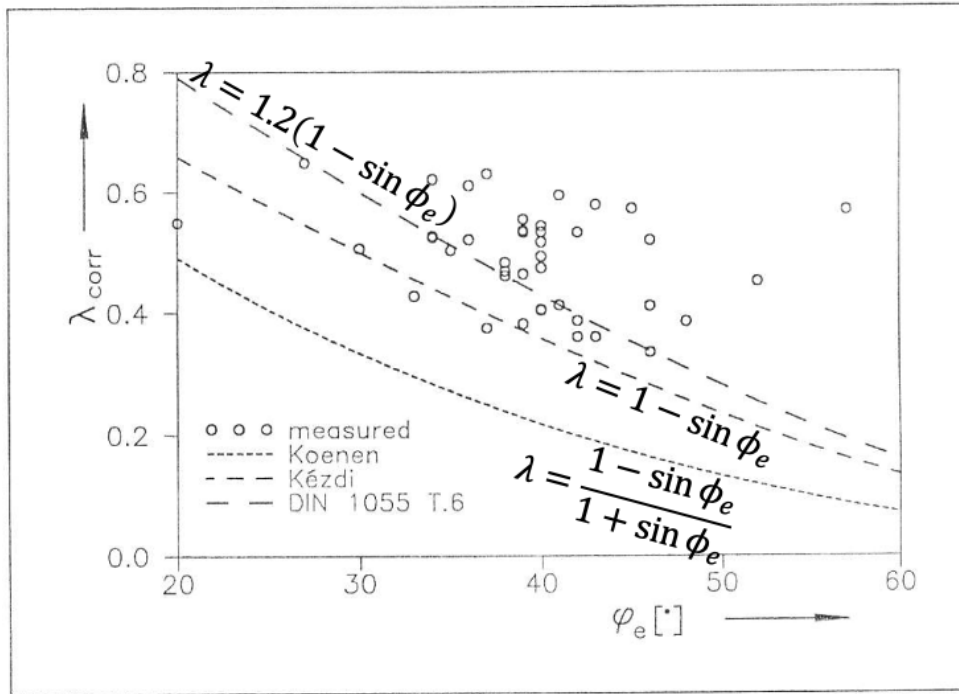
FIGURE 4.17. Measured Janssen's constants (λ), using a vertical normal stress estimated at the location of the measured lateral stress, plotted as a function of the effective angle of internal friction. This plot is from Kwade etal. [9].
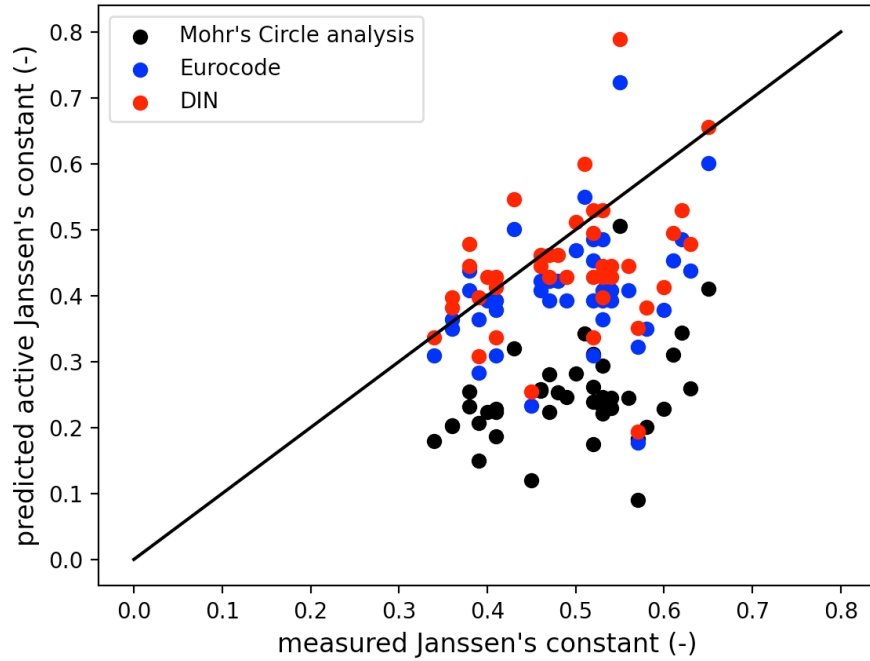
Figure 4.18. Predicted Janssen's constants plotted against measured Janssen's constants for the materials listed in Table 4.6. The predicted values come from the Mohr's circle analysis formula (Eq. (4.51)), the Eurocode recommendation (Eq. (4.25)), and the German DIN recommendation (Eq. (4.26)). The models generally under-predict the measured values.

The major principal stress at a point within an internally-yielding cohesionless material with an internal friction angle of 25° is 1.5 kPa.

1. Evaluate the minor principal stress and the angles between the minor principal plane and the slip planes (in the real world).
2. Draw the corresponding Mohr's circle.

SOLUTION:
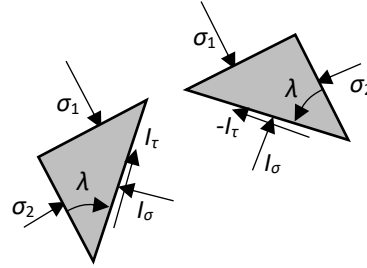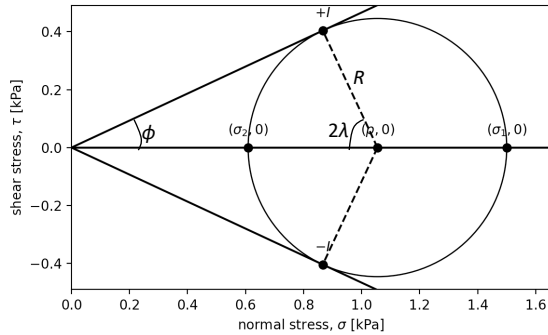
The radius of the Mohr's circle is,
$$R = \tfrac{1}{2}(\sigma_1 - \sigma_2),$$
(1)
and the hydrostatic pressure is,
$$p = \tfrac{1}{2}(\sigma_1 + \sigma_2).$$
(2)
The internal friction angle is related to the radius and pressure, assuming no cohesion, via,
$$\sin\phi = \frac{R}{p} = \frac{\tfrac{1}{2}(\sigma_1-\sigma_2)}{\tfrac{1}{2}(\sigma_1+\sigma_2)} = \frac{\sigma_1-\sigma_2}{\sigma_1+\sigma_2} \implies \frac{\sigma_1}{\sigma_2} = \frac{1-\sin\phi}{1+\sin\phi} \implies \sigma_2 = \sigma_1\left(\frac{1+\sin\phi}{1-\sin\phi}\right).$$
(3)
Using the given values of ϕ = 25° and σ_1 = 1.5 kPa, $\boxed{\sigma_2 = 0.61 \text{ kPa}}$, p = 1.05 kPa, and R = 0.45 kPa.

The angle from the internal yield points (I) to the minor principal plane in the Mohr's circle is,
$$2\lambda = \pm\left(\frac{\pi}{2} - \phi\right) \quad \text{(The sum of the internal angles of a triangle is 180°.)}$$
(4)
and, thus, the angles in the real world are,
$$\lambda = \pm\tfrac{1}{2}\left(\frac{\pi}{2} - \phi\right).$$
(5)
Using the given value for ϕ, 2λ = 65° $\implies$ $\boxed{\lambda = \pm 32.5°}$.

The stress state at the internal yield point ($I = (I_\sigma, I_\tau)$) is,
$$I_\sigma = p - R\cos(2\lambda),$$
(6)
$$I_\tau = \pm R\sin(2\lambda),$$
(7)
$$\implies \quad I = (0.87, \pm 0.40) \text{ kPa}.$$

The following Python code was used to perform the calculations and draw the Mohr's circle:

```
# IdealCoulomb_01.py

import matplotlib.pyplot as plt
import numpy as np

sigma_1 = 1.5  # kPa, major principal stress
phi = np.radians(25)  # deg/rad, internal friction angle

sigma_2 = sigma_1*(1 - np.sin(phi))/(1 + np.sin(phi))
print('sigma_2 = %.3f kPa' % sigma_2)

R = 0.5*(sigma_1 - sigma_2)
p = 0.5*(sigma_1 + sigma_2)
print('(p, R) = (%.3f, %.3f) kPa' % (p, R))


# Draw the Mohr's circle.
figure, axes = plt.subplots()
MohrsCircle = plt.Circle((p, 0), R, fill=False)  # make the Mohr's circle
axes.set_aspect(1)  # set the aspect ratio to one
axes.add_artist(MohrsCircle)  # add the Mohr's circle to the plot

# Draw Internal Yield Locus (IYL)
plt.plot([0, sigma_1], [0, sigma_1*np.tan(phi)], 'k-')
plt.plot([0, sigma_1], [0, -sigma_1*np.tan(phi)], 'k-')
I_sigma = p-R*np.cos(np.pi/2 - phi)
I_tau = R*np.sin(np.pi/2 - phi)
print('(I_sigma, I_tau) = (%.3f, %.3f) kPa' % (I_sigma, I_tau))
plt.plot(I_sigma, I_tau, 'ko')
plt.plot(I_sigma, -I_tau, 'ko')
plt.annotate('$+I$', (I_sigma, I_tau), textcoords='offset points', xytext=(0,10),
ha='center')
plt.annotate('$-I$', (I_sigma, -I_tau), textcoords='offset points', xytext=(0,10),
ha='center')

# Calculate the angle in the Mohr's circle from the +I to sigma_2.
two_lambda = np.pi/2 - phi
print('2*lambda = +/- %.3f deg' % (np.degrees(two_lambda)))
print('lambda = +/- %.3f deg' % (0.5*np.degrees(two_lambda)))

# Draw lines from the center of the Mohr's circle to the yield points.
plt.plot([p, I_sigma], [0, I_tau], 'k--')
plt.plot([p, I_sigma], [0, -I_tau], 'k--')

# Plot the major principal stress state and a label to the plot.
plt.plot(sigma_1, 0, 'ko')
plt.annotate('$(\sigma_{1}, 0)$', (sigma_1, 0), textcoords='offset points',
xytext=(0,10), ha='center')

# Plot the minor principal stress state and a label to the plot.
plt.plot(sigma_2, 0, 'ko')
plt.annotate('$(\sigma_{2}, 0)$', (sigma_2, 0), textcoords='offset points',
xytext=(0,10), ha='center')

# Plot the hydrostatic pressure state and a label to the plot.
plt.plot(p, 0, 'ko')
plt.annotate('$(p, 0)$', (p, 0), textcoords='offset points', xytext=(0,10),
ha='center')

axes.axhline(y=0, color='k')  # draw a horz line at y=0
```

```
        plt.xlim([0, 1.1*(p+R)])  # set the plot x-range
        plt.ylim([-1.1*R, 1.1*R])  # set the plot y-range
        plt.xlabel('normal stress, $\sigma$ [kPa]') # add the x-axis label
        plt.ylabel('shear stress, $\\tau$ [kPa]')  # add the y-axis label
        plt.show()  # show the plot
```

Running the Python code gives the following output:
```
    >>python3 ./IdealCoulomb_01.py
    sigma_2 = 0.609 kPa
    (p, R) = (1.054, 0.446) kPa
    (I_sigma, I_tau) = (0.866, 0.404) kPa
    2*lambda = +/- 65.000 deg
    lambda = +/- 32.500 deg
```

A cohesionless material has an internal friction angle of 40° and a wall friction angle of 20° (no adhesion). The hydrostatic pressure acting on the element is 50 kPa. Assume the material is yielding both internally and at the wall. For a material element adjacent to the wall:

1. Draw a Mohr's circle for the element (only the top half is needed), including the internal yield locus and wall yield locus. Label significant points and angles.
2. Calculate the normal and shear stress values on the plane on which internal yield occurs.
3. Calculate the normal and shear stress values on the wall plane for the <u>active</u> stress state. Call this stress state W_A. Hints: Let γ be the angle from the origin to W_A to the hydrostatic pressure. Apply the Law of Sines on triangle origin:W_A:hydrostatic pressure to find γ. Keep in mind that $\sin\gamma = \sin(\pi - \gamma)$. Lastly, make use of the geometry in the Mohrs circle to find the wall normal and shear stresses, i.e., you needn't memorize formulas for this calculation and instead can use the Mohrs circle geometry to get the appropriate formulas.

SOLUTION:
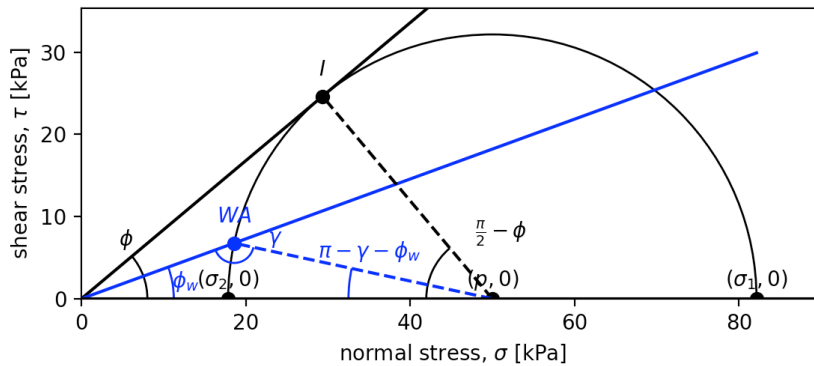
The radius of the Mohr's circle is,
$$R = p \sin\phi \;=> \; R = 32.1 \text{ kPa}. \tag{1}$$

Internal yielding occurs at,
$$\sigma_I = p - R\cos\left(\frac{\pi}{2} - \phi\right) \;=> \; \boxed{\sigma_I = 29.3 \text{ kPa}}, \tag{2}$$
$$\tau_I = R\sin\left(\frac{\pi}{2} - \phi\right) \;=> \; \boxed{\tau_I = 24.6 \text{ kPa}}. \tag{3}$$

The angle γ between the WYL and the line from $(p, 0)$ to the point WA is found using the Law of Sines,
$$\frac{\sin\phi_w}{R} = \frac{\sin\gamma}{p} \;=> \; \gamma = \sin^{-1}\left(\frac{p}{R}\sin\phi_w\right) \;=> \; \gamma = 147.9°. \tag{4}$$
Note that the obtuse angle value from the arcsine function is needed for the active stress state (the acute angle is used for the passive case).

The stress state at the wall for active yielding is,
$$\sigma_{WA} = p - R\cos(\pi - \gamma - \phi_w) \;=> \; \boxed{\sigma_{WA} = 18.6 \text{ kPa}}, \tag{5}$$
$$\tau_{WA} = R\sin(\pi - \gamma - \phi_w) \;=> \; \boxed{\tau_{WA} = 6.76 \text{ kPa}}. \tag{6}$$

The following Python code was used to perform the calculations and draw the figure.

```python
# IdealCoulomb_02.py

import matplotlib.patches as patches
import matplotlib.pyplot as plt
import numpy as np

p = 50  # kPa, hydrostatic stress
phi_deg = 40  # deg, internal friction angle
phiw_deg = 20  # deg, wall friction angle
phi_rad = np.radians(phi_deg)  # rad, internal friction angle
phiw_rad = np.radians(phiw_deg)  # rad, wall friction angle

# Find the Mohr's circle radius.
R = p*np.sin(phi_rad)
print('(p, R) = (%.1f, %.1f) kPa' % (p, R))

# Draw the Mohr's circle.
figure, axes = plt.subplots()
MohrsCircle = patches.Circle((p, 0), R, fill=False)  # make the Mohr's circle
axes.set_aspect(1)  # set the aspect ratio to one
axes.add_patch(MohrsCircle)  # add the Mohr's circle to the plot

# Plot the hydrostatic pressure state and a label.
plt.plot(p, 0, 'ko')
plt.annotate(r'$(p, 0)$', (p, 0), textcoords='offset points', xytext=(0,6), ha='center')

# Find and plot the major and minor principal stresses.
sigma_1 = p + R
sigma_2 = p - R
plt.plot(sigma_1, 0, 'ko')
plt.annotate(r'$(\sigma_1, 0)$', (sigma_1, 0), textcoords='offset points', xytext=(0,6), ha='center')
plt.plot(sigma_2, 0, 'ko')
plt.annotate(r'$(\sigma_2, 0)$', (sigma_2, 0), textcoords='offset points', xytext=(0,6), ha='center')

# Draw Internal Yield Locus (IYL).
plt.plot([0, sigma_1], [0, sigma_1*np.tan(phi_rad)], 'k-')
# Draw the angle phi.
phi_arc = patches.Arc([0, 0], 0.5*R, 0.5*R, angle=0, theta1=0, theta2=phi_deg, color='k', linestyle='-')
axes.add_patch(phi_arc)
plt.annotate(r'$\phi$', (0.2*R*np.cos(0.8*phi_rad), 0.38*R*np.sin(0.8*phi_rad)), textcoords='offset points', xytext=(0,0), ha='center', color='k')

# Draw Wall Yield Locus (WYL).
plt.plot([0, sigma_1], [0, sigma_1*np.tan(phiw_rad)], 'b-')
# Draw the angle phiw.
phiw_arc = patches.Arc([0, 0], 0.7*R, 0.7*R, angle=0, theta1=0, theta2=phiw_deg, color='b', linestyle='-')
axes.add_patch(phiw_arc)
plt.annotate(r'$\phi_w$', (0.4*R*np.cos(0.5*phiw_rad), 0.3*R*np.sin(0.4*phiw_rad)), textcoords='offset points', xytext=(0,0), ha='center', color='b')

# Find and plot the point at which internal yielding occurs.
I_sigma = p-R*np.cos(np.pi/2 - phi_rad)
I_tau = R*np.sin(np.pi/2 - phi_rad)
print('(I_sigma, I_tau) = (%.1f, %.1f) kPa' % (I_sigma, I_tau))
plt.plot(I_sigma, I_tau, 'ko')
plt.annotate(r'$I$', (I_sigma, I_tau), textcoords='offset points', xytext=(0,10), ha='center')

# Draw lines from the center of the Mohr's circle to the yield point.
plt.plot([p, I_sigma], [0, I_tau], 'k--')

# Draw the angle between point I and the minor principal stress.
I_arc = patches.Arc([p, 0], 0.5*R, 0.5*R, angle=0, theta1=(90+phi_deg), theta2=180, color='k', linestyle='-')
axes.add_patch(I_arc)
```

```
plt.annotate(r'$\frac{\pi}{2}-\phi$', (p+0.05*R*np.cos(np.pi/2-phi_rad), 0.3*R*np.sin(np.pi/2-
phi_rad)), textcoords='offset points', xytext=(0,0), ha='center', color='k')

# Find and plot the point at which active wall yielding occurs.
gamma_rad = np.pi - np.arcsin(p/R*np.sin(phiw_rad))  # obtuse angle
gamma_deg = np.degrees(gamma_rad)
print('gamma = %.1f deg' % gamma_deg)
WA_sigma = p-R*np.cos(np.pi-phiw_rad-gamma_rad)
WA_tau = R*np.sin(np.pi-phiw_rad-gamma_rad)
print('(WA_sigma, WA_tau) = (%.1f, %.2f) kPa' % (WA_sigma, WA_tau))
plt.plot(WA_sigma, WA_tau, 'bo')
plt.annotate(r'$WA$', (WA_sigma, WA_tau), textcoords='offset points', xytext=(0,10), ha='center',
color='b')

# Draw lines from the center of the Mohr's circle to the yield point.
plt.plot([p, WA_sigma], [0, WA_tau], 'b--')

# Draw the angle gamma.
gamma_arc = patches.Arc([WA_sigma, WA_tau], 0.15*R, 0.15*R, angle=0, theta1=(180+phiw_deg),
theta2=(180+phiw_deg+gamma_deg), color='b', linestyle='-')
axes.add_patch(gamma_arc)
plt.annotate(r'$\gamma$', (WA_sigma+5, WA_tau), textcoords='offset points', xytext=(0,0), ha='center',
color='b')

# Draw the angle pi-gamma-phiw.
WA_arc = patches.Arc([p, 0], 35, 35, angle=0, theta1=(gamma_deg+phiw_deg), theta2=180, color='b',
linestyle='-')
axes.add_patch(WA_arc)
plt.annotate(r'$\pi-\gamma-\phi_w$', (p-15, 5), textcoords='offset points', xytext=(0,0), ha='center',
color='b')


axes.axhline(y=0, color='k')  # draw a horz line at y=0
plt.xlim([0, 1.1*(p+R)])  # set the plot x-range
plt.ylim([0, 1.1*R])  # set the plot y-range
plt.xlabel('normal stress, $\sigma$ [kPa]') # add the x-axis label
plt.ylabel('shear stress, $\\tau$ [kPa]')  # add the y-axis label
plt.show()  # show the plot
```

Running the code produces the following output in addition to the figure.
```
>>python3 ./IdealCoulomb_02.py
(p, R) = (50.0, 32.1) kPa
(I_sigma, I_tau) = (29.3, 24.6) kPa
gamma = 147.9 deg
(WA_sigma, WA_tau) = (18.6, 6.76) kPa
```

Bibliography

[1] D. McGlinchey, "Bulk property characterization," Characterisation of Bulk Solids, D. McGlinchey, Ed., 2005.

[2] J. Zegzulka, D. Gelnar, L. Jezerska, A. Ramirez-Gomez, J. Necas, and J. Rozboj, "Internal friction angle of metla powders," Metals, vol. 8, 2018. DOI: 10.3390/met8040255.

[3] B. Hancock, "The wall friction properties of pharmaceutical powders, blends, and granulations," Journal of Pharmaceutic vol. 108, no. 1, pp. 457–463, 2019.

[4] H. Janssen, "Versuche uber getreidedruck in silozellen," Zeitschrift des Vereines Deutscher Ingenieure, vol. 39, pp. 1045–1049, 1895.

[5] E. 1, "Dd env 1991-4. basis of design and actions on structures. part 4. actions in silos and tanks," The European Union Per Regulation, Tech. Rep., 1996.

[6] D. 1. T.6, "Actions on structures - part 6: Design loads for buildings and loads in silo bins," Deutsches Institut f ur Normung, Tech. Rep., 1987.

[7] J. Horabik and R. Rusinek, "Pressure ratio of cereal grains determined in a uniaxial compression test," Agrophysics, vol. 16, pp. 23–28, 2002.

[8] A. Kwade, D. Schulze, and J. Schwedes, "Determination of the stress ratio in uniaxial compression tests. part 1," Powder Handling and Processing, vol. 6, no. 1, pp. 61–65, 1994.

[9] ——, "Determination of the stress ratio in uniaxial compression tests. part 2," Powder Handling and Processing, vol. 6, no. 1, pp. 199–203, 1994.

CHAPTER 5

Stresses in a Cylindrical Bin

In this chapter we develop a model for predicting the stresses in a cylindrical bin. Stress distributions are of considerable industrial interest since particulate materials are often stored in such bins. In addition, concepts encountered in these analyses, such as asymptotic stress behavior and switch stresses, appear in other systems.

The models in this chapter are based on the Method of Differential Slices, also frequently called "Janssen's Method" after one of the first people to use this approach for particulate materials [1], [2]. The Method of Differential Slices is just one type of model for predicting stress distributions. Although it is not the most quantitatively accurate modeling technique due to simplifying assumptions, it does predict observed trends and is a relatively simple modeling approach. These features make the Method of Differential Slices a good place to start when modeling stresses in bins.

5.1. Force Balance on a Differential Material Element

Consider a particulate material at rest in a cylindrical bin as shown Figure 5.1. The forces acting in the vertical direction on a thin slice of material, with differential thickness dz, include the force that the material below the slice exerts upward on the slice (F_{bottom}), the force that the material above the slice exerts downward on the slice (F_{top}), the shear force that the wall exerts on the slice (F_{sides}), and the weight of the slice, W. In this analysis, assume the material is slipping downward at the wall so the wall shear force acting on the material acts upwards. Downward slip is a reasonable assumption during filling of the bin since material already in the bin tends to slip downward as additional material is poured on top of it. Material discharging from the bin will also move downward against the walls.

Assuming the material slice does not accelerate in the vertical direction (e.g., it's static or moving at a constant speed),

$$\sum F_z = 0 = F_{\text{top}} - F_{\text{bottom}} - F_{\text{sides}} + W. \tag{5.1}$$

Assuming the vertical normal stress (σ_{zz}) is uniform across the slice, the downward acting force on the top of the element may be written as,

$$F_{\text{top}} = \sigma_{zz} \frac{\pi D^2}{4}, \tag{5.2}$$

where D is the cylindrical bin diameter and $\pi D^2/4$ is the cross-sectional area of the slice. The force on the bottom of the element acting upward is,

$$F_{\text{bottom}} = (\sigma_{zz} + d\sigma_{zz}) \frac{\pi D^2}{4}. \tag{5.3}$$

The additional $d\sigma_{zz}$ term exists since the vertical normal stress may change slightly over the differentially small distance dz. The frictional shear force exerted by the side walls is,

$$F_{\text{sides}} = \tau_w (\pi D dz), \tag{5.4}$$

where τ_w is the shear stress exerted by the wall on the material and πD is the circumference of the circular bin cross-section. Finally, the weight of the differentially thin element of material is,

$$W = \rho_b g \frac{\pi D^2}{4} dz, \tag{5.5}$$
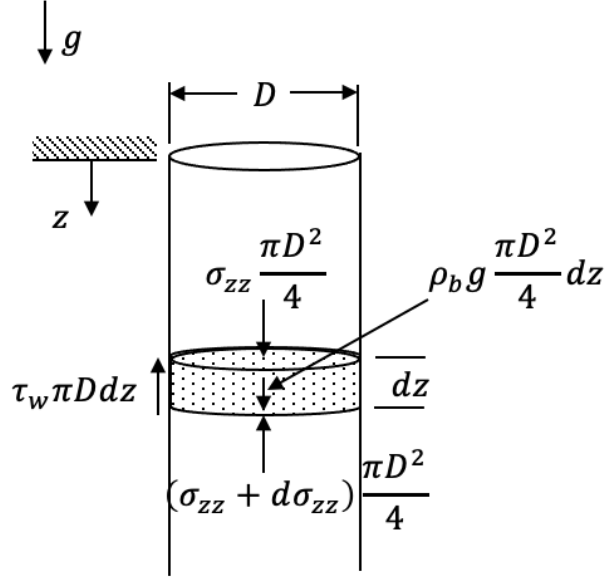
FIGURE 5.1. Forces in the vertical direction acting on a thin material element in a cylindrical bin.

where ρ_b is the bulk density of the material (assumed uniform across the cross-section) and g is the acceleration due to gravity.

Substituting the previous expressions into the force balance and simplifying,

$$\sigma_{zz}\frac{\pi D^2}{4} - (\sigma_{zz} + d\sigma_{zz})\frac{\pi D^2}{4} - \tau_w\left(\pi D dz\right) + \rho_b g\frac{\pi D^2}{4}dz = 0, \tag{5.6}$$

$$\frac{d\sigma_{zz}}{dz} + \frac{4}{D}\tau_w = \rho_b g. \tag{5.7}$$

To simplify this differential equation further, we must relate the shear stress at the wall to the vertical normal stress. To do this, first assume that the vertical normal stress is related to the radial normal stress via Janssen's constant, K (Chapter 4.4),

$$\sigma_{rr} = K\sigma_{zz}. \tag{5.8}$$

In addition, the shear stress at the wall can be related to the radial normal stress via a wall friction coefficient, μ_w,

$$\tau_w = \mu_w \sigma_{rr}. \tag{5.9}$$

Substituting Eqs. (5.8) and (5.9) into Eq. (5.7),

$$\frac{d\sigma_{zz}}{dz} + \frac{4\mu_w K}{D}\sigma_{zz} = \rho_b g. \tag{5.10}$$

To obtain a closed form solution to this differential equation, first assume the bulk density, wall friction coefficient, and Janssen's constant do not change with depth. Next, solve the homogeneous part of the differential equation,

$$\frac{d\sigma_{zz,H}}{dz} + \frac{4\mu_w K}{D}\sigma_{zz,H} = 0, \tag{5.11}$$

$$\int \frac{d\sigma_{zz,H}}{\sigma_{zz,H}} = \int -\frac{4\mu_w K}{D}dz, \tag{5.12}$$

$$\ln \sigma_{zz,H} = \frac{-4\mu_w K}{D}z + C, \tag{5.13}$$

$$\sigma_{zz,H} = C \exp\left(-\frac{4\mu_w K}{D}z\right), \tag{5.14}$$

where C is an unknown constant. The particular part of the solution is simply,

$$\frac{4\mu_w K}{D}\sigma_{zz,P} = \rho_b g, \tag{5.15}$$

$$\sigma_{zz,P} = \frac{\rho_b g}{(4\mu_w K)/D}. \tag{5.16}$$

Summing the homogeneous and particular solutions gives,

$$\sigma_{zz} = \frac{\rho_b g D}{4\mu_w K} + C \exp\left(-4\mu_w K\frac{z}{D}\right). \tag{5.17}$$

The constant C may be found using a boundary condition. In this case, we'll assume that at $z = 0$, i.e., the free surface, there is a uniform applied vertical normal stress of $\sigma_{zz,0}$, which is known as a <u>surcharge stress</u>. Using the boundary condition $\sigma_{zz}(z=0) = \sigma_{zz,0}$, the previous equation becomes,

$$\sigma_{zz} = \frac{\rho_b g D}{4\mu_w K}\left[1 - \exp\left(-4\mu_w K\frac{z}{D}\right)\right] + \sigma_{zz,0}\exp\left(-4\mu_w K\frac{z}{D}\right). \tag{5.18}$$

The corresponding radial normal and wall shear stresses are,

$$\sigma_{rr} = K\sigma_{zz} = \frac{\rho_b g D}{4\mu_w}\left[1 - \exp\left(-4\mu_w K\frac{z}{D}\right)\right] + K\sigma_{zz,0}\exp\left(-4\mu_w K\frac{z}{D}\right), \tag{5.19}$$

$$\tau_w = \mu_w\sigma_{rr} = \frac{\rho_b g D}{4}\left[1 - \exp\left(-4\mu_w K\frac{z}{D}\right)\right] + \mu_w K\sigma_{zz,0}\exp\left(-4\mu_w K\frac{z}{D}\right), \tag{5.20}$$

$$\tag{5.21}$$

We can make the previous equations dimensionless by dividing by the term in front of the square brackets,

$$4\mu_w K\left(\frac{\sigma_{zz}}{\rho_b g D}\right) = 1 - \exp\left(-4\mu_w K\frac{z}{D}\right) + 4\mu_w K\left(\frac{\sigma_{zz,0}}{\rho_b g D}\right)\exp\left(-4\mu_w K\frac{z}{D}\right), \tag{5.22}$$

$$4\mu_w\left(\frac{\sigma_{rr}}{\rho_b g D}\right) = 1 - \exp\left(-4\mu_w K\frac{z}{D}\right) + 4\mu_w K\left(\frac{\sigma_{zz,0}}{\rho_b g D}\right)\exp\left(-4\mu_w K\frac{z}{D}\right), \tag{5.23}$$

$$4\left(\frac{\tau_w}{\rho_b g D}\right) = 1 - \exp\left(-4\mu_w K\frac{z}{D}\right) + 4\mu_w K\left(\frac{\sigma_{zz,0}}{\rho_b g D}\right)\exp\left(-4\mu_w K\frac{z}{D}\right). \tag{5.24}$$

Notes:

(1) Refer to Chapter 4.4 for a review on Janssen's constant.
(2) A sketch of the stress as a function of depth is shown in Figure 5.2 for zero surcharge ($\sigma_{zz,0} = 0$). Note that the trend shown in the figure is the same regardless of whether it is the vertical, radial, or shear stress. The stresses asymptote to a constant value with increasing depth. The friction with the wall is the reason for this asymptotic behavior since the wall shear stress supports part of the material weight. More mathematically, taking the limit of Eq. (5.18), assuming zero surcharge, as $\mu_w \to 0$,

$$\lim_{\mu_w \to 0}(\sigma_{zz}) = \frac{(\rho_b g D)\left(4K\frac{z}{D}\right)}{4K} = \rho_b g z, \tag{5.25}$$

which is the hydrostatic relation for an incompressible fluid.
(3) With zero surcharge, the stresses approach the hydrostatic relation in the vicinity of the free surface where wall effects are not yet significant, i.e., when $z/D \ll 1$. For example, considering the vertical normal stress and using a Taylor Series expansion for the exponential term,

$$\sigma_{zz} = \frac{\rho_b g D}{4\mu_w K}\left[1 - \exp\left(-4\mu_w K\frac{z}{D}\right)\right], \tag{5.26}$$

$$= \frac{\rho_b g D}{4\mu_w K}\left\{1 - \left[1 - 4\mu_w K\frac{z}{D} + \frac{\left(-4\mu_w K\frac{z}{D}\right)^2}{2!} + \frac{\left(-4\mu_w K\frac{z}{D}\right)^3}{3!} + \cdots\right]\right\}, \tag{5.27}$$
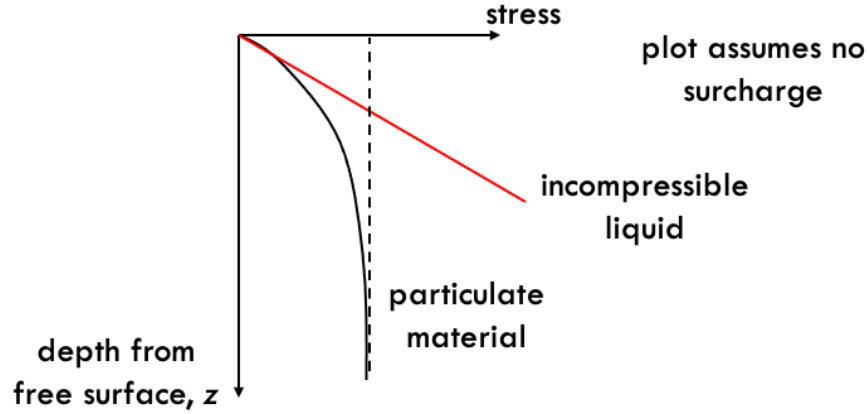
FIGURE 5.2. A sketch of the stress in a cylindrical bin (could be vertical, radial, or shear) as a function of depth from the free surface for zero surcharge. The figure also shows the hydrostatic pressure distribution for an incompressible fluid for comparison.

FIGURE 5.3. (left) A photograph of grain bins. (right) A photograph of tanks containing a liquid.

$$= \frac{\rho_b g D}{4\mu_w K} \left(4\mu_w K \frac{z}{D} \right) \qquad \left(\text{since } \frac{z}{D} \ll 1 \right), \tag{5.28}$$

$$= \rho_b g z. \tag{5.29}$$

(4) The asymptotic value of the vertical normal stress (including a surcharge stress) is found by taking the limit of Eq. (5.18) as $z/D \to \infty$,

$$\lim_{z/D \to \infty} \sigma_{zz} = \frac{\rho_b g D}{4\mu_w K} \left[1 - \lim_{z/D \to \infty} \exp \left(-4\mu_w K \frac{z}{D} \right) \right] + \sigma_{zz,0} \lim_{z/D \to \infty} \exp \left(-4\mu_w K \frac{z}{D} \right), \tag{5.30}$$

$$= \frac{\rho_b g D}{4\mu_w K}. \tag{5.31}$$

Note that the asymptotic stress is independent of the surcharge stress. The asymptotic stress increases with increasing bin diameter, decreasing wall friction coefficient, and decreasing Janssen's constant. Thus, unlike the hydrostatic pressure relation for incompressible fluids, there is no "pressure penalty" when building a tall bin containing a particulate material. This asymptotic effect is why grain bins tend to be tall and narrow while tanks containing liquids tend to be short and squat (Figure 5.3). However, unlike a liquid tank, bins holding particulate materials have a shear stress acting on the bin wall.

(5) The asymptotic stress in Eq. (5.31) is technically only reached at infinite depth. However, when $4\mu_w K(z/D) = 3$, the stresses are approximately 95% of their asymptotic value. For example, if
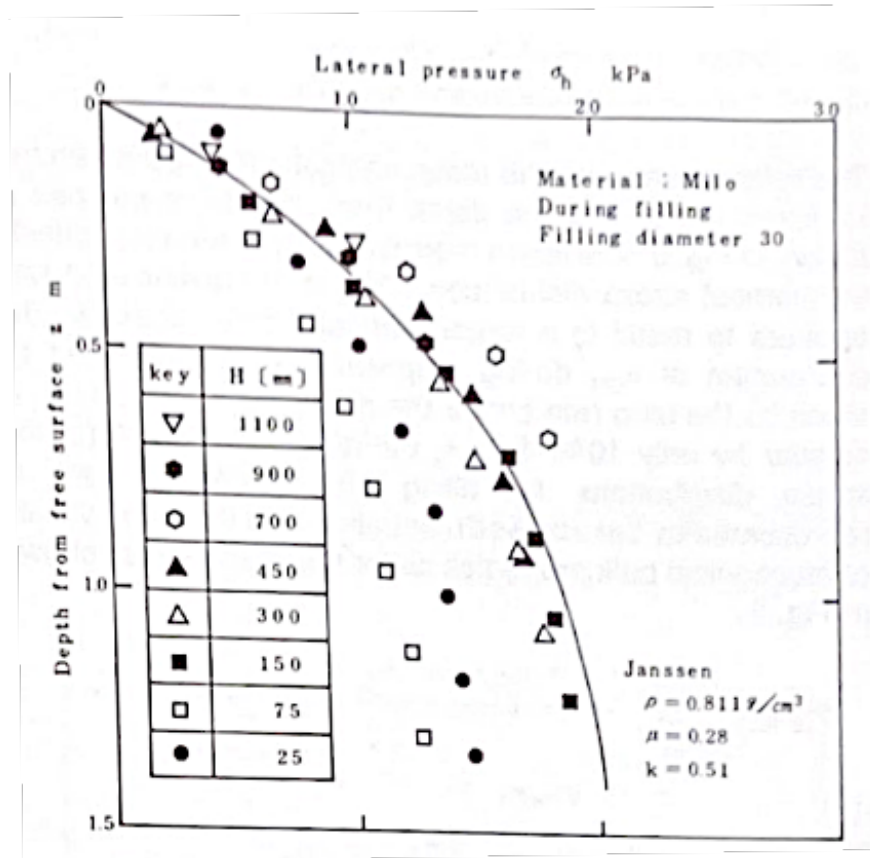
FIGURE 5.4. Experimental measurements of the radial normal stress as a function of depth from the free surface (no surcharge) for different fill levels of Milo (a beverage powder). Included in the figure is Janssen's prediction where Janssen's constant is a fitted parameter. This plot is from Suzuki et al. [3].

the wall friction angle is $\phi_w = 20°$ so $\mu_w = \tan \phi_w = 0.36$ and $K = 0.4$, then the stress reaches 95% of its asymptotic value when the depth is approximately five bin diameters ($z/D \approx 5.2$). The larger the wall friction coefficient and Janssen's constant, the shallower the depth to reach 95% of the asymptotic stresses.

(6) Experimental measurements support the model predictions. Figure 5.4 shows experimental measurements of the radial normal stress as a function of depth from the free surface (no surcharge) for different fill levels of Milo (a beverage powder). Included in the figure is a fit using the Janssen prediction where Janssen's constant is a fitted parameter. The asymptotic behavior is clearly observed.

(7) The surcharge has no impact on the asymptotic stress as is evident from Eq. (5.31) as well as in Figure 5.5. Janssen's assumption of a uniform vertical normal stress is known to be incorrect (discussed in a following note). In particular, this assumption results in large error near the free surface when a surcharge is present. Thus, the trends in Figure 5.5 should only be viewed qualitatively and not quantitatively.

(8) The stress derivation given in this section assumes that the wall friction is fully activated, meaning that the material is either slipping or in an incipient state of slipping against the wall. In a real system, the material may not be slipping and, thus, the previous derivation is a limiting case.
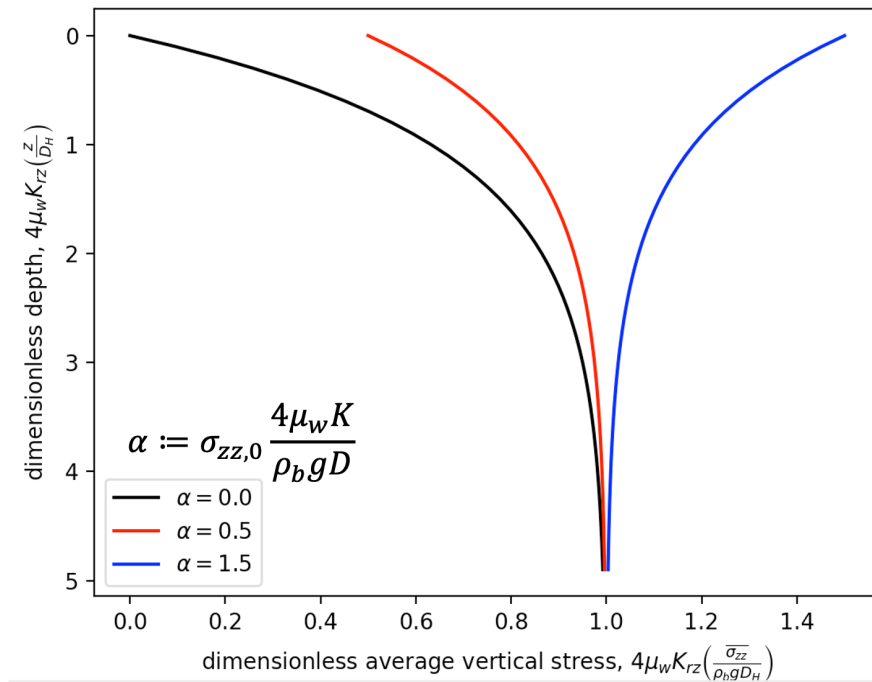
FIGURE 5.5. A plot of dimensionless vertical stress as a function of dimensionless depth from the free surface for different dimensionless surcharge stresses using Eq. (5.22). Note that the asymptotic stress values are identical regardless of the surcharge stress.

(9) The bulk density, wall friction angle, and Janssen's constant can vary as the applied stresses vary. These variations can be accounted for in the stress analysis by numerically solving the differential equation (Eq. (5.11)) with appropriate fits or numerical data for the stress-varying parameters.

(10) For non-circular bin cross-sections, a hydraulic diameter may be used in place of the diameter. The hydraulic diameter, D_H, is defined as,

$$D_H := \frac{4A}{P}, \tag{5.32}$$

where A is the bin cross-sectional area and P is the cross-sectional perimeter. For example, for a rectangular cross-sectional bin,

$$D_H = \frac{4LB}{2L + 2B} = \frac{2LB}{L + B}, \tag{5.33}$$

where L and B are the lengths of the bin sides. The predictions using a hydraulic diameter for a non-circular cross section won't be as accurate since the model derivation assumes uniform stresses across the cross section.

5.2. Active and Passive States

During filling and storage in a cylindrical bin, the system is mostly in the active state as material is compressed vertically during filling (Figure 5.6, left). During discharge, the system moves closer to a passive state near the exit since the vertical stress decreases as material dilates vertically when the exit is opened and the vertical stress becomes small (Figure 5.6, right). Far from the exit, however, the system will continue to be in an active state. For the purpose of simplifying the following explanation, assume that the discharging material is in an active state far from the exit and in a passive state near the exit (Figure 5.7). The division between the active and passive regions is called a switch plane.
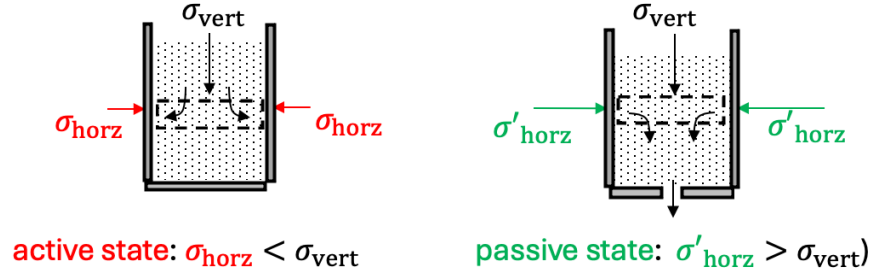
FIGURE 5.6. (left) The active stress state during filling of a cylinder. (right) The passive stress state during discharge of a cylinder.
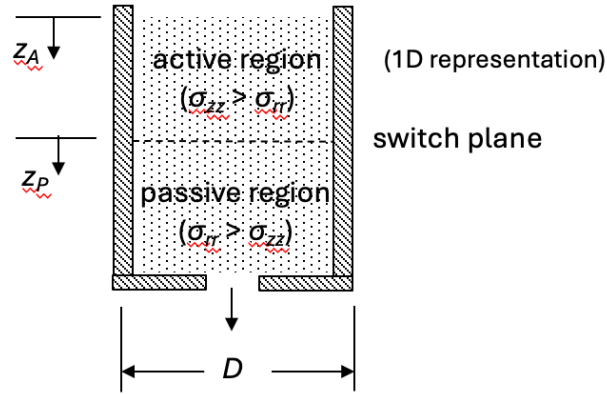
FIGURE 5.7. A simple model illustrating a switch plane in a discharging cylinder.

Now use Janssen's analysis in each region of the cylinder, subject to appropriate boundary conditions and Janssen's constants. Note that this analysis breaks down in the near vicinity of the exit since the vertical stress should go to zero there. In the active region, assuming no surcharge,

$$\sigma_{zz} = \frac{\rho_b g D}{4\mu_w K_A} \left[1 - \exp\left(-4\mu_w K_A \frac{z_A}{D} \right) \right], \tag{5.34}$$

$$\sigma_{rr} = \frac{\rho_b g D}{4\mu_w} \left[1 - \exp\left(-4\mu_w K_A \frac{z_A}{D} \right) \right]. \tag{5.35}$$

For a sufficiently deep active zone, the stresses approach their asymptotic values,

$$\lim_{z_A \to \infty} (\sigma_{zz}) = \frac{\rho_b g D}{4\mu_w K_A}, \tag{5.36}$$

$$\lim_{z_A \to \infty} (\sigma_{rr}) = \frac{\rho_b g D}{4\mu_w}. \tag{5.37}$$

Just below the switch plane, assuming a deep active region,

$$\sigma_{zz}(z_P = 0) = \sigma_{zz}(z_A \to \infty) = \frac{\rho_b g D}{4\mu_w K_A}, \tag{5.38}$$

since the vertical stress must be continuous at the switch plane as can be proven by considering a vertical force balance on a material element at the switch plane. Note that there is no such restriction on the radial stress. Now apply Janssen's analysis to the passive zone using the active zone asymptotic stress as the surcharge stress for the passive zone,

$$\sigma_{zz} = \frac{\rho_b g D}{4\mu_w K_P} \left[1 - \exp\left(-4\mu_w K_P \frac{z_P}{D} \right) \right] + \frac{\rho_b g D}{4\mu_w K_A} \exp\left(-4\mu_w K_P \frac{z_P}{D} \right), \tag{5.39}$$
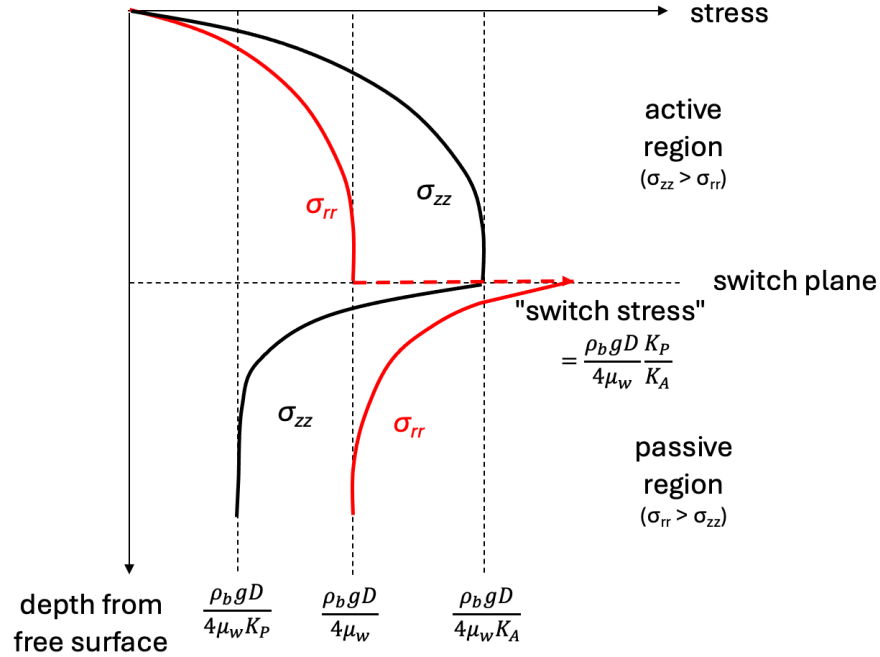
FIGURE 5.8. A sketch showing the vertical and radial stresses in a vertical cylinder with active and passive zones.

$$\sigma_{rr} = \frac{\rho_b g D}{4\mu_w} \left[1 - \exp\left(-4\mu_w K_P \frac{z_P}{D}\right) \right] + \frac{\rho_b g D K_P}{4\mu_w K_A} \exp\left(-4\mu_w K_P \frac{z_P}{D}\right). \tag{5.40}$$

For a sufficiently deep passive zone,

$$\lim_{z_P \to \infty} (\sigma_{zz}) = \frac{\rho_b g D}{4\mu_w K_P}, \tag{5.41}$$

$$\lim_{z_P \to \infty} (\sigma_{rr}) = \frac{\rho_b g D}{4\mu_w}. \tag{5.42}$$

Of particular interest is the radial stress just below the switch plane. Here the radial stress has its maximum value,

$$\sigma_{rr}(z_P = 0) = \frac{\rho_b g D K_P}{4\mu_w K_A}. \tag{5.43}$$

Since $K_P > K_A$, there is a sudden increase in the radial stress at the switch plane. This large radial stress is called a <u>switch stress</u>. A sketch showing the stresses from the previous analysis is shown in Figure 5.8.

Notes:

(1) The largest (radial) wall stress occurs when the bin is opened. During filling the bin entirely in an active state, but during discharge an active zone is located above a passive zone. Thus, one should consider the stresses during discharge to ensure that the largest wall stresses have been considered.

(2) A similar switch stress occurs in the junction between the vertical (e.g., cylindrical) and converging (e.g., conical) sections of a hopper. This topic is addressed in the next chapter.

(3) Plots of the lines of major principal stress are often helpful for visualizing stress fields. For the active state, the major principal stress along the centerline is σ_{zz} since there is no shear stress at the centerline due to symmetry and $\sigma_{zz} > \sigma_{rr}$ in the active state. Thus, the slope of the major principal stress line at the centerline is vertical. To determine the direction of the major principal stress at the wall, refer to the active state Mohr's circle shown in Figure 5.9a. The angle from the vertical normal stress (state Z_A) to the major principal stress in the Mohr's circle is $\omega - \phi_w$ in the

counter-clockwise direction, where ω is found using Eq. (4.30). Thus, in the "real world" the angle from the vertical normal stress to the major principal stress is $\frac{1}{2}(\omega - \phi_w)$ in the counter-clockwise direction. A sketch of the corresponding major principal stress lines are shown to the left of the Mohr's circle. Note that when the wall is frictionless ($\phi_w = 0$), $\omega = 0$ and the lines of major principal stress are vertical everywhere.

A similar analysis can be performed for the passive state (Figure 5.9b). For this case, $\sigma_{rr} > \sigma_{zz}$ along the centerline so the slope of the major principal stress line is horizontal there. The angle in the Mohr's circle from the radial stress at the wall to the major principal stress is $\omega + \phi_w$ in the clockwise direction and, thus, the "real world" angle from the radial wall stress to the major principal stress is $\frac{1}{2}(\omega + \phi_w)$. If the wall is frictionless, then the lines of major principal stress are horizontal everywhere.

5.3. The Distribution Factor for a Cylindrical Bin

Janssen assumed a uniform vertical normal stress, but this assumption cannot be correct. From symmetry the shear stress τ_{rz} at the centerline must be zero, making the vertical and radial normal stresses principal stresses at the centerline. At a frictional wall the shear stress is non-zero. Thus, the shear stress, and normal stresses, can vary over a horizontal cross-section. Figure 5.10 shows experimental measurements of the vertical normal stress as a function of radius in a cylindrical bin in two different experiments. Clearly the stress does not remain constant over the cross-section.

In Janssen's analysis (Figure 5.1), we should have used an average vertical normal stress,

$$\overline{\sigma_{zz}}A = \int_A \sigma_{zz}dA \implies \overline{\sigma_{zz}} = \frac{1}{A}\int_A \sigma_{zz}dA, \tag{5.44}$$

where A is the cross-sectional area of the material element in the bin. Repeating Eq. (5.7), but using an average vertical normal stress,

$$\frac{d\overline{\sigma_{zz}}}{dz} + \frac{4}{D}\tau_w = \rho_b g. \tag{5.45}$$

When writing the wall shear stress in terms of the radial and vertical normal stresses, the values specifically at the wall, indicated by a subscript "w", should be used, i.e.,

$$\sigma_{rr,w} = K_w \sigma_{zz,w}, \tag{5.46}$$

$$\tau_w = \mu_w \sigma_{rr,w}, \tag{5.47}$$

where K_w is Janssen's constant evaluated at the wall (Eq. (4.51)). Substituting these expressions into the differential equation gives,

$$\frac{d\overline{\sigma_{zz}}}{dz} + \frac{4\mu_w K_w}{D}\sigma_{zz,w} = \rho_b g. \tag{5.48}$$

Walker [5] defined a <u>Distribution Factor, $\mathcal{D}$,</u> to relate the vertical normal stress at the wall to the average vertical normal stress,

$$\mathcal{D} := \frac{\sigma_{zz,w}}{\overline{\sigma_{zz}}}. \tag{5.49}$$

Re-writing the differential equation using the distribution factor,

$$\frac{d\overline{\sigma_{zz}}}{dz} + \frac{4\mu_w K_w \mathcal{D}}{D}\overline{\sigma_{zz}} = \rho_b g. \tag{5.50}$$

Assuming $\mathcal{D}$ (and ρ_b, g, μ_w, and K_w) does not vary with the depth z, the solution to the differential equation with zero surcharge is similar to the previous Janssen relation,

$$\overline{\sigma_{zz}} = \frac{\rho_b gD}{4\mu_w K_w \mathcal{D}}\left[1 - \exp\left(-4\mu_w K_w \mathcal{D}\frac{z}{D}\right)\right]. \tag{5.51}$$

To determine the value for the distribution function, Walters [6] made use of Mohr's circles for material elements at the bin centerline, the wall, and at some arbitrary radius in between. In particular, he assumed:

(A) Active state
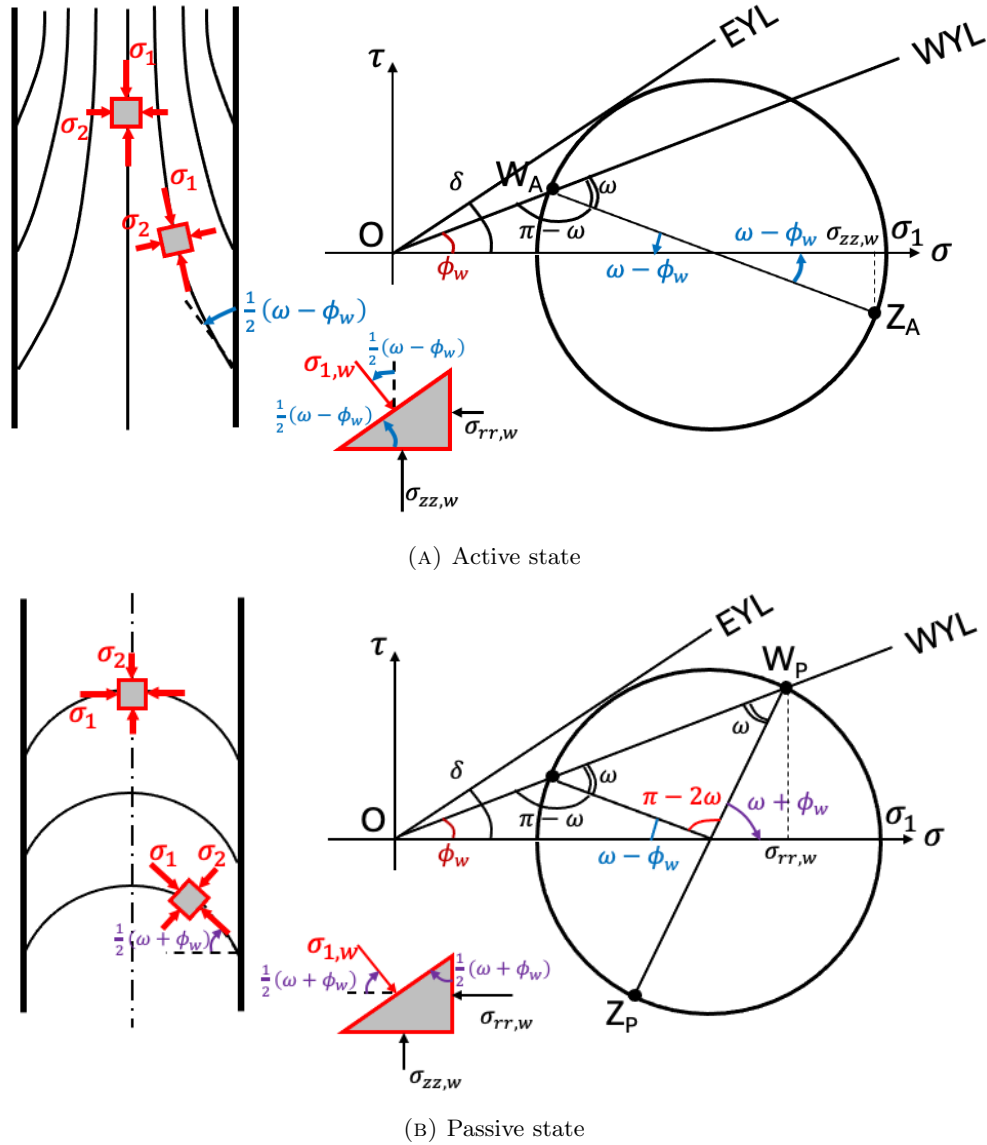
(B) Passive state

FIGURE 5.9. (right) The Mohr's circles corresponding to a material element at a vertical wall. (left) The corresponding lines of major principal stress. Conditions for active and passive stress states are shown.

(1) that the radial normal stress (σ_{rr}) is independent of the radius, and (2) that the shear stress varies linearly with the radius, i.e.,

$$\tau_{rz} = \underbrace{\tau_{rz,w}}_{=\tau_w} \left(\frac{r}{D/2} \right). \tag{5.52}$$

Recall that $\tau_{rz} = 0$ at the centerline ($r = 0$) from symmetry.

Assumption 2 is strictly only true at large depths where the vertical stress has reached its asymptotic value so the force balance on the material element is,

$$\tau_{rz}(2\pi r dz) = \rho_b g(\pi r^2 dz) \implies \tau_{rz} = \frac{1}{2}\rho_b g r. \tag{5.53}$$
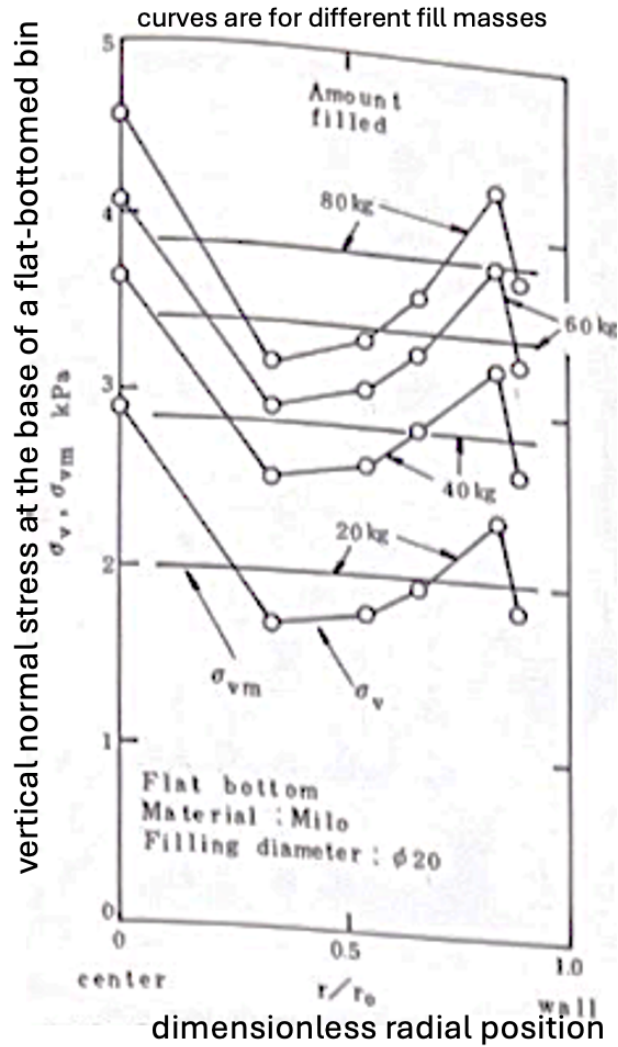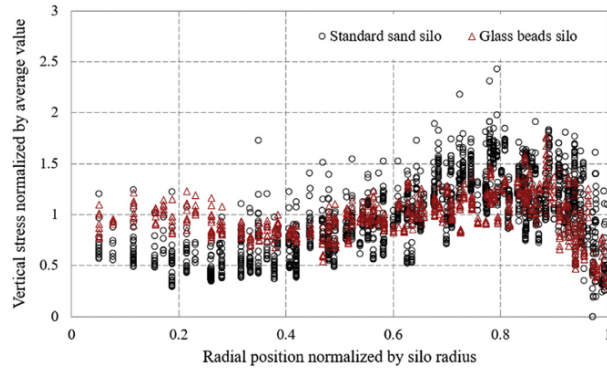
FIGURE 5.10. Vertical normal stress as a function of dimensionless radial position for cylindrical bins containing various granular materials. The left figure from Liu et al. [4] and the right figure is from Suzuki et al. [3].

Assumption 1 can be shown to be incorrect via the following argument. From the solid mechanics Equilibrium Equations in cylindrical coordinates assuming axisymmetric and asymptotic (in z) conditions,

$$\frac{d\sigma_{rr}}{dr} = \frac{\sigma_{\theta\theta} - \sigma_{rr}}{r}. \tag{5.54}$$

Since $\sigma_{\theta\theta} \neq \sigma_{rr}$, in general ($\sigma_{\theta\theta}$ is a principal stress while σ_{rr} isn't), σ_{rr} will be a function of r.

Despite the questionable assumptions, we'll continue with the analysis following Walker's approach. Consider the Mohr's circles for material elements at the centerline, wall, and at an arbitrary radius shown in Figure 5.11. Since we're assuming that the radial normal stress is constant, the radial states at the centerline, at an arbitrary radius, and the wall, R_c, R_r, and R_w, respectively, must all align vertically. Note that the radial and vertical stresses are principal stresses at the centerline. Considering the Mohr's circle through point R_r and using Pythagorean's Theorem for triangle $\Delta p_r R_c R_r$,

$$x_r^2 = \tau_{rz,r}^2 + (p_r - \sigma_{rr})^2, \tag{5.55}$$

where x_r and p_r are, respectively, the radius and hydrostatic pressure of the Mohr's circle for the arbitrary radius Mohr's circle. The previous equation is identical for the active and passive states, although in the passive state the terms in the parentheses are flipped. Note that from triangle $\Delta p_r OE$,

$$\sin \delta = \frac{x_r}{p_r} \implies p_r = \frac{x_r}{\sin \delta}. \tag{5.56}$$

Substituting the previous equation into the one prior to that, re-arranging, and solving for x_r,

$$x_r^2 = \tau_{zr,r}^2 + \left[\left(\frac{x_r}{\sin \delta} \right) - \sigma_{rr} \right]^2, \tag{5.57}$$

$$x_r^2 = \tau_{rz,r}^2 + \left(\frac{x_r}{\sin \delta} \right)^2 - 2 \left(\frac{x_r}{\sin \delta} \right) \sigma_{rr} + \sigma_{rr}^2, \tag{5.58}$$

$$\left(1 - \frac{1}{\sin^2 \delta} \right) x_r^2 + 2 \left(\frac{\sigma_{rr}}{\sin \delta} \right) x_r - \left(\sigma_{rr}^2 + \tau_{rz,r}^2 \right) = 0, \tag{5.59}$$

$$\left(\frac{\sin^2 \delta - 1}{\sin^2 \delta} \right) x_r^2 + 2 \left(\frac{\sigma_{rr}}{\sin \delta} \right) x_r - \left(\sigma_{rr}^2 + \tau_{rz,r}^2 \right) = 0, \tag{5.60}$$

$$\left(\frac{-\cos^2 \delta}{\sin^2 \delta} \right) x_r^2 + 2 \left(\frac{\sigma_{rr}}{\sin \delta} \right) x_r - \left(\sigma_{rr}^2 + \tau_{rz,r}^2 \right) = 0, \tag{5.61}$$

$$x_r = \left(\frac{-\sin \delta}{2 \cos^2 \delta} \right) \left[-2 \left(\frac{\sigma_{rr}}{\sin \delta} \right) \pm \sqrt{ \frac{4 \sigma_{rr}^2}{\sin^2 \delta} - \frac{4 \cos^2 \delta}{\sin^2 \delta} \left(\sigma_{rr}^2 + \tau_{rz,r}^2 \right) } \right], \tag{5.62}$$

$$x_r = \left(\frac{\sin \delta}{\cos^2 \delta} \right) \left[\left(\frac{\sigma_{rr}}{\sin \delta} \right) \pm \frac{1}{\sin \delta} \sqrt{ \sigma_{rr}^2 - \cos^2 \delta \left(\sigma_{rr}^2 + \tau_{rz,r}^2 \right) } \right], \tag{5.63}$$

$$x_r = \left(\frac{1}{\cos^2 \delta} \right) \left[\sigma_{rr} \pm \sqrt{ \sigma_{rr}^2 \sin^2 \delta - \tau_{rz,r}^2 \cos^2 \delta } \right], \tag{5.64}$$

$$x_r = \left(\frac{\tan \delta}{\cos \delta} \right) \left[\sigma_{rr} \pm \sqrt{ \sigma_{rr}^2 \sin^2 \delta - \tau_{rz,r}^2 \cos^2 \delta } \right]. \tag{5.65}$$

The positive square root is used for the active case and the negative root is for the passive case.

We can also obtain the following from the center of the Mohr's circle,

$$p_r = \frac{1}{2} (\sigma_{zz,r} + \sigma_{rr}) \implies \sigma_{zz,r} = 2p_r - \sigma_{rr}. \tag{5.66}$$

Substituting Eq. (5.56) into this equation gives,

$$\sigma_{zz,r} = 2 \left(\frac{x_r}{\sin \delta} \right) - \sigma_{rr}. \tag{5.67}$$
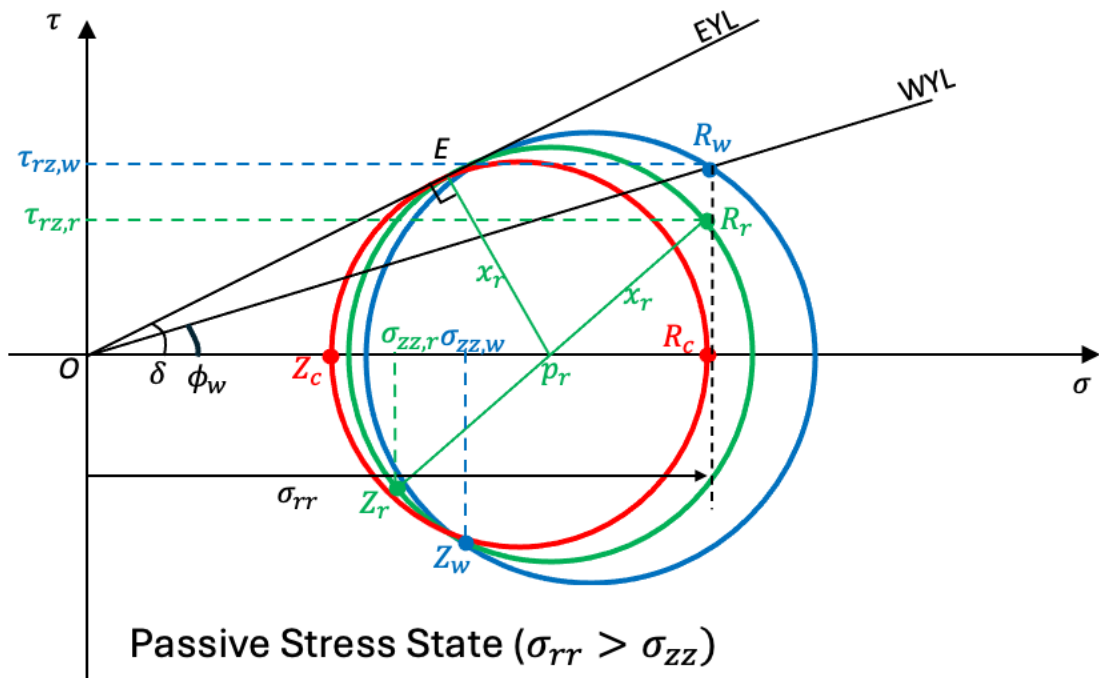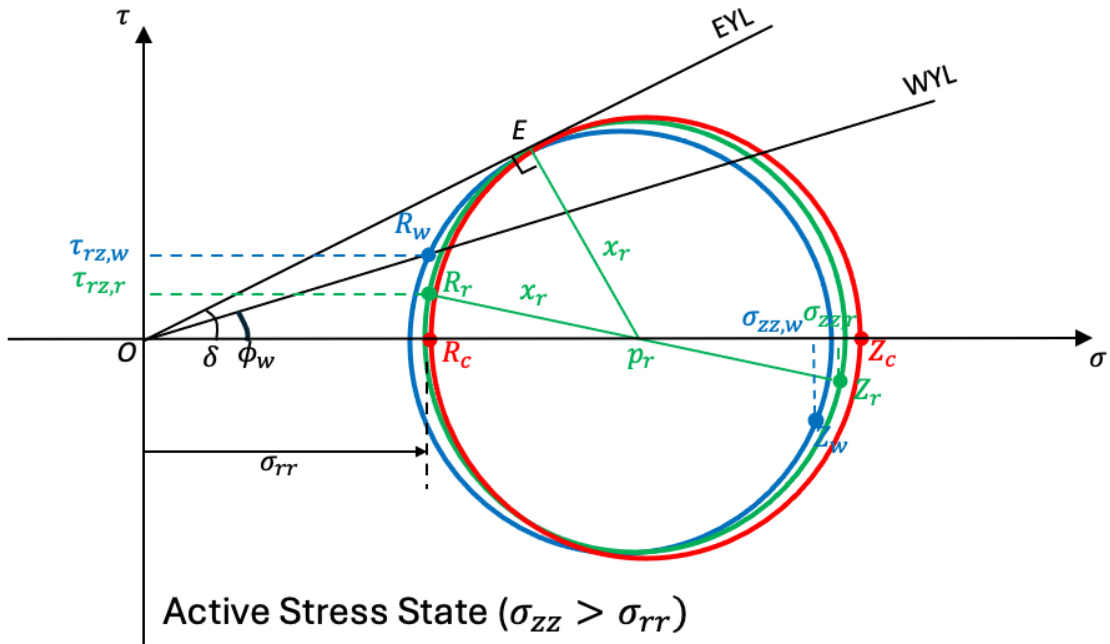
FIGURE 5.11. Mohr's circles for material elements at the centerline (red), at the wall (blue), and at an arbitrary radius (green).

Substituting Eqs. (5.52) and (5.65) into the previous equation gives,

$$\sigma_{zz,r} = \frac{2}{\sin\delta}\left(\frac{\tan\delta}{\cos\delta}\right)\left[\sigma_{rr} \pm \sqrt{\sigma_{rr}^2\sin^2\delta - \tau_w^2\left(\frac{r}{D/2}\right)^2\cos^2\delta}\right] - \sigma_{rr}, \tag{5.68}$$

$$= \left(\frac{2}{\cos^2\delta}\right)\left[\sigma_{rr} \pm \sqrt{\sigma_{rr}^2\sin^2\delta - 4\sigma_{rr}^2\left(\frac{\tau_w}{\sigma_{rr}}\right)^2\left(\frac{r}{D}\right)^2\cos^2\delta}\right] - \left(\frac{2}{\cos^2\delta}\right)\frac{\sigma_{rr}\cos^2\delta}{2}, \tag{5.69}$$

$$= \left(\frac{2}{\cos^2\delta}\right)\left[\sigma_{rr} - \frac{1}{2}(\cos^2\delta)\sigma_{rr} \pm \sigma_{rr}\sqrt{\sin^2\delta - 4\tan^2\phi_w\left(\frac{r}{D}\right)^2\cos^2\delta}\right], \tag{5.70}$$

$$= \left(\frac{2\sigma_{rr}}{\cos^2\delta}\right)\left[1 - \frac{1}{2}(\cos^2\delta) \pm \sqrt{\sin^2\delta - 4\tan^2\phi_w\cos^2\delta\left(\frac{r}{D}\right)^2}\right], \tag{5.71}$$

$$= \left(\frac{\sigma_{rr}}{\cos^2\delta}\right)\left[1 + 1 - \cos^2\delta \pm 2\sqrt{\sin^2\delta - 4\sin^2\delta\left(\frac{\tan\phi_w}{\tan\delta}\right)^2\left(\frac{r}{D}\right)^2}\right], \tag{5.72}$$

$$\sigma_{zz,r} = \left(\frac{\sigma_{rr}}{\cos^2\delta}\right)\left[1 + \sin^2\delta \pm 2\sin\delta\sqrt{1 - 4c\left(\frac{r}{D}\right)^2}\right], \tag{5.73}$$

where,

$$c := \left(\frac{\tan\phi_w}{\tan\delta}\right)^2. \tag{5.74}$$

The average vertical stress on a horizontal circular cross section is,

$$\overline{\sigma_{zz}} = \frac{1}{\pi D^2/4}\int_0^{D/2}\sigma_{zz,r}(2\pi r dr). \tag{5.75}$$

Substituting Eq. (5.73) into the previous integral and expanding,

$$\overline{\sigma_{zz}} = \frac{1}{\pi D^2/4}\int_0^{D/2}\left(\frac{\sigma_{rr}}{\cos^2\delta}\right)\left[1 + \sin^2\delta \pm 2\sin\delta\sqrt{1 - 4c\left(\frac{r}{D}\right)^2}\right](2\pi r dr), \tag{5.76}$$

$$= \frac{8}{D^2}\left(\frac{\sigma_{rr}}{\cos^2\delta}\right)\int_0^{D/2}\left[1 + \sin^2\delta \pm 2\sin\delta\sqrt{1 - 4c\left(\frac{r}{D}\right)^2}\right](r dr), \tag{5.77}$$

$$= \frac{8}{D^2}\left(\frac{\sigma_{rr}}{\cos^2\delta}\right)\left\{\frac{D^2}{8} + \frac{D^2}{8}\sin^2\delta \pm \frac{(\sin\delta)D^2\left[(1-c)^{3/2} - 1\right]}{6c}\right\}, \tag{5.78}$$

$$= \left(\frac{\sigma_{rr}}{\cos^2\delta}\right)\left\{1 + \sin^2\delta \pm \frac{4\sin\delta\left[(1-c)^{3/2} - 1\right]}{3c}\right\}, \tag{5.79}$$

$$\overline{\sigma_{zz}} = \left(\frac{\sigma_{rr}}{\cos^2\delta}\right)\left(1 + \sin^2\delta \pm 2y\sin\delta\right), \tag{5.80}$$

where,

$$y := \frac{2}{3c}\left[1 - (1-c)^{3/2}\right]. \tag{5.81}$$

Now recall that the Janssen constant at the wall (Eq. (4.51)) is,

$$K_w = \frac{\sigma_{rr,w}}{\sigma_{zz,w}} \implies \sigma_{zz,w} = \frac{\sigma_{rr,w}}{K_w} = \frac{\sigma_{rr}}{K_w}, \tag{5.82}$$

where the last equality is because the radial normal stress is assumed constant along a horizontal cross section. From the definition of the distribution factor (Eq. (5.49)),

$$\mathcal{D} = \frac{\sigma_{zz,w}}{\overline{\sigma_{zz}}} = \frac{\sigma_{rr}}{K_w\left(\frac{\sigma_{rr}}{\cos^2\delta}\right)\left(1 + \sin^2\delta \pm 2y\sin\delta\right)}, \tag{5.83}$$

$$= \frac{\cos^2 \delta}{K_w \left(1 + \sin^2 \delta + \kappa 2y \sin \delta\right)}, \tag{5.84}$$

where $\kappa = +1$ for the active case and $\kappa = -1$ for the passive case.

Notes:

(1) For convenience, several of the previous expressions are re-written here:

$$\sigma_{zz,w} = \mathcal{D}\overline{\sigma_{zz}}, \tag{5.85}$$

$$\sigma_{rr,w} = K_w \sigma_{zz,w}, \tag{5.86}$$

$$\mathcal{D} = \frac{\cos^2 \delta}{K_w \left(1 + \sin^2 \delta + \kappa 2y \sin \delta\right)}, \tag{5.87}$$

$$K_w = \frac{1 - \kappa \sin \delta \cos(\omega - \kappa \phi_w)}{1 + \kappa \sin \delta \cos(\omega - \kappa \phi_w)}, \tag{5.88}$$

$$\sin \omega = \frac{\sin \phi_w}{\sin \delta}, \tag{5.89}$$

$$c = \left(\frac{\tan \phi_w}{\tan \delta}\right)^2, \tag{5.90}$$

$$y = \frac{2}{3c} \left[1 - (1 - c)^{3/2}\right], \tag{5.91}$$

$$\kappa = \begin{cases} +1 & \text{active case} \\ -1 & \text{passive case} \end{cases}. \tag{5.92}$$

(2) A plot of the active and passive distribution factors as functions of the effective angle of internal friction for a range of wall friction angles is shown in Figure 5.12. For the active state, the distribution factor ranges between $0.6 < \mathcal{D}_A < 1$. If $\phi_w < \delta - 5°$, then $0.9 < \mathcal{D}_A < 1$ and $\mathcal{D}_A$ can reasonably be assumed to equal one. For the passive state, $1 < \mathcal{D}_P < 3$. Keep in mind that $\mathcal{D}$ is assumed to be independent of depth and that σ_{rr} is constant, neither of which is exactly true and, thus, the precise value of $\mathcal{D}$ is not well known. In practice, $\mathcal{D}_A$ is usually assumed equal to one for simplicity and because the error of this assumption is typically small. Although the precise value for the distribution factor for the passive case isn't known, it does appear to be significant and a safety factor should be considered in stress calculations.

(3) Examining Eq. (5.73) shows that the vertical normal stress is expected to decrease monotonically from the centerline to the wall for the active case (increase monotonically for the passive case). This trend doesn't match the experimental trends shown in Figure 5.10. Thus, although defining a distribution factor to account for a non-uniform vertical stress is worthwhile, the assumptions of a constant radial stress and the distribution factor being independent of the depth need to be improved to better match experimental observations.

5.4. Summary

Summarizing the significant points in this chapter:

(1) The Method of Differential Slices (aka Janssen's method) is a simple model for estimating stresses in bins.
(2) Stresses asymptote with depth due to wall shear stresses supporting some of the material weight.
(3) During filling of a cylindrical bin, the material is close to being in an active stress state. During discharge, the material near the exit is in a passive state.
(4) A (radial) wall switch stress occurs when the stress state changes from active to passive in a cylindrical bin.
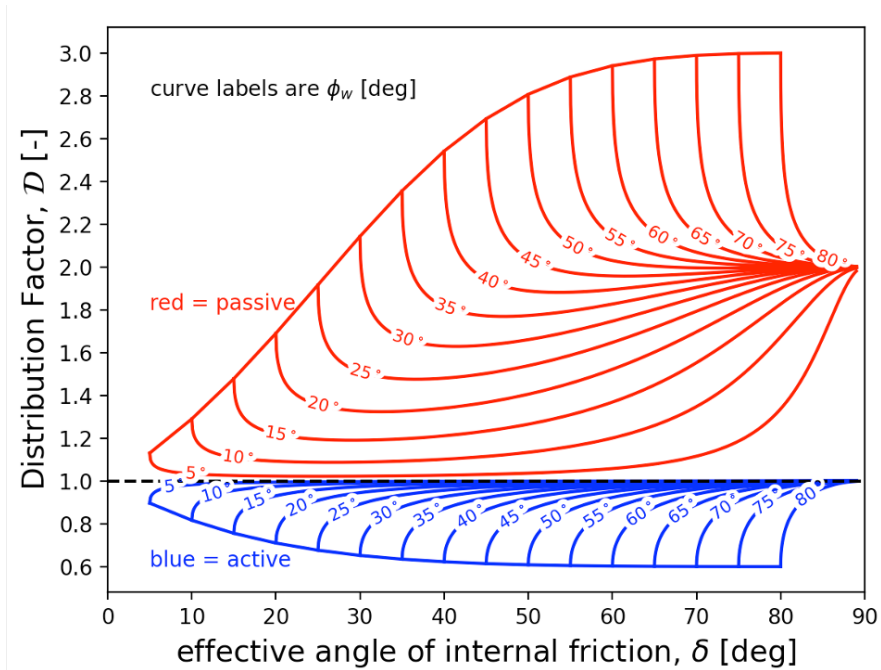
FIGURE 5.12. A plot of the active and passive distribution factors as functions of the effective angle of internal friction for a range of wall friction angles.

(5) A distribution factor can be defined to relate the vertical normal stress at the wall to the average vertical normal stress. The model presented here for the distribution factor assumes the radial stress is a constant (not accurate) and that the shear stress is proportional to the radius (only true at large depths). If the wall friction angle is smaller than the effective angle of internal friction by $5°$, then $\mathcal{D}_A \approx 1$. For the passive case, $1 < \mathcal{D}_P < 3$. Including the distribution factor in the calculation of the switch stress can provide a conservative value for design purposes.

A flat-bottomed steel silo 12 ft in diameter and 60 ft high is to be built.
1. Estimate the maximum normal stress acting on the silo <u>side</u> walls if the silo is filled with a particulate material with a specific weight of 62.4 lb$_f$/ft^3, an effective angle of internal friction of 40°, and a wall friction angle of 20°. Assume an active stress state during filling and a distribution factor of one.
2. Estimate the total force the silo <u>base</u> must support.
3. Estimate the maximum normal stress if the silo is filled with water with a specific weight of 62.4 lb$_f$/ft^3.
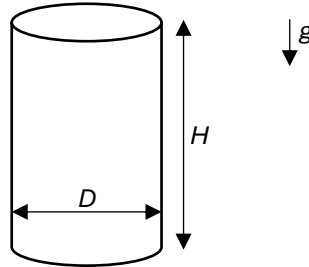
SOLUTION:
Use the Method of Differential Slices (Janssen's method) to estimate the stresses. From the derivation in lecture for a cylindrical bin filled with constant property material and no surcharge,

$$\sigma_{zz,w} = \frac{\rho_b g D}{4\mu_w K_{w,A} \mathcal{D}_A}\left[1 - \exp\left(-4\mu_w K_{w,A}\mathcal{D}_A \frac{z}{D}\right)\right],$$ (1)

$$\sigma_{rr,w} = K_{w,A}\sigma_{zz,w} = \frac{\rho_b g D}{4\mu_w \mathcal{D}_A}\left[1 - \exp\left(-4\mu_w K_{w,A}\mathcal{D}_A \frac{z}{D}\right)\right],$$ (2)

$$F_{\text{base}} = \overline{\sigma_{zz}}\big|_{z=H} \frac{\pi D^2}{4}.$$ (3)

In the previous equations,

$$\mu_w = \tan\phi_w,$$ (4)

$$K_{w,A} = \frac{1-\sin\delta\cos(\omega-\phi_w)}{1+\sin\delta\cos(\omega-\phi_w)} \text{ (It's acceptable to also use the Eurocode 1 or DIN values.),}$$ (5)

$$\sin\omega = \frac{\sin\delta}{\sin\phi_w},$$ (6)

$$\mathcal{D} = \frac{\sigma_{zz,w}}{\sigma_{zz}}.$$ (7)

Using the given data,

$\rho_b g$ = 62.4 lb$_f$/ft^3, D = 12 ft, H = 60 ft, δ = 40°, ϕ_w = 20°, $\mathcal{D}_A \approx 1$,

=> μ_w = 0.364, ω = 32.147°, $K_{w,A}$ = 0.228,

=> $\sigma_{zz,w}\big|_{z=H}$ = 1825.79 psf, $\boxed{\sigma_{rr,w}\big|_{z=H} = 417 \text{ psf}}$, $\boxed{F_{\text{base}} = 206000 \text{ lb}_f}$.

If using the Eurocode 1 Janssen coefficient,

$$K_{\text{Eurocode}} = 1.1(1-\sin\delta) = 0.393,$$ (8)

=> $\sigma_{zz,w}\big|_{z=H}$ = 1234.01 psf, $\boxed{\sigma_{rr,w}\big|_{z=H} = 485 \text{ psf}}$, $\boxed{F_{\text{base}} = 140000 \text{ lb}_f}$.

If using the German DIN Janssen coefficient,

$$K_{\text{DIN}} = 1.2(1-\sin\delta) = 0.429,$$ (9)

=> $\sigma_{zz,w}\big|_{z=H}$ = 1146.90 psf, $\boxed{\sigma_{rr,w}\big|_{z=H} = 492 \text{ psf}}$, $\boxed{F_{\text{base}} = 130000 \text{ lb}_f}$.

Clearly, the choice of Janssen's coefficient makes a significant difference in calculating the vertical stress and force, but has less of an effect on the radial wall stress.

For an incompressible liquid with the same specific weight evaluated at z = H,

$\sigma_{rr} = \rho g z$ => $\boxed{\sigma_{rr} = 3740 \text{ psf}}$.   (10)

The following Python code was used to perform the calculations.

```
# janssen_01.py

import numpy as np
import matplotlib.pyplot as plt

def K_w_fcn(delta_rad, phiw_rad, kappa):  # fcn to find Janssen's coefficient
    # kappa_A = +1, kappa_P = -1
    omega_rad = np.arcsin(np.sin(phiw_rad)/np.sin(delta_rad))
    print('omega = %.3f deg' % np.degrees(omega_rad))
    return((1 - kappa*np.sin(delta_rad)*np.cos(omega_rad - kappa*phiw_rad))/(1 +
kappa*np.sin(delta_rad)*np.cos(omega_rad - kappa*phiw_rad)))

def K_Eurocode_fcn(delta_rad):  # Eurocode 1 value for Janssen's coefficient.
    return(1.1*(1-np.sin(delta_rad)))

def K_DIN_fcn(delta_rad):  # German DIN value for Janssen's coefficient.
    return(1.2*(1-np.sin(delta_rad)))


# The given parameters.
gamma_b = 62.4  # lbf/ft^3, bulk specific weight
D = 12  # ft, bin diameter
delta_deg = 40  # deg, effective angle of internal friction
phiw_deg = 20  # deg, wall friction angle
z = 60  # ft, material depth
ScriptD_A = 1  # -, active distribution factor

# Convert from degrees to radians.
delta_rad = np.radians(delta_deg)
phiw_rad = np.radians(phiw_deg)

# Calculate the wall friction coefficient.
mu_w = np.tan(phiw_rad)
print('mu_w = %.3f' % mu_w)

# Calculate the active wall Janssen coefficient.
K_wA = K_w_fcn(delta_rad, phiw_rad, 1)
print('K_wA = %.3f' % K_wA)

# Calculate the vertical stress at the wall of the bin base.
sigma_zzw = gamma_b*D/4/mu_w/K_wA/ScriptD_A*(1 - np.exp(-4*mu_w*K_wA*ScriptD_A*z/D))
print('sigma_zzw = %.3f psf' % sigma_zzw)

# Calculate the radial stress at the wall of the bin base.
sigma_rrw = K_wA*sigma_zzw
print('sigma_rrw = %.3f psf' % sigma_rrw)

# Calculate the vertical force on the base.
F_base = sigma_zzw*np.pi*D*D/4
print('F_base = %.3f lbf' % F_base)

# Using the Eurocode Janssen coefficient.
print('Using K_Eurocode:')
K_Euro = K_Eurocode_fcn(delta_rad)
print('K_Eurocode = %.3f' % K_Euro)

# Calculate the vertical stress at the wall of the bin base.
sigma_zzw = gamma_b*D/4/mu_w/K_Euro/ScriptD_A*(1 - np.exp(-4*mu_w*K_Euro*ScriptD_A*z/D))
print('sigma_zzw = %.3f psf' % sigma_zzw)

# Calculate the radial stress at the wall of the bin base.
sigma_rrw = K_Euro*sigma_zzw
print('sigma_rrw = %.3f psf' % sigma_rrw)

# Calculate the vertical force on the base.
F_base = sigma_zzw*np.pi*D*D/4
print('F_base = %.3f lbf' % F_base)
```

```
# Using the German DIN Janssen coefficient.
print('Using K_DIN:')

K_DIN = K_DIN_fcn(delta_rad)
print('K_DIN = %.3f' % K_DIN)

# Calculate the vertical stress at the wall of the bin base.
sigma_zzw = gamma_b*D/4/mu_w/K_DIN/ScriptD_A*(1 - np.exp(-4*mu_w*K_DIN*ScriptD_A*z/D))
print('sigma_zzw = %.3f psf' % sigma_zzw)

# Calculate the radial stress at the wall of the bin base.
sigma_rrw = K_DIN*sigma_zzw
print('sigma_rrw = %.3f psf' % sigma_rrw)

# Calculate the vertical force on the base.
F_base = sigma_zzw*np.pi*D*D/4
print('F_base = %.3f lbf' % F_base)

# Calculate the maximum normal stress for water.
print('H2O:  rho*g*z = %.3f psf' % (gamma_b*z))
```

Running the code produces the following output:
```
>> python3 ./janssen_01.py
mu_w = 0.364
omega = 32.147 deg
K_wA = 0.228
sigma_zzw = 1825.791 psf
sigma_rrw = 416.649 psf
F_base = 206492.051 lbf
Using K_Eurocode:
K_Eurocode = 0.393
sigma_zzw = 1234.006 psf
sigma_rrw = 484.882 psf
F_base = 139562.765 lbf
Using K_DIN:
K_DIN = 0.429
sigma_zzw = 1146.901 psf
sigma_rrw = 491.625 psf
F_base = 129711.399 lbf
H2O:  rho*g*z = 3744.000 psf
```

You are tasked with estimating the maximum hoop stress, i.e., circumferential stress, acting on a cylindrical silo's wall during filling and discharge. The silo under consideration has a diameter of 10 m and a wall thickness of 15 cm. The silo will be filled with an incompressible material with a bulk density of 720 kg/m^3. The wall friction angle is 20° and the material's effective angle of internal friction is 40°, both of which may be assumed to be constant. Include a distribution factor in your analysis.
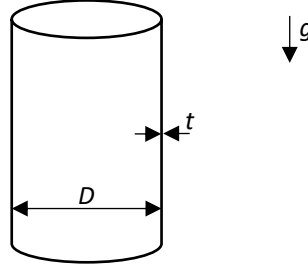
SOLUTION:
The maximum radial stress is the switch stress occurring during discharge and assuming asymptotic behavior for the active region. The asymptotic vertical stress at the wall for the active state is,

$$\sigma_{zz,w,\infty,A} = \frac{\rho_b g D}{4\mu_w K_{w,A}\mathfrak{D}_A}. \tag{1}$$

Thus, the wall radial stress at the switch plane in the passive region is,

$$\sigma_{rr,w,P,\text{switch}} = K_{w,P}\sigma_{zz,w,\infty,A} = \frac{\rho_b g D K_{w,P}}{4\mu_w K_{w,A}\mathfrak{D}_A}. \tag{2}$$

where,

$$\mu_w = \tan\phi_w, \tag{3}$$

$$K_w = \frac{1-\kappa\sin\delta\cos(\omega-\kappa\phi_w)}{1+\kappa\sin\delta\cos(\omega-\kappa\phi_w)} \quad (\kappa_A = +1, \kappa_P = -1), \tag{4}$$

$$\sin\omega = \frac{\sin\phi_w}{\sin\delta}, \tag{5}$$

$$\mathfrak{D}_A = \frac{\cos^2\delta}{K_{w,A}(1+\sin^2\delta+2y\sin\delta)}, \tag{6}$$

$$y = \frac{2}{3c}\left[1-(1-c)^{3/2}\right], \tag{7}$$

$$c = \left(\frac{\tan\phi_w}{\tan\delta}\right)^2. \tag{8}$$

Using the given values,

ρ_b = 700 kg/m^3, g = 9.81 m/s^2, ϕ_w = 20°, δ = 40°,

=> μ_w = 0.364, ω = 32.15°, $K_{w,A}$ = 0.228, $K_{w,P}$ = 2.303, c = 0.188, y = 0.951, $\mathfrak{D}_A$ = 0.975,

=> $\sigma_{rr,w,P,\text{switch}}$ = 501.9 kPa.
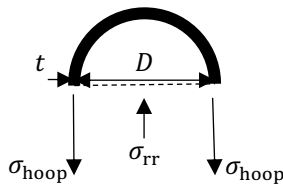
The hoop stress may be found by balancing lateral forces on half the cylindrical bin cross-section,

$$2\sigma_{\text{hoop}}tL = \sigma_{rr}DL \quad => \quad \sigma_{\text{hoop}} = \sigma_{rr}\left(\frac{D}{2t}\right), \tag{5}$$

where L is the distance into the page. Using the previously calculated and the given values,

$$\boxed{\sigma_{\text{hoop}} = 16.7 \text{ MPa}}. \tag{6}$$

The following Python code was used to perform the calculations.

```
# janssen_05.py

import numpy as np

def K_w_fcn(delta_rad, phiw_rad, kappa):
    omega_rad = np.arcsin(np.sin(phiw_rad)/np.sin(delta_rad))
    return ( (1-kappa*np.sin(delta_rad)*np.cos(omega_rad -
kappa*phiw_rad))/(1+kappa*np.sin(delta_rad)*np.cos(omega_rad - kappa*phiw_rad)) )

def ScriptD_fcn(delta_rad, phiw_rad, kappa):
    K_w = K_w_fcn(delta_rad, phiw_rad, kappa)
    c = (np.tan(phiw_rad)/np.tan(delta_rad))**2
    y = 2/3/c*(1-(1-c)**1.5)
    print('(c, y) = (%.3f, %.3f)' % (c, y))
    return( (np.cos(delta_rad))**2/(K_w*(1+(np.sin(delta_rad))**2 + kappa*2*y*np.sin(delta_rad))) )

# The given parameters:
D = 10  # m, diameter
t = 0.15  # m, wall thickness
rhob = 720 # kg/m^3, bulk density
g = 9.81  # m/s^2, gravitational acceleration
delta_deg = 40  # deg, effective angle of internal friction
delta_rad = np.radians(delta_deg)  # convert to radians
phiw_deg = 20  # deg, wall friction angle
phiw_rad = np.radians(phiw_deg)  # convert to radians

mu_w = np.tan(phiw_rad)  # wall friction coefficient
print('mu_w = %.3f' % mu_w)

omega_rad = np.arcsin(np.sin(phiw_rad)/np.sin(delta_rad)) # angle omega
print('omega = %.3f deg' % np.degrees(omega_rad))

K_wA = K_w_fcn(delta_rad, phiw_rad, 1)  # active Janssen coeff at the wall
K_wP = K_w_fcn(delta_rad, phiw_rad, -1)  # passive Janssen coeff at the wall
print('(K_wA, K_wP) = (%.3f, %.3f)' % (K_wA, K_wP))

ScriptD_A = ScriptD_fcn(delta_rad, phiw_rad, 1)  # active distribution factor
print('ScriptD_A = %.3f' % ScriptD_A)

# Determine the radial switch stress, i.e., the largest stress radial stress.
sigma_rr_switch = (rhob*g*D*K_wP)/(4*mu_w*K_wA*ScriptD_A)
print('sigma_rr_switch = %.1f kPa' % (sigma_rr_switch/1000))

# Calculate the corresponding hoop stress.
sigma_hoop_switch = sigma_rr_switch*(D/2/t)
print('sigma_hoop_switch = %.1f MPa' % (sigma_hoop_switch/1e6))
```

Running the code provides the following output.

```
>> python3 ./janssen_05.py
mu_w = 0.364
omega = 32.147 deg
(K_wA, K_wP) = (0.228, 2.303)
(c, y) = (0.188, 0.951)
ScriptD_A = 0.975
sigma_rr_switch = 501.9 kPa
sigma_hoop_switch = 16.7 MPa
```

Derive an expression for the force required to push a uniform plug of material of length L upward through a vertical pipe of diameter D. Assume the material bulk density is ρ_b, the wall friction coefficient is μ_w and Janssen's coefficient is K. Assume all of these quantities are constants.

Sketch how the force increases with increasing material length in the pipe.
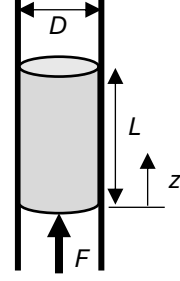
SOLUTION:
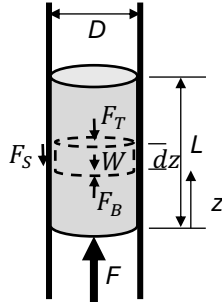
Assume the material is slipping upwards.

Balance forces in the vertical direction on a differentially thin material element,

$$\sum F_V = 0 = F_B - F_T - F_S - W, \tag{1}$$

where,

$$F_B = \overline{\sigma_{zz}} \frac{\pi D^2}{4}, \tag{2}$$

$$F_T = (\overline{\sigma_{zz}} + d\overline{\sigma_{zz}}) \frac{\pi D^2}{4}, \tag{3}$$

$$F_S = \tau_w (\pi D dz), \tag{4}$$

$$W = \rho_b g \frac{\pi D^2}{4} dz. \tag{5}$$

Substitute and simplify,

$$\overline{\sigma_{zz}} \frac{\pi D^2}{4} - (\overline{\sigma_{zz}} + d\overline{\sigma_{zz}}) \frac{\pi D^2}{4} - \tau_w (\pi D dz) - \rho_b g \frac{\pi D^2}{4} dz = 0, \tag{6}$$

$$\frac{d\overline{\sigma_{zz}}}{dz} + \frac{4}{D} \tau_w = -\rho_b g. \tag{7}$$

Relate the shear stress at the wall to the radial stress at the wall via the wall friction coefficient,

$$\tau_w = \mu_w \sigma_{rr,w}. \tag{8}$$

Relate the radial normal stress at the wall to the vertical normal stress at the wall using Janssen's coefficient,

$$\sigma_{rr,w} = K_w \sigma_{zz,w}. \tag{9}$$

Relate the vertical stress at the wall to the average vertical stress using a distribution factor,

$$\sigma_{zz,w} = \mathcal{D} \overline{\sigma_{zz}}. \tag{10}$$

Substitute Eqs. (8) – (10) into Eq. (7),

$$\frac{d\overline{\sigma_{zz}}}{dz} + \frac{4\mu_w K_w \mathcal{D}}{D} \overline{\sigma_{zz}} = -\rho_b g. \tag{11}$$

Solve the previous differential equation assuming the material bulk density, gravitational acceleration, wall friction coefficient, Janssen coefficient, and distribution factor don't vary with the elevation,

$$\overline{\sigma_{zz}} = -\frac{\rho_b g D}{4\mu_w K_w \mathcal{D}} + C \exp\left(-4\mu_w K_w \mathcal{D} \frac{z}{D}\right), \tag{12}$$

where C is a constant of integration. This constant may be found from the boundary condition applied at $z = L$ where the stress is zero,

$$\overline{\sigma_{zz}}(z = L) = 0 = -\frac{\rho_b g D}{4\mu_w K_w \mathcal{D}} + C \exp\left(-4\mu_w K_w \mathcal{D} \frac{L}{D}\right) \Rightarrow C = \frac{\rho_b g D}{4\mu_w K_w \mathcal{D}} \exp\left(4\mu_w K_w \mathcal{D} \frac{L}{D}\right). \tag{13}$$

Thus, the vertical stress distribution is,

$$\overline{\sigma_{zz}} = -\frac{\rho_b g D}{4\mu_w K_w \mathcal{D}} + \frac{\rho_b g D}{4\mu_w K_w \mathcal{D}} \exp\left(4\mu_w K_w \mathcal{D} \frac{L}{D}\right) \exp\left(-4\mu_w K_w \mathcal{D} \frac{z}{D}\right),$$ (14)

$$\overline{\sigma_{zz}} = \frac{\rho_b g D}{4\mu_w K_w \mathcal{D}} \left\{ \exp\left[4\mu_w K_w \mathcal{D} \left(\frac{L-z}{D}\right)\right] - 1 \right\}.$$ (15)

The force applied by the piston is,

$$F = \overline{\sigma_{zz}}(z=0)\frac{\pi D^2}{4} = \frac{\pi D^2}{4} \frac{\rho_b g D}{4\mu_w K_w \mathcal{D}} \left\{ \exp\left[4\mu_w K_w \mathcal{D}\left(\frac{L}{D}\right)\right] - 1 \right\}.$$ (16)

In dimensionless form,

$$\boxed{F\left(\frac{16\mu_w K_w \mathcal{D}}{\pi \rho_b g D^3}\right) = \exp\left[4\mu_w K_w \mathcal{D}\left(\frac{L}{D}\right)\right] - 1}.$$ (17)

A plot of the dimensionless force as a function of the dimensionless length is shown below.

Note that the force increases exponentially with the length of material in the cylinder and extremely large forces are required to push long lengths of material through the pipe. Thus, granular materials are rarely "pumped" through pipes, unlike fluids.
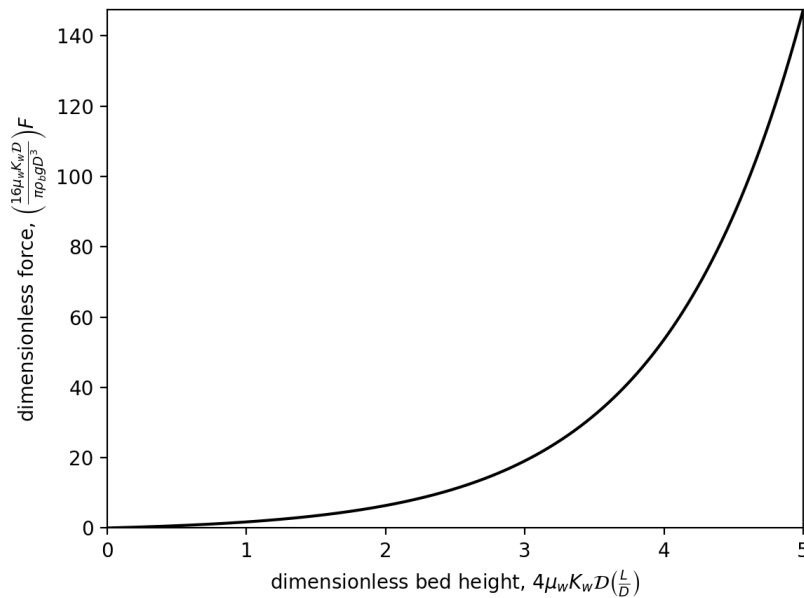
The following Python code was used to generate the plot.

```
# janssen_06.py

import numpy as np
import matplotlib.pyplot as plt

def F_prime(Lprime):  # dimensionless force
    return (np.exp(Lprime)-1)

Lprime_values = np.linspace(0,5,1000)  # range of dimensionless length

F_values = F_prime(Lprime_values)  # calculate dimensionless force values

# Plot the results.
plt.plot(Lprime_values, F_values, color='k', linestyle = 'solid', marker='')
plt.xlabel(r'dimensionless bed height, $4 \mu_w K_w \mathcal{D} \left(\frac{L}{D}\right)$')
plt.ylabel(r'dimensionless force, $\left(\frac{16 \mu_w K_w \mathcal{D}}{\pi \rho_b g D^3}\right) F$')
plt.margins(x=0,y=0)
plt.show()
```

Bibliography

[1] H. Janssen, "Versuche uber getreidedruck in silozellen," <u>Zeitschrift des Vereines Deutscher Ingenieure</u>, vol. 39, pp. 1045–1049, 1895.

[2] M. Sperl, "Experiments on corn pressure in silo cells - translation and comment of janssen's paper from 1895," <u>Granular Matter</u>, vol. 8, pp. 59–65, 2006. DOI: [10.1007/s10035-005-0224-z](10.1007/s10035-005-0224-z).

[3] M. Suzuki, T. Akashi, and K. Matsumoto, "Flow behaviour and stress conditions in small and medium silos," <u>Bulk Solids Handling</u>, vol. 5, no. 3, pp. 611–620, 1985.

[4] Y.-Y. Liu, D.-L. Zhang, B.-B. Dai, J. Su, Y. Li, and A. Yeung, "Experimental study on vertical stress distribution underneath granular silos," <u>Powder Technology</u>, vol. 381, pp. 601–610, 2012.

[5] D. Walker, "An approximate theory for pressures and arching in hoppers," <u>Chemical Engineering Science</u>, vol. 21, pp. 975–997, 1966.

[6] J. Walters, "A theoretical analysis of stresses in silos with vertical walls," <u>Chemical Engineering Science</u>, vol. 28, pp. 13–21, 1973.

CHAPTER 6

Stresses in a Conical Hopper

In addition to cylindrical bins, conical hoppers are also common geometries found in industrial applications. In this chapter we apply the Method of Differential Slices to a conical hopper. Although not provided in this chapter, the same analysis can be performed for a wedge-shaped hopper (aka a planar or slot hopper).

6.1. Force Balance on a Differential Material Element

Consider an axi-symmetric conical hopper containing a material with constant properties, as shown in Figure 6.1. For this geometry, we'll put the coordinate system at the hopper apex for convenience. We'll also assume the hopper has a half-angle from the vertical of θ. Assume the material is in an incipient state of downward slip, as if it was discharging from the hopper, for example. As with the analysis for a cylindrical bin, we'll balance forces in the vertical direction on a thin horizontal element, which can be written as,

$$\sum F_z = 0 = F_{\text{bottom}} - F_{\text{top}} - W + F_{\text{sides}}. \tag{6.1}$$

The force that the material below the element exerts upward on the element is,

$$F_{\text{bottom}} = \overline{\sigma_{zz}} A, \tag{6.2}$$

where $\overline{\sigma_{zz}}$ is the average vertical normal stress acting on the element and A is the cross-sectional area of the element. The force that the material above the element exerts downward on the element is,

$$F_{\text{top}} = \overline{\sigma_{zz}} A + d\left(\overline{\sigma_{zz}} A\right), \tag{6.3}$$

Note that both the average vertical normal stress and the element area can change over the small distance dz; hence, the differential term includes both the stress and area. The material (differential) weight acts
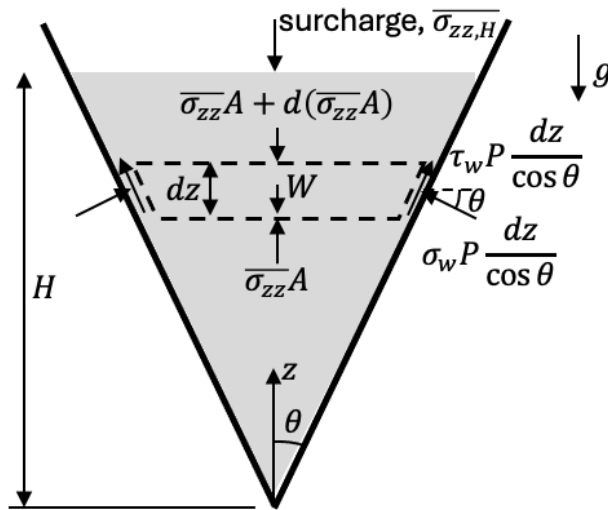
Figure 6.1. Forces in the vertical direction on a thin material element in a conical hopper.
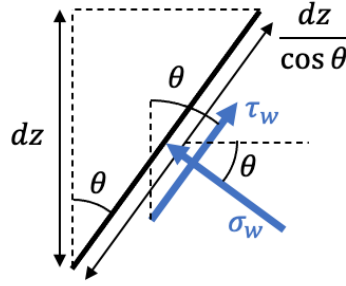
FIGURE 6.2. A schematic showing the length of the element at the inclined wall along with the angles for determining the vertical components of the normal and shear stresses at the wall.

downward and is given by,

$$W = \rho_b g dV = \rho_b g A dz, \tag{6.4}$$

where ρ_b is the material bulk density, g is the acceleration due to gravity, and dV is the differential volume of the element, which is given by $dV = Adz$. As the element thickness approaches zero, the small volume of material in the corners of the element becomes exceedingly small and can be neglected. Lastly, the force acting at the sides of the element include a wall normal force and a wall tangential force. The vertical components of these forces are given by,

$$F_{\text{sides}} = \sigma_w P \left(\frac{dz}{\cos \theta} \right) \sin \theta + \tau_w P \left(\frac{dz}{\cos \theta} \right) \cos \theta, \tag{6.5}$$

where σ_w and τ_w are the normal and tangential stresses at the wall and P is the perimeter of the element. Note that the inclined distance of the element along the wall is $dz/\cos \theta$, as shown in Figure 6.2.

Substituting these terms into the force balance and simplifying,

$$\overline{\sigma_{zz}}A - [\overline{\sigma_{zz}}A + d(\overline{\sigma_{zz}}A)] - \rho_b g A dz + \sigma_w P \left(\frac{dz}{\cos \theta} \right) \sin \theta + \tau_w P \left(\frac{dz}{\cos \theta} \right) \cos \theta = 0, \tag{6.6}$$

$$- d(\overline{\sigma_{zz}}A) - \rho_b g A dz + P \left(\frac{dz}{\cos \theta} \right) (\sigma_w \sin \theta + \tau_w \cos \theta) = 0, \tag{6.7}$$

$$- A d\overline{\sigma_{zz}} - \overline{\sigma_{zz}}dA + P \left(\frac{dz}{\cos \theta} \right) (\sigma_w \sin \theta + \tau_w \cos \theta) = \rho_b g A dz, \tag{6.8}$$

$$\frac{d\overline{\sigma_{zz}}}{dz} + \frac{1}{A}\frac{dA}{dz}\overline{\sigma_{zz}} - \frac{P}{A}\left(\frac{1}{\cos \theta} \right) (\sigma_w \sin \theta + \tau_w \cos \theta) = -\rho_b g. \tag{6.9}$$

For a conical hopper, which has a circular cross section, the area and perimeter of the element are,

$$A = \frac{\pi D^2}{4}, \tag{6.10}$$

$$P = \pi D, \tag{6.11}$$

where D is the diameter at the elevation z, i.e.,

$$D = 2z \tan \theta. \tag{6.12}$$

Note that,

$$\frac{1}{A}\frac{dA}{dz} = \left(\frac{4}{\pi D^2} \right) \left(\frac{\pi 2D}{4}\frac{dD}{dz} \right), \tag{6.13}$$

$$= \frac{2}{D}(2 \tan \theta), \tag{6.14}$$

$$= \frac{2}{2z\tan\theta}\left(2\tan\theta\right), \tag{6.15}$$

$$= \frac{2}{z}. \tag{6.16}$$

In addition, the wall shear stress is related to the wall normal stress via the wall friction angle, ϕ_w,

$$\tau_w = \sigma_w\tan\phi_w. \tag{6.17}$$

Substituting these expressions into the force balance and simplifying gives,

$$\frac{d\overline{\sigma_{zz}}}{dz} + \frac{2}{z}\overline{\sigma_{zz}} - \frac{\pi D}{\pi D^2/4}\left(\frac{1}{\cos\theta}\right)(\sigma_w\sin\theta + \sigma_w\tan\phi_w\cos\theta) = -\rho_b g, \tag{6.18}$$

$$\frac{d\overline{\sigma_{zz}}}{dz} + \frac{2}{z}\overline{\sigma_{zz}} - \frac{2}{z\tan\theta}\left(\frac{1}{\cos\theta}\right)\sigma_w(\sin\theta + \tan\phi_w\cos\theta) = -\rho_b g, \tag{6.19}$$

$$\frac{d\overline{\sigma_{zz}}}{dz} + \frac{2}{z}\overline{\sigma_{zz}} - \frac{2}{z\sin\theta}\sigma_w(\sin\theta + \tan\phi_w\cos\theta) = -\rho_b g, \tag{6.20}$$

$$\frac{d\overline{\sigma_{zz}}}{dz} + \frac{2}{z}\overline{\sigma_{zz}} - \sigma_w\frac{2}{z}\left(1 + \frac{\tan\phi_w}{\tan\theta}\right) = -\rho_b g. \tag{6.21}$$

At this point we have a differential equation involving the average vertical normal stress ($\overline{\sigma_{zz}}$) and the normal stress at the wall (σ_w). We can relate the normal stress at the wall to the average vertical stress using a Mohr's circle applied to a material element at the wall and a distribution factor.

First, consider the Mohr's circle for a material element adjacent to the wall in a passive state as shown in Figure 6.3. The corresponding material element is shown in Figure 6.4. Assume the material element is yielding internally, thus touching the effective yield locus (EYL) at point I, and yielding at the wall, thus touching the wall yield locus (WYL) at point W_P. As shown in Figure 6.4, the radial stress plane is at an angle θ in the counter-clockwise direction from the wall plane which means that the radial plane stress state R_P is rotated an angle 2θ in the counter-clockwise direction from the wall stress state W_P in the Mohr's circle. The vertical stress state Z_P is located $180°$ from the radial stress state in the Mohr's circle. Recall that for a passive stress state, $\sigma_{rr,w} > \sigma_{zz,w}$ and, thus, point R_P is located to the right of point Z_P in the Mohr's circle. From the right triangle ΔOIp,

$$\sin\delta = \frac{R}{p} \implies R = p\sin\delta. \tag{6.22}$$

Let ω be the angle between lines $\overline{OW_P}$ and $\overline{pW_P}$. From the Law of Sines on triangle ΔOW_Pp,

$$\frac{\sin\omega}{p} = \frac{\sin\phi_w}{R}. \tag{6.23}$$

Substituting Eq. (6.22) into Eq. (6.23),

$$\sin\omega = \frac{\sin\phi_w}{\sin\delta}. \tag{6.24}$$

Since the interior angles of a triangle sum to π radians, the angle between line $\overline{Op}$ and $\overline{pW_p}$ must be $\pi - \omega - \phi_w$. The other angles in Figure 6.3 may be found from similar geometric arguments.

Using the Mohr's circle geometry, the wall normal stress, radial normal stress, and vertical normal stress can be written, respectively, as,

$$\sigma_w = p + R\cos(\omega + \phi_w), \tag{6.25}$$

$$\sigma_{rr,w} = p + R\cos(\omega + \phi_w + 2\theta), \tag{6.26}$$

$$\sigma_{zz,w} = p - R\cos(\omega + \phi_w + 2\theta). \tag{6.27}$$

Making use of Eq. (6.22), the previous equations become,

$$\sigma_w = p\left[1 + \sin\delta\cos(\omega + \phi_w)\right], \tag{6.28}$$

$$\sigma_{rr,w} = p\left[1 + \sin\delta\cos(\omega + \phi_w + 2\theta)\right], \tag{6.29}$$
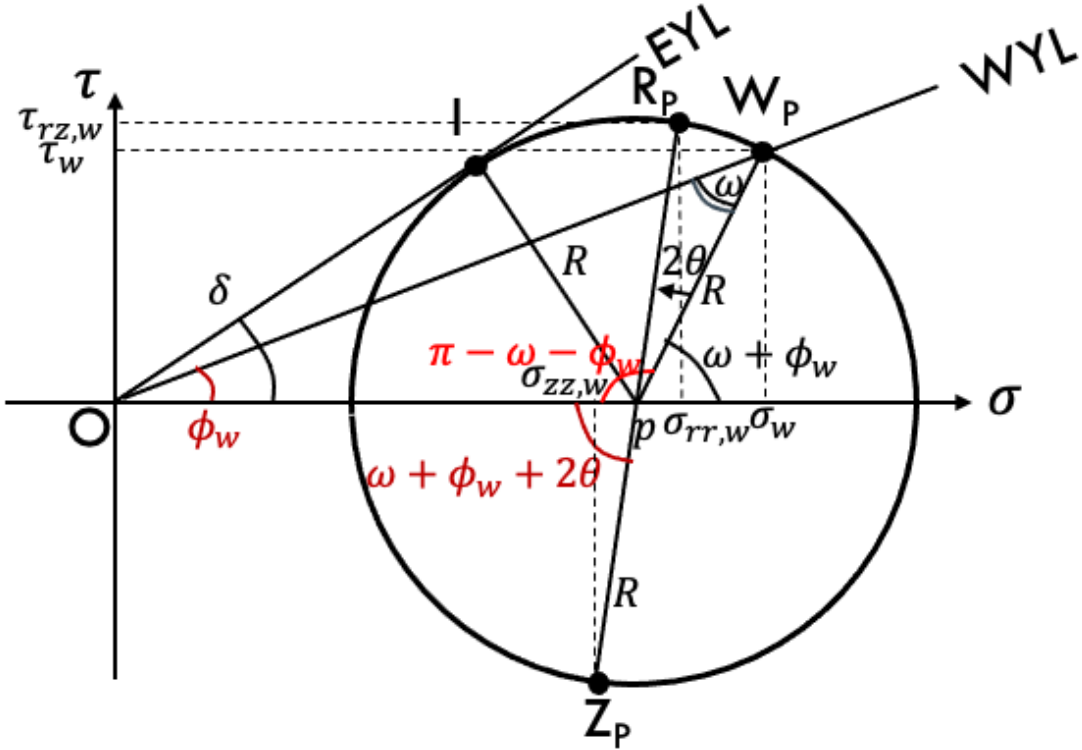
Figure 6.3. A Mohr's circle for a material element in a passive state adjacent to the wall in a conical hopper. Recall that in a passive state $\sigma_{rr,w} > \sigma_{zz,w}$.
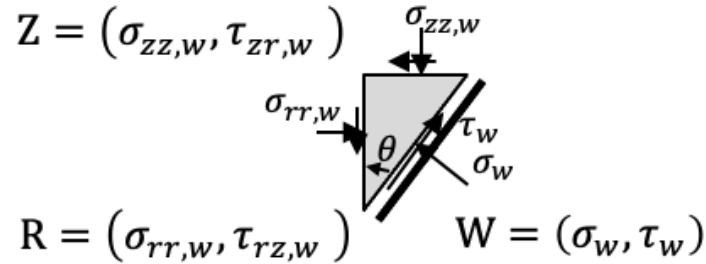
Figure 6.4. A material element located at the wall in a conical bin. The wall stress state is $W = (\sigma_w, \tau_w)$, the radial stress state is $R = (\sigma_{rr,w}, \tau_{rz,w})$, and the vertical stress state is $Z = (\sigma_{zz,w}, \tau_{zr,w} = -\tau_{rz,w})$.

$$\sigma_{zz,w} = p\left[1 - \sin\delta\cos(\omega + \phi_w + 2\theta)\right]. \tag{6.30}$$

Thus, we can write the ratios,

$$\frac{\sigma_w}{\sigma_{zz,w}} = \frac{1 + \sin\delta\cos(\omega + \phi_w)}{1 - \sin\delta\cos(\omega + \phi_w + 2\theta)}, \tag{6.31}$$

$$\frac{\sigma_{rr,w}}{\sigma_{zz,w}} = K_{w,P} = \frac{1 + \sin\delta\cos(\omega + \phi_w + 2\theta)}{1 - \sin\delta\cos(\omega + \phi_w + 2\theta)}. \tag{6.32}$$

where K_w is Janssen's constant at the wall.
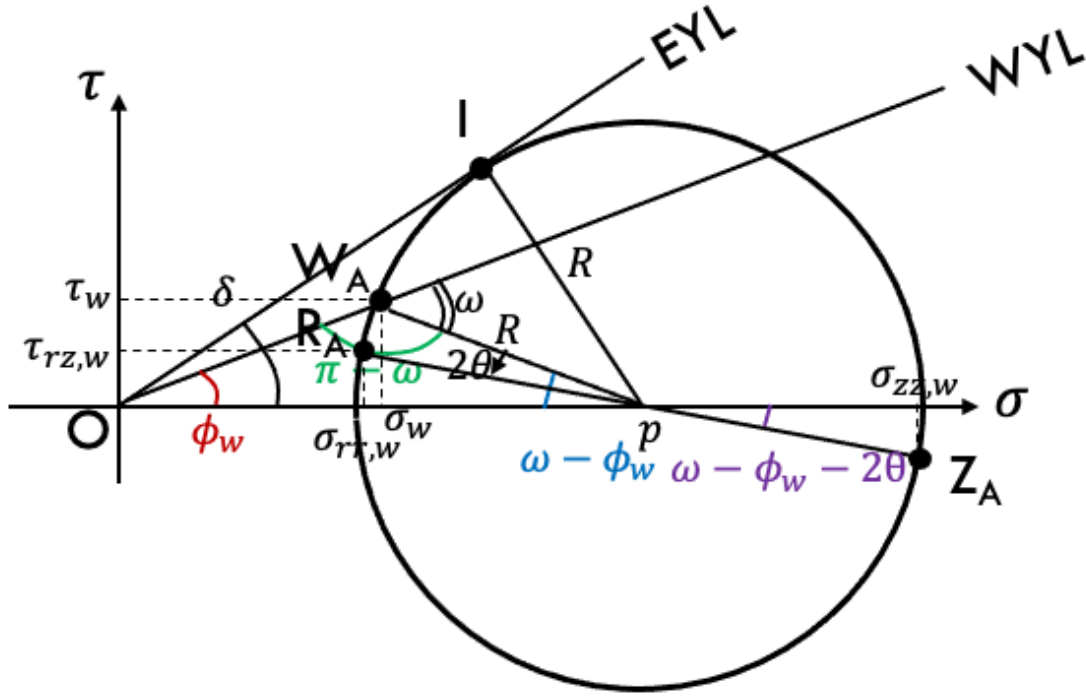
FIGURE 6.5. A Mohr's circle for a material element in an active state adjacent to the wall in a conical hopper. Recall that in an active state $\sigma_{zz,w} > \sigma_{rr,w}$.

We can perform a similar analysis for the active state using the Mohr's circle shown in Figure 6.5. For this case, the stress ratios are,

$$\frac{\sigma_w}{\sigma_{zz,w}} = \frac{1 - \sin\delta\cos(\omega - \phi_w)}{1 + \sin\delta\cos(\omega - \phi_w - 2\theta)}, \tag{6.33}$$

$$\frac{\sigma_{rr,w}}{\sigma_{zz,w}} = K_{w,A} = \frac{1 - \sin\delta\cos(\omega - \phi_w - 2\theta)}{1 + \sin\delta\cos(\omega - \phi_w - 2\theta)}. \tag{6.34}$$

The stress ratios for the passive and active cases may be written more compactly as,

$$\frac{\sigma_w}{\sigma_{zz,w}} = \frac{1 - \kappa\sin\delta\cos(\omega - \kappa\phi_w)}{1 + \kappa\sin\delta\cos(\omega - \kappa\phi_w - \kappa 2\theta)}, \tag{6.35}$$

$$\frac{\sigma_{rr,w}}{\sigma_{zz,w}} = K_w = \frac{1 - \kappa\sin\delta\cos(\omega - \kappa\phi_w - \kappa 2\theta)}{1 + \kappa\sin\delta\cos(\omega - \kappa\phi_w - \kappa 2\theta)}. \tag{6.36}$$

where $\kappa = +1$ for the active case and $\kappa = -1$ for the passive case.

From Eq. (6.35), we now have an expression relating σ_w to $\sigma_{zz,w}$ which can be substituted into Eq. (6.21). To relate $\sigma_{zz,w}$ to $\overline{\sigma_{zz}}$, make use of a distribution factor, $\mathcal{D}$, which is defined as,

$$\mathcal{D} := \frac{\sigma_{zz,w}}{\overline{\sigma_{zz}}} \implies \sigma_{zz,w} = \mathcal{D}\overline{\sigma_{zz}}. \tag{6.37}$$

Substituting Eqs. (6.35) and (6.37) into Eq. (6.21) results in,

$$\frac{d\overline{\sigma_{zz}}}{dz} + \frac{2}{z}\overline{\sigma_{zz}} - \sigma_{zz,w}\left[\frac{1 - \kappa\sin\delta\cos(\omega - \kappa\phi_w)}{1 + \kappa\sin\delta\cos(\omega - \kappa\phi_w - \kappa 2\theta)}\right]\frac{2}{z}\left(1 + \frac{\tan\phi_w}{\tan\theta}\right) = -\rho_b g, \tag{6.38}$$

$$\frac{d\overline{\sigma_{zz}}}{dz} + \frac{2}{z}\overline{\sigma_{zz}} - \mathcal{D}\overline{\sigma_{zz}}\left[\frac{1 - \kappa\sin\delta\cos(\omega - \kappa\phi_w)}{1 + \kappa\sin\delta\cos(\omega - \kappa\phi_w - \kappa 2\theta)}\right]\frac{2}{z}\left(1 + \frac{\tan\phi_w}{\tan\theta}\right) = -\rho_b g, \tag{6.39}$$
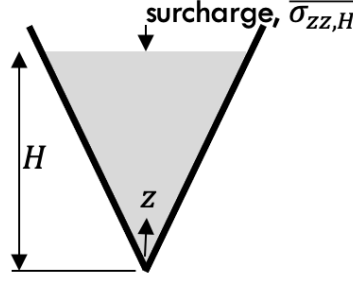
FIGURE 6.6. At the free surface of the material ($z = H$) the average vertical applied stress, i.e., the surcharge, is assumed to be $\overline{\sigma_{zz,H}}$.

$$\frac{d\overline{\sigma_{zz}}}{dz} + \frac{2}{z}\left\{1 - \mathcal{D}\left[\frac{1 - \kappa\sin\delta\cos(\omega - \kappa\phi_w)}{1 + \kappa\sin\delta\cos(\omega - \kappa\phi_w - \kappa 2\theta)}\right]\left(1 + \frac{\tan\phi_w}{\tan\theta}\right)\right\}\overline{\sigma_{zz}} = -\rho_b g, \tag{6.40}$$

$$\frac{d\overline{\sigma_{zz}}}{dz} + \frac{C}{z}\overline{\sigma_{zz}} = -\rho_b g, \tag{6.41}$$

where,

$$C := 2\left\{1 - \mathcal{D}\left[\frac{1 - \kappa\sin\delta\cos(\omega - \kappa\phi_w)}{1 + \kappa\sin\delta\cos(\omega - \kappa\phi_w - \kappa 2\theta)}\right]\left(1 + \frac{\tan\phi_w}{\tan\theta}\right)\right\}. \tag{6.42}$$

Equation (6.41) can be solved analytically by multiplying the entire equation by z^C and separating variables,

$$\frac{d\overline{\sigma_{zz}}}{dz}z^C + \frac{C}{z}\overline{\sigma_{zz}}z^C = -\rho_b g z^C, \tag{6.43}$$

$$z^C d\overline{\sigma_{zz}} + \overline{\sigma_{zz}}Cz^{C-1} = -\left(\rho_b g z^C\right)dz, \tag{6.44}$$

$$d\left(z^C\overline{\sigma_{zz}}\right) = -\left(\rho_b g z^C\right)dz. \tag{6.45}$$

Integrating both sides of the previous equation assuming the properties (δ, ϕ_w, ρ_b), gravitational acceleration (g), and distribution factor ($\mathcal{D}$) do not vary with the height z, we obtain,

$$z^C\overline{\sigma_{zz}} = \begin{cases} -\left(\frac{\rho_b g}{C+1}\right)z^{C+1} + c_1 & C \neq -1 \\ -\rho_b g \ln z + c_1 & C = -1 \end{cases}, \tag{6.46}$$

$$\overline{\sigma_{zz}} = \begin{cases} -\left(\frac{\rho_b g}{C+1}\right)z + c_1 z^{-C} & C \neq -1 \\ -\rho_b g z \ln z + c_1 z & C = -1 \end{cases}. \tag{6.47}$$

where c_1 is an unknown constant of integration. Note that we'll address the constant distribution factor assumption later in this chapter.

To determine the integration constant c_1, make use of a boundary condition at the free surface of the material. Assume the average vertical applied stress at the free surface, i.e., the surcharge, is (Figure 6.6),

$$\overline{\sigma_{zz}}\big|_{z=H} = \overline{\sigma_{zz,H}}. \tag{6.48}$$

Substitute into Eq. (6.47) and solve for the constant c_1,

$$\overline{\sigma_{zz,H}} = \begin{cases} -\left(\frac{\rho_b g}{C+1}\right)H + c_1 H^{-C} & C \neq -1 \\ -\rho_b g H \ln H + c_1 H & C = -1 \end{cases}, \tag{6.49}$$

$$c_1 = \begin{cases} \overline{\sigma_{zz,H}}H^C + \left(\frac{\rho_b g}{C+1}\right)H^{1+C} & C \neq -1 \\ \frac{\overline{\sigma_{zz,H}}}{H} + \rho_b g \ln H & C = -1 \end{cases}. \tag{6.50}$$

Thus,

$$\overline{\sigma_{zz}} = \begin{cases} \overline{\sigma_{zz,H}} H^C z^{-C} - \left(\frac{\rho_b g}{C+1}\right)\left(z - H^{1+C} z^{-C}\right) & C \neq -1 \\ -\rho_b g z \ln z + \frac{\overline{\sigma_{zz,H}}}{H} z + \rho_b g z \ln H & C = -1 \end{cases}. \tag{6.51}$$

The previous equation may be written in dimensionless form as,

$$\frac{\overline{\sigma_{zz}}}{\rho_b g H} = \begin{cases} \left(\frac{\overline{\sigma_{zz,H}}}{\rho_b g H} + \frac{1}{C+1}\right)\left(\frac{z}{H}\right)^{-C} - \left(\frac{1}{C+1}\right)\left(\frac{z}{H}\right) & C \neq -1 \\ \left[\frac{\overline{\sigma_{zz,H}}}{\rho_b g H} - \ln\left(\frac{z}{H}\right)\right]\left(\frac{z}{H}\right) & C = -1 \end{cases}. \tag{6.52}$$

Re-writing some previous equations for convenience,

$$C := 2\left\{1 - \mathcal{D}\left[\frac{1 - \kappa \sin\delta \cos(\omega - \kappa\phi_w)}{1 + \kappa \sin\delta \cos(\omega - \kappa\phi_w - \kappa 2\theta)}\right]\left(1 + \frac{\tan\phi_w}{\tan\theta}\right)\right\}, \tag{6.53}$$

$$\sin\omega = \frac{\sin\phi_w}{\sin\delta}, \tag{6.54}$$

$$\mathcal{D} := \frac{\sigma_{zz,w}}{\overline{\sigma_{zz}}}, \tag{6.55}$$

$$\frac{\sigma_w}{\sigma_{zz,w}} = \frac{1 - \kappa \sin\delta \cos(\omega - \kappa\phi_w)}{1 + \kappa \sin\delta \cos(\omega - \kappa\phi_w - \kappa 2\theta)}, \tag{6.56}$$

$$\frac{\sigma_{rr,w}}{\sigma_{zz,w}} = K_w = \frac{1 - \kappa \sin\delta \cos(\omega - \kappa\phi_w - \kappa 2\theta)}{1 + \kappa \sin\delta \cos(\omega - \kappa\phi_w - \kappa 2\theta)}, \tag{6.57}$$

$$\tau_{rz,w} = \sigma_w \tan\phi_w, \tag{6.58}$$

where $\kappa = +1$ for the active state and $\kappa = -1$ for the passive state.

Of particular interest is the value of the stress at the cone's vertex ($z = 0$) since that is where feeding equipment and valves are typically located. Taking the limit of Eq. (6.52) as $z/H \to 0$,

$$\lim_{z/H \to 0}\left(\frac{\overline{\sigma_{zz}}}{\rho_b g H}\right) = \begin{cases} \left(\frac{\overline{\sigma_{zz,H}}}{\rho_b g H} + \frac{1}{C+1}\right)\lim_{z/H \to 0}\left(\frac{z}{H}\right)^{-C} - \left(\frac{1}{C+1}\right)\lim_{z/H \to 0}\left(\frac{z}{H}\right) & C \neq -1 \\ \lim_{z/H \to 0}\left[\frac{\overline{\sigma_{zz,H}}}{\rho_b g H} - \ln\left(\frac{z}{H}\right)\right]\left(\frac{z}{H}\right) & C = -1 \end{cases}, \tag{6.59}$$

$$= \begin{cases} 0 & C < 0 \quad \text{(including } C = -1\text{)} \\ \infty & C > 0 \\ \frac{\overline{\sigma_{zz,H}}}{\rho_b g H} + 1 & C = 0 \end{cases}. \tag{6.60}$$

Thus, negative values of C result in zero stress at the vertex, which implies that the stresses acting on discharge equipment would be small. Positive values of C result in unbounded stresses at the vertex, which isn't physically reasonable (hoppers don't explode when filled with powder, fortunately). When $C = 0$ the vertex stress is equal to what would be expected for hydrostatic loading.

Figure 6.7 plots the dimensionless average vertical normal stress as a function of dimensionless height from the cone's vertex (Eq. (6.52)) for various values of C, assuming no surcharge stress. Consistent with Eq. (6.60), when $C > 0$ the stresses increase from zero at the free surface (no surcharge) and diverge to infinity approaching the vertex. When $C = 0$ the stress profile is linear with depth, indicating hydrostatic loading. When $C < 0$ the stress first increases with depth from the free surface, reaches a maximum, then decreases to zero at the vertex. For negative values of C but close to a value of zero, the stress remains close to the hydrostatic case until close to the vertex.

The parameter C in Eq. (6.42) is a complex function of the effective angle of internal friction (δ), the wall friction angle (ϕ_w), and the hopper wall half angle (θ). Walters [1] assumed that the wall shear stress should point upwards ($\tau_{rz,w} \geq 0$) otherwise the vertical stress gradient with depth would be larger than hydrostatic. From the active state Mohr's circle (Figure 6.5), we see that,

$$\tau_{rz,w} \geq 0 \implies \omega - \phi_w - 2\theta \geq 0 \implies \theta \leq \frac{1}{2}\left(\omega - \phi_w\right). \tag{6.61}$$
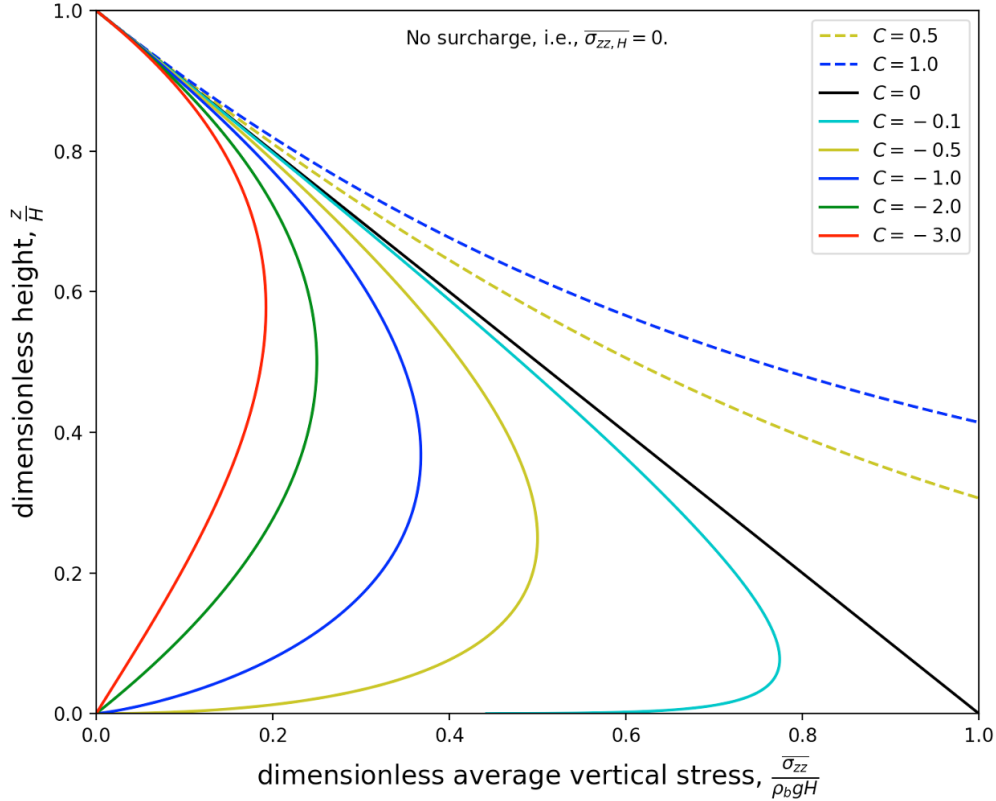
FIGURE 6.7. The dimensionless average vertical normal stress (horizontal axis) plotted as a function of the dimensionless height above the vertex (vertical axis) for a conical hopper for various values of C (refer to Eq. (6.52)). Note that zero surcharge stress is assumed, i.e., $\overline{\sigma_{zz,H}} = 0$.

For wall angles larger than this critical value, the stress state is likely not internally yielding or yielding at the wall [2]. Figure 6.8 plots this maximum wall angle as a function of the wall friction angle for various effective internal friction angles.

For the passive state the shear stress will always be positive, but there is the limitation that the point R_p in Figure 6.3 should remain to the right of the point I. Mathematically,

$$\omega + \phi_w + 2\theta \leq \pi - \left(\frac{\pi}{2} - \delta\right) \implies \theta \leq \frac{1}{2}\left(\frac{\pi}{2} + \delta - \omega - \phi_w\right). \tag{6.62}$$

Figure 6.8 also plots this limiting hopper wall half angle as a function of the wall friction angle. Walters [1] assumed that large wall angles were unlikely to be in mass flow, i.e., not yielding at the wall or internally, and, thus, the current analysis would not hold.

6.2. The Distribution Factor for a Conical Hopper

Now examine the distribution factor $\mathcal{D}$ for a conical hopper. The analysis here is similar to the one presented for a cylinder in Section 5.3. The average vertical stress can be determined from,

$$\overline{\sigma_{zz}} = \frac{1}{\pi D^2/4} \int_0^{D/2} \sigma_{zz,r}(2\pi r dr), \tag{6.63}$$

where $\sigma_{zz,r}$ is the value of the vertical stress at radius r. As with the distribution factor analysis for a cylinder, the two assumptions by Walters [1] are used: (1) the radial stress remains constant with radius, and
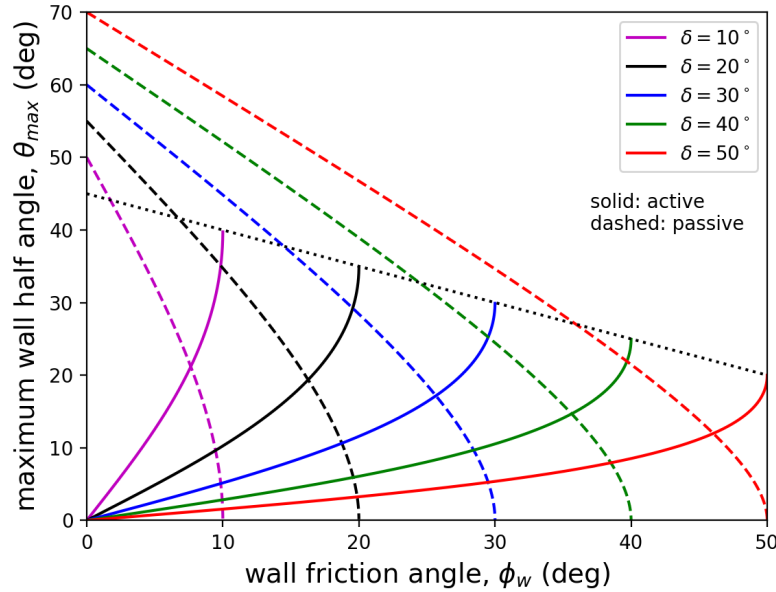
FIGURE 6.8. The maximum wall half angle (θ) plotted as a function of the wall friction angle (ϕ_w) for various effective angles of internal friction (δ) using Eqs. (6.61) (solid lines) and (6.62) (dashed lines) for the active and passive states, respectively. Note that $\phi_w \leq \delta$.

(2) the distribution factor is independent of elevation. The first assumption was shown to be incorrect in the previous chapter. The second assumption was true at large depths in cylindrical bins where the vertical stress asymptotes, but in the conical geometry the vertical stress doesn't asymptote. The only location where the shear stress varies linearly with radius is at the stress maximum where $\partial \overline{\sigma_{zz}}/\partial z = 0$ (and the vertical normal stresses on a material element balance). Despite these poor assumptions, we will continue the analysis for completeness.

Figure 6.9 shows two material elements in the conical bin: one at the centerline (red) and one adjacent to the wall (blue). The corresponding Mohr's circles for the two elements for the passive and active cases are shown in Figures 6.10. The material elements are assumed to be yielding internally and the element adjacent to the wall is assumed to be yielding at the wall (point W on the Mohr's circle). In the real world, to go from the wall plane to the plane on which the radial normal stress acts we move in the counter-clockwise direction by an angle θ. Thus, in the Mohr's circle we rotate in the counter-clockwise direction an angle 2θ to go from stress state W to stress state R. Comparing these two Mohr's circles to those used in the cylindrical bin distribution factor derivation (Figures 5.11) we see that the Mohr's circles are nearly identical except the radial stress aligns with point R_w, which is at angle η with respect to the origin, rather than point W, which is at ϕ_w. Thus, the expression for the distribution factor derived for the cylinder geometry can be used for the conical geometry except the term $\tau_{rz,w}/\sigma_{rr}$ should equal $\tan \eta$ instead of $\tan \phi_w$. In addition the expression for K_w should be Eq. (6.36). Thus, the distribution factor for a conical hopper is,

$$\mathcal{D} = \frac{\cos^2 \delta}{K_w \left(1 + \sin^2 \delta + \kappa 2y \sin \delta\right)}, \tag{6.64}$$

where,

$$K_w = \frac{1 - \kappa \sin \delta \cos(\omega - \kappa \phi_w - \kappa 2\theta)}{1 + \kappa \sin \delta \cos(\omega - \kappa \phi_w - \kappa 2\theta)}, \tag{6.65}$$

$$\sin \omega = \frac{\sin \phi_w}{\sin \delta}, \tag{6.66}$$
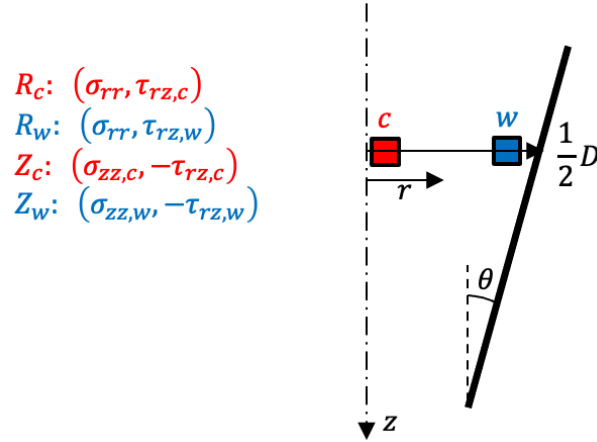
FIGURE 6.9. Two material elements in the conical hopper. One at the hopper's centerline (red) and one adjacent to the wall (blue). The elements' stress states on radial faces are noted by R and the stress states on the vertical faces are identified by Z.

$$y = \frac{2}{3c}\left[1 - (1-c)^{3/2}\right], \tag{6.67}$$

$$c = \left(\frac{\tan\eta}{\tan\delta}\right)^2, \tag{6.68}$$

with $\kappa = +1$ for the active state and $\kappa = -1$ for the passive state. The angle η can be found from the geometry in the Mohr's circles,

$$\tan\eta = \frac{\tau_{rz,w}}{\sigma_{rr,w}}, \tag{6.69}$$

$$= \frac{R\sin(\omega - \kappa\phi_w - \kappa 2\theta)}{p - \kappa R\cos(\omega - \kappa\phi_w - \kappa 2\theta)}, \tag{6.70}$$

$$= \frac{p\sin\delta\sin(\omega - \kappa\phi_w - \kappa 2\theta)}{p\left[1 - \kappa\sin\delta\cos(\omega - \kappa\phi_w - \kappa 2\theta)\right]}, \tag{6.71}$$

$$\tan\eta = \frac{\sin\delta\sin(\omega - \kappa\phi_w - \kappa 2\theta)}{1 - \kappa\sin\delta\cos(\omega - \kappa\phi_w - \kappa 2\theta)}, \tag{6.72}$$

where,

$$\sin\omega = \frac{\sin\phi_w}{\sin\delta}. \tag{6.73}$$

Note that when $\theta = 0$, $\eta = \phi_w$. Plots of the angle η as a function of the wall friction angle for various effective internal friction angles and wall half angles are shown in Figure 6.11.

Now let's return to parameter C in Eq. (6.53). This parameter is a complex function of the effective angle of internal friction (δ), the wall friction angle (ϕ_w), and the hopper wall half angle (θ). Figure 6.12 plots active and passive state values for C as a function of the wall friction angle for a variety of effective angles of internal friction at three different hopper wall half angles. These plots also take into account the limiting angles given by Eqs. (6.61) and (6.62). For all angles, $C < 0$ resulting in the stresses approaching zero at the hopper apex.

Notes:

(1) There is some disagreement as to the what the state of stress is within the hopper after filling. Nedderman [3] argues that as material fills the hopper, the material slides downward along the wall. As a result, the material is compressed laterally by the converging walls resulting in $\sigma_{rr,w} > \sigma_{zz,w}$
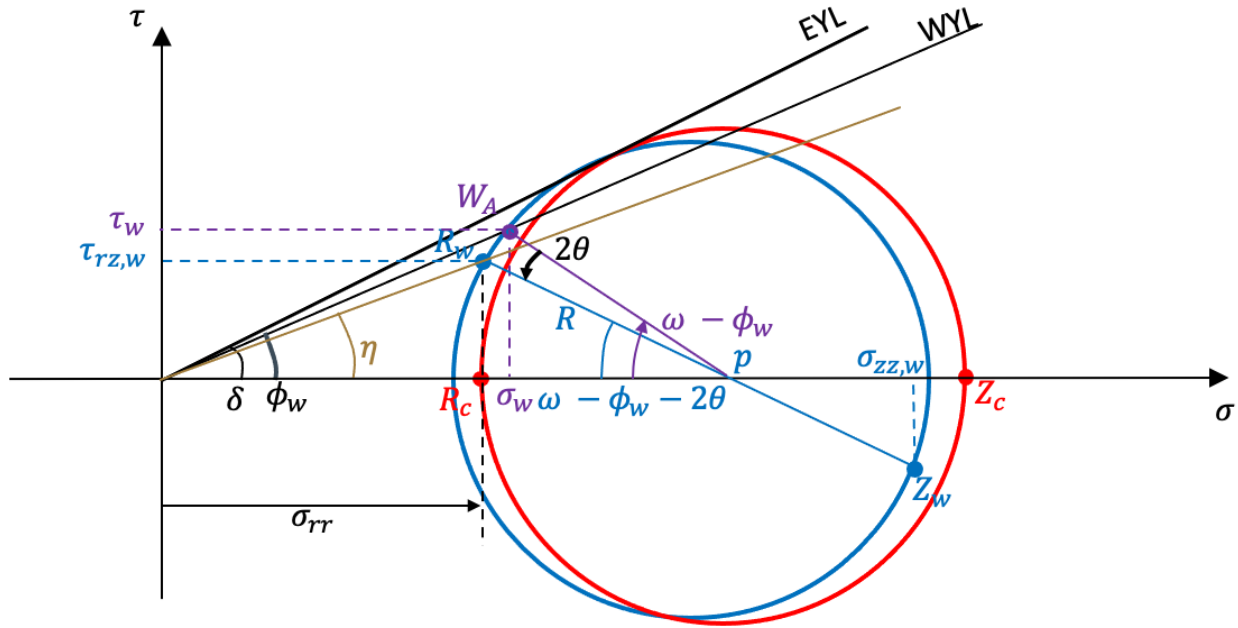
(A) Active state
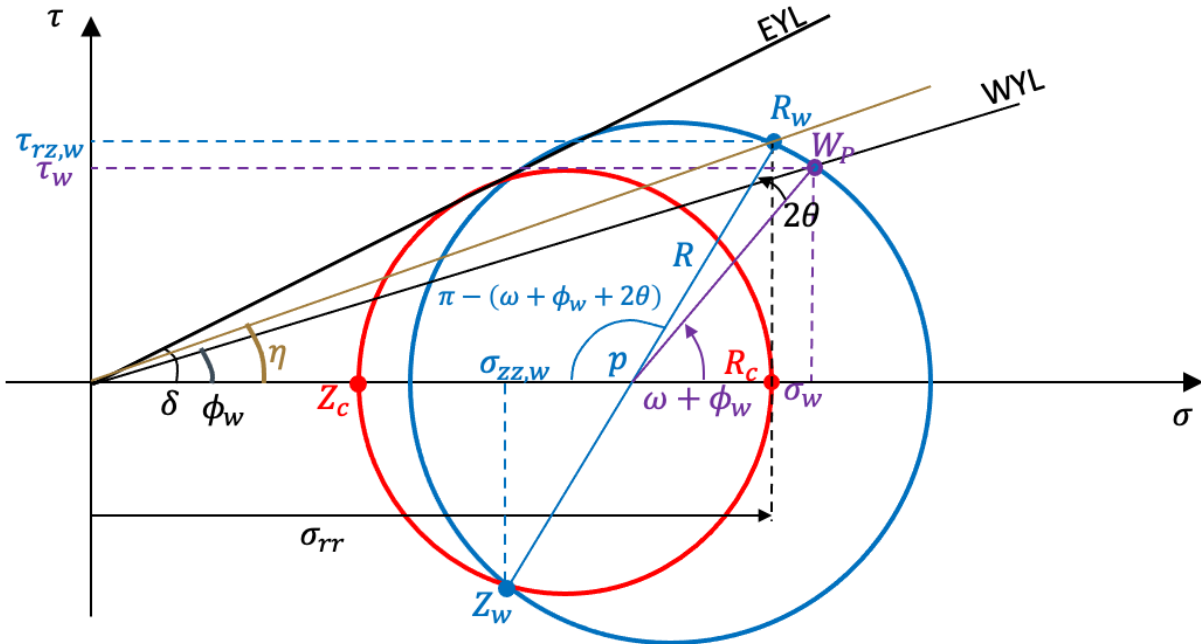
(B) Passive state

FIGURE 6.10. The Mohr's circles for centerline (red) and wall (blue) material elements.

and a passive stress state. In contrast, Schulze [2] states that, in general, the vertical stresses are larger than the horizontal stresses after filling. Other studies (e.g., McLean [4]) have shown that the material compressibility and hopper compliance can affect the filling stress state. Regardless of the

(A) $\theta = 10°$

(B) $\theta = 20°$

(C) $\theta = 30°$
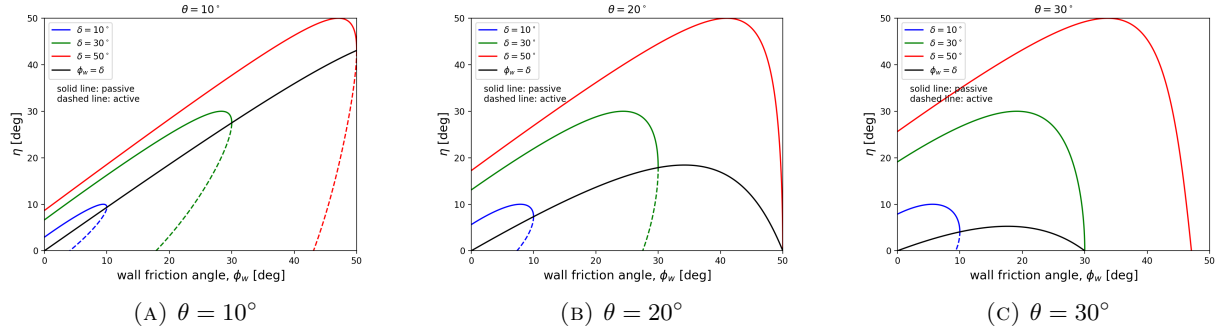
FIGURE 6.11. The angle η as a function of the wall friction angle (ϕ_w) for various effective internal friction angles (δ) and wall half angles (θ). Equation (6.72) was used to produce the plots.

(A) Active, $\theta = 10°$

(B) Active, $\theta = 20°$

(C) Active, $\theta = 30°$

(D) Passive, $\theta = 10°$

(E) Passive, $\theta = 20°$

(F) Passive, $\theta = 30°$
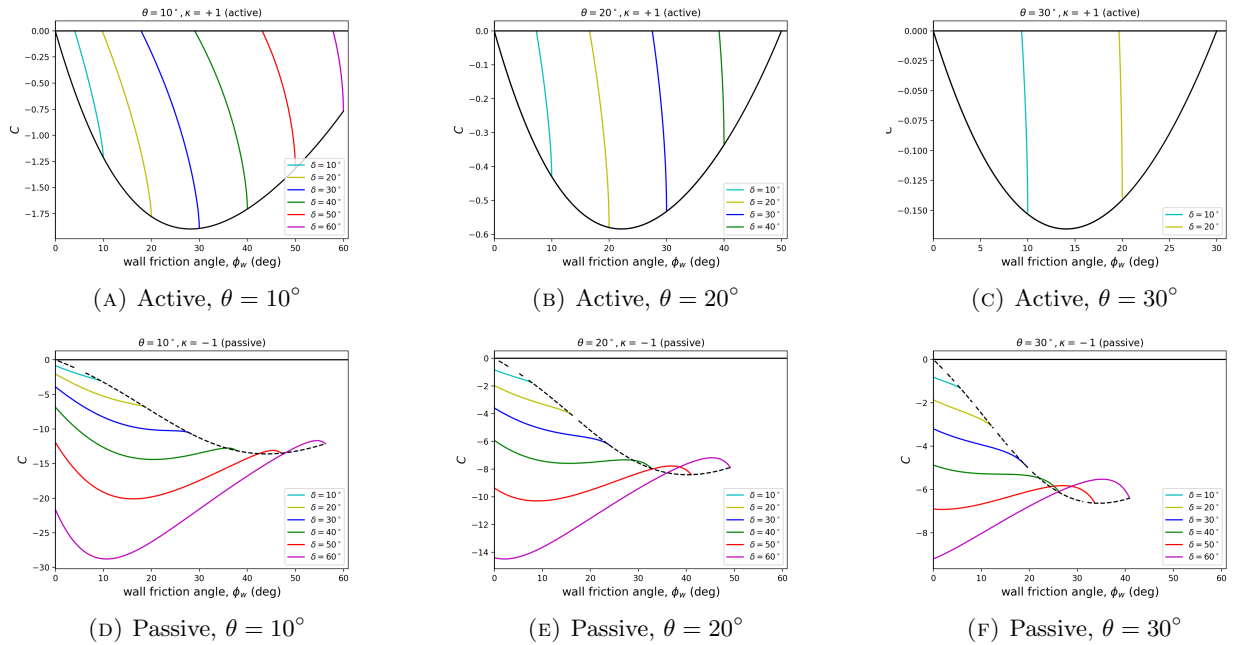
FIGURE 6.12. The parameter C (Eq. (6.42)) plotted as a function of the wall friction angle (ϕ_w) for various values of the effective angle of internal friction (δ) for three different wall half angles from the vertical (θ). The dashed termination lines correspond to the limiting angles given by Eqs. (6.61) and (6.62).

actual stress state, the active case generally provides a more conservative estimate of the stresses since it is close to hydrostatic, except near the apex.

(2) During discharge, the conical hopper is observed to be in a passive stress state. As the material moves toward the exit, it is compressed laterally by the walls and elongates vertically. Thus, $\sigma_{rr} > \sigma_{zz}$.

(3) Other models, for example, those assuming a radial stress field (e.g., Jenike [5]), provide better predictions for the stress state in a conical hopper than what's presented here, but the trends from the Method of Differential Slices model are consistent with observations and still provide valuable insight.

(A) Active

(B) Passive
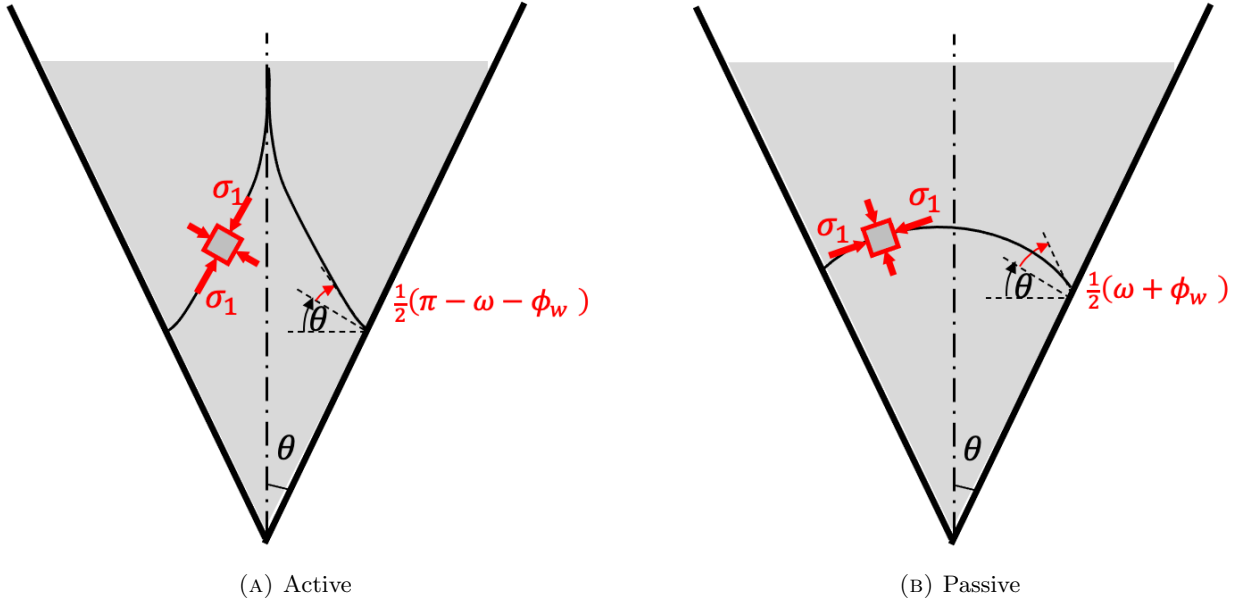
FIGURE 6.13. Sketches of the lines of major principal stress in a conical hopper.

(4) Lines of major principal stress within a conical hopper are sketched in Figure 6.13. As with the cylindrical bin, the vertical and radial stresses along the centerline are principal stresses. For the active state, $\sigma_{zz} > \sigma_{rr}$ and the slope of the major principal stress line at the centerline is vertical. For the passive state, $\sigma_{rr} > \sigma_{zz}$ and the major principal stress line slope at the centerline is horizontal. Referring to Figures 6.5 and 6.3, at the wall the angles of the major principal stress line with respect to the wall normal are $\frac{1}{2}(\pi - \omega + \phi_w)$ and $\frac{1}{2}(\omega + \phi_w)$, for the active and passive states, respectively.

6.3. The Switch Stress

In many industrial applications a cylindrical bin has a conical hopper attached to its bottom to facilitate discharge of material (Figure 6.14). A switch stress is observed at the junction of the two geometries. This section combines the models from this chapter and the previous one to predict the magnitude of the switch stress. Assume the material in the cylinder is in an active state since it's far from the exit, and reaches its asymptotic values,

$$(\overline{\sigma_{zz,\infty}}, \sigma_{rr,w} = \sigma_w)\big|_{\text{cyl,int}} = \left(\frac{\rho_b g D}{4 \tan \phi_w K_{w,A,cyl} \mathcal{D}_{A,cyl}}, K_{w,A,cyl}(\mathcal{D}_{A,cyl}\overline{\sigma_{zz}})\right). \tag{6.74}$$

The interface average vertical stress is the surcharge vertical stress for the conical hopper. The corresponding vertical stress at the wall in the conical bin, assuming a passive state is,

$$\sigma_{zz,w} = \mathcal{D}_{P,cone}\overline{\sigma_{zz}}. \tag{6.75}$$

The wall stress at the interface in the conical section is,

$$\sigma_{w,cone,int} = \sigma_{zz,w}\left[\frac{1 + \sin\delta\cos(\omega + \phi_w)}{1 - \sin\delta\cos(\omega + \phi_w + 2\theta)}\right]. \tag{6.76}$$

Combining Eqs. (6.74) – (6.76),

$$\sigma_{w,cone,int} = \frac{\rho_b g D \mathcal{D}_{P,cone}}{4 \tan \phi_w K_{w,A,cyl} \mathcal{D}_{A,cyl}}\left[\frac{1 + \sin\delta\cos(\omega + \phi_w)}{1 - \sin\delta\cos(\omega + \phi_w + 2\theta)}\right]. \tag{6.77}$$
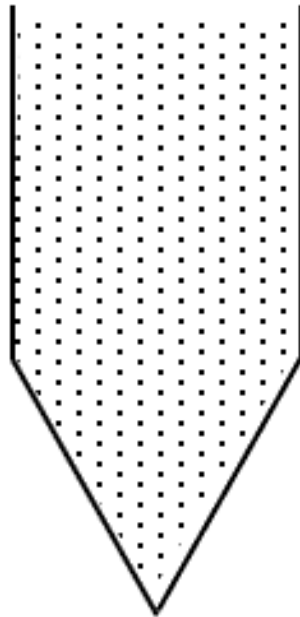
FIGURE 6.14. A sketch of a cylindrical bin with a conical hopper at the bottom. Material in the cylindrical portion is assumed to be in an active state while material in the conical section is assumed to be in a passive state.

Since $K_{A,\text{cyl}} < 1$, $\mathcal{D}_{P,\text{cone}} > 1$, $\mathcal{D}_{A,\text{cyl}} < 1$, and the term in square brackets is > 1, the wall stress increases abruptly, i.e., there is a switch stress at the interface between the cylindrical and conical sections.

Notes:

(1) A similar analysis can be performed for the conical section being in an active state. A switch stress occurs for that case as well.
(2) Figure 6.15 shows examples of the lines of major principal stress and the corresponding vertical and wall stresses for systems during filling, assuming the cylinder and cone are both in an active state, and during discharge where the cylinder remains in an active state but the cone is in a passive state. A wall switch stress appears in both systems.
(3) Discrete element method computer simulations also show the presence of switch stresses. Figure 6.16 shows the principal stresses in a two-dimensional particulate material discharging from a vertical bin with a wedge-shaped hopper. The orientation of the crosses in the figure reflect the orientation of the major and minor principal stresses while the the length of the cross arms correspond to the stress magnitudes (the larger length being the major principal stress). The figure shows that the major principal stress direction in the vertical section approaches a vertical orientation while the major principal stress direction in the hopper is arch-shaped, consistent with the sketch in Figure 6.15b. The largest stress magnitude, corresponding to a switch stress, occurs at the interface between the vertical and hopper sections. Note that the stresses decrease toward the hopper exit as predicted.
(4) Figure 6.17 shows experimental results of the wall stresses in a cylinder-cone system. A switch stress is clearly observed at the interface.

6.4. Enstad's Conical Hopper Model

Another Method of Differential Slices model for predicting the stresses in a conical hopper comes from Enstad [7]. This model consists of a vertical force balance on a differential spherical cap element (Figure 6.18)

(A) After filling with the cylinder and cone in active states.

(B) During discharge with the cylinder in an active state and cone in a passive state.

.
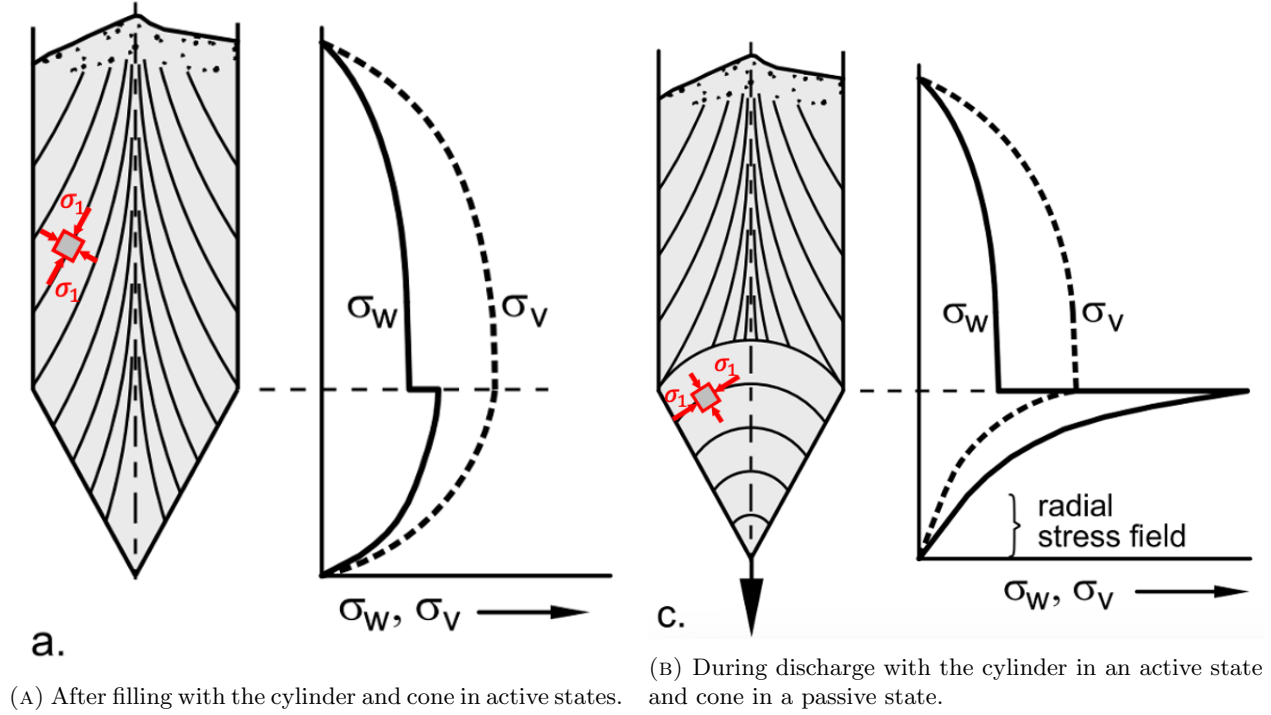
FIGURE 6.15. Examples of the lines of major principal stress and the corresponding vertical and wall stresses for cylinder-cone systems during (left) filling, assuming the cylinder and cone are both in an active state, and (right) during discharge where the cylinder remains in an active state but the cone is in a passive state. A wall switch stress appears in both systems. These figures are slightly modified from [2]

rather than a horizontal, planar element. The model assumes that: (1) the material is in a passive stress state and is yielding internally and at the wall, and (2) the stress on the upper and lower surfaces of the spherical cap are minor principal stresses.

Figure 6.19 shows the Mohr's circle for the material element in Figure 6.18. This Mohr's circle is identical to the one used in the planar element analysis in Figure 6.3. Of particular note, the angle from the wall normal stress to the major principal stress is $\omega + \phi_w$ in the clockwise direction in the Mohr's circle, which means that the same angle in the real world is $\beta := \frac{1}{2}(\omega + \phi_w)$ with the same orientation, where,

$$\sin\omega = \frac{\sin\phi_w}{\sin\delta}, \tag{6.78}$$

and,

$$\sin\delta = \frac{R}{p}, \tag{6.79}$$

consistent with previous analyses. Note that the minor principal stress is aligned in the radial direction of the spherical cap. The cap radius, R_{cap} is found by applying the Law of Sines to triangle ΔOAB,

$$\frac{\sin\theta}{R_{\text{cap}}} = \frac{\sin[\pi - (\theta + \beta)]}{r} = \frac{\sin(\theta + \beta)}{r}, \tag{6.80}$$

$$R_{\text{cap}} = r\left[\frac{\sin\theta}{\sin(\theta + \beta)}\right], \tag{6.81}$$

where r is the radius from the cone apex out to the spherical cap.
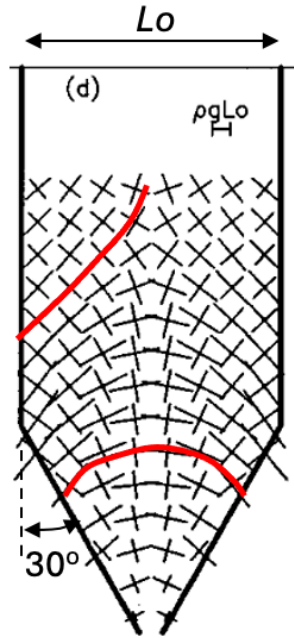
Figure 6.16. Results from two-dimensional discrete element method computer simulations of a particulate material discharging from a cylinder-cone system. The crosses in the figure show the orientation and magnitudes of the major and minor principal stresses. This figure is from Potapov and Campbell [6].
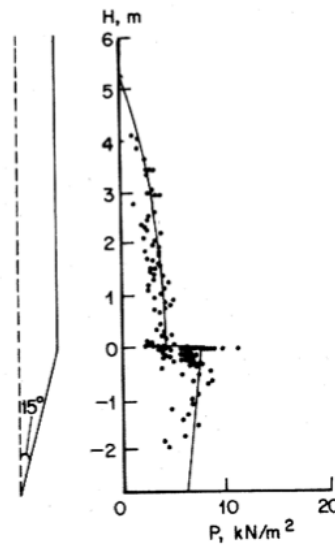
Figure 6.17. Experimental measurements of the wall stress in a cylinder-cone system. The switch stress at the interface is clearly visible.

Now examine a vertical force components acting on the element. The element weight acts downward with magnitude,

$$W = \rho_b g dV_{\text{total}}, \tag{6.82}$$
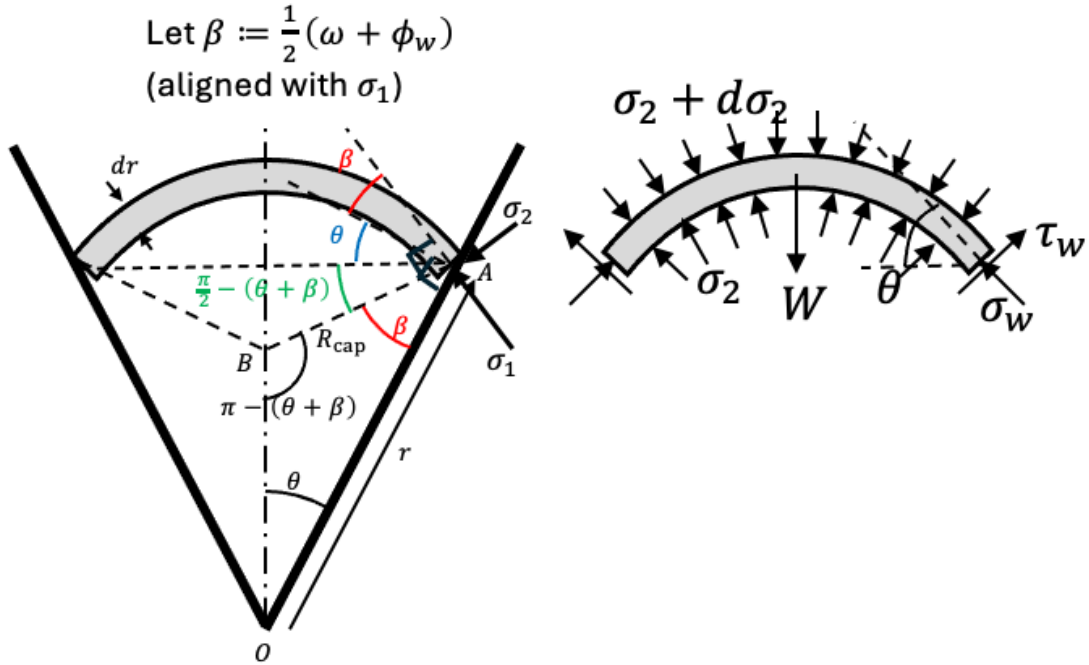
FIGURE 6.18. The geometry and force balance for the spherical cap element used in the Enstad model.
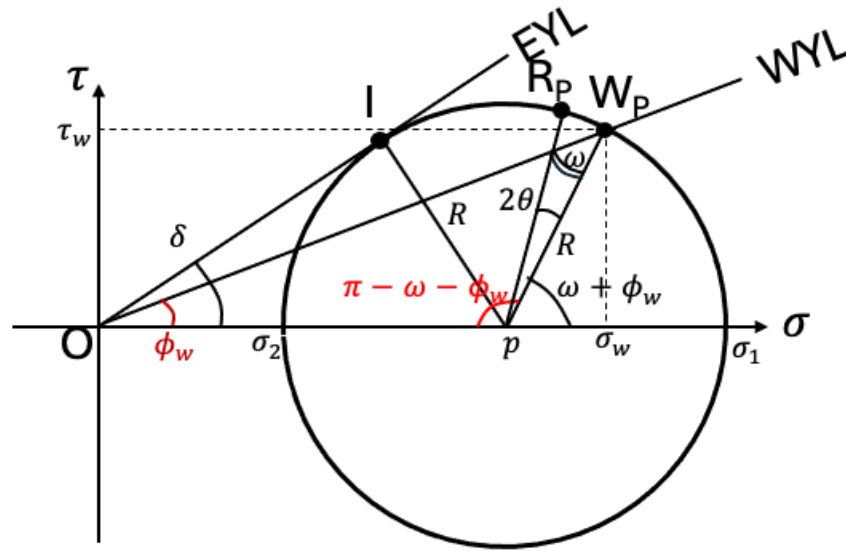
FIGURE 6.19. The Mohr's circle used in the Enstad model.

where dV_{total} is the differential volume of the spherical cap (to be addressed momentarily). The wall normal and shear stresses also have components in the vertical direction,

$$F_{\text{wall}} = (\sigma_w \sin\theta + \tau_w \cos\theta)[2\pi(r\sin\theta)dr], \tag{6.83}$$

where $2\pi(r\sin\theta)$ is the perimeter of the cap element and dr is the cap differential thickness. Acting on the top and bottom surfaces of the element are minor principal stresses, which have vertical force components of,

$$F_{\text{bottom}} = \sigma_2 \pi (r\sin\theta)^2, \tag{6.84}$$

$$F_{\text{top}} = \sigma_2 \pi (r\sin\theta)^2 + d\left[\sigma_2 \pi (r\sin\theta)^2\right]. \tag{6.85}$$

Balancing forces in the vertical direction,

$$\sum F_{\text{vertical}} = 0 = -W + F_{\text{wall}} + F_{\text{bottom}} - F_{\text{top}}, \tag{6.86}$$

$$\begin{aligned}- \rho_b g dV_{\text{total}} + (\sigma_w \sin\theta + \tau_w \cos\theta)[2\pi(r\sin\theta)dr] + \sigma_2\pi(r\sin\theta)^2 \\ - \left\{\sigma_2\pi(r\sin\theta)^2 + d\left[\sigma_2\pi(r\sin\theta)^2\right]\right\} = 0,\end{aligned} \tag{6.87}$$

$$- \rho_b g dV_{\text{total}} + (\sigma_w \sin\theta + \tau_w \cos\theta)[2\pi(r\sin\theta)dr] - d\left[\sigma_2\pi(r\sin\theta)^2\right] = 0. \tag{6.88}$$

At this point, refer back to the Mohr's circle (Figure 6.19) to obtain expressions for the wall normal stress, wall shear stress, and minor principal stress,

$$\sigma_w = p + R\cos(\omega + \phi_w) = p\left[1 + \sin\delta\cos(\omega + \phi_w)\right], \tag{6.89}$$

$$\tau_w = \sigma_w \tan\phi_w, \tag{6.90}$$

$$\sigma_2 = p - R = p(1 - \sin\delta), \tag{6.91}$$

where Eq. (6.79) has been used to eliminate the radius R in the previous equations.

Now determine the differential volume of the spherical cap element (V_{total}). To find this volume, first determine the volume of all the material from the cone vertex up to the top of the spherical cap. This volume is the sum of the volumes of a cone and a spherical cap,

$$V_{\text{total}} = V_{\text{cone}} + V_{\text{cap}}, \tag{6.92}$$

where,

$$V_{\text{cone}} = \frac{\pi}{3}(r\sin\theta)^2(r\cos\theta), \tag{6.93}$$

and,

$$V_{\text{cap}} = \frac{\pi}{3}R_{\text{cap}}^3 \left[2 + \cos(\theta + \beta)\right]\left[1 - \cos(\theta + \beta)\right]^2, \tag{6.94}$$

$$= \frac{\pi}{3}\left\{r\left[\frac{\sin\theta}{\sin(\theta + \beta)}\right]\right\}^3 \left[2 + \cos(\theta + \beta)\right]\left[1 - \cos(\theta + \beta)\right]^2, \tag{6.95}$$

making use of Eq. (6.81). Thus,

$$V_{\text{total}} = \frac{\pi}{3}(r\sin\theta)^2(r\cos\theta) + \frac{\pi}{3}\left\{r\left[\frac{\sin\theta}{\sin(\theta + \beta)}\right]\right\}^3 \left[2 + \cos(\theta + \beta)\right]\left[1 - \cos(\theta + \beta)\right]^2. \tag{6.96}$$

Now differentiate with respect to r to get the differential cap volume,

$$dV_{\text{total}} = \pi r^2 \sin^2\theta f(\theta, \beta)dr, \tag{6.97}$$

where,

$$f(\theta, \beta) := \cos\theta + \left[\frac{\sin\theta}{\sin^3(\theta + \beta)}\right]\left[2 + \cos(\theta + \beta)\right]\left[1 - \cos(\theta + \beta)\right]^2. \tag{6.98}$$

Substitute into Eq. (6.88) the expressions for the wall normal, wall shear, and minor principal stresses as well as the element differential volume,

$$\begin{aligned}- \rho_b g \pi r^2 \sin^2\theta f(\theta, \beta)dr \\ + p\left[1 + \sin\delta\cos(2\beta)\right](\sin\theta + \tan\phi_w\cos\theta))[2\pi(r\sin\theta)dr] \\ - d\left[p(1 - \sin\delta)\pi(r\sin\theta)^2\right] = 0.\end{aligned} \tag{6.99}$$

where $\beta = \frac{1}{2}(\omega + \phi_w)$. Now expand the differential term and move the element weight to the right-hand side of the equation,

$$
\begin{aligned}
p\left[1 + \sin\delta\cos(2\beta)\right]&(\sin\theta + \tan\phi_w\cos\theta)[2\pi(r\sin\theta)dr] \\
&- dp(1 - \sin\delta)\pi r^2\sin^2\theta - p(1-\sin\delta)\pi\left(2r\sin^2\theta dr\right) \\
&= \rho_b g\pi r^2\sin^2\theta f(\theta,\beta)dr.
\end{aligned}
\tag{6.100}
$$

Dividing by $(1 - \sin\delta)\pi r^2\sin^2\theta dr$,

$$
2p\frac{\left[1 + \sin\delta\cos(2\beta)\right](\sin\theta + \tan\phi_w\cos\theta)}{(1-\sin\delta)r\sin\theta} - \frac{dp}{dr} - \frac{2}{r}p = \rho_b g\left[\frac{f(\theta,\beta)}{1 - \sin\delta}\right].
\tag{6.101}
$$

Re-arrange the terms to bring the dp/dr expression to the front, combine the p terms, and multiply through by -1,

$$
\frac{dp}{dr} - \left\{\frac{\left[1 + \sin\delta\cos(2\beta)\right](1 + \tan\phi_w\cot\theta)}{1 - \sin\delta} - 1\right\}\frac{2}{r}p = -\rho_b g\left[\frac{f(\theta,\beta)}{1 - \sin\delta}\right].
\tag{6.102}
$$

Writing the previous expression more compactly,

$$
\frac{dp}{dr} - \frac{X}{r}p = -\rho_b gY,
\tag{6.103}
$$

where,

$$
X := 2\left\{\frac{[1 + \sin\delta\cos(2\beta)](1 + \tan\phi_w\cot\theta)}{1 - \sin\delta} - 1\right\},
\tag{6.104}
$$

$$
Y := \frac{f(\theta,\beta)}{1 - \sin\delta}.
\tag{6.105}
$$

The solution to this ODE is,

$$
p = c_1 r^X + \frac{\rho_b gY}{X - 1}r,
\tag{6.106}
$$

where c_1 is a constant of integration. To find this unknown constant, assume the minor principal stress at the free surface, located at $r = R$, is $\sigma_{2,0}$ as shown in Figure 6.20. Note that from Eq. (6.91),

$$
\sigma_{2,0} = p_0(1 - \sin\delta) \implies p_0 = \frac{\sigma_{2,0}}{1 - \sin\delta}.
\tag{6.107}
$$

Thus, at the free surface,

$$
p_0 = c_1 R^X + \frac{\rho_b gY}{X - 1}R \implies c_1 = \left(p_0 - \frac{\rho_b gY}{X - 1}R\right)R^{-X}.
\tag{6.108}
$$

Finally,

$$
p = \left(p_0 - \frac{\rho_b gY}{X - 1}R\right)\left(\frac{r}{R}\right)^X + \frac{\rho_b gY}{X - 1}r,
\tag{6.109}
$$

or, in dimensionless form,

$$
\frac{p}{\rho_b gR} = \left(\frac{p_0}{\rho_b gR} - \frac{Y}{X - 1}\right)\left(\frac{r}{R}\right)^X + \left(\frac{\rho_b gY}{X - 1}\right)\left(\frac{r}{R}\right).
\tag{6.110}
$$

The wall normal stress can be found using Eq. (6.89),

$$
\frac{\sigma_w}{\rho_b gR} = \left[\left(\frac{p_0}{\rho_b gR} - \frac{Y}{X - 1}\right)\left(\frac{r}{R}\right)^X + \left(\frac{\rho_b gY}{X - 1}\right)\left(\frac{r}{R}\right)\right][1 + \sin\delta\cos(2\beta)].
\tag{6.111}
$$

Notes:

(1) The Enstad and Walters models are compared for two different sets of parameters in Figure 6.21. Both show similar trends with the maximum wall stress located in similar locations.
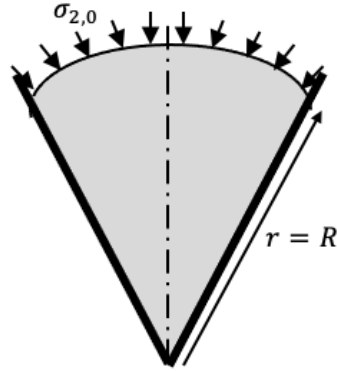
FIGURE 6.20. The free surface boundary condition used in the Enstad model.

(A) $(\theta, \delta, \phi_w) = (15°, 40°, 10°)$

(B) $(\theta, \delta, \phi_w) = (20°, 30°, 10°)$
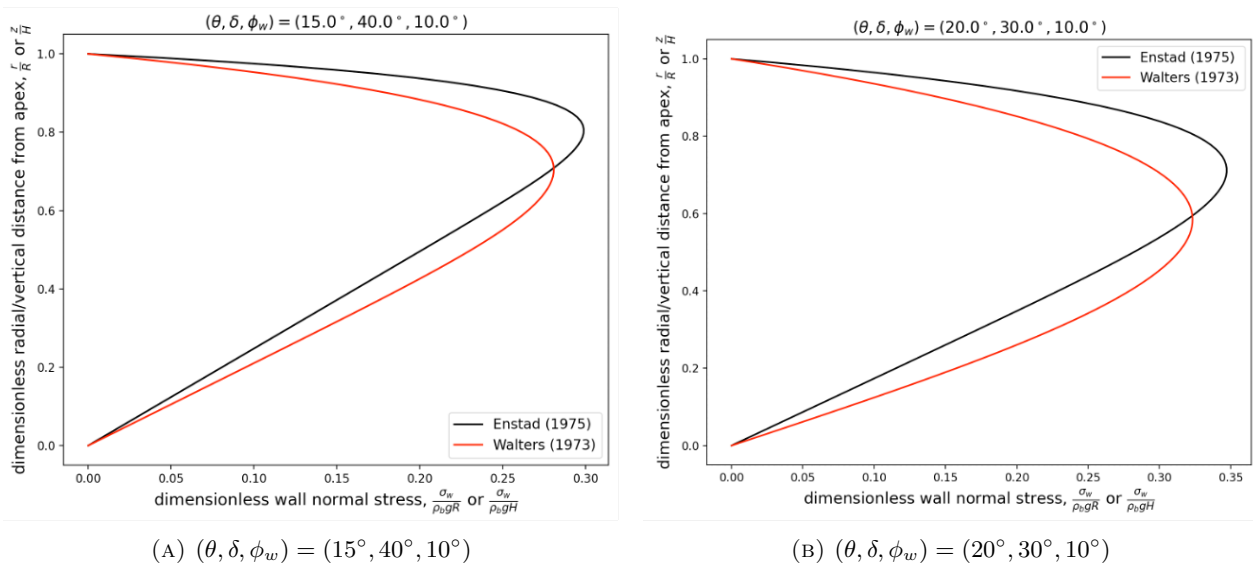
FIGURE 6.21. Comparisons of the dimensionless wall stresses predicted by the Enstad and Walters models for two different sets of parameters. There is no surcharge for either case, passive states of stress are assumed, and the distribution factor for the Walters model is assumed to be one.

6.5. Summary

The following items summarize the most significant points in this chapter:

(1) The Method of Differential Slices can be applied to conical and wedge-shaped bins. Walters [1] used a disk element, Enstad [7] used a spherical cap element.

(2) A passive stress state is observed in converging bins during discharge. The stress state during filling is not well defined. The active state provides a more conservative estimate of the stresses.

(3) For conical and wedge-shaped bins, the stresses approach zero toward the apex of the bin. The active state is closer to being hydrostatic until near the apex. The load on outlet devices is small!

(4) A wall switch stress is observed at the interface between the cylindrical and conical portions of a bin. Special attention should be given to this region when designing a storage vessel.

The dimensionless average vertical stress in a conical hopper as a function of the dimensionless vertical height from the vertex is,

$$\frac{\overline{\sigma_{zz}}}{\rho_b g H} = \begin{cases} \left(\frac{1}{C+1}\right)\left(\frac{z}{H}\right)^{-C} - \left(\frac{1}{C+1}\right)\left(\frac{z}{H}\right) & C \neq -1 \\ -\left(\frac{z}{H}\right)\ln\left(\frac{z}{H}\right) & C = -1 \end{cases}$$

Derive an expression for the maximum dimensionless average vertical stress and its dimensionless location. Plot the dimensionless location of the dimensionless maximum average vertical stress for various values of the constant $C \leq 0$.

SOLUTION:

To find the maximum, take the derivative of the expression with respect to the dimensionless height and set the expression equal to zero,

$$\frac{d}{d(z/H)}\left(\frac{\overline{\sigma_{zz}}}{\rho_b g H}\right) = 0 = \begin{cases} -\left(\frac{1}{C+1}\right)\left[C\left(\frac{z}{H}\right)^{-C-1} + 1\right] & C \neq -1 \\ 1 + \ln\left(\frac{z}{H}\right) & C = -1 \end{cases} \tag{1}$$

Solving for the dimensionless height,

$$\boxed{\left(\frac{z}{H}\right)_{\text{max}} = \begin{cases} \left(-\frac{1}{C}\right)^{\frac{-1}{C+1}} & C \neq -1 \\ \exp(-1) \approx 0.37 & C = -1 \end{cases}} \tag{2}$$

Note that,

$$\lim_{C \to 0}\left(-\frac{1}{C}\right)^{\frac{-1}{C+1}} = 0. \tag{3}$$

The value of the maximum average vertical stress is found by substituting Eq. (2) into the original expression,

$$\left.\frac{\overline{\sigma_{zz}}}{\rho_b g H}\right|_{\text{max}} = \begin{cases} \left(\frac{1}{C+1}\right)\left(-\frac{1}{C}\right)^{\frac{C}{C+1}} - \left(\frac{1}{C+1}\right)\left(-\frac{1}{C}\right)^{\frac{-1}{C+1}} & C \neq -1 \\ -\exp(-1)\ln(\exp(-1)) & C = -1 \end{cases}, \tag{4}$$

$$\boxed{\left.\frac{\overline{\sigma_{zz}}}{\rho_b g H}\right|_{\text{max}} = \begin{cases} -\left(\frac{1}{C+1}\right)\left[\left(-\frac{1}{C}\right)^{\frac{-1}{C+1}} - \left(-\frac{1}{C}\right)^{\frac{C}{C+1}}\right] & C \neq -1 \\ \exp(-1) \approx 0.37 & C = -1 \end{cases}} \tag{5}$$

Note that,

$$\lim_{C \to 0}\left[\left(\frac{1}{C+1}\right)\left(-\frac{1}{C}\right)^{\frac{C}{C+1}} - \left(\frac{1}{C+1}\right)\left(-\frac{1}{C}\right)^{\frac{-1}{C+1}}\right] = 1 + 0 = 1. \tag{6}$$

Equations (2) and (5) are plotted as a dotted line in the following figure for various values of $C \leq 0$.
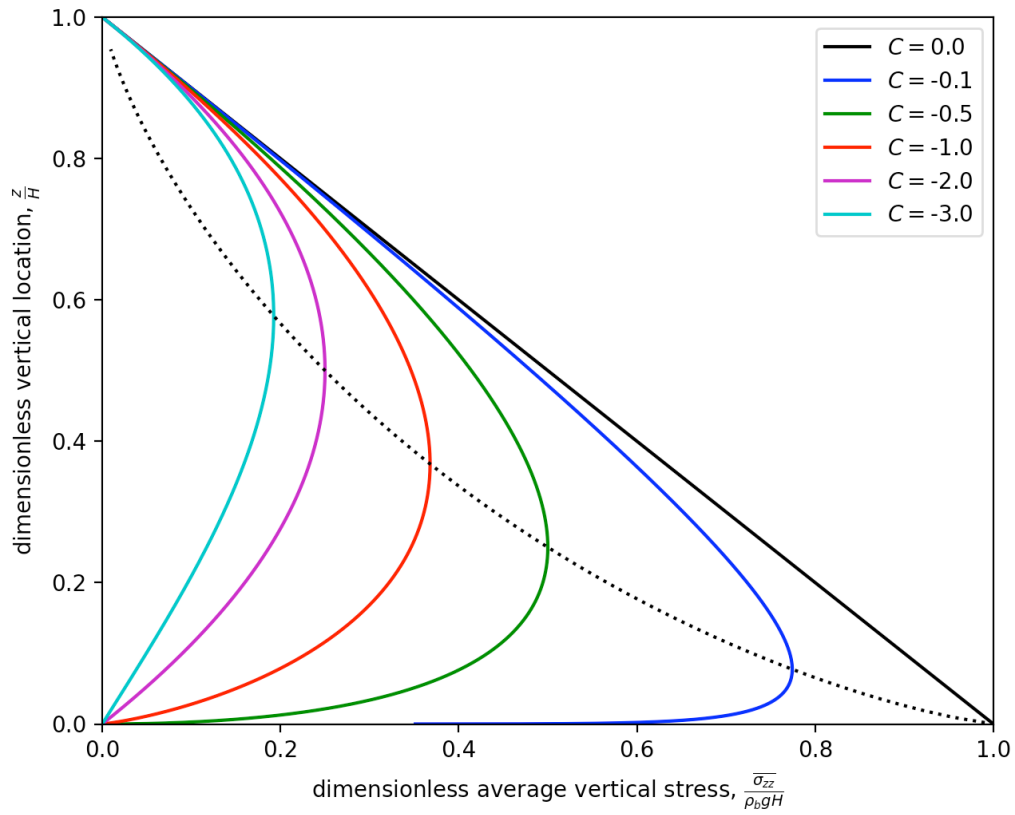
The following Python code was used to generate the figure.

```python
# MoDS_05.py

import numpy as np
import matplotlib.pyplot as plt

def sigma_zz_prime (zprime, sigma_zz_prime_0, C):
    # Avg vertical normal stress as a function of dimensionless height.
    if (C != -1):
        return (sigma_zz_prime_0*zprime**(-C) - 1/(C+1)*zprime*(1-zprime**(-C-1)))
    else:
        return ((sigma_zz_prime_0 - np.log(zprime))*zprime)

def Location(C):
    # Dimensionless location of the maximum stress.
    if (C == -1):
        return(np.exp(-1))
    else:
        return((-1/C)**(-1/(C+1)))

def Value(C):
    # Dimensionless value of the maximum stress.
    if (C == -1):
        return(np.exp(-1))
    else:
        return(-(1/(C+1))*((-1/C)**(-1/(C+1)) - (-1/C)**(C/(C+1))))

colors = ['k', 'b', 'g', 'r', 'm', 'c', 'y']

# First, plot some stress vs. height plots.
zprime = np.linspace(0, 1, 100000)
C_Values = [0, -0.1, -0.5, -1, -2, -3]  # C values to use for plotting
color_index = 0
for C in C_Values:
    plt.plot(sigma_zz_prime(zprime, 0, C), zprime, linestyle='-', color=colors[color_index],
label=r'$C=$%.1f' % C)
    color_index += 1

# Now find the locations and values of the stress maximums.
Location_Values = []  # array for holding the max location values
Stress_Values = []  # array for holding the max stress values

C_Values = np.linspace(0, -100, 10000)  # C values to use for plotting

for C in C_Values:
    Location_Values = np.append(Location_Values, Location(C))
    Stress_Values = np.append(Stress_Values, Value(C))

plt.plot(Stress_Values, Location_Values, linestyle=':', color='k')
plt.xlabel(r'dimensionless average vertical stress, $\frac{\overline{\sigma_{zz}}}{\rho_b g H}$')
plt.ylabel(r'dimensionless vertical location, $\frac{z}{H}$')
plt.xlim([0, 1])
plt.ylim([0, 1])
plt.legend()
plt.show()
```

Estimate the maximum wall stress in the discharging hopper shown below. The incompressible, cohesionless material has a bulk density of 700 kg/m³ and has an effective angle of internal friction of 50°. The wall friction angle is 15°. Assume the cylindrical bin is in an active stress state and the converging conical section is in a passive state. Use distribution factors in both the cylindrical and conical sections.

$D = 1$ m
$\theta = 15°$

Assume very deep.
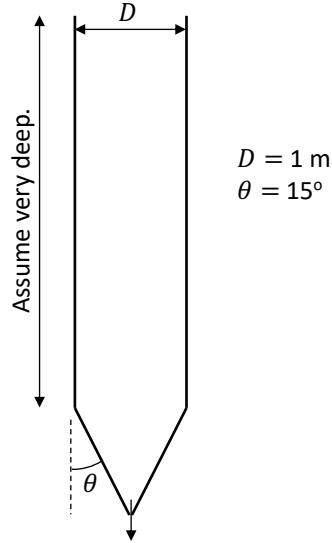
SOLUTION:
From the geometry, the vertical distance from the cone apex to the bottom of the conical section is,

$$\tan\theta = \frac{\frac{1}{2}D}{H} \Rightarrow H = \frac{\frac{1}{2}D}{\tan\theta} \Rightarrow H = 1.866 \text{ m.} \tag{1}$$

The largest wall stress will be a switch stress occurring at the interface between the cylindrical bin and the conical wall section and, thus, we must calculate the wall normal stress at the top portion of the conical section.

The average vertical normal stress and wall normal stress (which is equal to the radial normal stress) at the bottom of a deep cylindrical bin, assuming an active stress state, are,

$$\overline{\sigma_{zz,\text{cyl},\infty}} = \frac{\rho_b g D}{4 \tan\phi_w K_{A,\text{cyl}} \mathcal{D}_{A,\text{cyl}}} \Rightarrow \overline{\sigma_{zz,\text{cyl},\infty}} = 48.06 \text{ kPa,} \tag{2}$$

where,

$$K_{A,\text{cyl}} = \frac{1 - \sin\delta \cos(\omega - \phi_w)}{1 + \sin\delta \cos(\omega - \phi_w)} \Rightarrow K_{A,\text{cyl}} = 0.1342, \tag{3}$$

$$\mathcal{D}_{A,\text{cyl}} = \frac{1}{K_{A,\text{cyl}}} \left[\frac{\cos^2\delta}{1 + \sin^2\delta + 2\sin\delta y} \right] \Rightarrow \mathcal{D}_{A,\text{cyl}} = 0.9936, \tag{4}$$

with,

$$\sin\omega = \frac{\sin\phi_w}{\sin\delta} \Rightarrow \omega = 19.75°, \tag{5}$$

$$c = \left(\frac{\tan\phi_w}{\tan\delta} \right)^2 \Rightarrow c = 0.0506, \tag{6}$$

$$y = \frac{2}{3c} \left[1 - (1-c)^{3/2} \right] \Rightarrow y = 0.9873. \tag{7}$$

The wall normal stress at the interface between the cylindrical and conical sections is,

$$\sigma_{w,\text{cone,int}} = \sigma_{zz,w,\text{cone,int}} \left[\frac{1 + \sin\delta \cos(\omega + \phi_w)}{1 - \sin\delta \cos(\omega + \phi_w + 2\theta)} \right] \Rightarrow \sigma_{w,\text{cone,int}} = 186.4 \text{ kPa,} \tag{8}$$

where,

$$\sigma_{zz,w,\text{cone,int}} = \mathcal{D}_{P,\text{cone}} \overline{\sigma_{zz,\text{cone,int}}} = \mathcal{D}_{P,\text{cone}} \overline{\sigma_{zz,\text{cyl},\infty}} \Rightarrow \sigma_{zz,w,\text{cone,int}} = 77.02 \text{ kPa,} \tag{9}$$

$$\mathcal{D}_{P,\text{cone}} = \frac{1}{K_{P,\text{cone}}} \left[\frac{\cos^2\delta}{1 + \sin^2\delta - 2\sin\delta y} \right] \Rightarrow \mathcal{D}_{P,\text{cone}} = 1.603, \tag{10}$$

$$K_{P,\text{cone}} = \frac{1 + \sin\delta \cos(\Omega + \eta)}{1 - \sin\delta \cos(\Omega + \eta)} \Rightarrow K_{P,\text{cone}} = 1.9709, \tag{11}$$

$$\tan \eta = \frac{\sin \delta \sin(\omega + \phi_w + 2\theta)}{1 + \sin \delta \cos(\omega + \phi_w + 2\theta)} \ \Rightarrow \ \eta = 27.57^\circ, \tag{12}$$

$$\sin \Omega = \frac{\sin \eta}{\sin \delta} \ \Rightarrow \ \Omega = 37.17^\circ, \tag{13}$$

$$c = \left(\frac{\tan \eta}{\tan \delta}\right)^2 \ \Rightarrow \ c = 0.1920, \tag{14}$$

$$y = \frac{2}{3c}\left[1 - (1-c)^{3/2}\right] \ \Rightarrow \ y = 0.9503. \tag{15}$$

Thus, the maximum wall stress is 186 kPa, which occurs in the conical section at the interface between the cylindrical and conical sections.

The following Python code was used for the calculations.

```
# MoDS_04.py

import numpy as np
from scipy.optimize import bisect

def K_fcn(delta_rad, eta_rad, kappa):
    omega_rad = np.arcsin(np.sin(eta_rad)/np.sin(delta_rad))
    print('omega = %.4f deg' % np.degrees(omega_rad))
    return ( (1-kappa*np.sin(delta_rad)*np.cos(omega_rad -
kappa*eta_rad))/(1+kappa*np.sin(delta_rad)*np.cos(omega_rad-kappa*eta_rad)) )

def ScriptD_fcn(delta_rad, eta_rad, theta_rad, kappa):
    K = K_fcn(delta_rad, eta_rad, kappa)
    c = (np.tan(eta_rad)/np.tan(delta_rad))**2
    y = 2/3/c*(1-(1-c)**1.5)
    print('K = %.4f' % K)
    print('(c, y) = (%.4f, %.4f)' % (c, y))
    return(1/K*((np.cos(delta_rad))**2/(1+(np.sin(delta_rad))**2+kappa**2*np.sin(delta_rad)*y)))

def Eta_fcn(delta_rad, phiw_rad, theta_rad, kappa):
    omega_rad = np.arcsin(np.sin(phiw_rad)/np.sin(delta_rad))
    return(np.arctan((np.sin(delta_rad)*np.sin(omega_rad-kappa*phiw_rad-kappa**2*theta_rad))/(1-
kappa*np.sin(delta_rad)*np.cos(omega_rad-kappa*phiw_rad-kappa**2*theta_rad))))


rhob = 700  # kg/m^3, bulk density
g = 9.81  # m/s^2, gravitational acceleration
D = 1.0  # m, cylindrical bin diameter
phiw_deg = 15  # deg, wall friction angle
delta_deg = 50  # deg, effective angle of internal friction
theta_deg = 15  # deg, conical wall half angle

phiw_rad = np.radians(phiw_deg)
delta_rad = np.radians(delta_deg)
theta_rad = np.radians(theta_deg)

# Calculate the conical section vertical height from the apex.
H = 0.5*D/np.tan(theta_rad)
print('H = %.4f m' % H)

print('\nIn the cylindrical section:')
# Calculate the active Janssen's constant for the cylinder.
K_A_cyl = K_fcn(delta_rad, phiw_rad, 1)
print('K_A_cyl = %.4f' % K_A_cyl)

# Calculate the active distribution constant for the cylinder.
ScriptD_A_cyl = ScriptD_fcn(delta_rad, phiw_rad, theta_rad, 1)
print('ScriptD_A_cyl = %.4f' % ScriptD_A_cyl)

# Calculate the asymptotic average vertical normal stress in the cylindrical bin.
sigma_zz_bar_cyl_inf = rhob*g*D/4/np.tan(phiw_rad)/K_A_cyl/ScriptD_A_cyl
print('sigma_zz_bar_cyl_inf = %.4f kPa' % (sigma_zz_bar_cyl_inf/1000))

print('\nIn the conical section:')
```

```
    # Calculate the angle eta in the conical section for the passive state.
    eta_rad = Eta_fcn(delta_rad, phiw_rad, theta_rad, -1)
    print('eta = %.4f deg' % np.degrees(eta_rad))

    # Calculate the passive distribution factor in the conical section.
    ScriptD_P_cone = ScriptD_fcn(delta_rad, eta_rad, theta_rad, -1)
    print('ScriptD_P_cone = %.4f' % ScriptD_P_cone)

    # Calculate the vertical normal stress in the conical bin at the wall at the interface.
    sigma_zz_w_cone_int = ScriptD_P_cone*sigma_zz_bar_cyl_inf
    print('sigma_zz_w_cone_int = %.4f kPa' % (sigma_zz_w_cone_int/1000))

    # Calculate the wall normal stress in the conical section at the interface.
    omega_rad = np.arcsin(np.sin(phiw_rad)/np.sin(delta_rad))
    sigma_w_cone_int = sigma_zz_w_cone_int*(1+np.sin(delta_rad)*np.cos(omega_rad+phiw_rad))/(1-
    np.sin(delta_rad)*np.cos(omega_rad+phiw_rad+2*theta_rad))
    print('sigma_w_cone_int = %.4f kPa' % (sigma_w_cone_int/1000))
```

Running the Python code produces the following output.
```
>> python3 ./MoDS_04.py
H = 1.8660 m

In the cylindrical section:
omega = 19.7468 deg
K_A_cyl = 0.1342
omega = 19.7468 deg
K = 0.1342
(c, y) = (0.0506, 0.9873)
ScriptD_A_cyl = 0.9936
sigma_zz_bar_cyl_inf = 48.0612 kPa

In the conical section:
eta = 27.5727 deg
omega = 37.1741 deg
K = 1.9709
(c, y) = (0.1920, 0.9503)
ScriptD_P_cone = 1.6026
sigma_zz_w_cone_int = 77.0223 kPa
sigma_w_cone_int = 186.4306 kPa
```

Bibliography

[1] J. Walters, "A theoretical analysis of stresses in axially-symmetric hoppers and bunkers," Chemical Engineering Science, vol. 28, pp. 779–789, 1973.

[2] D. Schulze, Powers and Bulk Solids: Behavior, Characterization, Storage and Flow, 2nd. Springer, 2021. DOI: 10.1007/978-3-030-76720-4.

[3] R. Nedderman, Statics and Kinematics of Granular Materials. Cambridge University Press, 1992. DOI: 10.1017/CBO9780511600043.

[4] A. McLean, "Initial stress fields in converging channels," Bulk Solids Handling, vol. 5, pp. 45–54, 1985.

[5] A. Jenike, "Gravity flow of bulk solids (Bulletin 108)," Bulletin of the University of Utah, vol. 52, no. 29, Oct. 1961.

[6] A. Potapov and C. Campbell, "Computer simulation of hopper flow," Physics of Fluids, vol. 8, pp. 2884–2894, 1996.

[7] G. Enstad, "On the theory of arching in mass flow hoppers," Chemical Engineering Science, vol. 30, pp. 1273–1283, 1975.

CHAPTER 7

Types of Hopper Flows

7.1. Introduction

The definitions for a hopper, bin, and silo are not widely agreed upon and the terms are often used interchangeably. All of these devices are used to store materials, at least for some period of time. Following are formal definitions for the different devices, but like others, these definitions are not strictly followed in these notes:

- Hopper: A container that is discharged from the bottom, which consists of inclined walls. Above this inclined wall section, there may or may not be a section with vertical walls (Figure 7.1a). Hoppers are meant for shorter term storage.
- Bin: A container with vertical walls and typically a flat bottom, although inclined walls may also be used (Figure 7.1b). Bins are meant for longer term storage of material, in contrast to a hopper.
- Silo: A tall bin (Figure 7.1c).

There are many hopper designs as shown in Figure 7.2. The choice of the narrowing section depends on various factors, such as space constraints, material characteristics, and exit conditions. Typical materials used to construct hoppers, bins, and silos include:

- concrete: economical when building large hoppers; corrosion and wear resistant; stiff
- carbon steel, stainless steel, aluminum: flexible construction; sanitary
- plastic: only used for small applications

Notes:

(1) The internal surface of the vessel will change over time due to wear as material slides against it and, thus, the flow patterns within the vessel may change over time, especially with mass flow hoppers.
(2) Internal liners are often used to control wear, but contamination can be a concern.
(3) Venting is sometimes used in thin-walled vessels to avoid air pressure differences with the surrounding atmosphere and potential buckling of the vessel walls.

(A) A hopper.   (B) A bin.   (C) A silo.

FIGURE 7.1. Examples of a hopper, bin, and silo.
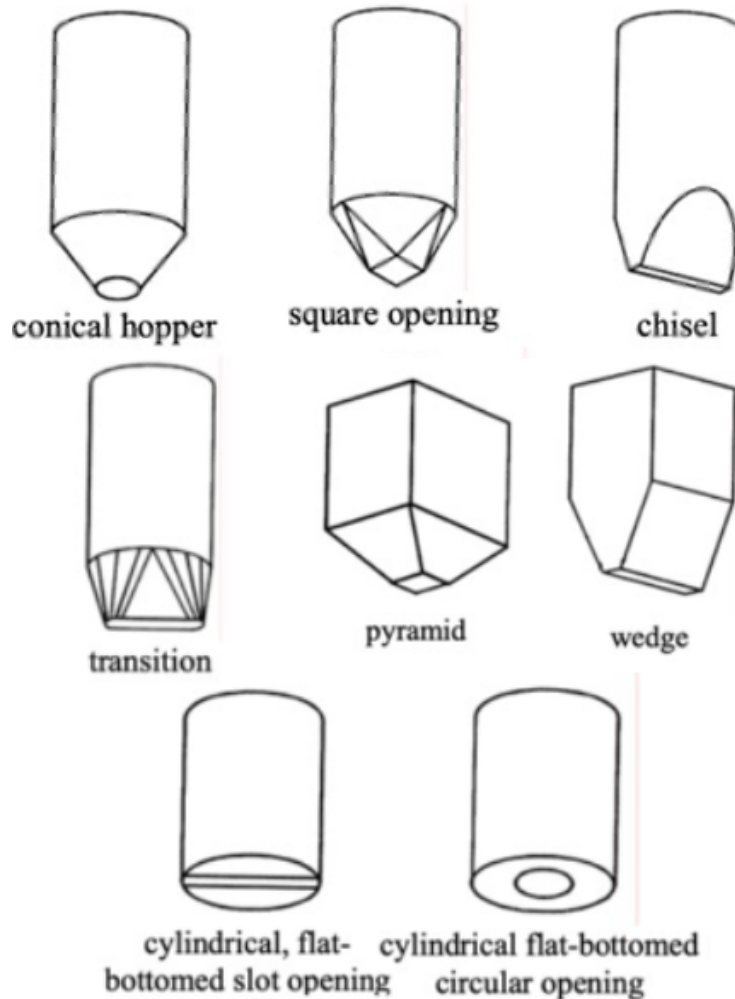
FIGURE 7.2. Different hopper designs. This figure is from Chase [1].

(4) Square and rectangular hopper cross-sections are common since they're easier to manufacture than circular cross sections. In addition, a square cross-section gives a larger cross-sectional area than a circular cross-section for the same aspect ratio, resulting in a smaller hopper height for the same volume capacity. The downsides to square and rectangular cross-sectioned hoppers are that the flat walls are susceptible to bending, which means that thicker walls must be used than for circular cross-sections. In addition, the inclined edges found in polygonal cross-sections, i.e., the valleys, can cause material build-up since they're less steep than the flat walls (Figure 7.3), i.e., $\theta_V > \theta_S$.

(5) Wedge-shapes can be approximately 10° to 12° less steep than conical hoppers and still produce mass flow. In addition, hoppers with circular exits need to have an exit diameter approximately twice the width of a rectangular exit to avoid cohesive bridging. These topics are discussed further in Chapter 9.

7.2. Hopper Flow Modes

The flow through a hopper is of three types: mass flow, funnel flow, and expanded flow. Each type of flow mode is described in this section. Examples of different hopper flow modes are available at the following links:
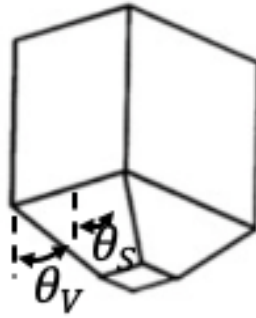
FIGURE 7.3. A square cross-sectioned hopper illustrating that the valleys are less steep than the sides, i.e., $\theta_V > \theta_S$.

- https://www.youtube.com/watch?v=w_Yd8or3PCk
- https://www.youtube.com/watch?v=NantWOoPT8Q

In <u>mass flow</u>, all of the material within the hopper flows during discharge, but not necessarily at the same speed (Figure 7.4a). Mass flow is typically desired in hopper flow for the following reasons.

(1) Mass flow produces "first in, first out" flow. In other words, the material that first fills the hopper is also the first material out of the hopper when discharged. There is less of a concern that long residence times in the hopper will occur and result in damaged, spoiled, or highly compacted material.

(2) There are no stagnant regions within the hopper and the entire capacity of the hopper can be used. All of the material within the hopper is flowing.

(3) There are well-developed models for predicting the stress and velocity fields in mass flow hoppers. Predictions for the other flow modes are not as well developed.

(4) When discharging, the free surface of a mass flow hopper is nearly flat until near the end of discharge. A flatter free surface results in less particle segregation during discharge since material won't flow down a free surface and be subject to shear-induced percolation.

(5) The material in the hopper is less likely to flood. Flooding occurs when air is entrained within the powder, causing the material to flow like a liquid, often in an uncontrolled manner. In mass flow the material moves more consistently and, thus, there is a reduced likelihood that air will get entrained in gaps within the material.

(6) The flow rate from the hopper and the material's bulk density at the exit are more consistent than for the other flow modes.

Although there are many advantages to mass flow, there are a few disadvantages.

(1) Mass flow hoppers tend to have steep hopper walls and, thus, tend to be taller than funnel flow hoppers, which have more shallow hopper walls.

(2) Because material flows along the walls of a mass flow hopper, wear on the walls can be significant.

(3) The stresses on the hopper walls tends to be larger for mass flow than funnel flow. In funnel flow, stagnant material at the walls acts to dissipate stresses caused by flowing material.

In <u>funnel flow</u> (aka core flow), material at the walls remains stagnant while material flows in a core region (Figure 7.4b). Funnel flow is the flow mode most often encountered in practice since many hoppers don't have walls steep enough to produce mass flow. The advantages of funnel flow include the following.

(1) Funnel flow hoppers require less head space since the walls are shallower (larger wall angle from the vertical).

(A) Mass flow.   (B) Funnel flow.   (C) Expanded flow.
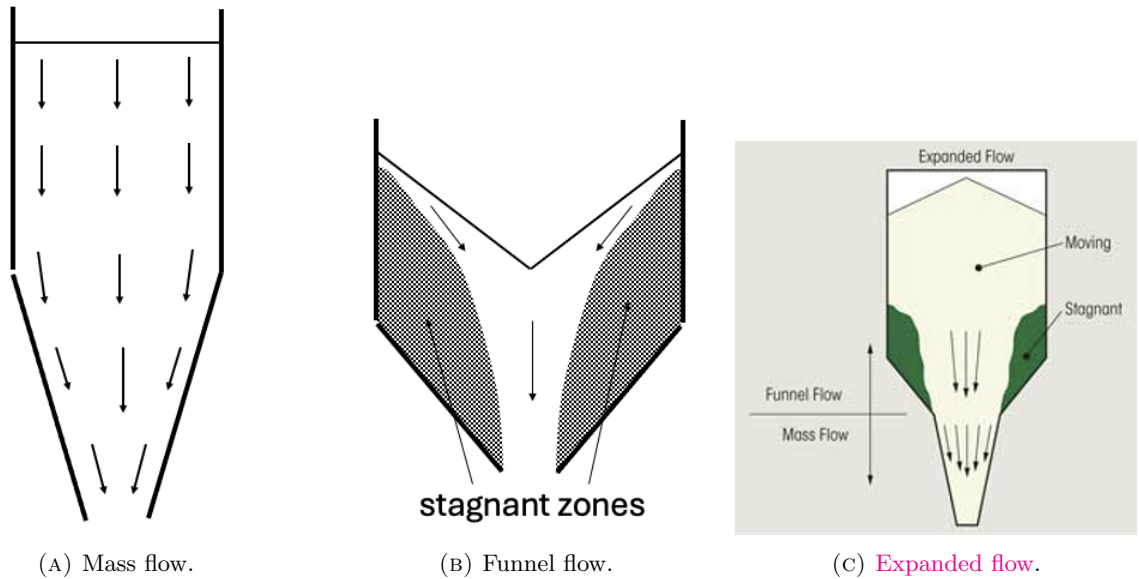
Figure 7.4. Schematics illustrating different flow modes within a hopper.

(2) The stresses on the hopper walls are reduced while the material is flowing since stresses transmitted from the flowing zone are dissipated in the stagnant material.

(3) There is less erosion of the hopper walls since material is stagnant there.

Unfortunately there are many negatives to funnel flow.

(1) The hopper operates in a "first in – last out" mode, which means that much of the material poured first into the hopper is the last material out of the hopper. The stagnant material can become damaged, spoil, or pack more tightly as a function of time.

(2) Because there are regions of stagnant material, the full capacity of the hopper isn't utilized. Furthermore, there may be material that remains in the bin even after discharge.

(3) Ratholes, which are an extreme case of funnel flow, may form and collapse during discharge. Collapsing ratholes can put significant stress on the hopper walls, increase the chances of flooding, and pose a safety risk

(4) During discharge the material free surface is sloped resulting in avalanching flow down the free surface and segregation of free-flowing particles with different properties, especially size differences.

(5) The flow rate from a funnel flow hopper is more likely to be intermittent.

(6) To correct flow problems, flow aids such as wall vibrators, air cannons, and mixer blades, are often required. These devices increase the complexity and costs of storage and discharge.

The last flow mode presented here is expanded flow. Expanded flow consists of a mass flow hopper located beneath a funnel flow hopper (Figure 7.4c). The mass flow hopper activates a flow channel in the hopper designed to prevent the formation of a rathole. The advantages of expanded flow include the following.

(1) Less headroom is required than a mass flow hopper due to the presence of the funnel flow region.

(2) Wear on the hopper walls is reduced in the funnel flow region due to the stagnant material there.

(3) The flow in expanded flow hoppers is better than the flow in funnel flow hoppers. A funnel flow hopper can be retrofitted with a mass flow section to produce expanded flow.

The downsides of expanded flow are as follows.

(1) There are still regions of stagnant material in the hopper.

(2) Segregation can still be an issue at the free surface.
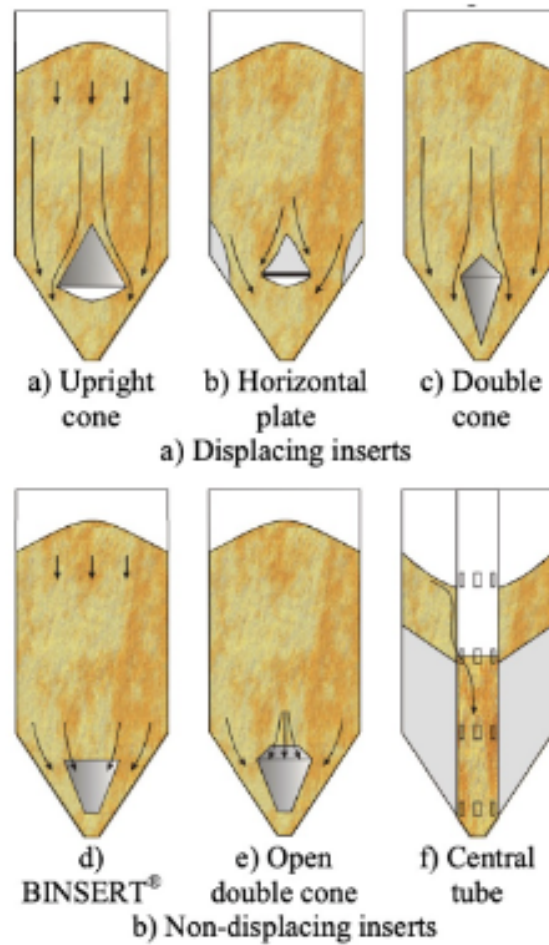
Figure 7.5. Examples of different types of hopper inserts. This figure is from Härtl [2].

Notes:

(1) Hopper inserts (Figure 7.5) can be used to convert funnel flow to mass flow by promoting flow along hopper walls. Inserts must be carefully designed otherwise cohesive arching may be exacerbated. In addition, inserts must be designed to support the significant loads they often encounter. Inserts are sometimes installed in retrofit applications and can be used for purposes other than flow, such as blending, injecting gas, or modifying material and wall stresses.

(2) A study performed by L. ter Borg at Bayer [3] involved performing flow tests on 500 different particulate materials. ter Borg tabulated the percentage of hoppers that resulted in mass flow as a function of the hopper wall angle measured from the vertical. The results are shown in Table 7.1. Interestingly, a 45° wall angle resulted solely in funnel flow conditions. Even a 15° wall angle from the vertical still resulted in 30% of the materials in funnel flow. It's clear that designing for mass flow is more challenging than one might initially expect. Note that 30° (from the vertical) conical hopper walls are common since they are straightforward to construct from flat sheet metal (see, for example, https://www.blocklayer.com/cone-patternseng).

angle from the vertical (°)	% of hoppers in mass flow
45	0
30	25
20	50
15	70

TABLE 7.1. Percentage of hoppers in mass flow in ter Borg's study [3] as a function of the hopper wall angle from the vertical.
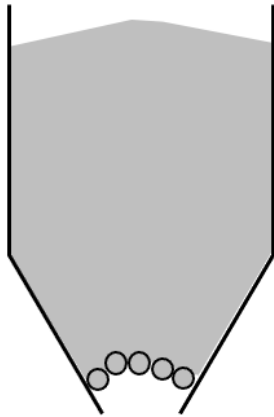
(A) A schematic of a mechanical arch.

(B) A stone arch.

FIGURE 7.6. Examples of mechanical arches.

7.3. Hopper Flow Problems

This section briefly reviews common problems encountered in hopper flows.

Mechanical arching occurs when particles mechanically wedge into place and support the weight of the material above it, preventing flow (Figure 7.6). Mechanical arching typically only occurs when the exit diameter is smaller than $8 - 12$ particle diameters. Mechanical arching isn't a common hopper flow problem, except for special cases. Vibration can destabilize a mechanical arch, but the arch will likely reform once the vibration stops. The research paper by To et al. [4] provides a probabilistic model for why mechanical arching (aka jamming) is unlikely to occur for larger diameter openings.

Cohesive bridging (aka cohesive arching) occurs when the strength developed in the material is sufficient to support the load from the material above it (Figure 7.7). Cohesive bridging is a common hopper flow problem. Cohesive bridges most commonly form near a hopper exit but can also form anywhere within a bin if the bin diameter is sufficiently small. A sufficiently large bin/exit diameter is required to ensure that the weight of the material will collapse the arch and maintain flow. Vibration and air injection may help collapse a cohesive bridge, but can potentially result in other problems, such as flooding. Improper application of vibration can sometimes exacerbate cohesive arching.

Material build-up on hopper walls is common when funnel flow occurs (Figure 7.8). The extreme case of material build-up is known as a rathole (discussed later in this section). Material build-up results in stagnant material, intermittent flow, and large dynamic loads when the material collapses. Material buildup is best avoided by using mass flow hoppers. Common methods for trying to eliminate material build-up include subjecting the hopper to vibration (using a vibrating motor or via hammering the side), injecting air via an air cannon at the wall to blast material from the side walls, or injecting air, e.g., with an air lance, to help fluidize the material.

(A) A schematic of a cohesive bridge.

(B) A photograph of a cohesive bridge.

(C) A photograph of a cohesive bridge.

(D) A photograph of a cohesive bridge [5].
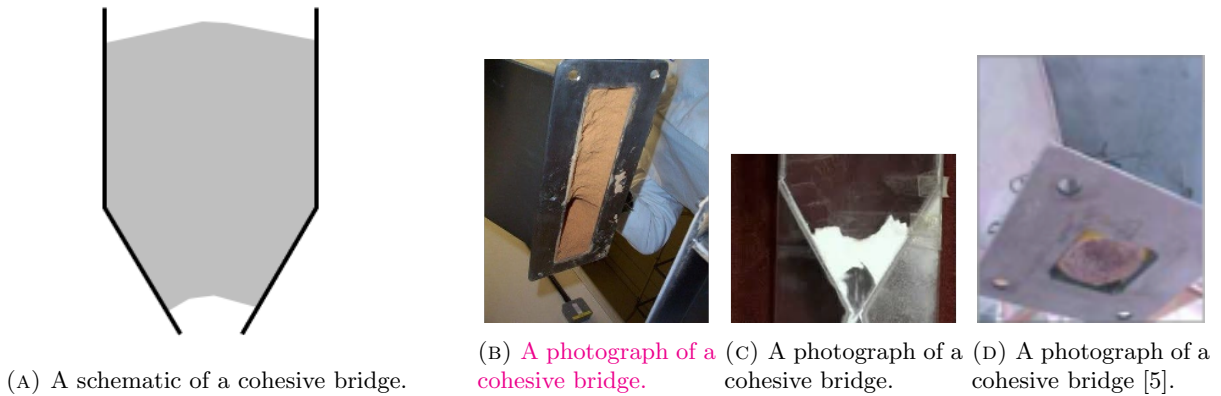
FIGURE 7.7. Examples of cohesive bridges.

(A) A schematic of material build-up at the hopper wall.

(B) A photograph of material build-up.
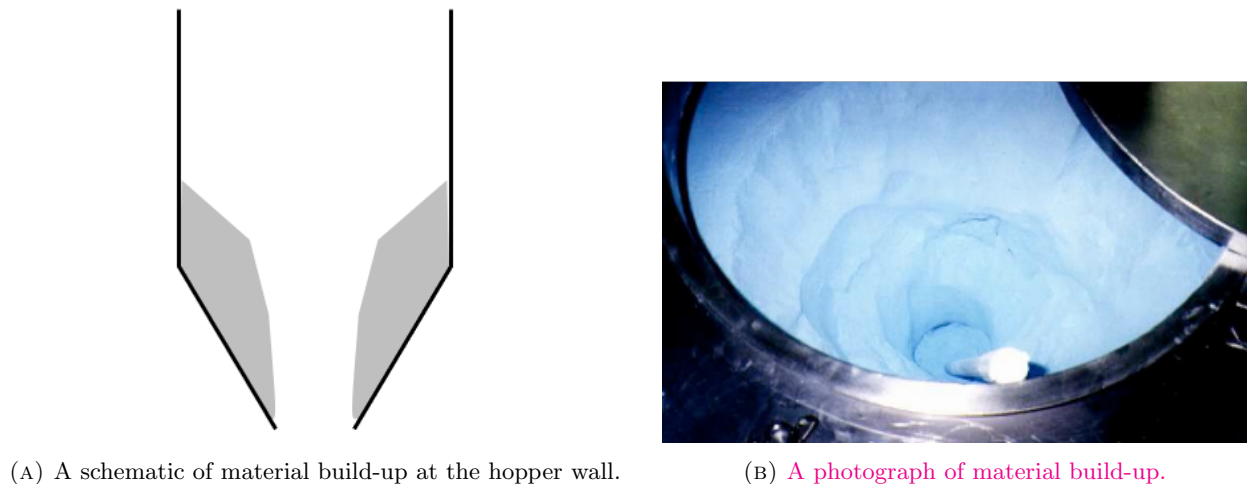
FIGURE 7.8. Examples of material build-up at the hopper wall.

A rathole is when flow only occurs in a narrow core of the material and stable, stagnant regions of material remain after partial discharge of the hopper (Figure 7.9). Ratholes are particularly problematic since they can collapse, resulting in large dynamic stresses on the hopper structure and flooding, whereby falling powder is aerated and flows in an uncontrolled, liquid-like manner. An interesting video discussing the significance of ratholing called "The Million Dollar Rathole" is available online.

Slow discharge from a hopper can occur if the material has low permeability. As material discharges, the counter-flow of air into the hopper may slow down the flow rate (Figure 7.10). In come cases, rather than having a continuous discharge of material, the flow may be irregular with material exiting in discrete "chunks" (e.g., "plop, plop" flow). A video example of the intermittent flow associated with counter-flowing air is available at: https://youtu.be/Ml6Etm9pPrU.

Flooding (aka flushing) occurs when an aerated powder flows from a hopper in an uncontrolled, liquid-like manner (Figure 7.11). Flooding typically only occurs for fine powders (Geldart Group A or smaller), which have small permeability. Flooding may also occur during rapid filling and discharge, where the powder becomes and remains aerated. Flooding may also occur when a rathole or cohesive bridge collapses. Improper injection of air, such as when trying to induce stalled flow, may also result in flooding. A short video showing flooding is available at: https://www.youtube.com/watch?v=PmTnUOcAnuY.
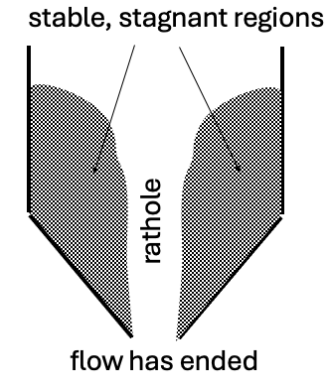
(A) A schematic of a rathole.

(B) A photograph of a rathole (courtesy of B. Hancock).

(C) A photograph of a rathole [5].

Figure 7.9. Examples of ratholes.
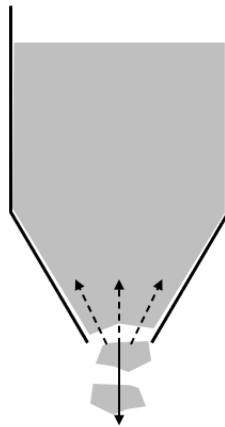
Figure 7.10. A schematic of hopper discharge slowed by incoming air.

Figure 7.11. An illustration of flooding from a hopper.

Segregation is the unintentional de-mixing of a previously blended particulate material (Figure 7.12). Many physical processes can cause segregation, but one of the most common is shear-induced percolation. Shear-induced percolation occurs when smaller particles fall between the gaps of larger particles in a shear flow. Shear flows commonly occur at the free surface of a flowing material. In particular, funnel flows have significant shear flow at the free surface due to the V-shaped surface that appears during discharge. In addition, filling of a hopper can result in segregation as material falling onto a mound also results in significant shear flow. Segregation is most significant for freely-flowing materials since particles must be able to move relative to one another to segregate. Additional information on shear-induced segregation during hopper discharge is available in Ketterhagen et al. [6], [7] and Anand et al. [8].

Eccentric loading of bin walls can occur when the flow channel in the hopper is off-center (Figure 7.13). Since bin walls are often thin-walled structures, eccentric loading can result in buckling of the walls. Off-center flow in the bin usually occurs for funnel flows or asymmetry at the bin outlet, e.g., an eccentric outlet, a partially open gate valve, or a poorly designed exit feeder. The wall loads caused by a flow channel are smaller at the flow channel, but larger at the edges of the channel.

Buckling of the bin walls can occur if a low permeability material bridges within the bin (Figure 7.14). As downstream material flows while upstream material bridges, a void will form between the two regions. If the material has low permeability, then air may not fill the void rapidly enough to maintain atmospheric pressure within the void. As a result, the air pressure in the void can drop below atmospheric pressure and buckling of the bin walls may occur.

Silo quaking/honking can occur during discharge as a result of stick-slip movement of material against the silo walls (Figure 7.15). The vibrations can be below the audible range (quaking) or in the audible range (honking). This phenomenon is most noticeable with hard, brittle, and coarse materials in metal bins. It is believed that most silos experience this issue, but with small amplitudes. Large vibration and noise can potentially cause structural damage and fatigue, and can present a health concern. Shocks (sudden pressure changes) can also occur due to sudden changes in flow.

The last hopper problem presented here is Thermal Ratcheting (Figure 7.16). Consider a bin located outdoors. During the day, the Sun heats the bin walls causing the bin to expand and the material inside to settle. At night, the bin walls cool and contract, causing the radial stresses to increase significantly since the stresses required to move the material upwards are exceedingly large (a passive stress state - refer to Chapter 5). Over successive thermal cycles, the radial stresses during cooling may exceed the bin strength and cause bin failure. This phenomenon is known as thermal ratcheting. A similar effect can occur for materials that swell due to temperature or moisture absorption.

Additional examples of hopper/bin problems are shown in Figure 7.17. In addition, the following videos provide additional hopper/bin problem examples:

(1) A dramatic example of poor flow (caking) leading to tragedy: https://en.wikipedia.org/wiki/Oppau_explosion.
(2) Grain silo collapse videos:
   (a) https://www.youtube.com/watch?v=5yZ8s8Rwo-Y
   (b) https://www.youtube.com/watch?v=nljxk1auzHQ
(3) https://www.facebook.com/jordan.white.39545/videos/10211881599893153/

Storage and flow problems can have consequences on manufacturing performance such as:

(1) caking of material stored under large loads and extended storage times, which requires significant effort to clear from storage vessels,
(2) unacceptable product uniformity due to mass differences and segregation,
(3) low process yields due to inefficient material handling and high reject levels,
(4) equipment damage or uncontrolled flow,
(5) need for force feeders, vibrators, custom hoppers, etc., and
(6) irreproducible manufacturing operations.

(A) An initially well-mixed material with two particle sizes (yellow particles are small, black particles are large) that segregated after flowing through the hopper.

(B) An illustration of shear-induced percolation on a sloped free surface.
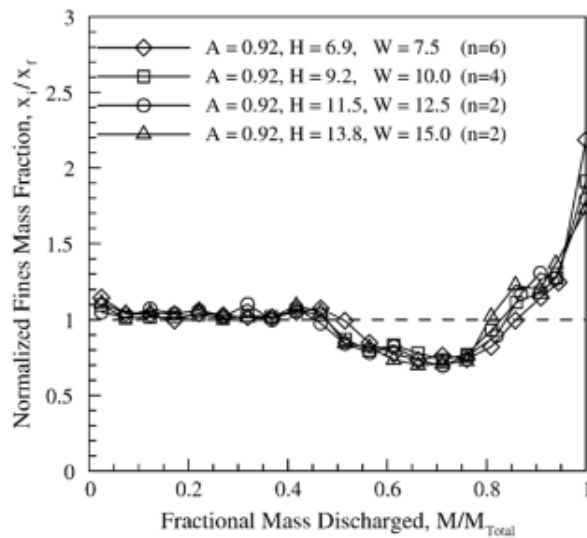
(C) Segregation results from a simulated hopper flow of a blend of fine and coarse particles [7]. The vertical axis is the mass fraction of fine particles at the exit plane normalized by the overall mass fraction of fines. The horizontal axis is the fraction of total mass discharged from the hopper. A fines mass fraction of one indicates a well blended mixture, a value greater than one is fines-rich, and a value less than one is coarse-rich. The different symbols are for hoppers of different dimensions.

FIGURE 7.12. Examples of particle segregation.

7.4. Summary

Following is a summary of the significant points in this chapter.

(1) There are three hopper flow modes: mass flow (usually what is wanted), funnel flow (more common), and expanded flow (often for a retrofit).
(2) Many flow problems exist, including bridging, material build-up, ratholes, segregation, ...
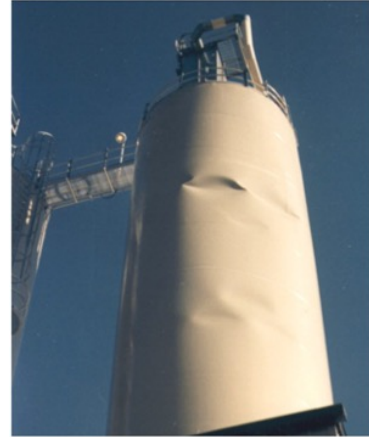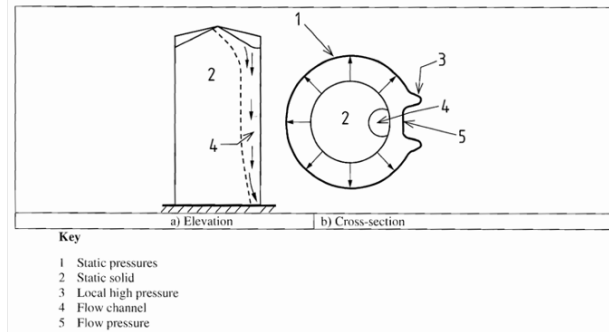
(A) A schematic of eccentric loading on a bin's wall due to off-center discharge of material within the bin [9].

(B) A photograph of a silo that has buckled due to eccentric wall loading.

FIGURE 7.13. Examples of eccentric loading of the hopper walls due to an off-center flow channel.
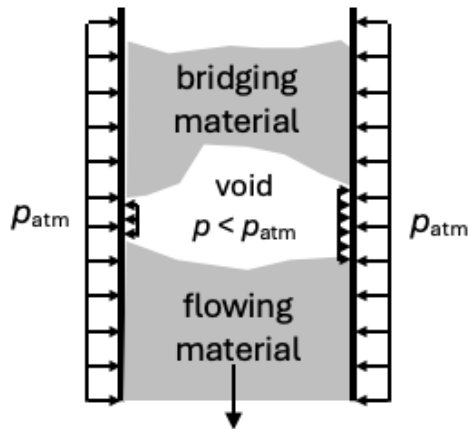
(A) A schematic illustrating the mechanism causing wall buckling due to air pressure differences.

(B) A photograph of a silo with buckled walls caused by pressure differences.

FIGURE 7.14. Examples of eccentric loading of the hopper walls due to an off-center flow channel.

(3) Poor flow can impact manufacturing performance and cause structural and safety concerns.
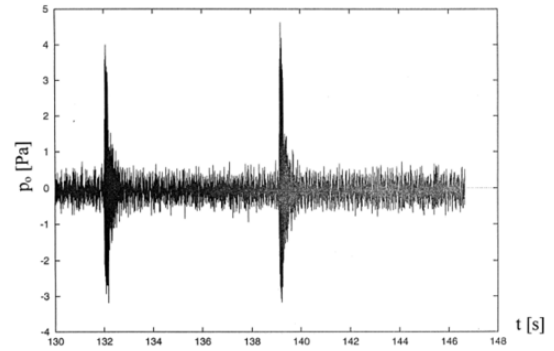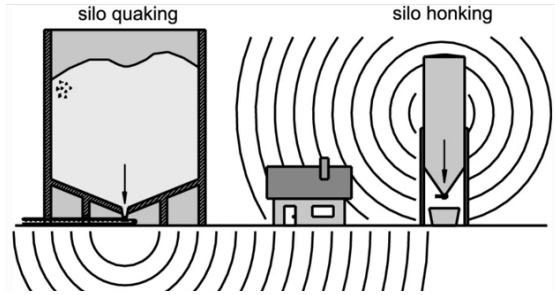
(A) A schematic illustrating silo quaking and silo honking. Figure from Schulze [10].

(B) Sound pressure time profile outside a honking silo. Figure from Tejchman [11].

FIGURE 7.15. Examples of silo quaking and honking.
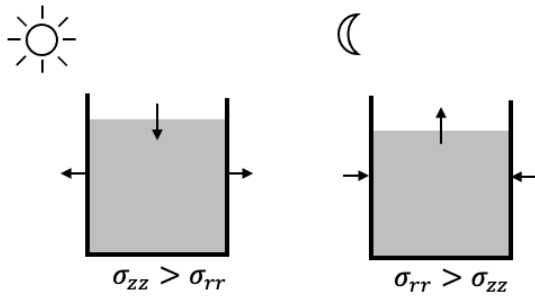
(A) Schematics illustrating the phenomenon of thermal ratcheting.

(B) Photographs of the thermal ratcheting failure of a bin containing 9000 tons of fly ash. Photographs from Dogangun et al. [12].

FIGURE 7.16. Examples of thermal ratcheting.
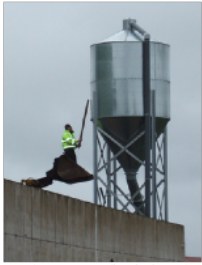
(A) From McGee [13].

(B) From McGlinchey [14].

(C) From http://jenike.mmcis.com/Training/fos.html.
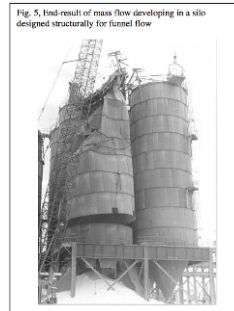
(D) From Carson [15].

(E) From Marinelli [16].

(F) From http://www.youtube.com/watch?v=s2Rc8fZCjtI.

(G) From http://www.bulksolidsflow.com/index.php?option=com_content&view=article&id=5&Itemid=3.

FIGURE 7.17. Many examples of hopper/bin flow problems.

Bibliography

[1] G. Chase, Solids notes. chapter 10, University of Akron, 1998.

[2] J. Härtl, "A study of granular solids in silos with and without an insert," Ph.D. dissertation, The University of Edinburgh, 2008.

[3] K. Jacob, Bin and hopper design, Lecture Notes, Mar. 2000.

[4] K. To, P.-Y. Lai, and H. Pak, "Jamming of granular flow in a two-dimensional hopper," Physical Review Letters, vol. 86, no. 1, pp. 71–74, 2001.

[5] J. Johanson, "Troubleshooting bins, hoppers and feeders," Chemical Engineering Progress, no. 4, pp. 24–36, 2002.

[6] W. Ketterhagen, J. Curtis, C. Wassgren, A. Kong, P. Narayan, and B. Hancock, "Granular segregation in discharging cylindrical hoppers: A discrete element and experimental study," Chemical Engineering Science, vol. 62, pp. 6423–6439, 2007.

[7] W. Ketterhagen, J. Curtis, C. Wassgren, and B. Hancock, "Modeling granular segregation in flow from quasi-three-dimensional wedge-shaped hoppers," Powder Technology, vol. 179, pp. 126–143, 2008.

[8] A. Anand, J. Curtis, C. Wassgren, B. Hancock, and W. Ketterhagen, "Segregation of cohesive granular materials during discharge from a rectangular hopper," Granular Matter, vol. 12, pp. 193–200, 2010.

[9] E. 1, "En 1991-4: Actions on structures – part 4: Silos and tanks," European Committee for Normalisation, Tech. Rep., 2006.

[10] D. Schulze, Powers and Bulk Solids: Behavior, Characterization, Storage and Flow, 2nd. Springer, 2021. DOI: 10.1007/978-3-030-76720-4.

[11] J. Tejchman, "Technical concept to prevent the silo honking," Powder Technology, vol. 106, no. 1-2, pp. 7–22, 1999.

[12] A. Dogangun, Z. Karaca, A. Durmus, and H. Sezen, "Cause of damage and failures in silo structures," Journal of Performance of Constructed Facilities, vol. 23, no. 2, 2009.

[13] E. McGee, "The benefits of powder characterization," SHAPA Technical Bulletin Number 14, 2009. [Online]. Available: https://www.shapa.co.uk/technical-downloads/Updated%5C%20Papers%5C%20May%5C%202015/powder_characterisation.pdf.

[14] D. McGlinchey, Bulk Solids Handling: Equipment Selection and Operation. Blackwell, 2008.

[15] J. Carson, "Silo failures: Case histories and lessons learned," in Handbook of Conveying and Handling of Particulate Solids, A. Levy and H. Kalman, Eds. Elsevier, 2001, pp. 153–166.

[16] J. Marinelli, Lecture notes for "particulate systems" (che 53600 at purdue university), 2018.

CHAPTER 8

Shear Cell Testing

The properties used in bin and hopper design are often obtained from shear cell testing. These are fundamental powder properties corresponding to the Jenike modeling framework as well as the Ideal Coulomb material model. They are not flow indices, although they are sometimes used in that manner. There are devices other than shear cells that can be used for the powder property measurements described in this chapter, including triaxial testers, uniaxial testers, and biaxial testers, but shear cells are the most commonly used device and are the only device discussed in these notes. More information on these other testing devices is available in Schwedes [1].

Notes:

(1) The standard nomenclature used in shear cell testing uses similar symbols making it easy to get confused. Thus, these notes will use symbols that are not standard, but hopefully are easier to associate with the physical quantities of interest.

8.1. The Material Flow Function (mFF)

Let's begin with a simple thought experiments. Imagine making a snowball (Figure 8.1). If you pack the snowball loosely, i.e., apply a small consolidation stress, the snowball will have little strength, i.e., it's easy to break apart (aka yield). However, if you pack the snowball tightly, i.e., apply a large consolidation stress, then the snowball has more strength. A powder's strength is a function of the consolidation stress applied to the powder (or alternately, its solid fraction). One goal of shear cell testing is to (indirectly) measure a powder's yield strength as a function of the stress used to compact the powder (aka the consolidation stress).

The <u>unconfined yield strength</u> of a powder (f_c) is the maximum principal stress that a powder's free surface can withstand before yielding. The unconfined yield strength is important since, in order for material in the hopper to remain flowing, the local stresses acting on the powder should exceed the powder's local unconfined

FIGURE 8.1. A photograph of a snowball.
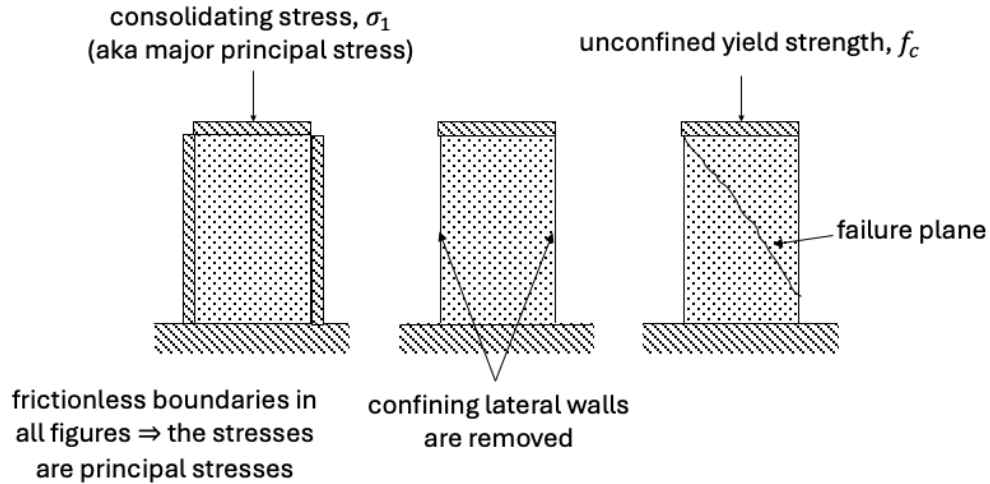
FIGURE 8.2. An illustration of a simple experiment used to determine a material's flow function.
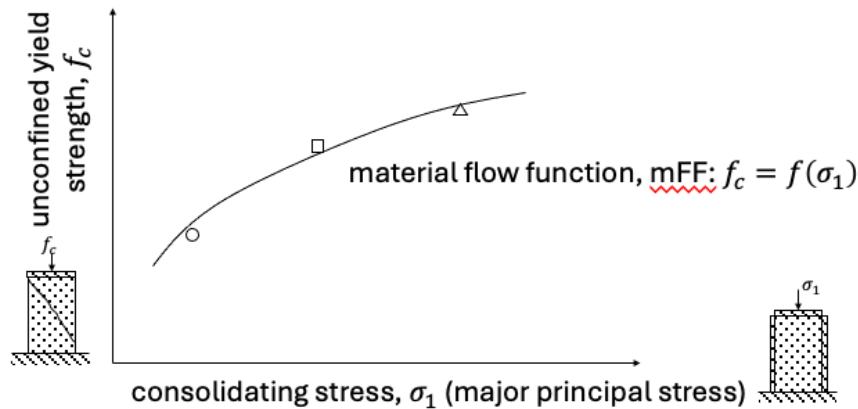
FIGURE 8.3. An example of a material flow function (mFF).

yield strength. If this is the case, then a stable free surface won't form and the powder will continue to flow (i.e., yield).

The underlined material flow function (mFF) is the relationship between the powder's unconfined yield strength (f_c) and the consolidation stress (σ_1), which is also the major principal stress, used to consolidate the powder. The material flow function is primarily a function of the powder properties, although environmental conditions, such as temperature and relative humidity, can also play a role.

An illustration of a simple unconfined yield strength measurement is shown in Figure 8.2. Here, a cylindrical container is used to consolidate the sample. The walls of the container are assumed frictionless, which makes the normal stresses applied by the walls principal stresses. The stress applied on the lid of the container is the major principal stress (σ_1) (aka consolidation stress) and it consolidates the material uniformly to some solid fraction. The applied stress is removed along with the side walls to create a free, or unconfined, surface. A new stress is applied to the lid. The stress at which the material yields is the unconfined yield strength (f_c). A plot of a typical material flow function is shown in Figure 8.3.

Notes:
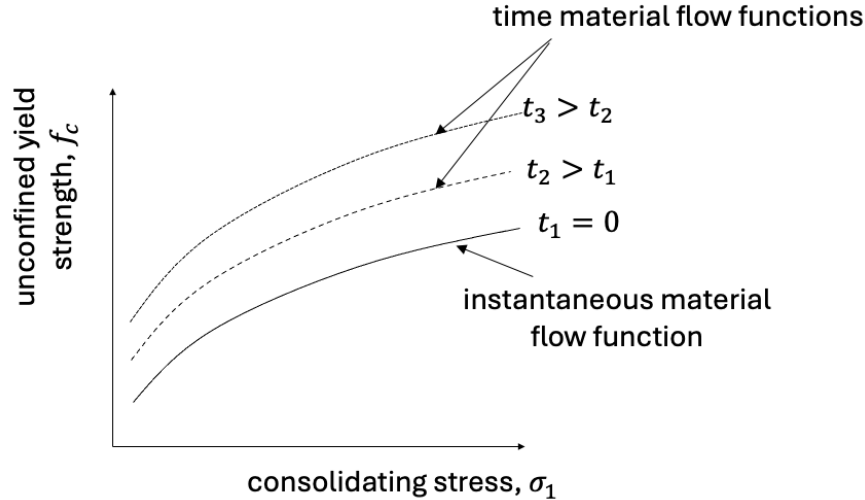
FIGURE 8.4. An illustration of how a material flow function changes due to time consolidation.

(1) The simple experiment shown in Figure 8.2 cannot be used in practice for many materials since the unconfined yield strength may be small enough that the material weight collapses the column when the side walls are removed.

(2) Material flow functions frequently change with time and environmental conditions as inter-particle forces change due:
- escape of interstitial air with a corresponding increase in bulk density,
- external vibrations due to machinery, traffic, wind, etc., cause an increase in bulk density,
- moisture collects on particle surfaces resulting in increased cohesion caused by the formation of liquid bridges,
- evaporation of water results in precipitation of dissolved salts, forming solid bridges between particles, and
- fragmentation or plastic deformation of particles under pressure (creep) results in an increase in the contact area between particles and, thus, an increase in cohesion,
- changes in the particle surface due to chemical reactions, e.g., crystallization or fermentation.

This phenomenon whereby the powder strength changes over time is known as Time Consolidation. An illustration of material flow functions as a function of time is shown in Figure 8.4. The material flow function performed immediately after the powder has been loaded into the measurement device for testing is referred to as the "instantaneous material flow function" while the flow functions at later times are known as "time material flow functions". It is essential that material flow functions be prepared over the range of conditions anticipated for the powder, e.g., the storage times, temperatures, humidities, and loads, otherwise the properties used in design calculations will not be representative of the powder's true state.

(3) A material flow factor, (mff) is the inverse slope, measured from the origin, of a point on the material flow function (mFF), i.e.,

$$\text{mff} := \frac{\sigma_1}{f_c}. \tag{8.1}$$

The material flow factor is used in hopper design calculations and is often reported as a comparative measure of a powder's flowability. It's important to note, however, that the material flow factor is not a constant and, thus, reporting a single value for the parameter should be considered with caution. At the very least, the consolidation stress at which the material flow factor is determined should be reported. Jenike [2] provided qualitative characterization of a powder's flow behavior based on the material flow factor as described in Table 8.1 and shown in Figure 8.5. As the material

material flow factor (mff)	flow behavior
mff < 1	hardened
$1 <$ mff < 2	very cohesive
$2 <$ mff < 4	cohesive
$4 <$ mff < 10	easy flowing
$10 <$ mff	free flowing

TABLE 8.1. Qualitative flow behavior for various ranges of the material flow factor (mff).
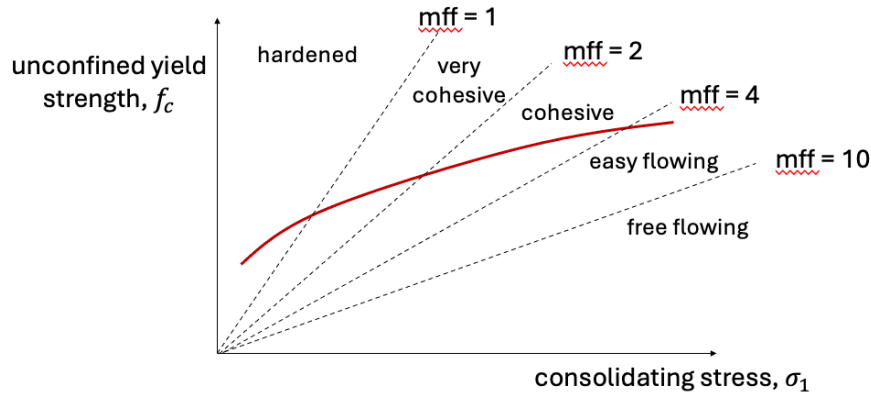
FIGURE 8.5. Qualitative flow behavior for various values of the material flow factor (mff). As the material flow factor increases, the flow behavior improves. The colored line in the figure is an example material flow function (mFF). Note that the material flow factor changes for this material depending on the consolidation stress.

flow factor increases, i.e., the unconfined yield strength decreases for a given consolidation stress, the flow behavior improves.

8.2. Shear Cell Testing

Shear cell testing is used to determine a material's flow function (mFF) as well other useful parameters, such as cohesion and internal friction and wall friction angles. Unlike the uniaxial compaction experiment shown in Figure 8.2, shear cell testing can be performed on materials with small strength. Another key aspect of shear cell testing is that the material is tested in a well-defined, repeatable state (i.e., solid fraction). Most index style measurement devices have ill-defined testing states. For example, filling material into a flow-through-an-orifice cup does not put the material into a uniform and known solid fraction prior to testing.

Notes:

(1) Shear cells usually measure flow properties at quasi-static conditions, i.e., small shear strain rates, which may not be representative of the strain rates in actual flowing conditions. Similarly, the consolidation stresses usually applied in shear cell testing are larger than those encountered at the free surface of a flowing material.
(2) Shear cells do not directly measure the consolidation stress and unconfined yield strength, but instead use Mohr's circle analysis to determine those values.

Several shear cell designs have been proposed. Figure 8.6 shows the shear cell design originally used by Jenike [2]. The powder is loaded into a split cylindrical testing vessel. The cylinder is split so the top portion (the ring) can translate over the fixed bottom portion (the base). The base and lid are roughened to prevent powder slippage against the the vessel surfaces. A vertical load is applied to the lid to consolidate the

(A) A photograph of the shear cell.
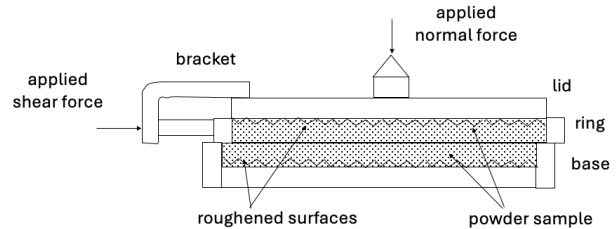
(B) A schematic of the shear cell.

FIGURE 8.6. The Jenike translational shear cell.

material. A shear force is then applied to the side of the ring and the force at which the material begins to move is recorded. A more detailed description of how a shear cell test is performed is described in a following section. Since the translation is in a single direction, the shear cell has a limited displacement, less than 10 mm for example. Since the displacement is small, conditioning the material to a consistent repeatable initial state via shear can be challenging (described in more detail in a following section). The displacement rate during testing is slow - on the order of 1 mm/min. An ASTM standard [3] provides detailed information on the Jenike shear cell and its operation.

One of the most common shear cell designs is the annular (aka ring) shear cell (Figure 8.7). In this device, the material is contained within an annulus (Figure 8.7b), with the lid and base roughened by vertical vanes to prevent slipping against the cell walls. A vertical load is applied to the lid and the torque required to rotate the sample base, is recorded. A significant advantage of the annular shear cell over the translational shear cell is that large shear strains can be applied to the material, which helps in material preparation. Another advantage of this device is that the measurements are highly automated, minimizing operator bias in the results. As with the translational shear cell, the shear strain rates are small. Examples of annular shear cells include ones described at https://www.dietmar-schulze.de/ringschergeraete_e.html and https://www.brookfieldengineering.com/products/powder-flow-testers/pft-powder-flow-testers. ASTM standards also exist for annular shear cells, such as the one for the Schulze ring shear tester [4].

The last shear cell device discussed here is the Peschl-style shear cell (Figure 8.8). The Peschl shear cell is also a rotational shear cell and operates in much the same way as an annular shear cell, but the material is contained within a cylindrical sample vessel, not an annular vessel. An example of a Peschl-style shear cell is the one available with the FT4 rheometer. An ASTM standard for operating a Peschl-style shear cell is also available [5].

Comparisons between shear cell designs have been performed [6]. There is little difference in the results from different shear cell designs for freely-flowing materials; however, differences are observed for cohesive, compressible materials. These findings indicate that shear cell design and procedures can have an impact on the shear cell results. As a final comment, the uncertainty in shear cell measurements and the propagation of that uncertainty into property measurements is rarely reported in shear cell testing. These uncertainties would help put the differences in these comparative shear cell tests into perspective as well as establish an appropriate degree of confidence in property measurements.

8.3. Some Comments on Solid Fraction

Although the material flow function (mFF) is the relationship between the consolidation stress (major principal stress) used to compact the powder and the resulting unconfined yield strength, it's really the powder's solid fraction (aka relative density) that governs the powder's strength. The consolidation stress simply sets the powder's solid fraction. Hence, the powder's solid fraction is monitored during shear cell testing.

(A) A photograph of the full shear cell device.

Shear cell approx. 30 ml, 2 EURO coin

(B) A photograph of the testing cell base and lid.

Figure 8.7. An annular shear shear cell. The images are from https://www.dietmar-schulze.com/.
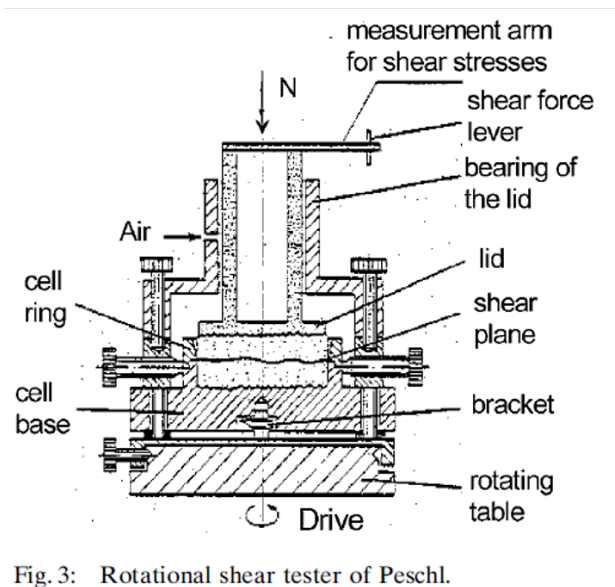
Fig. 3:   Rotational shear tester of Peschl.

(A) A schematic of the full shear cell device. This figure is from [6].
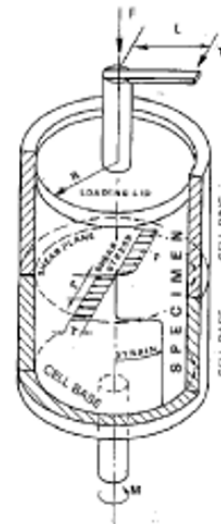
FIG. 1 Schematic View of a Rotational Split Level Shear Cell

(B) A schematic of material movement in the shear cell. This figure is from [7].

Figure 8.8. A Peschl shear shear cell.

Depending on the powder's initial configuration, a powder's solid fraction can change when sheared. A loosely-packed (aka under-consolidated) powder will densify when sheared at a sufficiently large normal load whereas a tightly-packed (aka over-consolidated) powder will dilate when sheared for a sufficiently small normal load. Densification of an under-consolidated powder occurs because the particles start in a loosely-packed configuration for the given load and then move into a more tightly packed state as the particles move relative to each other (Figure 8.9a). For a tightly-packed configuration for a given load, the particles must move over each other, i.e., dilate, when sheared (Figure 8.9b). This dilation is referred to as the Reynolds'
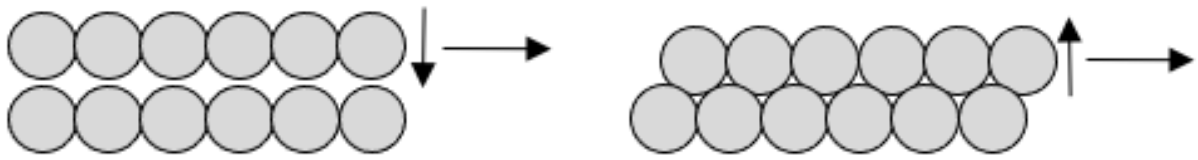
(A) Particles in an under-consolidated state.

(B) Particles in an over-consolidated state.

FIGURE 8.9. Particles subject to shear in under- and over-consolidated states.

(A)

(B)
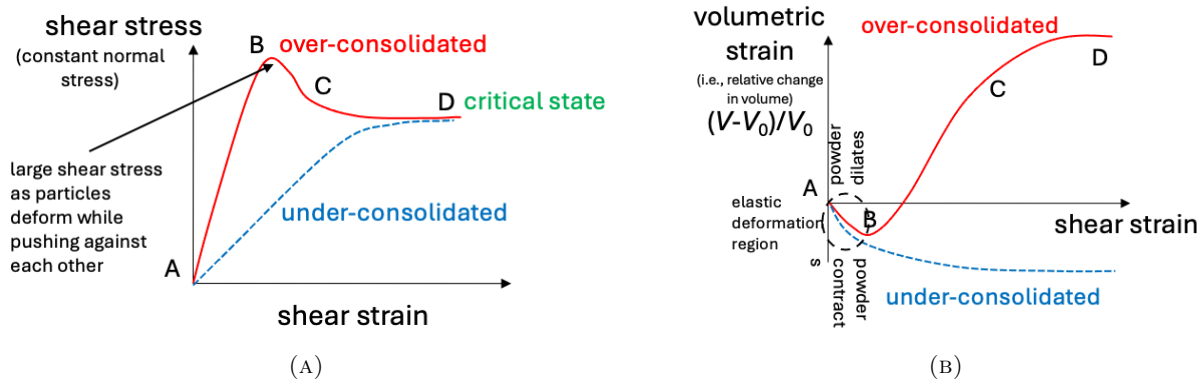
FIGURE 8.10. The shear stress required to deform a powder bed and the corresponding volumetric strain of the powder bed as functions of shear strain for powder beds under- and over-consolidated at the given normal stress.

Principle of Dilatancy. Powder for which the solid fraction doesn't change when sheared at a given normal stress is said to be in its critical state.

Notes:

(1) Videos demonstrating the Reynolds' Principle of Dilatancy are available at `https://www.youtube.com/watch?v=kzw80pyUI8g` and `https://www.youtube.com/watch?v=B_qRh5Y-hO8`.
(2) The critical state for a powder is independent of the powder's initial packing configuration. It only depends on the applied consolidation stress.
(3) A plot of the shear stress required to shear a powder at a given normal stress as a function of shear strain is shown in Figure 8.10a. Curves are shown for under- and over-consolidated initial states. Figure 8.10b shows the powder's volumetric strain (i.e., the relative change in volume) as a function of shear strain for the same powder. For an under-conolidated powder, increasing shear stress causes the bed to deform and consolidate until reaching the critical state. For an over-consolidated powder, the shear shear stress is initially large as the tightly packed particles compress against each other and consolidate. Eventually a critical shear stress is reached and the particles move over each other and dilate. The shear stress then decreases and the bed dilates until reaching its critical state for the given normal stress.
(4) When the material is under-consolidated, it will tend to densify uniformly over the entire bulk of the bed. However, when the material is over-consolidated, only a narrow region of the material, approximately 8-10 particle diameters thick, will dilate and yield. This region is known as a shear band or slip plane (Figure 8.11). Hence, with over-consolidation, dilation and failure tends to be localized, with regions of un-dilated material on either side.
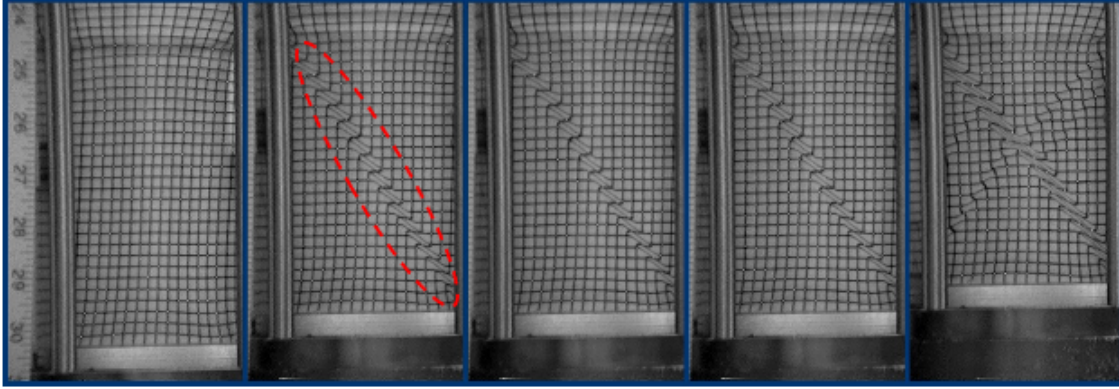
FIGURE 8.11. Formation of a shear band, highlighted by the red dashed line, in a uniaxially compressed bed of sand. This figure is from http://web.utk.edu/~alshibli/research/MGM/F75-Ottawa.php.

Another important observation is that when a sufficiently large pressure is applied to a particulate material, the particles will re-arrange, elastically and plastically deform, and fracture (usually at higher loads). When the pressure is removed, the elastic deformation of the particles is recovered, but the bulk deformation due to the other effects remains. Usually the elastic deformation is much smaller than the non-recoverable deformations and, thus, is often neglected. Hence, we assume that volume changes due to an applied pressure is irreversible. A common empirical model for powder consolidation is shown in Figure 8.12. In this model, known as Walker's equation, the specific volume (v) of a particulate material decreases logarithmically with increasing pressure (p),

$$v = v_0 - \lambda \ln\left(\frac{p}{p_0}\right), \tag{8.2}$$

where v_0 is the material's specific volume at a reference pressure p_0 and λ is a fitting parameter. Note that the specific volume is related to the material's bulk density (ρ_b), bed porosity (ϵ), and true density (ρ_true) via,

$$v = \frac{1}{\rho_b} = \frac{1}{(1-\epsilon)\rho_\text{true}}. \tag{8.3}$$

As the applied pressure approaches zero, the material's specific volume approaches its value at incipient fluidization (v_{mf}), i.e., when the particles are barely touching each other. Now consider a material that has been consolidated to specific volume v_1 using a pressure p_1 (refer to Figure 8.12). As the pressure gradually increases to p_2, the specific volume decreases logarithmically from v_1 to v_2. When the pressure is removed (State 3), the specific volume remains at v_2 since the consolidation is irreversible. If a new pressure is applied, but is smaller than the pressure used to consolidate the material to its current state, e.g., $p_4 < p_2$, then the bed specific volume will remain unchanged since the new pressure won't be enough to further consolidate the material. The specific volume will remain unchanged if the pressure is removed again (State 5). If a new pressure is gradually applied, e.g., up to p_6, the material's specific volume will remain constant until reaching p_2. Pressures larger than p_2 will result in the specific volume decreasing logarithmically to State 6.

Notes:

(1) Bulk density (or solid fraction) is often measured in a uniaxial compression test, also known as an oedometer test (Figure 8.13). The height of material in the testing cell (H) should be much smaller than the cell diameter (D) and the walls should be lubricated so wall shear stresses are negligible. If the wall shear stresses are zero, then the vertical normal stress will be uniform and the major principal stress.
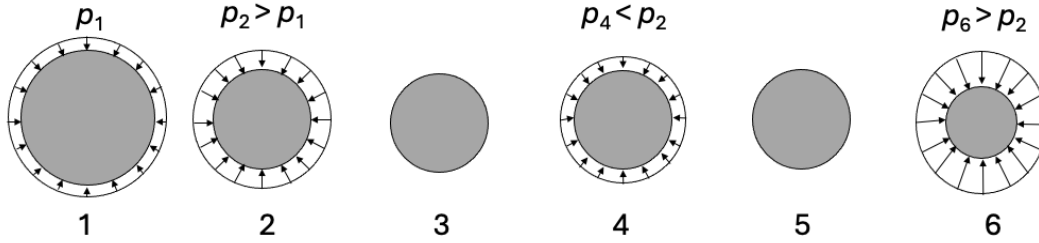
(A) Sketch of a particulate materials volumetric response to different applied pressures.
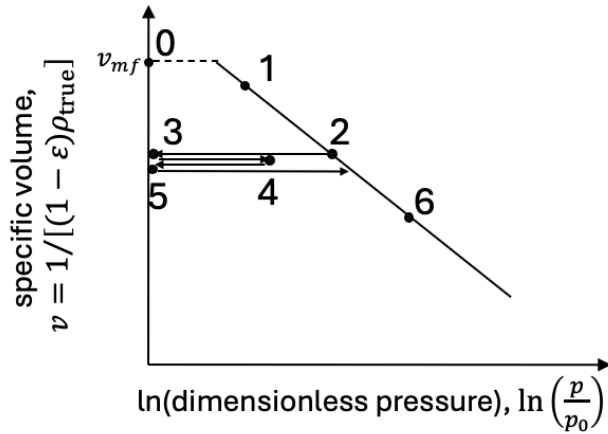
(B) A plot of the particulate material's specific volume as a function of the applied pressure.

FIGURE 8.12. The Walker model for how a particulate material's specific volume changes in response to an applied pressure.
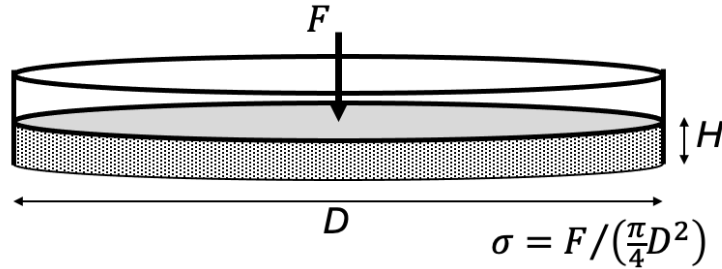
FIGURE 8.13. A sketch of an oedometer test for measuring a powder's bulk density as a function of the consolidation stress.

(2) There have been many empirical fits proposed for how bulk density (ρ_b) varies with the applied consolidation stress (σ) [8]. Common fits include:

$$\frac{1}{\rho_b} = \frac{1}{\rho_{b,0}} - \lambda \ln\left(\frac{\sigma}{\sigma_0}\right) \qquad \text{(Walker equation [9])} \qquad (8.4)$$

$$\frac{\rho_b}{\rho_{b,0}} = \frac{1}{2^\beta}\left(1 + \frac{\sigma}{\sigma_0}\right)^\beta \qquad \text{(Johanson and Cox [10])} \qquad (8.5)$$
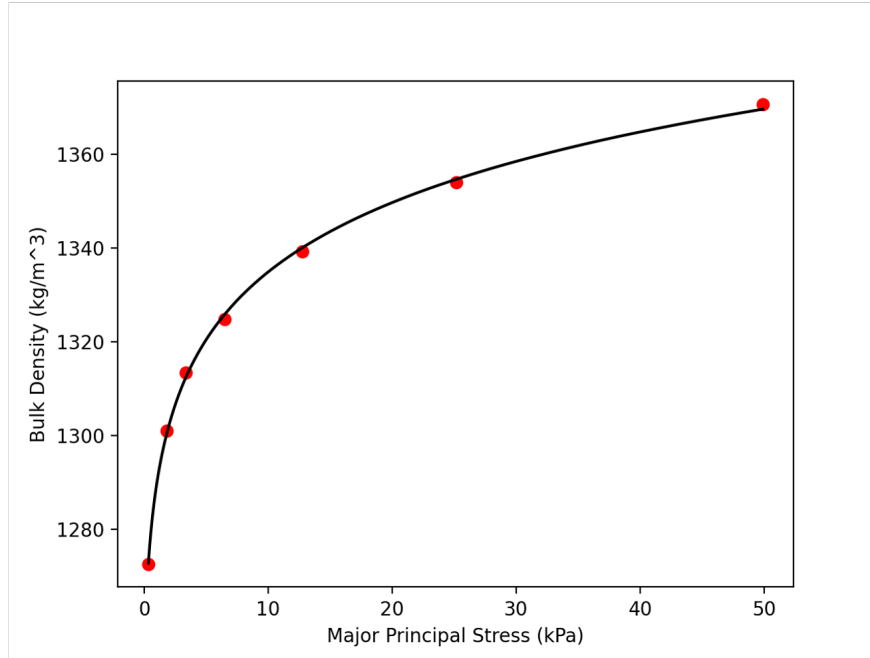
FIGURE 8.14. The bulk density of sand as a function of the applied major principal stress. The data are from Gu et al. [8]. The curve fit is Eq. 8.5.
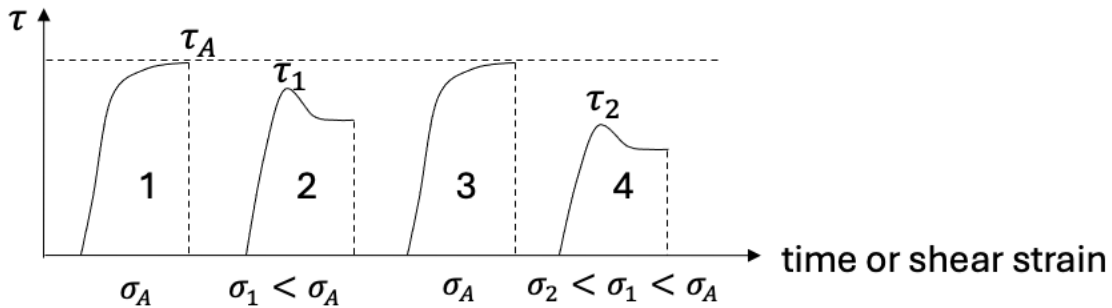
FIGURE 8.15. The measured shear stress in a typical shear cell testing procedure as a function of shear strain or time. In the figure, τ is the shear stress and σ is the normal stress. Steps 1 through 4 are described in the text.

$$\frac{\rho_b}{\rho_{b,0}} = \frac{1}{2}\left[1 + \left(\frac{\sigma}{\sigma_0}\right)^\beta\right] \qquad \text{(Gu et al. [8])} \qquad (8.6)$$

$$\frac{\rho_b}{\rho_{b,0}} = \left(\frac{\sigma}{\sigma_0}\right)^\beta \qquad \text{(Jenike [2], for } \frac{\sigma}{\sigma_0} \gg 1). \qquad (8.7)$$

In the previous equations, λ and β are fitting parameters and $\rho_{b,0}$ is the bulk density at consolidation stress σ_0. An example fit to experimental data is shown in Figure 8.14.

8.4. Shear Cell Testing Procedures

In this section, a typical shear cell testing procedure is described and typical measurements are presented. The steps in the procedure are as follows (Figure 8.15):
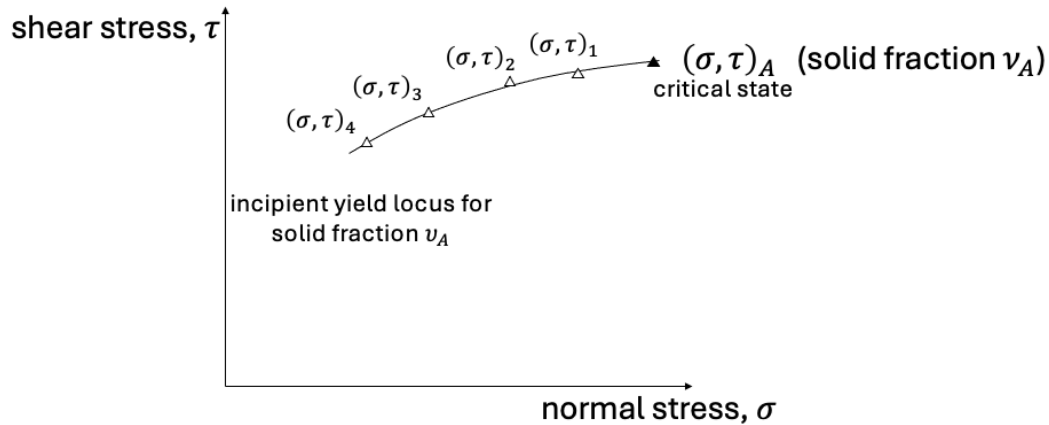
FIGURE 8.16. An incipient yield locus for solid fraction ν_A.

(1) Apply a normal stress σ_A to the powder and shear the bed until reaching the critical state for this normal stress. The corresponding critical state shear stress is τ_A. The powder solid fraction is now ν_A. The powder should start in an under-consolidated state so the entire powder bed is at the same solid fraction ν_A (refer to the previous discussion regarding shear band formation). This step is called the pre-shear step and $(\sigma, \tau)_A$ is also called $(\sigma, \tau)_{\text{pre}}$. A key feature of the pre-shear step is that it puts the bed in a consistent state with a nearly uniform solid fraction. Thus, testing always starts in a well-defined, uniform state.

(2) Remove the normal stress σ_A and apply a smaller normal stress σ_1. Since $\sigma_1 < \sigma_A$, the bed solid fraction at the start of the test is still ν_A. The powder will now be in an over-consolidated state for normal stress σ_1. Shear the bed and record the maximum shear stress during the test, τ_1. This is the shear stress at incipient yield, i.e., when the bed first starts to plastically yield in shear, for the normal stress σ_1 when the bed has solid fraction ν_A.

(3) Re-prepare the bed at the same initial solid fraction ν_A following Step 1. Note that the bed is in an under-consolidated state at the start of pre-shear since $\sigma_1 < \sigma_A$. The material densifies when sheared during this step.

(4) Follow Step 2, but use an even smaller normal stress $\sigma_2 < \sigma_1$. Again, the bed will start in an over-consolidated state at this normal stress. The maximum shear stress at incipient yield is τ_2 for the normal stress σ_2 when the bed has solid fraction ν_A.

(5) Repeat the procedures several times and plot the incipient yield shear stress values as a function of the applied normal stresses (Figure 8.16). The resulting curve is known as an incipient yield locus. Note that this curve is generated at the solid fraction ν_A, which corresponds to the critical-state for $(\sigma, \tau)_A$. The incipient yield locus is the locus of shear stresses that results in incipient yield of the powder given an applied normal stress for a powder with a solid fraction ν_A. The stress state $(\sigma, \tau)_A$ is called the end-point stress state or the termination stress state for this yield locus since a normal stress larger than σ_A would result in a solid fraction larger than ν_A.

(6) Repeat Steps 1 - 5, but with different end-point (or critical-state) normal stresses. The resulting plot will now show incipient yield loci for different solid fractions (Figure 8.17).

Notes:

(1) In traditional shear cells, it's challenging to test at small normal stresses. The hydrostatic stress due to gravity can affect the measurement. Extrapolating properties to smaller normal stresses has significant uncertainty. One novel shear cell that may provide data at small normal stresses
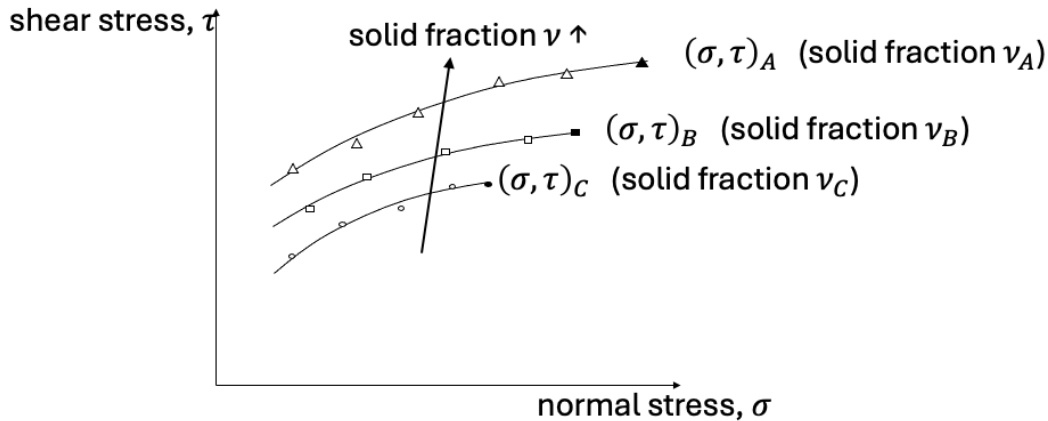
FIGURE 8.17. Incipient yield loci for several different solid fractions.

application	material bulk density (kg/m^3)				—
	0 – 150	150 – 300	300 – 600	600 – 1200	1200 – 2500
container up to 20 L, dosage of small amounts	0.4 kPa	0.8 kPa	1.6 kPa	2.5 kPa	4 kPa
container up to 100 L, barrels	0.8 kPa	1.5 kPa	2.5 kPa	5 kPa	10 kPa
Intermediate Bulk Containers (IBCs), sacks packed on pallets, small silos	1.5 kPa	2.5 kPa	5 kPa	10 kPa	20 kPa
medium size and large silos	3 kPa	7 kPa	12 kPa	25 kPa	50 kPa

TABLE 8.2. Estimates of the consolidation stresses for different material bulk densities and vessel sizes. The data in this table comes from Schulze [12].

is the Sevilla Powder Tester [11], which uses fluidizing air to counteract the influence of gravity-induced hydrostatic stresses. Additional research needs to examine this type of tester to verify its applicability at small normal stresses.

(2) Typically only three to five points are required to produce an incipient yield locus. The loads used in the shear cell should reflect the loads anticipated in practice. In general, the consolidating stresses are typically due to the weight of the material (refer to Chapter 5). Table 8.2 provides estimates of the consolidation stresses for different material bulk densities and vessel sizes.

(3) In Jenike's analysis [2], he includes the end point state as part of the incipient yield locus (Figure 8.18a). Experimentally, there is some evidence that if the material is pre-sheared at the end point state $(\sigma, \tau)_A$, stopped, then sheared again at normal stress σ_A as if performing an incipient yield test, the corresponding incipient yield shear stress is slightly larger than ν_A. The exact cause for this behavior isn't widely agreed upon. Regardless of the cause, it has been suggested that the end point state should not be part of the incipient yield locus since the solid fraction at the critical state while the material is moving is slightly smaller than the solid fraction once motion ceases (Figure 8.18b).

(4) The locus of end point stress states is called the termination locus (Figure 8.19). The termination locus is often observed to lie on a straight line that passes through the origin. The angle between the termination locus and the horizontal axis is the angle of kinematic friction, ϕ_{sf}. Recall that
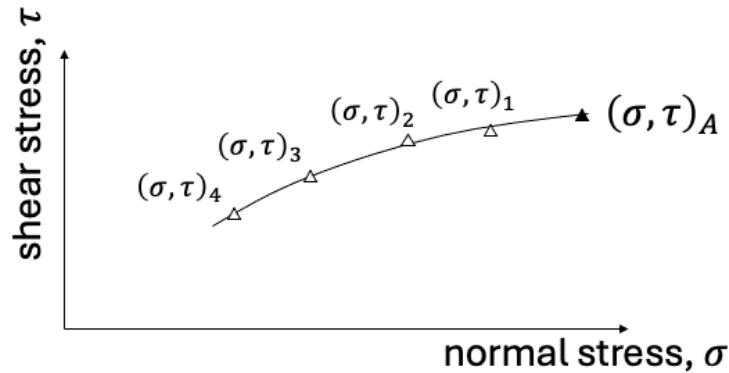
(A) The end point stress state as part of the incipient yield locus.
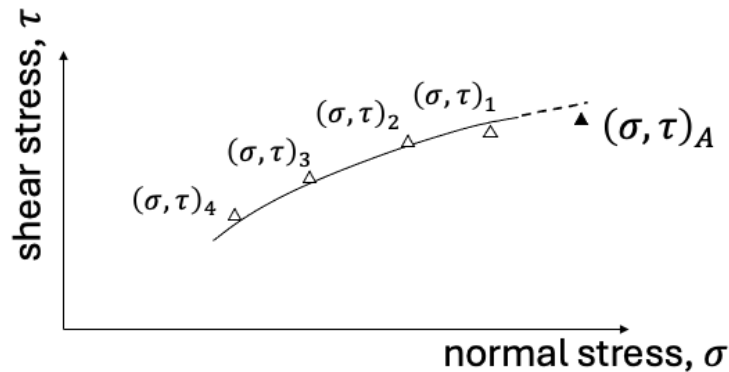
(B) The end point stress state is not part of the incipient yield locus.

FIGURE 8.18. Incipient yield loci including and not including the end point stress state.

the end point stresses are at the critical states for different solid fractions. Since the termination locus passes through the origin, we observe that materials behave effectively like they're cohesionless when flowing even if they are cohesive when yielding incipiently.

(5) The internal friction angle (ϕ), cohesion (c), and tensile strength (T) may be found by fitting a line to an incipient yield locus (Figure 8.20; refer to Chapter 4). These fitting values would be specifically for the solid fraction corresponding to the incipient yield locus and incipient yield loci at other solid fractions may have different values. Note that many incipient yield loci have significant curvature at small normal stresses and, thus, extrapolation of the line to the vertical axis can have significant error. Sometimes only a few experimental data points nearest to the origin are used in the line fitting to account for the curvature and obtain more accurate values for the cohesion and tensile strength. Rather than using a straight line fit, the Warren-Spring equation (Eq. (4.4)) can account for the curvature near the origin and has been observed to fit experimental data well.

(6) The incipient yield loci are similar to, but not identical to the internal yield loci in the Ideal Coulomb material model (Chapter 4). First, the incipient yield loci are a function of the material's solid fraction whereas the internal yield loci (in the model) are not a function of the solid fraction. Second, an incipient yield locus does not extend beyond the end-point stress state whereas an internal yield locus does. Lastly, the incipient yield loci are the the stress conditions for incipient yielding of the material. Once the material starts to flow due to shear, the solid fraction decreases (the Reynolds Principal of Dilatancy) and the material reaches the critical state for the new solid fraction. The Ideal Coulomb material model does not have this same feature.
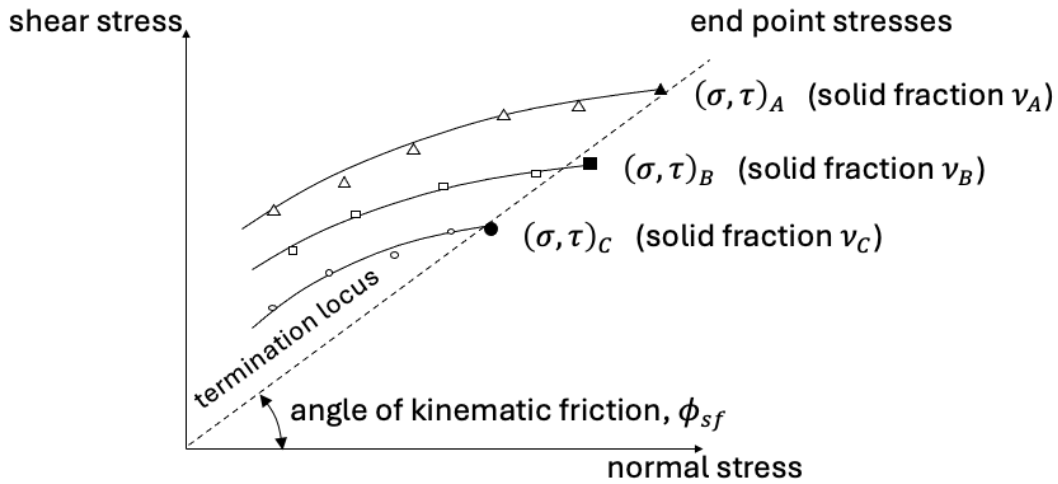
FIGURE 8.19. The termination locus, which passes through the end point stresses. The angle of kinematic friction is also shown in the figure.
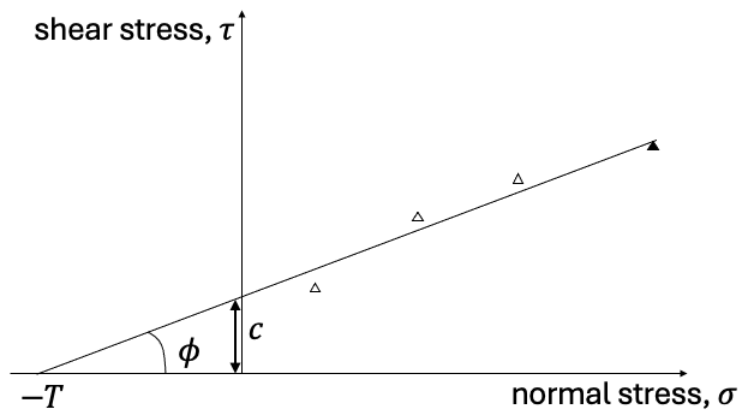
FIGURE 8.20. A line fitted to an incipient yield locus. The angle ϕ is the internal friction angle, c is the cohesion, and T is the tensile strength.

The consolidation stress (σ_1) and unconfined yield strength (f_c) for a given solid fraction can be found from the incipient yield loci using Mohr's circles as shown in Figure 8.21. The consolidation stress is the major principal stress that sets the solid fraction of the material. Thus, the Mohr's circle corresponding to the consolidation stress should pass through the end point state and be tangent to the incipient yield locus (since a Mohr's circle extending past the yield locus would have a different solid fraction). If one does not include the end point stress state in the incipient yield locus (Figure 8.18b), then the convention is to draw a Mohr's circle tangent to the incipient yield locus at a normal stress smaller than the end point normal stress, but includes the end point stress state in the Mohr's circle (even though it technically corresponds to a slightly smaller solid fraction). The unconfined yield strength is found from a Mohr's circle that is tangent to the incipient yield locus, because the material is yielding, and passes through the origin, since the origin corresponds to an unconfined surface. As described in Chapter 4, the effective angle of internal friction (δ) may be found from the consolidation stress Mohr's circle.

Notes:
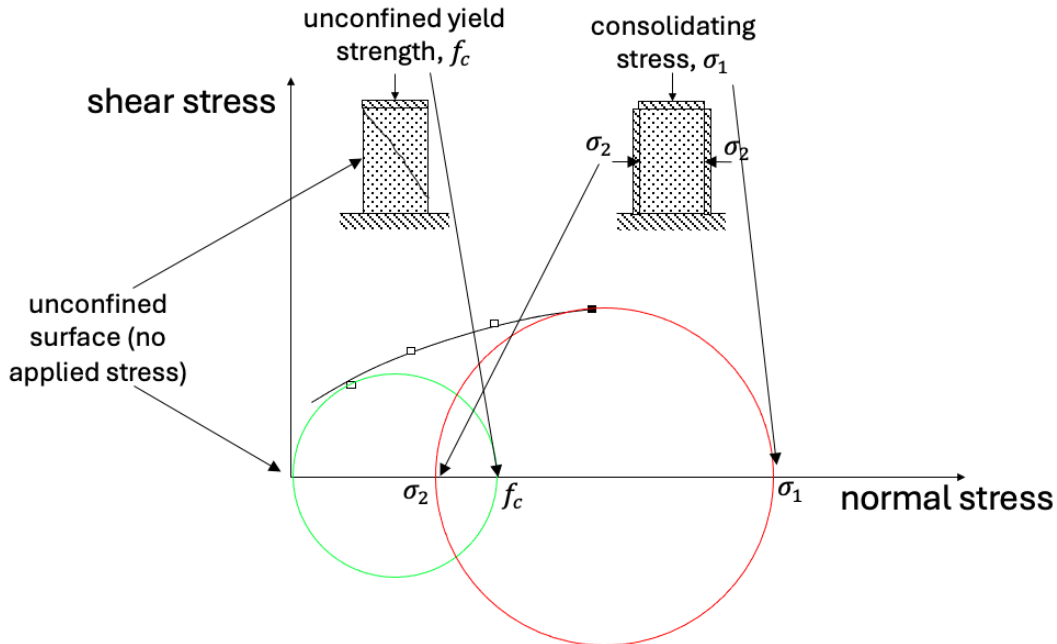
FIGURE 8.21. A diagram showing how the consolidation stress (σ_1) and unconfined yield strength (f_c) are found from an incipient yield locus using Mohr's circles.

(1) The major principal stress (σ_1) is not aligned with the shear cell applied normal stress (σ) as shown in Figure 8.22a. If the failure plane in the shear cell is assumed to be horizontal as shown in the figure due to the geometry of the shear cell (the actual failure surface may not be so well defined according to [1]), then the applied normal stress is normal to the plane and the shear stress at failure is tangential to the plane. Using the Mohr's circle shown in Figure 8.22b, the corresponding consolidation stress will be rotated clockwise from the failure plane by an angle θ in the real-world.

8.5. Wall Friction Shear Cell Testing

A shear cell may also be used to determine the friction angle between the powder and a wall surface. For this type of measurement, the lower portion of the shear cell is removed and the powder comes into direct contact with a "coupon" of the wall material (Figure 8.23). The wall material coupons should reflect actual wall conditions, e.g., the same material, the same surface finish, and the same finish orientation. In practice, wall properties may change over time due to wear and environmental conditions. These changes should be considered during testing.

Wall friction tests are often performed at a constant speed, resulting in measurements of the kinematic wall friction angle. These values are useful for mass flow hoppers where material slides at the walls. In a kinematic wall friction test, the largest expected normal stress is applied on the shear cell lid and the shear stress required to move the powder against the wall coupon at steady state is measured (Figure 8.24). The normal stress is then decreased and the test is performed again. Following this procedure, the wall friction angle can be measured.

For time consolidation testing, static wall friction angle measurements are usually made since the material presumably has been at rest against the wall for some period of time. Here, a preparatory-shear normal stress is applied to the material and the sample is sheared to critical state to obtain a uniform solid fraction bed (Figure 8.25). Next, a normal stress smaller than the preparatory-shear test is applied to the material, called
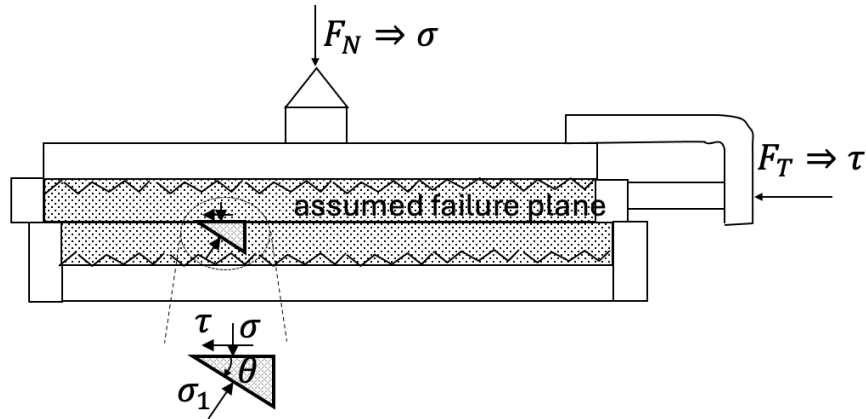
(A) Geometry of the assumed yield surface in the shear cell and corresponding stresses.
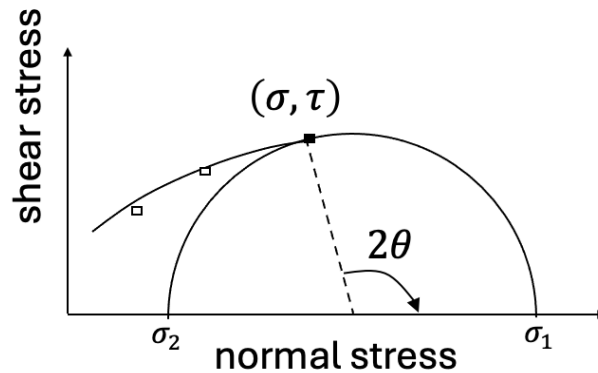
(B) Mohr's circle showing the angle between the failure surface at critical state and the major principal stress.

FIGURE 8.22. Shear cell yield surface geometry, stresses, and Mohr's circle.
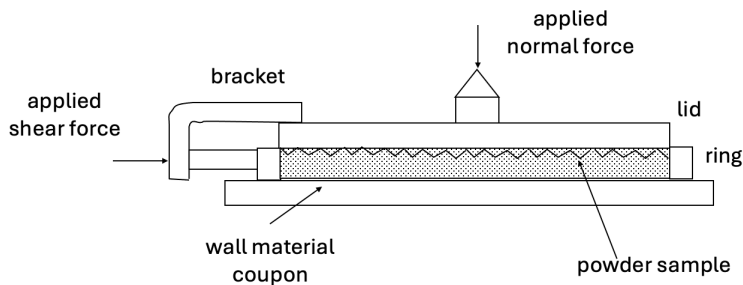
FIGURE 8.23. A schematic showing a shear cell designed to measure a wall friction angle.

the pre-shear wall normal stress, and the material is sheared to the critical state. The $(\sigma_w, \tau_w)_{\mathrm{pre}}$ stress state corresponds to material flowing at these stress conditions. The shear stress is removed and the material then sits under the $\sigma_{w,\mathrm{pre}}$ wall normal stress for a prescribed period of time to allow for time consolidation of the sample. At the end of this time, the maximum wall stress required to initiate yielding is recorded. This is the stress required to re-start movement of material at a hopper wall.

Notes:
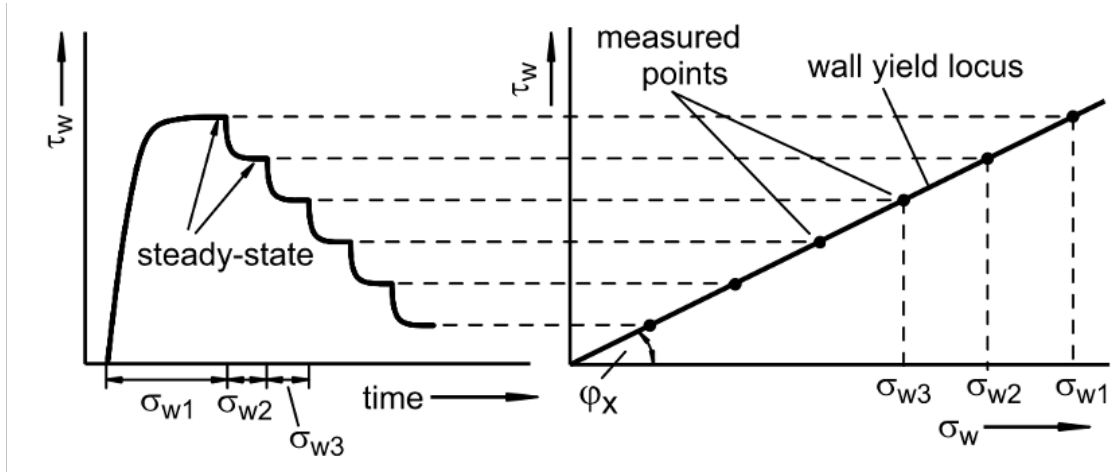
Figure 8.24. (left) The shear stress required to move the powder against a wall coupon as a function of time as different normal stresses (σ_w) are applied. (right) The steady state wall shear stress plotted against normal stress. The wall kinematic friction angle is ϕ_x in this figure. Note that these figures are from Schulze [12].
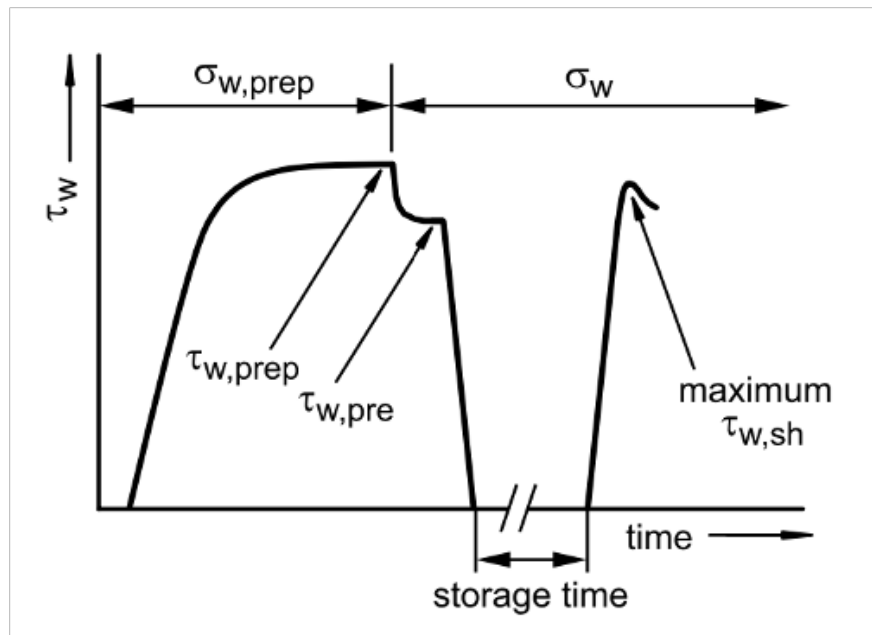
Figure 8.25. A plot showing the procedure for a wall time consolidation shear cell test. Note that this figure is from Schulze [12].

(1) Rao et al. [13] report that, at least for sand, the incipient yield internal friction angle (ϕ_{inc}) and incipient yield wall friction angle ($\phi_{w,\mathrm{inc}}$) increase with an increase in the particle density. Furthermore, for rounded sang grains, the critical state wall friction angle can be related to the internal friction angle via,

$$\frac{\phi_{w,\mathrm{inc}}}{\phi_{\mathrm{inc}}} = 1.0 - 0.80 \exp\left[-15\left(\frac{R_a}{D_{av}}\right)^{0.54}\right], \tag{8.8}$$

where the quantity in the rounded parentheses is the relative roughness of the wall surface with R_a being the average roughness of the wall surface and D_{av} the weighted average particle size.

8.6. Summary

Shear cell testing is a key part of designing vessels for storing and transporting powders. A summary of the important points from this chapter are listed below.

(1) Shear cell testing is commonly used to measure properties needed for bin and hopper design. Mohr's circles are used in the analysis of shear cell results to obtain the consolidation stress and unconfined yield strength.
(2) The significant properties obtained from shear cell testing include bulk density (or solid fraction), internal friction angle, cohesion, effective internal friction angle, wall friction angle, and the material flow function. It is difficult to obtain properties at small consolidation stresses.
(3) It is important to understand the concepts of under- and over-consolidation and the critical state and the powder behavior in these states.
(4) Materials should be tested over the range of anticipated conditions, e.g., time consolidation, loads, temperature, humidity, different manufacturing conditions, etc. Reliable predictions cannot be made with inaccurate material properties.

Fit the following shear cell incipient yield locus data using,

a.   an ideal Coulomb material model,
$$\tau = (\tan\phi)\sigma_N + c,$$
where ϕ and c are fitting constants. Report your values for ϕ and c.

b.   and the Warren-Spring equation,
$$\left(\frac{\tau}{c}\right)^n = \frac{\sigma_N}{T} + 1,$$
where C, T, and n are fitting constants. Report your values for C, T, and n.

c.   Plot the data and the two curve fits.

σ_N [kPa]	τ [kPa]
0.4	1.0
0.7	1.1
1.3	1.4
3.4	2.1
4.7	2.6
6.3	3.0
8.7	3.6

SOLUTION:
Use the Python code at the end of this document to fit the data and create the plot.
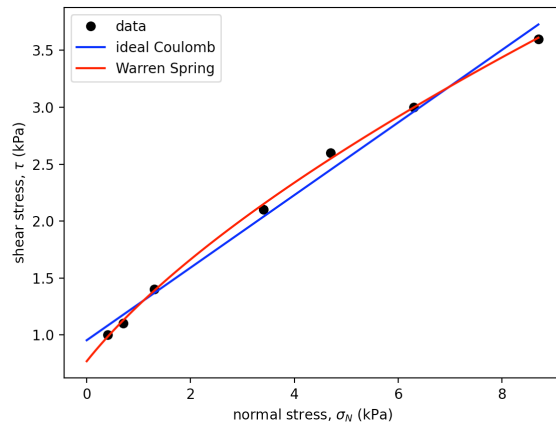
Ideal Coulomb material fit values: (ϕ, c) = (17.694°, 0.952 kPa).
Warren-Spring fit values: (C, T, n) = (0.768 kPa, 0.860 kPa, 1.555).

```
# shearcell_03.py

import matplotlib.pyplot as plt
import numpy as np
from scipy.optimize import curve_fit

def IdealCoulomb(sigma_N, phi, c):
    return(np.tan(phi)*sigma_N + c)

def WarrenSpring(sigma_N, C, T, n):
    return(C*((sigma_N/T + 1)**(1/n)))

# IYL data values in kPa.
data = np.array([[0.4, 1.0],
                 [0.7, 1.1],
                 [1.3, 1.4],
                 [3.4, 2.1],
                 [4.7, 2.6],
                 [6.3, 3.0],
```

```
                    [8.7, 3.6]])

# Fit the data with the ideal Coulomb material IYL.
popt, pcov = curve_fit(IdealCoulomb, data[:,0], data[:,1])
phi, c = popt
print('(phi, c) = (%.3f deg, %.3f kPa)' % (np.degrees(phi), c))

# Fit the data with the Warren-Spring IYL.
popt, pcov = curve_fit(WarrenSpring, data[:,0], data[:,1])
C, T, n = popt
print('(C, T, n) = (%.3f kPa, %.3f kPa, %.3f)' % (C, T, n))

# Plot the data points.
plt.plot(data[:,0], data[:,1], color='k', marker='o', linestyle='', label='data')

# Plot the corresponding ideal Coulomb material IYL fit.
sigma_N = np.linspace(0, np.amax(data[:,0]), 100)
plt.plot(sigma_N, IdealCoulomb(sigma_N, phi, c), color='b', marker='', linestyle='-', label='ideal
Coulomb')

# Plot the corresponding Warren-Spring IYL fit.
plt.plot(sigma_N, WarrenSpring(sigma_N, C, T, n), color='r', marker='', linestyle='-', label='Warren
Spring')

plt.xlabel('normal stress, $\\sigma_N$ (kPa)')
plt.ylabel('shear stress, $\\tau$ (kPa)')
plt.legend()
plt.show()
```

Incipient yield loci (IYL) for an ideal Coulomb material are given by,

$$\tau = \mu\sigma + c.$$

where μ = tanϕ is the internal friction coefficient, ϕ is the internal friction angle, and c is the cohesion. Assume the values for ϕ and c, are known values (found from shear cell testing, for example). In addition, assume the end-point stress state $(\sigma, \tau)_{EP}$ is known and <u>is</u> part of the IYL.
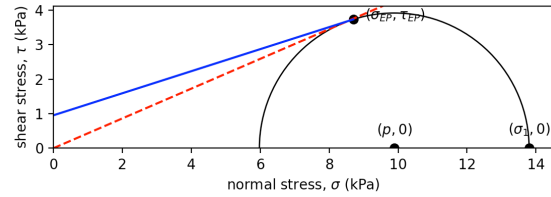
a.   Derive an expression (or set of expressions) to find the consolidation stress, σ_1, in terms of ϕ, c, and $(\sigma, \tau)_{EP}$.
b.   Using your expressions from (a) calculate σ_1 when (ϕ, c) = (17.694°, 0.952 kPa) and σ_{EP} = 8.7 kPa.
c.   Calculate the effective angle of internal friction for this Mohr's circle.

Note that the expressions in (a) need not be explicit for σ_1 and numerical methods can be used in (b) and (c).

SOLUTION:
The IYL is given by,

$$\tau = \mu\sigma + c. \tag{1}$$

Find the slope of this curve,

$$\frac{d\tau}{d\sigma} = \mu. \tag{2}$$

Write the equation of a Mohr's circle,

$$(\sigma - p)^2 + \tau^2 = R^2. \tag{3}$$

The slope at any point on the Mohr's circle is,

$$2(\sigma - p) + 2\tau\frac{d\tau}{d\sigma} = 0 \implies \frac{d\tau}{d\sigma} = -\left(\frac{\sigma - p}{\tau}\right) = \frac{p - \sigma}{\tau}. \tag{4}$$

Substitute Eq. (1) into Eq. (3) since the internal yield locus (IYL) at the end-point state will be a point on the Mohr's circle,

$$\boxed{R = \sqrt{(\sigma_{EP} - p)^2 + (\mu\sigma_{EP} + c)^2}}. \tag{5}$$

Also set the slopes the same since the IYL is tangent to the Mohr's circle,

$$\frac{p - \sigma_{EP}}{\tau} = \mu. \tag{6}$$

Substitute Eq. (1) in for the shear stress,

$$\frac{p - \sigma_{EP}}{\mu\sigma_{EP} + c} = \mu \implies \boxed{p = \sigma_{EP} + \mu(\mu\sigma_{EP} + c)}. \tag{7}$$

Once the pressure is found, then the radius of the Mohr's circle may be found using Eq. (6). The effective angle of internal friction is given by,

$$\boxed{\sin\delta = \frac{R}{p}}. \tag{8}$$

The following Python code is used to solve the previous expressions for the given values of (ϕ, c, σ_{EP}) to obtain $\boxed{\sigma_1 = 13.8 \text{ kPa}}$. The effective angle of internal friction is $\boxed{\delta = 23.3°}$. Other quantities of interest are (p, R) = (9.89, 3.91) kPa.
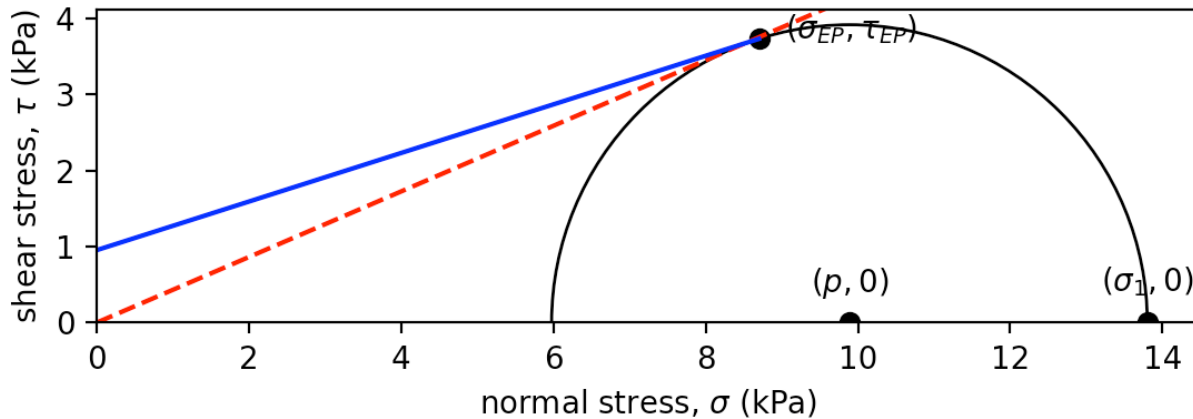
Following is the Python code used for the calculations.

```
# shearcell_02.py

import numpy as np
import matplotlib.pyplot as plt
from scipy.optimize import fsolve

def IYL(sigma, mu, c):  # incipient yield locus
    return(mu*sigma + c)

phi = np.radians(17.694)  # given internal friction angle [rad]
mu = np.tan(phi)  # internal friction coefficient [-]
c = 0.952  # given cohesion [kPa]
sigma_EP = 8.7  # given end-point normal stress [kPa]
tau_EP = IYL(sigma_EP, mu, c)

# Set up the plot.
fig, axes = plt.subplots()

# Solve for the hydrostatic pressure, the radius, and plot the pressure point.
p = sigma_EP + mu*(mu*sigma_EP + c)
R = np.sqrt((sigma_EP - p)**2 + (mu*sigma_EP + c)**2)
print('(p, R) = (%.3f, %.3f) kPa' % (p, R))
plt.plot(p, 0, 'ko')
plt.annotate('$(p, 0)$', (p, 0), textcoords='offset points', xytext=(0,10), ha='center')

MohrsCircle = plt.Circle((p, 0), R, fill=False)  # make the Mohr's circle
axes.set_aspect(1)  # set the aspect ratio to one
axes.add_artist(MohrsCircle)  # add the Mohr's circle to the plot

# Plot the end-point stress state.
plt.plot(sigma_EP, tau_EP, 'ko')
plt.annotate('$(\sigma_{EP}, \\tau_{EP})$', (sigma_EP, tau_EP), textcoords='offset points',
xytext=(30,0), ha='center')

# Plot the consolidation stress.
sigma_1 = p+R  # Find the consolidation stress.
print('sigma1 = %.3f kPa' % sigma_1)
plt.plot(sigma_1, 0, 'ko')
plt.annotate('$(\sigma_1, 0)$', (sigma_1, 0), textcoords='offset points', xytext=(0,10), ha='center')

# Calculate the effective angle of internal friction.
delta = np.arcsin(R/p)
print('delta = %.2f deg' % (np.degrees(delta)))
plt.plot([0, p], [0, p*np.tan(delta)], color='r', marker='', linestyle='--')

# Plot the IYL.
# Obtain a series of normal stresses for plotting a smooth line.
```

```
sigma = np.linspace(0, sigma_EP, 100)
plt.plot(sigma, IYL(sigma, mu, c), color='b', marker='', linestyle='-')

# Label the axes and set the scale limits.
plt.xlabel('normal stress, $\\sigma$ (kPa)')
plt.ylabel('shear stress, $\\tau$ (kPa)')
plt.xlim([0, 1.05*(p+R)])
plt.ylim([0, 1.05*R])
plt.show()
```

Running the Python code gives the following output (and the plot):
```
> python3 ./shearcell_02.py
(p, R) = (9.889, 3.913) kPa
sigma1 = 13.802 kPa
delta = 23.31 deg
```

Incipient yield loci (IYL) for an ideal Coulomb material are given by,

$$\tau = \mu\sigma + c.$$

where $\mu = \tan\phi$ is the internal friction coefficient, ϕ is the internal friction angle, and c is the cohesion. Assume the values for ϕ, c, and the end-point stress σ_{EP} are known values (found from shear cell testing, for example). In addition, assume the end-point stress state $(\sigma, \tau)_{EP}$ is known and is part of the IYL.
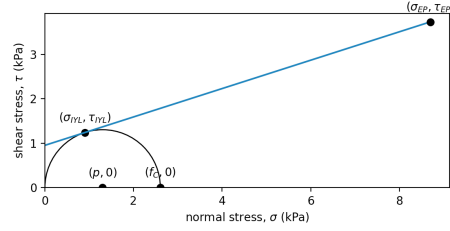
a. Derive an expression (or set of expressions) to find the unconfined yield strength, f_C, in terms of ϕ and c.
b. Using your expressions from (a) calculate f_C when $(\phi, c, \sigma_{EP}) = (17.694°, 0.952\text{ kPa}, 8.7\text{ kPa})$.

Note that the expressions in (a) need not be explicit for σ_1 and numerical methods can be used in (b).

SOLUTION:
The IYL is given by,

$$\tau = \mu\sigma + c. \tag{1}$$

Find the slope of this curve,

$$\frac{d\tau}{d\sigma} = \mu. \tag{2}$$

Write the equation of a Mohr's circle,

$$(\sigma - p)^2 + \tau^2 = R^2. \tag{3}$$

The slope at any point on the Mohr's circle is,

$$2(\sigma - p) + 2\tau \frac{d\tau}{d\sigma} = 0 \;\Rightarrow\; \frac{d\tau}{d\sigma} = -\left(\frac{\sigma - p}{\tau}\right) = \frac{p - \sigma}{\tau}. \tag{4}$$

Substitute Eq. (1) into Eq. (3) since the internal yield locus (IYL) will be a point on the Mohr's circle,

$$R = \sqrt{(\sigma_{IYL} - p)^2 + (\mu\sigma_{IYL} + c)^2}. \tag{5}$$

Also set the slopes the same since the IYL is tangent to the Mohr's circle,

$$\frac{p - \sigma_{IYL}}{\tau} = \mu. \tag{6}$$

Substitute Eq. (1) in for the shear stress,

$$\frac{p - \sigma_{IYL}}{\mu\sigma_{IYL} + c} = \mu \;\Rightarrow\; p = \sigma_{IYL} + \mu(\mu\sigma_{IYL} + c). \tag{7}$$

One of the points on the unconfined yield strength Mohr's circle must go through the origin. Thus, we know that for this Mohr's circle,

$$p = R \quad \text{(since } \sigma_2 = p - R = 0\text{)}. \tag{8}$$

With this in mind, we can re-write Eq. (5) as,

$$p = \sqrt{(\sigma_{IYL} - p)^2 + (\mu\sigma_{IYL} + c)^2}. \tag{9}$$

Substituting Eq. (7) into this expression gives,

$$\sigma_{IYL} + \mu(\mu\sigma_{IYL} + c) = \sqrt{[\mu(\mu\sigma_{IYL} + c)]^2 + (\mu\sigma_{IYL} + c)^2}, \tag{10}$$

$$[\sigma_{IYL} + \mu(\mu\sigma_{IYL} + c)]^2 = [\mu(\mu\sigma_{IYL} + c)]^2 + (\mu\sigma_{IYL} + c)^2, \tag{11}$$

$$\sigma_{IYL}^2 + 2\sigma_{IYL}\mu(\mu\sigma_{IYL} + c) + [\mu(\mu\sigma_{IYL} + c)]^2 = [\mu(\mu\sigma_{IYL} + c)]^2 + (\mu\sigma_{IYL} + c)^2, \tag{12}$$

$$\sigma_{IYL}^2 + 2\sigma_{IYL}\mu(\mu\sigma_{IYL} + c) - (\mu\sigma_{IYL} + c)^2 = 0, \tag{13}$$

$$\sigma_{IYL}^2 + 2\mu^2\sigma_{IYL}^2 + 2\mu c\sigma_{IYL} - \mu^2\sigma_{IYL}^2 - 2\mu c\sigma_{IYL} - c^2 = 0, \tag{14}$$

$$(1 + \mu^2)\sigma_{IYL}^2 - c^2 = 0, \tag{15}$$

$$\sigma_{IYL} = \frac{c}{\sqrt{1 + \mu^2}}. \tag{16}$$

Note that this is the normal stress that falls on the IYL as well as the Mohr's circle for the unconfined yield strength. To find the unconfined yield strength, substitute Eq. (16) into Eq. (7) and multiply by two (since $f_C = 2p$),

$$\boxed{f_C = 2p = 2[\sigma_{IYL} + \mu(\mu\sigma_{IYL} + c)]}. \tag{18}$$

The following Python code is used to solve the previous expressions for the given values of (ϕ, c, $\sigma_{N,EP}$) to obtain f_C = 2.61 kPa. Other quantities of interest are $p = R = 1.30$ kPa and $(\sigma, \tau)_{IYL} = (0.907, 1.24)$ kPa.
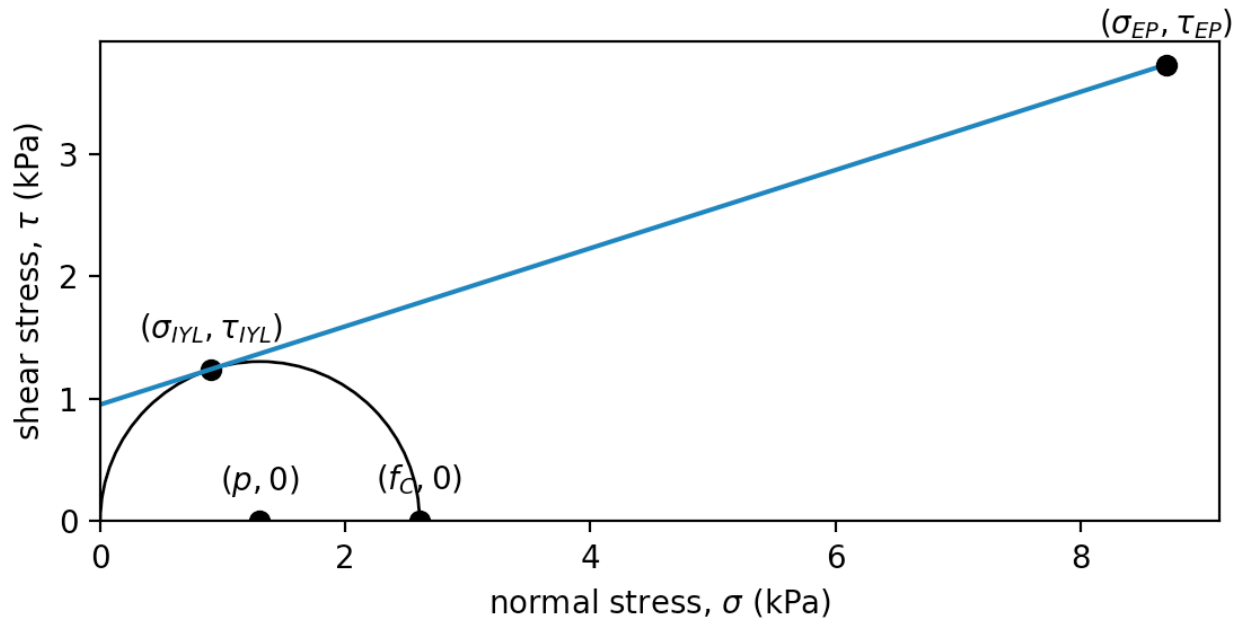
Following is the Python code used for the calculations.

```
# shearcell_02.5.py

import matplotlib.pyplot as plt
import numpy as np
from scipy.optimize import fsolve

def IdealCoulomb(sigma, phi, c):  # IYL
    return(np.tan(phi)*sigma + c)

# Set up the plot.
figure, axes = plt.subplots()

# Input parameters
c = 0.952  # kPa, cohesion
phi = np.radians(17.694)  # rad(deg), internal friction angle
mu = np.tan(phi)  # -, internal friction coefficient
sigma_EP = 8.7  # kPa
tau_EP = IdealCoulomb(sigma_EP, phi, c)
print('(phi, c, sigma_EP, tau_EP) = (%.3f deg, %.3f kPa, %.3f kPa, %.3f kPa)' % (np.degrees(phi), c,
sigma_EP, tau_EP))

# Find the normal stress on the IYL corresponding to the unconfined yield strength.
sigma_IYL = c/np.sqrt(1 + mu**2)
tau_IYL = IdealCoulomb(sigma_IYL, phi, c)
f_C = 2*(sigma_IYL + mu*(mu*sigma_IYL + c))
p = R = f_C/2
print('f_C = %.3f kPa' % f_C)
print('p = R = %.3f kPa' % p)
print('(sigma_IYL, tau_IYL) = (%.3f, %.3f) kPa' % (sigma_IYL, tau_IYL))

# Draw the Mohr's circle for the unconfined yield strength.
MohrsCircle = plt.Circle((0.5*f_C, 0), 0.5*f_C, fill=False)  # make the Mohr's circle
axes.set_aspect(1)  # set the aspect ratio to one
axes.add_artist(MohrsCircle)  # add the Mohr's circle to the plot

# Plot the unconfined yield strength point and label it.
plt.plot(f_C, 0, 'ko')
```

```
    plt.annotate('$(f_C, 0)$', (f_C, 0), textcoords='offset points', xytext=(0,10), ha='center')

    # Plot the pressure point and label it.
    plt.plot(p, 0, 'ko')
    plt.annotate('$(p, 0)$', (p, 0), textcoords='offset points', xytext=(0,10), ha='center')

    # Plot the common point on the IYL and Mohr's circle.
    plt.plot(sigma_IYL, tau_IYL, 'ko')
    plt.annotate('$(\\sigma_{IYL}, \\tau_{IYL})$', (sigma_IYL, tau_IYL), textcoords='offset points',
    xytext=(0,10), ha='center')

    # Plot the IYL.
    sigma = np.linspace(0, sigma_EP, 100)  #  a bunch of points for a smooth line
    plt.plot(sigma, IdealCoulomb(sigma, phi, c), marker='', linestyle='-')

    # Plot the endpoint stress point and label it.
    plt.plot(sigma_EP, tau_EP, 'ko')
    plt.annotate('$(\\sigma_{EP}, \\tau_{EP})$', (sigma_EP, tau_EP), textcoords='offset points',
    xytext=(0,10), ha='center')

    # Add plot labels and set the axis limits.
    plt.xlabel('normal stress, $\\sigma$ (kPa)')
    plt.ylabel('shear stress, $\\tau$ (kPa)')
    plt.xlim([0, 1.05*sigma_EP])
    plt.ylim([0, 1.05*tau_EP])
    plt.show()
```

Running the code provides the following output.

```
>  python3 ./shearcell_02.5.py
(phi, c, sigma_EP, tau_EP) = (17.694 deg, 0.952 kPa, 8.700 kPa, 3.728 kPa)
f_C = 2.606 kPa
p = R = 1.303 kPa
(sigma_IYL, tau_IYL) = (0.907, 1.241) kPa
```

A series of shear cell experiments were performed on powdered sugar with the results shown in the following figures. The applied normal stresses are located near the bottom of the figures.

Endpoint (aka pre-shear) stress of 1000 Pa:
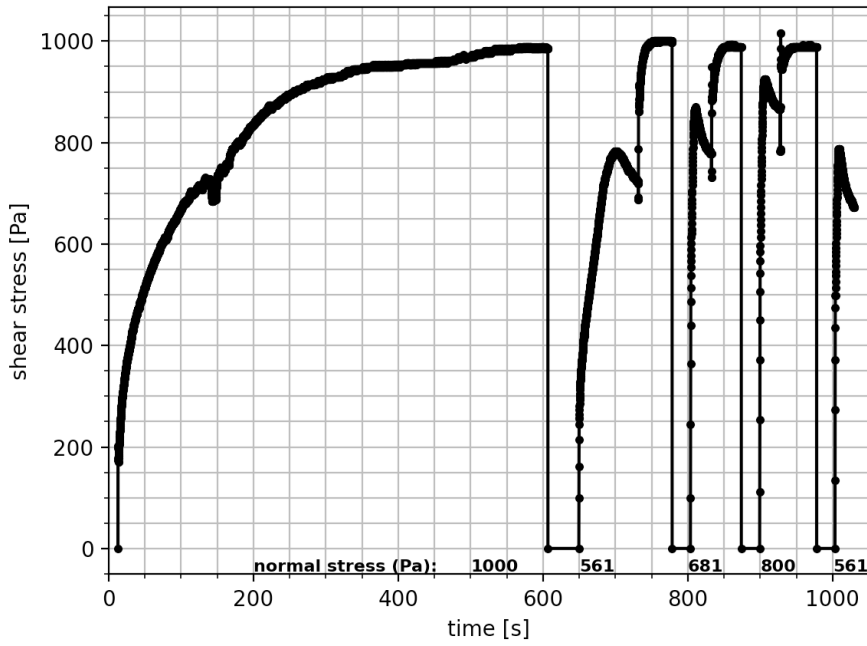
Endpoint (aka pre-shear) stress of 2000 Pa:
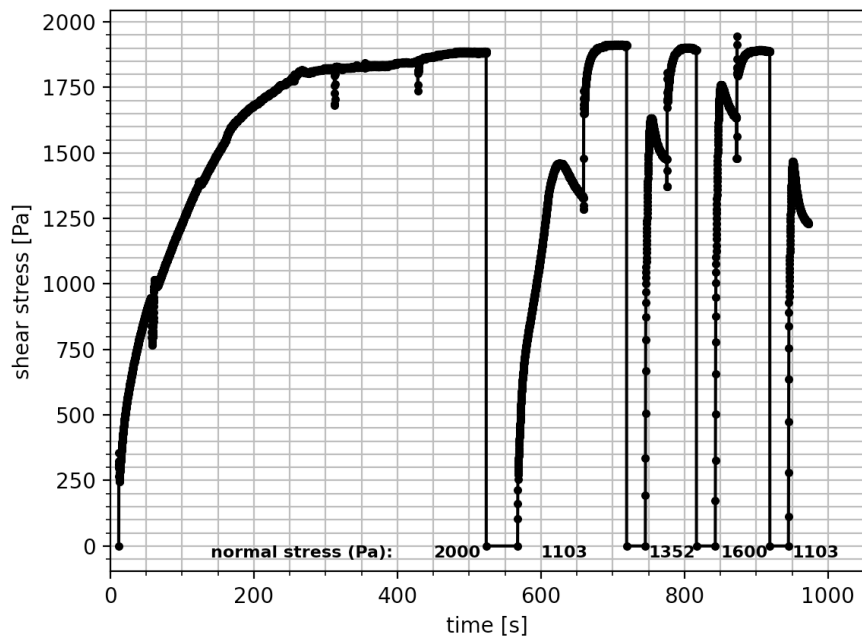
Endpoint (aka pre-shear) stress of 4000 Pa:
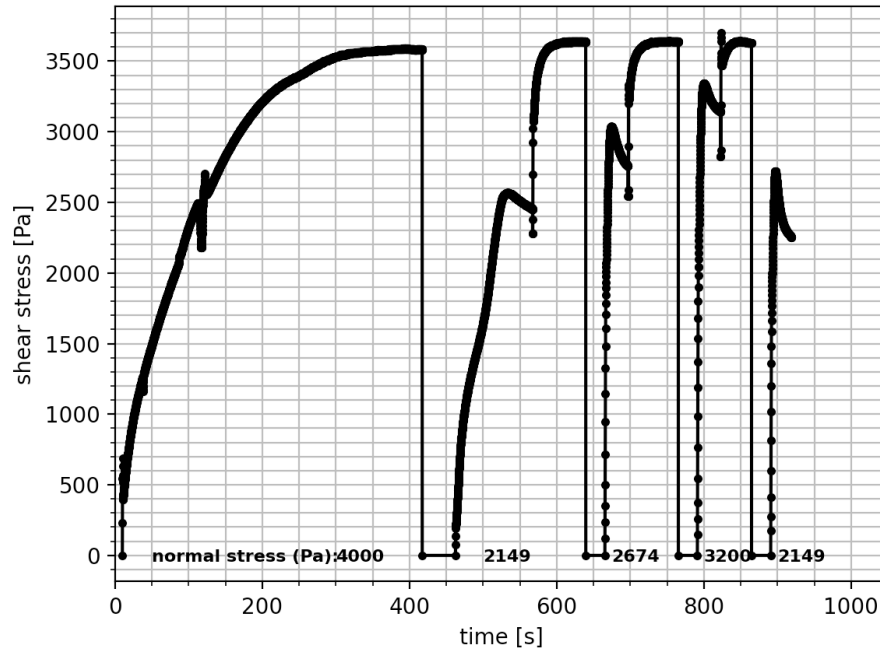
a. Plot the incipient yield loci data points and a linear fit to the data points (extend it to the vertical axis) for each end-point stress.
b. Determine the consolidation stress-unconfined yield strength for each incipient yield locus. Plot the material's flow function.
c. Plot the internal friction angle, effective angle of internal friction, and cohesion as functions of the consolidation stress.

Hints:
1. There'll be uncertainty in reading the plots. Don't worry if your values are slightly different than a colleague's values.
2. A numerical curve fit for fitting the incipient yield loci will be more accurate than plotting by hand. For example, consider using the `curve_fit` function in the Python `scipy.optimize` library.
3. Make use of the derivations given in lecture to obtain the consolidation stress and unconfined yield strength from the incipient yield loci.

SOLUTION:

First, determine the yielding shear stress for each applied normal stress for each end-point condition. These values are summarized in the following plots and table. Note that there will be some uncertainty when reading the plots.

Endpoint (aka pre-shear) stress of 1000 Pa:
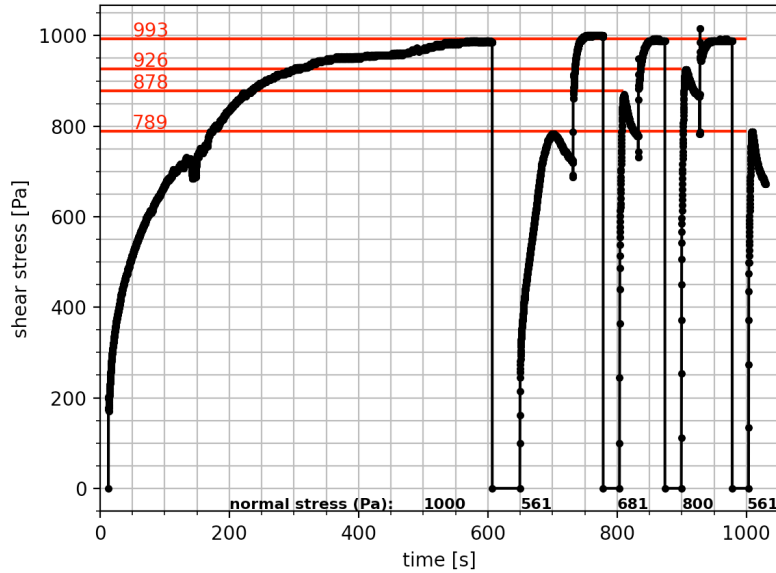
Endpoint (aka pre-shear) stress of 2000 Pa:
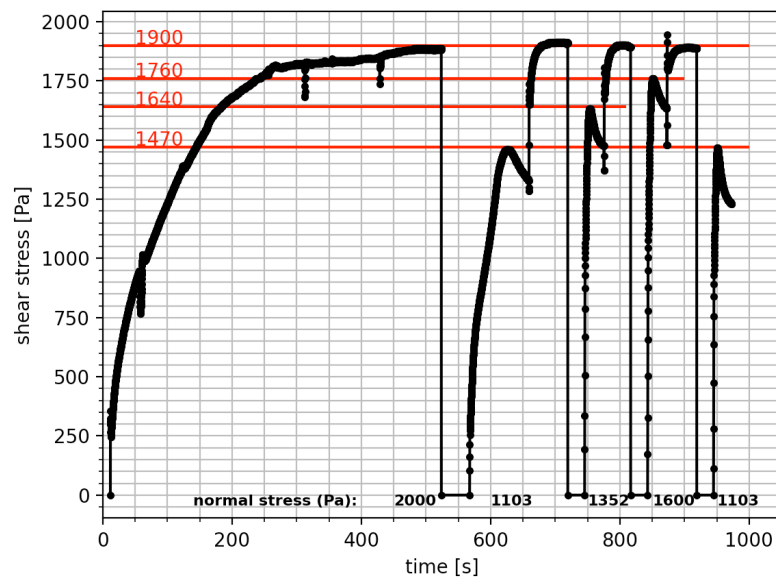
Endpoint (aka pre-shear) stress of 4000 Pa:
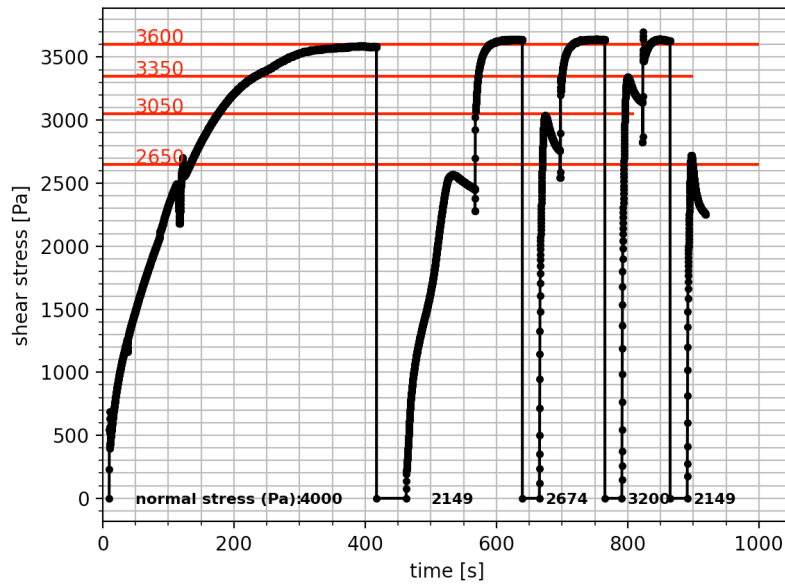
$(\sigma, \tau)_{EP}$ = (1000, 993) Pa		$(\sigma, \tau)_{EP}$ = (2000, 1900) Pa		$(\sigma, \tau)_{EP}$ = (4000, 3600) Pa	
σ [Pa]	τ [Pa]	σ [Pa]	τ [Pa]	σ [Pa]	τ [Pa]
561	789	1103	1470	2149	2650
681	878	1352	1640	2674	3050
800	926	1600	1760	3200	3350

The data, linear fits to the data of the ideal Coulomb material form ($\tau = \mu\sigma + c$), and the Mohr's circles for determining the consolidation stress and unconfined yield strength are shown in the following figure. The corresponding numerical data are given in the table following the figure. The algorithms for consolidation stress and unconfined yield strength are taken from the lecture material.
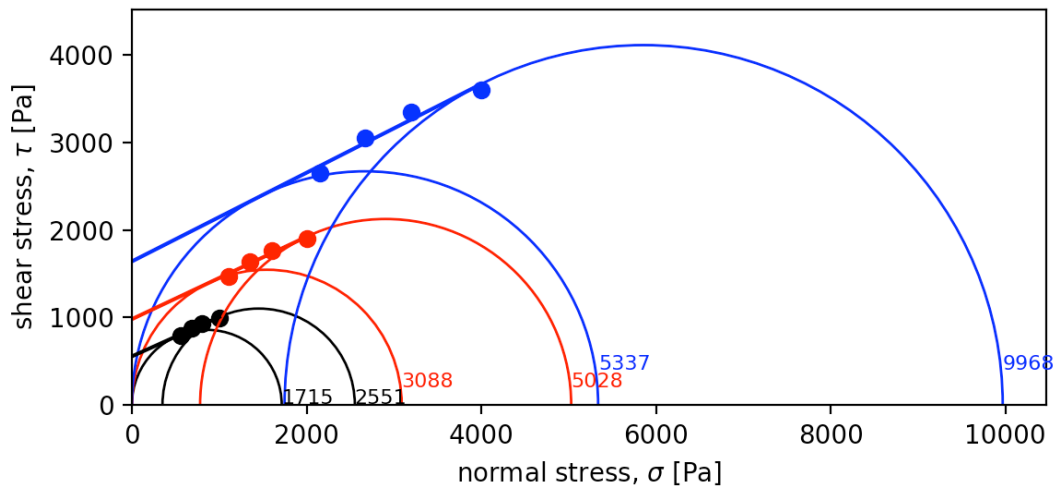
consolidation stress, σ_1 [Pa]	unconfined yield strength, f_c [Pa]	internal friction angle, ϕ [deg]	effective angle of internal friction, δ [deg]	cohesion, c [Pa]
2550	1720	24.2	49.3	555
5030	3090	25.2	47.0	980
9970	5340	26.9	44.6	1640

Following is the material flow function for the powdered sugar using the consolidation stress and unconfined yield strength values from the previous table. Note that a quadratic fit to the data is also included in the plot (but wasn't a required deliverable for this problem).
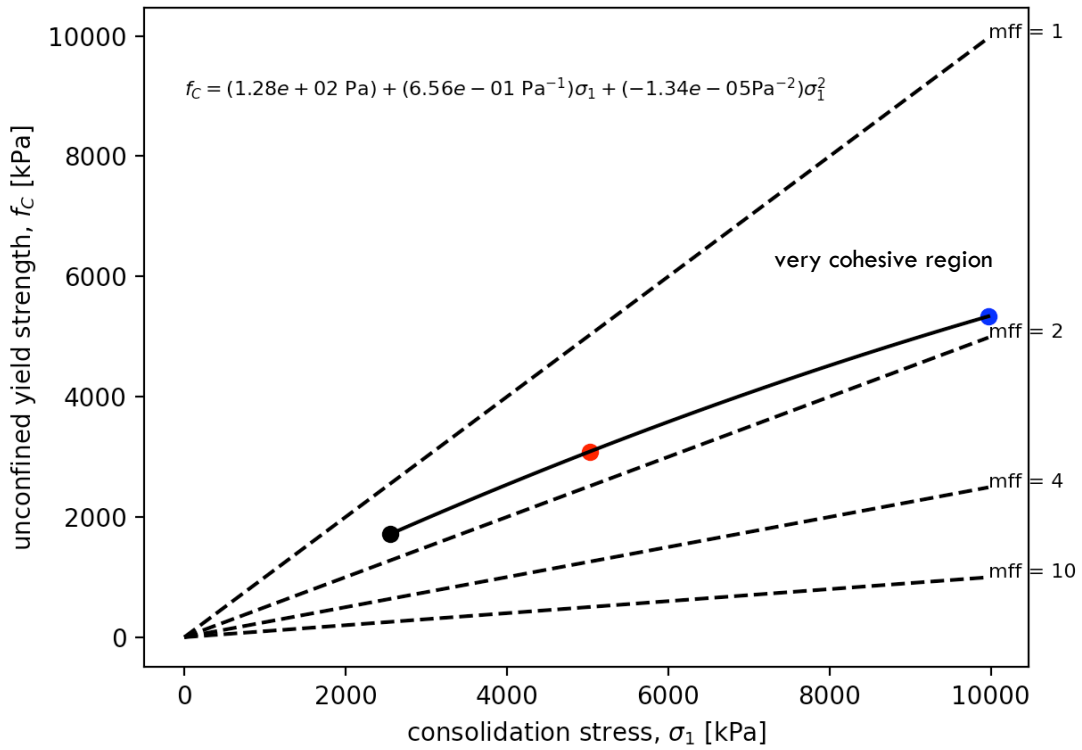
Following are plots of the internal friction angle, effective angle of internal friction, and cohesion as functions of the consolidation stress for each yield locus. The numerical values are given in the previous table.
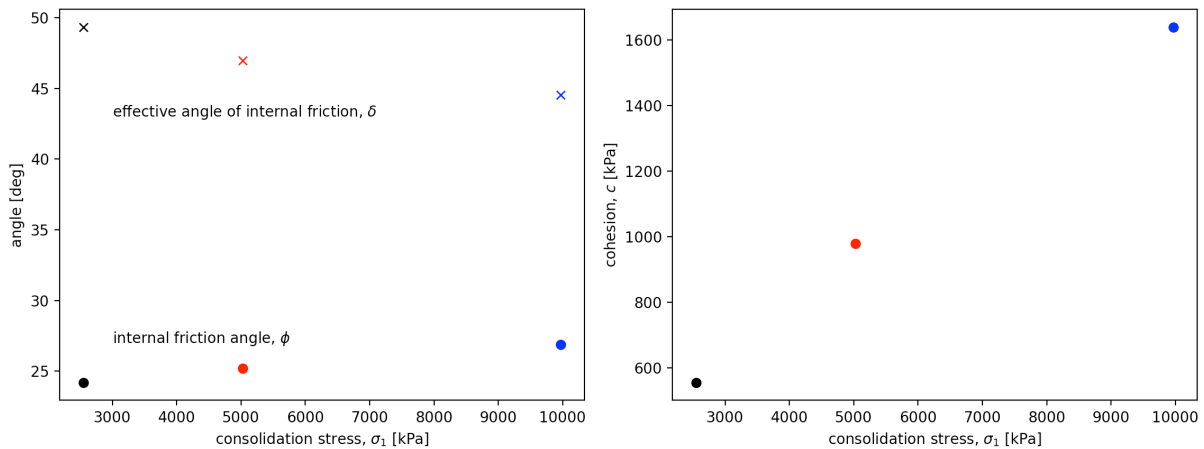
The following Python code was used to perform the calculations and generate the plots.

```
# shearcell_05.py

import numpy as np
import matplotlib.pyplot as plt
import matplotlib.patches as patches
from scipy.optimize import curve_fit

def IdealCoulomb(sigma, phi_rad, c):
    # Ideal Coulomb material model incipient yield locus (linear).
    return(np.tan(phi_rad)*sigma + c)

def Get_Sigma1_fC_delta(phi_rad, c, sigma_EP):
    # Function to return the consolidation stress, unconfined yield
    # strength, and effective angle of internal friction assuming a
    # linear incipient yield locus.  Use the equations derived in
    # lecture.

    mu = np.tan(phi_rad)

    p = sigma_EP + mu*(mu*sigma_EP + c)
    R = np.sqrt((sigma_EP - p)**2 + (mu*sigma_EP + c)**2)
    sigma1 = p + R

    sigma_IYL = c/np.sqrt(1 + mu**2)
    tau_IYL = IdealCoulomb(sigma_IYL, phi_rad, c)
    fC = 2*(sigma_IYL + mu*(mu*sigma_IYL + c))

    delta_rad = np.arcsin(R/p)

    return(sigma1, fC, delta_rad, p, R)

def QuadraticFit(x, c0, c1, c2):
    # Quadratic curve fit used for the material flow function.
    return(c0 + c1*x + c2*x**2)

# Specify the shear cell data.  The first datapoint is the end-point
# stress (sigma_EP, tau_EP).  The remainder are incipient yield data
# (sigma, tau).
dataset_1 = [[1000, 993], [561, 789], [681, 878], [800, 926]]
dataset_2 = [[2000, 1900], [1103, 1470], [1352, 1640], [1600, 1760]]
dataset_3 = [[4000, 3600], [2149, 2650], [2674, 3050], [3200, 3350]]

# Extract the normal and shear stresses.
sigma_1 = np.array([item[0] for item in dataset_1])
tau_1 = np.array([item[1] for item in dataset_1])
sigma_2 = np.array([item[0] for item in dataset_2])
tau_2 = np.array([item[1] for item in dataset_2])
sigma_3 = np.array([item[0] for item in dataset_3])
tau_3 = np.array([item[1] for item in dataset_3])

# Plot the yield loci.
figure, axes = plt.subplots()
plt.scatter(sigma_1, tau_1, color='k')
plt.scatter(sigma_2, tau_2, color='r')
plt.scatter(sigma_3, tau_3, color='b')
plt.xlabel(r'normal stress, $\sigma$ [Pa]')
plt.ylabel(r'shear stress, $\tau$ [Pa]')

# Fit straight lines to each incipient yield locus to obtain the
# internal friction angle and cohesion.
[phi_rad_1, c_1], cov = curve_fit(IdealCoulomb, sigma_1, tau_1)
print('(phi_1, c_1) = (%.2f deg, %.2f kPa)' % (np.degrees(phi_rad_1), c_1))
sigma_range = np.linspace(0, max(sigma_1), 100)
plt.plot(sigma_range, IdealCoulomb(sigma_range, phi_rad_1, c_1), color='k', linestyle='-')
[phi_rad_2, c_2], cov = curve_fit(IdealCoulomb, sigma_2, tau_2)
print('(phi_2, c_2) = (%.2f deg, %.2f kPa)' % (np.degrees(phi_rad_2), c_2))
sigma_range = np.linspace(0, max(sigma_2), 100)
```

```
plt.plot(sigma_range, IdealCoulomb(sigma_range, phi_rad_2, c_2), color='r', linestyle='-')
[phi_rad_3, c_3], cov = curve_fit(IdealCoulomb, sigma_3, tau_3)
print('(phi_3, c_3) = (%.2f deg, %.2f kPa)' % (np.degrees(phi_rad_3), c_3))
sigma_range = np.linspace(0, max(sigma_3), 100)
plt.plot(sigma_range, IdealCoulomb(sigma_range, phi_rad_3, c_3), color='b', linestyle='-')

# Find the consolidation stress and unconfined yield strength for each incipient yield locus.
(sigma1_1, fC_1, delta_rad_1, p_1, R_1) = Get_Sigma1_fC_delta(phi_rad_1, c_1, sigma_1[0])
print('(sigma1_1, fC_1) = (%.2f, %.2f) kPa, delta_1 = %.2f deg' % (sigma1_1, fC_1,
np.degrees(delta_rad_1)))
(sigma1_2, fC_2, delta_rad_2, p_2, R_2) = Get_Sigma1_fC_delta(phi_rad_2, c_2, sigma_2[0])
print('(sigma1_2, fC_2) = (%.2f, %.2f) kPa, delta_2 = %.2f deg' % (sigma1_2, fC_2,
np.degrees(delta_rad_2)))
(sigma1_3, fC_3, delta_rad_3, p_3, R_3) = Get_Sigma1_fC_delta(phi_rad_3, c_3, sigma_3[0])
print('(sigma1_3, fC_3) = (%.2f, %.2f) kPa, delta_3 = %.2f deg' % (sigma1_3, fC_3,
np.degrees(delta_rad_3)))

# Plot the corresponding Mohr's circles.
MohrsCircle = patches.Circle((p_1, 0), R_1, fill=False, color='k')
axes.add_patch(MohrsCircle)
plt.text(sigma1_1, 10, '%d' % sigma1_1, color='k', fontsize=8)
MohrsCircle = patches.Circle((0.5*fC_1, 0), 0.5*fC_1, fill=False, color='k')
axes.add_patch(MohrsCircle)
plt.text(fC_1, 10, '%d' % fC_1, color='k', fontsize=8)
MohrsCircle = patches.Circle((p_2, 0), R_2, fill=False, color='r')
axes.add_patch(MohrsCircle)
plt.text(sigma1_2, 200, '%d' % sigma1_2, color='r', fontsize=8)
MohrsCircle = patches.Circle((0.5*fC_2, 0), 0.5*fC_2, fill=False, color='r')
axes.add_patch(MohrsCircle)
plt.text(fC_2, 200, '%d' % fC_2, color='r', fontsize=8)
MohrsCircle = patches.Circle((p_3, 0), R_3, fill=False, color='b')
axes.add_patch(MohrsCircle)
plt.text(sigma1_3, 400, '%d' % sigma1_3, color='b', fontsize=8)
MohrsCircle = patches.Circle((0.5*fC_3, 0), 0.5*fC_3, fill=False, color='b')
axes.add_patch(MohrsCircle)
plt.text(fC_3, 400, '%d' % fC_3, color='b', fontsize=8)
axes.set_aspect(1)
axes.set_xlim(left=0)
axes.set_ylim(bottom=0)
plt.show()

# Fit the material flow function with a quadratic curve.
[c0, c1, c2], cov = curve_fit(QuadraticFit, [sigma1_1, sigma1_2, sigma1_3], [fC_1, fC_2, fC_3])

# Plot the material flow function.
plt.plot(sigma1_1, fC_1, 'ko')
plt.plot(sigma1_2, fC_2, 'ro')
plt.plot(sigma1_3, fC_3, 'bo')
# Add the quadratic curve fit.
sigma1_range = np.linspace(sigma1_1, sigma1_3, 100)
plt.plot(sigma1_range, QuadraticFit(sigma1_range, c0, c1, c2), color='k', linestyle='-')
# Add flow factor lines.
ff_values = [1, 2, 4, 10]
for ff in ff_values:
    plt.plot([0, sigma1_3], [0, 1/ff*sigma1_3], color='k', linestyle='--')
    plt.text(sigma1_3, 1/ff*sigma1_3, 'mff = %d' % ff, color='k', fontsize=8)
plt.xlabel(r'consolidation stress, $\sigma_1$ [kPa]')
plt.ylabel(r'unconfined yield strength, $f_C$ [kPa]')
plt.text(0, 9000, r'$f_C = (%0.2e$ Pa$) + (%.2e$ Pa$^{-1})\sigma_1 + (%.2e$Pa$^{-2})\sigma_1^2$' %
(c0, c1, c2), color='k', fontsize=8)
plt.show()

# Plot the internal friction angle and effective angle of internal
# friction as functions of the consolidation stress.
plt.plot(sigma1_1, np.degrees(phi_rad_1), 'ko')
plt.plot(sigma1_2, np.degrees(phi_rad_2), 'ro')
plt.plot(sigma1_3, np.degrees(phi_rad_3), 'bo')
plt.plot(sigma1_1, np.degrees(delta_rad_1), 'kx')
plt.plot(sigma1_2, np.degrees(delta_rad_2), 'rx')
```

```
plt.plot(sigma1_3, np.degrees(delta_rad_3), 'bx')
plt.xlabel(r'consolidation stress, $\sigma_1$ [kPa]')
plt.ylabel(r'angle [deg]')
plt.text(3000, 27, r'internal friction angle, $\phi$', color='k', fontsize=10)
plt.text(3000, 43, r'effective angle of internal friction, $\delta$', color='k', fontsize=10)
plt.show()

# Plot the cohesion as a function of the consolidation stress.
plt.plot(sigma1_1, c_1, 'ko')
plt.plot(sigma1_2, c_2, 'ro')
plt.plot(sigma1_3, c_3, 'bo')
plt.xlabel(r'consolidation stress, $\sigma_1$ [kPa]')
plt.ylabel(r'cohesion, $c$ [kPa]')
plt.show()
```

Running the Python code produces the following text output:

```
>> python3 ./shearcell_05.py
(phi_1, c_1) = (24.19 deg, 554.81 kPa)
(phi_2, c_2) = (25.21 deg, 979.70 kPa)
(phi_3, c_3) = (26.87 deg, 1639.31 kPa)
(sigma1_1, fC_1) = (2551.93, 1715.03) kPa, delta_1 = 49.34 deg
(sigma1_2, fC_2) = (5028.62, 3088.42) kPa, delta_2 = 46.98 deg
(sigma1_3, fC_3) = (9968.19, 5337.04) kPa, delta_3 = 44.56 deg
/opt/miniconda3/lib/python3.8/site-packages/scipy/optimize/minpack.py:828: OptimizeWarning: Covariance
of the parameters could not be estimated
  warnings.warn('Covariance of the parameters could not be estimated',
```

Note that the warning was generated for the quadratic fit to the material flow function.

Bibliography

[1] J. Schwedes, "Review of testers for measuring flow properties of bulk solids," Granular Matter, vol. 5, pp. 1–43, 2003.

[2] A. Jenike, "Gravity flow of bulk solids (Bulletin 108)," Bulletin of the University of Utah, vol. 52, no. 29, Oct. 1961.

[3] "Astm d6128-22. standard test method for shear testing of bulk solids using the jenike shear cell," American Society for Testing and Materials, 100 Barr Harbor Drive, P.O. Box C700, West Conshohocken, PA, USA, Standard, Oct. 2022.

[4] "Astm d6673-16. standard test method for bulk solids using schulze ring shear tester," American Society for Testing and Materials, 100 Barr Harbor Drive, P.O. Box C700, West Conshohocken, PA, USA, Standard, Dec. 2016.

[5] "Astm d7891-15. standard test method for shear testing of powders using the freeman technology ft4 powder rheometer shear cell," American Society for Testing and Materials, 100 Barr Harbor Drive, P.O. Box C700, West Conshohocken, PA, USA, Standard, May 2015.

[6] R. Schmitt and H. Feise, "Influence of tester geometry, speed and procedure on the results from a ring shear tester," Particle and Particle Systems Characterization, vol. 21, no. 5, pp. 403–410, 2004.

[7] "Astm d6682-01. standard test method for measuring shear stresses of powders using peschl rotational split level shear tester," American Society for Testing and Materials, 100 Barr Harbor Drive, P.O. Box C700, West Conshohocken, PA, USA, Standard, Oct. 2008.

[8] Z. Gu, P. Arnold, and A. McLean, "Consolidation-related bulk density and permeability models for bulk solids," Powder Technology, vol. 72, pp. 39–44, 1992.

[9] R. Nedderman, Statics and Kinematics of Granular Materials. Cambridge University Press, 1992. DOI: 10.1017/CBO9780511600043.

[10] J. Johanson and B. Cox, "Practical solutions to fine particle handling," Powder Handling and Processing, vol. 1, no. 1, pp. 61–65, 1989.

[11] A. CZastellanos, J. Valverde, and M. Quintanilaa, "The sevilla powder tester: A tool for characterizing the physical properties of fine cohesive powders at very small consolidations," KONA, vol. 22, pp. 66–81, 2004.

[12] D. Schulze, Powers and Bulk Solids: Behavior, Characterization, Storage and Flow, 2nd. Springer, 2021. DOI: 10.1007/978-3-030-76720-4.

[13] K. Rao, M. Allam, and R. Robinson, "Interfacial friction between sands and solid surfaces," ICE Proceedings Geotechnica, vol. 131, pp. 75–82, 1998. DOI: 10.1680.igeng.1998.30112.

CHAPTER 9

Hopper Design

The objectives of basic hopper design involve ensuring mass flow within the hopper, which is most affected by the hopper wall angle, and avoiding cohesive bridging (aka doming), which is controlled by the exit diameter (Figure 9.1). The methodology for achieving both of these objectives is described in this chapter for symmetric conical and wedge-shaped hoppers using the approach originally derived by Jenike [1], [2].

Jenike [1], [2] performed a solid mechanics analysis to determine the stress field in symmetric wedge and conical hoppers. Assuming an ideal Coulomb material, he calculated the maximum wall angle to produce mass flow in these hoppers and derived the minimum exit diameter required to prevent bridging. Jenike found that the stresses in a mass flow hopper are a function of:

- the material's effective angle of internal friction, δ,
- the material-wall friction angle, ϕ_w, and
- the angle between the hopper wall and the vertical, θ.

The parameters affecting the minimum exit diameter to avoid cohesive bridging are:

- the material's flow function, mFF,
- the material's specific weight (bulk density multiplied by gravitational acceleration), and
- the hopper flow factor, hff, which is a function of δ, ϕ_w, and θ (discussed later in this chapter).

Deriving and solving the equations to generate the conditions required to produce mass flow and prevent cohesive bridging is beyond the scope of these notes. The analysis involves the Equilibrium Equations from solid mechanics, Mohr's circles, and the Method of Characteristics for solving the equations. Fortunately,
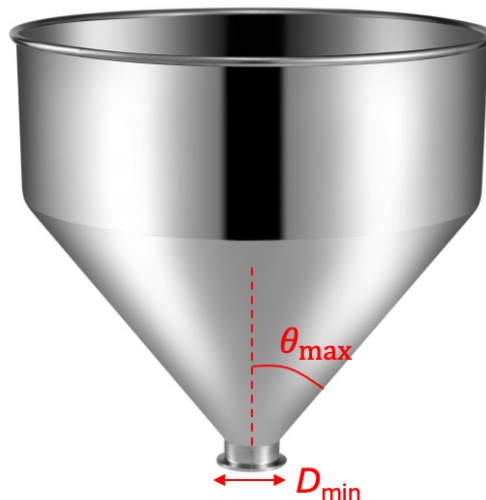
FIGURE 9.1. A photograph of a conical hopper showing the maximum wall half angle from the vertical $\theta_{\max}$ for mass flow and the minimum exit diameter to avoid cohesive bridging $D_{\min}$.

Jenike produced plots that allow one to easily look up the maximum hopper wall half angle from the vertical to ensure mass flow as well as a simple analysis for determining the minimum exit size. This chapter focuses on applying Jenike's results rather than deriving the underlying equations.

9.1. Maximum Hopper Wall Half Angle to Produce Mass Flow

An example of one of Jenike's design charts is shown in Figure 9.2. This chart is specifically for a conical hopper and a material with an effective angle of internal friction of $\delta = 50°$. The vertical axis in the chart is the wall friction angle (ϕ_w) and the horizontal axis is the hopper wall half angle from the vertical (θ). The lower left corner of the figure corresponds to mass flow conditions while the upper right corner is funnel flow. The black line spanning the figure from the upper-left to the lower-right corresponds to critical conditions separating the two flow regimes. The curves in the lower left-half of the figure correspond to different hopper flow factor (hff) values (discussed later in this chapter).

To determine the maximum hopper wall half angle from the vertical to produce mass flow, one first chooses the correct design chart (in this case, for a conical hopper and an effective angle of internal friction of $\delta = 50°$), then draws a horizontal line from the correct wall friction angle on the vertical axis until it touches the black dividing line, then draws a vertical line downward to the hopper wall half angle on the horizontal axis. The red lines in the figure provide an example for a wall friction angle of $\phi_w = 20°$. The maximum wall half angle from the vertical to produce mass flow in a conical hopper with this material is $\theta_{\max} = 26°$. Note that this wall angle does not include a safety margin. It's customary to include a three degree margin for conical hoppers since the transition between mass flow and funnel flow is abrupt so the maximum hopper wall half angle should be $\theta_{\max} = 23°$.

Notes:

(1) Decreasing the wall friction angle (ϕ_w), e.g., through the use of wall liners, increases the critical wall angle ($\theta_{\max}$) required for mass flow. For example, in the previous example, if the wall friction angle is changed from $\phi_w = 20°$ to $\phi_w = 15°$ the maximum hopper wall angle (without a safety margin) increases from $\theta_{\max} = 26°$ to $\theta_{\max} = 32°$ (Figure 9.3).

(2) Design charts for wedge-shaped hoppers (aka symmetrical slot hoppers) are also available. These charts assume the hopper depth (L) is at least three times the exit width (B) so the effects from the front and back walls can be neglected (Figure 9.4). The Jenike charts for wedge hoppers look similar to those for conical hoppers, but with an important difference: there is an intermediate flow region separating the mass flow and funnel flow regions (Figure 9.5). The flow in the intermediate region could be mass flow or funnel flow depending on the material height in the hopper [3]. Thus, the transition between mass and funnel flow is more gradual than for a conical hopper. As a result, a safety margin is not typically included for wedge hopper wall angles. To be conservative, Jenike included a dashed line near the mass flow-intermediate flow boundary which is used to determine the maximum hopper wall half angle for mass flow. For example, in Figure 9.5, the maximum hopper wall half angle to produce mass flow is $34°$ for a wedge hopper containing material with an effective angle of internal friction of $\delta = 50°$ and a wall friction angle of $\phi_w = 20°$.

(3) For the same effective internal friction and wall friction angles, the critical mass flow angle for a wedge hopper is about $10°$ to $12°$ larger than for a conical hopper. The vertical gradient in the cross-sectional area is smaller for wedge hoppers compared to conical hoppers. Thus, the material compresses less laterally in a wedge hopper as it flows toward the exit, making it easier for the material to discharge. The larger critical wall angle means that wedge hoppers are often considered for new hopper construction as well as for retrofits since wedge hoppers require less head space for the same material volume.

(4) Additional design charts for conical and wedge hoppers at different effective angles of internal friction are given at the end of this chapter in Section 9.6.
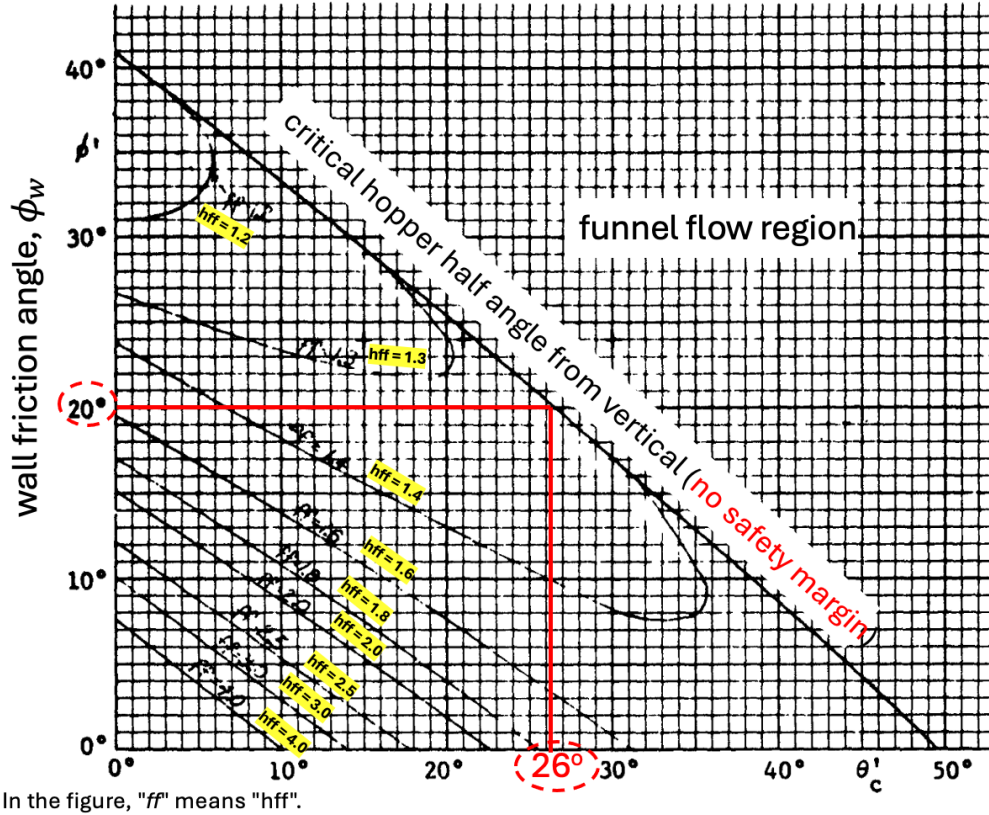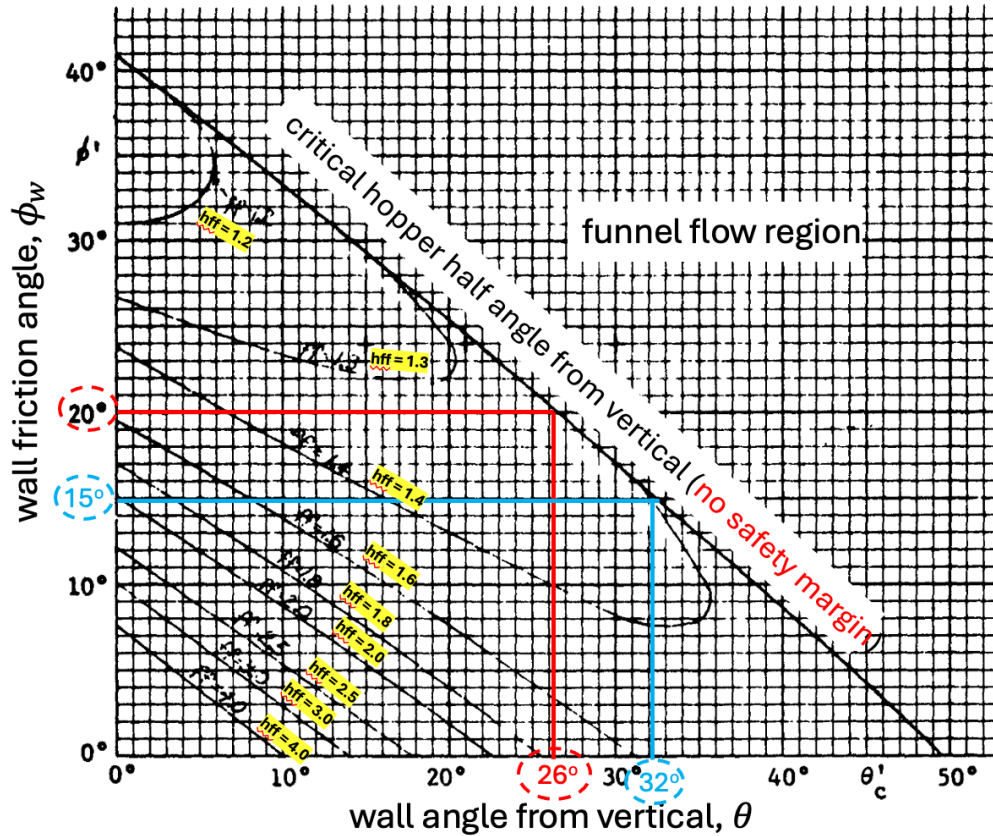
FIGURE 9.2. The Jenike design chart for determining the maximum hopper wall half angle to produce mass flow for a material with an effective angle of internal friction of $\delta = 50°$ in a conical hopper. The red lines in the figure correspond to an example with a wall friction angle of $\phi_w = 20°$ giving a critical hopper wall angle of $\theta_{\max} = 26°$ (without a safety margin). This design chart is from Jenike [2].

(5) Behara et al. [4] provide mathematical expressions for the critical hopper wall half angle,

conical hopper:
$$\theta_{\max} = 90° - \frac{1}{2}\arccos\left(\frac{1 - \sin\delta}{2\sin\delta}\right) - \frac{1}{2}\left[\phi_w + \arcsin\left(\frac{\sin\phi_w}{\sin\delta}\right)\right], \tag{9.1}$$

wedge hopper:
$$\theta_{\max} = \left[60.5° + \frac{1}{15.07}\arctan\left(\frac{50° - \delta}{7.73°}\right)\right]\left[1 - \frac{\phi_w}{42.3° + 0.131\delta\exp(0.06)}\right], \tag{9.2}$$

where δ is the effective angle of internal friction and ϕ_w is the wall friction angle, both of which should be in degrees and not radians. Recall that $\phi_w \leq \delta$ (Chapter 4). These expressions do not include a safety margin. For improved safety, subtract $3°$ from the calculated $\theta_{\max}$ values for the conical hopper. For wedge hoppers the transition between mass flow and funnel flow is more gradual and a safety margin is not needed. Figure 9.6 plots Eqs. (9.1) and (9.2) using the Python code given in Listing 9.1.

LISTING 9.1. Python code to determine the maximum hopper wall half angle to produce mass flow in conical and wedge hoppers.

```
def HopperCriticalAngle(delta, phiw, Type):
    # angles in radians, returns radians
    # Evaluate the critical half angle from the vertical for different
    # hopper types to ensure mass flow.
```

FIGURE 9.3. The Jenike design chart for determining the maximum hopper wall half angle to produce mass flow for a material with an effective angle of internal friction of $\delta = 50°$ in a conical hopper. The blue lines in the figure correspond to an example with a wall friction angle of $\phi_w = 15°$ giving a critical hopper wall angle of $\theta_{\max} = 32°$ (without a safety margin). This design chart is from Jenike [2].
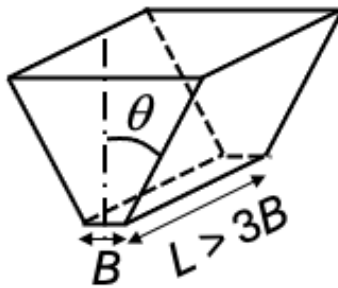
FIGURE 9.4. A schematic of a wedge hopper geometry for which the front and back wall effects can be neglected.

```
# Found using the expressions in Arnold and McLean (1976).

sin_delta = np.sin(delta)
sin_phiw = np.sin(phiw)
```
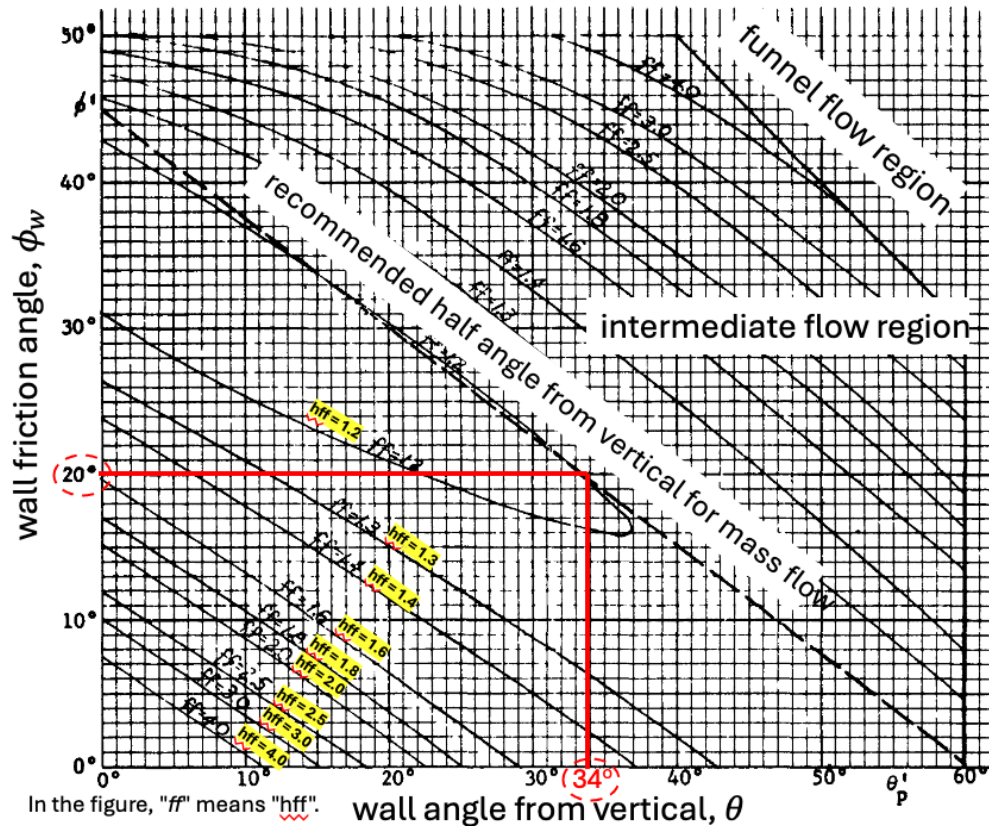
FIGURE 9.5. The Jenike design chart for determining the maximum hopper wall half angle to produce mass flow for a material with an effective angle of internal friction of $\underline{\delta = 50°}$ in a $\underline{\text{wedge}}$ hopper. The red lines in the figure correspond to an example with a wall friction angle of $\phi_w = 20°$ giving a critical hopper wall angle of $\theta_{\max} = 34°$. This design chart is from Jenike [2].

```
if (Type == 'Conical'):
    # Critical hopper angle for a conical hopper.
    return(np.radians(90) - 0.5*np.arccos((1-sin_delta)/(2*sin_delta)) -
        ↪ 0.5*(phiw + np.arcsin(sin_phiw/sin_delta)))
elif (Type == 'Slot'):
    # Critical angle for a symmetric slot hopper.
    return ((np.radians(60.5) + np.arctan((np.radians(50)-delta)/np.radians
        ↪ (7.73))/15.07)*(1-phiw/(np.radians(42.3) + 0.131*np.exp(0.06)*
        ↪ delta)))
else:
    print('Don\'t␣know␣how␣to␣evaluate␣for␣a␣\'%s\'␣hopper.' % Type)
    quit()
```

9.2. Minimum Hopper Exit Size to Avoid Cohesive Bridging

If a powder ceases to flow in a hopper (or other device), then an unconfined (aka free) surface exists (Figure 9.7). In order to ensure that flow continues in the device, the powder must yield at the unconfined surface.
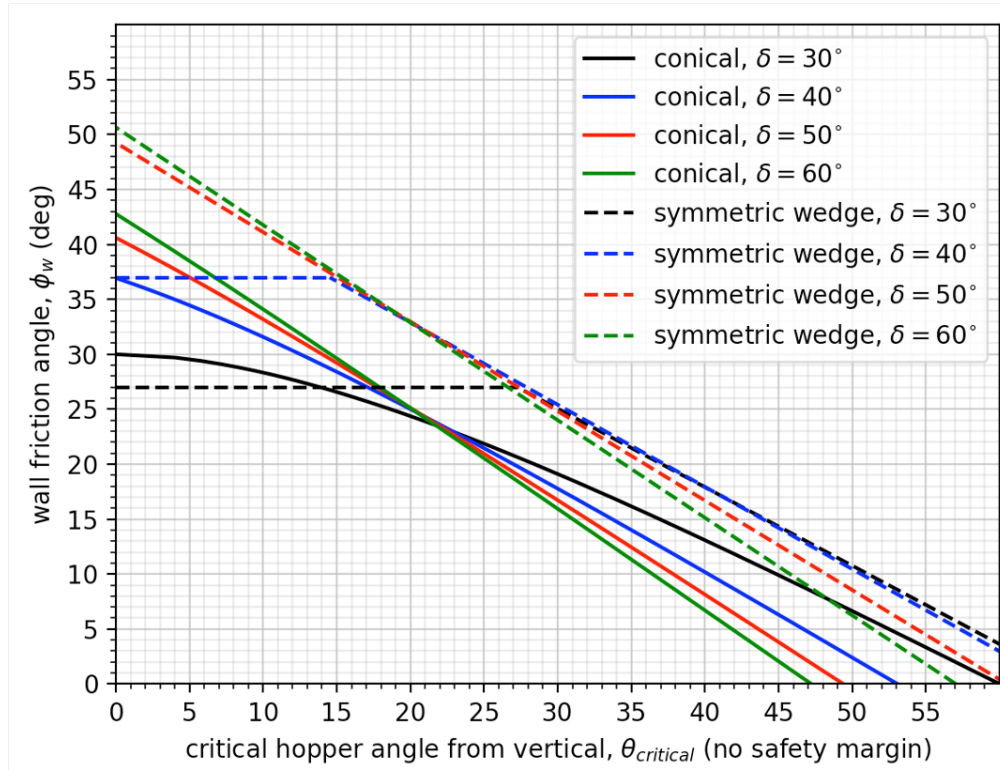
FIGURE 9.6. The critical hopper angle to produce mass flow in conical and wedge hoppers. The curves are plotted using Eqs. (9.1) and (9.2) implemented in the Python code in Listing 9.1.
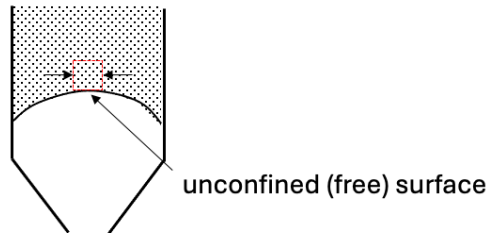
FIGURE 9.7. A schematic showing an unconfined surface when a cohesive arch forms in a hopper.

The stresses applied to the powder at the free surface by the walls must exceed the powder's unconfined yield strength (f_c) at that location. Thus, we need to know the stresses applied to the powder by the walls in order to determine if the powder will flow.

Jenike found that in a mass flow hopper, the ratio of the consolidation stress acting on the material (σ_1) to the major principal stress applied to the material at the wall (σ_{app}) is a constant, which he defined as the hopper flow factor (hff),

$$\text{hff} := \frac{\sigma_1}{\sigma_{\text{app}}}. \tag{9.3}$$

Determining the hff requires solving two simultaneous differential equations, which is beyond the scope of these notes. The solution is a function of the effective angle of internal friction (δ), the wall friction angle
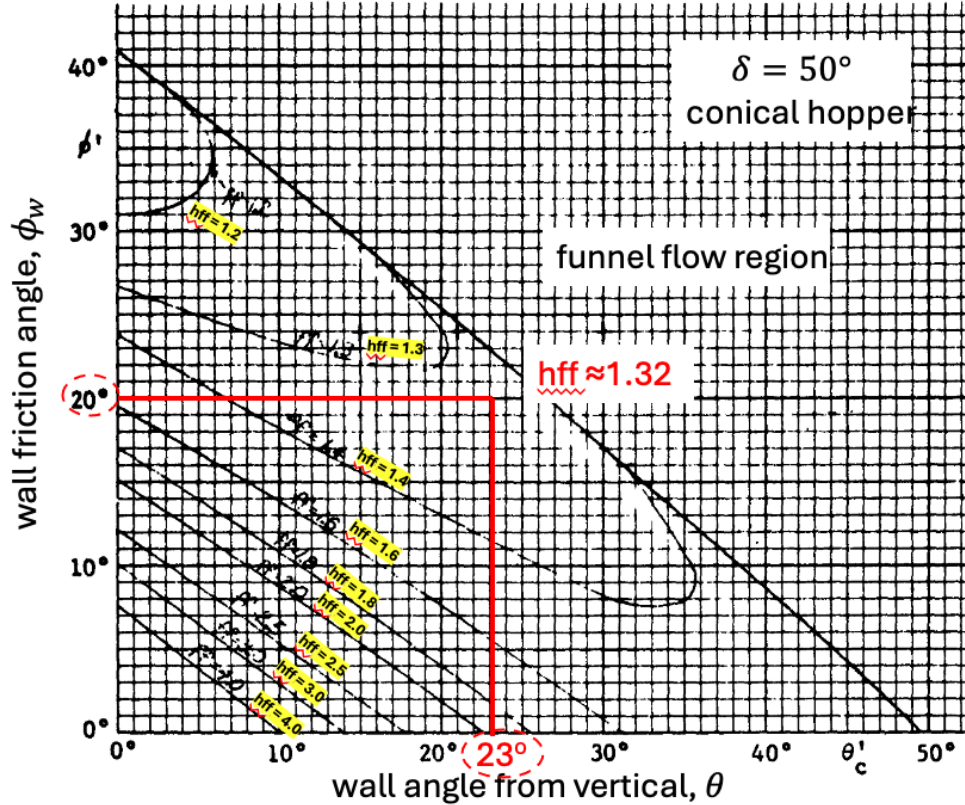
FIGURE 9.8. The hopper design chart for a conical hopper and a material with an effective angle of internal friction of $\delta = 50°$. For a wall friction angle of $\phi_w = 20°$ and a hopper wall half angle of $23°$, the hopper flow factor is hff ≈ 1.32. This chart is from Jenike [2].

(ϕ_w), and the wall half angle from the vertical (θ). Typical values for the hff are between 1.1 and 1.7. Fortunately, Jenike included in his design charts curves allowing one to estimate hopper flow factor values. For example, referring to Figure 9.8, for a material with an effective angle of internal friction of $\delta = 50°$ contained within a conical hopper with a wall half angle of $23°$ and a wall friction angle of $20°$, the hopper flow factor is hff ≈ 1.32. Similarly, the hopper flow factor for a wedge hopper at the same conditions is hff ≈ 1.20 (Figure 9.9).

Notes:

(1) Arnold and McLean [5] provide expressions for calculating the hopper flow factor,

$$\text{hff} = H(\theta)\frac{Y(1 + \sin\delta)}{2(X - 1)\sin\theta}, \tag{9.4}$$

$$X = \frac{2^m \sin\delta}{1 - \sin\delta}\left[\frac{\sin(2\beta + \theta)}{\sin\theta} + 1\right], \tag{9.5}$$

$$Y = \frac{\{2\left[1 - \cos(\beta + \theta)\right]\}^m (\beta + \theta)^{1-m} \sin\theta + \sin\beta \left[\sin(\beta + \theta)\right]^{1+m}}{(1 - \sin\delta)\left[\sin(\beta + \theta)\right]^{2+m}}, \tag{9.6}$$

$$H(\theta) = \left(\frac{130° + \theta}{65°}\right)^m \left(\frac{200° + \theta}{200°}\right)^{1-m}, \tag{9.7}$$
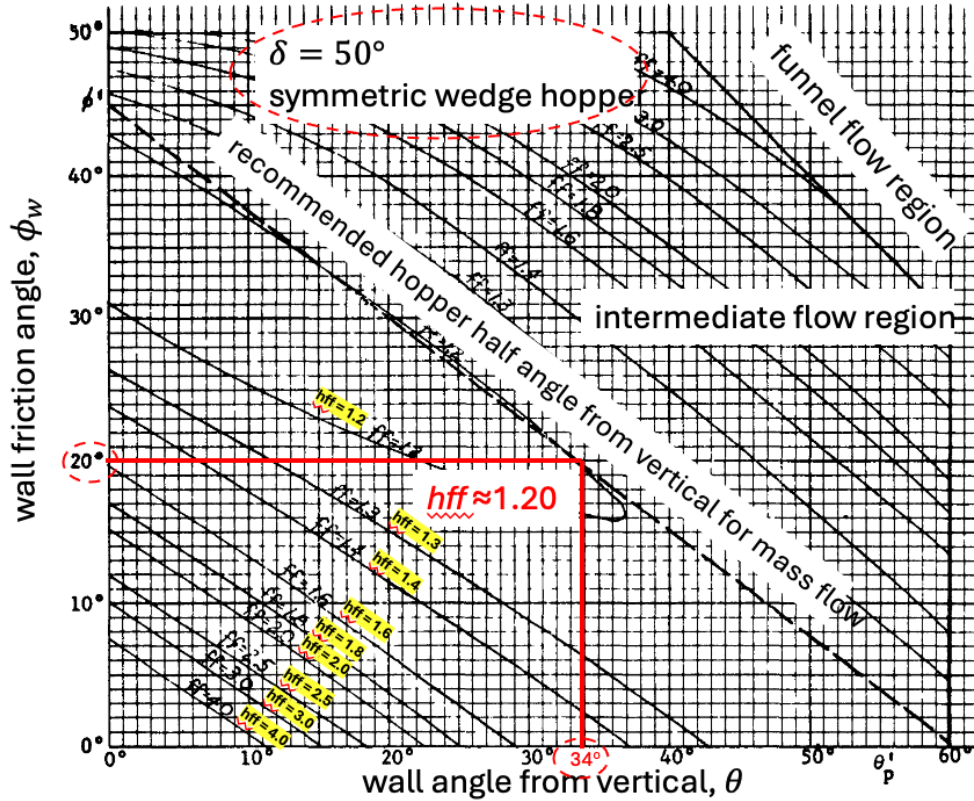
FIGURE 9.9. The hopper design chart for a <u>wedge</u> hopper and a material with an effective angle of internal friction of $\delta = 50°$. For a wall friction angle of $\phi_w = 20°$ and a hopper wall half angle of $34°$, the hopper flow factor is hff ≈ 1.20. This chart is from Jenike [2].

$$\beta = \frac{1}{2}\left[\phi_w + \arcsin\left(\frac{\sin\phi_w}{\sin\delta}\right)\right], \tag{9.8}$$

where $m = 1$ for a conical hopper and $m = 0$ for a wedge hopper. Python functions for evaluating the function $H(\theta)$ and the hopper flow factor (hff) are given in Listing 9.2. Note that these expressions are slightly different than the values from Jenike.

LISTING 9.2. Python code for calculating the function H(theta) and the hopper flow factor using the expressions in Arnold and McLean (1976).

```
def H(theta, Type): # theta in radians, return is dimensionless
    # Found using the expressions in Arnold and McLean (1976).
    if (Type == 'Conical'):
        return((130+np.degrees(theta))/65)
    elif (Type == 'Slot'):
        return((200+np.degrees(theta))/200)
    else:
        print('Don\'t know how to evaluate H(theta) for a \'%s\' hopper.' %
            ↪ Type)
        quit()

def HopperFlowFactor(delta, phiw, theta, Type): # angles in radians, return is
    ↪ dimensionless
```

```
# Found using the expressions in Arnold and McLean (1976).

sin_delta = np.sin(delta)
sin_phiw = np.sin(phiw)
sin_theta = np.sin(theta)
beta = 0.5*(phiw + np.arcsin(sin_phiw/sin_delta))
sin_beta = np.sin(beta)
sin_beta_plus_theta = np.sin(beta+theta)

# Now find the hff for the given hopper angle.
if (Type == 'Conical'):
    X = 2*sin_delta/(1-sin_delta)*(np.sin(2*beta+theta)/sin_theta + 1)
    Y = ((2*(1-np.cos(beta+theta)))*sin_theta + sin_beta*(
        ↪ sin_beta_plus_theta)**2) / ((1-sin_delta)*(sin_beta_plus_theta)
        ↪ **3)
elif (Type == 'Slot'):
    X = sin_delta/(1-sin_delta)*(np.sin(2*beta+theta)/sin_theta + 1)
    Y = ((beta+theta)*sin_theta + sin_beta*sin_beta_plus_theta) / ((1-
        ↪ sin_delta)*(sin_beta_plus_theta)**2)
else:
    print('Don\'t␣know␣how␣to␣evaluate␣the␣HopperFlowFactor␣for␣a␣\'%s\'␣
        ↪ hopper.' % Type)
    quit()

H_theta = H(theta, Type)
hff = H_theta*Y*(1+sin_delta)/(2*(X-1)*sin_theta)
return(hff)
```

Recall that in order to ensure that material doesn't form a bridge, we want the applied stress (σ_{app}) to equal or exceed the unconfined yield strength of the material (f_c), i.e., for flow we should have,

$$\sigma_{\mathrm{app}} \geq f_c \implies \frac{1}{\mathrm{hff}}\sigma_1 \geq \mathrm{mFF}(\sigma_1). \tag{9.9}$$

This criterion is shown graphically in Figure 9.10. The critical applied stress (CAS) is where the applied stress equals the unconfined yield strength. Note that if the material flow function (mFF) is always less than the 1/hff line, then a cohesive arch will never form. If the material flow function is always greater than the 1/hff line, then gravity alone will not break the arch and some other means of promoting flow must be used.

To determine the required critical applied stress at the hopper exit to ensure flow, we can perform a force balance on a thin, uniform arch of material as shown in Figure 9.11. For this analysis, assume the only forces acting on the arch are the applied stress from the walls and the weight of the material in the arch. Neglecting the weight of the material above the arch serves as a conservative scenario since the weight of overlying material would help to collapse the arch. During discharge, the major principal stress applied to the material at the wall acts on a plane that is at an angle β with respect to the wall (refer to Chapter 6).

The upward acting force resulting from the (major principal) applied stress at the wall acts over the perimeter area of the arch and is given by,

$$F_{\mathrm{up}} = [f_1(\theta)r\,dr]\sigma_{\mathrm{app}}\sin(\theta - \beta), \tag{9.10}$$

where $f_1(\theta)$ is a function of the arch geometry. Note that the perimeter area is proportional to $r\,dr$ where r is the radius from the hopper's apex. The downward acting force, i.e., the arch weight, is proportional to the arch volume,

$$F_{\mathrm{down}} = \rho_b g[f_2(\theta)r^2 dr], \tag{9.11}$$
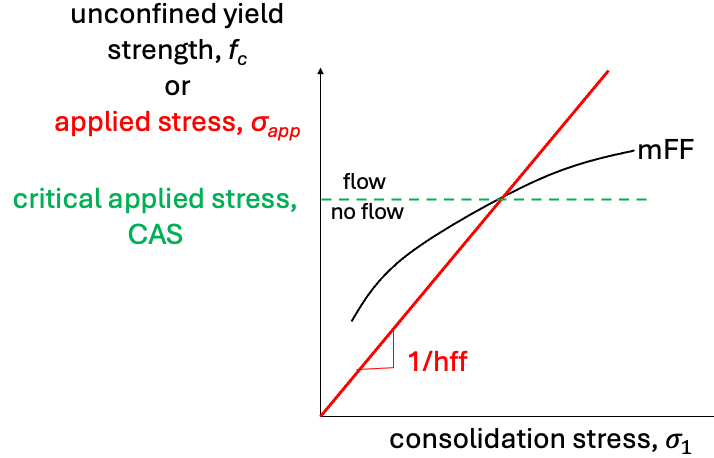
FIGURE 9.10. The critical applied stress (CAS) is the applied stress at which the applied stress ($\sigma_{\mathrm{app}} = \sigma_1/\mathrm{hff}$) equals the unconfined yield strength ($f_c = \mathrm{mFF}(\sigma_1)$). Consolidation stresses larger than the critical applied stress will result in flow (the applied stress is larger than the material strength) while consolidation stresses smaller than the critical applied stress result in no flow.
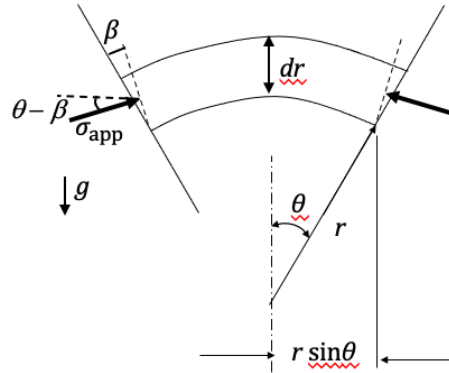
FIGURE 9.11. A free body diagram of a thin arch of material at the hopper exit. Two forces are assumed to act on the arch, the force applied at the walls and the material weight.

where $f_2(\theta)$ is also a function of the arch geometry. Note here that the volume is proportional to $r^2 dr$. Now determine the exit radius (from the hopper apex), r_b, at which the upward and downward acting forces are equal,

$$\sum F_z = 0 = F_{\mathrm{up}} - F_{\mathrm{down}}, \tag{9.12}$$

$$0 = [f_1(\theta) r_b dr]\sigma_{\mathrm{app}} \sin(\theta - \beta) - \rho_b g[f_2(\theta) r_b^2 dr], \tag{9.13}$$

$$r_b = \frac{f_1(\theta)}{f_2(\theta)} \frac{\sigma_{\mathrm{app}} \sin(\theta - \beta)}{\rho_b g}. \tag{9.14}$$

To be conservative, let F_{up} be as large as possible (more likely to form an arch), which means choosing β such that $\sin(\theta - \beta) = 1$. Thus, the previous equation becomes,

$$r_b = f_3(\theta) \frac{\sigma_{\mathrm{app}}}{\rho_b g} \tag{9.15}$$

The exit diameter, D, is related to the radius via (Figure 9.11),

$$D = 2r_b \sin(\theta). \tag{9.16}$$

In addition, when the arch is just about to yield, the applied stress should equal the critical applied stress, i.e., $\sigma_{\text{app}} = \text{CAS}$. The hopper diameter for these conditions is the minimum diameter at which the arch will yield. Thus,

$$D_{\min} = H(\theta) \frac{\text{CAS}}{\rho_b g}, \tag{9.17}$$

where $H(\theta)$ is a function accounting for the arch geometry. An analysis can be performed to determine the form of $H(\theta)$, but is outside the scope of these notes.

Notes:

(1) As discussed in previous chapters, the bulk density is a function of the consolidation stress. It's value in Eq. (9.17) should correspond to the consolidation stress at the exit.
(2) The minimum exit width for a wedge hopper (Figure 9.4) is,

$$B_{\min} = H(\theta) \frac{\text{CAS}}{\rho_b g}. \tag{9.18}$$

(3) Plots for the function $H(\theta)$ for various exit geometries are given in Figure 9.12. Several curve fits have been proposed for $H(\theta)$, including the one given in Eq. (9.7) as well as the following [4]:

$$\text{circular exit:} \quad H(\theta) = 2.0 + \frac{\theta}{60°}, \tag{9.19}$$

$$\text{square exit:} \quad H(\theta) = 1.8 + \frac{\theta}{70°}, \tag{9.20}$$

$$\text{rectangular exit:} \quad H(\theta) = 1.0 + \frac{\theta}{180°}. \tag{9.21}$$

For exit dimensions between the rectangular and square shapes, Woodcock and Mason [6] recommend interpolating between the two curves. It's important to note from Figure 9.12 that circular exit diameters must be approximately twice the width of rectangular exits to avoid bridging. Thus, not only can wedge hoppers have larger wall angles than conical hoppers to produce mass flow (Section 9.1), but the exit openings can be smaller than circular exits to avoid cohesive bridging.

To summarize, the hopper design process involves the following steps:

(1) Determine the wall friction angle, ϕ_w, effective angle of internal friction (δ), and the material flow function (mFF) from shear cell testing.
(2) Determine the material bulk density as a function of the consolidation stress, for example from an oedometer test.
(3) Determine the hopper wall angle for mass flow ($\theta_{\max}$) and the hopper flow factor (hff) using the Jenike design charts.
(4) Calculate the Critical Applied Stress (CAS) using the hff and mFF.
(5) (If the properties vary with σ_1, then repeat steps $1 - 4$, using the σ_1 found in Step 4.)
(6) Calculate the powder bulk density at σ_1.
(7) Calculate the minimum outlet diameter.

Note that time consolidation behavior of the material should be considered during the design process.

9.3. Designing to Avoid the Formation of a Rathole

Sometimes funnel flow in a hopper can't be avoided; however, it's best to try to at least avoid the formation of a rathole (aka pipe) due to their potential for damage, safety risks, and exceedingly poor flow behavior. Ratholes form because the stresses applied to the material by the walls are smaller than the material's
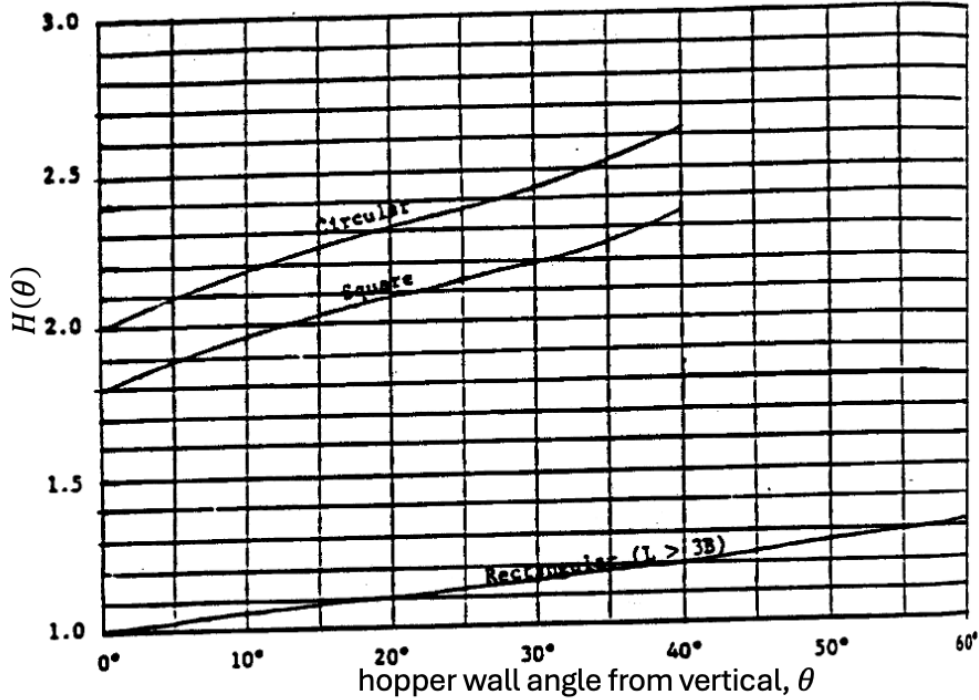
FIGURE 9.12. Plots of the function $H(\theta)$ for various hopper exit geometries. This figure is from Jenike [2].

unconfined yield strength. Ratholes won't form in mass flow hoppers, but they can form in funnel flow, especially as the fill level increases since larger consolidation stresses result in increased material strength.

As with hopper design, the detailed analysis for determining the conditions for avoiding rathole formation are not presented here. The reader is referred to the work by Jenike [1], [2], Johanson [7], and Hill and Cox [8] for more in-depth analyses. Instead, the final design criterion is presented. To avoid the formation of a rathole, the minimum exit diameter of the hopper (D_{rh}) should be [2],

$$D_{\mathrm{rh}} = G(\phi)\frac{f_c}{\rho_b g}, \tag{9.22}$$

where $G(\phi)$ is a function of the material's internal friction angle and f_c is the unconfined yield strength at the maximum expected consolidation stress. A plot of $G(\phi)$ is given in Figure 9.13, but a simple curve fit to the relation is given by Mehos [9],

$$G(\phi) = 4.3\tan\phi. \tag{9.23}$$

Cohesive bridging will not occur if ratholing doesn't occur for a circular exit; thus, D_{rh} should be used as the minimum exit diameter for a circular exit for a funnel flow hopper. For a slot-style exit, the exit diagonal length, $\sqrt{B^2 + L^2}$, should be $\geq D_{\mathrm{rh}}$. To avoid cohesive bridging for a slot exit in funnel flow, the recommendation is to follow the procedures for sizing $B_{\min}$, but using a hopper flow factor of hff $= 1.7$. The maximum consolidation stress may be estimated using Janssen's equation assuming vertical walls over the entire hopper height (Chapter 5),

$$\sigma_1 = \frac{\rho_b g D_H}{4K_a \tan\phi_w}\left[1 - \exp\left(-4K_A \tan\phi_w \frac{z}{D_H}\right)\right], \tag{9.24}$$

with the largest depth z and a hydraulic diameter for the bin, D_H (Eq. (5.32)).
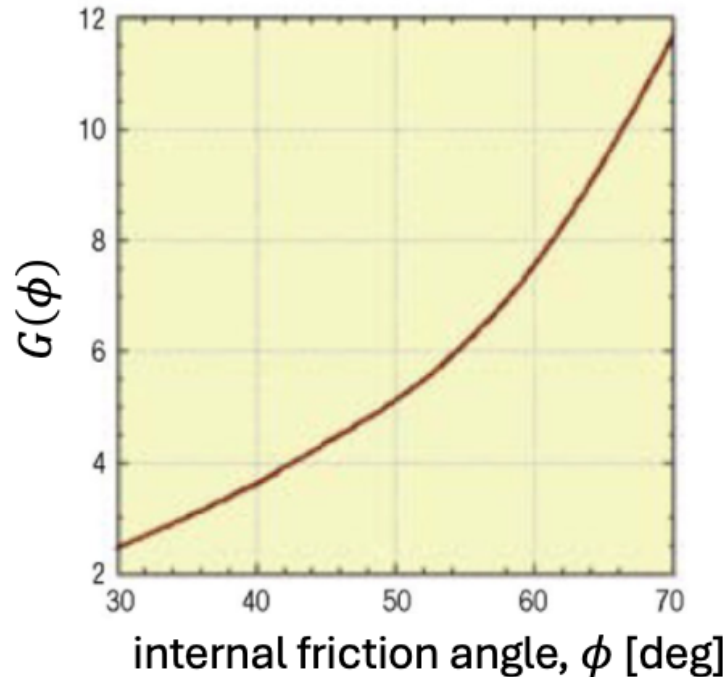
FIGURE 9.13. A plot of the the rathole function $G(\phi)$. This figure is from Mehos and Morgan [10].

9.4. Rules of Thumb for Improving Hopper Flow

Based on the analyses presented in this chapter, several general recommendations can be made for improving flow behavior in hoppers. These recommendations include the following.

(1) Decrease the hopper wall angle from the vertical (θ), which makes it more more likely that mass flow occurs in the hopper. Having a small hopper wall angle may not be possible due to space constraints.
(2) Replace a conical hopper with a wedge-shaped hopper. Wedge-shaped hoppers have a larger critical wall angle, by about $10°$ to $12°$, than conical hoppers, for the same material and wall properties.
(3) Reduce wall friction angle (ϕ_w) via the use of liners. Reducing the wall friction angle increases the critical hopper wall angle for mass flow.
(4) Increase the hopper exit diameter ($D_{\min}$ or $B_{\min}$). Increasing the exit diameter decreases the likelihood of cohesive bridging.
(5) Change from a circular exit to a rectangular exit. The width of a rectangular exit can be approximately half the size of a circular exit and still avoid arching.
(6) Decrease the fill height, particularly if the hopper operates in funnel flow. Decreasing the fill height decreases the maximum consolidation stress and material strength and, thus, reduces the chance of ratholing.
(7) Add a flow aid such as fumed silica, talc, or stearic acid into the material. Flow aids reduce the material's effective internal friction angle, wall friction angle, and unconfined yield strength by modifying particle-particle interactions. However, adding a flow aid may be expensive or not allowed due to purity requirements. In addition, the addition of a flow aid requires an additional blending step, which increases the complexity of processing.

9.5. Summary

The following list summarizes the major points in the chapter.

(1) The Jenike design procedure can be used to design simple hoppers for mass flow and avoid cohesive bridging.
(2) For funnel flow hoppers, one should attempt to design the hopper to avoid ratholing.
(3) For details on the testing procedures and analyses used in the Jenike design procedure, refer to Jenike [1] (aka Bulletin 108) and Jenike [2] (aka Bulletin 123).

9.6. Additional Hopper Design Charts

This section provides additional Jenike hopper design charts.
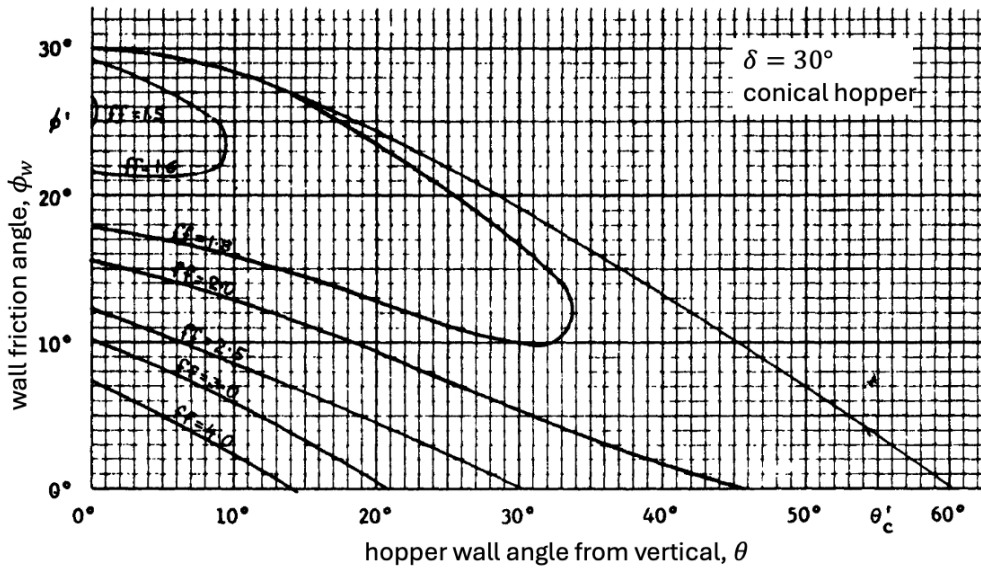
FIGURE 9.14. The Jenike design chart for determining the maximum hopper wall half angle to produce mass flow for a material with an effective angle of internal friction of $\delta = 30°$ in a <u>conical</u> hopper. The "ff" in the plot is the hopper flow factor (hff). This design chart is from Jenike [2].
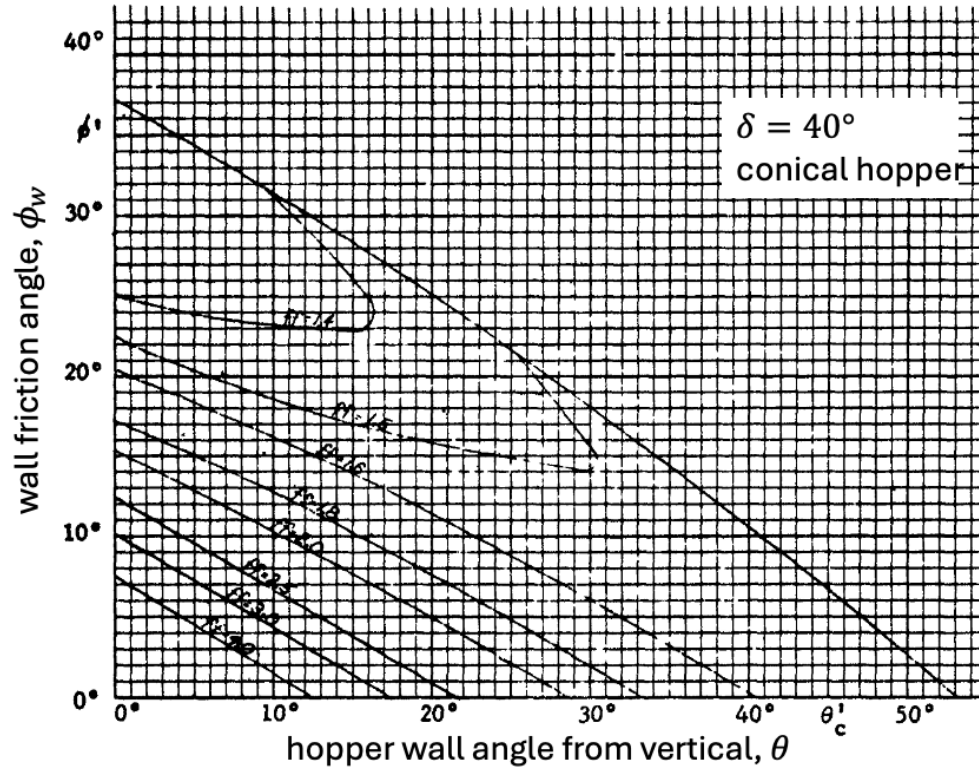
Figure 9.15. The Jenike design chart for determining the maximum hopper wall half angle to produce mass flow for a material with an effective angle of internal friction of $\delta = 40°$ in a conical hopper. The "ff" in the plot is the hopper flow factor (hff). This design chart is from Jenike [2].
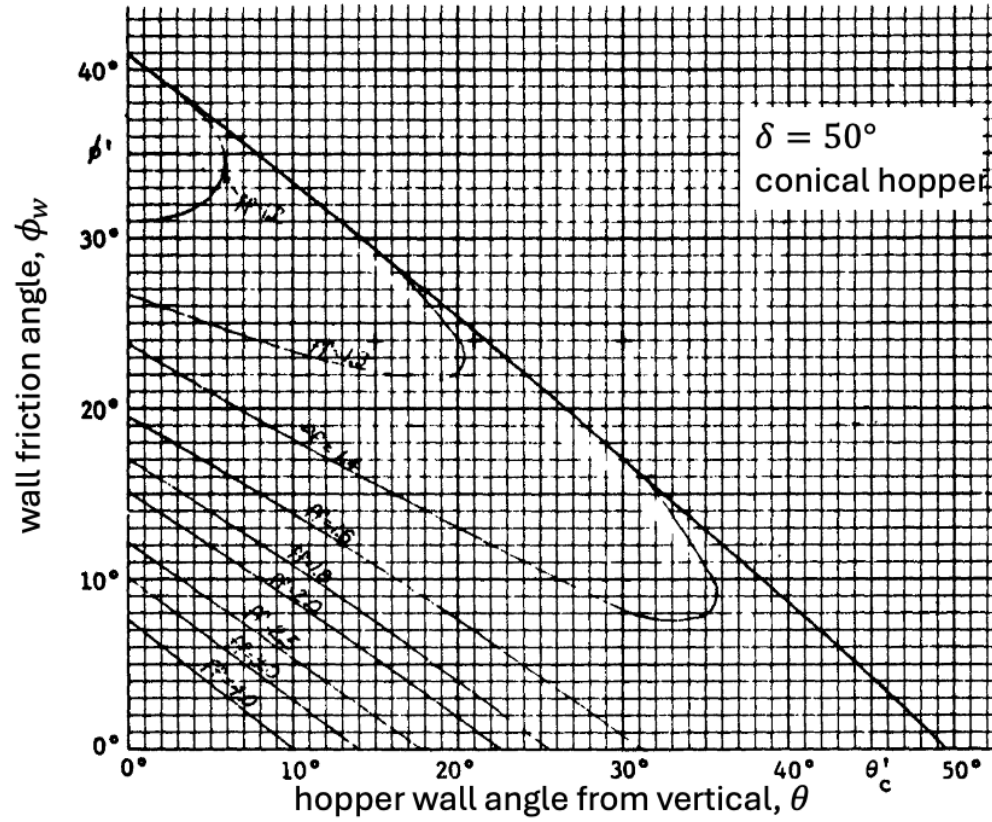
FIGURE 9.16. The Jenike design chart for determining the maximum hopper wall half angle to produce mass flow for a material with an effective angle of internal friction of $\delta = 50°$ in a <u>conical</u> hopper. The "ff" in the plot is the hopper flow factor (hff). This design chart is from Jenike [2].
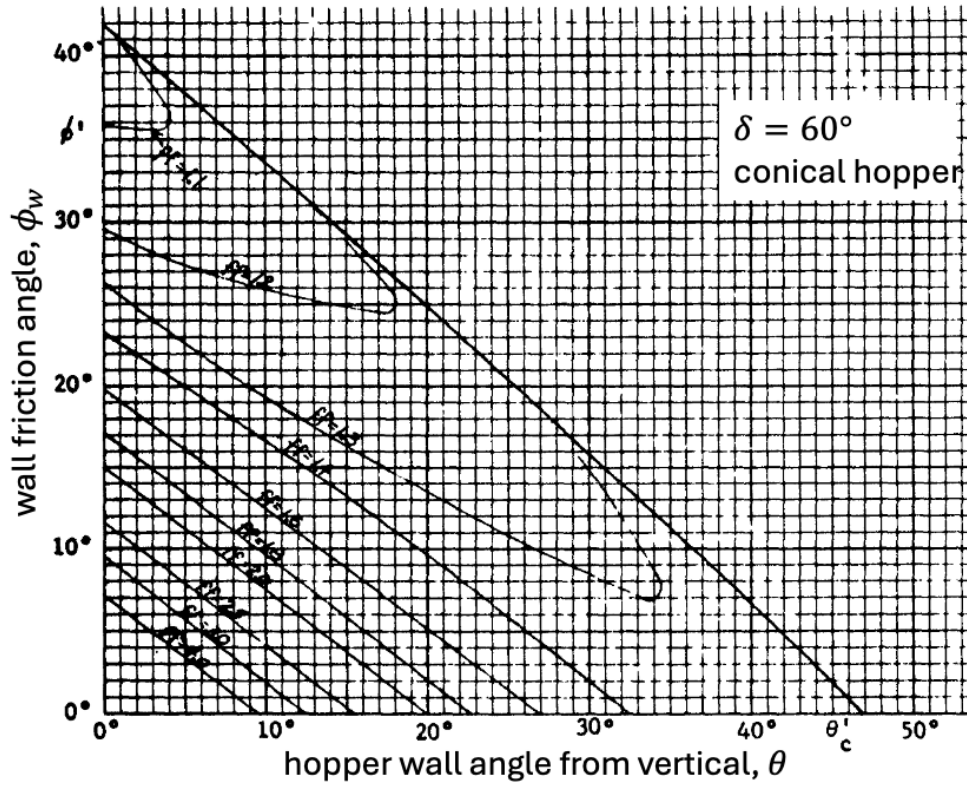
Figure 9.17. The Jenike design chart for determining the maximum hopper wall half angle to produce mass flow for a material with an effective angle of internal friction of $\delta = 60°$ in a <u>conical</u> hopper. The "ff" in the plot is the hopper flow factor (hff). This design chart is from Jenike [2].
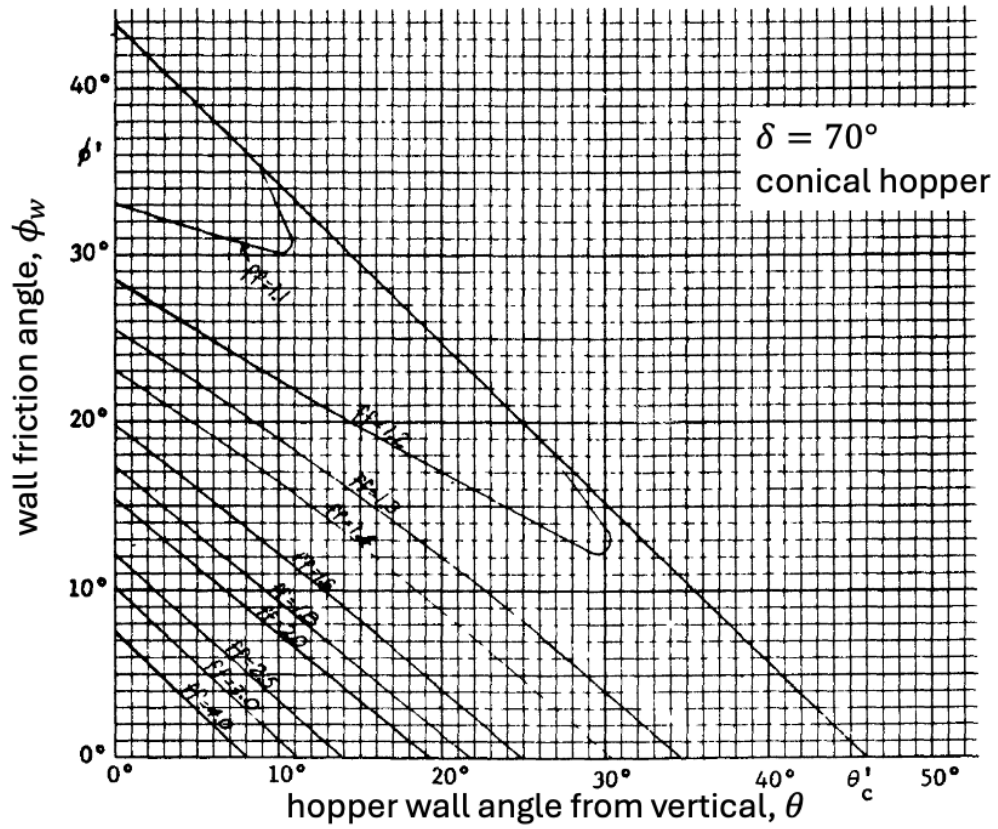
FIGURE 9.18. The Jenike design chart for determining the maximum hopper wall half angle to produce mass flow for a material with an effective angle of internal friction of $\delta = 70°$ in a conical hopper. The "ff" in the plot is the hopper flow factor (hff). This design chart is from Jenike [2].
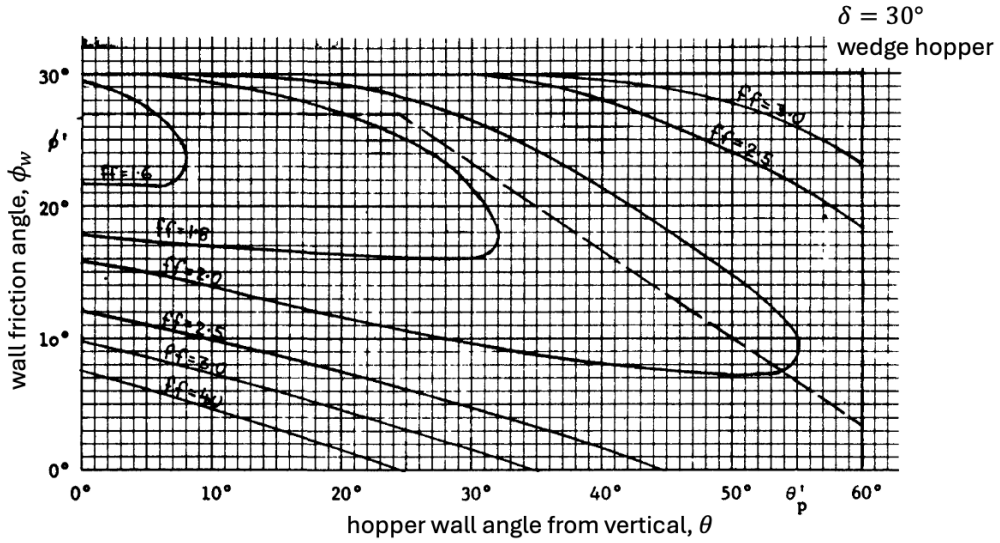
FIGURE 9.19. The Jenike design chart for determining the maximum hopper wall half angle to produce mass flow for a material with an effective angle of internal friction of $\delta = 30°$ in a wedge hopper. The "ff" in the plot is the hopper flow factor (hff). This design chart is from Jenike [2].
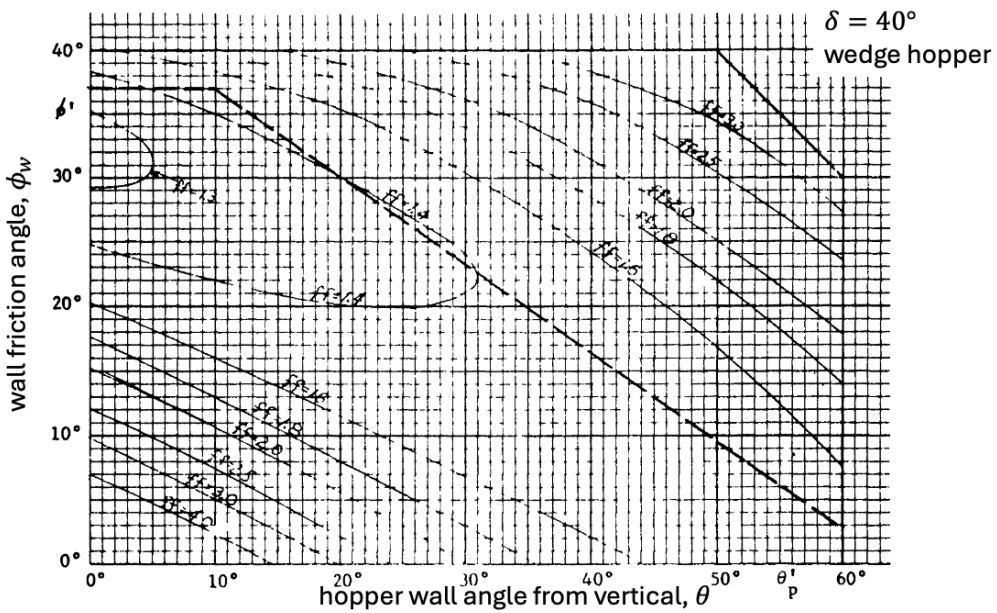
FIGURE 9.20. The Jenike design chart for determining the maximum hopper wall half angle to produce mass flow for a material with an effective angle of internal friction of $\delta = 40°$ in a wedge hopper. The "ff" in the plot is the hopper flow factor (hff). This design chart is from Jenike [2].
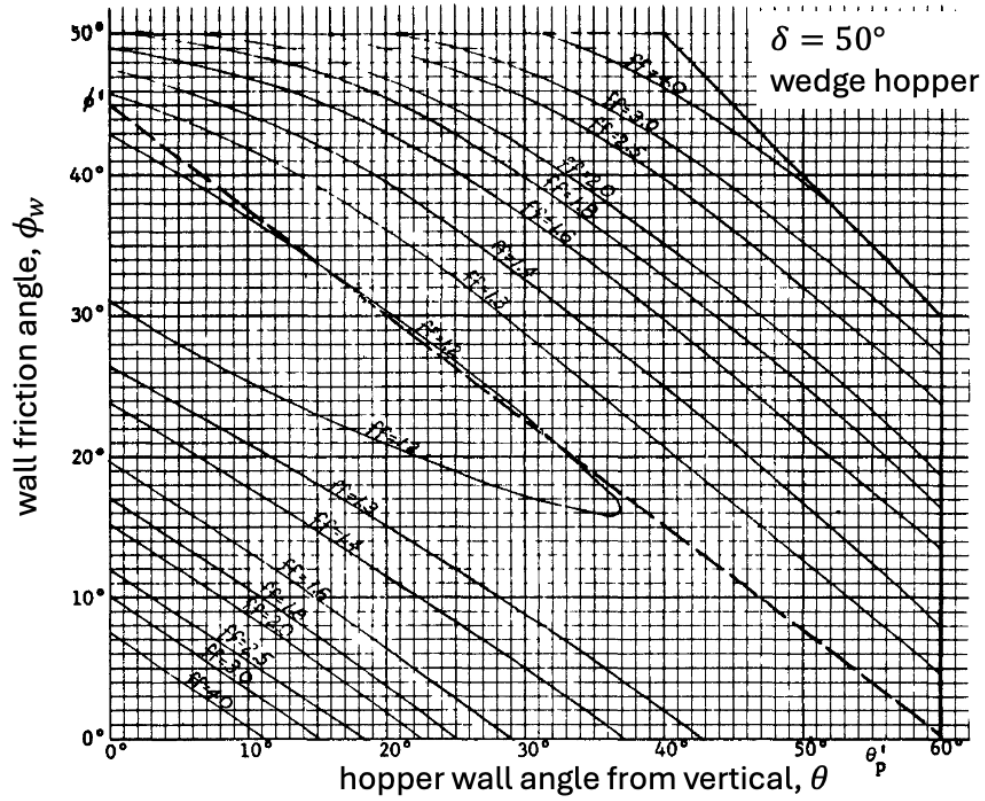
Figure 9.21. The Jenike design chart for determining the maximum hopper wall half angle to produce mass flow for a material with an effective angle of internal friction of $\delta = 50°$ in a wedge hopper. The "ff" in the plot is the hopper flow factor (hff). This design chart is from Jenike [2].
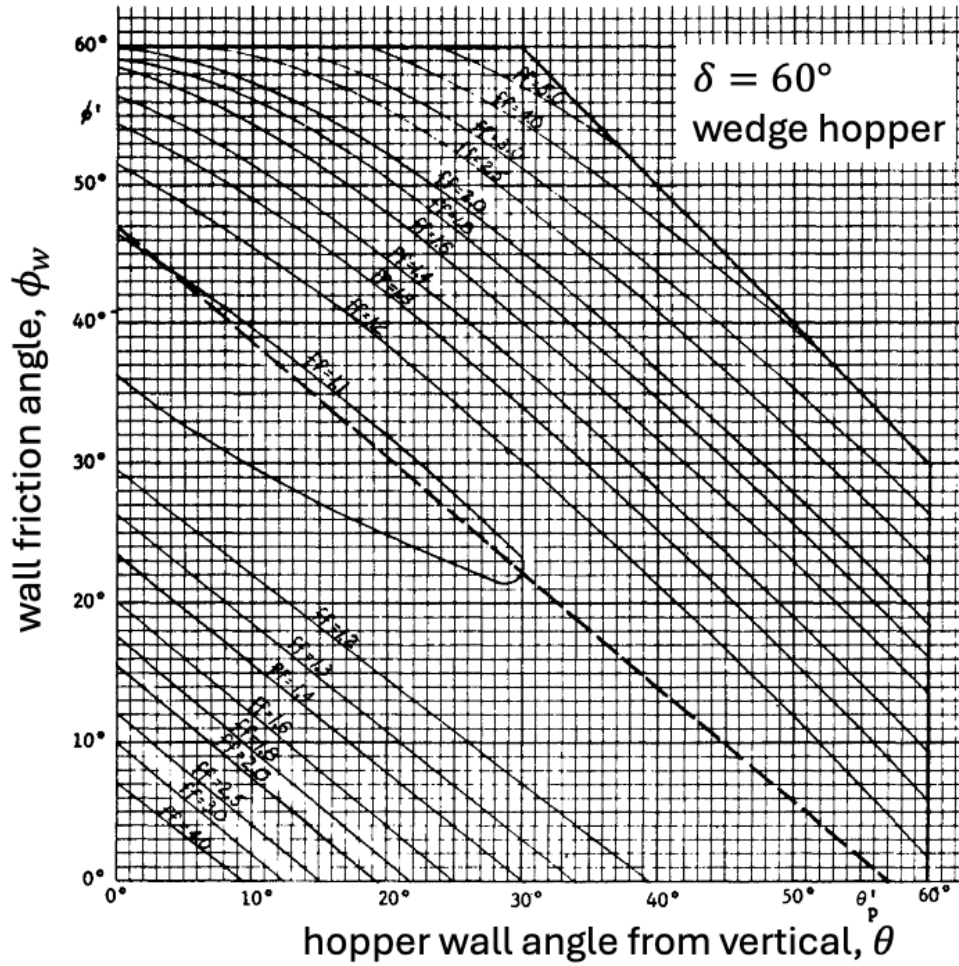
FIGURE 9.22. The Jenike design chart for determining the maximum hopper wall half angle to produce mass flow for a material with an effective angle of internal friction of $\delta = 60°$ in a wedge hopper. The "ff" in the plot is the hopper flow factor (hff). This design chart is from Jenike [2].
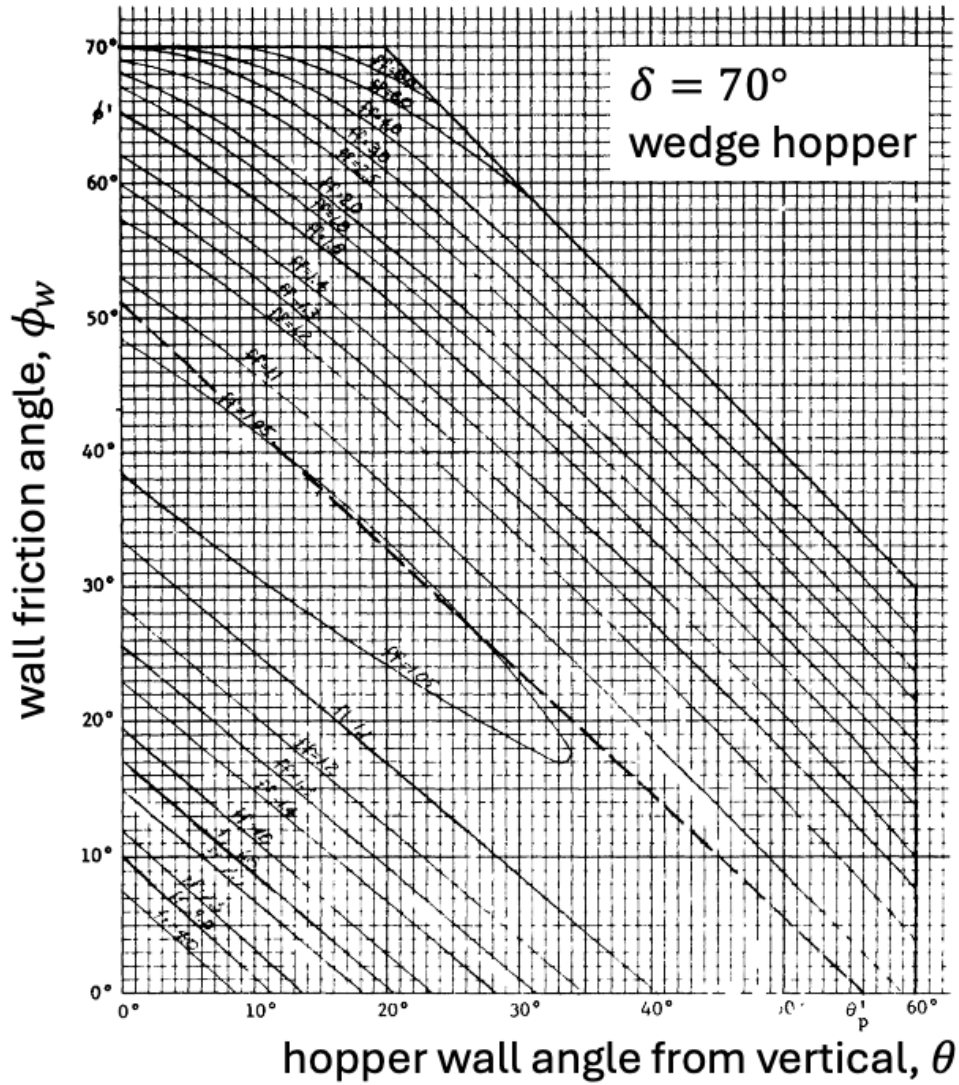
FIGURE 9.23. The Jenike design chart for determining the maximum hopper wall half angle to produce mass flow for a material with an effective angle of internal friction of $\delta = 70°$ in a wedge hopper. The "ff" in the plot is the hopper flow factor (hff). This design chart is from Jenike [2].

You are contracted to design a conical hopper through which a material with a bulk density of 1700 kg/m^3 and an effective angle of internal friction of 40º can be emptied safely. The hopper is constructed of a material that gives a wall friction angle of 20º. Four sets of shear tests have been conducted on the material and the results for the material flow function are listed in the table below and are shown in the attached plot.

consolidation stress [kPa]	1.1	1.75	2.75	3.25
unconfined yield strength [kPa]	0.9	1.35	1.75	1.95
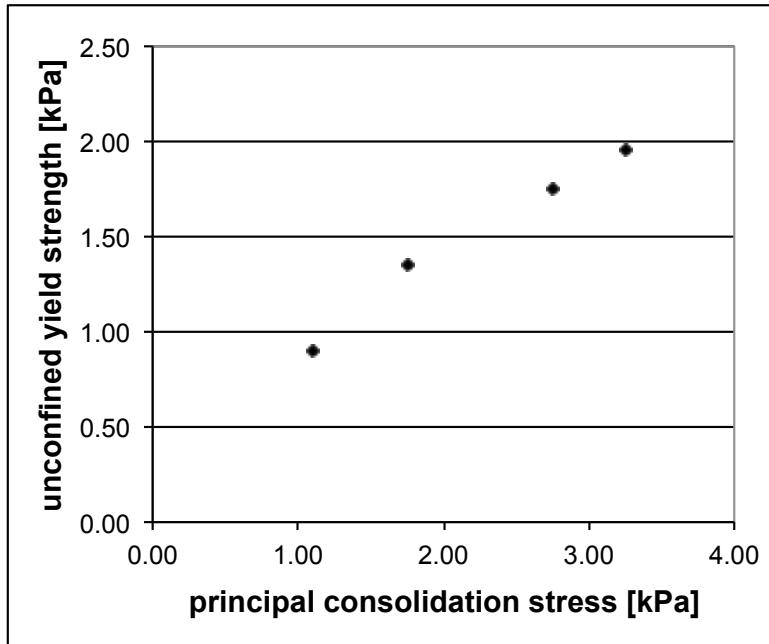
a. Determine the maximum hopper wall angle (measured from the vertical) to ensure mass flow.
b. Determine the minimum hopper exit diameter to avoid bridging.

SOLUTION
Using a design chart (Figure 1) for a conical hopper with an effective angle of internal friction of $\delta = 40°$ and a wall friction angle of $\phi_w = 20°$, the minimum wall angle to ensure mass flow (including a 3° safety factor) is $\theta = 25°$. The hopper flow factor, also read from the design chart, is hff ≈ 1.47.

The minimum hopper exit diameter to avoid bridging is given by:

$$D_{min} = H(\theta)\frac{CAS}{\rho_b g} \tag{1}$$

where $H(\theta) \approx 2.39$ (found from design chart Fig. 2), $\rho_b = 1700$ kg/m^3, and $g = 9.81$ m/s^2. The critical applied stress (CAS) is found from the intersection of the powder's flow function and the inverse of the hopper flow factor as shown in Fig. 4 $\Rightarrow$ CAS ≈ 1.7 kPa. Thus, the minimum exit diameter is: $D_{min} = 0.24$ m.
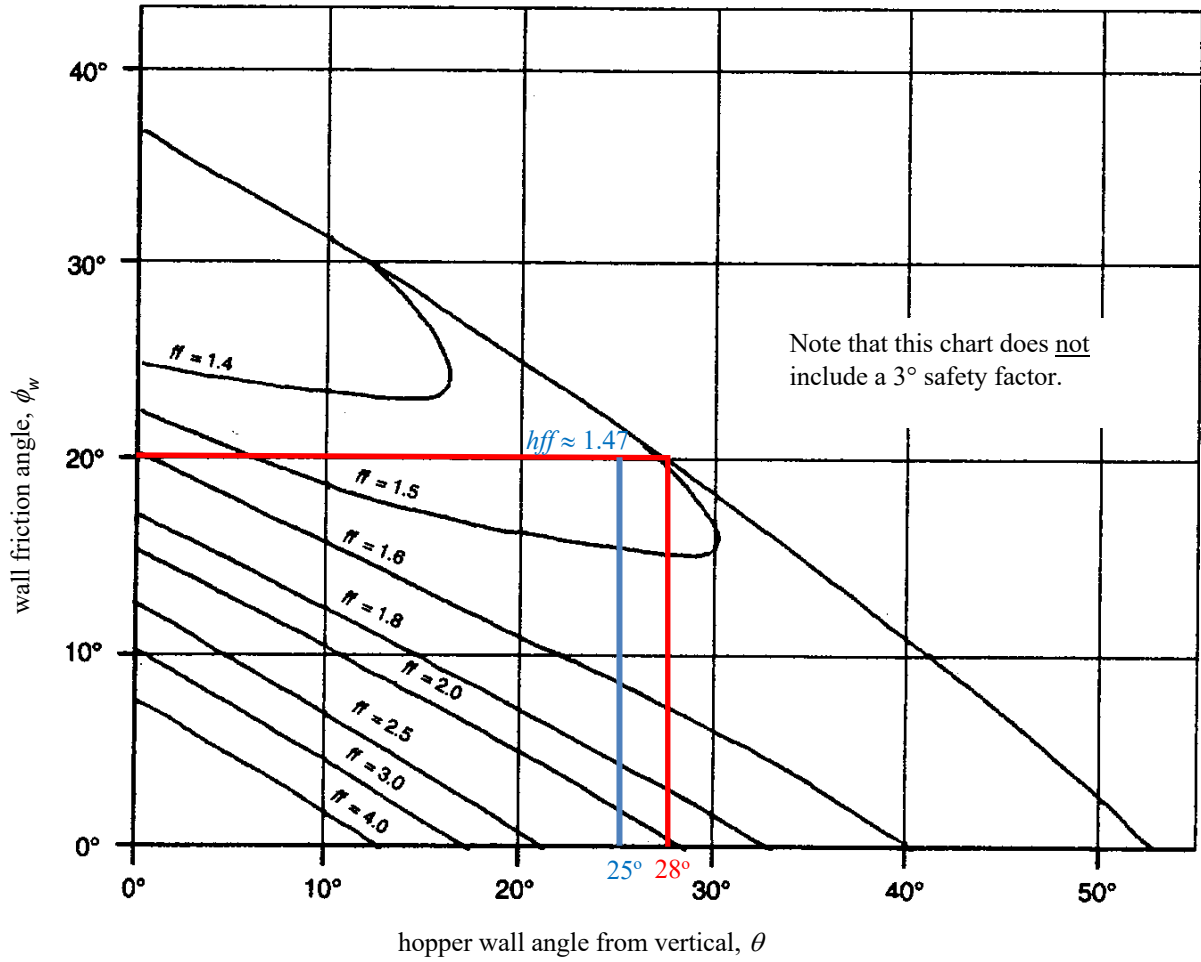
Figure 1. Conical hopper design chart for a powder with an effective angle of internal friction of δ = 40°.

The chart shows:
- Vertical axis: wall friction angle, ϕ_w (0° to 40°)
- Horizontal axis: hopper wall angle from vertical, θ (0° to 50°)
- Contour lines labeled: ff = 1.4, ff = 1.5, ff = 1.6, ff = 1.8, ff = 2.0, ff = 2.5, ff = 3.0, ff = 4.0
- Note that this chart does not include a 3° safety factor.
- $hff \approx 1.47$
- Markings at 25° and 28°

hopper wall angle from vertical, θ
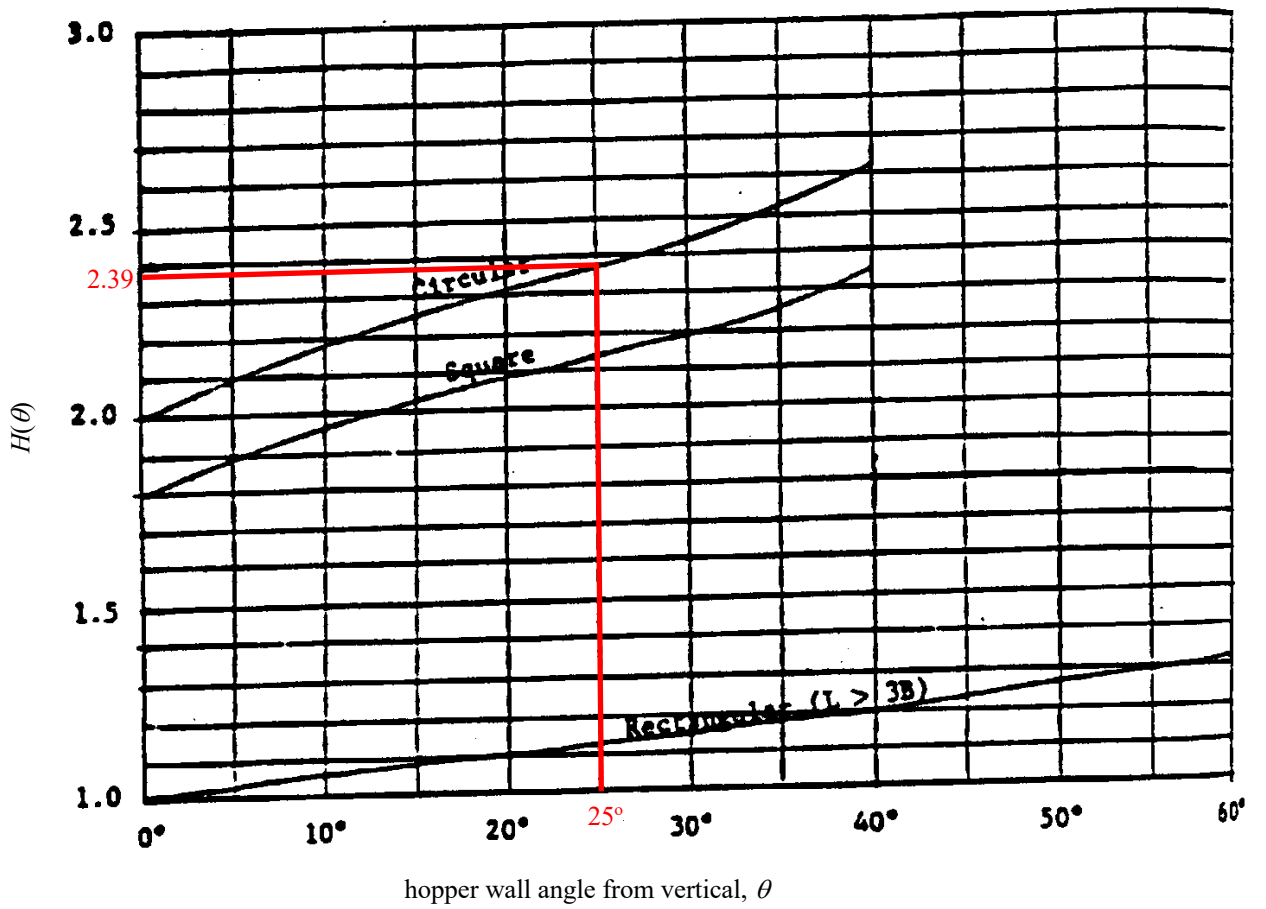
Figure 2. Minimum outlet diameter function $H(\theta)$ design chart.
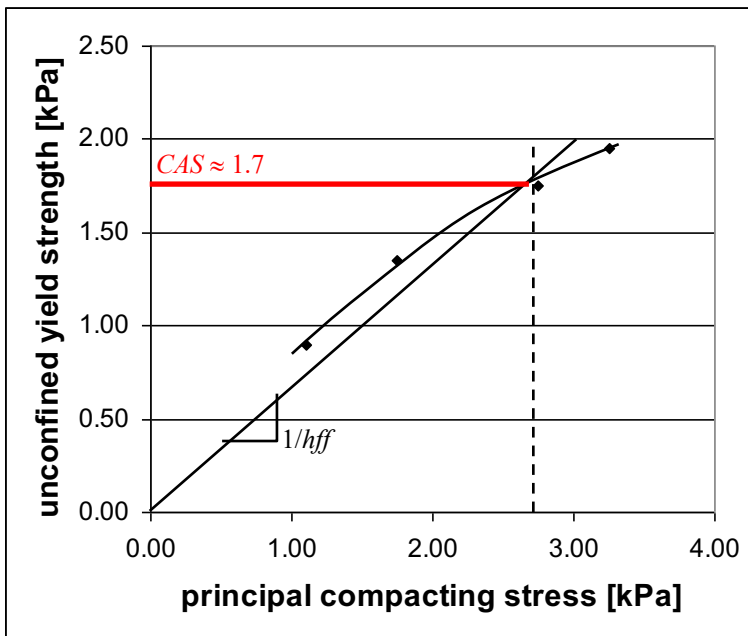
Note:
$1/hff = 1/1.47 = 0.680$

Figure 3. Plot to determine the critical applied stress (CAS).

Design a mass flow, slot hopper with a rectangular exit ($L > 3B$) for coal with the following testing data and a (constant) wall friction angle of $\phi_w = 18°$.

σ_1 [Pa]	f_c [Pa]	ρ_b [kg/m³]	δ [deg]
3175	2104	717	57
6541	3719	734	54
21204	9718	813	49
36026	14532	853	45

[This example problem was originally developed by K. Jacob and M. Kodam at Dow Chemical.]

SOLUTION:

For convenience, fit the mFF (f_c as a function of σ_1) to a quadratic curve,
$$f_c = (-2.979 * 10^{-6})\sigma_1^2 + (4.944 * 10^{-1})\sigma_1 + (5.847 * 10^2),$$ (1)
where σ_1 and f_c are in Pa.
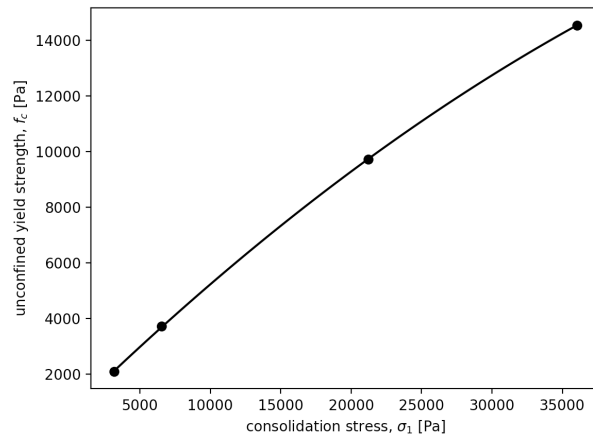
Fit the bulk density as a function of the consolidation stress to a power law curve,
$$\rho_b = (3.869 * 10^2)\sigma_1^{7.481*10^{-2}},$$ (2)
where ρ_b is in kg/m³.
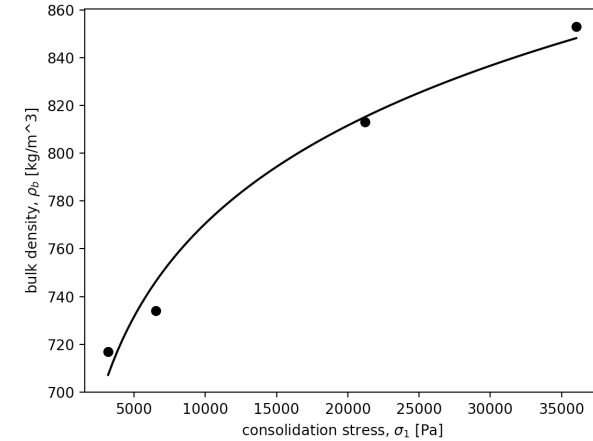
Lastly, fit the effective angle of internal friction as a function of the consolidation stress using an asymptoting exponential curve,

$$\delta = (40.36° - 58.59°)[1 - \exp(-3.719 * 10^{-5}\sigma_1)] + 58.59°, \tag{3}$$

where δ is in degrees and σ_1 is in Pa.
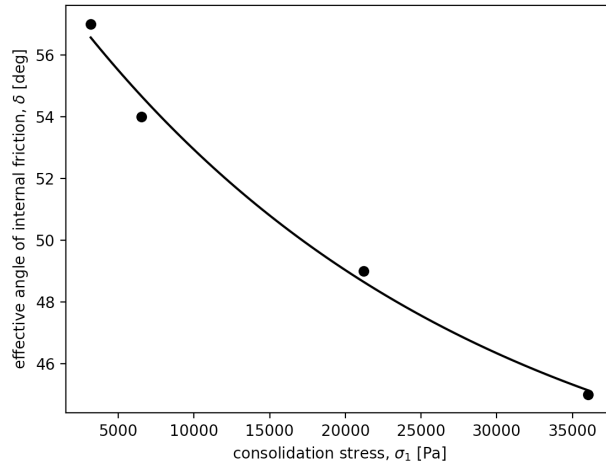
Since the properties are functions of the consolidation stress (σ_1), an iterative solution will be needed. The following algorithm has been used and implemented in a Python program provided at the end of this solution.

1. Make an initial guess for the consolidation stress (σ_1) corresponding to the critical applied stress (CAS).
2. Calculate the effective angle of internal friction (δ) using Eq. (3).
3. Calculate the minimum hopper half angle from the vertical (θ) to ensure mass flow.
4. Calculate the hopper flow factor (hff)
5. Determine the consolidation stress corresponding to the critical applied stress using,

$$mFF(\sigma_1) = \frac{1}{hff}\sigma_1. \tag{4}$$

6. Is the σ_1 in Step 4 the same as the σ_1 in Step 1? If not, then use the σ_1 from Step 4 as the new value for σ_1 and go to Step 2. If the two values for σ_1 are sufficiently close, then proceed to Step 6.
7. Calculate the critical applied stress (CAS),

$$CAS = mFF(\sigma_1) = \frac{1}{hff}\sigma_1. \tag{5}$$

8. Calculate the bulk density (ρ_b) corresponding to this σ_1 using Eq. (2).
9. Calculate the function $H(\theta)$ using,

$$H(\theta) = 1 + \frac{\theta}{180°}. \tag{6}$$

10. Calculate the minimum exit width to avoid cohesive bridging,

$$B_{\min} = H(\theta)\frac{CAS}{\rho_b g}. \tag{7}$$

Using the algorithm,

σ_1 = 1480 Pa,
CAS = 1310 Pa,
θ = 37.0°,
δ = 57.6°,
hff = 1.13,
ρ_b = 668 kg/m³,
$H(\theta)$ = 1.21
$B_{\min}$ = 0.24 m.

Note that the converged value of σ_1 is smaller than the values in the given table. Thus, we extrapolated parameter values, which is not ideal. It would have been better to obtain experimental data in the table at smaller consolidation stresses to improve confidence in the predictions.

The following Python code was used to perform the calculations.

```python
# hopper_design_11.py

import numpy as np
import matplotlib.pyplot as plt
from scipy.optimize import curve_fit
from scipy.optimize import fsolve

def H(theta):  # theta in degrees
    # A function to calculate the pre-factor for the minimum outlet dimension.
    return(1+theta/180)

def Slot_thetacrit(delta, phiw):  # angles in degrees
    # Calculate the critical half angle from the vertical for a wedge hopper.
    # Found using the expressions in Arnold and McLean (1976).

    return(60.5 + np.degrees(np.arctan((50 - delta)/7.73))/15.07)*(1-phiw/(42.3 +
0.131*np.exp(0.06)*delta))

def Slot_hff(delta, phiw, theta):  # angles in degrees
    # Calculate the hopper flow factor for a wedge hopper.
    # Found using the expressions in Arnold and McLean (1976).
    m = 0  # slot hopper

    phiw_rad = np.radians(phiw)
    sin_delta = np.sin(np.radians(delta))
    sin_phiw = np.sin(np.radians(phiw))
    theta_rad = np.radians(theta)
    sin_theta = np.sin(theta_rad)

    beta_rad = 0.5*(phiw_rad + np.arcsin(sin_phiw/sin_delta))
    X = ((2**m)*sin_delta)/(1-sin_delta)*(np.sin(2*beta_rad+theta_rad)/sin_theta + 1)
    Y = (((2*(1-np.cos(beta_rad+theta_rad)))**m) * ((beta_rad+theta_rad)**(1-m)) * np.sin(theta_rad) +
np.sin(beta_rad)*(np.sin(beta_rad+theta_rad))**(1+m)) / ((1-
sin_delta)*(np.sin(beta_rad+theta_rad))**(2+m))
    H_theta = H(theta)

    hff = H_theta*(Y*(1+sin_delta))/(2*(X-1)*sin_theta)
    return(hff)

def mFF(sigma1, mFF_c0, mFF_c1, mFF_c2):
    # The material flow function fit with a quadratic equation. mFF_c0, mFF_c1, and mFF_c2 are fit
parameters
    return(mFF_c2*sigma1**2 + mFF_c1*sigma1 + mFF_c0)

def compressibility(sigma1, rhob_c, rhob_n):
    # The bulk density as a function of the consolidation stress, fit with a power law.  rhob_c and
rhob_n are fit parameters.
    return(rhob_c*sigma1**rhob_n)

def eff_friction(sigma1, delta0, delta_inf, delta_beta):
    # The effective friction angle as a function of the consolidation stress, fit with an asymptoting
exponential function.  delta_0, delta_inf, and delta_beta are fit parameters.
    return((delta_inf-delta0)*(1-np.exp(-delta_beta*sigma1))+delta0)

def CAS_fcn(sigma1, mFF_c0, mFF_c1, mFF_c2, hff):
    # The function for finding the critical applied stress:  mFF = sigma1/hff
    return(mFF(sigma1, mFF_c0, mFF_c1, mFF_c2) - sigma1/hff)

g = 9.81  # gravitational acceleration [m/s^2]
phiw = 18  # the given wall friction angle [deg]
# The given data:  sigma1 [Pa], fc [Pa], rhob [kg/m^3], delta [deg]
data = np.array([[3175, 2104, 717, 57],
                 [6541, 3719, 734, 54],
                 [21204, 9718, 813, 49],
                 [36026, 14532, 853, 45]])
```

```python
    # Obtain single arrays for each parameter.
    sigma1 = data[:,0]
    fc = data[:,1]
    rhob = data[:,2]
    delta = data[:,3]

    # First, find the fitting parameters for the mFF.
    popt, pcov = curve_fit(mFF, sigma1, fc)
    mFF_c0, mFF_c1, mFF_c2 = popt
    print('mFF fit parameters: (mFF_c0, mFF_c1, mFF_c2) = (%.3e, %.3e, %.3e)' % (mFF_c0, mFF_c1, mFF_c2))

    # Now find the fitting parameters for the compressibility.
    popt, pcov = curve_fit(compressibility, sigma1, rhob)
    rhob_c, rhob_n = popt
    print('compressibility fit parameters: (rhob_c, rhob_n) = (%.3e, %.3e)' % (rhob_c, rhob_n))

    # Lastly, find the fitting parameters for the effective internal friction angle.
    popt, pcov = curve_fit(eff_friction, sigma1, delta, p0=(delta[0], delta[-1], 1e-4))  # make an initial
    guess based on the end points of the data
    delta0, delta_inf, delta_beta  = popt
    print('effective friction angle fit parameters: (delta0, delta_inf, delta_beta) = (%.3e, %.3e, %.3e)'
    % (delta0, delta_inf, delta_beta))

    # Plot the given data and curve fits.
    sigma1_fit = np.linspace(np.amin(sigma1), np.amax(sigma1), 100)  # sigma1 values to make the fitting
    curve smooth
    plt.plot(sigma1, fc, color='k', marker='o', linestyle='')
    plt.plot(sigma1_fit, mFF(sigma1_fit, mFF_c0, mFF_c1, mFF_c2), color='k', marker='', linestyle='-')
    plt.xlabel('consolidation stress, $\sigma_1$ [Pa]')
    plt.ylabel('unconfined yield strength, $f_c$ [Pa]')
    plt.show()

    plt.plot(sigma1, rhob, color='k', marker='o', linestyle='')
    plt.plot(sigma1_fit, compressibility(sigma1_fit, rhob_c, rhob_n), color='k', marker='', linestyle='-')
    plt.xlabel('consolidation stress, $\sigma_1$ [Pa]')
    plt.ylabel('bulk density, $\\rho_b$ [kg/m^3]')
    plt.show()

    plt.plot(sigma1, delta, color='k', marker='o', linestyle='')
    #delta0, delta_inf, delta_beta = [57, 45, 0.0001]
    plt.plot(sigma1_fit, eff_friction(sigma1_fit, delta0, delta_inf, delta_beta), color='k', marker='',
    linestyle='-')
    plt.xlabel('consolidation stress, $\sigma_1$ [Pa]')
    plt.ylabel('effective angle of internal friction, $\delta$ [deg]')
    plt.show()

    # Iterate to find the consolidation stress.
    sigma1_new = 1000  # Make an initial guess for the consolidation stress [Pa].
    sigma1 = 0  #  Set the 'old' sigma1 so we go through the following loop at least once.

    while (not np.isclose(sigma1, sigma1_new, rtol=1e-3)):  # Are the old and new sigma1 values
    significantly different?
        sigma1 = sigma1_new
        # Calculate the effective friction angle.
        delta = eff_friction(sigma1, delta0, delta_inf, delta_beta)
        # Calculate the critical hopper angle.
        theta = Slot_thetacrit(delta, phiw)
        # Calculate the hopper flow factor.
        hff = Slot_hff(delta, phiw, theta)
        print('(sigma1, delta, theta, hff) = (%.3f Pa, %.3f deg, %.3f deg, %.2f)' % (sigma1, delta, theta,
    hff))

        # Find the consolidation stress at the critical applied stress.
        sigma1_new = fsolve(CAS_fcn, x0=sigma1, args=(mFF_c0, mFF_c1, mFF_c2, hff))  # use sigma1 as an
    initial guess
        print('sigma1_new = %.3f Pa' % sigma1_new)

    # We now have a converged consolidation stress.  Calculate the critical applied stress.
    print('Converged values:')
```

```
CAS = mFF(sigma1_new, mFF_c0, mFF_c1, mFF_c2)
print('(sigma1_new, CAS) = (%.3f, %.3f) Pa' % (sigma1_new, CAS))
# Calculate the critical wall angle.
theta = Slot_thetacrit(delta, phiw)
print('theta = %.3f deg' % theta)
# Calculate the effective angle of internal friction.
print('delta = %.3f deg' % eff_friction(sigma1_new, delta0, delta_inf, delta_beta))
# Calculate the hopper flow factor.
hff = Slot_hff(delta, phiw, theta)
print('hff = %.3f' % hff)
# Calculate the bulk density.
rhob = compressibility(sigma1_new, rhob_c, rhob_n)
print('rhob = %.3f kg/m^3' % rhob)
# Calculate the function H(theta)
H_theta = H(theta)
print('H(theta) = %.3f' % H_theta)
# Calculate the minimum exit opening.
Bmin = H_theta*CAS/(rhob*g)
print('Bmin = %.3f m' % Bmin)
```

Running the Python code produces the following output:

```
>> python3 ./hopper_design_11.py
mFF fit parameters: (mFF_c0, mFF_c1, mFF_c2) = (5.847e+02, 4.944e-01, -2.979e-06)
compressibility fit parameters: (rhob_c, rhob_n) = (3.869e+02, 7.481e-02)
effective friction angle fit parameters: (delta0, delta_inf, delta_beta) = (5.859e+01, 4.036e+01,
3.719e-05)
(sigma1, delta, theta, hff) = (1000.000 Pa, 57.927 deg, 36.925 deg, 1.13)
sigma1_new = 1468.828 Pa
(sigma1, delta, theta, hff) = (1468.828 Pa, 57.624 deg, 36.956 deg, 1.13)
sigma1_new = 1480.596 Pa
(sigma1, delta, theta, hff) = (1480.596 Pa, 57.616 deg, 36.956 deg, 1.13)
sigma1_new = 1480.894 Pa
Converged values:
(sigma1_new, CAS) = (1480.894, 1310.327) Pa
theta = 36.956 deg
delta = 57.616 deg
hff = 1.130
rhob = 667.980 kg/m^3
H(theta) = 1.205
Bmin = 0.241 m
```

A wedge hopper with outlet dimensions of $(B, L)_{exit} = (0.5, 1.5)$ m has a half wall angle from the vertical of 45°. The rectangular bin section above the hopper has cross-sectional dimensions $(B, L)_{bin} = (1, 1.5)$ m. The hopper is used to store coal with the following properties. Assume the system has a constant wall friction angle of $\phi_w = 18°$ and a constant internal friction angle of $\phi = 35°$.

σ_1 [Pa]	f_c [Pa]	ρ_b [kg/m³]	δ [deg]
3175	2104	717	57
6541	3719	734	54
21204	9718	813	49
36026	14532	853	45

Use the following empirical fits to the table data,
$$f_c = (-2.979 * 10^{-6})\sigma_1^2 + (4.944 * 10^{-1})\sigma_1 + (5.847 * 10^2) \quad [\sigma_1 \text{ and } f_c \text{ are in Pa}],$$
$$\rho_b = (3.869 * 10^2)\sigma_1^{7.481*10^{-2}} \quad [\rho_b \text{ is in kg/m}^3].$$

a. Show that the hopper produces funnel flow.
b. Verify that the hopper outlet dimensions are sized to prevent cohesive bridging.
c. Calculate the maximum fill height of the hopper to ensure a rathole does not form.
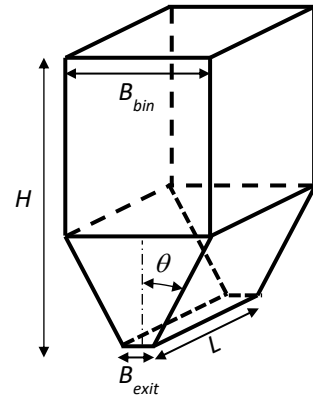
SOLUTION:
First, check to see if the hopper wall angle results in mass flow or funnel flow. Calculate the critical hopper half angle for this wedge hopper using the following plot.
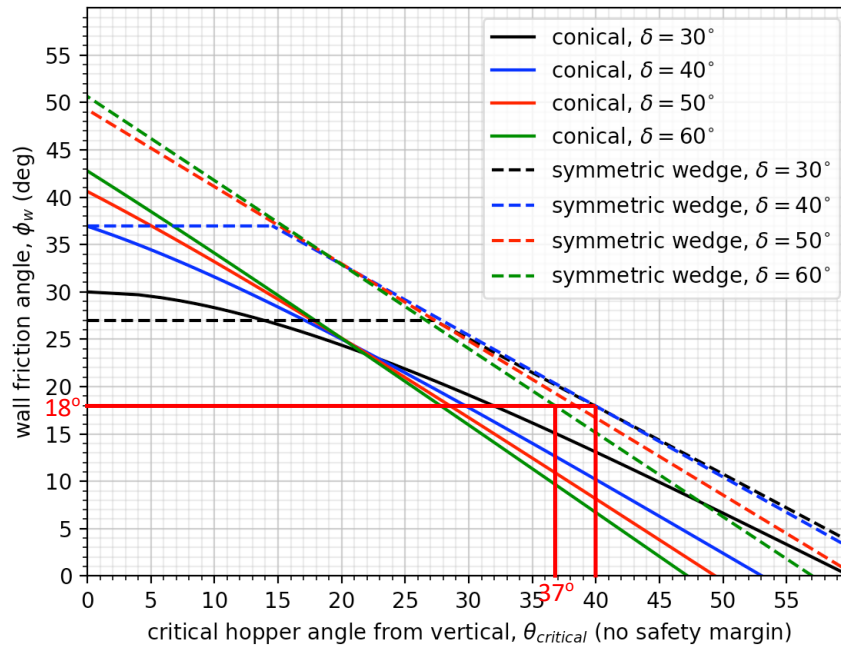
We observe that over the range $\delta = 40° - 60°$ the critical hopper wall half angle for mass flow in a wedge hopper is between 37° and 40°. Since the given hopper wall half angle is 45°, we conclude that the current wedge hopper produces funnel flow.

Since we have funnel flow, calculate the minimum exit dimension to avoid cohesive bridging. For funnel flow, assume a hopper flow factor of $hff = 1.7$. The consolidation stress and corresponding critical applied stress for this hopper flow factor and the given material flow function is,

$$mFF(\sigma_1) = \frac{1}{hff}\sigma_1 \quad \Rightarrow \quad \sigma_1 = 5329 \text{ Pa,}$$

(1)

$$CAS = \frac{1}{hff}\sigma_1 \quad \Rightarrow \quad CAS = 3135 \text{ Pa,}$$

(2)

Calculate the corresponding bulk density at this consolidation stress using the given compressibility expression,

$$\rho_b = 735.2 \text{ kg/m}^3.$$

Calculate the function $H(\theta)$ for a slot exit,

$$H(\theta) = 1 + \frac{\theta}{180°} \quad \Rightarrow \quad H(\theta) = 1.25.$$

(3)

Calculate the minimum exit dimension to avoid cohesive bridging in this funnel flow hopper,

$$B_{\text{min,exit}} = H(\theta)\frac{CAS}{\rho_b g} \quad \Rightarrow \quad B_{\text{min,exit}} = 0.543 \text{ m.}$$

(4)

Since the given hopper exit has $B_{\text{exit}} < B_{\text{min,exit}}$, we conclude that cohesive bridging will not occur.

Now determine the maximum fill level to avoid the formation of a rathole. Note that for the given bin dimensions,

$$D_{H,\text{bin}} = \frac{4A_{\text{bin}}}{P_{\text{bin}}} = \frac{4B_{\text{bin}}L_{\text{bin}}}{2(B_{\text{bin}}+L_{\text{bin}})} \quad \Rightarrow \quad D_{H,\text{bin}} = 1.200 \text{ m.}$$

(5)

In addition, the exit diagonal dimension is,

$$D_{\text{diag,exit}} = \sqrt{B_{\text{exit}}^2 + L_{\text{exit}}^2} \quad \Rightarrow \quad D_{\text{diag,exit}} = 1.581 \text{ m.}$$

(6)

Determine the consolidation stress that gives,

$$D_{\text{diag,exit}} = D_{rh} = G(\phi)\frac{f_c}{\rho_b g} \quad \Rightarrow \quad \sigma_1 = 6951 \text{ Pa, } f_c = 3877 \text{ Pa, and } \rho_b = 749.9 \text{ kg/m}^3,$$

(7)

where $f_c = mFF(\sigma_1)$ and $\rho_b = \text{fcn}(\sigma_1)$ are the functions given in the problem statement and,

$$G(\phi) = 4.3\tan\phi.$$

(8)

Use a numerical method to find this consolidation stress.

Now solve for the depth H_{max} corresponding to this consolidation stress and bulk density (Eq. (7)) using the following Janssen equation,

$$\sigma_1 = \frac{\rho_B g D_{H,\text{bin}}}{4K_A \tan\phi_w}\left[1 - \exp\left(-4K_A \tan\phi_w \frac{H_{\text{max}}}{D_{H,\text{bin}}}\right)\right] \quad \Rightarrow \quad H_{\text{max}} = 1.21 \text{ m,}$$

(9)

where $D_{H,\text{bin}}$ is given in Eq. (5) and $K_A = 0.4$. Although this function can be solved analytically, a numerical algorithm was used here to solve it.

Thus, to avoid the formation of rathole, the hopper should be filled to a depth of no more than $\boxed{H_{\text{max}} = 1.21 \text{ m}}$. Note that there may be other iterative schemes that can be used to determine this maximum depth.

The following Python code was used to perform the calculations.

```
# hopper_design_12.py

import numpy as np
import matplotlib.pyplot as plt
from scipy.optimize import fsolve

def H(theta):  # theta in degrees
    # A function to calculate the pre-factor for the minimum outlet dimension.
    return(1+theta/180)

def Slot_thetacrit(delta, phiw):  # angles in degrees
    # Calculate the critical half angle from the vertical for a wedge hopper.
    # Found using the expressions in Arnold and McLean (1976).

    return(60.5 + np.degrees(np.arctan((50 - delta)/7.73))/15.07)*(1-phiw/(42.3 +
0.131*np.exp(0.06)*delta))

def Slot_hff(delta, phiw, theta):  # angles in degrees
    # Calculate the hopper flow factor for a wedge hopper.
    # Found using the expressions in Arnold and McLean (1976).
    m = 0  # slot hopper

    phiw_rad = np.radians(phiw)
    sin_delta = np.sin(np.radians(delta))
    sin_phiw = np.sin(np.radians(phiw))
    theta_rad = np.radians(theta)
    sin_theta = np.sin(theta_rad)

    beta_rad = 0.5*(phiw_rad + np.arcsin(sin_phiw/sin_delta))
    X = ((2**m)*sin_delta)/(1-sin_delta)*(np.sin(2*beta_rad+theta_rad)/sin_theta + 1)
    Y = (((2*(1-np.cos(beta_rad+theta_rad)))**m) * ((beta_rad+theta_rad)**(1-m)) * np.sin(theta_rad) +
np.sin(beta_rad)*(np.sin(beta_rad+theta_rad))**(1+m)) / ((1-
sin_delta)*(np.sin(beta_rad+theta_rad))**(2+m))
    H_theta = H(theta)

    hff = H_theta*(Y*(1+sin_delta))/(2*(X-1)*sin_theta)
    return(hff)

def mFF(sigma1):
    # The material flow function fit with a quadratic equation.
    # consolidation stress in [Pa]
    # return fc in [Pa]
    return((-2.979e-6)*sigma1**2 + (4.944e-1)*sigma1 + (5.847e2))

def compressibility(sigma1):
    # The bulk density as a function of the consolidation stress.
    # consolidation stress in [Pa]
    # returns bulk density in [kg/m^3]
    return((3.869e2)*sigma1**(7.481e-2))

def eff_friction(sigma1):
    # The effective friction angle as a function of the consolidation stress.
    # consolidation stress in [Pa]
    # returns delta in [deg]
    return((-18.23)*(1-np.exp((-3.719e-5)*sigma1))+58.59)

def CAS_fcn(sigma1, hff):
    # The function for finding the critical applied stress:  mFF = sigma1/hff
    # consolidation stress in [Pa] and hff is dimensionless
    # returns the CAS in [Pa]
    return(mFF(sigma1) - sigma1/hff)

def G(phi):
    # The pre-factor for the critical rathole diameter calculation.
    # phi in [deg]
    # returns a dimensionless value
    return(4.3*np.tan(np.radians(phi)))
```

```
def D_rh_fcn(sigma1, D_diagexit, G_phi):
    # The function for finding the consolidation stress to satisfy:  D_rh = D_diagexit.
    # sigma1 in [Pa], D_diagexit in [m], G_phi is dimensionless
    fc = mFF(sigma1)  # calculate the unconfined yield strength
    rhob = compressibility(sigma1)  # calculate the bulk density
    return(G_phi*fc/rhob/g - D_diagexit)

def Janssen_fcn(z, sigma1, D_Hbin, phiw, K_A):
    # Calculate the consolidation stress using an active Janssen expression.
    # z in [m], sigma1 in [Pa], D_H in [m], phiw in [deg], K_A is dimensionless
    rhob = compressibility(sigma1)  # calculate the bulk density
    tan_phiw = np.tan(np.radians(phiw))  # calculate the wall friction coefficient
    return(sigma1 - rhob*g*D_Hbin/4/K_A/tan_phiw*(1-np.exp(-4*K_A*tan_phiw*z/D_Hbin)))

g = 9.81  # gravitational acceleration [m/s^2]
theta = 45  # the given hopper wall half angle from vertical [deg]
phiw = 18  # the given wall friction angle [deg]
phi = 35  # the given material internal friction angle [deg]
B_exit = 0.5  # exit short dimension [m]
L_exit = 1.5  # exit long dimension [m]
B_bin = 1.0  # bin short dimension [m]
L_bin = 1.5  # bin long dimension [m]

# First determine the minimum exit dimension to prevent cohesive bridging.
# Find the consolidation stress and corresponding critical applied stress using a hopper flow factor
of hff = 1.7 for funnel flow.
hff = 1.7
sigma1 = fsolve(CAS_fcn, x0=(5000), args=(hff))
CAS = mFF(sigma1)

# Calculate the minimum dimension pre-factor.
H_theta = H(theta)

# Calculate the bulk density.
rhob = compressibility(sigma1)

# Calculate the minimum dimension to avoid cohesive bridging.
B_minexit = H_theta*CAS/rhob/g
print('(sigma1, CAS, H(theta), rhob) = (%.3f, %.3f) Pa, %.3f, %.3f kg/m^3' % (sigma1, CAS, H_theta,
rhob))
print('B_minexit = %.3f m' % B_minexit)

# Calculate the bin hydraulic diameter.
D_Hbin = 4*(B_bin*L_bin)/(2*(B_bin+L_bin))
# Calculate the exit diagonal dimension.
D_diagexit = np.sqrt(B_exit**2 + L_exit**2)
print('(D_Hbin, D_diagexit) = (%.3f, %.3f) m' % (D_Hbin, D_diagexit))

G_phi = G(phi)
print('G(phi) = %.3f' % G_phi)

# Determine the consolidation stress corresponding to when D_rh = D_diagexit.
sigma1 = fsolve(D_rh_fcn, x0=(1000), args=(D_diagexit, G_phi))
fc = mFF(sigma1)
rhob = compressibility(sigma1)
print('(sigma1, fc, rhob) = (%.3f Pa, %.3f Pa, %.3f kg/m^3)' % (sigma1, fc, rhob))

# Determine the depth corresponding to this consolidation stress using a Janssen relation.
K_A = 0.4
H_max = fsolve(Janssen_fcn, x0=(1), args=(sigma1, D_Hbin, phiw, K_A))
print('H_max = %.3f m' % H_max)
```

Running the Python code produces the following output:
```
>> python3 ./hopper_design_12.py
(sigma1, CAS, H(theta), rhob) = (5329.425, 3134.956) Pa, 1.250, 735.177 kg/m^3
B_minexit = 0.543 m
(D_Hbin, D_diagexit) = (1.200, 1.581) m
```

```
G(phi) = 3.011
(sigma1, fc, rhob) = (6917.039 Pa, 3861.953 Pa, 749.658 kg/m^3)
H_max = 1.208 m
```

Bibliography

[1] A. Jenike, "Gravity flow of bulk solids (Bulletin 108)," Bulletin of the University of Utah, vol. 52, no. 29, Oct. 1961.

[2] ——, "Storage and flow of solids (Bulletin (123)," Bulletin of the University of Utah, vol. 53, no. 26, Nov. 1964.

[3] E. Benink, "Flow and stress analysis of cohesionless bulk materials in silos related to codes," Ph.D. dissertation, The University of Twente, Enschede, The Netherlands, 1990.

[4] S. Behara, S. Das, Z. Hatvani, and M. Paul, "Flowability studies of bulk materials for design of hopper using a jenike shear cell," Powder Handling and Processing, vol. 14, no. 2, pp. 96–101, 2002.

[5] P. Arnold and A. McLean, "Improved analytical flowfactors for mass-flow hoppers," Powder Technology, vol. 15, pp. 279–281, 1976.

[6] C. Woodcock and J. Mason, Bulk Solids Handling An Introduction to the Practice and Technology. Blackie Academic and Professional, 1987.

[7] K. Johanson, "Rathole stability analysis for aerated powder materials," Powder Technology, vol. 141, pp. 161–170, 2004.

[8] J. Hill and G. Cox, "Cylindrical cavities and classical rat-hole theory occurring in bulk materials," International Journal for Numerical and Analytical Methods in Geomechanics, vol. 24, pp. 971–990, 2000.

[9] G. Mehos, "Using solids flow property testing to design mass- and funnel-flow hoppers," Powder and Bulk Engineering, 2020.

[10] G. Mehos and D. Morgan, "Hopper design principles," Chemical Engineering, 2016. [Online]. Available: https://www.chemengonline.com/hopper-design-principles/?printmode=1.

CHAPTER 10

Mass Flow Rate from a Bin or Hopper

In this chapter we examine the discharge rate from a hopper. First, a simple dimensional analysis is performed. Next, analytical models for the flow rate are presented. Finally, the mass flow rate for fine (i.e., small) particles where fluid effects are significant is presented.

10.1. Dimensional Analysis

Consider the discharge of a deep bed of coarse ($> 400 \, \mu\text{m}$, so fluid effects are negligible), cohesionless particles from a conical hopper. The parameters expected to influence the mass flow rate of material from the hopper (W, with dimensions of mass over time, i.e., M/T) include the bulk density of material (ρ_b, with dimensions of M/L^3, where L is length), the acceleration due to gravity (g, with dimensions of L/T), the hopper exit diameter (D, with dimensions of L), the hopper wall angle from the vertical (θ, with no dimensions), the material effective angle of internal friction (δ, with no dimensions), the wall friction angle (ϕ_w, with no dimensions), and the particle size (d, with dimensions of L),

$$W = f_1(\rho_b, g, D, \theta, \delta, \phi_w, d), \tag{10.1}$$

where f_1 is an unknown function. Note that the height of material in the hopper doesn't play a role since, according to Janssen's analysis, the stresses in the powder are independent of the height for sufficiently large heights. Applying the Buckingham-Pi Theorem,

$$\Pi = N_d - N_p = 8 - 3 = 5, \tag{10.2}$$

where Π is the number of dimensionless terms that can be used to describe the original equation (Eq. (10.1)), N_d is the number of terms in the original dimensional equation (W, ρ_b, g, D, θ, δ, ϕ_w, d), and N_p is the number of reference dimensions required to describe these parameters (M, L, T). The hopper wall angle, effective angle of internal friction, and wall friction angle are already dimensionless, which leaves two remaining Π terms. Using ρ_b, g, and d as repeating variables, these two remaining terms are,

$$\Pi_1 = \frac{W}{\rho_b g^{1/2} D^{5/2}}, \tag{10.3}$$

$$\Pi_2 = \frac{D}{d}. \tag{10.4}$$

Thus, the original dimensional relation (Eq. (10.1)) may instead be written in dimensionless form as,

$$\frac{W}{\rho_b g^{1/2} D^{5/2}} = f_2 \left(\frac{D}{d}, \theta, \delta, \phi_w \right). \tag{10.5}$$

Note that the function f_2 is different than the function f_1, in general. Neither of these functions can be determined from dimensional analysis alone and instead must be found either through experiments or other analysis.

Notes:

   (1) Consider a simple model known as the <u>free fall arch</u> in which we assume particles fall with zero initial speed from a spherical arch located at the hopper exit (Figure 10.1). The speed of the particles
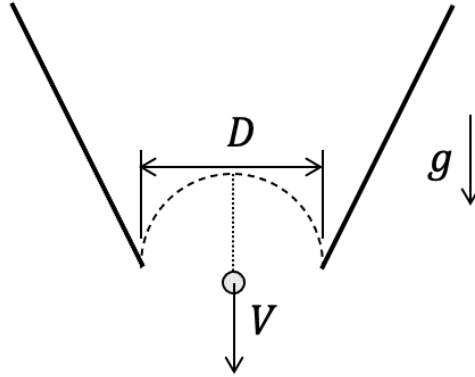
Figure 10.1. A sketch of the Free Fall Arch concept.
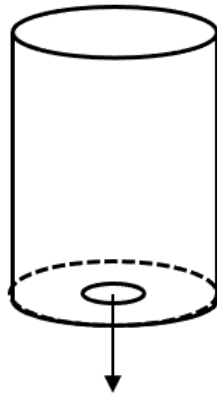
Figure 10.2. A sketch of a vertical cylindrical bin with a centered circular orifice – the Beverloo correlation geometry.

passing the exit plane is $V = \sqrt{2g(1/2D)} = \sqrt{gD}$ (balancing potential and kinetic energies). Thus, the mass flow rate from the hopper is,

$$W \propto \rho_b V D^2 = \rho_b g^{1/2} D^{5/2}, \tag{10.6}$$

which is consistent with the result from the dimensional analysis (Eq. (10.5)).

10.2. Beverloo's Correlation

Beverloo et al. [1] observed that mass flow rate experimental data for coarse, cohesionless particles from a cylindrical bin with a circular outlet (Figure 10.2) is fit well by the empirical relation,

$$\frac{W}{\rho_b g^{1/2} D^{5/2}} = c \left[1 - k \left(\frac{d}{D} \right) \right]^{5/2}, \tag{10.7}$$

or, in dimensional form,

$$W = c \rho_b g^{1/2} \left(D - kd \right)^{5/2}. \tag{10.8}$$

In the previous equations, c and k are fit parameters. These equations are known as the Beverloo Correlation. Note that Beverloo's correlation is consistent with the dimensional analysis performed in the previous section.

Notes:
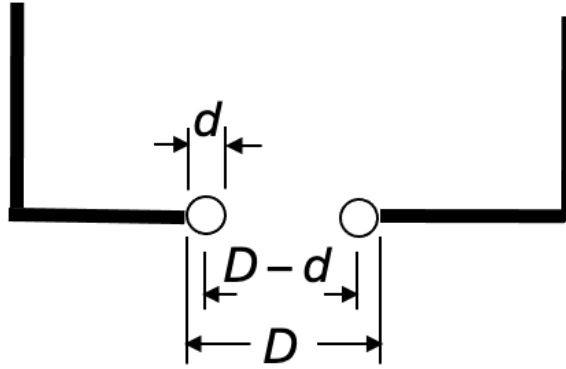
FIGURE 10.3. A sketch of the empty annulus concept.

(1) The bulk density should be the bulk density of the flowing material at the discharge plane. Since this value isn't typically known a priori, the loosely-filled, i.e., poured, bulk density is usually used. The predicted mass flow rate is typically within 5% of the measured value using this assumption [2].

(2) The constant c is reasonably approximated as $c \approx 0.58$, although very low friction materials may have larger values of c. There has been work on analytically deriving this constant, but it's outside the scope of these notes.

(3) The factor $D - kd$ accounts for the fact that the effective exit diameter through which particles flow is slightly smaller than the actual diameter due to the finite size of the particles. No particles can flow in the region located less than a particle radius next to the exit wall (Figure 10.3). In addition, the bulk density of the material is likely smaller near the exit edges due to dilation of the material at the walls. These phenomena are known as the empty annulus concept.

The parameter k depends on the geometry of the exit and the particle shape [3]. For spheres, a value of $k = 1.6$ should be used while for irregular shapes, a value of $k = 2.4$ is more appropriate.

(4) The Beverloo correlation is for coarse, cohesionless material that is unaffected by the surrounding fluid. A good rule of thumb is that the correlation can be used for particle sizes $> 400 \, \mu\text{m}$.

(5) Mechanical arches can form at the exit (non-cohesive arches) if the exit diameter is less than approximately $8 - 12$ particle diameters.

(6) The Beverloo correlation (Eq. (10.8)) is specifically for symmetric, flat-bottom bins with circular exits. For rectangular exits ($L > 3B$), Beverloo's correlation is,

$$W = 1.03\rho_b g^{1/2}(L - kd)(B - kd)^{3/2}. \tag{10.9}$$

Similar Beverloo correlation expressions for other geometries are listed in Table 10.1. Note that the expression for a rectangular exit in the table is equal to Eq. (10.9) in the limit as $L \gg B$.

(7) Although the Beverloo correlation is specifically for a flat-bottomed cylindrical bin, the expression can be modified to also work for symmetric hoppers. In these cases the constant c in the Beverloo correlation is a strong function of the hopper wall half angle measured from the vertical (θ). Rose and Tanaka [5] suggested the modified empirical correlation,

$$W = W_{\text{Beverloo}} F(\theta, \phi_d), \tag{10.10}$$

where W_{Beverloo} is the regular Beverloo correlation (Eq. (10.8)) and,

$$F(\theta, \phi_d) = \begin{cases} (\tan \theta)^{-0.35} & \theta \leq 90° - \phi_d \quad \text{(mass flow)}, \\ [\tan(90° - \phi_d)]^{-0.35} & \theta > 90° - \phi_d \quad \text{(funnel flow)} \end{cases} \tag{10.11}$$
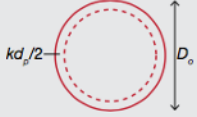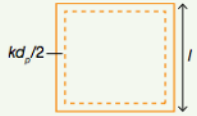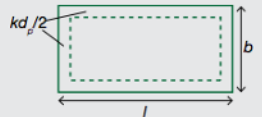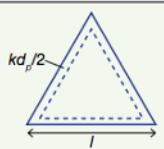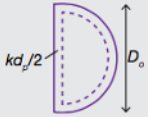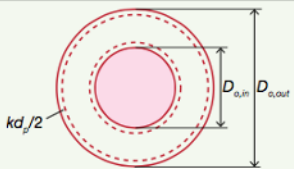
Table 4. Equations for calculating discharge rate through orifices of various shapes.	
Orifice Shape	**Discharge Rate Equation**
Circle	$W = C\rho_b \sqrt{g}\left(D_o - kd_p\right)^{5/2}$
Square	$W = \dfrac{4}{\pi} C\rho_b \sqrt{g}\left(l - kd_p\right)^{5/2}$
Rectangle	$W = \dfrac{4}{\pi} C\rho_b \left(b - kd_p\right)\left(l - kd_p\right)\sqrt{g\dfrac{2\left(b - kd_p\right)\left(l - kd_p\right)}{\left(b - kd_p\right)+\left(l - kd_p\right)}}$
Equlateral Triangle	$W = \dfrac{4}{\pi} C\rho_b \sqrt{g}\left[\dfrac{\sqrt{3}}{4}\left(l - \sqrt{3}kd_p\right)^2\right]\left[\dfrac{l - \sqrt{3}kd_p}{\sqrt{3}}\right]^{0.5}$
Semicircle	$W = \dfrac{4}{\pi} C\rho_b \sqrt{g}\left[\dfrac{\pi}{8}\left(D_o - kd_p\right)^2\right]\left[\dfrac{\dfrac{\pi}{2}\left(D_o - kd_p\right)^2}{\dfrac{\pi}{2}\left(D_o - kd_p\right)+\left(D_o - kd_p\right)}\right]^{0.5}$
Annulus	$W = C\rho_b \sqrt{g}\left[\left(D_{o,out} - \dfrac{kd_p}{2}\right)^2 - \left(D_{o,in} + \dfrac{kd_p}{2}\right)^2\right]\sqrt{D_{o,out} - D_{o,in} - kd_p}$

TABLE 10.1. Beverloo correlation style relations for estimating the mass flow rate through orifices of different geometries. This table is from Dhodapkar et al. [4].

The quantity ϕ_d is the angle between the stagnant zone boundary and the horizontal (Figure 10.4). Unfortunately, this angle typically needs to be determined experimentally. Nedderman [2] recommends using $\phi_d = 45°$ if no information is available so the previous expression becomes,

$$F(\theta, \phi_d) = \begin{cases} (\tan\theta)^{-0.35} & \theta \leq 90° - \phi_d \quad \text{(mass flow)}, \\ 1 & \theta > 90° - \phi_d \quad \text{(funnel flow)} \end{cases} \tag{10.12}$$

(8) Schulze and Schwedes [6] proposed a correlation for the mass flow rate from a vertically oriented outlet (Figure 10.5) similar to Beverloo's expression,

$$W = C_S \rho_b g^{1/2}(d_{SC} - kd)^{5/2}. \tag{10.13}$$

In this equation, the effective circular orifice diameter is,

$$d_{SC} = \cos\alpha(d_S - s\tan\alpha), \tag{10.14}$$

where d_S is the actual diameter of the outlet, s is the vertical wall thickness, and α is the angle between the upper free surface of the flowing material and the horizontal portion of the outlet. A summary of the measured constants k, C_S, and α for the materials they tested is given in Table 10.2.
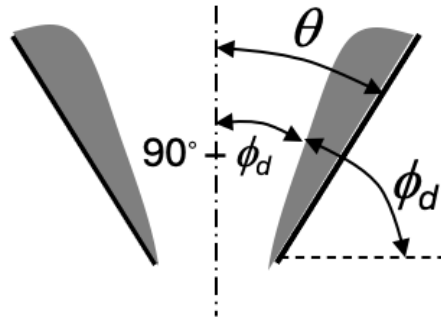
FIGURE 10.4. A sketch showing how the angle ϕ_d is defined in the Rose and Tanaka correlation.
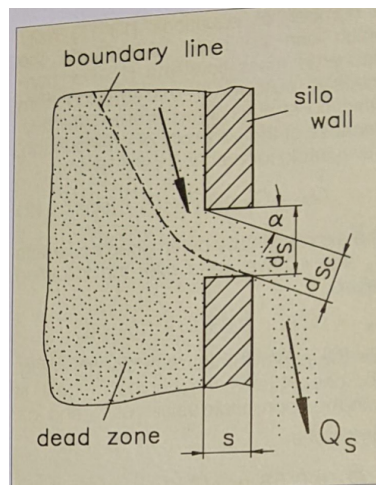
FIGURE 10.5. The geometry used in the empirical mass flow rate correlation for a vertically-oriented outlet. This figure is from Schulze and Schwedes [6].

Material	k	C_S	$\alpha\,(°)$
plastic pellets	1.7	0.298	28
brown coal coke	2.6	0.262	34
limestone	2.7	0.290	32
glass beads	1.5	0.345	22
rubber pellets	1.7	0.290	28

TABLE 10.2. Experimental values used in the empirical correlation for the mass flow rate through a vertically-oriented, circular outlet (Eq. (10.13)). These data are from Schulze and Schwedes [6].

10.3. Analytical Models

In addition to the empirical expressions developed by Beverloo and Rose and Tanaka, several researchers have also derived analytical models for the mass flow rate through a hopper. Several of these models are presented in this section.
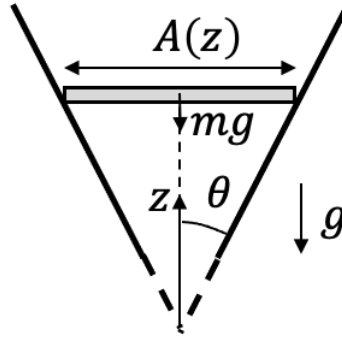
FIGURE 10.6. The geometry used in the Johanson [7] hopper flow rate analysis.

10.3.1. Johanson's Cohesionless Model

Johanson [7] developed an analytical model for a coarse, cohesive powder flowing through a hopper. The derivation for a cohesionless powder in a conical hopper (assuming the particle size is much smaller than the exit size) is given here, but the derivation for a cohesive powder is presented later in this section.

Apply Newton's Second Law in the vertical direction to a one-dimensional material element at the exit of a hopper (assume one-dimensional, uniform flow, Figure 10.6). Assume no forces act on the element other than weight since the powder is assumed to be in free fall at the exit,

$$\sum F_z = ma = -mg \implies a = -g. \tag{10.15}$$

From calculus, the acceleration of the material element may be written in terms of its speed as,

$$a = \frac{dv}{dt} = \frac{dv}{dz}\frac{dz}{dt} = v\frac{dv}{dz}. \tag{10.16}$$

Substituting this expression into the force balance,

$$v\frac{dv}{dz} = -g. \tag{10.17}$$

From Conservation of Mass, assuming a constant bulk density,

$$\rho_b v A = \text{constant} \implies v\frac{dA}{dz} + A\frac{dv}{dz} = 0 \implies \frac{dv}{dz} = -\frac{v}{A}\frac{dA}{dz}. \tag{10.18}$$

Substituting into the previous expression,

$$v\frac{v}{A}\frac{dA}{dz} = g. \tag{10.19}$$

For a conical hopper with a wall half angle from the vertical of θ,

$$\tan\theta = \frac{D/2}{z} \implies D = 2z\tan\theta \quad \text{or} \quad z = \frac{D}{2\tan\theta}, \tag{10.20}$$

$$A = \frac{\pi}{4}D^2 = \frac{\pi}{4}(2z\tan\theta)^2 \implies \frac{dA}{dz} = 2\pi z\tan^2\theta \implies \frac{1}{A}\frac{dA}{dz} = \frac{2}{z} = \frac{4\tan\theta}{D}. \tag{10.21}$$

Substitute these expressions into Eq. (10.19),

$$v^2 = \frac{gD}{4\tan\theta}. \tag{10.22}$$

Thus, the mass flow rate at the hopper exit (indicated by the subscript 'e') is,

$$W = \rho_b v_e A_e = \rho_b\sqrt{\frac{gD_e}{4\tan\theta}}\frac{\pi}{4}D_e^2 \implies \frac{W}{\rho_b g^{1/2} D_e^{5/2}} = \frac{\pi}{8}\frac{1}{\tan^{1/2}\theta}. \tag{10.23}$$

Notes:
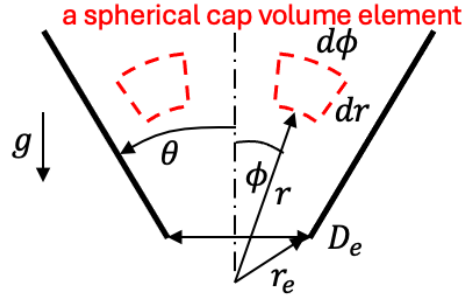
FIGURE 10.7. The geometry used in the Brown [8] and Carleton [9] hopper flow rate analyses.

(1) One could use $D_e - kd$ in place of D_e if particle size effects are significant.
(2) Johanson's analytical expression (Eq. (10.23)) is similar to the Beverloo/Rose and Tanaka empirical expressions (Eqs. (10.8) and (10.12)), except that in Beverloo's expression the leading constant is $c = 0.58$ while the Johanson's expression $\pi/8 \approx 0.39$ and the exponent in Rose and Tanaka's correlation is -0.35 while Johanson's exponent is -0.5.

10.3.2. Brown and Carleton's Cohesionless Models

Brown [8] and Carleton [9] developed analytical models similar to Johanson's, but assumed radial flow rather than purely vertical flow (Figure 10.7). For this model, assume a conical hopper, cohesionless particles and steady, incompressible, and radial flow toward the hopper apex. Also assume the particle size is much smaller than the exit size. From Conservation of Mass applied to a differential volume element,

$$\rho_b v(2\pi r^2 \sin\phi d\phi) = \rho_b (v + dv) \left[2\pi (r + dr)^2 \sin\phi d\phi \right], \tag{10.24}$$

$$vr^2 = (v + dv)\left[r^2 + 2rdr + (dr)^2 \right], \tag{10.25}$$

$$vr^2 = vr^2 + 2vrdr + v(dr)^2 + r^2 dv + 2rdvdr + dv(dr)^2, \tag{10.26}$$

$$0 = 2vrdr + r^2 dv, \tag{10.27}$$

$$\frac{dv}{dr} = -\frac{2v}{r}. \tag{10.28}$$

The (radial) acceleration of a material element may be written as,

$$\frac{dv}{dt} = \frac{dv}{dr}\frac{dr}{dt} = \frac{dv}{dr}v = -\frac{2v^2}{r}, \tag{10.29}$$

where the previous equation has been used. Since the net (radial) force on a material element is equal to the mass times the acceleration,

$$dF_{\text{net}} = (dm)\frac{dv}{dt} = -(dm)\frac{2v^2}{r}, \tag{10.30}$$

where $dm = \rho_b dV$ is the small mass in the small spherical cap volume element dV. Assuming only a net gravitational force acts in the radial direction at the exit (Figure 10.8),

$$-(dm)\frac{2v_{r_e}^2}{r_e} = -(dm)g\cos\phi, \tag{10.31}$$

$$\frac{2v_{r_e}^2}{r_e} = g\cos\phi \implies v_{r_e} = \sqrt{\frac{1}{2}gr_e\cos\phi}. \tag{10.32}$$

The exit diameter is,

$$D_e = 2r_2\sin\theta \implies r_e = \frac{D_e}{2\sin\theta}. \tag{10.33}$$
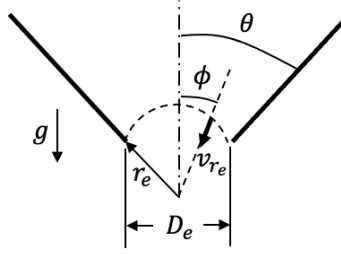
FIGURE 10.8. The exit geometry used in the Brown [8] and Carleton [9] hopper flow rate analyses.

Thus, the radial speed in the vicinity of the exit is,

$$v_{r_e} = \sqrt{\frac{gD_e \cos\phi}{4\sin\theta}}. \tag{10.34}$$

Note that experimental measurements show that this predicted velocity is inaccurate but, surprisingly, the predicted mass flow rate is reasonably predicted.

It is at this point the Brown [8] and Carleton [9] derivations diverge. Carleton assumed that ϕ is sufficiently small for mass flow to assume $\cos\phi \approx 1$. Thus, the mass flow rate is,

$$W = \rho_b v_{r_e} \frac{\pi}{4} D_e^2, \tag{10.35}$$

$$\frac{W_e}{\rho_b g^{1/2} D_e^{5/2}} = \frac{\pi}{8} \frac{1}{\sin^{1/2}\theta}. \tag{10.36}$$

This expression is similar to the one derived by Johanson [7] except Carleton has a $\sqrt{\sin\theta}$ while Johanson has a $\sqrt{\tan\theta}$. These trigonometric functions are similar, however, when θ is small.

In Brown's derivation, he found the mass flow rate by integrating the radial speed over the exit area taking into account the variation in ϕ,

$$W = \int_0^\theta \rho_b v_{r_e} 2\pi r_e^2 \sin\phi d\phi = \int_0^\theta \rho_b \sqrt{\frac{gD_e \cos\phi}{4\sin\theta}} 2\pi \left(\frac{D_e}{2\sin\theta}\right)^2 \sin\phi d\phi, \tag{10.37}$$

$$W = \frac{\pi}{4} \frac{\rho_b g^{1/2} D_e^{5/2}}{(\sin\theta)^{5/2}} \int_0^\theta \sqrt{\cos\phi} \sin\phi d\phi, \tag{10.38}$$

$$\frac{W}{\rho_b g^{1/2} D_e^{5/2}} = \frac{\pi}{6} \left[\frac{1 - (\cos\theta)^{3/2}}{(\sin\theta)^{5/2}}\right]. \tag{10.39}$$

Notes:

(1) Brown reported his expression as,

$$\frac{W}{\rho_b g^{1/2} D_e^{5/2}} = \frac{\pi}{4} \left[\frac{1 - (\cos\theta)^{1/2}}{\sqrt{2}(\sin\theta)^{3/2}}\right]. \tag{10.40}$$

This expression is numerically nearly identical to Eq. (10.39) but technically the two expressions are different. This author (Wassgren) is not sure how Eq. (10.40) was determined.

(2) Brown also derived an expression for a wedge-shaped hopper and found,

$$\frac{W_{\text{wedge}}}{\rho_b g^{1/2} L(B - kd)^{3/2}} = \frac{\theta^{1/2}}{\sqrt{2}\sin\theta}. \tag{10.41}$$

Comparisons of the various mass flow rate expressions presented in this chapter for coarse, cohesionless material in a conical hopper are shown in Figure 10.9. The analytical expressions are all nearly equal
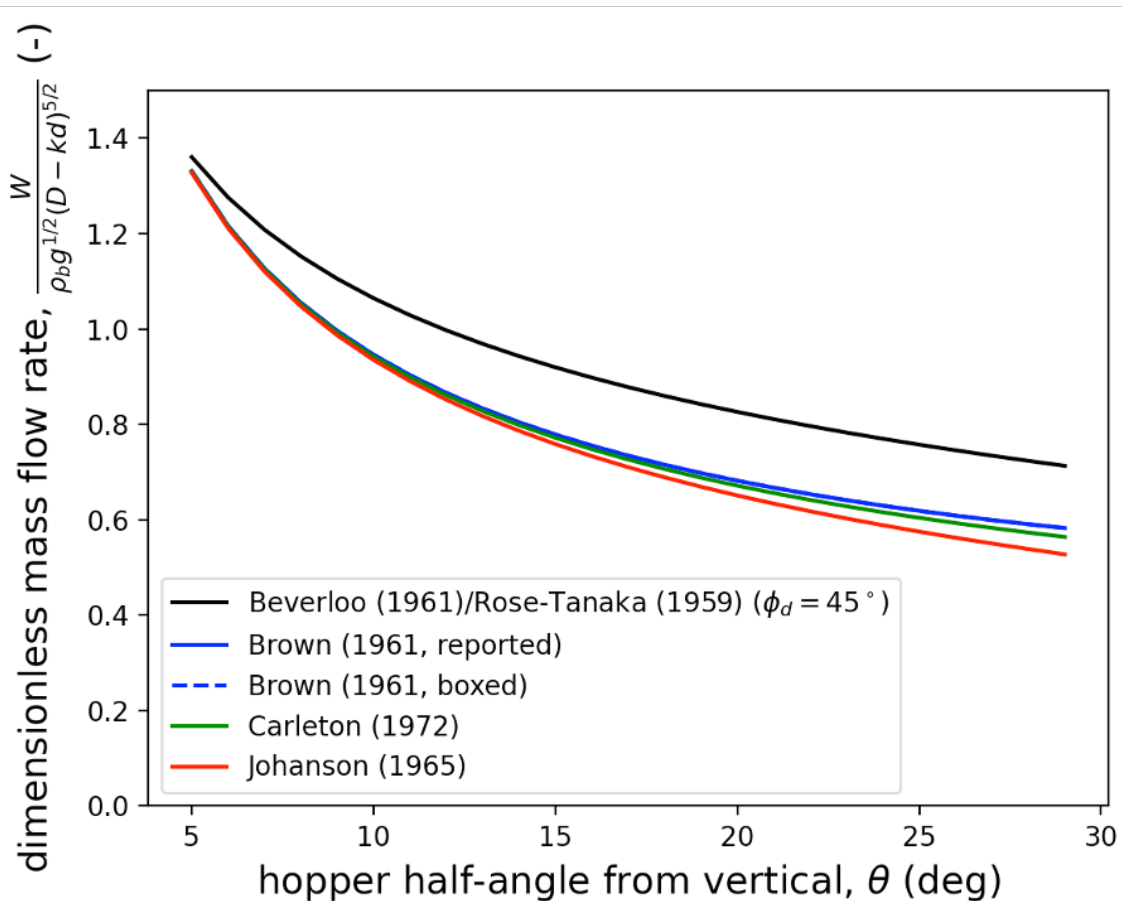
FIGURE 10.9. Plots of the dimensionless mass flow rate for a coarse, cohesionless material in a conical hopper as a function of the hopper half angle from the vertical for the Beverloo/Rose-Tanaka correlations (Eqs. (10.8) and (10.12)), the Johanson model (Eq. (10.19)), the Carleton model (Eq. (10.36)), and the two Brown expressions (Eqs. (10.39) and (10.40)). Note that the two Brown expressions overlap each other.

and only begin to deviate at large hopper wall half angles, which is where the mass flow assumption is more likely to become inaccurate. The Beverloo/Rose-Tanaka expression remains larger than the analytical expressions over the range of hopper wall half angles, although less so at smaller angles. The Beverloo/Rose-Tanaka expression is likely to be more accurate than the derived expressions since it is an empirical fit to experimental data with no derivation assumptions. There are additional mass flow rate analyses that make other assumptions and include the effects of stresses (refer to Nedderman [2] for an overview).

10.3.3. Johanson's Cohesive Model

The Johanson ([7]; partially re-derived by Mehos [10]) proposed a derivation for predicting the mass flow rate of cohesive (and non-cohesive) powders from hoppers with circular and rectangular exit geometries. The derivation is similar to the one used to predict the minimum bridge diameter to avoid cohesive bridging. Following is the derivation for a conical hopper, but a similar approach can be used for wedge hoppers. The derivation presented here has differences from Johanson's original work, which will be highlighted.
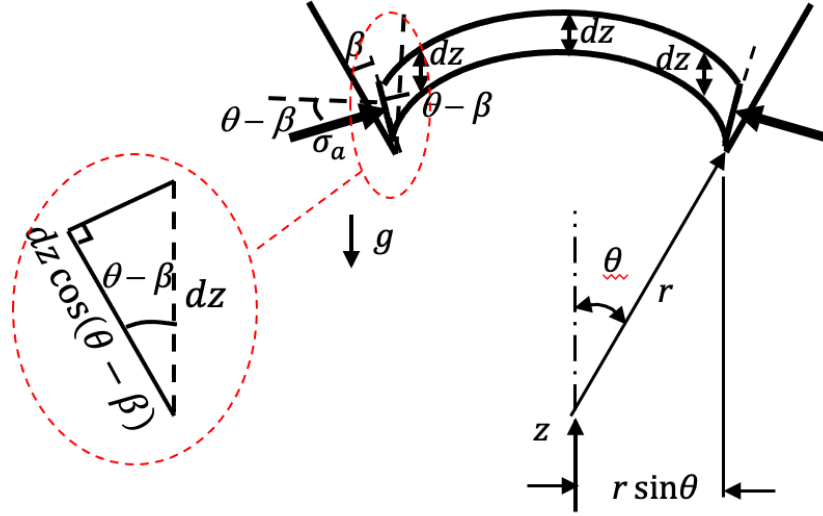
FIGURE 10.10. A drawing of the material element and geometry used in the Johanson [7] powder mass flow rate model.

Apply Newton's Second Law in the vertical direction to a thin element of material with vertical thickness dz located at the (conical) hopper outlet,

$$\sum F_z = ma = F_{\text{up}} - F_{\text{down}}. \tag{10.42}$$

The upward acting force is due to the applied major principal stress σ_a acting at the hopper walls, which acts at an angle β inclined from the hopper wall (similar to what was described in Chapter 9.2),

$$F_{\text{up}} = [2\pi(r\sin\theta)]dz\cos(\theta-\beta)]\,\sigma_a\sin(\theta-\beta) = \sigma_a 2\pi(r\sin\theta)dz\sin(\theta-\beta)\cos(\theta-\beta), \tag{10.43}$$

where the quantity is square brackets is the element perimeter area. Johanson neglected the arch curvature when writing the perimeter area. The downward acting force is due to the weight of the material element,

$$F_{\text{down}} = \rho_b g\left[\pi(r\sin\theta)^2 dz\right], \tag{10.44}$$

where the quantity in square brackets is the element volume (neglecting the arch curvature). Substitute the forces into Newton's Second Law and simplify,

$$\rho_b\left[\pi(r\sin\theta)^2 dz\right]a = \sigma_a 2\pi(r\sin\theta)dz\sin(\theta-\beta)\cos(\theta-\beta) - \rho_b g\left[\pi(r\sin\theta)^2 dz\right], \tag{10.45}$$

$$\rho_b a = \left(\frac{2}{r\sin\theta}\right)\sigma_a\sin(\theta-\beta)\cos(\theta-\beta) - \rho_b g. \tag{10.46}$$

To be conservative, let $\theta-\beta = 45°$ so $\sin(\theta-\beta)\cos(\theta-\beta) = \frac{1}{2}$ to maximize the upward force. For convenience, let $D := 2r\sin\theta$ be the outlet diameter. Divide the entire equation by the consolidation stress (σ_1) at the outlet and re-arrange,

$$\frac{\rho_b a}{\sigma_1} = \left(\frac{2}{D}\right)\frac{\sigma_a}{\sigma_1} - \frac{\rho_b g}{\sigma_1}, \tag{10.47}$$

$$a = g\left[\left(\frac{2\sigma_1}{\rho_b g D}\right)\frac{\sigma_a}{\sigma_1} - 1\right]. \tag{10.48}$$

Since the material is yielding, assume $\sigma_a = f_c$, where f_c is the unconfined yield strength of the material. Note that the ratio σ_1/f_c is the material flow factor (mff) at the consolidation stress. Thus, the previous equation may be written as,

$$a = g\left[\left(\frac{2\sigma_1}{\rho_b g D}\right)\frac{1}{\text{mff}} - 1\right]. \tag{10.49}$$

Now re-write the consolidation stress term. Recall from the previous chapter that the critical exit diameter to avoid cohesive bridging is,

$$D = H(\theta)\frac{\text{CAS}}{\rho_b g}, \tag{10.50}$$

where,

$$\text{CAS} = \frac{1}{\text{hff}}\sigma_1, \tag{10.51}$$

which gives,

$$D = \frac{H(\theta)}{\text{hff}}\frac{\sigma_1}{\rho_b g} \implies \frac{\sigma_1}{\rho_b g D} = \frac{\text{hff}_c}{H(\theta)}, \tag{10.52}$$

where the subscript "$_c$" is included on the hopper flow factor to signify that its value assumes the critical case. Note that Johanson used $H(\theta) = 2$ in his derivation. Substituting into the expression for the acceleration,

$$a = g\left[\frac{2}{H(\theta)}\frac{\text{hff}_c}{\text{mff}} - 1\right]. \tag{10.53}$$

Note again that Johanson's derivation had $H(\theta) = 2$.

The remainder of the derivation is identical to the previously presented one for cohesionless materials (Section 10.3.1). The final expression is,

$$W_{\text{conical}} = \rho_b\frac{\pi}{4}D^2\sqrt{\frac{gD}{4\tan\theta}\left(1 - \frac{2}{H(\theta)}\frac{\text{hff}_c}{\text{mff}}\right)}. \tag{10.54}$$

Notes:

(1) Johanson's [7] expression for a conical bin is,

$$W_{\text{conical}} = \rho_b\frac{\pi}{4}D^2\sqrt{\frac{gD}{4\tan\theta}\left(1 - \frac{\text{hff}_c}{\text{mff}}\right)}. \tag{10.55}$$

His expression for a wedge-shaped bin is,

$$W_{\text{wedge}} = \rho_b BL\sqrt{\frac{gB}{2\tan\theta}\left(1 - \frac{\text{hff}_c}{\text{mff}}\right)}. \tag{10.56}$$

(2) As a reminder,
 - hff_c is the hopper flow factor at the critical exit diameter, i.e., the minimum exit diameter at which arching can occur, $B_{\min}$ or $D_{\min} = H(\theta)\text{CAS}/(\rho_b g)$. Note that Johanson used $B_{\min}$ or $D_{\min} = 2(\text{CAS})/(\rho_b g)$.
 - The parameter mff is the material flow factor at the consolidation stress.
 - Ideally, ρ_b should be evaluated at the actual consolidation stress.

(3) For a non-cohesive material, $\text{hff}_c = 0$ since the critical exit diameter is zero. As a result, the term in parenthesis is equal to one and the prior Johanson expression for a cohesionless material is obtained.

(4) Another mass flow rate expression for cohesive materials was developed by Anand et al. [11]. They used discrete element method (DEM) computer simulations to predict the discharge rate of (liquid bridge) cohesive, spherical particles from a flat-bottomed bin. Recall from Eq. (10.9) that the Beverloo correlation for non-cohesive materials through a slot exit is,

$$W = 1.03\rho_b g^{1/2}(L - kd)(B - kd)^{3/2}. \tag{10.57}$$

For these cohesive materials, Anand et al. suggest using the following simulation-determined correlation for the shape factor k, presumably to account for the increase in effective particle shape due to agglomeration,

$$k = 1.9\exp(0.39\text{Bo}), \tag{10.58}$$
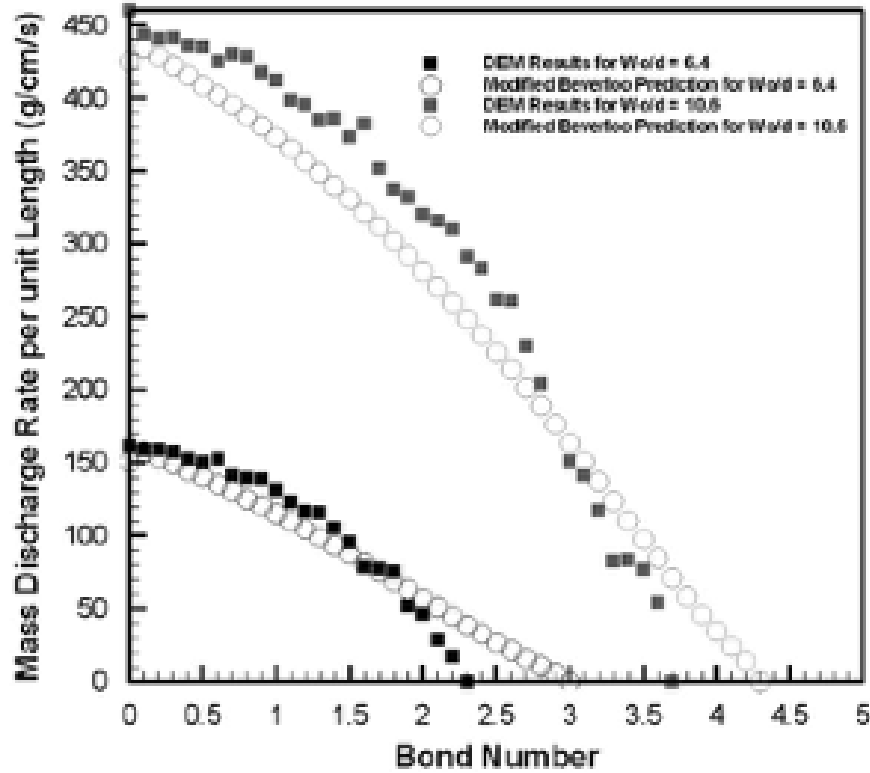
Figure 10.11. A plot comparing the mass flow rate from a wedge hopper from DEM simulations and the modified Beverloo model (Eqs. (10.57) and (10.58)) as functions of the Bond number (Eq. (10.59)). Results from two different dimensionless slot widths are shown.

where Bo is the Bond number, which is the ratio of a characteristic particle liquid bridge cohesive force to the particle weight,

$$\text{Bo} := \frac{F_{\text{coh}}}{W} = \frac{2\pi R \gamma}{\frac{4}{3}\pi R^3 \rho_p g} = \frac{3\gamma}{2R^2 \rho_p g}. \tag{10.59}$$

In the previous expression, γ is the liquid's surface tension, R is the particle radius, ρ_p is the particle density, and g is the acceleration due to gravity. A plot comparing the model mass flow rate predictions to DEM simulation results is shown in Figure 10.11.

10.4. The Mass Flow Rate for Fine Powders

The previous correlations are not accurate for fine powders ($< 400\,\mu\text{m}$) due to the influence of the surrounding fluid. Pressure gradients, permeability, and drag all act to modify the mass flow rate. For fine particles, the flow rate can be written with an effective gravitational acceleration as,

$$W = c\rho_b \left(g + \frac{1}{\rho_b} \frac{dp}{dr} \right)^{1/2} (D - kd)^{5/2}, \tag{10.60}$$

where dp/dr is the pressure gradient near the outlet. Determining the pressure gradient requires knowledge of the bed properties, gas properties, and geometry. It's a non-trivial calculation. There are many papers on this topic and won't be discussed further in these notes.

A powder bed's permeability is a measure of the ease with which a fluid, e.g., air, flows through a powder bed. A larger permeability means that a smaller pressure gradient is required to produce a given flow rate.
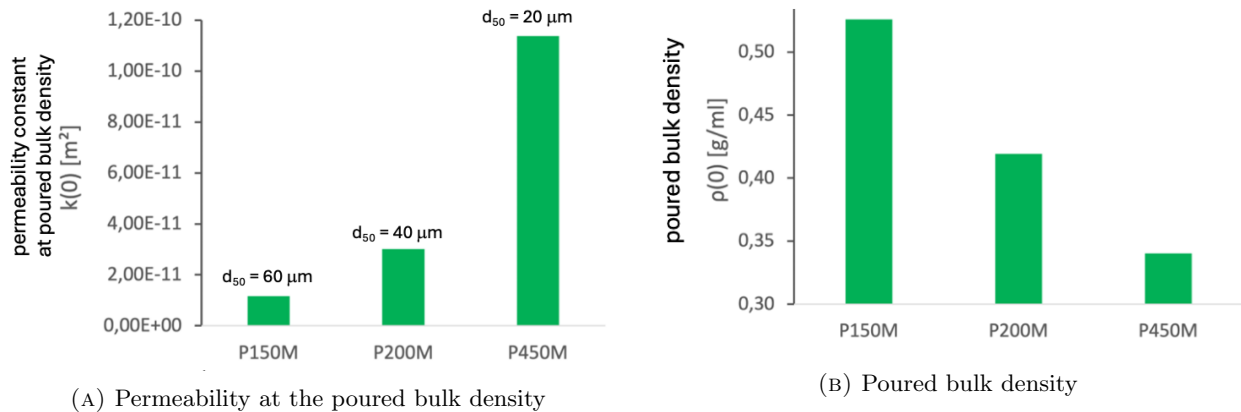
(A) Permeability at the poured bulk density

(B) Poured bulk density

FIGURE 10.12. (A) The permeability of different grades, i.e., particle sizes, of milled lactose powder at the poured bulk density. (B) The poured bulk density of the same lactose powder.

Darcy's Law provides a relationship between the pressure gradient and volumetric flow rate,

$$\mathbf{Q} = -\frac{KA}{\mu}\nabla p, \tag{10.61}$$

where $\mathbf{Q}$ is the volumetric flow rate (dimensions of L^3/T and a vector quantity) of the fluid, K (dimensions of L^2) is the bed's permeability, A (dimensions of L^2) is the bed's cross-sectional area, which includes the fluid and particle area, μ (dimensions of $M/(LT)$) is the fluid's dynamic viscosity, and p (dimensions of $M/(LT^2)$) is the pressure in the fluid. As the permeability increases, the volumetric flow rate also increases. One expression for estimating a particle bed's permeability is the Carman-Kozeny Equation,

$$K \propto d_{SV}^2 \frac{\epsilon}{180(1-\epsilon)^2}, \tag{10.62}$$

where d_{SV} (dimensions of L) is the particle equivalent sphere surface area-to-volume diameter and ϵ (dimensionless) is the bed's void fraction (aka porosity). As the bulk density increases for a given material, the bed porosity decreases and the permeability decreases. Similarly, as the particle's equivalent sphere surface area-to-volume diameter decreases, the permeability decreases. Thus, tightly packed beds consisting of small particles will generally have small permeability and a larger pressure gradient is needed to obtain a given volumetric flow rate of fluid through the bed.

Notes:

(1) Figure 10.12 shows permeability experimental measurements for different grades, i.e., particle sizes, of milled lactose powder at their poured bulk densities (note the small magnitude of the permeability). In Figure 10.12a the permeability increases as the particle size decrease, which appears to contradict the Carmen-Kozeny Equation (Eq. (10.62)). However, Figure 10.12b shows that the poured bulk density decreases as the particle size decreases. This behavior occurs because as particle size decreases, the powder becomes more cohesive and the bed becomes more porous. Thus, there are two counter-acting effects: a decreasing particle size but increasing void fraction. Evidently the increase in void fraction results in an increase in the bed permeability with decreasing particle size at the poured bulk density in this case.

An illustration of a low permeability powder discharging through a hopper is shown in Figure 10.13. The stresses acting on the powder decrease approaching the hopper exit (Chapter 6). As the stresses decrease, the powder bed dilates resulting in a decrease in the local air pressure. The negative (gage) pressure at the hopper exit results in an influx of air into the powder bed, primarily through the hopper exit. The flow of incoming air will slow the discharging powder flow rate. The smaller the bed permeability, the larger the exit pressure gradient will be since air cannot rapidly fill the void left by the particles (refer to the Carmen-Kozeny
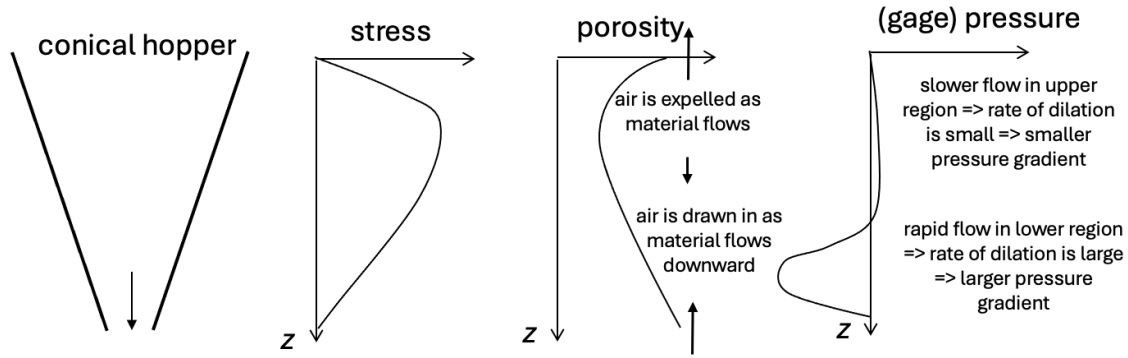
FIGURE 10.13. An illustration of a low permeability powder discharging from a hopper.

Equation, Eq. (10.62)), and the smaller the powder mass flow rate from the hopper. The reader can refer to Dhodapkar et al. [4] for additional detail.

Notes:

(1) A video showing mass flow of fine powder with air effects can be viewed at: http://www.youtube.com/watch?v=UKLQwOxFSaU.

To estimate the particle speed at the hopper outlet including air effects, Carleton [9] assumed a radial flow field in a conical hopper and applied a force balance to an individual particle (no neighbors) including the particle inertia, weight, and fluid drag (relative to stationary air - a poor assumption). The resulting analysis gives an equation implicit in the particle speed (V_0),

$$\frac{4V_0^2 \sin\theta}{D} + \frac{15\rho_F^{1/3}\mu_F^{2/3}V_0^{4/3}}{\rho_S d^{5/3}} = g, \tag{10.63}$$

where θ is the hopper wall half angle from the vertical, D is the hopper exit diameter, d is the particle diameter, ρ_F and ρ_P are the fluid and particle densities, respectively, μ_F is the fluid dynamic viscosity, and g is the acceleration due to gravity.

Notes:

(1) Equation (10.63) can be solved numerically for the particle speed. Alternately, Carleton provided a nomograph (Figure 10.14) for determining the particle speed.
(2) The volumetric flow rate from the hopper (Q) may be estimated using $Q = V_0 \frac{\pi}{4} D^2$. Note that Carleton's analysis does not provide a method for estimating the bulk density.

Air pressure differences can also be used to increase the mass flow rate from a hopper. Nedderman [2] states that the mass flow rate in the presence of a positive applied gage pressure above the powder bed in a hopper (Δp), assuming a narrow, smooth conical hopper and an incompressible powder and fluid, is,

$$W = W_0 \sqrt{1 + f(\text{Re}_e)\frac{\Delta p}{\rho_b g r_e}}, \tag{10.64}$$

where W_0 is the mass flow rate in the absence of pressure effects, ρ_b is the powder bulk density, g is the acceleration due to gravity, and r_e is the radius from the hopper apex to the actual exit location. The function of Reynolds number at the exit (Re_e) is,

$$f(\text{Re}_e) = \frac{150 + 5.25\text{Re}_e}{150 + 1.75\text{Re}_e}, \tag{10.65}$$

where,

$$\text{Re}_e = \frac{\rho_F v_e r_e}{\mu_F}, \tag{10.66}$$
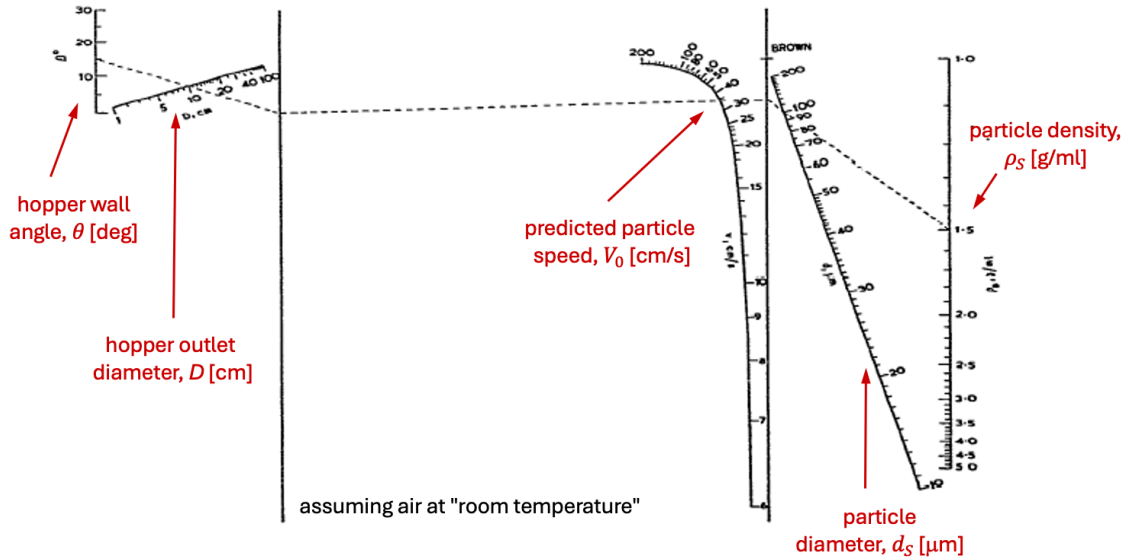
Figure 10.14. The particle speed nomograph provided by Carleton [9]. An example is given in this figure in which the hopper has a $\theta = 15°$ wall angle, $D = 10$ cm exit diameter and the particles have a $d = 100\,\mu\text{m}$ diameter and $\rho_S = 1.5$ g/ml density. Room temperature air and a gravitational acceleration of $g = 9.81$ m/s are assumed. The resulting particle exit speed is $V_0 = 35$ cm/s.

and v_e is the particle speed at the exit and ρ_F and μ_F are the fluid density and dynamic viscosity, respectively.

Notes:

(1) The most accurate approach to predicting the outlet mass flow rate in the presence of a fluid involves applying Conservation of Mass and the Linear Momentum Equation to differential material elements and then solving for the stress and velocity fields. This approach would include the gravitational, material, and fluid forces acting on the material elements. The resulting equations could be solved analytically, given sufficient assumptions, or numerically. Refer, for example, to the work by Lamptey and Thorpe [12] or Gu [13] for additional details.

(2) Methods for improving the flow of low permeability powders include:
   (a) Using a dual hopper arrangement to provide ventilation (Figure 10.15a). This technique decreases the pressure gradient near the hopper outlet [13].
   (b) Increasing the outlet size, resulting in a larger area through which air can flow.
   (c) Decreasing the fill level of the material in the hopper, which increases the pressure gradient for downward air flow from the upper free surface resulting in more air entering the powder bed from the top and reducing the air flow from the bottom.
   (d) Injecting a small amount of air into the powder bed near the exit, which decreases pressure gradient there (Figure 10.15b). The air flow rate should not be so large as to cause flooding, however.
   (e) Installing a standpipe at the hopper outlet (Figure 10.15c), ensuring that there are no voids in the standpipe, which decreases the pressure gradient at the exit which in turn decreases the upward flow of air [13].
   (f) Increase the air pressure at the top of the powder bed to increase the mass flow rate (refer to Eq. (10.64)).

(A) A dual hopper arrangement   (B) Injecting air into the powder bed   (C) Adding a standpipe to the hopper exit
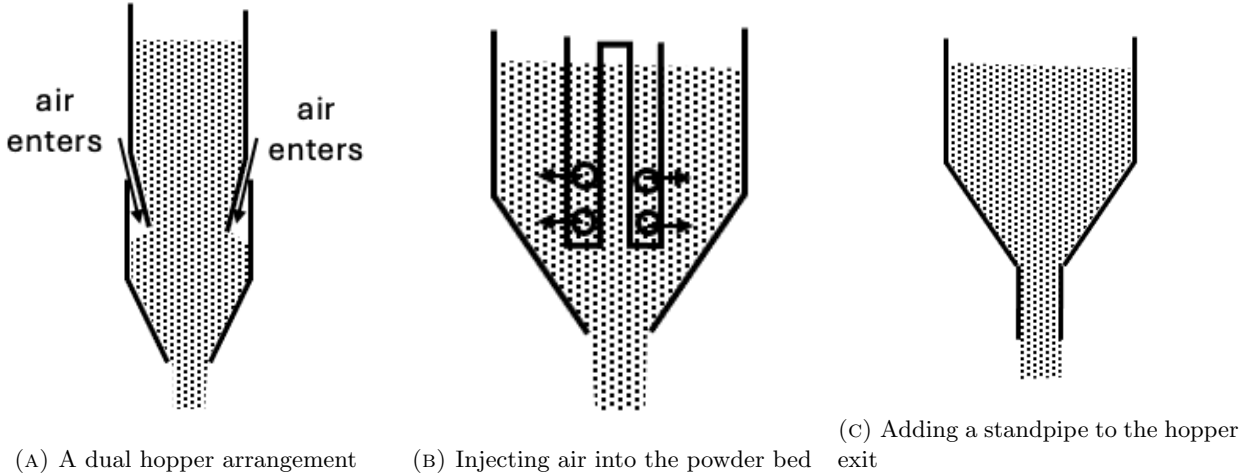
FIGURE 10.15. Methods for increasing the mass flow rate of low permeability powders from a hopper.

10.5. Measurement of Mass Flow Rate

Measurements of a powder's mass flow rate are often needed during manufacturing in order to control the process. Two methods for determining mass flow rate are described in this section: (1) methods relying on force or torque measurements, and (2) methods relying on the attenuation of radiation passing through the powder. Other methods exist and the reader is referred to [14] for additional detail.

Force measurements can be used with a linear momentum or moment of momentum analysis to determine a powder stream's mass flow rate. In devices such as the impact plate, diverting chute, and centripetal flow meter, a powder stream impacts or is diverted and the resulting force is measured. Applying the Linear Momentum Equation in the x-direction to the control volume surrounding the powder stream impacting the plate shown in Figure 10.16, gives,

$$\frac{d}{dt}\int_{\text{CV}} u_x \rho_b dV + \int_{\text{CS}} u_x(\rho_b \mathbf{u}_{rel} \cdot d\mathbf{A}) = F_{B,x} + F_{S,x}, \tag{10.67}$$

where,

$$\frac{d}{dt}\int_{\text{CV}} u_x \rho_b dV = 0 \quad \text{(assuming steady flow)}, \tag{10.68}$$

$$\int_{\text{CS}} u_x(\rho_b \mathbf{u}_{rel} \cdot d\mathbf{A}) = (V_2 \cos\theta)\dot{m} \quad \text{(assuming a uniform speed)}, \tag{10.69}$$

$$F_{B,x} = 0 \quad \text{(no body forces in the } x \text{ direction)}, \tag{10.70}$$

$$F_{S,x} = F_x \quad \text{(the measured force).} \tag{10.71}$$

Substituting and simplifying,

$$\dot{m} = \frac{F_x}{V_2 \cos\theta}. \tag{10.72}$$

The speed V_2 can be found via calibration or measured using an optical or Doppler shift method, for example.

If the Linear Momentum Equation is applied to the same control volume in the y direction,

$$\frac{d}{dt}\int_{\text{CV}} u_y \rho_b dV + \int_{\text{CS}} u_y(\rho_b \mathbf{u}_{rel} \cdot d\mathbf{A}) = F_{B,y} + F_{S,y}, \tag{10.73}$$
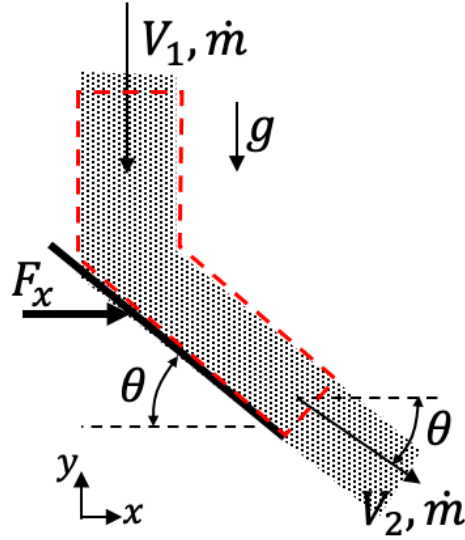
FIGURE 10.16. The control volume and free body diagram for an impact plate linear momentum analysis.

where,

$$\frac{d}{dt}\int_{\text{CV}} u_y \rho_b dV = 0 \quad \text{(assuming steady flow)},\tag{10.74}$$

$$\int_{\text{CS}} u_y (\rho_b \mathbf{u}_{rel} \cdot d\mathbf{A}) = (-V_1)(-\dot{m}) + (-V_2 \sin\theta)(\dot{m}) \quad \text{(assuming uniform speeds)},\tag{10.75}$$

$$F_{B,y} = -mg \quad \text{(material weight in the control volume)},\tag{10.76}$$

$$F_{S,y} = F_y \quad \text{(the measured force in the } y \text{ direction)}.\tag{10.77}$$

Substituting and simplifying,

$$\dot{m}(V_1 - V_2 \sin\theta) = -mg + F_y.\tag{10.78}$$

Now substitute in for V_2 using Eq. (10.72),

$$\dot{m}\left(V_1 - \frac{F_x}{\dot{m}\cos\theta}\sin\theta\right) = -mg + F_y,\tag{10.79}$$

$$\dot{m}V_1 - F_x \tan\theta = -mg + F_y,\tag{10.80}$$

$$\dot{m} = \frac{-mg + F_y + F_x \tan\theta}{V_1}.\tag{10.81}$$

If the material weight can be estimated or neglected, then the mass flow rate can be determined knowing the measured horizontal and vertical impact forces, the plate angle, and the impact speed.

Analysis for a rotary disk flow meter (aka Coriolis flow meter) is similar to that for the impact plate, but the Moment of Momentum Equation is used in place of the Linear Momentum Equation. Consider a powder stream that falls vertically onto a rotating disk and is then thrown off laterally as shown in Figure 10.17. From the Moment of Momentum Equation applied in the z direction to a control volume enclosing the material entering and exiting the spinning plate,

$$\frac{d}{dt}\int_{\text{CV}} (\mathbf{r}\times\mathbf{u})_z \rho_b dV + \int_{\text{CS}} (\mathbf{r}\times\mathbf{u})_z (\rho_b \mathbf{u}_{rel} \cdot d\mathbf{A}) = T_{B,z} + T_{S,z},\tag{10.82}$$
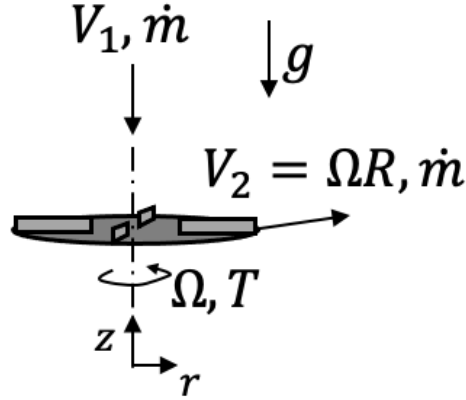
FIGURE 10.17. A moment of momentum analysis for a rotary disk used to determine a powder stream's mass flow rate.

where,

$$\frac{d}{dt}\int_{\text{CV}}(\mathbf{r}\times\mathbf{u})_z\rho_b dV = 0 \quad \text{(assuming steady flow)}, \tag{10.83}$$

$$\int_{\text{CS}}(\mathbf{r}\times\mathbf{u})_z(\rho_b\mathbf{u}_{rel}\cdot d\mathbf{A}) = [R\hat{\mathbf{e}}_r\times(V_r\hat{\mathbf{e}}_r+\Omega R\hat{\mathbf{e}}_\theta)]\dot{m} = \Omega R^2\dot{m} \tag{10.84}$$

(assuming the particles' tangential speeds equal the disk tangential speed),

$$T_{B,z} = 0 \quad \text{(no body torques in the } z \text{ direction)}, \tag{10.85}$$

$$T_{S,z} = T \quad \text{(the measured torque)}. \tag{10.86}$$

Substituting and simplifying,

$$\dot{m} = \frac{T}{\Omega R^2}. \tag{10.87}$$

Thus, measurements of the torque and rotational speed can be used to predict the mass flow rate.

The last method discussed in this section for measuring a powder stream's mass flow rate involves radiation attenuation. Often, x-rays or microwaves are used. The radiation is emitted with intensity I_{emitted}, passes through a powder stream of well-defined thickness x as shown in Figure 10.18, and is received with intensity I_{recieved}. The bulk density of the powder stream (ρ_b) is related to the radiation intensities via,

$$\frac{I_{\text{received}}}{I_{\text{emitted}}} = \exp\left(-\frac{\mu}{\rho_b}x\right), \tag{10.88}$$

where μ is a calibrated material-specific attenuation coefficient. The speed of the powder stream V can be found using cross-correlation from the receiver measurements at two known streamwise distances. The Doppler shift in a reflected signal could also be used to determine the stream's speed. The resulting mass flow rate is,

$$\dot{m} = \rho_b V A, \tag{10.89}$$

where A is the cross-sectional area of the powder stream and is related to x via the integration of path lengths. One example of an x-ray radiation attenuation device for measuring mass flow rate is given at: https://www.enurga.com/flowmeter.htm.

10.6. Summary

Summarizing the main points from this chapter:

- The mass flow rate from a hopper is independent of the material height for sufficiently large heights (a Janssen effect) ($W \propto D^{5/2}$).
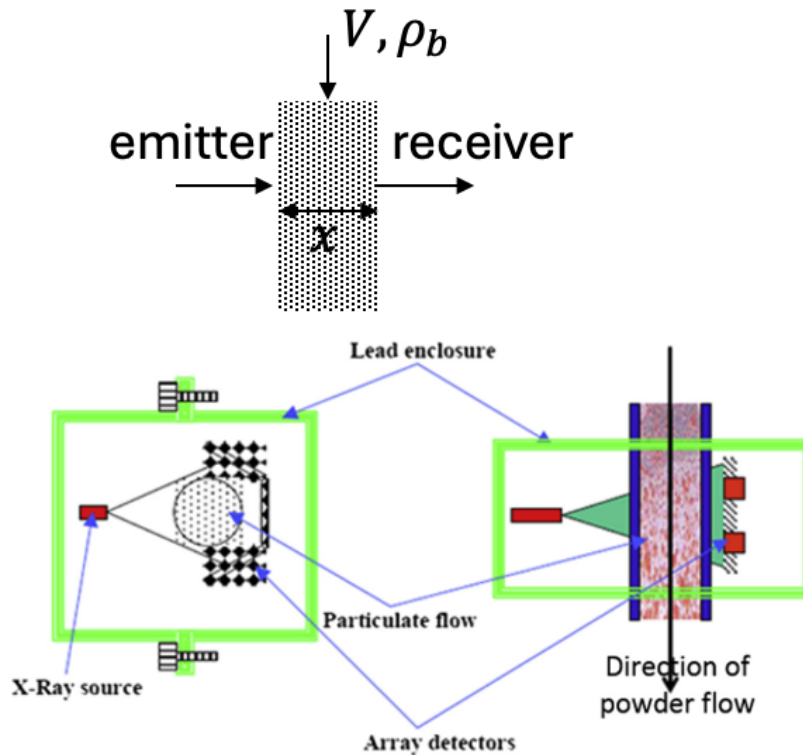
Figure 10.18. An illustration for how radiation attenuation through a flowing powder stream can be used to estimate a powder's bulk density. The bottom figure is from Ganesh et al. [15].

- A finite particle size results in the "empty annulus" effect $(D - kd)$.
- There are many estimates for predicting the mass flow rate of cohesionless particulates from a hopper, e.g., Beverloo/Rose-Tanaka, Brown, Carleton, Johanson, ...
- For cohesive powder mass flow rate, use the Johanson relation.
- The flow of fine powders is affected by the surrounding fluid. Often the flow rate is diminished as fluid flows counter to the powder during discharge.
- Various methods exist for measuring powder mass flow rate.

10.7. Related Standards

- ASAE D274.1, 2008, "Flow of grain and seeds through orifices", American Society of Agricultural and Biological Engineering.
- ASTM B964-23, 2023, "Standard test methods for flow rate of metal powders using the Carney funnel", ASTM Standards.
- ASTM B213-20, 2020, "Standard test methods for flow rate of metal powders using the Hall flowmeter funnel", ASTM Standards.

A particulate material consisting of spherical particles of diameter 400 μm has a bulk density of 800 kg/m³.

a. Estimate the mass flow rate through an orifice of 25 mm diameter in the base of a wide cylindrical, flat-bottomed bin.

b. Estimate the mass flow rate through a 25 mm diameter orifice in the base of a conical hopper of half-angle 20° from the vertical. The hopper is observed to be in mass flow.

c. Estimate the mass flow rate through a 40 mm x 15 mm rectangular orifice in the base of a wide cylindrical bin.

SOLUTION:

For part (a), estimate the mass flow rate using the Beverloo correlation,

$$W = 0.58\rho_b g^{1/2}(D - kd)^{5/2} \quad => \quad \boxed{W = 0.14 \text{ kg/s}}. \tag{1}$$

where ρ_b = 800 kg/m³, g = 9.81 m/s², D = 0.025 m, k = 1.6 (for spheres), and d = 400*10⁻⁶ m.

For part (b), several models can be used to estimate the mass flow rate,

$$\text{Beverloo (1961) with Rose-Tanaka (1959):} \quad W = 0.58\rho_b g^{1/2}(D - kd)^{5/2}(\tan\theta)^{-0.35} \quad => \quad \boxed{W = 0.19 \text{ kg/s}}. \tag{2}$$

$$\text{Brown (1961):} \quad W = \frac{\pi}{6}\rho_b g^{1/2}(D - kd)^{5/2}\left[\frac{1 - (\cos\theta)^{3/2}}{(\sin\theta)^{5/2}}\right] \quad => \quad W = 0.16 \text{ kg/s}. \tag{3}$$

$$\text{Carleton (1972):} \quad W = \frac{\pi}{8}\rho_b g^{1/2}(D - kd)^{5/2}(\sin\theta)^{-1/2} \quad => \quad W = 0.16 \text{ kg/s}. \tag{4}$$

$$\text{Johanson (1965):} \quad W = \frac{\pi}{8}\rho_b g^{1/2}(D - kd)^{5/2}(\tan\theta)^{-1/2} \quad => \quad W = 0.15 \text{ kg/s}. \tag{5}$$

The Beverloo/Rose-Tanaka relation is likely the best predictor since it is an empirical fit to experimental data whereas the other expressions come from analytical derivations.

For part (c), use the Beverloo correlation for a rectangular outlet,

$$W = 1.03\rho_b g^{1/2}(L - kd)(B - kd)^{3/2} \quad => \quad W = 0.18 \text{ kg/s}, \tag{6}$$

using L = 40 mm and B = 15 mm. Note that previous expression assumes $L > 3B$, which doesn't strictly hold here (L/B = 2.67). An expression where the L/B requirement is relaxed is given in Dhodapkar et al. (2016),

$$W = \frac{4}{\pi}C\rho_b g^{1/2}(B - kd)(L - kd)\sqrt{\frac{2(B-kd)(L-kd)}{(B-kd)+(L-kd)}} \quad => \quad \boxed{W = 0.23 \text{ kg/s}}, \tag{7}$$

where C is interpolated from the Dhodapkar et al. (2016) recommendations as,

$$C = \left(\frac{0.83 - 0.91}{4 - 2}\right)(2.67 - 2) + 0.91 \quad => \quad C = 0.88. \tag{8}$$

Reference:

Dhodapkar, S., Jacob, K., and Kodam, M., 2016, "Determining the discharge rates of particulate solids", *Chemical Engineering Progress*, Vol. 5, pp. 50 – 61.

Estimate the mass flow rate of iron ore powder from the wedge hopper shown below. The powder has the measured properties given in the figures. Assume the hopper is constructed of new steel plate, which has a measured wall friction angle of 25°. (This example is inspired by the one in Johanson, J.R., 1965, "Method of calculating the rate of discharge from hoppers and bins," *Transactions of the Society of Mining Engineers, V*ol. 232, p. 69 – 80.)
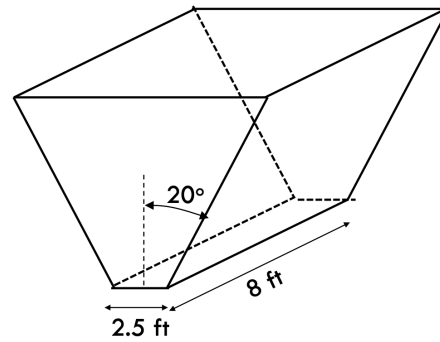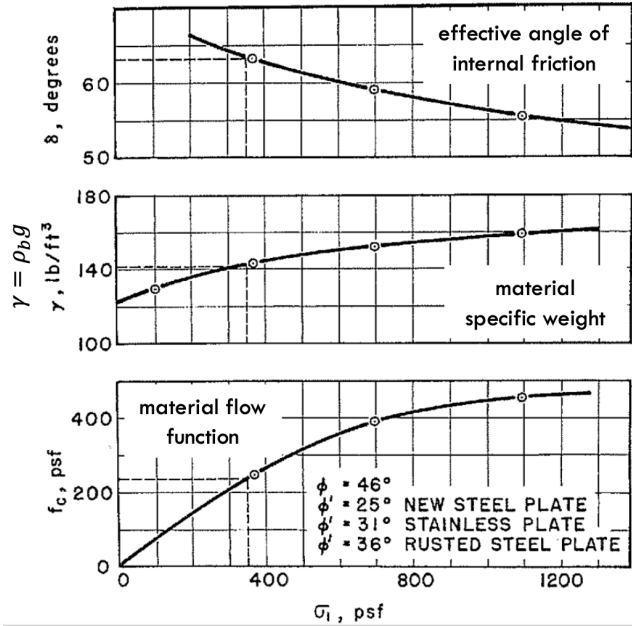
SOLUTION:

First, determine the critical hopper flow factor (hff_c) using the Jenike design chart for a wedge hopper, assuming an initial guess for the consolidation stress of $\sigma_{1,c}$ = 600 lb$_f$/ft^2. For this consolidation stress, the corresponding material properties are δ = 60° and $\gamma = \rho_b g$ = 153 lb$_f$/ft^3 (red lines in the following figure).
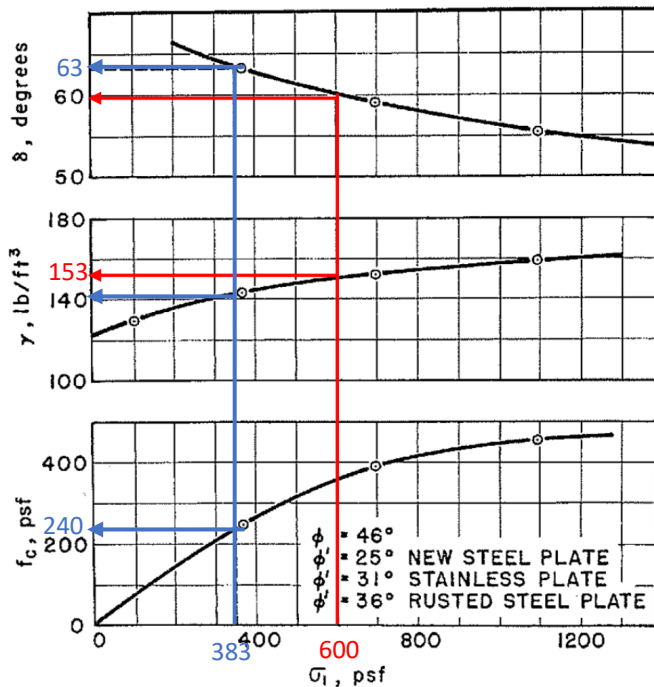
Using the Jenike design chart for a wedge hopper (see below) and $\delta = 60°$, we obtain $hff_c = 1.1$. The critical applied stress to avoid cohesive bridging at the exit is,

$$B_{\min} = H(\theta)\frac{CAS}{\rho_b g} \implies CAS = \sigma_{a,c} = \frac{\rho_b g B_{\min}}{H(\theta)}. \tag{1}$$

Recall that the hopper flow factor is defined as,

$$hff_c := \frac{\sigma_{1,c}}{\sigma_{a,c}} \implies \sigma_{1,c} = (hff_c)\sigma_{a,c}. \tag{2}$$
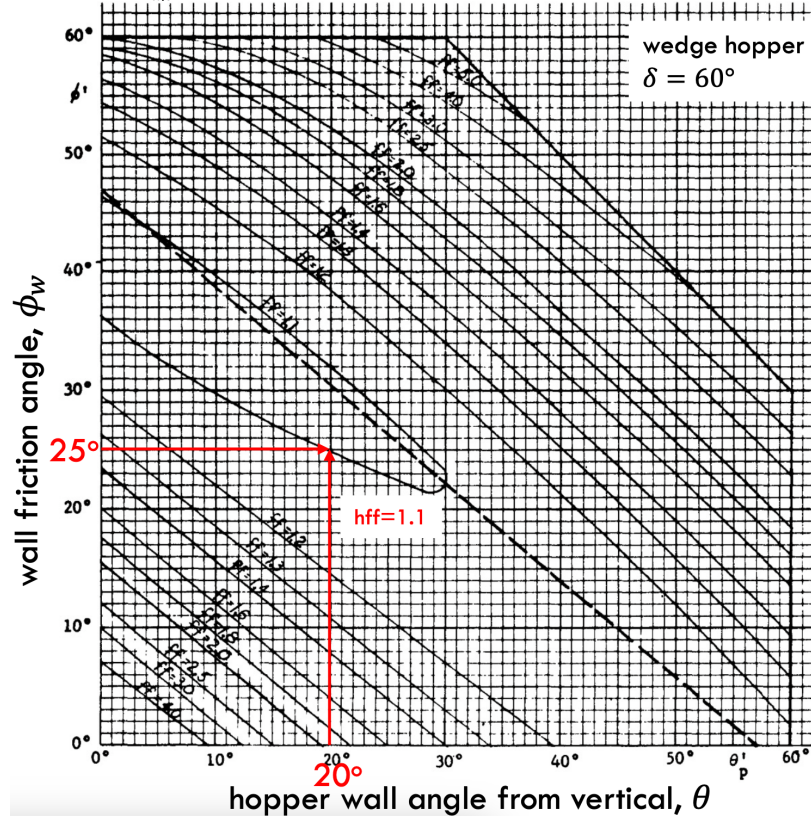
Using the assumed and given data,

$\rho_b g = 153$ lb$_f$/ft^3, $B_{\min} = 2.5$ ft, $H(\theta = 20°) = 1.1$ (refer to the following plot),
$\implies \sigma_{a,c} = 348$ lb$_f$/ft^2 (Eq. (1)) $\implies \sigma_{1,c} = 383$ lb$_f$/ft^2 (Eq. (2)).

C. Wassgren   244   2024-06-12
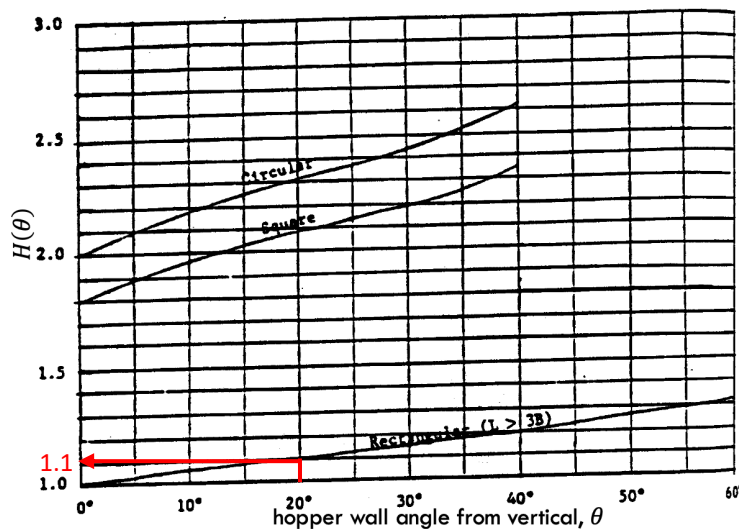
Return to the material properties plots for $\sigma_{1,c}$ = 383 lb$_f$/ft^2. For this consolidation stress, the corresponding material properties are δ = 63° and $\gamma = \rho_b g$ = 153 lb$_f$/ft^3 (blue lines in the plot). Since the new value for δ is close to δ = 60° and our plots for determining hff are coarse, we'll continue to use the value of hff_c = 1.1. Recalculating using Eqs. (1) and (2) gives $\sigma_{1,c}$ = 355 lb$_f$/ft^2. This value gives nearly the same material properties as $\sigma_{1,c}$ = 383 lb$_f$/ft^2 and, thus, we'll use $\gamma = \rho_b g$ = 153 lb$_f$/ft^3. From the plot we also obtain f_c = 240 lb$_f$/ft^2.

The actual material flow factor is,
$$\text{mff} = \frac{\sigma_{1,c}}{f_c} \quad \Rightarrow \quad \text{mff = 1.48.} \tag{3}$$

Now make use of Johanson's mass flow rate expression for cohesive powders in a hopper with a rectangular exit,
$$W = \rho_b BL \sqrt{\frac{Bg}{2\tan\theta}\left(1 - \frac{1}{H(\theta)}\frac{\text{hff}_c}{\text{mff}}\right)} \quad \Rightarrow \quad \boxed{W = 18\ 300\ \text{lb}_m\text{/s}}. \tag{4}$$
Here, $\rho_b g$ = 153 lb$_f$/ft^3 (ρ_b = 142 lb$_m$/ft^3, g = 32.2 ft/s^2), B = 2.5 ft, L = 8 ft, θ = 20°, $H(\theta)$ = 1.1, hff$_c$ = 1.1, and mff = 1.48.

Bibliography

[1] W. Beverloo, H. Leniger, and J. van de Velde, "The flow of granular solids through orifices," vol. 15, pp. 260–269, 1961.

[2] R. Nedderman, Statics and Kinematics of Granular Materials. Cambridge University Press, 1992. DOI: 10.1017/CBO9780511600043.

[3] C. Woodcock and J. Mason, Bulk Solids Handling An Introduction to the Practice and Technology. Blackie Academic and Professional, 1987.

[4] S. Dhodapkar, K. Jacob, and M. Kodam, "Determining the discharge rates of particulate solids," Chemical Engineering Progress, vol. 5, pp. 50–61, 2016.

[5] H. Rose and T. Tanaka, "Rate of discharge of granular materials from bins and hoppers," The Engineer (London), vol. 208, pp. 465–469, 1959.

[6] D. Schulze and J. Schwedes, "Tests on the application of discharge tubes," Bulk Solids Handling, vol. 12, no. 1, pp. 33–39, 1992.

[7] J. Johanson, "Method of calculating the rate of discharge from hoppers and bins," Transactions of the Society of Mining vol. 232, pp. 69–80, 1965.

[8] R. Brown, "Minimum energy theorem for flow of dry granules through apertures," Nature, vol. 191, no. 4787, pp. 458–461, 1961.

[9] A. Carleton, "The effect of fluid-drag forces on the discharge of free-flowing solids from hoppers," Powder Technology, vol. 6, no. 2, pp. 91–96, 1972.

[10] G. Mehos, "Maximum solids discharge rates from hoppers," Chemical Engineering Research and Design, vol. 191, pp. 564–567, 2023.

[11] A. Anand, J. Curtis, C. Wassgren, B. Hancock, and W. Ketterhagen, "Predicting discharge dynamics of wet cohesive particles from a rectangular hopper using the discrete element method (dem)," Chemical Engineering Science, vol. 64, pp. 5268–5275, 2009.

[12] B. Lamptey and R. Thorpe, "The discharge of solid-liquid mixtures from hoppers," Chemical Engineering Science, vol. 46, no. 9, pp. 2197–2212, 1990.

[13] Z. Gu, "Gravity flowrate of bulk solids from mass flow bins," Ph.D. dissertation, University of Wollongong, Australia, 1991.

[14] Y. Yan, "Mass flow measurement of bulk solids in pneumatic pipelines," Measurement Science and Technology, vol. 7, pp. 1687–1706, 1996.

[15] S. Ganesh, R. Troscinski, N. Schmall, J. Lim, Z. Nagy, and G. Reklaitis, "Application of x-ray sensors for in-line and noninvasive monitoring of mass flow rate in continuous tablet manufacturing," ournal of Pharmaceutical Sciences, vol. 106, no. 12, pp. 3591–3603, 2017.

CHAPTER 11

Discharge Devices

Often at the outlet of a hopper there's a device used to control the discharge rate. Common devices include conveyors, feeders (feeders control the flow more precisely than conveyors), or rotary valves. Rotary valves are also commonly used to block air flow between the hopper and a pneumatic conveying line. To obtain the desired flow rate, the hopper exit must be at least as large as the unobstructed exit flow rate found in the previous chapter, and typically even larger.

Exit device dynamics can significantly affect the flow pattern within the hopper. For example, asymmetric discharge may occur due to improper exit feeder design (Figure 11.1) or off-center filling. Asymmetric discharge can result in eccentric loading of the hopper. Unless properly designed to account for eccentric loading, structural failure of the hopper may occur [1], [2].

Notes:

(1) Discharge belts and screws cannot control flooding, but rotary valves can.
(2) Some bins/hoppers may have multiple outlets, which are more difficult to design in terms of structure and flow.
(3) Slide valves (Figure 11.2) are common at the exit of a hopper. These valves are used for maintenance purposes and should either be fully open during operation or fully closed.

11.1. Screw Feeders and Conveyors

Screw feeders and conveyors (aka augers) consist of a housing (aka trough or barrel), a screw, an inlet, an outlet, and a motor that turns the screw (Figure 11.3a). The screw (Figure 11.3b) is comprised of a shaft (aka core) about which the screw (aka flights) is attached. The distance between neighboring flights is called the screw "pitch". Material from a hopper falls into the empty volume between the screw flights and then is conveyed downstream as the screw turns until reaching the outlet at which point the material falls out.

Notes:

(1) A "standard pitch" screw is one where the screw pitch is equal to the screw diameter (Figure 11.4a). Standard pitch is commonly used for conveying material horizontally or at slight inclines. A "half
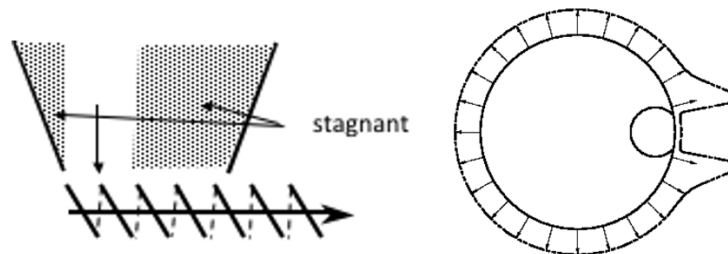
FIGURE 11.1. (left) Asymmetric discharge of a hopper into a screw feeder. (right) The radial stress distribution on a hopper's walls due to the presence of an asymmetric flow channel at the right side of the hopper.
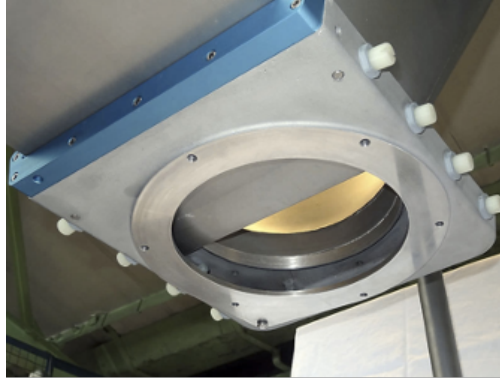
FIGURE 11.2. A photograph looking up at a slide valve located at the outlet of a hopper. A video of an operating slide value is available at: https://www.youtube.com/watch?v=bS9JNIK0qMk.

pitch" screw has a pitch equal to half the screw diameter (Figure 11.4b). Half pitch screws are used to convey material at large or vertical inclines.

(2) "Double flight" screws have two helical flights 180° out of phase (Figure 11.4c). Double flights are used to produce more uniform flow of the material.

(3) There are many screw flight designs. For example, some screws have cut-outs ("cut flights") and protruding sections ("cut and folded flights"). These various designs are optimized for handling materials with different properties as well as for controlling mixing during conveying. If the powder has a tendency to flood, then a screw with a core should be used, as opposed to a coreless screw, which is better for feeding cohesive materials.

(4) A screw feeder operates in much the same way as a screw conveyor. The primary difference is that feeders control the mass flow rate more precisely using closed loop control. One common method of feeder control relies on monitoring the material weight in the feed hopper, referred to as "gravimetric mode" or "loss-in-weight" feeding. When there is no closed loop control, the feeder is operating in "volumetric mode", relying on consistent filling of the screw flights to maintain a desired flow rate.

(5) If the hopper exit must be large to prevent bridging or ratholing, multiple feed screws might be used in a slot opening beneath the hopper (aka a "live bottom" screw feeder, Figure 11.5).

(6) A shroud covering the screw is typically used just downstream of the inlet to prevent a flooding material from overflowing the feeder.

(7) Feed screws typically aren't used in applications where there's an air pressure gradient between the hopper and outlet since there is no air lock or seal in the screw.

(8) Active cooling of the screw or barrel may be needed due to heat build up caused by the work on the material during operation.

(9) The effort required to clean a feed screw should not be underestimated. In general, cleaning procedures for any unit operation should be part of the overall system design.

(10) Screw flights should not be run further than the discharge opening to avoid potentially plugging the region near the end of the screw.

(11) The mass flow rate ($\dot{m}$) for a feed screw (aka "capacity") is equal to the material bulk density (ρ_b) multiplied by the material average speed (v) and the cross-sectional area of the material (A),

$$\dot{m} = \rho_b v A. \tag{11.1}$$

The cross-sectional area is,

$$A = \alpha \frac{\pi}{4}(D_f^2 - D_s^2), \tag{11.2}$$

where $0 \leq \alpha \leq 1$ is the fraction of the open screw volume/area that is filled with material ($\alpha = 1$ corresponds to a completely filled flight volume/area) and D_f and D_s are the diameters of the
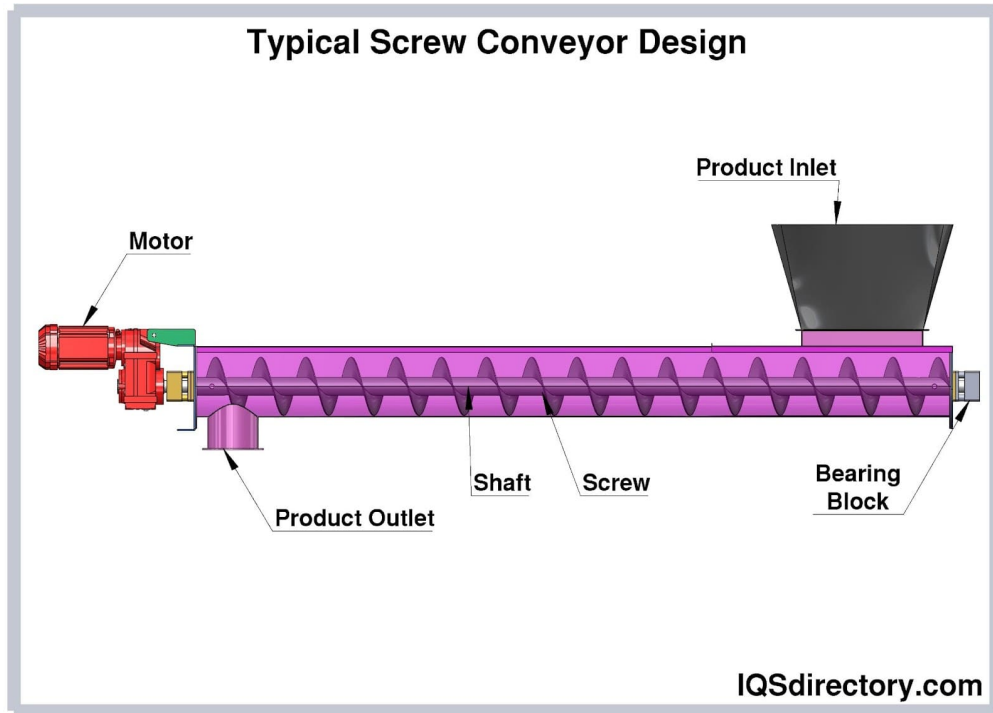
(A) Screw conveyor components
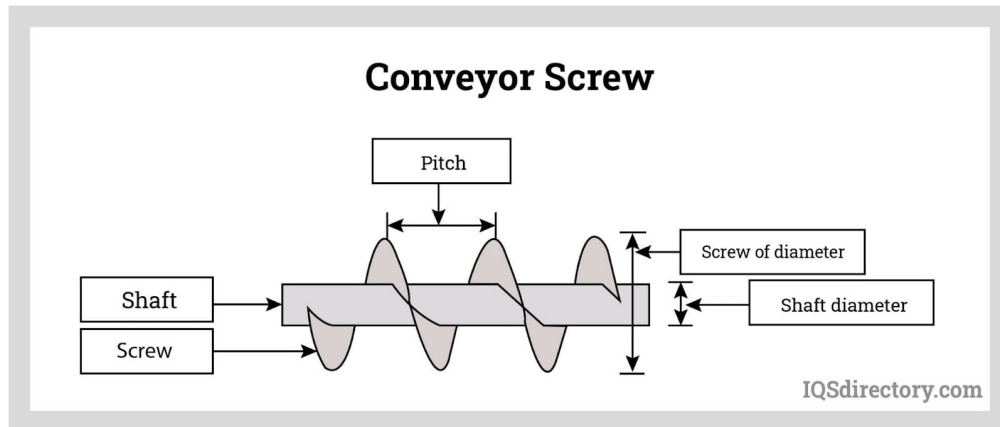
(B) Screw Parts

FIGURE 11.3. A schematic of a simple screw conveyor design. These figures are from https://www.screw-conveyors.com/screw-conveyor-design/.

screw flights and shaft, respectively. The speed at which material moves downstream in one screw revolution is,

$$v = \frac{L}{T} = \frac{\eta P}{2\pi/\omega}, \tag{11.3}$$

where L is the distance the material moves in one screw revolution and T is the time required for one revolution. The material moves a distance $L = \eta P$ where P is the screw pitch length and $0 \le \eta \le 1$ is the conveying efficiency of the screw, which is a complex function of the screw characteristics, material properties, and screw inclination angle. Lastly, ω is the rotational speed of the screw (with dimensions of $1/T$). Substituting the expressions for the area and speed into the mass flow rate

(A) A standard pitch screw

(B) A half-pitch screw

(C) A double flight screw
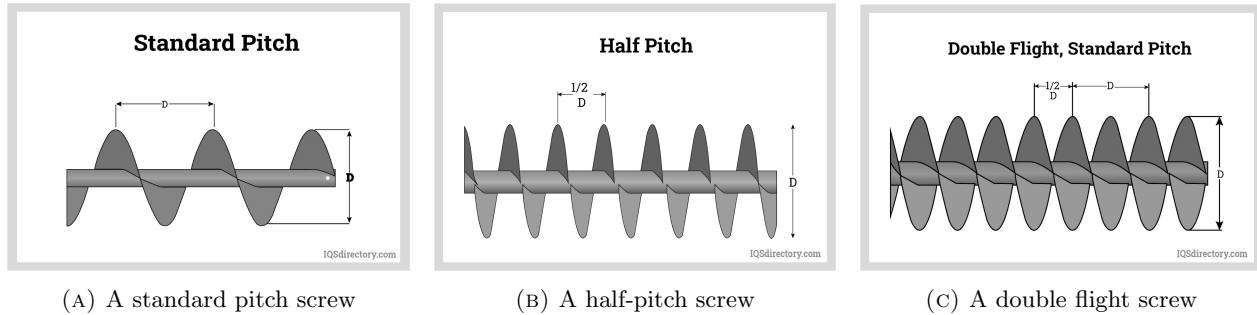
FIGURE 11.4. Illustrations of various screw designs. These figures are from https://www.screw-conveyors.com/screw-conveyor-design/.

FIGURE 11.5. A photograph of a "live bottom" screw feeder to be located at the bottom of a hopper with a large exit area. This photograph is from http://www.conveyoreng.com/products/screw-feeders-live-bottoms/?v=868f8823ca02.

expression,

$$\dot{m} = \frac{1}{8}\rho_b \eta \omega \alpha P(D_f^2 - D_s^2). \tag{11.4}$$

When locating a screw feeder/conveyor at the exit of a hopper, the screw should be designed so the hopper discharges uniformly rather than producing an asymmetric flow channel. If a constant pitch, constant shaft diameter screw in a constant area barrel is used, such as the one illustrated in Figure 11.1, then the flight volume on the upstream side of the screw will fill first with material from the hopper. As that material is conveyed downstream, no new material from the hopper enters the screw since the screw flight volume is already full. Thus, an asymmetric flow channel will form located at the upstream side of the screw. To discharge the hopper uniformly, the volume in the screw must increase gradually underneath the hopper to accommodate new material over the entire hopper exit. Of course, the screw spanwise width should also match the hopper's spanwise width.

Three common methods for increasing the screw fill volume are shown in Figure 11.6. The first approach involves increasing the screw pitch moving downstream (Figure 11.6a). In the second method, the screw shaft diameter decreases moving downstream (Figure 11.6b). Lastly, the trough/barrel diameter can be increased moving downstream (Figure 11.6c). Sometimes combinations of these three techniques are used simultaneously.

Notes:

(1) These increasing-volume screw design features are best suited for for slot-type hopper exits.

(A) A variable pitch screw

(B) A tapered screw core

(C) A tapered barrel
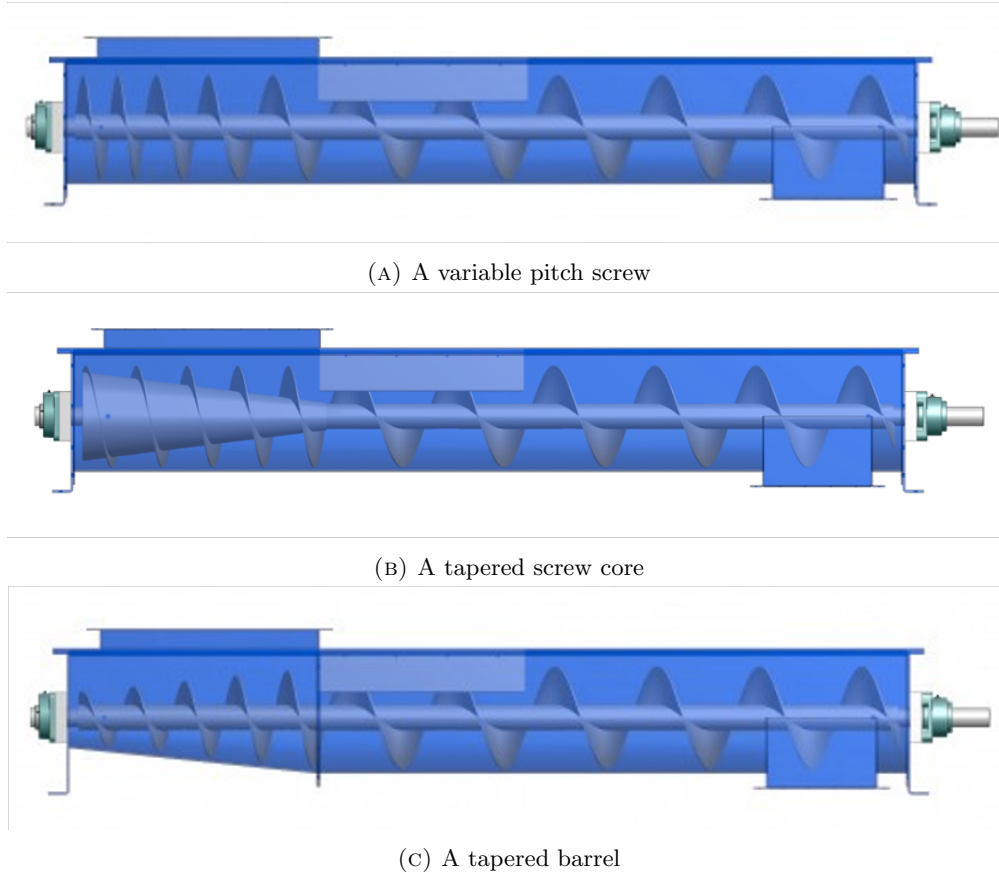
Figure 11.6. Three different screw designs for increasing the available volume into which material can flow from the hopper. These figures are from http://www.conveyoreng.com/products/screw-feeders-live-bottoms/. A video showing the discharge dynamics using a tapered shaft and variable pitch screw geometry is available at https://www.youtube.com/watch?v=ZjKbSnVESDc. A computer simulation of a variable pitch screw may be viewed at https://www.youtube.com/watch?v=PQi9U8_GAVQ.

(2) To determine area gradient in the streamwise direction to ensure uniform discharge from the hopper at a specified volumetric flow rate, apply Conservation of Mass to the control volume shown in Figure 11.7. This control volume surrounds a differentially small streamwise length of material discharging from the hopper into the feed screw. From Conservation of Mass, assuming steady state flow,

$$\rho_b v A + \rho_b \left(\frac{Q_H}{BL}\right)(Bdx) = \rho_b v A + d\left(\rho_b v A\right), \tag{11.5}$$

where Q_H is the (total) volumetric flow rate from the hopper, B is the distance into the page, L is the streamwise length of the hopper exit, v is the streamwise speed of the material, A is the cross-sectional screw area, and x is the downstream direction. Assuming a constant bulk density and constant streamwise speed,

$$\rho_b \left(\frac{Q_H}{L}\right)(dx) = \rho_b v dA, \tag{11.6}$$

$$\frac{dA}{dx} = \frac{1}{v}\left(\frac{Q_H}{L}\right). \tag{11.7}$$

$$\rho_b \left(\frac{Q_H}{BL}\right)(Bdx)$$

$$\rho_b vA \xrightarrow{\ \ dx\ \ } \rho_b vA + d(\rho_b vA)$$
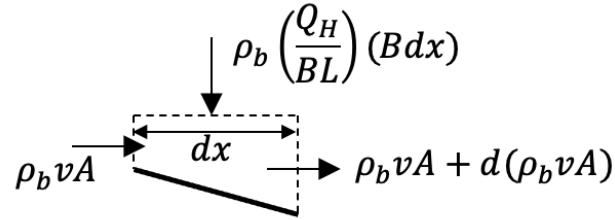
FIGURE 11.7. The control volume used in the Conservation of Mass analysis for determining the area gradient in the streamwise direction to ensure uniform discharge from a hopper.
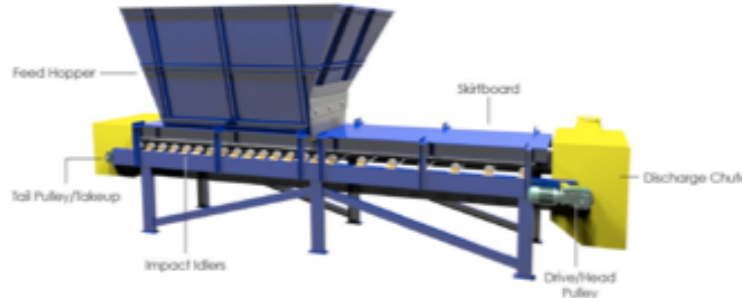
FIGURE 11.8. A schematic of a belt conveyor. This figure is from http://feeco.com/belt-feeders/.

For more information on feed screw design and interfacing with hoppers, the reader should refer to https://www.kwsmfg.com/wp-content/themes/va/pdf/Screw-Conveyor-Engineering-Guide-pt1.pdf, https://www.iqsdirectory.com/articles/screw-conveyors.html, Roberts [3], and Bates [4].

11.2. Belt Feeders and Conveyors

Belt feeders/conveyors (Figure 11.8) are also commonly used to control the flow at the exit of a hopper. A belt conveyor uses a looped belt with a width at least as big as the hopper width mounted on a set of pulleys at either end with the one on the discharge end being motorized to drive the belt. In between the end pulleys, the belt rests on rollers (aka idlers). Material from the hopper falls onto the moving belt and is conveyed downstream.

Notes:

(1) Belt conveyors are well suited for long, wide slot-style hopper exits and can handle large discharge loads. Belt conveyors can handle higher feed rates than screw conveyors and can convey material long distances.

(2) The belt mass flow rate (aka capacity, $\dot{m}$) is given by,

$$\dot{m} = \rho_b V A, \tag{11.8}$$

where V is the belt speed and A is the cross-sectional area of the material on the belt. Many belts have a trough-style cross section (Figure 11.9) to keep the material contained laterally on the belt. For this configuration, three idlers guide the belt at each streamwise support location with one idler under the bottom of the belt and an idler supporting each trough wall. The maximum cross-sectional area of material on the belt (A) is modeled as the sum of a trapezoidal area (A_T) and the area of a circular segment (A_{CS}),

$$A = A_T + A_{CS}, \tag{11.9}$$
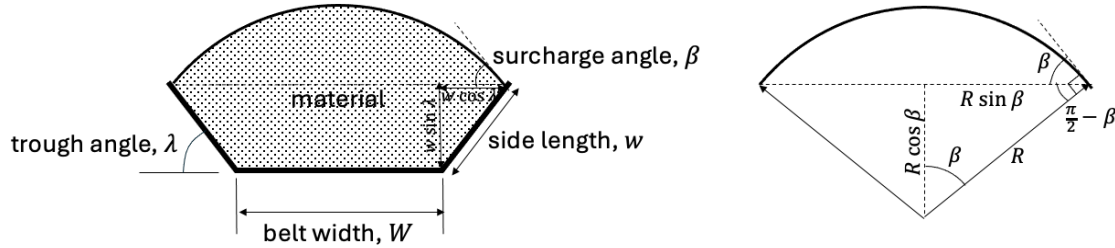
Figure 11.9. (left) A cross-sectional schematic of a trough-style belt. (right) The geometry used to calculate the circular segment cross-sectional area.

Material	Surcharge angle, λ (°)	Material	Surcharge angle, λ (°)
ammonium sulphate	10	Portland cement	25
graphite	10	gravel (pebbles)	10
iron ore (crushed fine)	20	limestone (3 mm)	10
potash ore	10	sand (foundry)	30
sugar (granulated)	10	talc (powdered)	10

Table 11.1. Surcharge angle values for various materials. This data is from `https://pdhonline.com/courses/m344/m344content.pdf`. More surcharge angle values are available at `https://www.engineeringtoolbox.com/bulk-material-conveyor-capacity-d_1558.html`.

where,

$$A_T = Ww\sin\lambda + 2\left[\frac{1}{2}(w\cos\lambda)(w\sin\lambda)\right] = Ww + w^2\cos\lambda\sin\lambda, \tag{11.10}$$

and,

$$A_{CS} = \underbrace{\frac{(2\beta)}{2}R^2}_{A_{\text{sector}}} - \underbrace{2\left[\frac{1}{2}(R\sin\beta)(R\cos\beta)\right]}_{A_{\text{triangle}}} = R^2\left(\beta - \sin\beta\cos\beta\right). \tag{11.11}$$

where W is the horizontal portion belt width, w is the length of a trough wall, λ is the trough angle with respect to the horizontal, β is the "surcharge angle" of the material, and,

$$2R\sin\beta = W + 2w\cos\lambda \implies R = \frac{W + 2w\cos\lambda}{2\sin\beta}. \tag{11.12}$$

Typical trough angles are $\lambda = 20°, 35°$, and $45°$. Values for the surcharge angle for various materials are given in Table 11.1. Typically, material is filled to less than 80% of the maximum area.

(3) Belt conveyors exert little shear on the discharging material and, thus, there is little heat generation during feeding. Belt conveyors are good for large, fragile, or cohesive materials.

(4) Materials prone to flooding, dust generation, or are adhesive are not well suited for belt feeding.

(5) Like screw feeders, belt feeders can be combined with weight sensors to monitor and control the mass flow rate from the hopper (gravimetric feeding).

(6) Belt conveyors are easier to clean than screw conveyors.

(7) Belt wear and associated maintenance should be monitored, especially when conveying abrasive materials.

(8) As with screw conveyors, the filling volume beneath the hopper exit should increase moving downstream on the belt in order to discharge the hopper uniformly (Figure 11.10).

(9) For more information on belt conveyor design, refer to `https://pdhonline.com/courses/m344/m344content.pdf`.
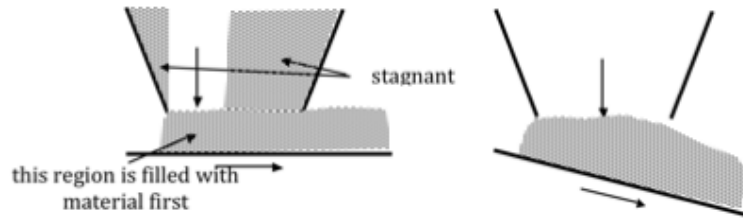
FIGURE 11.10. An illustration showing that a belt conveyor should be tilted to increase the fill volume moving downstream in order to discharge a hopper uniformly.
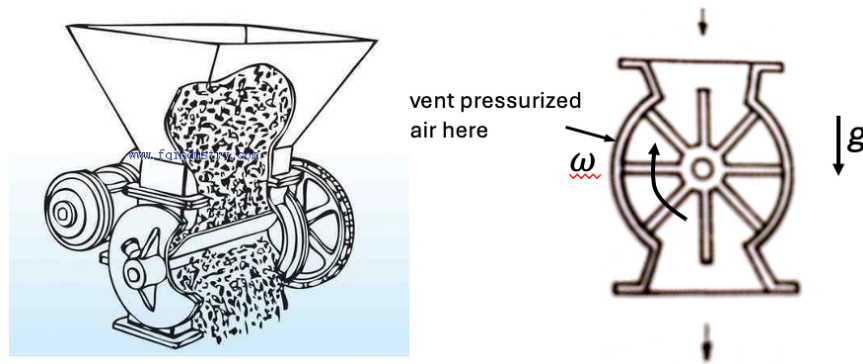
FIGURE 11.11. Illustrations of a rotary feeder/valve. The left figure is from http://www.fqindustry.com/news/What-is-a-rotary-feeder-4.html and the right figure is from Thomson [5].

11.3. Rotary Feeders/Valves

Rotary feeders/valves are often used to feed material into an environment with a different surrounding pressure. Screw and belt conveyors don't provide a seal between upstream and downstream environments, but rotary feeders do.

A rotary feeder consists of a housing within which a shaft with vanes or pockets rotates (Figure 11.11). Material in the hopper falls into an open cavity between neighboring shaft vanes. As the shaft rotates, the open cavity seals against the housing as the vanes move out of hopper discharge zone. At the bottom of the rotary feeder, the cavity opens again and material falls out into the discharge region.

Notes:

(1) Rotary valves are good for feeding floodable materials, but are not well suited for cohesive materials, which may not fill the cavity efficiently.
(2) Rotary valves are typically used for circular or square hopper exits.
(3) A simulation example of a rotary valve can be viewed at https://www.youtube.com/watch?v=rXOlotxOGmU.
(4) Material will preferentially fill the rotary valve cavities on the upstream side of the valve, i.e., where the cavity first opens up underneath the hopper. As a result, the hopper will discharge asymmetrically. To discharge the hopper more uniformly, a standpipe should be installed between the hopper and the rotary valve, as shown in Figure 11.12. The engineering rule of thumb is that the standpipe length should be at least twice the exit diameter. An example simulation showing the impact of a standpipe is available at https://www.youtube.com/watch?v=zun389BPTKc.

The flow rate through the feeder (Q) is governed largely by the rotor speed (ω). The relationship is not exactly linear since the speed with which powder falls into the cavity is governed by gravitational acceleration. The
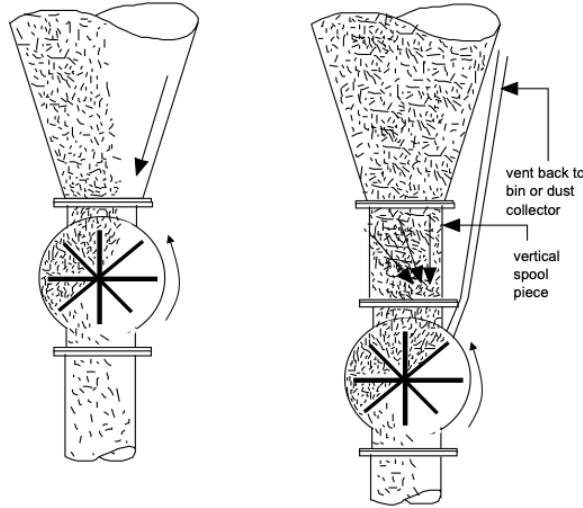
FIGURE 11.12. Illustrations of hopper flow without (left) and with (right) a standpipe between the hopper exit and a rotary valve. The figures are from Marinelli [6].

ratio of the characteristic time for material to fall into the cavity (T_{fall}) to the period of rotation (T_{rotate}) is a Froude number (Fr),

$$\left(\frac{T_{\text{fall}}}{T_{\text{rotate}}}\right)^2 \propto \left(\frac{\sqrt{R/g}}{1/\omega}\right)^2 = \frac{\omega^2 R}{g} = \text{Fr}, \tag{11.13}$$

where R is the radius of the rotary feeder and g is the acceleration due to gravity. When $\text{Fr} \ll 1$, then $T_{\text{fall}} \ll T_{\text{rotate}}$, i.e., material falls into the open cavity before the cavity can rotate very much, and the flow rate will be nearly proportional to the rotational speed, i.e., $Q \propto \omega$. However, as the Froude number increases, the open cavity volume may not fill completely since the cavity rotates quickly out of the filling zone. As a result, the flow rate increases at a rate that is less than linear with the rotational speed.

Notes:

(1) Typical rotary feeder rotational speeds are between 5 and 40 rpm.
(2) Typical volume fill efficiencies range between approximately 50 and 85%, depending on the material and rotational speed.
(3) The flow rate from the rotary valve will be periodic due to the opening and closing of cavities.
(4) If the hopper exit is large, the flow rate through the rotary valve can be reduced by using shallow pockets, thereby decreasing the volume of the pocket (Figure 11.13).

Rotary valves are well suited for feeding material into an environment with a different pressure, such as a pneumatic conveying line. When used in such applications, the gap between the rotating vanes and the housing must be small to prevent air leakage through the valve. Unfortunately, particles can get jammed in this small clearance, particularly just downstream of the filling zone (Figure 11.14a). To prevent jamming, an offset feed region can be used along with a flow control gate, as shown in Figure 11.14b. Particles are unlikely to get caught in the gap just downstream of the gate overhang. In addition to a flow control gate, rotary valves used in pressurized environments also incorporate a vent on the return side of the housing (Figure 11.14a). The vent is used to equalize the pressure in the open cavity before reaching the filling region.

Notes:

FIGURE 11.13. Illustration of a rotary valve with shallow pockets, which can be used to decrease the flow rate. This figure is from Thomson [5].

(A) vent
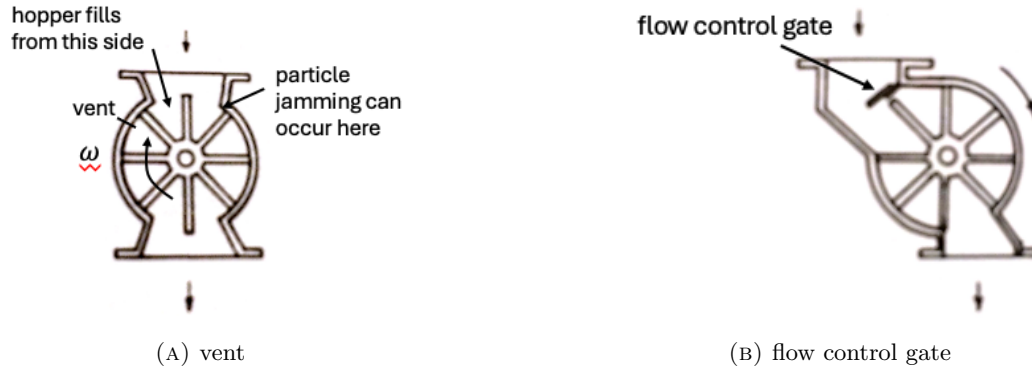
(B) flow control gate

FIGURE 11.14. Illustrations of a flow control gate and a vent in a rotary valve. These figures are from Thomson [5].
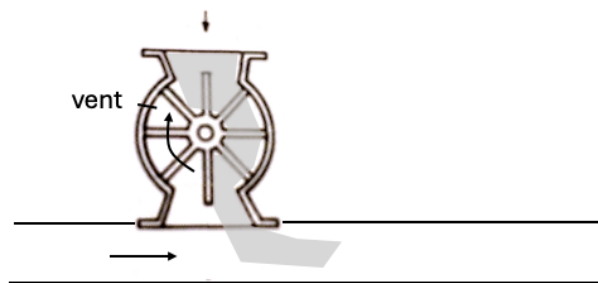
FIGURE 11.15. Illustration of a rotary valve feeding into a conveying line. The valve should be oriented to discharge material on the downstream side of the exit.

(1) Over time there will be increased air leakage through the vane/housing clearance due to abrasive wear of the valve vanes.
(2) If feeding into a pneumatic conveying line, a rotary valve should be oriented to discharge material at the downstream side of the exit to maintain a "clean" flow from the valve (Figure 11.15).

FIGURE 11.16. A wall vibrator attached to a hopper wall. This figure is from http://www.shake-it.com/product-line/mt-fast-hopper-trailer-vibrator/.

11.4. Discharge Aids

Often discharge aids, such as wall vibrators, vibrating dischargers, air injectors, and air cannons, are used to aid in the discharge of material from funnel flow hoppers. These devices are almost always added after the hopper has been installed and flow problems are observed. The type, location, and operation of discharge aids is almost always found empirically. There has been little research focused on providing design rules for discharge aids.

A wall vibrator is typically an unbalanced motor that is operated either electrically or pneumatically (Figure 11.16). Often the vibration frequency and amplitude can be controlled. The vibrator is usually attached to a wall against which material stagnates with the intention of inducing flow. Unfortunately, vibration, especially for compressible materials at small amplitudes and high frequencies, can sometimes cause material to pack more densely, exacerbating flow problems. Wall vibrators tend to be more effective at promoting flows in chutes, which have a free surface. A video showing a wall vibrator in action is available at https://www.youtube.com/watch?v=zsiIu4ZwggY. Another video that promotes the use of vibration is available at https://www.youtube.com/watch?v=T_HYfCsOXAI. This dramatic video doesn't actually show vibration in action, but it does show the dangerous situations people may be put in when flow problems exist.

Vibrating dischargers (aka bin activators) also use vibration in an attempt to improve flow from a hopper. As opposed to being attached to a hopper wall, the discharger is an insert installed at the hopper exit (Figure 11.17). The discharger vibrates the material as opposed to the hopper walls. As with a wall vibrator, material may pack more densely with a discharger if the material is compressible. An illustration of an operating discharger is available at https://www.youtube.com/watch?v=wuK8LUvfucU.

In addition to vibration, air is often injected into stagnant material in an effort to induce flow; however, air should not be used with materials prone to flooding. An air cannon (Figure 11.18) impulsively injects a fixed volume of air at hopper walls, usually at large pressures and speeds, and is particularly useful for breaking up time consolidated material. Often multiple air cannons are used in different regions of a hopper and are timed to go off in such a way as to keep material in motion. For more information on air cannons, please refer to https://www.youtube.com/watch?v=XsYoB_dvMjo.

Aeration pads (Figure 11.19) also inject air into the material at a wall in order to induce flow, but the air is at a lower pressure and speed than with an air cannon. The air from an aeration pad effectively reduces the wall friction angle and aerates the material near the wall, often leading to mass flow conditions. In some cases, the aeration pad design can also cause the hopper wall to vibrate, which also helps to improve flow conditions. An example video showing the installation and a demonstration of one type of aeration pad is available at https://youtu.be/1v4__fDyGyE?si=xGAx1A1WwnDYZuWT.
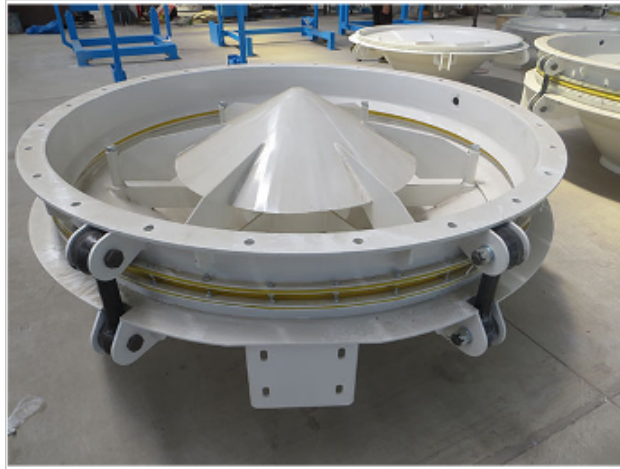
Figure 11.17. A vibrating discharger, which would be located at a hopper exit. This figure is from http://www.grainsilo.com/grain-silo-system/grain-handling/vibrating-discharger.html.

Figure 11.18. A photograph showing the installation of multiple (orange) air cannons on a hopper. This figure is from https://www.martin-eng.com/content/product_subcategory/491/air-cannons-products.

11.5. Hopper Level Sensors

In addition to discharging material effectively from a hopper or bin, one often needs to know how much material remains within the vessel. For small hoppers and bins, the entire device may placed on load cells to measure the weight of the device. This approach is often used in gravimetric feeding applications, e.g., loss-in-weight feeders. For large bins and hoppers, level detectors are often used to determine the location of the material free surface. Many designs have been proposed for detecting the free surface height.

Point-level detection relies on direct contact with the material at a fixed location within the hopper. This type of device determines if material exists at the sensor location and is most often located at the vessel wall. Examples of such devices include capacitance and pressure diaphragm sensors, rotary paddles, tilt switches, and vibrating rods (Figure 11.20 shows vibrating rod sensors installed in hopper). A capacitance sensor checks for disruptions in the sensor's local electric field caused by the presence of material. In a

(A) Aeration pads installed in a hopper. This figure is from https://techflow.net/installations/components-spares/aeration-pad.
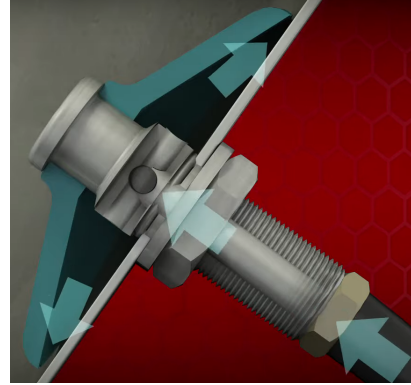
(B) Close up of one type of aeration pad design. This figure is from https://www.prospare.co.uk/product-categories/aeration/.

FIGURE 11.19. Aeration pads in a hopper.
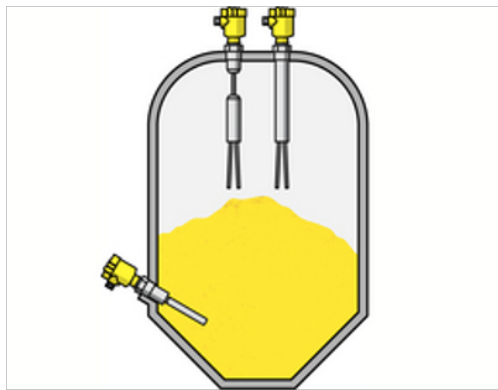
FIGURE 11.20. An illustration of multiple vibrating rod point-level sensors installed in a hopper. Point-level sensors detect if material is present at the sensor location. This figure is from http://www.tjvega.com.cn/cn-en/Level_switch_vibration_Measuring-principle.htm.

pressure diaphragm sensor, the normal stress generated by the material activates a switch in the sensor. Rotary paddles and vibrating rods operate by detecting the change in power required to rotate or vibrate a rod when submerged in a material (refer to https://www.youtube.com/watch?v=pQIiFTuzIuU and https://www.youtube.com/watch?v=TfljWiwlMOs for example videos). A tilt switch hangs vertically when no material is present, but tilts and triggers a switch then it rests on the material surface (refer to https://www.youtube.com/watch?v=brYJbhagucw for an illustration of the operation). One deficiency of wall-mounted sensors is that they will give inaccurate readings of the volume of material in funnel flow and rat-holed conditions since material at the walls remains stagnant, but material in the core may have discharged.

Continuous-level sensors can determine the height of the material free surface, not just whether or not material is present at a particular location as is provided by a point-level sensor. Continuous-level sensors usually involve remote sensing. Examples of such sensors include plumb-bob, ultrasonic, laser, and radar sensors. These sensors are typically mounted at the top of the vessel. A plumb-bob sensor (Figure 11.21a) operates by dropping a weight attached to a cable spooled from a pulley. When the weight contacts the material free surface, the torque on the pulley decreases and the length of unspooled cable can be used to measure the free

(A) An illustration of a plumb-bob level sensor.

(B) An illustration of a radar level sensor.

Figure 11.21. Examples of continuous-level sensors. Both figures are from https://www.azosensors.com/article.aspx?ArticleID=558.

surface height. Ultrasonic, laser, and radar sensors operate by directing sound, light, or radar waves onto the material free surface and timing the return of the reflected waves (Figure 11.21b). Knowing the wave speed and return wave time, the distance to the free surface can be determined.

11.6. Summary

The following bullet points summarize the major topics in this chapter:

(1) Discharge devices such as a screw feeder, belt feeder, or rotary valve are located at the hopper outlet to control the discharge rate.
(2) Discharge devices must be carefully designed to prevent asymmetric discharge from the hopper. Increasing the feeder volume in the downstream direction is needed for uniform discharge. The use of a vertical standpipe below the hopper exit can be helpful for isolating feeder dynamics from the hopper.
(3) Discharge aids such as vibrators, air cannons, and aeration pads are often used in an attempt to remedy flow problems. These devices are often applied via trial-and-error and may worsen flow problems.
(4) Various level sensor designs can be used to determine the fill level in a hopper. Funnel flow or ratholing can result in misleading measurements.

Calculate the mass flow rate for the conveying screw shown in the following figure. The screw has pitch length P, a screw flight diameter of D_f, a screw shaft diameter D_s, and rotates at a speed ω (e.g., in rad/s). The material has a bulk density of ρ_b. Assume the fraction of the screw volume filled with material is α ($0 \leq \alpha \leq 1$) and the conveying efficiency, i.e., the ratio of the axial distance the material moves in one screw revolution to the pitch length, is η (($0 \leq \eta \leq 1$).
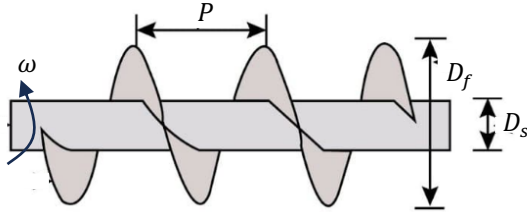
SOLUTION:
The cross-sectional area of material in the screw is,
$$A = \alpha \frac{\pi}{4}\left(D_f^2 - D_s^2\right). \tag{1}$$
Note that the fraction of area filled with material is equal to the fraction of volume filled, α. The speed at which this material moves downstream in one screw revolution is,
$$v = \frac{L}{T} = \frac{\eta P}{2\pi/\omega}, \tag{2}$$
where L is the distance moved in one screw rotation ($= \eta P$) and T is the time require for one revolution ($= 2\pi/\omega$, where ω is in rad/s). The mass flow rate is then,
$$\dot{m} = \rho_b v A \implies \dot{m} = \rho_b\left(\frac{\eta P}{2\pi/\omega}\right)\left[\alpha\frac{\pi}{4}\left(D_f^2 - D_s^2\right)\right] \implies \boxed{\dot{m} = \frac{1}{8}\rho_b \eta P \alpha \left(D_f^2 - D_s^2\right)\omega}. \tag{3}$$

Derive the required tilt angle τ for a belt conveyor to uniformly discharge a hopper at a belt speed of v. Assume the volumetric flow rate from the hopper is Q, the streamwise length of the hopper exit is L, and the spanwise width of the hopper exit (and belt width) is B.

hopper and belt have
width B into the page

Q L v τ
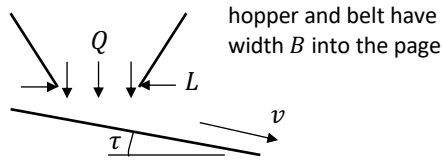
SOLUTION:
From the analysis given in the course notes,
$$\frac{dA}{dx} = \frac{1}{v_s}\left(\frac{Q}{L}\right),\tag{1}$$
where A is the cross-sectional area in the streamwise direction and v_s is the speed in the streamwise direction (not the inclined speed v). The cross-sectional area in the streamwise direction is,
$$A = B(x\tan\tau) \;=>\; \frac{dA}{dx} = B\tan\tau.\tag{2}$$
The inclined speed v and streamwise speed v_s are related via,
$$v_s = v\cos\tau.\tag{3}$$
Substituting Eqs. (2) and (3) into Eq. (1) and re-arranging,
$$B\tan\tau = \frac{1}{v\cos\tau}\left(\frac{Q}{L}\right),\tag{4}$$
$$\tan\tau\cos\tau = \frac{1}{v}\left(\frac{Q}{BL}\right),\tag{5}$$
$$\boxed{\sin\tau = \frac{1}{v}\left(\frac{Q}{BL}\right)}.\tag{6}$$

x

$x\tan\tau$

τ

$v_s = v\cos\tau$

τ

v

Bibliography

[1] R. Jenkyn and D. Goodwill, "Silo failures: Lessons to be learned," Engineering Digest, pp. 17–22, 1987.

[2] J. Carson and R. Jenkyn, "Load development and structural considerations in silo design," in Reliable Flow of Particulate Oslo, Norway, 1993.

[3] A. Roberts, "Design and performance criteria for screw conveyors in bulk solids operation," Bulk Solids Handling, vol. 22, no. 6, pp. 436–444, 2002.

[4] L. Bates, "Interfacing hoppers with screw feeders," Bulk Solids Handling, vol. 6, no. 1, pp. 65–78, 1986.

[5] F. Thomson, "Storage and flow of particulate solids," in Handbook of Powder Science & Technology, M. Fayed and L. Otten, Eds., 2nd ed., 1997, ch. 8, pp. 389–486.

[6] J. Marinelli, Lecture notes for "particulate systems" (che 53600 at purdue university), 2018.

CHAPTER 12

Chute Design

Chutes are used to transfer material from one unit operation to the next (Figure 12.1). They also help reduce material spillage and provide dust control. Unfortunately chute design is often overlooked since for fluids, transferring fluid between locations is much less problematic. Indeed, in manufacturing process drawings, chutes and other transfer hardware are usually just lines on a flow sheet. Poor flow in chutes can result in flow stoppages, small flow rates, degraded material, surface wear, dust generation, and conveyor belt abrasion (Figure 12.2). Thus, some care should be taken in proper chute design.

(A) Photo from https://forum.bulk-online.com/showthread.php?28819-Case-study-Transfer-Chute-Redesign-with-EDEM-BulkSim%C2%AE-Simulation.

(B) Photo from https://www.martin-eng.com/content/article/982/engineered-transfer-chutes-help-superior-midwest-energy-terminal-maintain-high-volume.
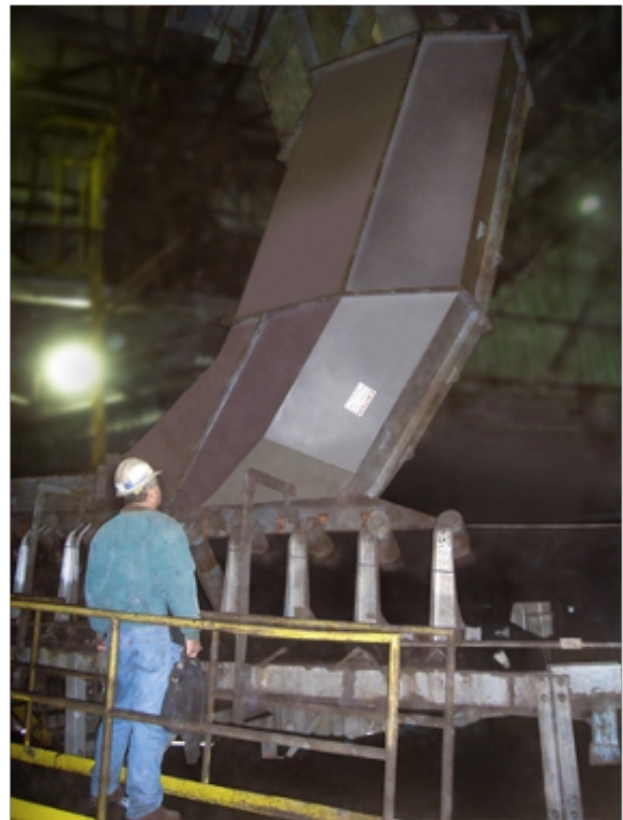
FIGURE 12.1. Photographs of chutes in manufacturing processes.

(A) Photo showing build-up of material in a chute.

(B) Another photo of material build-up in a chute.

FIGURE 12.2. Examples of problems encountered in particulate material transfer chutes. For an example of poor hood design on a chute, refer to https://www.youtube.com/watch?v=tTNDllS2QYg.
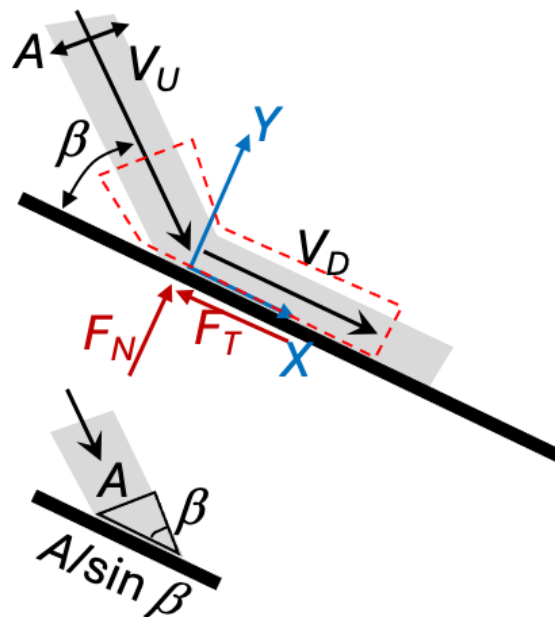
FIGURE 12.3. The control volume and free body diagram used in the linear momentum analysis of material impacting a chute. Note that V_U and V_D indicate the upstream and downstream speeds, respectively.

12.1. Preventing Flow Stoppages at Impact

To prevent material build-up, surfaces should be sufficiently steep and smooth to prevent material build-up, particularly after free fall of the material, but not so steep that material speeds and surface wear are excessive.

To analyze the speed of material after impact on a chute (Figure 12.3), apply the Linear Momentum Equation in the X and Y directions to a control volume surrounding the material (note that much of the analysis in this chapter comes from Dick and Royal [1]). Assume the material does not bounce on the surface, the system is at steady state, the material weight in the control volume is negligible, and the tangential force applied to the material is a Coulomb sliding friction force (i.e., $F_T = F_N \tan \phi_w$). In the Y direction,

$$\frac{d}{dt} \int_{CV} u_Y \rho dV + \int_{CS} u_Y \left(\rho \mathbf{u}_{rel} \cdot d\mathbf{A} \right) = F_{B,Y} + F_{S,Y}, \tag{12.1}$$

where,

$$\frac{d}{dt} \int_{CV} u_Y \rho dV = 0 \qquad \text{(steady conditions)}, \tag{12.2}$$

$$\int_{CS} u_Y \left(\rho \mathbf{u}_{rel} \cdot d\mathbf{A} \right) = (-V_U \sin \beta)(-\dot{m}), \tag{12.3}$$

$$F_{B,Y} = 0 \qquad \text{(neglecting material weight)}, \tag{12.4}$$

$$F_{S,Y} = F_N. \tag{12.5}$$

Substituting,

$$\dot{m} V_U \sin \beta = F_N. \tag{12.6}$$

Note that $\dot{m} = \rho_b V_U A$. Similarly, in the X-direction,

$$\frac{d}{dt} \int_{CV} u_X \rho dV + \int_{CS} u_X \left(\rho \mathbf{u}_{rel} \cdot d\mathbf{A} \right) = F_{B,X} + F_{S,X}, \tag{12.7}$$

where,

$$\frac{d}{dt} \int_{CV} u_X \rho dV = 0 \qquad \text{(steady conditions)}, \tag{12.8}$$

$$\int_{CS} u_X \left(\rho \mathbf{u}_{rel} \cdot d\mathbf{A} \right) = (V_U \cos \beta)(-\dot{m}) + (V_D)(\dot{m}), \tag{12.9}$$

$$F_{B,X} = 0 \qquad \text{(neglecting material weight)}, \tag{12.10}$$

$$F_{S,X} = -F_T = -F_N \tan \phi_w. \tag{12.11}$$

Substituting,

$$\dot{m} \left(-V_U \cos \beta + V_D \right) = -F_N \tan \phi_w. \tag{12.12}$$

Combining Eqs. (12.6) and (12.12),

$$\dot{m} V_U \sin \beta = -\frac{\dot{m}}{\tan \phi_w} \left(-V_U \cos \beta + V_D \right), \tag{12.13}$$

$$\sin \beta \tan \phi_w = \cos \beta - \frac{V_D}{V_U}, \tag{12.14}$$

$$\frac{V_D}{V_U} = \cos \beta - \sin \beta \tan \phi_w. \tag{12.15}$$

Note that for V_D/V_U to remain positive, i.e., no reverse flow and no stopping,

$$\cos \beta - \sin \beta \tan \phi_w > 0 \implies \tan \beta \tan \phi_w < 1. \tag{12.16}$$

Thus, to ensure that materials flows downstream after impact,

$$\beta + \phi_w < 90°. \tag{12.17}$$

Note that the average normal impact stress is estimated to be (refer to Figure 12.3 and Eq. (12.6)),

$$\overline{\sigma_N} = \frac{F_N}{A/\sin \beta} = \rho_b V_U^2 \sin^2 \beta. \tag{12.18}$$
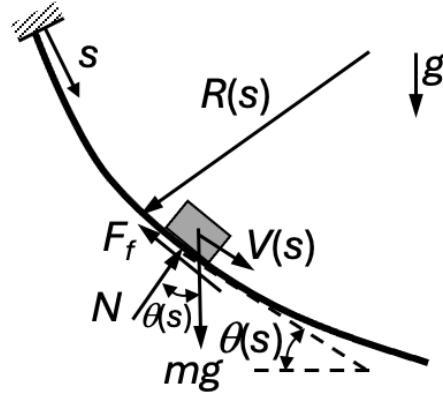
FIGURE 12.4. The geometry and free body diagram for a small element of material on a curved chute.

12.2. Preventing Flow Stoppages on Curved Chutes

Curved chutes are generally better at directing the flow of material rather than allowing material to free fall or using straight chutes with abrupt angle changes. To analyze material flow on a curved chute, consider the material element shown in Figure 12.4. Applying Newton's Second Law to the material element in the streamwise (s) direction,

$$ma_s = m\frac{dV}{dt} = m\frac{dV}{ds}\frac{ds}{dt} = mV\frac{dV}{ds} = mg\sin\theta - F_f = mg\sin\theta - N\tan\phi_w. \tag{12.19}$$

A force balance in the radial direction (towards the center of curvature) gives,

$$ma_r = m\frac{V^2}{R} = -mg\cos\theta + N. \tag{12.20}$$

Combining these two relations,

$$V\frac{dV}{ds} = g\sin\theta - \left(\frac{V^2}{R} + g\cos\theta\right)\tan\phi_w. \tag{12.21}$$

This differential equation can be integrated with respect to the location s using the boundary condition $V(s=0) = V_0$, keeping in mind that the chute angle and radius of curvature can vary with s, i.e., $\theta = \theta(s)$ and $R = R(s)$. The method of integration will depend on the form of $\theta(s)$ and $R(s)$ and may require numerical methods.

Notes:

(1) Consider a flow with an initial speed V_0 turned by some angle from the vertical using a constant radius chute. The flow speed at the end of the chute is found by solving Eq. (12.21),

$$V\frac{dV}{ds} = g\sin\left(\frac{\pi}{2} - \alpha\right) - \left[\frac{V^2}{R} + g\cos\left(\frac{\pi}{2} - \alpha\right)\right]\tan\phi_w, \tag{12.22}$$

$$\frac{V}{gR}\frac{dV}{d\alpha} = \cos\alpha - \left(\frac{V^2}{gR} + \sin\alpha\right)\tan\phi_w, \tag{12.23}$$

$$F'^2 V'\frac{dV'}{d\alpha} = \cos\alpha - (F'^2 V'^2 + \sin\alpha)\tan\phi_w, \tag{12.24}$$

where $F' := V_0/\sqrt{gR}$ and $V' := V/V_0$. The previous differential equation is subject to the boundary condition $V'(\alpha = 0) = 1$. Plots of the dimensionless speed as a function of angle for different values of F' and ϕ_w are given in Figure 12.5. From the plot, we observe that as $F' = V_0/\sqrt{gR}$ decreases
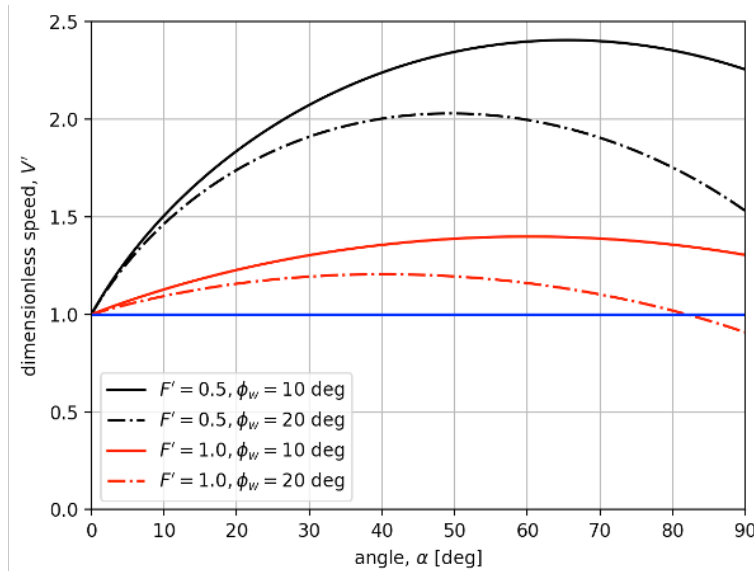
FIGURE 12.5. Plots of dimensionless material speed $V' = V/V_0$ on a chute with constant radius of curvature R plotted as a function of angle α for different values of the dimensionless initial speed $F' = V_0/\sqrt{gR}$ and wall friction angle ϕ_w.
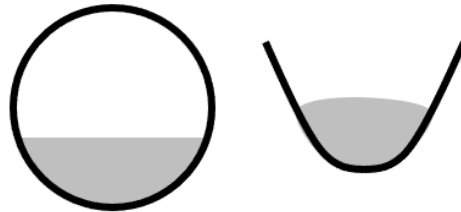
FIGURE 12.6. Circular and U-shaped chute cross sections.

(at a given wall friction angle), the dimensionless final speed, V', increases. Thus, for a given inlet speed, V_0, increasing the radius of curvature, R, which decreases F', results in a larger outlet speed. Thus, large radius of curvature turns are typically desired to maintain flow speed.

(2) Methods for controlling the flow on the chute include the following:
    (a) Use curved chute cross-sections, e.g., circular pipes and U-shaped troughs, to help center the load (Figure 12.6). Keeping the flow consistently in a particular region helps to reduce material buildup in the chute.
    (b) Minimize the use of rectangular cross-sectioned chutes. Often, square or rectangular sections are used since they're easy to fabricate and install, but these sections are more likely to disperse the material, entrain air, and result in a build up of material in the chute corners.
    (c) If material enters the chute with spanwise momentum, then rubber curtains, chains, and ribs in the chute can reduce the spanwise momentum to center the flow (Figure 12.7).
    (d) When transitioning from a chute to a belt, accelerating the material to the belt speed and loading tangentially onto the belt (to reduce the impact stress) can significantly reduce belt wear and minimize dusting (Figure 12.8).
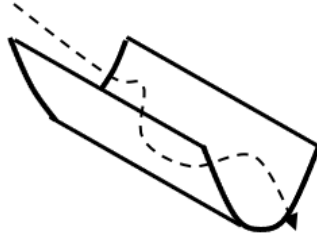
FIGURE 12.7. Circular and U-shaped chute cross sections.
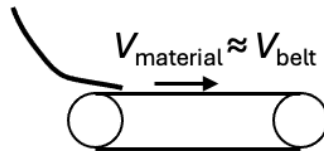
FIGURE 12.8. Matching the material speed at the end of a chute to a conveyor's belt speed.

12.3. Chute Fill Area

For an enclosed chute, which is often used to help contain dust, it is important that the chute not plug with material. A design rule-of-thumb to avoid plugging is to keep the material height in the chute (H) to less than one-third of the chute's diameter (D) at the minimum speed (assuming a circular cross-section), i.e.,

$$H < \frac{1}{3}D. \tag{12.25}$$

Consider the circular cross-section shown in Figure 12.6 through which material flows at volumetric flow rate Q,

$$Q = VA = V\frac{D^2}{8}(\alpha - \sin\alpha), \tag{12.26}$$

where V is the material speed and, from trigonometry,

$$\alpha - 2\cos^{-1}\left(1 - \frac{2H}{D}\right). \tag{12.27}$$

Notes:

(1) For $H/D = 1/3$, $\alpha = 141°$ and $Q = 0.23VD^2$.
(2) Although the bulk density of the material may change as it flows along a chute due to changes in velocity, centripetal acceleration, and material thickness (hydrostatic stress), it is reasonable to assume that these changes are small as long as the material doesn't become fluidized.

12.4. Reducing Chute Wear

For abrasive materials, it is important to minimize chute wear. From Archard's Wear Law, the wear volume on a surface (V) is given by,

$$V \propto \frac{N\Delta s}{H}, \tag{12.28}$$
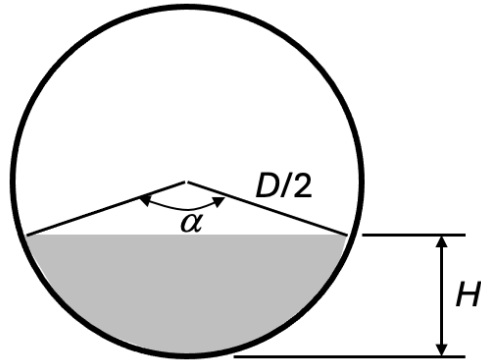
FIGURE 12.9. The geometry of a circular cross-sectioned chute of diameter D filled to height H.
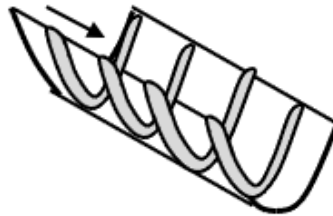
FIGURE 12.10. Illustration of spanwise ribs within a chute to reduce surface wear of the chute.

where N is the normal load acting on the surface, Δs is the sliding distance, and H is the surface hardness of the softer material. Thus, to reduce wear, one should design the chute curvature such that the normal force is small. Referring to Figure 12.4, the normal force on the chute is,

$$N = \frac{V^2}{R} + mg\cos\theta. \tag{12.29}$$

Decreasing the material speed on the chute (V), increasing the chute's radius of curvature (R), decreasing the mass of material on the chute (m), and increasing the chute angle from the horizontal (θ) will all act to decrease the normal force and wear.

Notes:

(1) An alternate approach for reducing wear is to use spanwise, abrasion-resistant ribs so the flowing material only contacts the chute surface at the rib surfaces (Figure 12.10). Nearly static material will build up between the ribs and, thus, flowing material mostly only contacts the stagnant material between the ribs. This approach is only recommended for large, non-cohesive materials, otherwise significant material build-up can occur.

(2) "Rock boxes" may be used at transfer points to reduce wear at junction points. A rock box is a transfer location where material accumulates so incoming material impacts accumulated material rather than the chute surface (Figure 12.11). Rock boxes are not good for for cohesive materials since significant build-up may occur and also friable materials since material breakage and dusting may occur. A discrete element method (DEM) simulation showing a rock box may be viewed at https://www.youtube.com/watch?v=QgVNvYZb3pI.

(3) Replaceable liners may also be used on the chute surface to reduce wear of the chute. However, use of liners can result in potential contamination of the material, the surface finish of the liner will
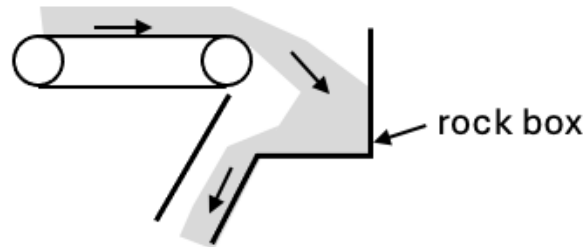
FIGURE 12.11. Illustration of a "rock box".

change over time, and fasteners used to hold the liner in place and protruding into the flow may result in material build-up sites.
(4) Methods for minimizing dust generation include:
    (a) enclosing the chute,
    (b) reducing air entrainment and material attrition by keeping the material in contact with the chute surface, concentrating the material stream, keeping impact angles small to avoid sudden dilation of the material, minimizing changes in the material velocity, and matching material and belt velocities at transfer points.

12.5. Chutes Used to Fill Hoppers

When filling a hopper from a chute, one should try to minimize or at least be aware of potential segregation issues. For example, consider the chute used to fill three hoppers as shown in Figure 12.12. If the material in the chute is prone to shear-induced percolation segregation whereby smaller particles tend to preferentially fall through the gaps between larger particles when the material is sheared as it flows down the chute surface, then the first hopper filled from the chute will have a larger concentration of smaller or fine particles. The last hopper to be filled will tend to have a larger concentration of larger or coarse particles.

Another potential source of filling non-uniformity occurs if the material is prone to elutriation segregation. As material enters the hopper from above, air is displaced and moves upwards. Fine particles will remain suspended in the air longer and will settle on the bed surface. Thus, there will tend to be a layer of fine particles on the bed free surface within the hopper while coarse particles are deeper within the bed (Figure 12.13). To avoid this phenomenon, the hopper should be filled using a tangential inlet so the material swirls around the hopper walls while settling rather than falling directly from above as would be the case for a central inlet.

12.6. Summary

Following is a summary of the important points from this chapter:

(1) Design impact points to avoid flow stoppages.
(2) Use large radius chutes to maintain stream speed.
(3) Don't fill chutes more than one-third full.
(4) Use curved chute cross-sections to concentrate the flow.
(5) Design the chute to minimize wear and dusting.
(6) Be aware of potential segregation during filling of hoppers and bins.
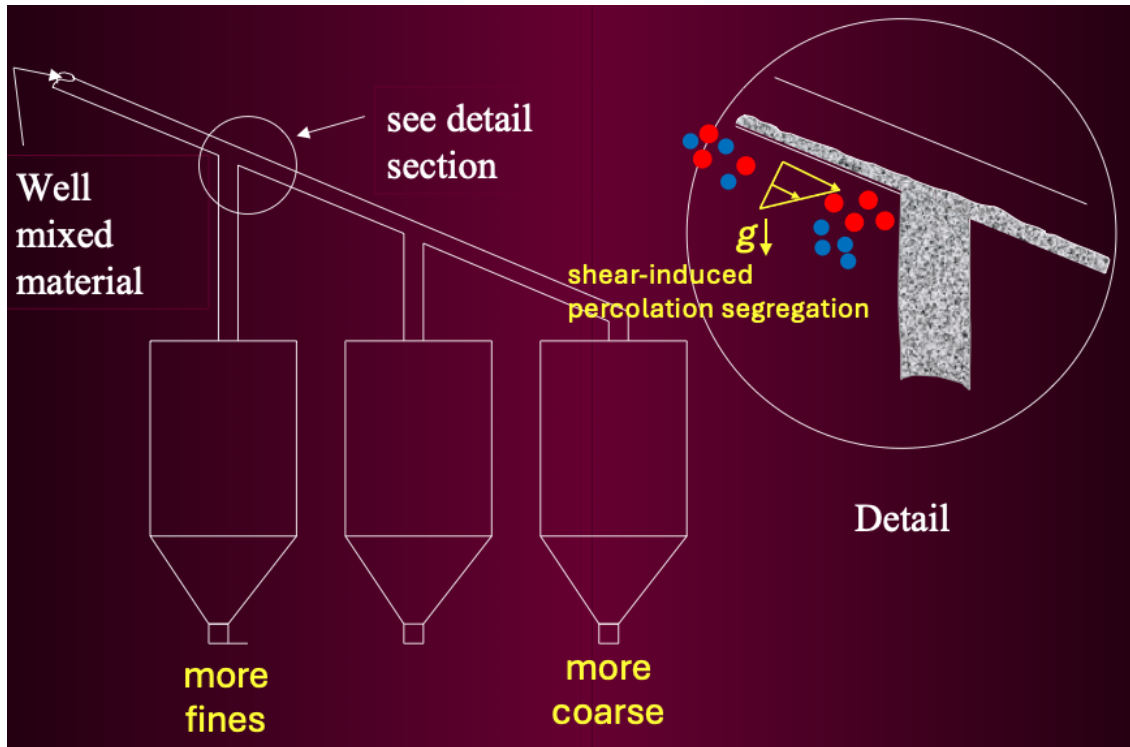
FIGURE 12.12. Illustration of a chute used to fill three hoppers. Due to segregation in the chute, the first hopper to be filled will tend to have more fine material while the last hopper will tend to have more coarse material. This figure is slightly modified from the ones presented in Marinelli [2] and Carson et al. [3].
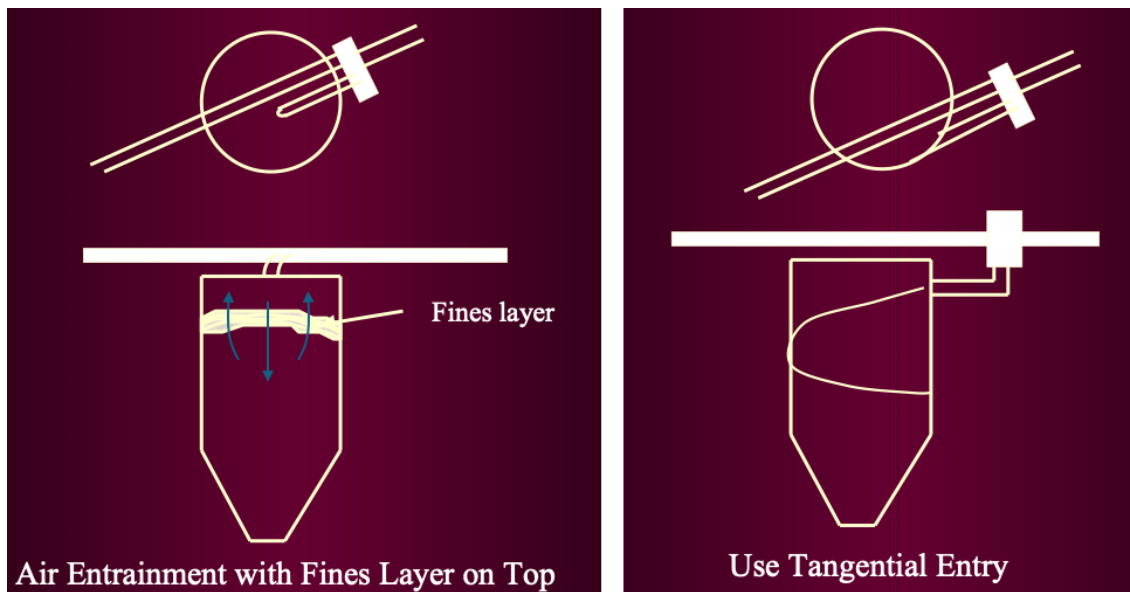
FIGURE 12.13. Illustration of elutriation segregation caused by a central filling port at the top of the hopper (left) versus using a tangential entry inlet (right), which reduces elutriation segregation. This figure is from Marinelli [2].

Material falls vertically from rest a distance of 2 m. The material impacts a flat plate that directs the flow at an angle of 40° from the horizontal. The friction angle between the material and wall is 20°.
a. What is the speed at which the material impacts the plate?
b. What is the material speed down the plate immediately after impacting the plate?
c. What is the maximum turning angle of the flow to prevent material build-up?
d. What will be the material's speed a distance 2 m downstream of the impact location?

SOLUTION:

$g = 9.81$ m/s^2
$H = 2$ m
$L = 2$ m
$\theta = 40°$
$\beta = 50°$
$\phi_w = 20°$
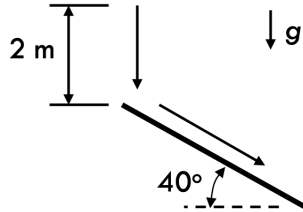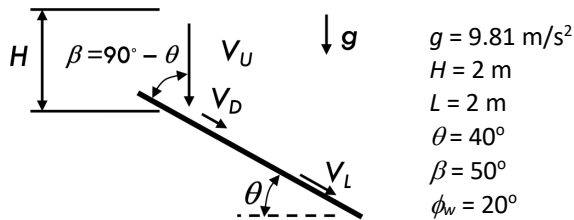
The speed just before impacting the plate (V_U) is,
$$V_U = \sqrt{2gH} \quad \text{(equating kinetic and potential energies).}$$ (1)

The speed immediately after impacting the plate (V_D) is,
$$\frac{V_D}{V_U} = \cos\beta - \sin\beta \tan\phi_w.$$ (2)

The maximum turning angle to prevent flow stoppages is,
$$\beta_{\max} = 90° - \phi_w.$$ (3)

To find the speed a distance L down the surface, solve the following differential equation,
$$V\frac{dV}{ds} = g\sin\theta - \left(\frac{V^2}{R} + g\cos\theta\right)\tan\phi_w,$$ (4)
Subject to the boundary condition $V(s = 0) = V_D$. Note that for this case, θ is a constant and R is infinite. Thus, Eq. (4) becomes,
$$\int_{V_D}^{V_L} VdV = (g\sin\theta - g\cos\theta \tan\phi_w)\int_0^L ds,$$ (5)
$$\frac{1}{2}(V_L^2 - V_D^2) = (g\sin\theta - g\cos\theta \tan\phi_w)L,$$ (6)
$$V_L = \sqrt{V_D^2 + 2gL(\sin\theta - \cos\theta \tan\phi_w)}.$$ (7)

Substituting the given values,
  $V_U = 6.3$ m/s,
  $V_D = 2.3$ m/s,
  $\beta_{\max} = 70°$,
  $V_L = 4.41$ m/s.

You are asked to design a constant radius chute to transfer material with a wall friction coefficient of 15° from a vertical speed of 1 m/s to a horizontal belt conveyor with a speed of 2 m/s. What radius of curvature should be used?
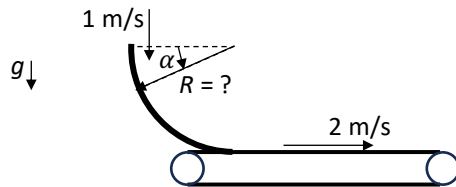
SOLUTION:
From the course notes, the differential equation governing the material movement on the chute is,

$$F'^2 V' \frac{dV'}{d\alpha} = \cos\alpha - (F'^2 V'^2 + \sin\alpha)\tan\phi_w, \tag{1}$$

where $V'(\alpha = 0) = 1$, $F' := V_0/\sqrt{gR}$, and $V' := V/V_0$. In this case, $V_0 = 1$ m/s, $g = 9.81$ m/s^2, $\phi_w = 15°$, and $V(\alpha = \frac{\pi}{2}) = 2$ m/s => $V'(\alpha = \frac{\pi}{2}) = 2$. Note that R is currently unknown which means that F' is also unknown.

To find the value for F' that gives the target of $V'(\alpha = \frac{\pi}{2}) = 2$, iteratively solve the differential equation in Eq. (1) until the target chute exit speed is found. Performing these calculations computationally (Python code given at the end of this solution) gives the result: $F' = 0.471$ => $\boxed{R = 0.46 \text{ m}}$.

A plot of the material speed on the chute as a function of the angle α is given below.
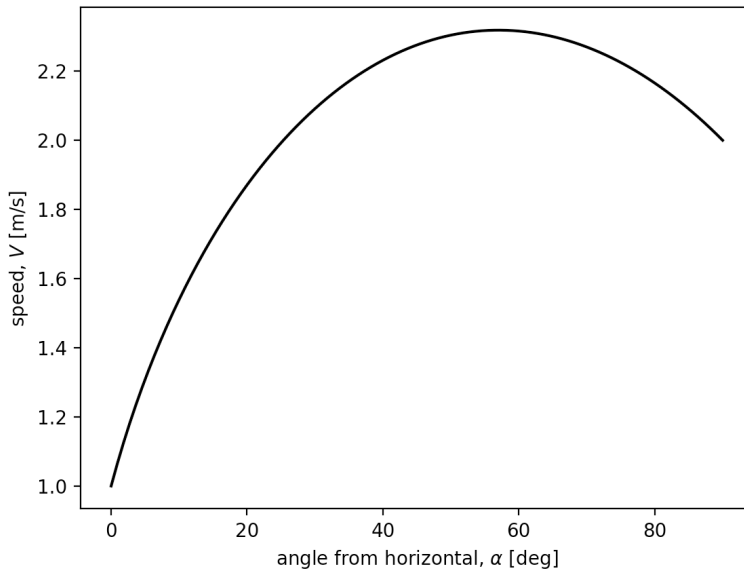
The Python code used to perform the calculations follows.

```python
# chute_02.py

import numpy as np
import matplotlib.pyplot as plt
from scipy.integrate import odeint
from scipy.optimize import fsolve

def ode(V_prime, alpha, phiw, F_prime):
    # The ode used to calculate the dimensionless material speed on
    # the chute as a function of the angle alpha.
    cos_alpha = np.cos(alpha)
    sin_alpha = np.sin(alpha)
    tan_phiw = np.tan(phiw)

    dV_prime_dalpha = (cos_alpha - (F_prime**2 * V_prime**2 +
sin_alpha)*tan_phiw)/(F_prime**2 * V_prime)
    return(dV_prime_dalpha)

def DimensionlessFinalSpeed(F_prime, V0_prime, Vf_target_prime, phiw, alpha):
    # Function used to find the difference between the dimensionless
    # final speed on the chute and the target dimensionless final
    # speed.
    V_prime = odeint(ode, V0_prime, alpha, args=(phiw, F_prime))  # speed on chute
    Vf_prime = V_prime[-1]  # dimensionless final speed on the chute
    return(Vf_prime - Vf_target_prime)

# Initialize variables.
V0 = 1  # initial speed [m/s]
g = 9.81  # gravitational acceleration [m/s^2]
phiw = np.radians(15)  # wall friction angle [rad]
alpha = np.linspace(0, np.pi/2, 100)  # range of chute angles [rad]
V0_prime = V0/V0  # dimensionless initial speed
Vf_target = 2  # target final speed [m/s]
Vf_target_prime = Vf_target/V0

# Pick an initial guess for the chute radius.
R = 1  # [m]
F0_prime = V0/np.sqrt(g*R)

# Iterate to find when the DimensionlessFinalSpeed function is zero,
# i.e., the final speed on the chute matches the target final speed.
F_prime = fsolve(DimensionlessFinalSpeed, F0_prime, args=(V0_prime, Vf_target_prime, phiw,
alpha))

print('F_prime = %.3f' % F_prime)
R = ((V0/F_prime)**2)/g  # This is the desired chute radius.
print('R = %.3f m' % R)

# Calculate the speed on the chute for this F_prime value so we can
# plot it.
V_prime = odeint(ode, V0_prime, alpha, args=(phiw, F_prime))

# Plot the data using two axes
fig, ax = plt.subplots()
ax.set_xlabel(r'angle from horizontal, $\alpha$ [deg]')
ax.set_ylabel(r'speed, $V$ [m/s]')
ax.plot(np.degrees(alpha), V0*V_prime, color='k', marker='', linestyle='-')
plt.show()
```

A chute is to be designed to handle a mass flow rate of 10,000 lb$_m$/h with a bulk density of 50 lb$_m$/ft³. The material's free fall height onto the chute is 2 ft, the material wall friction angle is 20°, and the chute angle from the vertical is 20°.
a.   Show that the material flow on this chute?
b.   What is the recommended minimum (circular) chute diameter?
(Note that this example is originally from K. Jacob and M. Kodam.)

$\dot{m} = 10000$ lb$_m$/h

2 ft

20°

$D = ?$

SOLUTION:

$\dot{m}$

H

β

20°

$D = ?$
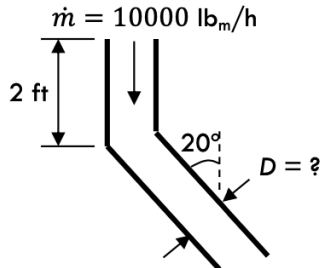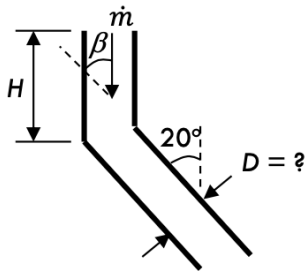
First check the flow/no-flow chute angle criterion: $\beta + \phi_w < 90°$ in order to flow. Here, β = 20° and ϕ_w = 20° => $\beta + \phi_w = 40° < 90°$ and, thus, the material should flow on this chute.

The impact speed of material on the chute is,
$$V_I = \sqrt{2gH},\tag{1}$$
where g = 32.2 ft/s² and H = 2 ft, which gives V_I = 11.3 ft/s. The speed after impact is,
$$V_D = V_I(\cos\beta - \sin\beta\tan\phi_w),\tag{2}$$
which results in V_D = 9.3 ft/s.

The minimum chute diameter at the given mass flow rate is found from,
$$\dot{m} = \rho_b V_D A_{cs} = \rho_b V_D \frac{D^2}{8}(\alpha - \sin\alpha),\tag{3}$$
where A_{cs} is the chute cross-sectional (circular) area, D is the circle diameter, and α is the total angle out to the material surface (refer to the figure). Using the given values of $\dot{m}$ = 10 000 lb$_m$/h, ρ_b = 50 lb$_m$/ft³, an angle of α = 141.1°, which corresponds to H/D = 1/3, and the calculated value for V_D, the recommended minimum chute diameter is D = 0.16 ft.
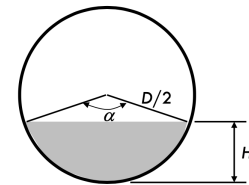
Bibliography

[1] D. Dick and T. Royal, "Design principles for chutes to handle bulk solids," Bulk Solids Handling, vol. 12, no. 3, pp. 447–450, 1992.

[2] J. Marinelli, Lecture notes for "particulate systems" (che 53600 at purdue university), 2018.

[3] J. Carson, T. Royal, and D. Goodwill, "Understanding and eliminating particle segregation problems," Bulk Solids Handling, vol. 6, no. 1, pp. 139–144, 1986.

CHAPTER 13

Influence of Particle and Environmental Properties on Powder Bulk Properties

This chapter describes the influence that particle properties and environmental conditions have on a powder's bulk density and flow behavior. In particular, the following particle-level properties are examined:

- particle size and size distribution,
- particle shape and roughness,
- particle density,
- inter-particle friction, and
- inter-particle cohesion.

The environmental conditions examined here include:

- temperature,
- humidity,
- external loads, and
- storage duration.

13.1. Particle Size and Size distribution

The forces that act to keep a particle in motion are either an inertial force or the particle weight, both of which are proportional to the particle mass, which in turn is proportional to the cube of the particle size, x^3. The forces acting to resist a particle's movement include frictional and cohesive forces, which act at the particle's surface. Thus, these forces are proportional to the particle's surface area, which in turn is proportional to the square of the particle size, x^2. The ratio of the characteristic resistance force to the characteristic movement force is known as a <u>Bond number, Bo</u>, which is related to the particle size by,

$$\text{Bo} := \frac{\text{characteristic resistance force}}{\text{characteristic movement force}} \propto \frac{x^2}{x^3} = \frac{1}{x}. \tag{13.1}$$

As the particle size (x) decreases, i.e., as the Bond number increases, the resistance force becomes increasingly significant compared to the movement force and the particle doesn't move as easily. Thus, we expect a powder's flow behavior to generally become worse as the particle size decreases. Examples demonstrating the influence of particle size on powder flow behavior are shown in Figure 13.1.

Notes:

(1) Various researchers have developed empirical expressions relating the particle size to bulk flow properties. For example, Köhler and Schubert [3] proposed the following material flow function (mFF) expression for free-flowing alumina powders,

$$f_c = b_0 + b_1 d_{50}^{-b_2} \sigma_1, \tag{13.2}$$

where d_{50} is the median particle diameter of the particle size distribution and $b_i > 0$ are fitting parameters. As the median particle size decreases, the bulk strength increases. Podczeck and
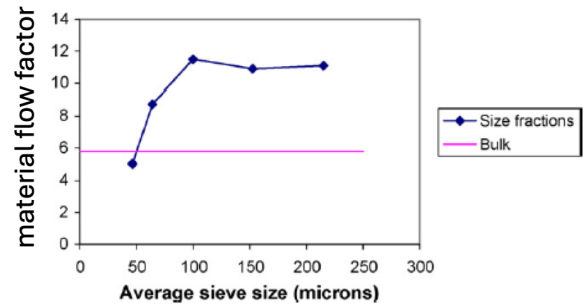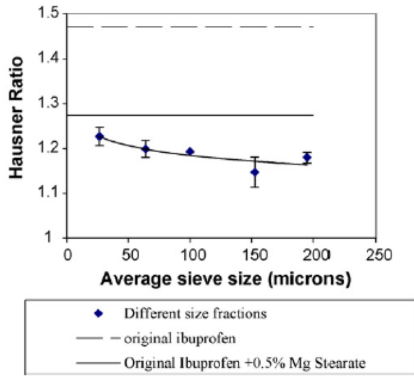
(A) The Hausner Ratio of different size fractions of ibuprofen. As the particle size decreases, the flow behavior becomes worse. This figure is from Liu et al. [1].

(B) The material flow factor (mff) of different size fractions of lubricated ibuprofen. As the size decreases, the flow behavior worsens. This figure is from Liu et al. [1].
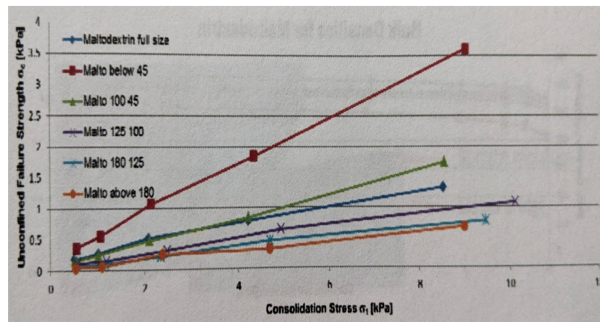
(C) The material flow functions (mFFs) of different size fractions of maltodextrin. As the size decreases, the material strength increases and the flow behavior worsens. This figure is from Wolfson [2].

Figure 13.1. Examples demonstrating that powder flow behavior becomes worse as particle size decreases.

Miah [4] developed an expression for the internal friction angle of unlubricated pharmaceutical powders,

$$\phi = b_0 + b_1 \exp\left(AR\right) - b_2 \ln d_{vs}, \tag{13.3}$$

where AR is the particle aspect ratio, d_{vs} is the weighted mean of the surface area distribution, and $b_i > 0$ are fitting parameters. As the particle size increases, the internal friction angle decreases.

Powders comprised of smaller particles also tend to pack in more porous configurations (Figure 13.2). The relatively large resistance forces allow particles to pack in stable configurations that have significant void regions. These voids would collapse for particles with weak cohesive or frictional forces. Note that as previously discussed in Chapter 2, the more compressible the powder, the worse the flow behavior.

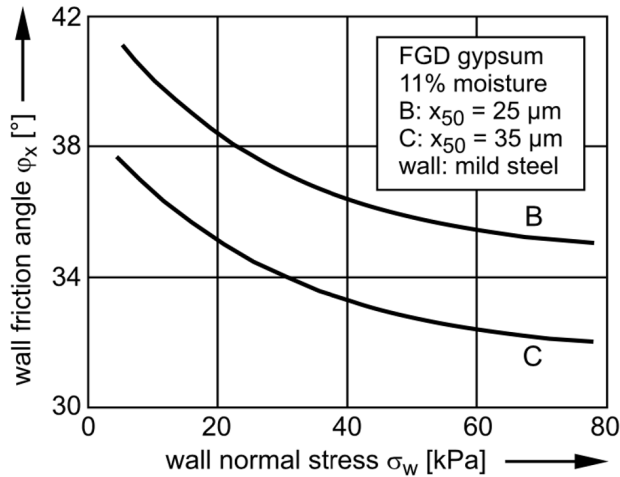The wall friction angle also increases as particle size decreases. Figure 13.3 plots the wall friction angle as a function of the wall normal stress for two different particle sizes of gypsum against a mild steel wall. The smaller particles have a a larger wall friction angle for the same normal stress.

In general, a broader particle size distribution (PSD) results in more efficient packing of particles, but the relationship can be complex. Particles of different size can pack with small porosity since small particles can fit into the voids between the large ones, as shown in Figure 13.4. In this figure, the porosity of a binary blend of spheres is shown as a function of the fraction of large particles for different size ratios. A minimum
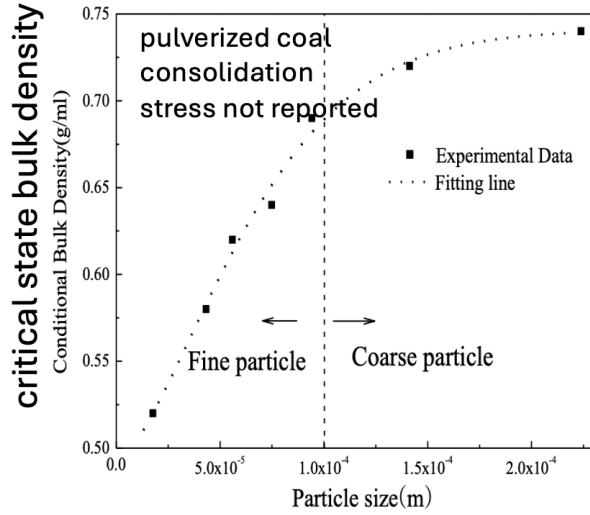
(A) A plot of the critical state bulk density from a shear cell test for different sizes of coal particles. Bulk density decreases as particle size decreases. Plot from Liu et al. [5].
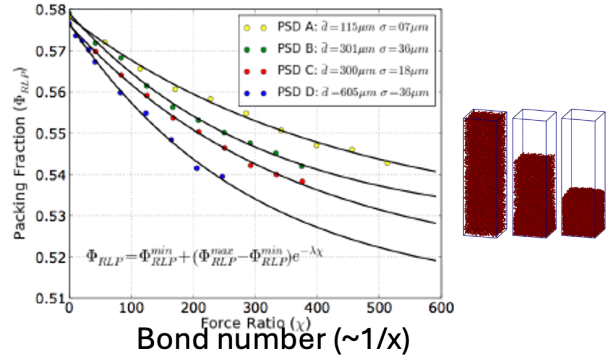
(B) The poured solid fraction of simulated particle size distributions (different curves) as a function of Bond number. As Bond number increases due to a decrease in particle size, the packing fraction decreases. Plot from Ely [6].

FIGURE 13.2. Experimental and simulation data showing how packing fraction decreases as particle size decreases.

FIGURE 13.3. Wall friction angle as a function of wall normal stress for two different particle sizes of gypsum against a mild steel wall. The smaller particle size has a larger wall friction angle. This figure is from Schulze [7].

bed porosity is observed, which is a function of the fraction of large particles and the particle size ratio. Note that for free flowing mixtures containing particles of different size, the particles may segregate and, thus, the packing fraction may change during handling.

In general, as the width of the PSD increases, flow behavior becomes worse. Figure 13.5 shows the material flow functions (mFFs) of limestone powder with different particles size distributions. The three size distributions highlighted in the figure have similar median particle sizes, but the distribution widths are different.
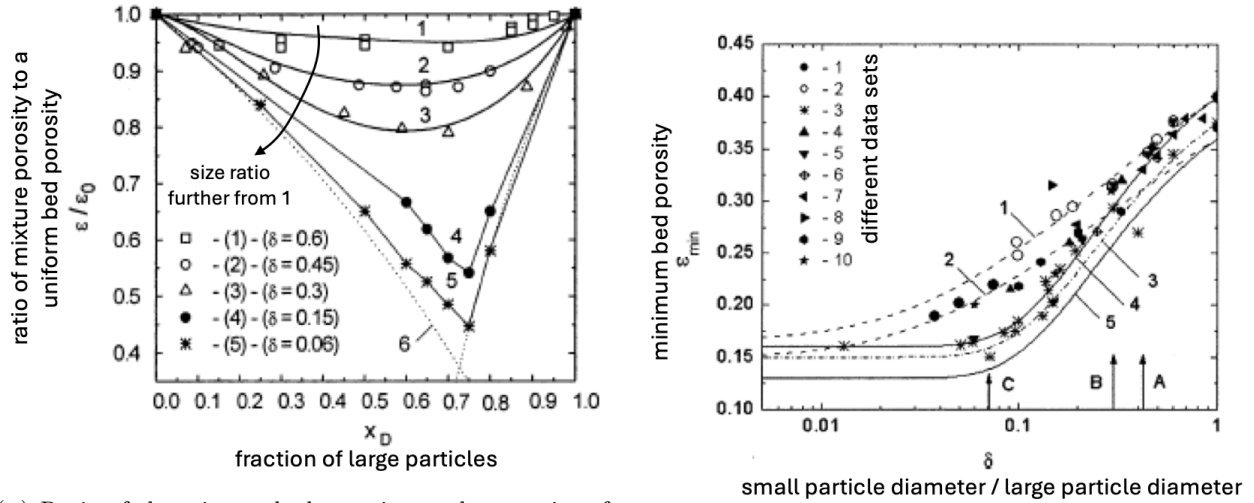
(A) Ratio of the mixture bed porosity to the porosity of a bed of uniform spheres as a function of the fraction of large particles for different size ratios. The bed porosity of the mixture is always smaller than the porosity of the uniform spheres.

(B) The minimum bed porosity as a function of the particle size ratio. As the difference in size increases (smaller ratio in the figure), the minimum bed porosity decreases.
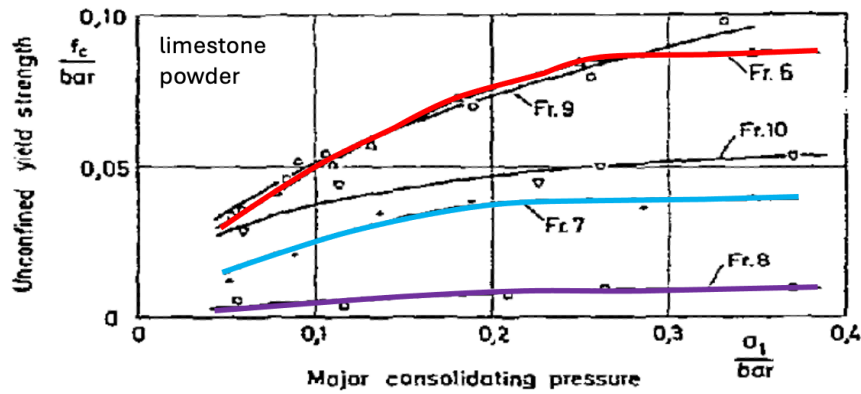
FIGURE 13.4. The packing of binary blends of spheres. Both plots are from Dias et al. [8].

FIGURE 13.5. Material flow functions (mFFs) for limestone powder with different particle size distributions. Powders Fr. 6, 7, and 8 have similar median sizes, but the breadth of $PSD_{Fr.\ 6} > PSD_{Fr.\ 7} > PSD_{Fr.\ 8}$. Thus, increasing PSD breadth results in a stronger powder. This figure is from Kurz and Münz [9].

As the PSD width increases, the mFF values are larger, i.e., the powder becomes stronger, and the flow behavior worsens. Conceptually, the broader the size distribution, the more efficiently the particles can pack and, consequently, the harder it is to shear the material.

Notes:

(1) Empirical fits to experimental bulk flow properties that incorporate the particle size distribution have been proposed [10], [11]. For example, Leyva and Mullarney [10] developed the following empirical expression, which works best for single component pharmaceutical powders,

$$\text{mff} = \exp\left(b_0 + b_1 \ln d_{10} + b_2 \ln d_{50} + b_3 \ln d_{90} + b_4 \ln d[4, 3]\right), \tag{13.4}$$
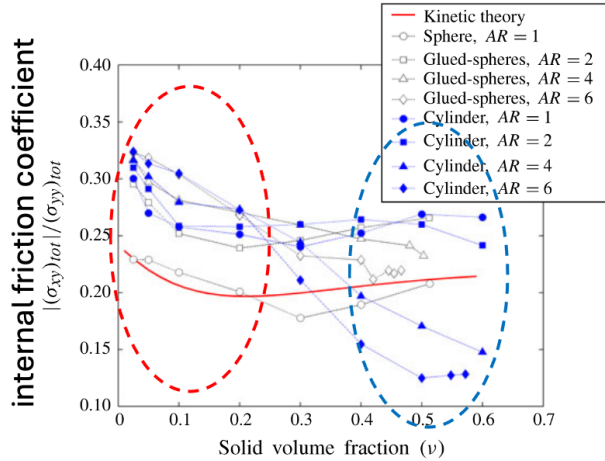
(A) Plot of the internal friction angle as a function of solid volume fraction for cylindrical rods, both smooth and bumpy (comprised of glued-spheres), with various aspect ratios. Also included in the plots are trends for spheres and predictions from kinetic theory.
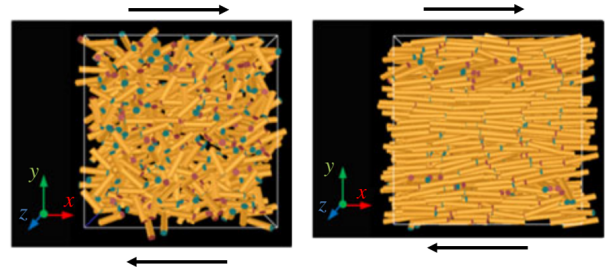
(B) Discrete element method computer simulations of short aspect ratio (left) and long aspect ratio (right) cylinders in a shear flow. The high aspect ratio cylinders pack more tightly and flow better than the small aspect ratio cylinders.

FIGURE 13.6. DEM simulations of spheres and cylinders in a shear flow. At small solid fractions, spheres have smaller internal friction than cylinders. At larger solid fractions, long cylinders can align and, as a result, have smaller internal friction.

where mff is the material flow factor and the d_{10}, d_{50}, d_{90}, and $d[4, 3]$ (the volume mean diameter) are obtained from the particle size distribution measured using laser diffraction. The b_i are fitting parameters. Unfortunately, the exact consolidation stress at which the mff was determined was not reported.

13.2. Particle Shape and Roughness

Particle shape can also have a significant influence on bulk solids packing and flow. In general, irregularly shaped particles have larger bed porosity and poorer flow behavior, but a general statement can't be made regarding the influence of shape. Indeed, some particle shapes, such as elongated rods, may pack inefficiently and flow poorly when oriented randomly, yet pack very efficiently and flow well when aligned (Figure 13.6).

Figure 13.7 plots the bed voidage (i.e., porosity) for particles of different sphericity (a sphere has a sphericity of one). As particles become more spherical, they pack more tightly. However, as shown in Figure 13.8, sphero-cylindrical particles with a length twice their radius pack even more efficiently than spheres. Even ellipsoidal particles can pack more tightly than spheres as shown by the M&M candies in Figure 13.9. These examples demonstrate that the exact geometry of the particles matter.
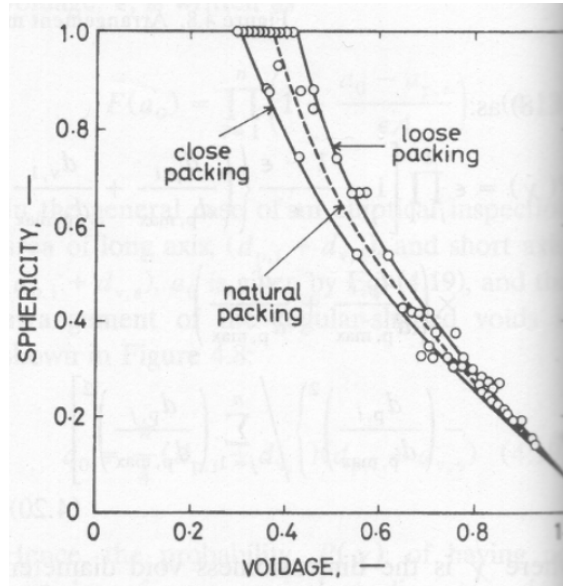
FIGURE 13.7. Bed voidage (i.e., porosity) on the horizontal axis and particle sphericity on the vertical axis. As particles become more spherical, they pack more tightly. This figure is from Crosby [12].
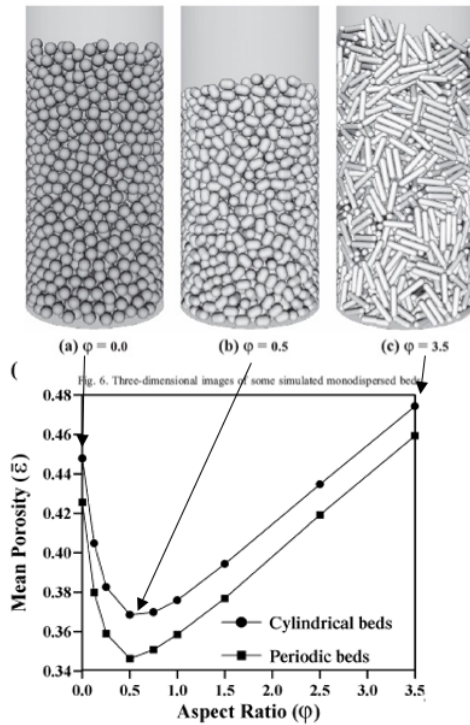

FIGURE 13.8. The porosity of beds comprised of sphero-cylinders with different aspect ratios. In this work, an aspect ratio of zero corresponds to a sphere. A minimum bed porosity occurs at an aspect ratio of 0.5. This figure is from Abreu et al. [13].
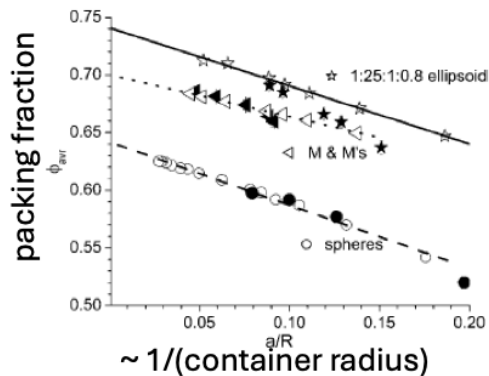
FIG. 2. Packing fraction as a function of inverse spherical container size. Empty symbols and lines are data and extrapolation for simulated packing. The extrapolated values are as follows: for spheres, $\phi_0 = 0.642 \pm 0.002$; for mini M&M's, $\phi_0 = 0.700 \pm 0.002$, 1.25:1:0.8 ellipsoids $\phi_0 = 0.741 \pm 0.002$. Solid symbols are the corresponding experimental results.

FIGURE 13.9. The packing fraction of ellipsoids, M&M candies, and spheres contained within a sphere plotted as a function of the inverse of the containing sphere radius. Ellipsoids pack more tightly than M&Ms, which in turn pack more tightly than spheres. This figure is from Man et al. [14].

The surface roughness on a particle is also important, but as with particle shape, the details matter. Figure 13.10 shows that increasing surface roughness increases the porosity of a powder bed since the roughness increases the effective friction between particles, allowing the particles to rest in configurations that are stable with fewer contacts. Increasing wall roughness also increases wall friction angle as shown in Figure 13.11. However, for small particles with flat surfaces, adding surface roughness can reduce cohesion, increasing the packing fraction and improving flow (Figure 13.12). The surface roughness prevents particle surfaces from coming into close contact and, thus, reduces van der Waals cohesive forces, which vary inversely with the square of the separation distance. A video illustrating just how significant a small amount of surface roughness can be is available at https://www.youtube.com/watch?v=MM5lWf6pl6c.

13.3. Particle Density

Increasing particle density improves flow behavior. Recall that the Bond Number, Bo, is the ratio of a characteristic resistance force, e.g., van der Waals or liquid bridge cohesion, to a characteristic movement force, e.g., the particle's weight or inertial force. Resistance forces are independent of particle density while the weight and inertial force are proportional to density. Thus, the Bond number is inversely proportional to the particle density and increasing the density improves flow behavior.
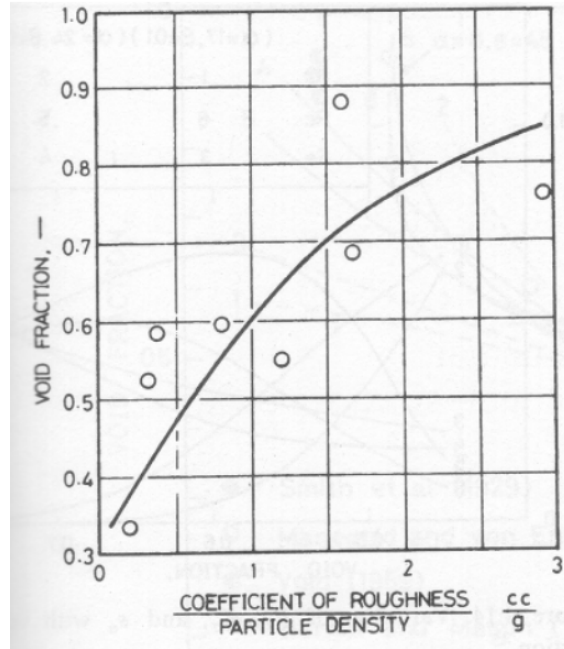
FIGURE 13.10. Increasing particle surface roughness increases the particle bed's void fraction. This figure is from Crosby [12].
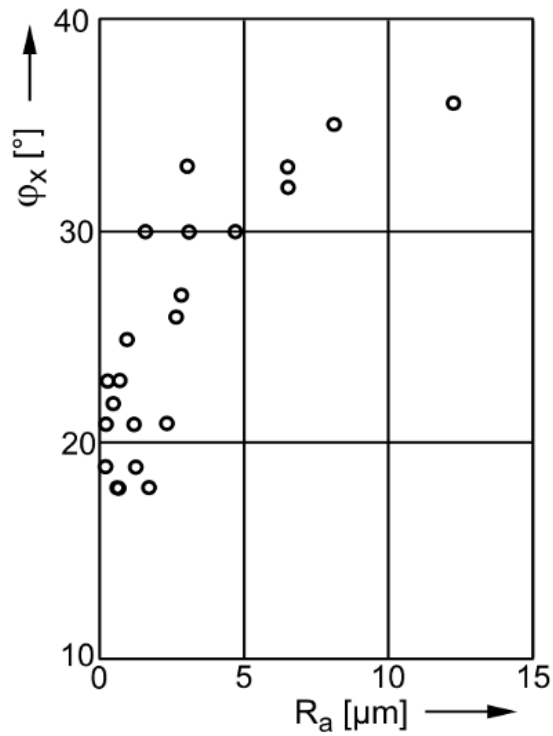

FIGURE 13.11. Increasing particle surface roughness increases the wall friction angle. This figure is from Schulze [7].
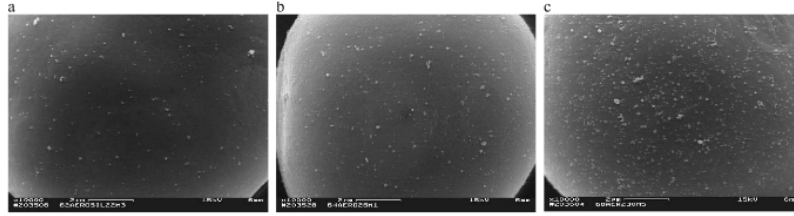
Fig. 4. Aerosil 200® agglomerates on cornstarch surface (0.2% Aerosil 200® in cornstarch): (a) 2 min blending time, (b) 6 min blending time, (c) 30 min blending time.
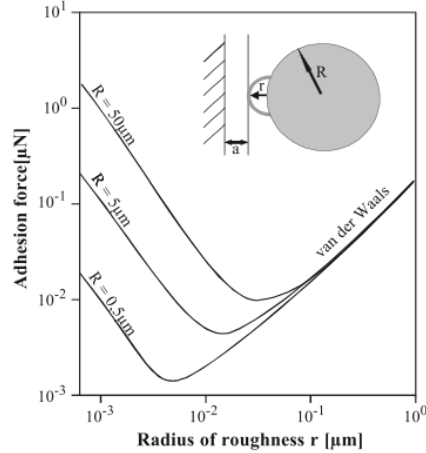

Fig. 1. Dependency of the adhesion force on the size of the surface roughness, Hamaker constant $A = 4 \times 10^{-20}$ J.

FIGURE 13.12. (top) Photographs of micron-sized particles with different amounts of much smaller, nano-sized particles on their surfaces. (bottom) A model demonstrating how the van der Waals force decreases due to the presence of a small bump, which acts to separate the particle from a surface. These figures are from Meyer and Zimmermann [15].

13.4. Inter-particle Friction and Cohesion

The effects of inter-particle friction and cohesion can be difficult to isolate from other effects such as particle shape or surface roughness. However, discrete element method (DEM) computer simulations can be used for such studies. In simulations of spherical particles with varying inter-particle and particle-wall friction (Figure 13.13), the bulk internal friction coefficient and bulk wall friction angle increase as particle-level friction increases up to a particle-particle and particle-wall friction coefficient of approximately 0.5. For larger values of the friction coefficients, particles rotate against each other rather than slide and the bulk friction angles remain nearly constant. For non-rolling particles, which are more representative of real particles with irregular shape, the bulk internal friction angle and bulk wall friction angle increase as particle-level friction increases.

As inter-particle cohesion increases, the Bond number increases and the bulk porosity increases (Figure 13.2b) and the flow behavior worsens (Figure 13.14). This behavior was discussed previously in Section 13.1.

There are several sources of inter-particle cohesion including van der Waals interactions, electrostatics, liquid bridges, and solid bridges. Van der Waals forces result from the (nearly always) attractive forces between molecules resulting from dipole moments caused by permanent or momentary imbalances in electron clouds and, as such, are much weaker than covalent or ionic bonds. The magnitude of a van der Waals force is a function of the particle geometry and material properties, but the force is short range, resulting in negligible cohesion when particle surfaces are separated by more than approximately 100 nm. As described
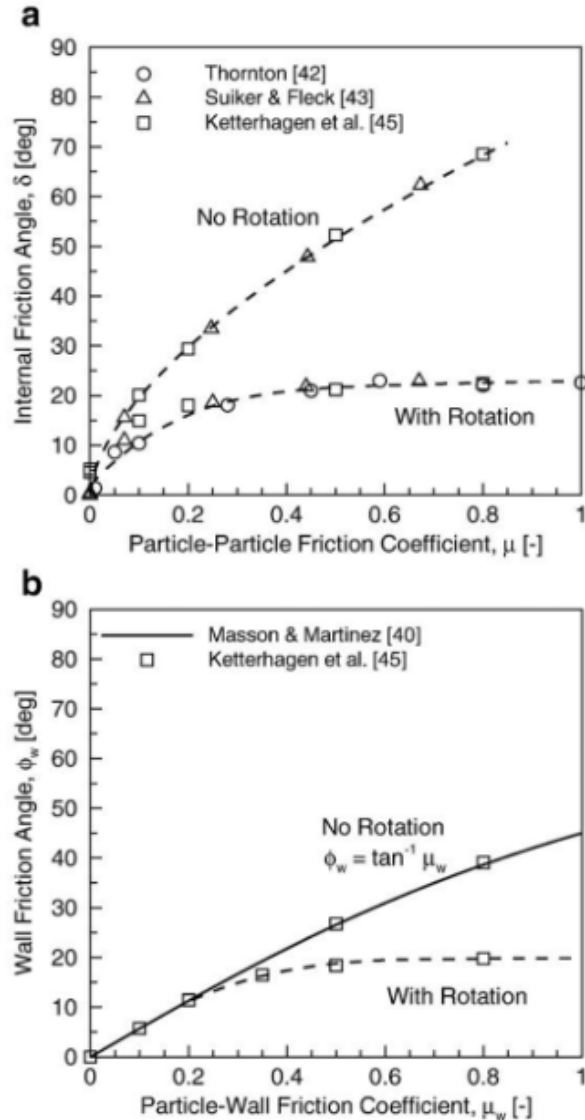
FIGURE 13.13. (top) Bulk internal friction angle as a function of the particle-particle friction coefficient and (bottom) bulk wall friction angle as a function of the particle-wall friction coefficient. Data and fitting curves are shown for spherical particles that can rotate or cannot rotate. Included in the figures are simulations and experiments from various authors. These figures are from Ketterhagen et al. [16].

in Section 13.2, adding a small amount of roughness to flat particle surfaces can be enough to separate the surfaces and greatly weaken the van der Waals forces.

Electrostatic forces can develop through tribocharging, which involves the transfer of electrons when dissimilar surfaces are in contact, or through the deposition of ions on particle surfaces. The distribution of charge on a particle's surface depends on the charge mobility. For insulating materials, the charge isn't mobile on the surface but on conductors the charge can move on the surface in response to surrounding electric fields. For example, charge can re-distribute as particles approach one another and tends to collect at asperities. The presence of a conductive liquid on a particle's surface, e.g., water resulting from high humidity, can
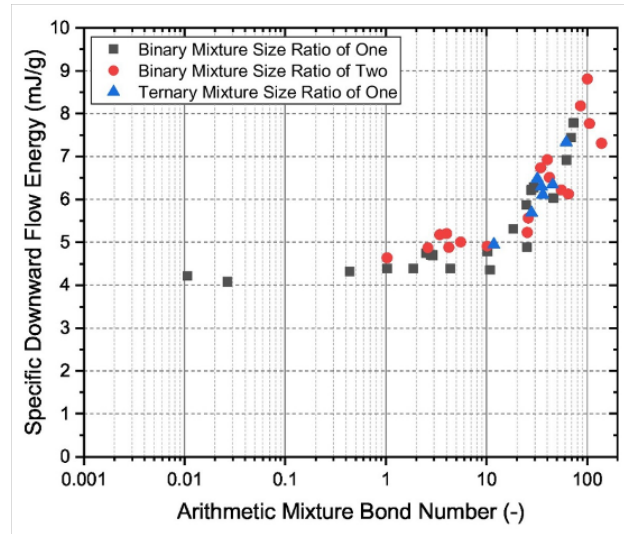
Figure 13.14. The specific energy required to rotate an FT4 rheometer blade downward through a bed of powder as a function of the powder mixture's Bond number. The larger the specific energy, the more difficult it is to move the blade through the powder. This figure is from Pasha et al. [17].
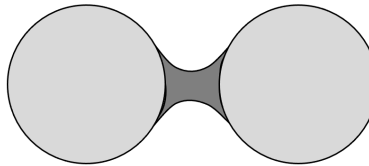

Figure 13.15. A sketch of a pendular liquid bridge between two spherical particles. There is a cohesive force between the two particles resulting from pressure and surface tension forces in the liquid bridge.

result in charge mobility and dissipation as excess charge finds a path to ground. Many pharmaceutical manufacturing facilities are held at a relative humidity of approximately 40% in order to reduce electrostatic forces (by increasing charge mobility on surfaces), while still being low enough to avoid liquid bridging (discussed in the following paragraph).

Liquid bridges on a particle's surface can result in cohesion due to surface tension and capillary pressure forces [18]. Small volumes of liquid, e.g., less than 13.6% by volume for equal sized spheres [19], result in strong, pendular liquid bridges (Figure 13.15) while large volumes of liquid can lead to total or near total immersion of the particles, which have weak or zero strength cohesive forces. Liquid bridge forces can be significantly stronger than van der Waals or electrostatic forces.

Solid bridges (Figure 13.16) are much stronger and more permanent than liquid bridges. Solid bridges can form from a variety of mechanisms, including:

- Polymeric bridges: A liquid solution with a polymer binder forms a liquid bridge. The liquid evaporates leaving behind a solid, polymeric bridge. Polymeric bridges are frequently used in wet granulation manufacturing processes.
- Saturated solution bridges: Here, a solvent dissolves some of the particle material creating a liquid bridge. When the solvent evaporates, the material re-crystallizes to form a solid bridge. Note that the material may re-crystallize into a different polymorphic form.
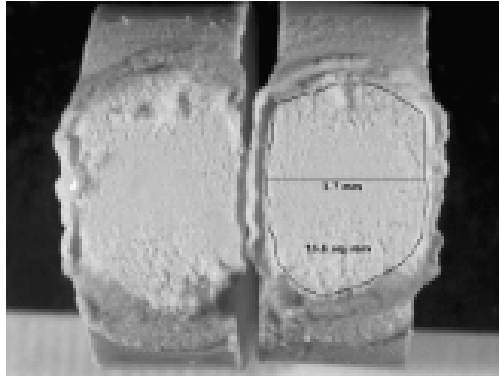
FIGURE 13.16. A photograph of a solid bridge that formed between two tablets. The bridge has been cut in half and the cross sections are shown. This figure is from Bika et al. [20].

- Solid binder bridges: A finely ground solid binder chemically reacts with any liquid present on the particle surface to produce a solid bridge.
- Melting/freezing: If the material melts, a liquid bridge may form. When the material cools, it can form a solid bridge.
- Sintering: When a bulk material is subject to stress and heat, it may melt at particle-particle contacts then resolidify to form a solid bridge.

13.5. Glass Transition Temperature

The glass transition temperature, T_g, is the temperature above which an amorphous material undergoes a reversible transition from a hard, "glassy" state into a soft, "rubbery" state. When the temperature is greater than T_g, the rubbery material can significantly deform, resulting in increased contact area between surfaces and a larger cohesive force.

Notes:

(1) The transition to a rubbery state occurs over a range of temperatures related to the molecular degrees of freedom of the material, but is usually reported as the single temperature, T_g.
(2) Glass transition is not a phase transition. Glass transition occurs at a temperature lower than the melting point, i.e., $T_g < T_{\text{melting}}$.
(3) The glass transition temperature typically decreases with increasing moisture content.

13.6. Critical Relative Humidity (CRH)

The Critical Relative Humidity (CRH), a material property, is the relative humidity (RH) at which a salt begins to absorb moisture from the atmosphere. The CRH decreases with increasing temperature for most salts (refer to [21] for a model used to predict the CRH). If the RH > CRH, then the material absorbs moisture and dissolves, yielding a saturated solution. If RH < CRH (due to a change in RH or temperature), then the solution can recrystallize and form a solid bridge. The CRH for mixtures or materials with impurities is smaller than the CRH for the individual components. Values for CRH for various materials are listed in Table 13.1.

13.7. Moisture Content

As discussed previously, external moisture can alter a powder bed's porosity and flow due to the presence of liquid bridge cohesive forces. At low moisture contents, as surface moisture increases, cohesion increases resulting in decreasing porosity and poorer flow behavior. Figure 13.17 shows results from discrete element

Salt	CRH @ 30 °C
calcium nitrate	46.7
ammonium nitrate	59.4
sodium nitrate	72.4
urea	72.5
ammonium chloride	77.2
diammonium phosphate	82.0
potassium chloride	84.0
potassium nitrate	90.5
monoammonium phosphate	91.6
monocalcium phosphate	93.6
potassium sulfate	96.3

TABLE 13.1. Critical Relative Humidity (CRH) values for various salts at a temperature of 30 °C. This data is from https://en.wikipedia.org/wiki/Critical_relative_humidity.

method (DEM) computer simulations, which include liquid bridges forces, and corresponding experiments of uniform spheres at different moisture contents. As the moisture content increases up to a critical value ($\approx$1-10% by mass), the bed becomes more porous due to the increased cohesivity of the liquid bridges. Beyond this critical point, the moisture content has little influence on the bed, at least up to a moisture content of approximately 20%.

Figure 13.17 shows experimental data for the material flow factor (mff) and bulk density of moist sand as the moisture content changes. Unlike the previously discussed DEM simulations, the sand's porosity reaches a maximum at a moisture content near 2%, but then decreases with increasing moisture content. The material flow factor decreases rapidly (worse flow behavior) up to the same moisture content of 2%, but then stabilizes at larger moisture contents. Figure 13.18 shows similar flow behavior for wetted, fine sand. The sand rapidly gains strength in going from zero moisture content to 3% moisture content, but then the strength stabilizes at larger moisture contents up to approximately 12%. Figure 13.20 demonstrates that the wall friction angle dependence on moisture content depends on the wall material. For gypsum against a mild steel wall, the wall friction angle increases with increasing moisture content. However, for gypsum against an ultrahigh molecular weight polyethylene wall, the wall friction angle decreases with increasing moisture content.

Caking, i.e., the undesirable agglomeration of material, due to moisture effects often starts at the surface of the material where it is exposed to humidity and temperature cycling. Over time, moisture may propagate deeper into the bed, especially since caking typically causes the material to contract and form cracks through which moisture can propagate.

13.8. Temperature

A powder's strength tends to increase as temperature increases due to the previously described influence of the glass transition temperature and critical relative humidity. Figure 13.21 plots the unconfined yield strength and material flow factor (mff) of sulfur as a function of temperature after storage for two weeks. The material strength increases rapidly with temperatures above 40 °C. Figure 13.22 shows similar behavior with temperature, but for a powder containing fat. In this figure, the material flow function (mFF) gains strength as temperature increases and the critical arching diameter increases rapidly for temperatures above 20 °C.

13.9. Applied Load

Larger applied loads, especially for materials that are static, increase a powder's bulk density and increase the powder's strength, as has been described in Chapters 2 and 8. The increase in strength is readily
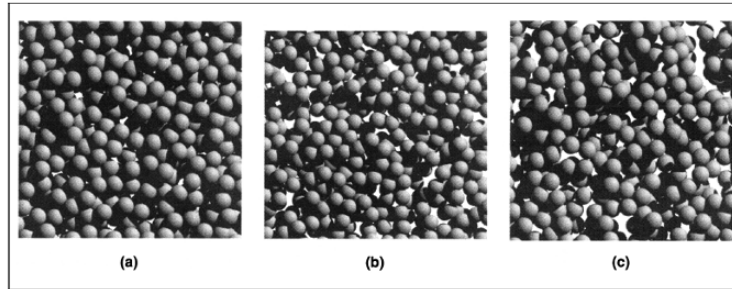
Figure 7. Internal packing structure of a thin layer of 1.9 particle diameter thickness for 0.25-mm particles at different liquid contents: (a) $M = 0.0\%$. (b) $M = 2\%$. and (c) $M = 20\%$.
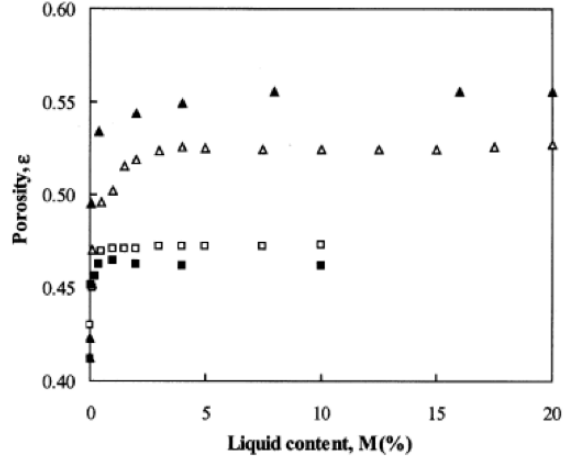

Figure 2. Porosity as a function of liquid content (water) for the packing of 1-mm (■) and 0.25-mm (▲) particles.

The experimental results of 1-mm (□) and 0.25-mm (△) particles are also plotted for comparison.

FIGURE 13.17. (top) Figures from discrete element method computer simulations of uniform spheres with liquid bridges formed at different moisture contents. As moisture content increases, porosity increases. (bottom) A plot of the bed porosity as a function of moisture content. This figure is from Yang et al. [22].

observed in material flow functions (mFF) which plot the powder's unconfined yield strength as a function of consolidation stress. In addition, large loads can not only cause particle re-arrangement within the bulk, but can also increase the contact area between particles through plastic deformation or fracture, which increases the bonding force between particles and worsens flow behavior.

If the material is under an applied load for an extended period of time and is viscoelastic, then the particles may creep, resulting in an increase in the contact area over time and further strengthening of the bulk. As described previously in Chapter 8, time consolidation testing of materials is essential for characterizing material flow behavior.

The effects of applied load can often be observed in bulk bags of powder. Caking due to pressure often is observed at the bottom of the bag where the pressure is the largest. It's usually recommended that materials that are sensitive to caking not be stacked one on top of another, but instead be stored on shelving so the loads on the material are not too great.
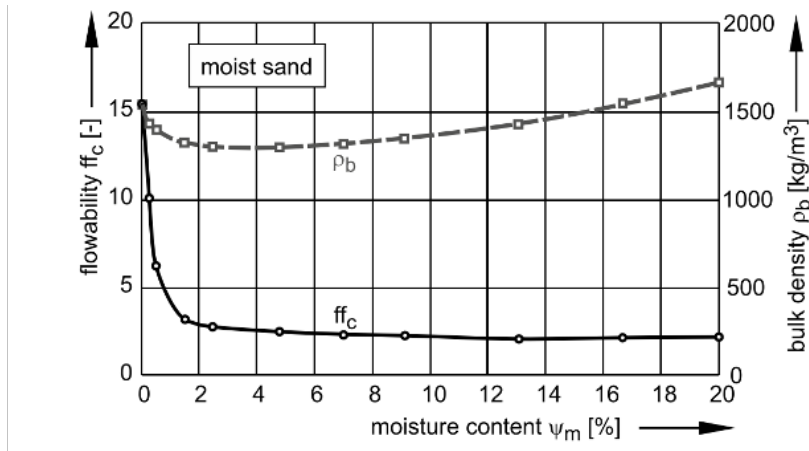
Fig. 8.3 Influence of moisture content on flowability and bulk density of sand (measured by the author with a ring shear tester, consolidation stress, σ_1, about 7.5 kPa)

FIGURE 13.18. The (left axis) material flow factor (mff) and (right axis) bulk density of wet sand plotted as functions of the moisture content. This figure is from Schulze [7].
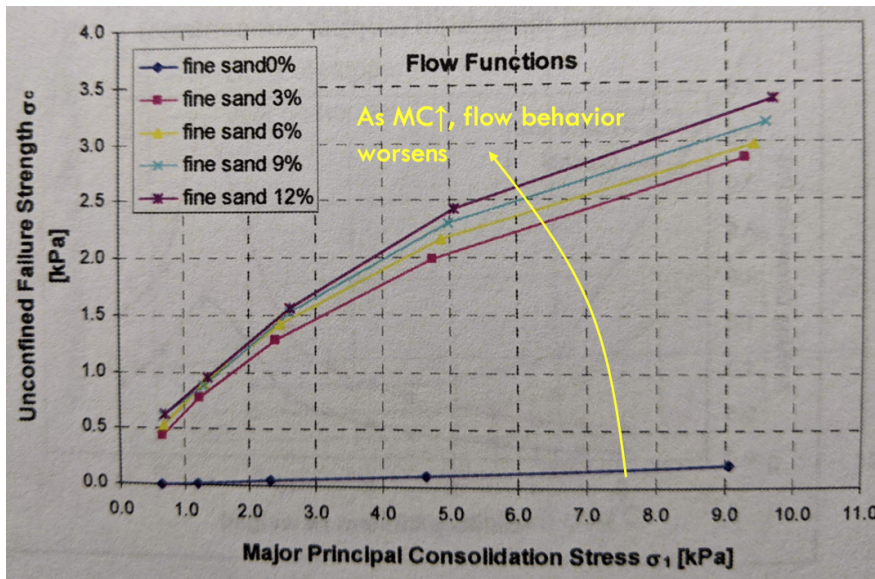

FIGURE 13.19. Material flow functions (mFFs) for dry and moist fine sand at different moisture contents. This figure is from Wolfson [2].

Fig. 8.5 Wall friction angle, φ_x, of FGD gypsum as a function of moisture content [2]
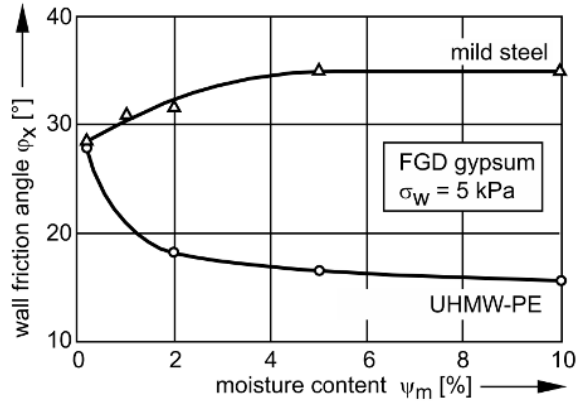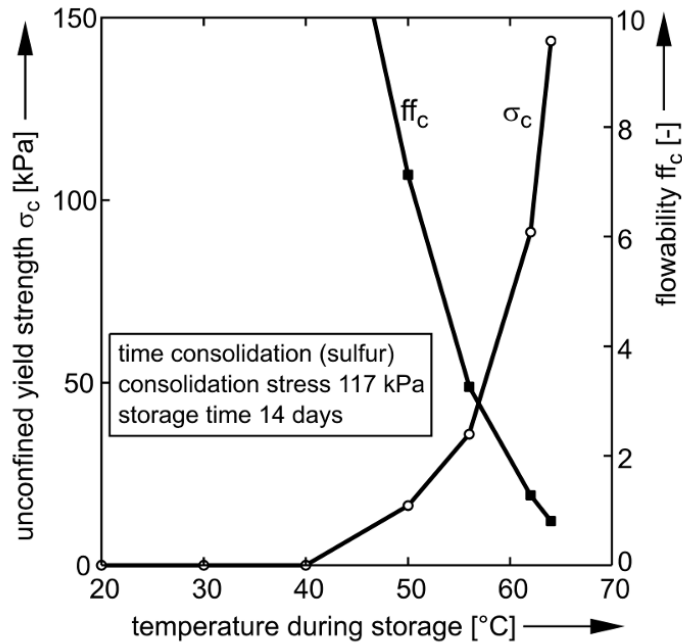
FIGURE 13.20. The wall friction angles between a gypsum powder and mild steel and ultra high molecular weight polyethylene walls plotted as a function of the moisture content. This figure is from Schulze [7].

Fig. 8.7 Time consolidation of sulfur granules [3]

FIGURE 13.21. The (left axis) unconfined yield strength and (right axis) material flow factor (mff) for sulfur as a function of temperature. This figure is from Schulze [7].
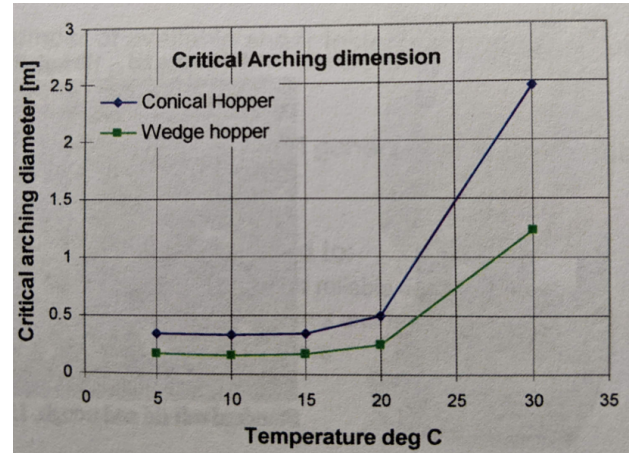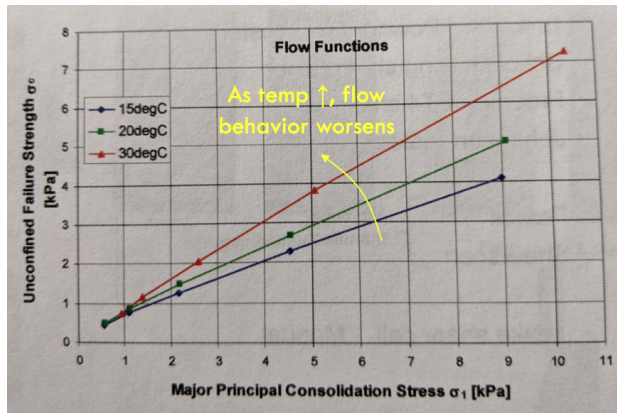
(A) The material flow function (mFF) at different temperatures.

(B) The critical arching dimension in a hopper as a function of temperature.

FIGURE 13.22. The influence of temperature on the flow behavior of a fatty powder. These figures are from Wolfson [2].

Bibliography

[1] L. Liu, I. Marziano, A. Benthan, J. Litster, E. White, and T. Howes, "Effect of particle properties on the flowability of ibuprofen powders," International Journal of Pharmaceutics, vol. 362, pp. 109–117, 2008.

[2] T. W. Centre, Flow properties and design principles, Storage and Flow of Bulk Solids short course notes, Kansas State University, Nov. 2016.

[3] T. Köhler and H. Schubert, "Influence of particle size distribution on the flow behavior of fine powders," Particle and Particle Systems Characterization, vol. 8, no. 1-4, pp. 101–104, 1991. DOI: 10.1002/ppsc.19910080119.

[4] F. Podczeck and Y. Miah, "The influence of particle size and shape on the angle of internal friction and the flow factor of unlubricated and lubricated powders," International Journal of Pharmaceutics, vol. 144, pp. 187–194, 1996. DOI: 10.1016/S0378-5173(96)04755-2.

[5] Y. Liu, X. Guo, H. Lu, and X. Gong, "An investigation of the effect of particle size on the flow behavior of pulverized coal," Procedia Engineering, vol. 102, pp. 698–713,

[6] D. Ely, "Dry powder segregation and flowability: Experimental and numerical studies," Ph.D. dissertation, Purdue University, West Lafayette, IN, U.S.A., 2011.

[7] D. Schulze, Powers and Bulk Solids: Behavior, Characterization, Storage and Flow, 2nd. Springer, 2021. DOI: 10.1007/978-3-030-76720-4.

[8] R. Dias, J. Teixeira, M. Mota, and A. Yelshin, "Particulate binary mixtures: Dependence of packing porosity on particle size ratio," Industrial & Engineering Chemistry Research, vol. 43, pp. 7912–7919, 2004.

[9] H. Kurz and G. Münz, "The influence of particle size distribution on the flow properties of limestone powders," Powder Technology, vol. 11, pp. 37–40, 1975.

[10] N. Leyva and M. Mullarney, "Modeling pharmaceutical powder-flow performance using particle size distribution data," Pharmaceutical Technology, vol. 33, no. 3, 2009.

[11] W. Yu, K. Muteki, L. Zhang, and G. Kim, "Prediction of bulk powder flow performance using comprehensive particle size and particle shape distributions," Journal of Pharmaceutical Sciences, vol. 100, no. 1, pp. 284–293, 2011. DOI: 10.1002/jps.22254.

[12] E. Crosby, Kagaku Kogaku, vol. 25, no. 2, pp. 124–130, 1961.

[13] C. Abreu, F. Tavares, and M. Castier, "Influence of particle shape on the packing and on the segregation of spherocylinders via monte carlo simulations," Powder Technology, vol. 134, pp. 167–180, 2003.

[14] W. Man, A. Donev, F. Stillinger, et al., "Experiments on random packings of ellipsoids," Physical Review Letters, vol. 94, 2005, Article 198001.

[15] K. Meyer and I. Zimmermann, "Effects of glidants in binary powder mixtures," Powder Technology, vol. 139, pp. 40–54, 2004.

[16] W. Ketterhagen, J. Curtis, C. Wassgren, and B. Hancock, "Predicting the flow mode from hoppers using the discrete element method," Powder Technology, vol. 195, pp. 1–10, 2009.

[17] M. Pasha, N. Hekiem, X. Jia, and M. Ghadiri, "Prediction of flowability of cohesive powder mixtures at high strain rate conditions by discrete element method," Powder Technology, vol. 372, pp. 59–67, 2020.

[18] F. Soulié, F. Cherblanc, M. E. Youssofi, and C. Saix, "Influence of liquid bridges on the mechanical behaviour of polydisperse granular materials," International Journal for Numerical and Analytical Methods in Geomechanics, vol. 30, no. 3, pp. 213–228, 2006. DOI: 10.1002/nag.476.

[19] C. Flemmer, "On the regime boundaries of moisture in granular materials," Powder Technology, vol. 66, no. 2, pp. 191–194, 1991.

[20] D. Bika, G. Tardos, S. Panmai, L. Farber, and J. Michaels, "Strength and morphology of solid bridges in dry granules of pharmaceutical powders," Powder Technology, vol. 150, pp. 104–116, 2005.

[21] M. Coelho and N. Harnby, "The effect of humidity on the form of water retention in a powder," Powder Technology, vol. 20, pp. 197–200, 1978.

[22] Y. Yang, R. Zou, and A. Yu, "Numerical study of the packing of wet coarse uniform spheres," AIChE Journal, vol. 49, no. 7, pp. 1656–1666, 2003.